High Accuracy Resonator Spectroscopy of Atmospheric Gases at Millimetre and Submillimetre Waves

M. Yu. Tretyakov

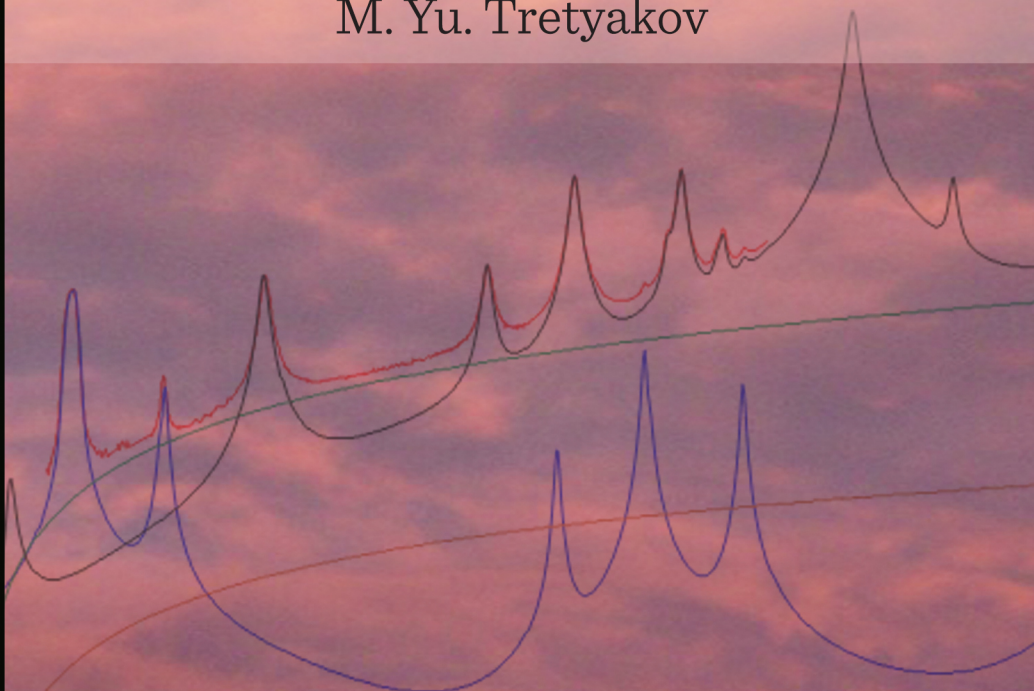

High Accuracy Resonator Spectroscopy of Atmospheric Gases at Millimetre and Submillimetre Waves

High Accuracy Resonator Spectroscopy of Atmospheric Gases at Millimetre and Submillimetre Waves

By

M. Yu. Tretyakov

Translated from Russian by Nadezhda Krivatkina
in close cooperation with the author

Proofreading by Eleanor Kate Brown

Cambridge
Scholars
Publishing

High Accuracy Resonator Spectroscopy of Atmospheric Gases at Millimetre and Submillimetre Waves

By M. Yu. Tretyakov

This book first published 2022

Cambridge Scholars Publishing

Lady Stephenson Library, Newcastle upon Tyne, NE6 2PA, UK

British Library Cataloguing in Publication Data
A catalogue record for this book is available from the British Library

ISBN (10): 1-5275-7581-0
ISBN (13): 978-1-5275-7581-3

CONTENTS

INTRODUCTION

Why atmosphere

Cognition of the surrounding world is closely connected with the evolution of civilisation and follows it step by step. At the initial stage, curiosity was the principal driving force, the pursuit of material goods frequently in the background. Later came the realisation that the familiar world is far from infinite, eternal and immutable. It is actually an infinitesimal, fragile framework capable of surviving under the conditions of unstable equilibrium for a brief moment of time at one of the interminable evolutionary stages of the Universe. The duration of this time flash may be cut short at any moment by various, negligible on the global scale, natural (meteor collision, volcanic eruption) or man-made (nuclear conflict, technological disaster) events. The established equilibrium will just break. The realisation of this fact gave a new impetus to learn more about the world so as to protect it. This requires understanding sources of danger, detecting, and preventing them well in advance, or at least forecasting a possible scenario of the upcoming event. At the state level, an understanding of the above implies rational environmental management as one of the priority areas in the development of science in all advanced countries worldwide. Therefore, the technologies of monitoring and forecasting the state of the atmosphere and hydrosphere are regarded to be the most important and even critical.

The atmosphere of the Earth is one of the key factors ensuring the existence of the familiar world. The Earth's atmosphere is the source of oxygen and humidity that are indispensable for life, protects all living beings against hard cosmic radiation, and also works as a greenhouse film raising the average temperature of the Earth by more than 30°C. The atmosphere balances two basic mechanisms determining the average temperature of the Earth — heating by solar radiation, on the one hand, and energy loss due to self-radiation and the resulting cooling down, on the other hand. This process is called the *radiation balance* of the planet, which implies that the amount of the energy emitted into space must always be equal to that received from the Sun, thereby guaranteeing a stable climate on the planet. Thus, there exists a direct relationship between the climate and the factors influencing the radiation balance. The

foremost of these are the solar radiation and the composition of the atmosphere. The oceans, the surface of the Earth, its vegetation, ice, and snow cover, as well as some other factors and processes of their interaction are also important, though to a lesser extent (fig. I.1).

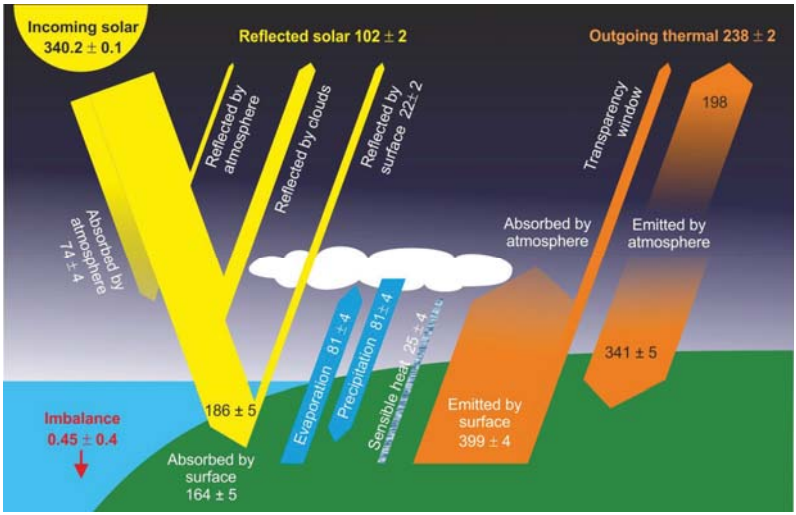

Fig. I.1. Approximate average annual radiation balance of the Earth [L'Ecuyer, 2015].

The author of the present work addresses different aspects of the atmosphere, with a focus on its major gas constituents and on the way, they absorb electromagnetic radiation and influence the radiation balance. Note that studying the problems of radiation propagation in the atmosphere is of great importance, and is closely connected with the development of systems for radio communication, radar and remote sensing, and weather forecasting.

To create a model of radiation propagation in the atmosphere one must know how the weak electromagnetic radiation of the wavelength range of interest interacts with the atmosphere, specifically, with its constituent gases. This interaction, or more precisely, the spectrum characterising the 'force' of radiation interaction with gas as a function of frequency, is the main subject of the study of molecular gas spectroscopy.

What is spectroscopy capable of?

Spectroscopy is a combination of theoretical and experimental methods that enable characterisation of the spectra of individual molecules and their ensembles, i.e., gases and their mixtures. These spectra possess the specific features of thermal motion of molecules and the effects of intermolecular interactions. Nitrogen and oxygen are the main constituents of the Earth's atmosphere, but it also contains molecules of all substances that can exist in the gas phase on our planet (fig. I.2). Despite the insignificant concentration, many of them take part in physical and chemical atmospheric processes and make a significant contribution to the global radiation balance.

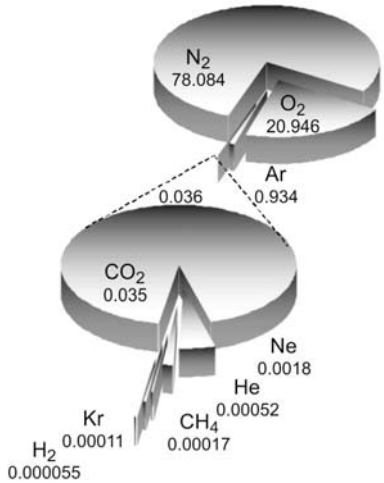

Fig. I.2. Approximate composition of dry atmospheric air with percentage indicated for each.

The most typical example is a molecule of water H_2O. Water vapour constitutes less than 1 % of the mass of the atmosphere but it is the main absorber of radiation. CO_2, O_3, CH_4, N_2O, and many other gases also have a strong immediate impact on the radiation balance (fig. I.3), although the fraction of even the most common of these molecules in the atmosphere is merely a few hundredths of a percent.

To control this atmospheric diversity and properly take into consideration the absorption of the radiation propagating in the atmosphere, spectroscopic databases, which contain detailed information needed for modelling

molecular spectra, are created. The most known ones are the open access international databases HITRAN (HIgh-resolution TRANsmission molecular absorption database) [Gordon, 2021] and GEISA (Gestion et Etude des Informations Spectroscopiques Atmosphériques = Management and Study of Atmospheric Spectroscopic Information) [Jacquinet–Husson, 2016].

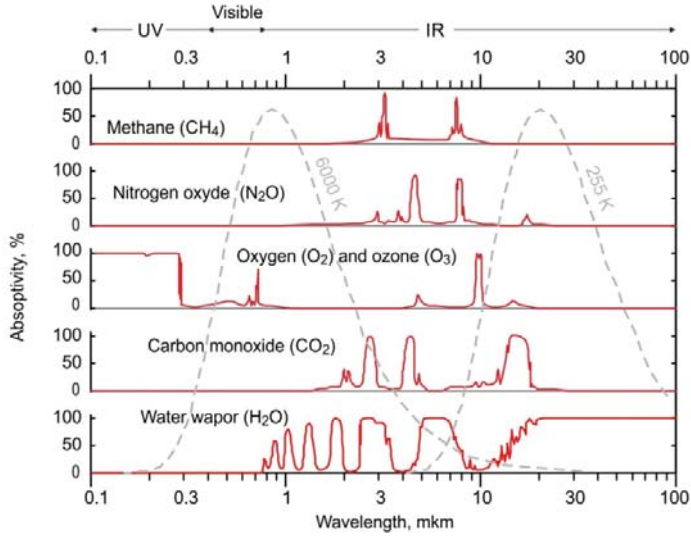

Fig. I.3. The contribution of major greenhouse gases to the absorption of the radiation that has passed through the atmosphere to the surface of the Earth [Peixoto, 1992]. The dashed curves show spectral density of the radiation power of the Sun (6000 K) and the Earth (255 K). The arrows on top indicate approximate borders of ultraviolet (UV), visible, and infrared (IR) ranges.

A huge amount of spectroscopic information, which is constantly updated and supplemented, has been accumulated by now. For instance, the HITRAN-2008 database [Rothman, 2009] contained a little more than 1 million spectral lines of atmospheric gases, whereas its current version HITRAN-2021 [Gordon, 2021] contains over 11 million lines belonging to 55 different molecules in 146 various isotopic combinations, and the ExoMol database [Tennyson, 2016] comprises billions of lines for NH_3, SO_2, H_2CO, CH_4, and other molecules. As a result, many projects on global monitoring of the atmosphere and the underlying surface of the planet that seemed fantastic not long ago can now be implemented from space satellites. As new achievements are made and new technically advanced

equipment is developed, mankind poses even more ambitious tasks, the solution of which demands new and more accurate spectroscopic data.

Despite the recent breakthrough in the field of direct numerical computations of molecular spectra on supercomputers, high accuracy experimental research of the radiation absorption by atmospheric gases and their mixtures in well controlled laboratory conditions is still of primary significance. The experiment is required not only for assessing the quality of the known or new calculated data but also for gaining an insight into the physical mechanisms affecting the magnitude of absorption that underlie the propagation models.

What is high accuracy needed for?

High accuracy is critically important for both the models and the underlying spectroscopic data used for calculating the radiation balance and the solution of remote sensing problems, as they are aimed at determining integrated absorption over very long paths with greatly differing conditions of radiation propagation. The calculations should take into account a large range of factors affecting the amount of absorption. With increasing distance from the surface, all major parameters — temperature, pressure, gas concentration — change, even without allowance for turbulent motions of the air (fig. I.4). Hence, the smallest error in the spectroscopic parameters or the inaccuracy of the propagation model may result in significant uncertainties in the interpretation of the computation results.

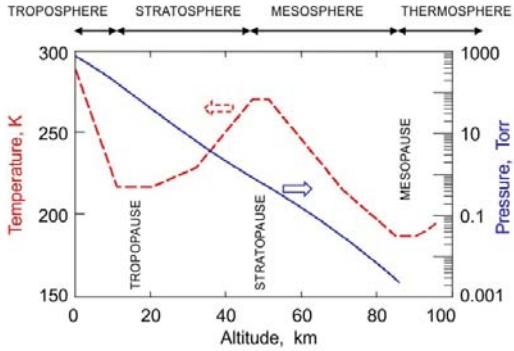

Fig. I.4. Approximate profiles of pressure (solid line, right scale) and temperature (dashed curve, left scale) of the Earth's atmosphere in the mid-latitudes (according to the data of the 'Standard Atmosphere calculator and table generator'). The division of the atmosphere into constituent layers is shown on top.

Why millimetres and submillimetres

Despite the fact that the millimetre and submillimetre waves, even if taken together, constitute only a minor part of the range of electromagnetic radiation interacting with the atmosphere, this monograph is dedicated to this wave range for several reasons.

The atmosphere in the millimetre and submillimetre ranges is more transparent for radiation than in the ultraviolet and visible ranges, especially in the conditions of fog, smoke, dust, and other factors of this sort. This occurs partly because of a much longer radiation wavelength compared to the characteristic size of volatile particles, which makes radiation scattering negligibly small.

The lines of the rotational spectra of all light molecules possessing a magnetic or an electric dipole moment and a small number of atoms fall within this range. This universality makes it extremely attractive for a quantitative molecular analysis, which is the basis of remote sensing of the atmosphere of the Earth and other planets. That is why the number of ground-based, airborne, and satellite-based instruments using the millimetre and submillimetre ranges for monitoring is growing every year.

The considered range is interesting and actively mastered by traditional radar and radiometry methods. The higher the operating frequency of the radiometer (the shorter its wavelength), the higher its spatial resolution and the smaller the size and weight of the instrument. Not a single large satellite mission on remote sensing of the Earth works without devices operating in the millimetre and submillimetre wavelength ranges.

Also worthy of note is the recent actively developing ‘teravision’ — visualisation using terahertz waves. These are the submillimetre waves that must pass through the atmosphere to illuminate or transilluminate the object. Finally, still another reason for choosing the considered range is the fact that the majority of physical mechanisms determining the characteristic features of the spectra of gases and gas mixtures are common for all spectral ranges. The microwave methods of research, that gave birth to high and superhigh resolution molecular spectroscopy and laid the bases for high accuracy millimetre and submillimetre spectroscopy, ensure higher quality data at a lower cost than the studies in other regions of electromagnetic radiation.

Why resonator

The longer the distance passed by the radiation interacting with matter, the weaker the interaction registered by the spectrometer. Therefore, the

interaction *path length* and the related sensitivity to radiation absorption are the two principal parameters characterising the instrument. The advantage of a resonator over a conventional gas cell is the possibility of achieving a very long path length. The radiation bouncing between the reflecting mirrors passes the distance between them many times. In a well-made desktop resonator, the radiation can pass several hundred metres. Such a path length in conventional gas cells is possible theoretically, but it is unfeasible in the millimetre and submillimetre ranges primarily because it is impossible to form a narrow non-divergent beam.

A rather long interaction path length may be attained in an open atmosphere in field conditions, but continuously varying, uncontrolled parameters of the object under study, that are quite natural for these conditions, create insurmountable difficulties for accurate measurements.

Still another merit of the *resonator spectrometer* (also referred to as the *cavity spectrometer*) is that for measuring the magnitude of absorption there is no need to know the path length as, in resonance conditions, an integer number of radiation half-waves fit in between the resonator mirrors. Consequently, the radiation-gas interaction path length may be expressed in units of the frequency at which the measurements are performed. In all other spectrometer types, the path length is a multiplier of the measured absorption. The geometrical length of a cell can be measured accurately, but the path length may differ significantly (always being longer) from the geometrical length because of unknown spatial radiation diagram and the presence of inevitable parasitic reflections, due to which part of the radiated power returns to the cell and interacts with the gas. The uncertainty of the length leads to ambiguity of the measured absorption.

Finally, the main advantage of the resonator spectrometer is the practicability of studying broad molecular lines (for example, pressure-broadened lines of atmospheric gases under ambient conditions) and non-resonant absorption slowly varying with frequency. This feature is also connected with a more regular field pattern inside the resonator compared to gas cells of other types. It is especially pronounced in traditional microwave video spectrometers, in which the radiation is transmitted through the studied gas and arrives at the radiation power receiver. The molecular lines in this case are observed as dips in the power *versus* frequency curve. The output power is frequency dependent in all real radiation sources. This dependence is aggravated by the interference of the source radiation with inevitable parasitic reflections from the receiver, gas cell windows, and other spectrometer elements. It is not a simple task to distinguish a broad molecular line from interference dips of comparable

width. The frequency period of the amplitude-frequency dependence of the radiation power in the spectrometer is the shorter the longer the gas cell length. There arises a contradiction: a large path length is demanded for a high spectrometer sensitivity, whereas for studying broad lines, the length must be small. As priority is always given to sensitivity, traditional spectrometers of the millimetre and submillimetre ranges are restricted to studying narrow lines corresponding to the uppermost atmospheric layers at extremely low pressures. Therefore, many physical mechanisms affecting the shape of gas spectra remain outside the performed research. One such mechanism is the collisional coupling of molecular lines (also referred to as spectral exchange, line interference, or line mixing). Some spectra consisting of closely spaced molecular lines cannot be represented as a sum of individual components. This effect occurs only at high pressures when the line contours overlap strongly. Another example is molecular spectra arising due to the collisions of molecules with each other. Collisional interaction leads to transient polarisation of molecules. So, even non-polar molecules of noble gases may form short-lived pair states and start to absorb radiation. The corresponding spectral manifestations of such processes are very broad because of a short time scale of collisions. In the millimetre and submillimetre ranges, they may be investigated only by means of resonator spectrometers.

The evolution of resonator spectroscopy

The history of the resonator spectroscopy started almost simultaneously with the high-resolution microwave spectroscopy. In the early spectrometers, the resonator was a box (sometimes the size of a room) with polished copper walls, in which the problem of a huge number of spatial modes excited in such a cavity was solved by means of a fan ‘mixing’ the radiation inside the box and a large number of thermocouples measuring the temperature of the gas heated by the radiation (see, for instance, Becker [1946]). Charles Townes and Arthur Schawlow, the authors of the classical book ‘Microwave Spectroscopy’ [Townes, 1955] widely known in the spectroscopic community, stated that the use of a resonator allows measuring absorption in broad lines and obtaining long path lengths in a gas cell of small size. A few years later, in a paper on the theory of the cavity spectrometer [Beers, 1959] it was shown that, other conditions being equal, its limiting sensitivity may be up to 300 times higher than that of the video spectrometer with a conventional 3-metere cell. Beer’s paper was published at a time when the culture of work with open resonators with two reflecting surfaces (Fabry-Perot resonators) had been formed. In

the 1960s it gave an impetus to creating resonator spectrometers, considered at that time as an alternative to video spectrometers that would provide a better sensitivity retaining the high resolution inherent to the microwave spectroscopy. A typical example is a resonator spectrometer created by E. Valkenburg, and V. Derr [Valkenburg, 1966] that was used to investigate the high-resolution spectra of D_2O molecules [Benedict, 1970] and N_2O molecules [Pearson, 1970] in the 70—310 GHz range. The real sensitivity of the resonator spectrometers, on account of their technical features, proved not to be higher than that of conventional video spectrometers. The main reason for this was complexity of employing modulation methods, which was mentioned by Beers but was undervalued by other researchers.

The resonator spectrometers did not reach a record sensitivity in investigations of high-resolution spectra, but they demonstrated their advantages both in accurate measurements of the magnitude of absorption coefficient [Gilbert, 1970] and in studies of broad atmospheric lines [Frenkel, 1966-1] and even of non-resonant absorption [Frenkel, 1966-2].

The next impetus for the development of the resonator spectroscopy was offered by systems of remote sensing and radars that demanded accurate models of millimetre and submillimetre wave radiation propagation in the atmosphere, whereas the high-resolution molecular spectroscopy could not provide sufficient information. Typical examples of the instruments capable of solving these tasks are the spectrometers developed by Hans Liebe [Liebe, 1975, 1984, 1992] and at the University of Lille (France) [Bauer, 1986].

The progress in the modern resonator spectroscopy was stimulated by the increasing requirements for accuracy in the radiation propagation models, as well as by the desire to find a modulation method efficient for the resonator spectrometer and to realise its potential advantage in sensitivity. A possible approach to the solution of this problem is fast, repeated recording of the resonant response in the frequency domain over a maximum short time stipulated by the resonator time constant. A special high-accuracy frequency modulation of the exciting radiation is used for recording, this approach is used in the spectrometer created at the Institute of Applied Physics in Nizhny Novgorod [Krupnov, 2000; Tretyakov, 2009; Koshelev, 2018-1].

Another approach with analogous underlying physics is pulse excitation of a resonator and recording of its response in the time domain over the same minimal time. The attempt to implement this approach was made at the Ohio State University (USA) [Meshkov, 2005]. This approach was, for the time being, fully realised and demonstrated record sensitivity

to radiation absorption in molecular lines ($5 \cdot 10^{-13}$ cm^{-1}) only in the resonator spectrometer of the IR wavelength range [Burkart, 2014], in which the reflection coefficient of the mirrors can be an order of magnitude higher than in the millimetre and submillimetre ranges.

The structure of the book

The first chapter of the book is a brief introduction to the molecular gas spectroscopy, in which the basic definitions, terminology, and concepts needed for modelling atmospheric absorption in the millimetre and submillimetre wavelength ranges are introduced. Special attention is given to resonant molecular lines and non-resonant absorption. The physical mechanisms determining line shape and leading to non-resonant absorption are also addressed. The second chapter is dedicated to the resonator spectroscopy technique. The principles of the operation of the resonator spectrometer and of all systems needed for its functioning are considered in detail. The absorption measurement methods are surveyed. The resonator spectrometer developed at the Institute of Applied Physics of the Russian Academy of Sciences (IAP RAS) is considered as a practical example. Its basic parameters are compared with analogous parameters of the other best-known instruments of such class. Chapter 3 is primarily a retrospective overview of the studies of the specific features of atmospheric absorption in the millimetre and submillimetre wavelength ranges. Particular attention is paid to the information regarding the spectra of atmospheric gases obtained using the resonator spectroscopy. The results of analogous investigations employing other methods are presented for comparison. The theoretical fundamentals on the oxygen and water vapour spectra are provided at the beginning of the corresponding sections. A significant part of Chapter 3 is devoted to the investigation of non-resonant absorption and experimental analysis of its causes. The contribution of the resonator spectrometry to the research concerned with the absorption of the millimetre and submillimetre waves by the Earth's atmosphere is summarized in the Conclusion. The materials presented in the Appendices may be helpful to the readers interested in practical details. They may also be useful for a deeper understanding of the processes and phenomena considered in the book.

CHAPTER 1

THE BASICS OF ATMOSPHERIC ABSORPTION MODELLING

1.1. Absorption coefficient

The absorption of sunlight by the atmospheric air has been attracting the attention of researchers for about three centuries. Back in the 1720s, the French physicist Pierre Bouguér assessed the transparency of the atmosphere by measuring changes of the solar light at different heights. In 1729, he published the 'Essay on the Gradation of Light' ('Essai d'Optique, sur la gradation de la lumiere') [Bouguér, 1729], in which he proposed methods for measuring attenuation of the light propagating through the atmosphere and was the first to formulate the basic law of spectroscopy known as the Bouguér law (also referred to as the Beer–Lambert–Bouguér law).

For quantitative measurements of light attenuation or radiation absorption by a medium, it is convenient to use a characteristic that is related only to the medium and depends neither on the radiation properties nor on the interaction volume. The radiation receiver response is usually proportional to the power W of the radiation absorbed by the medium on the path having length Δl. Therefore, the amount of radiation absorption by gas may be characterised by a relative change of the radiation power normalised to the interaction path length:

$$\frac{1}{\Delta l}\frac{\Delta W}{W}.$$

Assuming the radiation wavefront to be plane, in the limit as the path length approaches zero, this quantity is called the *absorption coefficient*:

$$\alpha = \lim_{\Delta l \to 0}\left(\frac{1}{\Delta l}\frac{\Delta W}{W}\right) = \frac{1}{W}\frac{dW}{dl}. \qquad (1.1)$$

Most generally, the absorption coefficient is defined as the relative change in the radiation energy per unit volume of the medium per unit time. By solving this differential equation, taking into consideration that it is more convenient to regard α to be positive, we obtain the formula for the radiation power variation during propagation in the medium known as the Beer–Lambert–Bouguér law:

$$W(l) = W_0 \cdot \exp(-\alpha \cdot l), \tag{1.2}$$

where W_0 is the initial power, and l is the distance passed by the radiation.

In classical electrodynamics, the propagation of electromagnetic waves is described by Maxwell's equations, from which it follows that, in a nonconducting medium having dielectric constant ε and magnetic permeability μ, any Cartesian component of electromagnetic field, E and B, must meet the wave equation

$$\nabla^2 u - \frac{1}{\upsilon^2}\frac{\partial^2 u}{\partial t^2} = 0, \tag{1.3}$$

where the constant $\upsilon = \dfrac{c}{\sqrt{\mu\varepsilon}}$ characterises the wave propagation velocity in the medium (c is the speed of light in vacuum). The quantity $n = \sqrt{\mu\varepsilon}$ is called the index of refraction or *refractive index* of the medium and is a complex value:

$$n = n_1 + in_2. \tag{1.4}$$

The wave equation has a solution in the form of a plane wave

$$u = \exp(i\mathbf{k}\cdot\mathbf{r} - i\omega t), \tag{1.5}$$

where the circular frequency ω and the absolute value of the wave vector $\mathbf{k}$ are related by

$$k = \frac{\omega}{\upsilon} = \frac{\omega}{c}n. \tag{1.6}$$

If the wave is propagating only in the x direction, the fundamental solution will be written as

$$u(x,t) = A\exp(ikx - i\omega t) + B\exp(-ikx - i\omega t). \tag{1.7}$$

From the relations (1.4) and (1.6) we obtain

$$u(x,t)=\left[A\exp\left(-\frac{\omega}{c}n_2x\right)\exp\left(i\frac{\omega}{c}n_1x\right)\right.$$
$$\left.+B\exp\left(\frac{\omega}{c}n_2x\right)\exp\left(-i\frac{\omega}{c}n_1x\right)\right]e^{-i\omega t}, \qquad (1.8)$$

from which it is clear that during the wave propagation in conventional dielectrics ($n_2 > 0$), the wave amplitude decreases exponentially as

$$u(x,t)=A\exp\left(-\frac{\omega}{c}n_2x\right)\exp\left(-i\omega\left(t+\frac{n_1}{c}x\right)\right). \qquad (1.9)$$

Considering that the wave power is proportional to its amplitude squared and comparing the form of the solution (1.9) with the expression (1.2), we obtain the following formula for the absorption coefficient of the medium:

$$\alpha=\frac{2\omega}{c}n_2\,. \qquad (1.10)$$

For strict compliance with the Beer–Lambert–Bouguér law, the following conditions shall be met:

1) The absorbing medium shall be homogeneous throughout the interaction volume.
2) The medium shall not be turbid, i.e., it must not scatter radiation.
3) The radiation shall propagate through the medium with all its beams being of equal length of the interaction with the absorbing medium.
4) The radiation intensity shall be sufficiently small so as not to disturb the thermodynamic balance of the medium (in particular, the energy distribution of the gas molecules shall be Boltzmann distribution).
5) The radiation shall be monochromatic or at least have a spectral width narrower than the characteristic scale of the dependence of the absorption coefficient of the medium on radiation frequency.

Let us consider how radiation interacts with gases and why the result of the interaction depends on radiation frequency.

The origin of this interaction is the same as the interaction of the electric field with spaced apart unlike charges (electric dipole) or the magnetic field with a current loop (magnetic dipole). In either case, additional energy of the object, arising as a result of the object's dipole moment interaction with the field, is equal to the scalar product of the dipole moment and the field intensity.

The electric dipole arises in molecules because different atoms attract electrons of the neighbouring atoms in a different way (electronegativity

of atoms), leading to a nonuniform distribution of positive and negative charges in the molecule, and to the appearance of the electric dipole moment. The presence of spin in the nuclei and electrons in the molecules or the orbital motion of unpaired electrons is equivalent to the magnetic dipole (fig. 1.1).

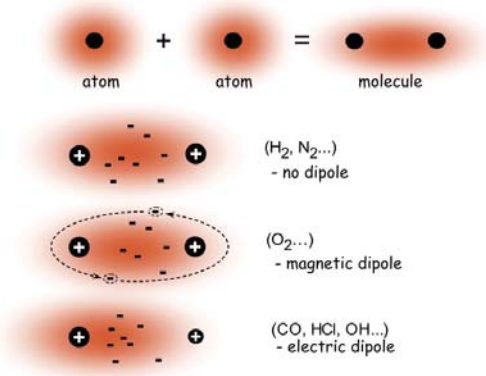

Fig. 1.1. Dipole moment in a diatomic molecule.

Thus, the electric and magnetic components of radiation may interact with the molecules, triggering changes in spin orientation, rotation of a molecule as a whole, vibration of atoms, electron transitions to higher orbitals, and so on. In all cases, the interaction results in the conversion of the radiation energy to one or another form of a molecule's internal energy.

The dependence of the interaction on the radiation frequency originates from the quantum nature of light. A molecule can absorb only one radiation quantum (photon) at each moment of time, this results in an abrupt change in its state, for example, it starts to rotate or to vibrate[1]. As the energy of a quantum is directly proportional to the radiation frequency, and the energy needed to excite motions of different types in a molecule may differ strongly, the result of the radiation–molecules interaction strongly depends on the radiation frequency.

Moreover, in each spectral region corresponding to some type of motion, the radiation may interact with molecules in a resonant or non-resonant manner. Resonant interaction and absorption are typical for

[1] Strictly speaking, two or more photons may be absorbed by a molecule simultaneously (see, for example, Bonch-Bruevich [1965] and references therein). However, this probability is many orders of magnitude smaller than a one-photon transition and may be disregarded in the majority of cases.

individual molecules. They occur only at definite frequencies, for instance, the ones related to changes in the angular velocity (frequency of rotation) of a molecule or to changes in the vibrational frequency of atoms. Non-resonant absorption is caused by the inelastic (non-instantaneous, leading to changes in internal energy) interaction of molecules with each other. Even at the instant of collision, that may be regarded to be almost elastic from the classical point of view, the field of one molecule induces charge redistribution in another one, resulting in a transient induced dipole moment. Inelastic collision may cause short-term 'adhesion' of molecules and formation of a new object absorbing radiation. In either case a new additional absorption mechanism comes into play that acts for a very short time and, hence, its manifestation in the frequency domain is very smooth compared to the resonant lines. Such smooth broadband spectral features are responsible for non-resonant absorption.

The general dependence of absorption coefficient on frequency is called the *spectrum of gas*. Different types of motion in a molecule correspond to different regions of the spectrum: the spectrum of nuclear magnetic and electron spin (paramagnetic) resonance, rotational spectrum, vibrational spectrum, electron spectrum, and others. The region of frequencies where the resonant interaction occurs is called *the spectral line of gas*.

In section 1.2 we will show where particular frequencies of spectral lines come from, specifically, when a molecule rotating as a whole changes its angular speed. Different aspects of non-resonant absorption will be addressed in section 1.3.

1.2. Resonant lines

In this section we will consider how molecules absorb radiation and what happens in this case. Assume that a hypothetical gas consists of identical molecules that do not possess translational motion and do not interact with each other but are in thermodynamic equilibrium. The spectrum of such a gas depends on the properties of the individual molecules and is actually a stick diagram, in which the lines are delta functions at certain frequencies multiplied by the corresponding amplitudes. We will also address different aspects of resonant line shapes and, in particular, the way molecular motion and almost elastic collisions affect the spectrum of individual molecules.

1.2.1. Spectrum stick diagram

A detailed analysis of the classical [Townes, 1955; Gordy, 1984; Herzberg, 1949-1, -2] and more recent [Jensen, 2000; Banker, 2004] *ab initio* methods of calculating spectra of different molecules based on numerical solution of the Schrödinger equation is not directly related to this book. Here, we intend to demonstrate why, how, and what should be taken into consideration in modelling the spectra of atmospheric absorption in the millimetre and submillimetre wavelength ranges that are the domains of the rotational molecular spectra.

Molecular rotation

In classical physics, the rotations of macroscopic objects are described by angular momentum (the rotational equivalent of linear momentum) and rotational kinetic energy, the essential parameters of the objects being the values of the principal moments of inertia with respect to three mutually perpendicular axes of rotation. This allows the rotation to be considered as a combination of the components along these axes. The rotational spectra of molecules are calculated analogously. This approach is physically correct when the displacement of the atoms in a molecule, from the equilibrium positions, are small compared to the distance between the atoms (bond length). The principal moments of inertia are generally designated in ascending order by I_A, I_B and I_C. According to the values of the moments of inertia, all molecules are divided into groups which are unambiguously related to the geometrical structure of the molecules.

1. *Linear molecules are the molecules in which all atoms are arranged along one line.* Typical atmospheric representatives are the molecules of carbon dioxide (CO_2), nitrous oxide (N_2O), and carbonyl sulphide (OCS). Diatomic molecules such as carbon oxide (CO), molecular oxygen (O_2) or nitrogen (N_2) are the simplest cases of linear molecules. The moment of inertia with respect to the axis of a linear molecule I_A is infinitesimal, as it is determined by the size of the atoms that are negligibly small compared to the bond length and by the electron mass, which is much less than the mass of the atoms. It can be asserted that, under normal conditions, linear molecules do not rotate about their axis, as the energy of such rotation greatly exceeds the average thermal energy of the molecules. The moments of inertia, I_B and I_C, corresponding to the rotation in two mutually perpendicular planes passing through the axis of the molecule are identical. Therefore, it can be assumed that in linear molecules $I_B = I_C$, $I_A = 0$.

2. *Symmetric tops are the molecules with two identical moments of inertia and one moment of inertia different from them and from zero.* Typical representatives are, for example, molecules of ammonia (NH_3) and methyl fluoride (CH_3F). These molecules have a symmetry axis at the rotation about which they resemble tops; that's where the name of the group comes from. Obviously, in this case too, the moments of inertia corresponding to the rotation of mutually perpendicular planes passing through the axis of the molecule are identical. If these moments of inertia are greater than the moment of inertia with respect to the symmetry axis ($I_B = I_C > I_A$), the top is called oblate, and if they are smaller ($I_A = I_B < I_C$), the top is called prolate. Accordingly, the molecule of ammonia is an oblate top, and the molecule of methyl fluoride is a prolate top.

3. *Spherical tops are the molecules with three identical moments of inertia* ($I_A = I_B = I_C$). An example is a tetrahedron-shaped molecule of methane (CH_4).

4. *Asymmetric tops are the molecules that have three different moments of inertia* ($I_A \neq I_B \neq I_C$). The majority of molecules are asymmetric tops. Typical atmospheric representatives are molecules of water (H_2O), nitrogen dioxide (NO_2), ozone (O_3), sulphur dioxide (SO_2), and hydrogen sulphide (H_2S).

We will consider the rotational spectrum in the simplest case of a diatomic molecule, since much of this consideration can be generalised to more complex molecules.

To begin with, we will assume that the atoms are rigidly bonded with each other (fig. 1.2), i.e., we will use *the rigid top approximation*.

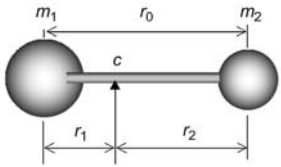

Fig. 1.2. Rigid diatomic molecule. m_1, m_2 and r_1, r_2 are, respectively, atomic masses and distances from the position of the centre of mass (c), and r_0 is bond length.

The principal axis of rotation of such a molecule is normal to its axis and passes through the centre of mass, the position of which is found from the equilibrium condition (the equality of rotational momenta):

$$m_1 r_1 = m_2 r_2 . \qquad (1.11)$$

The moment of inertia with respect to this axis is defined by

$$I_C = m_1 r_1^2 + m_2 r_2^2 = \frac{m_1 m_2}{m_1 + m_2} r_0^2 = \mu \cdot r_0^2 , \tag{1.12}$$

where μ is the reduced atomic mass. A classical angular momentum **J** of such a system rotating with angular velocity ω_r is

$$\mathbf{J} = I_C \boldsymbol{\omega}_r . \tag{1.13}$$

The kinetic energy of rotation of such a system is

$$E = \frac{I_C \omega_r^2}{2} = \frac{\mathbf{J}^2}{2 I_C} . \tag{1.14}$$

Quantum mechanics postulates that the square of the angular momentum is quantised, i.e., it can take on only discrete values proportional to the square of Planck's constant *ħ*:

$$\mathbf{J}^2 = \hbar^2 J(J+1), J = 0, 1, 2... \tag{1.15}$$

The number *J* is called a *rotational quantum number*. The absolute value of the vector of angular momentum at large values of *J* is an integer number of Planck's constants:

$$|\mathbf{J}| \approx J\hbar.$$

Therefore, the angular momentum is frequently represented as a vector having length *Jħ*.

The dependence of the kinetic energy on the rotational quantum number is found by the substitution of (1.15) into (1.14):

$$E = hBJ\left(J+1\right), \tag{1.16}$$

where $h = 2\pi \cdot \hbar$, and $B = \frac{h}{8\pi^2 I_c}$ is the *rotational constant* of the molecule.

Exactly the same expression may be rigorously derived for the energy of rotation of a diatomic molecule from the solution of the Schrödinger equation (see, for example, Townes [1955]), from which follows quantisation of rotational energy. Values of the energy determine the position of rotational *energy levels* (stationary molecular states) usually depicted as a diagram (fig. 1.3).

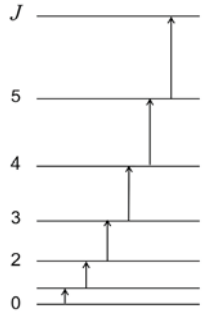

Fig. 1.3. Diagram of rotational energy levels of a diatomic molecule. The arrows show allowed transitions with photon absorption.

A molecule can interact with radiation, absorb a photon, and make a transition from one rotational level to another, only if it has a permanent electric or magnetic moment. Undoubtedly, the necessary condition for absorption to occur is to meet the law of conservation of energy, i.e., the change in the molecule energy must be equal to the energy of the absorbed photon:

$$\Delta E = h\nu . \tag{1.17}$$

Moreover, since the rotational state of the molecule changes as a result of the interaction with the field, i.e., its angular momentum changes, according to the laws of conservation the angular momentum of the field shall change as well. However, a plane electromagnetic wave has no definite angular momentum. To solve this problem, the field is expanded into *multipole waves* (see, for example, Rose [1955] or Berestetskii [1982]). The individual terms of this expansion correspond to the photons having various values of angular momentum, which may be absorbed by molecules. The main term of this expansion is dipole waves. All the other terms of the expansion in molecular spectroscopy may be neglected in most cases (*dipole approximation*). Photons in this case may be in two states corresponding to the projections of their spin (angular momentum) onto the propagation direction equal to $+\hbar$ and $-\hbar$ (in classical electrodynamics this corresponds to the right and left circular polarisations of the electromagnetic wave). Consequently, the molecule that has absorbed a photon can change its total angular momentum only by $\hbar$. This means that, at each act of the interaction of the molecule-dipole with radiation, the rotational quantum number can change only by unity:

$$\Delta J = \pm 1 . \tag{1.18}$$

This relation is referred to as the *selection rule* for dipole transitions. The selection rule also follows from the solution of the Schrödinger equation. It determines the molecular energy levels between which transitions are allowed when the molecule interacts with the field. All other transitions are *forbidden*. For the rotational spectrum of a polar diatomic molecule, only the transitions to the neighbouring levels are *allowed*. The plus sign corresponds to the absorption of a photon by a molecule, and the minus sign to photon emission. The transitions with photon absorption are shown by arrows in fig. 1.3.

The substitution of the values of the energy levels from (1.16) into (1.17) applying the selection rule (1.18) yields an expression for the frequencies at which the molecule can absorb radiation:

$$\nu = 2B\left(J+1\right). \tag{1.19}$$

They are the frequencies of the rotational spectrum lines at which the resonant interaction of radiation with a rigid diatomic molecule occurs. From the expression (1.19), it follows that the lines of this spectrum are spaced apart by the same distance equal to 2*B*. Such a spectrum is called *equidistant.*

In real conditions, atoms in a molecule are not rigorously bonded; the distance between them during the rotation of the molecule will increase due to centrifugal forces stretching the molecule: the higher the rotation speed (or the value of J), the greater the stretching. If the stretching is small, we can speak of an elastic deformation of the molecule. Then, according to classical physics, an increase in the moment of inertia I_C and the related decrease of the rotational constant *B* must be proportional to the square of angular velocity or the square of angular momentum (1.14), i.e., in conformity with (1.15), the rotational constant at the state *J* may be written as

$$B_J = B - DJ(J+1), \tag{1.20}$$

where *D* is the linear centrifugal stretching constant.

The substitution of this expression into (1.16) yields the energies of the levels

$$E = hBJ\left(J+1\right) - hDJ^2\left(J+1\right)^2. \tag{1.21}$$

The frequencies of rotational lines of a nonrigid molecule obtained by analogy with the derivation of (1.19) are

$$\nu = 2B\left(J+1\right) - 4D\left(J+1\right)^3. \tag{1.22}$$

For the majority of molecules, the constant D is very small, not more than $10^{-4}B$. Therefore, the rotational spectrum of diatomic molecules is almost equidistant, but its lines are gradually approaching each other with increasing J.

A still more exact expression for line frequencies may be obtained by taking into consideration nonlinearity of the centrifugal stretching or, which is the same, anharmonicity of the molecule's field of force. This is done by means of still another small molecular constant H, the magnitude of which depends on the geometry of the molecule (see, for instance, Gordy [1984]). For the energy of the levels, we obtain

$$E = hBJ\left(J+1\right) - hDJ^2\left(J+1\right)^2 + hHJ^3\left(J+1\right)^3, \qquad (1.23)$$

and for the frequencies

$$\nu = 2B\left(J+1\right) - 4D\left(J+1\right)^3 + H\left(J+1\right)^3\left[\left(J+2\right)^3 - J^3\right]. \quad (1.24)$$

The expression (1.23) is actually a power series expansion of energy in terms of $J(J+1)$, which may be expanded, if necessary, to any number of terms. It should be kept in mind that all the other terms of this series do not have such a clear physical meaning as the initial ones. Values of molecular constants are determined by the best possible fit with the experimentally measured line frequencies. For example, the frequencies of the rotational spectrum lines of a molecule of carbon monoxide CO reproducing all currently known accurate measurements may be calculated by three constants: B =57.635968019(28) GHz, D = 0.18350489(16) MHz, and H = 0.17168(10) Hz [Winnewisser, 1997]. The uncertainties of the values of constants related to a measurement error are indicated in parentheses in units of the last significant digit. This notation of a parameter uncertainty will be used throughout this book.

Let us now consider what the amplitude of the spectral lines depends on, i.e., what determines the value of the gas absorption coefficient at the resonance frequency. The radiation power absorbed by the gas is equal to the energy of the absorbed quanta per unit time, which is equal to the number of quanta absorbed per unit time multiplied by the energy of one quantum (we assume for definiteness that there occurs a rotational transition from level a to level b):

$$\Delta E = N_q \cdot h\nu_{ab}. \qquad (1.25)$$

The number of the absorbed quanta is equal to the number of molecules able to absorb a quantum, multiplied by the probability of absorption:

$$N_q = N_{ab} p_{ab}. \tag{1.26}$$

If the medium is in thermodynamic equilibrium with the field, then the number of molecules at the level *a* (energy level *population*) is defined by the Boltzmann distribution

$$N_a = N \exp\left(-\frac{E_a}{kT}\right), \tag{1.27}$$

where N is the total number of molecules, E_a is the energy of the low level, k is the Boltzmann constant, and T is the temperature of gas.

It should be taken into consideration that, in the resonant field, the molecules of the lower-level *a* will absorb photons and jump to the upper-level *b*, and the molecules of the level *b* will, at the same time, emit photons indistinguishable from the photons of the field and will drop to level *a*. We will show below that both processes are equiprobable for the millimetre and submillimetre wavelength ranges. This means that the resulting decrease of the number of field photons, which from the point of view of an external observer corresponds to the number of molecules able to absorb a photon and characterises the radiation power absorbed by the gas, will be proportional to the difference of the populations of levels *a* and *b*:

$$N_a - N_b = N_a\left(1-\exp\left(-\frac{E_b - E_a}{kT}\right)\right) = N_a\left(1-\exp\left(-\frac{h\nu_{ab}}{kT}\right)\right). \tag{1.28}$$

It should be taken into account that molecules in different states may have equal energies. Such states are called *degenerate.* The number of the states having the same energy is referred to as the degree of degeneracy. Such states include, in particular, rotational states of molecules with different projections of the total angular momentum in the absence of a permanent external field. In conformity with the quantisation rules, the projection of the total angular momentum of such a system may have values equal to the integer number of Planck's constants:

$$\mathrm{J}_z = m\hbar\,,\ m = 0, \pm 1, \pm 2 \ldots\,. \tag{1.29}$$

Consequently, in a molecule with the angular momentum characterised by the rotational quantum number J, m may take on values from $-J$ to $+J$,

i.e., the total of $(2J + 1)$ values. The considered rotational state has exactly this number of projections of the total angular momentum onto an arbitrary direction, which is equal to the degree of *rotational degeneracy* of this state:

$$g_J = 2J + 1 . \tag{1.30}$$

With the application of the external field, the energy of the molecules having the same total angular momentum will depend on the magnitude of its projection onto the direction of the field. Therefore, the energies of their *J*-th level will be different. The degeneracy is cancelled by the field. The level splits into sublevels. The total number of various molecular states Z is called the *total internal partition sum*, also known as the internal partition function, or the statistical sum that can be calculated as

$$Z = \sum_i g_i \exp\left(-\frac{E_i}{kT} \right). \tag{1.31}$$

With the degeneracy taken into account, the population of level a is

$$N_a = N \frac{g_a}{Z} \exp\left(-\frac{E_a}{kT} \right). \tag{1.32}$$

Thus, the total number of molecules able to make a contribution to the absorption of photons from the field can be found as

$$N_{ab} = N \frac{g_a}{Z} \exp\left(-\frac{E_a}{kT} \right) \left(1 - \exp\left(-\frac{h\nu_{ab}}{kT} \right) \right). \tag{1.33}$$

The probability p_{ab} of resonant photon absorption by a molecule is determined by two factors. The first of them is the radiation energy density $\rho(\nu_{ab})$, which is a product of the number of photons per unit volume and the photon energy. The more photons, the higher the probability that the molecule will 'collide' with a photon and absorb it. The second factor is the quantity related to the dipole moment of the molecule that is referred to as the *Einstein coefficient* for stimulated transitions B_{ab}. The larger the dipole moment, the stronger the interaction with the field and, hence, the probability of the transition. At rotational transitions, the dipole moment plays the role of a 'handle' by means of which the field rotates the molecule. This is obvious for diatomic molecules which have actually one axis of rotation normal to the axis of the molecule and a dipole moment directed along the molecule's axis. In more complex molecules with two or more different principal moments of inertia, for the excitation of a

definite type of rotation, of primary importance is the magnitude of the dipole moment projection onto the axis normal to the axis of this rotation, rather than the magnitude of the dipole moment. For instance, in symmetric top molecules, the total dipole moment (it is always oriented along the symmetry axis in such molecules) is responsible for the excitation of rotation about the axis normal to the symmetry axis of the molecule, and the probability of the transitions corresponding to such a rotation is high. The field cannot excite rotation about the symmetry axis because the magnitude of the dipole moment projection onto the direction normal to this axis is equal to zero. Despite the fact that the energy levels corresponding to such rotation not only exist but are populated as a result of molecular collisions, no transitions between them occur under the action of the field, as their probability is zero. The magnitude of the projection for each specific case may be assessed from purely geometrical considerations. One should take into account not only the dipole moment orientation with respect to the molecular frame, but also the spatial distribution of molecular dipoles. For molecules rotating in the electromagnetic field, this distribution is not homogeneous, as the condition (1.29) must be fulfilled. In quantum mechanics the equivalent of the dipole moment projection is a module of the matrix element of the dipole moment of the transition $|\mu_{ab}|$ defined as an absolute value of the vector of the dipole moment of the molecule, $\boldsymbol{\mu}$, averaged over the initial and final states

$$\mu_{ab} = \mu_{ba} = \left\langle \psi_a \left| \boldsymbol{\mu} \right| \psi_b \right\rangle , \tag{1.34}$$

where ψ_a and ψ_b are the wave functions of states a and b. The probability of the transition is proportional to the square of this function.

The equivalence of the dipole projection to its matrix element is readily demonstrated on an example of the simplest case of diatomic molecules excited by a linearly polarised radiation. We remind the reader that, in this case, the dipole is directed along the axis of interatomic bond and normally to the vector of the angular momentum of the molecule. Note that only the magnitude of the projection, rather than its sign (or 'phase' of the matrix element), influences the efficiency of the molecule–field interaction. This means that only one quarter of the coordinate plane, not even one quarter of the spatial sphere, can be taken to estimate the average value of the dipole moment projection. Suppose that we want to excite in gas the transition from one of the upper rotational levels to the next one. This means that J is large, hence, the number of the projections of the angular momentum of the molecule onto the axis normal to the plane of polarisation is also large. It is obvious that in this case the dipole

moment of the molecules is, on average, oriented at an angle of 45° to the plane of polarisation, and the magnitude of the projection squared is $\mu^2/2$. For comparison, the exact expression for the square of the matrix element of the transition $J \to J + 1$ of diatomic molecules, with all possible orientations taken into consideration, has the following form [Townes, 1955]:

$$\left|\mu_{ab}\right|^2 = \mu^2 \frac{J+1}{2J+1}, \tag{1.35}$$

which is in agreement with the above qualitative estimate.

Thus, the probability that a molecule will absorb a photon with resonance frequency ν_{ab} is written as

$$p_{a\to b} = \rho\left(\nu_{ab}\right) B_{ab} = \rho\left(\nu_{ab}\right) \frac{8\pi^3}{3h^2} \left|\mu_{ab}\right|^2. \tag{1.36}$$

The probability of a molecule radiating a photon under the action of a resonant field is, generally, higher than the probability of absorption by the value of the probability of spontaneous radiation

$$p_{b\to a} = \rho\left(\nu_{ab}\right) B_{ab} + A_{ba}, \tag{1.37}$$

where A_{ba} is the Einstein coefficient for spontaneous emission that is related to the coefficient of stimulated transitions ($B_{ab} = B_{a\to b} = B_{b\to a}$) by

$$A_{ba} = B_{ab} \frac{8\pi h \nu_{ab}^3}{c^3}, \tag{1.38}$$

where c is the speed of radiation propagation.

In the visible range, spontaneous transitions should be taken into consideration no less carefully than the stimulated one, but the probability of such transitions decreases in proportion to the cube of frequency and becomes negligibly small in the millimetre and submillimetre wavelength ranges. Therefore, it can be assumed that

$$p_{ab} = p_{a\to b} = p_{b\to a}. \tag{1.39}$$

If we assume that the radiation interacts with gas in a cell of small length Δl, with a cross section S, then for the molecule concentration n and the radiation energy density ρ the following relations will be true:

$$n = \frac{N}{S\Delta l}, \quad \rho(\nu_{ab}) = \frac{W}{Sc}. \tag{1.40}$$

Then, for the absorption coefficient at the frequencies corresponding to the resonant rotational lines we obtain

$$\alpha_{ab} = \frac{1}{\Delta l}\frac{\Delta W}{W} = \frac{8\pi^3 \nu_{ab}}{3hc}|\mu_{ab}|^2 n \frac{g_a}{Z}\exp\left(-\frac{E_a}{kT}\right)\left(1-\exp\left(-\frac{h\nu_{ab}}{kT}\right)\right). \quad (1.41)$$

This expression is valid for molecules of all types. Moreover, it is true for all other types of electric dipole transitions, as it determines the intensity of a molecular spectral line.

The expression (1.41) may be simplified, taking into account that for the rotational transitions the energy $h\nu$ is almost always lower than kT, which enables power series expansion of the corresponding exponent and allows neglecting nonessential terms. A further simplification is possible for the rotational spectra of diatomic molecules. By neglecting the vibrational states almost unpopulated under normal conditions, we can write the partition function in the form

$$Z = \sum_{J=0}^{\infty}(2J+1)\exp\left(-\frac{hBJ(J+1)}{kT}\right). \quad (1.42)$$

For the majority of molecules under normal conditions, $hB << kT$. Therefore, summation may be replaced by integration which can be calculated explicitly:

$$Z \approx \int_0^{\infty}(2t+1)\exp\left(-\frac{hBt(t+1)}{kT}\right)dt = \frac{kT}{hB}. \quad (1.43)$$

With the expression (1.35) taken into consideration, we obtain

$$\alpha_J = n\frac{8\pi^3 \nu_0^2 hB}{3c(kT)^2}\mu^2(J+1)\exp\left(-\frac{hBJ(J+1)}{kT}\right), \quad (1.44)$$

where ν_0 is the transition frequency.

In a more general case, it is impossible to calculate the partition sum using analytical methods. For solving practical tasks, it is possible to apply a semi-empirical approach, when the values of Z are calculated numerically in a wide temperature range, and the result is approximated by an analytical function. The coefficients of approximation of the Z values by a third-order polynomial calculated in the 70–3000 K range for most of the atmospheric molecules can be found, for example, in the paper by Gamache [2000]. In the majority of cases, with the exception of heavy molecules with many vibrational degrees of freedom, the approximation error is less than 1 %. More extended numerical data on partition sums,

albeit without any functional approximation, can be found in work by Gamache [2017].

Using the expressions (1.24) and (1.44) and the known values of the molecular constants B, D, and H, it is possible to plot stick diagrams of rotational spectra for most polar diatomic molecules. A diagram of the carbon oxide spectrum is given as an example in fig. 1.4, *a.* The rotational spectrum of linear molecules is absolutely the same.

The spectrum of symmetric tops, on the one hand, is complicated by the appearance of one more principal axis of rotation. As a result, for the description of energy levels and molecular spectra it is necessary to introduce one more rotational quantum number K characterising the projection of the total angular momentum onto the symmetry axis of the molecule and, hence, takes on the values from 0 to J. On the other hand, only the $J, K \rightarrow J + 1, K$ transitions are allowed in such molecules, i.e., $\Delta K = 0$. This is explained by the above-mentioned impossibility of the resonant field to spin a molecule about the symmetry axis. Thereby we can say that the spectrum of such molecules (fig. 1.4, *b*) consists of a series of transitions, each of which corresponds to a definite value of K, and its form is almost indistinguishable from the series of lines of the rotational spectrum of diatomic molecules.

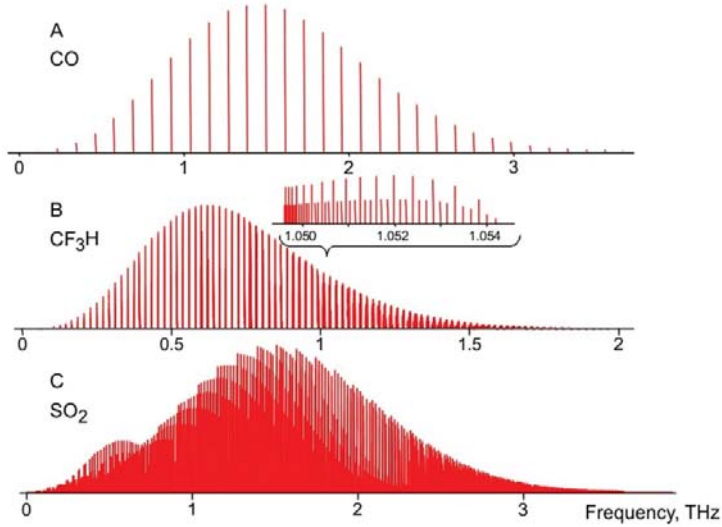

Fig. 1.4. Stick diagrams of the rotational spectrum of a linear CO molecule (*a*), CF_3H symmetric top molecules (*b*) (the inset shows the K-structure of one of rotational transitions) and SO_2 asymmetric top molecule (*c*) at room temperature.

The asymmetric top spectra are still more complex, as a molecule can rotate simultaneously about all three principal axes. Three quantum numbers are needed in this case for describing the energy level and the spectrum. The numbers characterising the magnitude of the total angular momentum J and its two projections K_a and K_c are used as a rule. Nevertheless, in this case too, the entire rotational spectrum can be resolved into individual series similar to the series of lines of a diatomic molecule, each corresponding to a definite type of rotation (fig. 1.4, *c*).

Vibrations in molecules

Nonrigid bonding of atoms in molecules leads not only to the centrifugal stretching of molecules during rotation. The elasticity of bonding means that a molecule can have a vibrational energy corresponding to the energy of periodic stretching and compression with a definite frequency dependent on the mass of atoms and bond elasticity.

Only one type of vibration corresponding to periodic changes in the bond length is possible for diatomic molecules. Here, we can also draw an analogy with a classical harmonic oscillator. The bonding force F acting on atoms at a small deviation from their equilibrium position obeys Hooke's law

$$F = -\kappa\left(r - r_e\right), \tag{1.45}$$

where r is the internuclear distance, r_e is the equilibrium distance or bond length, and κ is the force constant of bonding corresponding to a classical elasticity coefficient. The stored (potential) energy is a parabola

$$E = \frac{\kappa}{2}\left(r - r_e\right)^2 . \tag{1.46}$$

The vibrational frequency referred to as the *fundamental frequency* is described by the expression

$$\nu_V = \frac{1}{2\pi}\sqrt{\frac{\kappa}{\mu}}, \tag{1.47}$$

where μ is the reduced mass from the expression (1.12). In contrast to classical physics, in quantum mechanics the vibrational energy of a harmonic oscillator can take only discrete values corresponding to the vibrational energy levels, characterised by the vibrational quantum number V:

$$E_V = h\nu_V \left(V + \frac{1}{2}\right), V = 0, 1, 2 \ldots \qquad (1.48)$$

The state without vibrations ($V = 0$) is called the *ground state*. Note that the ground state has non-zero energy. When such a system interacts with radiation, the frequencies of the allowed ($\Delta V = \pm 1$) transitions between the vibrational levels corresponding to the energy conservation law coincide with the classical analogue:

$$\nu = \frac{E_{V+1} - E_V}{h} = \nu_{V+1} . \qquad (1.49)$$

In fact, the potential energy of a diatomic molecule is similar to the energy of a harmonic oscillator only in the close vicinity of the equilibrium state (fig. 1.5).

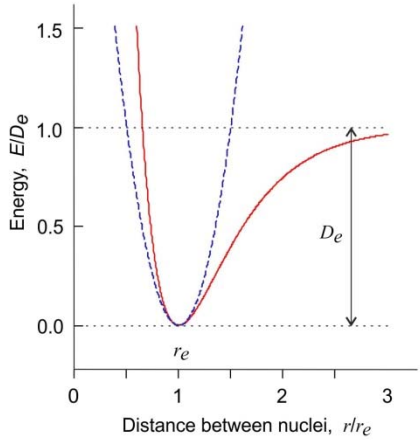

Fig. 1.5. The internal potential energy of a diatomic molecule (solid curve) and the potential energy of a harmonic oscillator (dashed curve) as a function of internuclear distance.

Short-range interatomic forces rapidly start to counteract the compression of the real bond. The bond is known to weaken on stretching, and the molecule can dissociate into atoms that will have a total energy equal to the dissociation energy which is smaller than the molecular equilibrium energy (D_e) by the magnitude of the nonzero energy of the ground state.

The vibrational energy of real diatomic molecules may be represented in the form of a series

$$\frac{E_V}{h} = \nu_V\left(V+\frac{1}{2}\right) - \nu_V x\left(V+\frac{1}{2}\right)^2 + \nu_V y\left(V+\frac{1}{2}\right)^3 + \nu_V z\left(V+\frac{1}{2}\right)^4 + \ldots, \tag{1.50}$$

where *x, y,* and *z* are the anharmonicity constants. Anharmonicity enables transitions from any to any vibrational energy level. At small vibrational perturbations, the contribution of anharmonicity is rather small for all molecules; therefore, for the frequency of vibrational transitions the approximate expression

$$\nu \approx \nu_V V,\ V = 0, 1, 2 \ldots \tag{1.51}$$

is fulfilled, from which, it follows that the field can excite vibrations of the bond length in the molecule at the fundamental frequency ($V = 1$) as well as at its harmonics or overtones ($V = 2, 3, 4...$).

More complex molecules have several fundamental frequencies (ν_1, ν_2, ν_3 ...). In a general form, their number is found as follows. A nonlinear molecule consisting of N atoms has $3N$ degrees of freedom. Three of them correspond to the translational motion of a molecule as a whole, three more to molecular rotation. The remaining $3N - 6$ correspond to different fundamental vibrations. The number is almost the same for linear, including diatomic, molecules, except that they have only two rotational degrees of freedom and, hence, $3N - 5$ fundamental vibrations. The vibrations directed along the bond axes are referred to as *valence vibrations* or *stretching vibrations*. Their number corresponds to the number of bonds and is equal to $N - 1$. The remaining $2N - 5$ different vibrations for nonlinear and $2N - 4$ for linear molecules correspond to the change of angles between the bonds and are called the *deformation* or *bending vibrations*. Each fundamental vibration is characterised by its quantum number (V_1, V_2, V_3...). Several fundamental vibrations can be excited simultaneously in any combination with each other and their overtones. The vibrational state of the molecule is specified by a set of vibrational quantum numbers.

Despite the fact that in most ordinary atmospheric molecules all vibrations occur at frequencies greatly exceeding typical rotational frequencies, they shall be taken into consideration in the analysis of the absorption spectra in the millimetre and submillimetre ranges. This is associated with a high sensitivity of spectrometers, which allows for the observation of the lines corresponding to pure rotational transitions in molecules in excited vibrational states. The vibrations are excited due to the collisions of molecules during thermal motion.

For simplicity let us come back to a diatomic molecule. A vibrating molecule can interact with a resonant field exciting its rotation like a molecule in the ground state. A huge number of vibrations takes place during one turn; therefore, the rotation can be described using the moment of inertia corresponding to an average bond length. The bond stretches more than it compresses because of the asymmetry of the potential (fig. 1.5), consequently the average moment of inertia is a little more and the corresponding effective rotational constant B_V is a little less than the corresponding magnitudes for a molecule in the ground state. The centrifugal constant will change similarly. Almost everything related to the molecular spectrum in the ground state is applicable to the rotational spectrum in the excited vibrational state. Consequently, the general form of the spectrum stick diagram remains almost unchanged, although the intensity is much weaker. The latter is explained by a lower population of excited vibrational-rotational states as compared to the ground state under normal conditions. The ratio of the number of molecules in such states N_V to the number of molecules in the ground state N_0 determines the extent to which the intensity of rotational lines in the vibrational state is less than the intensity of the corresponding lines in the ground state, which is found from the Boltzmann distribution:

$$\frac{N_V}{N_0} = \exp\left(-\frac{h\nu_V V}{kT}\right), \tag{1.52}$$

where the product $\nu_V V$ is the frequency of vibrations.

We will demonstrate the manifestation of vibrational states in the rotational spectra of gases in the millimetre and submillimetre wavelength ranges on an example of a molecule of carbonyl sulphide (OCS). This molecule, like all linear three-atomic molecules, possesses four fundamental vibrations. Two of them are stretching vibrations, which correspond to symmetric (both bonds are stretched or compressed simultaneously) and antisymmetric (one bond is stretched and the other is compressed and vice versa) vibrations. Two other vibrations are deformational. They occur in two mutually perpendicular planes, when a molecule apparently ‘breaks’ at the site of the central atom and bends without changes in the bond lengths. It is obvious that, if the molecule is not rotating, then both these vibrations occur with equal energies and frequencies, which means that they are degenerate. Therefore, such molecules have only three fundamental frequencies and their vibrational state has three quantum numbers. The rotation of the molecule in the plane of vibrations results in the appearance of the Coriolis force, the magnitude of which depends on the speed of rotation. This interaction of vibrations and rotation changes

the energy of the state. The rotation in the mutually perpendicular plane occurs independent of vibrations, i.e., the degeneracy of bending vibrations is lifted during rotation. This means that to identify the vibrational state of the molecule, it is necessary to indicate in which of the two planes the vibrations occur.

In fig. 1.6, one can see the stick diagrams of the rotational spectrum of carbonyl sulphide based on experimental data [Burenin, 1981-1, Burenin, 1981-2] relating to successive tenfold vertical stretching of the scale. Clearly, at each scaling (equivalent to an increase in the spectrometer sensitivity) increasingly more characteristic series of spectral lines becomes apparent. This procedure of revealing a greater number of lines with increasing sensitivity can be repeated (hypothetically getting rid of technical limitations) many times. The natural limit is the observation of the lines of a highly excited vibrational state, the energy of which is sufficient to break an intramolecular bond. Such excitation will lead to dissociation of the molecule.

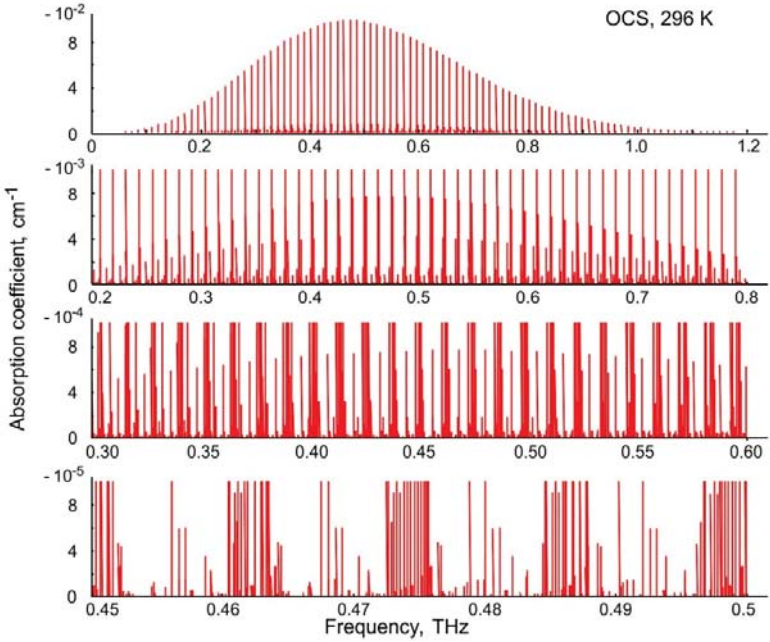

Fig. 1.6. Stick diagram of the rotational spectrum of OCS molecule at room temperature at successive (downright) tenfold stretching of the vertical scale and twofold stretching of the horizontal scale.

Part of the observed series (quite a substantial part) is formed thanks to the existence of different stable isotopes of atoms entering the molecule. According to the nomenclature of the International Union of Pure and Applied Chemistry (IUPAC), identical molecules with different combinations of isotopes of atoms are called the *isotopologues*. A small change in the nuclei masses leads to a small change of molecular constants, hence, the different series of lines corresponding to the isotopologues do not overlap. A relative amount of isotopologues under standard conditions and the corresponding ratios of intensities of the line series are defined as products of natural isotopic abundance of atoms. The most abundant isotopologue (93.719 %) for OCS is $^{16}O^{12}C^{32}S$. Its rotational spectrum dominates in the upper diagram in fig. 1.6. The next of the intense line series belongs to the pure rotational transitions of the molecules in the bending vibrational state excited by collisions, ν_2. Thus, the lines of the rotational spectrum even of such simple molecules under normal conditions may be found with sufficient instrumental sensitivity in any part of the millimetre and submillimetre wavelength ranges.

Inversion motion

To complete the picture, one more type of atomic motion in molecules should be mentioned. This motion resembles vibrations but has no classical analogue, therefore its interpretation faces some difficulties, notably the *inversion motion* caused by tunnelling. The best-known example is a molecule of ammonia (NH_3), which is an oblate symmetric top. The atom of ammonia is sitting rather close to the plane of hydrogen atoms. The internal energy of the molecule in the ground vibrational state is too small for a nitrogen atom to reach the hydrogen plane. The peak of the potential energy (fig. 1.7) impedes this process. Nevertheless, it appears as if the nitrogen atom passes through the plane of the hydrogens and the molecule ‘turns inside out’.

Such a transition is known as tunnelling, as for the ammonia atom to overcome the potential barrier it must make a tunnel in it. This motion is very much like the ‘umbrella’ vibration ν_2, when an atom of N vibrates symmetrically with respect to the plane of H atoms so that the angle of N—H-bonds changes, but their lengths remain unchanged. The vibration energy of this type may be much higher than the height of the potential barrier and, in full conformity with a classical oscillator, the nitrogen atom will be, in turn, on the left or on the right of the plane of hydrogen atoms.

The fundamental frequency ~932 cm^{-1} [2] of such a vibration is more than a thousand times higher than the frequency of the *inversion transitions,* related to the splitting of each vibrational-rotational energy level (including the ones above the barrier) into two sublevels due to the presence of a potential barrier (fig. 1.7). The magnitude of the splitting depends on the energy level.

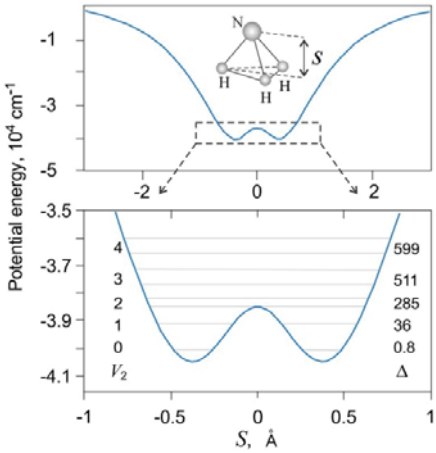

Fig. 1.7. The function of the internal potential energy of an ammonia molecule *versus* the distance between the ammonia atom and the plane of hydrogen atoms. The bottom picture shows the low part of the potential: the positions and magnitude of the inversion splitting Δ of the ground and several first excited vibrational levels (umbrella motion).

What motion do these transitions correspond to? Suppose that the transition from the low to the upper inversion level corresponds to the excitation of the periodic inversion motion with a frequency equal to the frequency of the transition (analogously to the way vibrations occur when the corresponding quantum is absorbed in molecules). Since ammonia is a symmetric top, it has a dipole moment oriented along the axis of motion of

[2] In spectroscopy the frequency is frequently expressed in inverse centimetres rather than in Hertz, which corresponds to λ^{-1}, where λ is the respective wavelength in centimetres. This unit is sometimes called the 'spectroscopic wavenumber' (frequently just 'wavenumber') or rarely 'the kayser' after Heinrich Kayser and abbreviated as K, where 1 K = 1 cm^{-1}. The wavenumber is proportional to frequency and to photon energy. That is why spectroscopists use the wavenumber as a unit of energy.

the ammonia atom at inversion. If there is no inversion motion, then according to classical physics, the molecule will interact with a permanent gradient electric field and will be pulled in the region of a stronger field. With the excitation of a periodic inversion motion, the average dipole moment tends to zero and the interaction with the field does not occur. Charles Hard Townes understood this property of ammonia molecules and used it in the first molecular maser created in 1953, the work for which he was awarded the Nobel prize in 1964. A molecular beam was transmitted through the region of a permanent gradient electric field. The unexcited molecules at the low level escaped from the beam, whereas the ones performing an inversion motion continued to move rectilinearly, reached the resonator, and emitted coherently. The maser started to operate. Moreover, the dependence of the inversion transition frequency on the rotational quantum numbers [Townes, 1955] corresponds to the alleged motion. The higher the velocity of the molecular rotation about its axis (the growth of J at $K = 0$), the more oblate the top is becoming under the action of centrifugal forces, and the easier the nitrogen passes through the barrier. The frequency of the inversion transition is increasing, indeed. As the speed of the molecular rotation about the axis normal to the symmetry axis increases (the growth of J at $K=J$), the centrifugal forces, on the contrary, pull the nitrogen away from the hydrogen plane and impede inversion. The frequency of the inversion transition decreases. This confirms the validity of the above arguments. However, the analysis of the *wave functions* [3] relating to the inversion levels (see, for example, fig. 25.6 from the book [Papoušek, 1982]) shows that the probability of finding a nitrogen atom on the left and on the right is the same, both in the upper and in the low state. Moreover, the probability of passing through the barrier or tunnelling (see, for example, Landau [1977]; Razavy [2003]) depends only on the energy of the level and on the height of the potential barrier. The energy of the low level, the so-called *energy of zero vibrations* corresponding to $V = 0$ in the expression (1.48), according to the current quantum-chemical calculations [Huang, 2008-2], is ~7430 cm^{-1} (including ~470 cm^{-1} in umbrella vibrations), the barrier height is ~1790 cm^{-1}. The inversion splitting of the levels at which the ammonia maser works is only ~0.8 cm^{-1}. The corresponding change of the probability of tunnelling is negligibly small.

[3] The wave function is used in quantum mechanics for describing the state of the system. It is a function of the system coordinates and is physically meaningless per se, but the square of its absolute value is interpreted as the probability density of detecting the system at a given point of its configuration space.

From this follows the principal difference between the vibrational and inversion motions. A molecule can be routinely transferred from the ground vibrational to the excited state and back, i.e., it is possible to make the molecule vibrate and to cease the vibrations, whereas the inversion motion occurs continuously, independent of the state of the molecule, even if it does not interact with anything. The vibrational state can be excited at fundamental frequency harmonics, and the inversion motion at each state of the molecule can take place at one frequency only. The inversion frequency can be increased or decreased by transferring the molecule to the energy level which is closer to or farther from the top of the potential barrier. This does not contradict the observed dependence of the inversion transition frequency on the rotational state considered above, since the increase of J at $K = 0$ corresponds to the growth and at $K = J$ to the decrease of rotational energy. The states of the molecule with a nitrogen atom on the left and on the right of the hydrogen plane are energetically identical. It might seem that by exciting the inversion transition we do not excite the inversion motion of the molecule; we only change its frequency. Then, it is impossible to cease the inversion motion. And yet the maser works…

1.2.2. Molecular line shape

The question concerning the shape of a molecular spectral line corresponding to the molecular transition from level *a* to level *b* may be formulated as follows: will gas consisting of such molecules absorb radiation at frequency detuning upwards or downwards the resonance frequency of the transition? As the answer is obviously positive, we just need to clarify the frequency interval in which absorption takes place (the width of the spectral line) and the dependence of the absorbed power on frequency detuning (i.e., spectral line shape).

It is reasonable to consider the absorption *line shape* independent of its integrated intensity, the physical meaning of which will be clarified a little later. The integrated intensity of spectral lines (1.41) is characterised by the properties of the relevant transitions and is constant for each line, depending only on molecular concentration and temperature. It will be shown below that the line shape is determined by the mechanisms common for all transitions and may be different depending on which mechanism is dominating under the conditions of line observation. Therefore, the absorption coefficient for each individual line at frequency ν_0 can be represented as a product of the integrated intensity α_{ab} and the frequency-dependent intensity distribution or the function of line shape

(sometimes referred to as the *profile* or the *contour*) $I(\nu, \nu_0)$ having unit area:

$$\alpha_{line}(\nu) = \alpha_{ab} \cdot I(\nu, \nu_0) \ , \qquad \int_{-\infty}^{+\infty} I(\nu, \nu_0) d\nu = 1 . \qquad (1.53)$$

Note that, from the expressions (1.53), follows a conclusion important for practical applications: the integrated line intensity α_{ab} is the area bounded by the line contour:

$$\alpha_{ab} = \int_{-\infty}^{+\infty} \alpha_{line}(\nu) d\nu . \qquad (1.54)$$

This is the crux of the considered term. It is convenient to normalise the integrated intensity to the molecular concentration:

$$S_{ab} = \frac{\alpha_{ab}}{n} . \qquad (1.55)$$

At a fixed temperature, the normalised line intensities are tabulated in the spectroscopic databases. For a known molecular concentration, the relations (1.54)—(1.55) are used to measure the line intensity in a pure gas or, the other way round, to determine the concentration of the absorbing gas in the mixture with other gases by numerical integration of the experimental recording of a line with known (or pre-measured) intensity of the absorbing gas. The form of the function $I(\nu, \nu_0)$ is of no significance in this case. Infinite integration limits are valid if the spectrum has only one line. In fact, the integration is performed over the entire frequency range in which the absorption in the line exceeds the experimental noise. A possible contribution of other lines and of non-resonant absorption should also be taken into consideration. In the case of dense spectra, it is convenient to employ the notion *absorption cross section* in a given frequency range, that is an integrated spectrum intensity in this range, normalised to the concentration of absorbing molecules.

It is also handy to consider a molecular line shape as a power spectrum of the process running in time and corresponding to the molecule-field interaction. The evolution of the vector of the molecule's dipole moment is used in this case, which comprehensively characterises all changes in the molecular motion during its interaction with electromagnetic radiation (see, for example, Hartmann [2008] and references therein). The line shape in gas is determined by the time evolution of the induced polarisation, comprised of the dipole radiation of the individual molecules

synchronised by the resonant electromagnetic field and emitting photons which are indistinguishable from the photons of the field. For example, when excited by a linearly polarised resonance radiation of vibrational motion in a hypothetic gas of polar diatomic molecules fixed in space, the dipole moments of all the molecules will be arranged in the direction of the electric field vector and will vibrate in-phase with the oscillations of the electric field. The application of a resonant field corresponding to the rotational molecular transition will result in precession of the vector of angular momentum of molecules synchronously with the phase of the electric component of the field. To ensure exact correspondence between the resonant line shape and the spectrum of gas polarisation evolution it is necessary to produce polarisation in gas by a sufficiently long pulse of resonance radiation and register the process of polarisation evolution immediately after switching off the radiation [Rohart, 1994]. Note that in both cases the electromagnetic radiation should be weak and should not disturb the thermodynamic equilibrium of the gas. Then, the gas may be regarded to be similar to a radiating oscillator, and the relevant well-developed mathematical approach can be used for modelling line shape.

The molecular line shape in gas is determined more rigorously, if the molecules are considered as moving oscillators (radiating dipoles) subject to random perturbations [Fano, 1963]. Recall that the absorption and the stimulated emission are equivalent because in both cases, molecular transitions occur under the influence of the resonant field. The emission spectrum averaged over all fluctuations of each oscillator is equal to zero because the oscillation phases and all directions of motion are equiprobable. Therefore, to find the emission spectrum of such an oscillator one should consider the correlation between its successive positions in space over short time intervals, i.e., autocorrelation. If the perturbation process is stationary, the autocorrelation function does not depend on running time and determines the way the oscillator moves and emits. The autocorrelation function is statistical averaging over the fluctuations. Actually, it is an ensemble averaging — averaging over different phases, velocities and spatial distribution of molecules-oscillators in gas. The line shape as the spectrum of radiation power (or *power spectral density*) of the oscillators subject to Brownian motion is a Fourier image of the dipole autocorrelation function of a single oscillator, calculated over all possible (and strictly speaking, infinite) intervals of time (see the Wiener — Khintchine theorem [Wiener, 1930; Khintchine, 1934]). A rigorous derivation of the relation between the absorption shape and the correlation function of the dipole moment operator for the absorbing molecule can be found, e.g., in Gordon [1968].

Natural broadening

The resonance frequency of the transition obeys the energy conservation law

$$E_a - E_b = h\nu_0 . \tag{1.56}$$

This does not mean that a spectral line may be represented by means of a delta function at frequency ν_0, as the accuracy of determining values of energy levels is limited by the *uncertainty principle*. The uncertainty of the energy δE depends on the duration of the molecule's stay in a definite state, in other words, on the *lifetime* Δt of this energy state:

$$\Delta t \cdot \delta E \approx \hbar . \tag{1.57}$$

The corresponding uncertainty of the frequency which characterises the range within which the molecule will absorb radiation that is, in fact, the resonant line width, can be found from (1.56) and (1.57):

$$\Delta\nu = \frac{1}{2\pi\Delta t_a} + \frac{1}{2\pi\Delta t_b}, \tag{1.58}$$

where Δt_a and Δt_b are the lifetimes of the molecule in states a and b, respectively.

Even if a molecule is stationary (i.e., it is localised in space and its translational motion is frozen but it can rotate and vibrate) and fully isolated from the interaction with the field and other molecules, the lifetime of its energy state is finite and is determined by the probability of spontaneous transitions to lower levels:

$$\Delta t_a = \frac{1}{\sum_k A_{ak}}. \tag{1.59}$$

For a hypothetic gas consisting of such stationary molecules, the relevant line width, called the *natural width* in this case, is determined by the sum of the probabilities of all possible spontaneous transitions from both energy levels. In the presence of an external electromagnetic field (for example, broadband solar radiation), the line width of such a gas will also be determined by the lifetimes of the transition levels, which now depend on the probability of stimulated transitions to other levels:

$$\Delta t_a = \frac{1}{\sum_k \rho(\nu_{ak}) B_{ak}}, \tag{1.60}$$

The corresponding mechanism is called the *radiative broadening*.

The line shape in gas under the conditions of natural or radiative broadening is readily found from qualitative considerations making use of the aforementioned temporal approach.

Imagine an ensemble of N two-level molecules in the upper state a just after switching off the transition-resonant field. Over the time interval dt their amount will decrease by

$$-dN = A_{ab} N dt, \tag{1.61}$$

where A_{ab} is the probability of spontaneous transition. From this, it follows that the number of such molecules changes with time as

$$N(t) = N_0 \exp(-A_{ab} t). \tag{1.62}$$

The radiation amplitude $P(t)$ of coherent oscillations of an ensemble of such molecules-oscillators at the frequency $\nu_{ab} = \nu_0 = \omega_0/2\pi$ will, respectively, decrease with time as

$$P(t) = P_0 \exp(-A_{ab} t) \exp(i\omega_0 t). \tag{1.63}$$

This process corresponds exactly to the decay of oscillations of a harmonic oscillator with a damping constant $1/A_{ab}$. Its spectrum is determined by the Fourier integral which may be written, omitting insignificant amplitude factors, in the form

$$P(\omega) \propto \int_0^\infty \exp\left(-A_{ab} t\right) \exp\left(i\omega t\right) \exp\left(-i\omega_0 t\right) dt = \frac{1}{i\left(\omega - \omega_0\right) - A_{ab}}, \tag{1.64}$$

and the energy spectrum of this process determining line shape

$$|P(\omega)|^2 \propto \frac{1}{(\omega-\omega_0)^2 + \left(A_{ab}/2\right)^2} \tag{1.65}$$

is the well-known *Lorentz profile*. Passing over to the linear frequency ($\nu = \omega/2\pi$) and performing the normalisation (1.53), we obtain the shape of a naturally or radiatively broadened line

$$I_R(\nu, \nu_0) = \frac{1}{\pi} \frac{\Delta\nu_R}{\left(\nu - \nu_0\right)^2 + \Delta\nu_R^2}. \tag{1.66}$$

The width of such a line is $\Delta\nu_R = A_{ab}/4\pi$ (or $B_{ab}/4\pi$ for radiative broadening) that is a half-width of the profile at its half maximum amplitude (fig. 1.8).

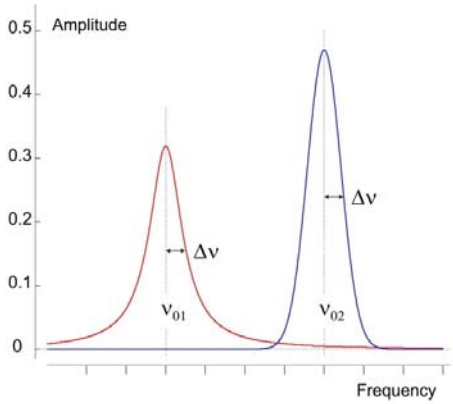

Fig. 1.8. The Lorentz (*on the left,* frequency ν_{01}) and Doppler (*on the right*, frequency ν_{02}) profiles of unit area for the same width $\Delta\nu$.

Generally, the width of a naturally or radiatively broadened line can be described by the effective lifetime of a molecule-oscillator:

$$\Delta t_{ab} = \frac{\Delta t_a \Delta t_b}{\Delta t_a + \Delta t_b},$$

(1.67)

and (1.58) transforms to

$$\Delta\nu_R = \frac{1}{2\pi\Delta t_{ab}}. \qquad (1.68)$$

For the lines of the rotational spectra of most atmospheric molecules under normal conditions of the Earth's atmosphere, the influence of the radiative, more so that of the natural broadening, is negligibly small compared to two other mechanisms — the thermal translational motion of molecules and their collisions. The latter two are the principal mechanisms determining the width and shape of almost all observable resonant molecular lines.

Doppler broadening

If a molecule absorbs radiation at the frequency $\nu_0 = \nu_{ab}$, then the frequency of the radiation absorbed by the molecule with the projection of

velocity υ onto the direction of radiation propagation will differ from ν_0 by the value of the Doppler shift

$$\nu = \nu_0 \left(1 - \frac{\upsilon}{\upsilon_{\text{ph}}}\right), \tag{1.69}$$

where υ_{ph} is the phase velocity of radiation propagation which can nearly always be regarded to be equal to the speed of light. Under thermodynamic equilibrium under normal conditions, a great number of molecules move equiprobably in all directions. Therefore, instead of the absorption at the resonance frequency ν_0, a continuous absorption with intensity distribution $I(\nu)$ will be observed in some spectral interval in the vicinity of ν_0. The probability of radiation absorption by a molecule in the frequency interval $d\nu$ near the frequency ν is equal in this case to the probability that the molecule will have the projection of velocity υ onto the direction of radiation propagation in the interval of velocities $d\upsilon$. This probability is determined by the Maxwell distribution:

$$I(\nu)d\nu = \text{M}(\upsilon)d\upsilon = \text{M}\big(\upsilon(\nu)\big)\frac{d\upsilon(\nu)}{d\nu}d\nu, \tag{1.70}$$

$$\text{M}(\upsilon) = \frac{1}{\upsilon_0\sqrt{\pi}}\exp\left(-\frac{\upsilon^2}{\upsilon_0^2}\right), \quad \upsilon_0 = \sqrt{\frac{2kT}{M}},$$

where υ_0 is the most probable speed of a molecule having mass M at temperature T. Expressing $\upsilon(\nu)$ from (1.69) and substituting it into (1.70), yields the following expression for $I(\nu)$

$$I(\nu) = \frac{c}{\nu_0\upsilon_0\sqrt{\pi}}\exp\left[-\frac{c^2}{\upsilon_0^2}\left(\frac{\nu-\nu_0}{\nu_0}\right)^2\right]. \tag{1.71}$$

It is a Gaussian function meeting the normalisation condition (1.49), half width of which at $1/e$ maximum is characterised by

$$D = \nu_0\frac{\upsilon_0}{c} = \frac{\nu_0}{c}\sqrt{\frac{2kT}{M}}. \tag{1.72}$$

Thus, if molecular collisions in gas in thermodynamic equilibrium are so rare that they can be neglected, the line shape (referred to as a *Doppler profile*, fig. 1.8) has the form:

$$I_D(\nu,\nu_0)=\frac{1}{D\sqrt{\pi}}\exp\left[-\left(\frac{\nu-\nu_0}{D}\right)^2\right]. \tag{1.73}$$

For convenience of estimations, the width of the Doppler profile can be described, by analogy with the Lorentz profile, by the value of half width at half maximum:

$$\Delta\nu_D = D\sqrt{\ln 2}=\frac{\nu_0}{c}\sqrt{\ln 2\frac{2kT}{M}}. \tag{1.74}$$

The Doppler broadening is a predominant mechanism specifying the line shape in the upper atmospheric layers.

Collisional broadening

The collisional interaction of molecules is a basic physical mechanism determining the thermodynamic properties of gases and the shape of their spectra. So, it is not surprising that it is the subject matter of numerous monographs and review articles (e.g., Camy-Peyret, [2003]; Hartmann [2008]; Buldyreva [2011], Hartmann [2018]), as well as continuously appearing in new research papers. The survey of up-to-date, high-accuracy methods of calculating the spectral line shape under the conditions of collisional interaction of molecules can be found in May [2013]. Here, we will consider only the most significant consequences of molecular collisions, the influence of which on the line shape of atmospheric molecules should be taken into consideration to provide sufficient accuracy of the correspondence between models and experimental data.

According to classical molecular physics, molecules are rigid spheres that do not attract each other and move at the same (mean thermal) speed. Their collisions are determined by the effective *collisional interaction cross section* (sometimes referred to as the collisional cross section or the interaction cross section) σ and the *mean free path length* L_F. The collisional cross section is an area of a 'circle-target'. If another molecule enters this circle, there occurs collision. The *free path length* is the distance on passing which the molecules collide with a probability equal to unity. The relationship between the collisional cross section and the free path length is derived as follows (see, for instance, Hirschfelder [1954]). At normal incidence of an infinitely small particle on area S, the probability P_c of its collision with spheres (or normally located targets having area σ), provided the particle flies over distance L, is equal to the

ratio of the total area overlapped by the targets to the area *S*. The number of targets in the volume *LS* is *nLS*, and their sum area is $\Sigma = \sigma nLS$, hence

$$P_c = \frac{\Sigma}{S} = \sigma nL. \tag{1.75}$$

The free path length is by definition $L_F = L$ at $P = 1$, i.e.

$$L_F = \frac{1}{n\sigma}. \tag{1.76}$$

The relationship between the collisional cross section and the radius *r* of a rigid-sphere molecule is drawn from the following considerations. If all the molecules are stationary and a similar molecule is incident on them on passing distance *L*, then this molecule will collide with all the molecules the centres of which are in a circular cylinder having base radius 2*r* and height *L* (fig. 1.9). The number of molecules in the cylinder is $n4\pi r^2 L$. It is obvious that the mean free path length is equal to the height of the cylinder in which there is only one molecule:

$$L_F = \frac{1}{n4\pi r^2}. \tag{1.77}$$

Comparison of this equation with (1.76) shows that the radius of a rigid molecule-sphere is equal to half the radius of the collisional cross section.

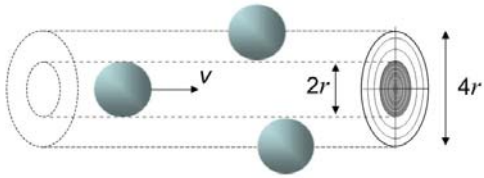

Fig. 1.9. The cross section of collisional interaction and the size of molecules-spheres.

The average time between the collisions Δt_c is defined as the ratio of the mean free path length to the mean relative thermal speed of molecules, υ_r. As all the directions of molecule motion are equiprobable, it can be shown that two arbitrary colliding molecules move, on the whole, normally to each other. Consequently, the speed of their relative motion is $\sqrt{2}$ times higher than the mean thermal speed, and

$$\Delta t_c = \frac{L_F}{\upsilon_r} = \frac{1}{n\sigma\upsilon_r} = \frac{1}{n\sigma}\sqrt{\frac{\pi M}{16kT}}. \qquad (1.78)$$

In quantum mechanics, molecular collision is usually considered as a process when the field formed by charges of one molecule starts to interact with the field of the other molecule, thereby perturbing energy states of both colliding partners. The strongest perturbation arises when the speed of the relative translational motion of the molecules in collisions is close to the speed of their vibrational or rotational motion. Then the interaction is close to the static one and occurs at large enough distances between the molecules. Under normal conditions, strong interaction most often takes place for the rotational motion. Therefore, the most probable effect of collision is the perturbation of rotational molecular states.

Under normal conditions, nearly all gases can be regarded to be ideal. This means that it is possible to make a few assumptions that will greatly simplify the case, and to focus on the principal factors influencing the shape of resonant lines.

The first assumption is that only two molecules participate in each collision. It is the *pair (or binary) collisions approximation*. It is based on the fact that, even at atmospheric pressure, the density of gas is so low that the average distance between the molecules is much larger than their characteristic size and the probability of collisions in which three molecules take part simultaneously (*ternary collisional event*) is very low. For conventional light molecules, such events become significant at pressures of hundreds of atmospheres.

The second assumption is the *impact approximation*. It implies that, given a low gas density, the period during which a moving molecule 'does not feel' the presence of the neighbours is much longer than the period of effective interaction between two colliding molecules, i.e., the mean time between the collisions is much longer than the duration of the collisions which may be considered to be instantaneous.

As molecules have a large number of internal degrees of freedom, under these approximations the collisions may be divided into two groups:

1) Inelastic collisions, when the internal energy of the molecule interacting with a resonant field changes due to the translational energy of the colliding pair. This means that the molecule makes a nonradiative transition to another energy level. In this case, it is said that the *collisional relaxation* of the excited molecular state takes place. In terms of the temporal approach to the analysis of line shape, the result of such a collision is the shortening of the time of the interaction of the molecule with the field. All the considerations made in the derivation of the line

shape under natural and radiative broadening conditions (1.66) hold true for this group.

2) Elastic or adiabatic collisions, when the internal energy of the molecules does not change and after the collision, they preserve the same energy state. The rotational or vibrational frequency of the molecules during the interaction changes in proportion to the interaction force. As a result, on collision, the molecule will acquire phase incursion in its rotational or vibrational motion. Under the impact approximation this means that the phase changes abruptly by an arbitrary magnitude.

For assessing the relationship between the elastic and inelastic collisions, following Charles Townes [1955], we will estimate the energy needed to change the phase by the amount $\Delta\varphi$ that will allow us to consider the trains of molecular oscillations before and after collisions as independent ones. A change by more than 1 radian is regarded to be sufficient. Such a phase variation during an elastic collision having duration t' means that

$$\Delta\varphi = \omega t' = 2\pi\nu' t' \geq 1, \text{ or } \nu' \geq \frac{1}{2\pi t'},$$

where ν' is the characteristic change of frequency that may be approximately assessed through the interaction energy W' as $h\nu' = W'$. The duration of the collision can be estimated as the time of flight of a molecule that has passed a distance equal to its size. The size of the molecule is several angstroms and the mean thermal speed under ordinary conditions is several hundred meters per second. Consequently, $t' \sim 10^{-13}$ s and $1/(2\pi t') \sim 6$ THz, which is higher that the frequency of rotational transitions for the majority of atmospheric molecules. Therefore, the energy required for a marked change of phase is higher than the energy needed for the transition of the molecule to the neighbouring rotational level. The fast change of the interaction energy also facilitates the transition. The characteristic time of the change is usually shorter or comparable to the period of rotation. This means that the resonance frequency of the transition will also be present in the interaction spectrum. Still, another factor favourable for the transition is the fact that the energy of the translational motion of molecules $3kT/2$ under typical atmospheric conditions is also higher than the transition energy. All this leads to the conclusion that, under ordinary conditions, the fraction of elastic collisions is small and most of the collisions result in changes in the rotational states of the molecules.

Thus, under normal conditions, the main factor influencing the shape of the observed lines is a collision-induced decrease of the lifetime of a

molecule in a state resonant with the field. Therefore, by analogy with the natural and radiative broadening, the shape of a collision-broadened line normalised to the area will correspond to the following expression

$$I_c(\nu,\nu_0)=\frac{1}{\pi}\frac{\Delta\nu_c}{(\nu-\nu_0)^2+\Delta\nu_c^2},\qquad \Delta\nu_c=\frac{1}{2\pi\Delta t_c},\qquad (1.79)$$

where Δt_c is the mean time between the collisions.

Note that the substitution of such a line shape into the expressions (1.53) and (1.54) yields a very simple expression for the integrated intensity

$$\alpha_{ab}=\pi\cdot\alpha_{line}(\nu_0)\cdot\Delta\nu_c,\qquad (1.80)$$

which can be used for measuring the integrated intensity of collision-broadened lines.

The collisional interaction energy and, hence, the result of the interaction depend not only on the charge distribution in molecules and their relative speeds, but also on the distance of the closest approach, in a flight with retained rectilinear trajectory b_p, that is usually called the *impact parameter* (fig. 1.10).

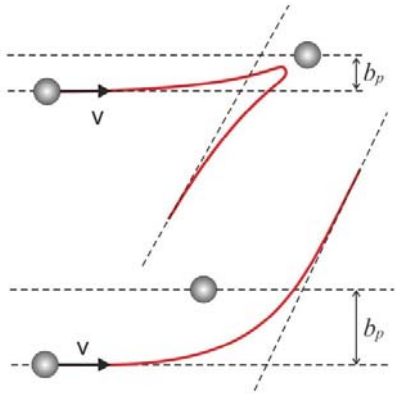

Fig. 1.10. Approximate trajectories of relative molecular motion during collisions.

The effective collisional cross section can be written as [Townes, 1955]:

$$\sigma=\int_0^\infty 2\pi b_p\cdot S(b_p)\,db_p,\qquad (1.81)$$

where the factor $2\pi b_p db_p$ is proportional to the probability of collision during motion with an impact parameter b_p, and $S(b_p)$ is the weight factor characterising the degree of perturbation of the molecular state by this collision. For small impact parameters, $S(b_p) = 1$, which means that any such collision leads to a change in the molecular state, thus contributing to line broadening. For large impact parameters, $S(b_p)$ is proportional to the probability of a collisional transition of the molecule to other states. The larger the bp and the faster the interaction force between molecules decreases with increasing distance, the lower the transition probability.

Collisions at a distance, that do not change the state of the molecule, lead to the above-mentioned changes of the phase of molecular oscillations, rotational or vibrational. The Fourier analysis of the corresponding wave packets (trains of oscillations) shows that the phase shifts arising, as a result of such collisions, lead to a small but notable frequency shift of the observed line. The shift may have either a positive or a negative sign. The sign and the magnitude of the shift depend not only on a definite molecular transition, but on the collision partner as well. The origin of the frequency shift may be also understood from the classical considerations. If a rotating dipole is placed in an inhomogeneous electric field then the higher the field amplitude and the lower the rotation energy, the greater the change in rotation velocity., the higher the field amplitude and the lower the rotation energy. The interaction with the field leads to a change of the rotation energy. An analogous effect occurs when the molecule moves into the electric field of its collision partner. The rotational energy levels of the molecule-dipole shift, the shift value being different for different energy levels. So, the frequencies of the transitions change respectively. This shifting of the line frequency is the second most significant collisional effect determining the observed line shape.

Under the approximation of pair collisions, their number in unit time is directly proportional to the number of molecules per unit volume and, hence, to gas pressure p. The same conclusion follows from the classical expression for the mean time between the collisions (1.78). It is true for the collisions resulting in both the broadening of the line and its frequency shift. Therefore, both these effects depend linearly on pressure, and can be quantitatively described by changes of the line shape parameters normalised to the corresponding pressure change. Since at zero pressure the collisional line width is equal to zero and the line frequency corresponds to the transition frequency of a stationary molecule, we have

$$\gamma_c = \frac{\Delta\nu_c}{p}, \quad \delta_c = \frac{\nu_c - \nu_0}{p}, \tag{1.82}$$

where γ_c and δ_c are the coefficients of collisional broadening and shifting, respectively, and ν_c is the frequency of the centre of the observed line. The zero-pressure line frequencies, as well as the corresponding shifting and broadening parameters are tabulated in the spectroscopic databases. Thus, the width and frequency of the centre of the observed line — the line shape parameters — are regarded to be functions of pressure:

$$\Delta\nu_c = \gamma_c p, \qquad \nu_c = \nu_0 + \delta_c p. \tag{1.83}$$

Combined effect of broadening mechanisms (Voigt profile)

In real gases all basic broadening mechanisms act simultaneously, but natural and radiative broadening have a specific feature – they are not related to molecular collisions and motions. Natural, radiative, and collisional line broadenings are similar in the sense that all of them shorten the lifetime of the molecular state. As the result of their combined action, the width of the observed Lorentz line profile is the sum of the radiative (or natural) and collisional components:

$$\Delta\nu_L = \Delta\nu_R + \Delta\nu_c. \tag{1.84}$$

To understand the joint action of radiative and Doppler broadening, it may be helpful to consider the Brownian motion of decaying oscillators. For determining line shape, one must calculate the weighted averaging of individual oscillator profiles using the Maxwell distribution of the oscillator speeds as the weight factor. The Lorentz profiles should be taken instead of the delta-functions shifted by the Doppler correction assumed in the derivation of eq. (1.71). Such a summation ultimately converting to the integration is actually the convolution of the Doppler (Gaussian) and radiative (Loretz) line profiles:

$$I(\nu,\nu_0) = \int I_D(t,\nu_0)\, I_R(\nu - t,\nu_0)\, dt. \tag{1.85}$$

The corresponding line shape is called the *Voigt profile.* When the normalisation condition (1.53) is met, it has the form

$$I_V(\nu,\nu_0) = \frac{y}{\pi} \cdot \int_{-\infty}^{\infty} \frac{e^{-t^2}}{y^2 + (x-t)^2}\, dt, \tag{1.86}$$

where $x = \dfrac{\nu - \nu_0}{\Delta\nu_D} \cdot \sqrt{\ln 2}$, $y = \dfrac{\Delta\nu_R}{\Delta\nu_D} \cdot \sqrt{\ln 2}$ are the dimensionless variables.

Note that radiative (or natural) and Doppler broadening mechanisms are independent of each other and eq. (1.85) can be considered to be exact. Contrary to that, the collisional and Doppler mechanisms of broadening are not independent. The faster moving molecules collide more frequently; consequently, the spectral lines corresponding to their oscillation trains will be more broadened by the collisions than the analogous lines of slow molecules. Nevertheless, on average, all moving molecules collide over the same time period (1.78) related to the mean relative speed. The line profile in gas is composed of the line profiles of groups of molecules moving similarly to each other. The speed distribution of the molecules is almost symmetric with respect to the most probable speed. Taken together, this will all lead to averaging of more broadened or less broadened profiles of the groups of molecules. The result will be similar to the average broadening given by (1.79) for all molecules. Therefore, the independence of the Doppler and collisional broadening mechanisms is a rather good initial approximation for obtaining the product of their combined action. Consequently, in this case too, the line shape corresponds approximately to the convolution of the Doppler (Gaussian) and collisional (Loretz) profiles, i.e., to the Voigt profile. Thus, the Voigt profile is a universal function that is most often used for modelling the shape of resonant molecular lines. The difference between the real line and the Voigt profile appears only in cases with a large enough (10^2—10^3 and higher) signal-to-noise ratio of the recording. The calculated and experimental profiles almost coincide and the deviation between them can be seen only from the difference between the observed and the best fitted Voigt profiles (fig. 1.11). The real line is a little narrower and a little higher than the corresponding Voigt profile.

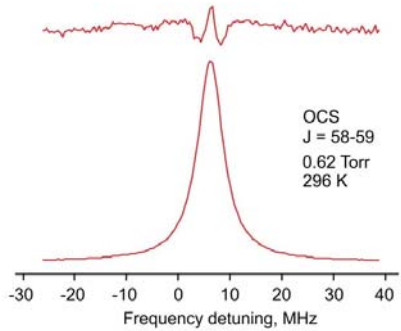

Fig. 1.11. The experimental recording of the line of pure rotational transition of a carbonyl sulphide molecule. The curve on top is a 20-fold magnification of the line deviation from the Voigt profile. The detuning is from the frequency of 716.560 GHz. Adopted from Koshelev [2012].

Line shape beyond the Voigt profile

When discussing subtle effects affecting a molecular line shape, researchers frequently use the concept of the *collisional relaxation rate* of molecules Γ that characterises the decay time of the polarisation induced in gas by resonance radiation (or the decay time of the coherent radiation of molecules) $\tau = 1/\Gamma$, and is unambiguously connected with the collisional line width $\Delta\nu_c = \Gamma/2\pi$. There are two fundamentally different physical phenomena responsible for the difference between the observed line shape and the Voigt profile:

1) the speed dependence of the collisional relaxation of a molecule, and
2) the elastic collisions of a molecule changing the direction of its motion, i.e., the velocity.

Let us consider these phenomena.

The speed dependence of collisional relaxation

Clearly, the frequency of the collisions leading to a collisional relaxation of the state of the molecules depends on the speed of their movement. Actually, we speak about the dependence of the collisional relaxation rate Γ on the relative speed of the molecules, υ_r. Note that only speed, i.e., the modulus of molecular velocity, is important in this case because of the isotropy of the velocity distribution for a gas at thermal equilibrium.

For determining the average relaxation rate, the function $\Gamma(\upsilon_r)$ shall be averaged with allowance for the molecules' velocity distribution:

$$\Gamma_0 = \langle \Gamma(\upsilon_r) \rangle = \int_0^\infty \Gamma(\upsilon_r) f(\upsilon_r) d\upsilon_r , \qquad (1.87)$$

where $f(\upsilon_r)$ is the Maxwell distribution.

If $f(\upsilon_r)$ were symmetric, with respect to the most probable speed and Γ depended linearly on υ_r, the observed line shape would correspond exactly to the Lorentz (Voigt) profile derived, assuming that all the molecules move at the same mean speed. In this case, the contributions of the groups of molecules moving with some offset upwards from the mean speed and forming broader absorption profiles will be exactly compensated by the contributions of the groups of molecules moving with the same offsets, but downwards from the mean speed and forming more narrow profiles. As an example of real dependences, we present in fig. 1.12 the result of numerical theoretical computations of the pressure-normalised dependence of $\Gamma/(2\pi)$ on υ_r for the lines of one of the rotational transitions of an OCS

molecule, together with the shape of the corresponding $f(\upsilon_r)$ function. The $\Gamma(\upsilon_r)$ slope is changing appreciably within the width of the distribution function, decreasing with the increase of speed. The resulting real line is a little narrower and higher than the corresponding Lorentz (Voigt) profile.

For line shape modelling, this effect may be taken into consideration in different ways. The easiest way is to use a simplified form of the molecular interaction potential (more details can be found in section 1.3.2) that has only a long-range component $V(r) \sim r^{-q}$, where r is the intermolecular distance and q = 3, 4, 5…, depending on the dominant interaction type in the considered gas (dipole-dipole, dipole-quadrupole, quadrupole-quadrupole, and so on). In this case, the function $\Gamma(\upsilon_r)$ has the simple form

$$\Gamma(\upsilon_r) = \Gamma\left(\bar{\upsilon}_r\right) \cdot \left(\frac{\upsilon_r}{\bar{\upsilon}_r}\right)^a, \quad a = \frac{q-3}{q-1}, \tag{1.88}$$

($\bar{\upsilon}_r$ is the mean relative speed, and a or q is assumed to be the empirical parameter of the model that takes the effect into account). Note that (1.88) can be expressed analytically through the hypergeometrical function [Berman, 1972; Pickett, 1980-1].

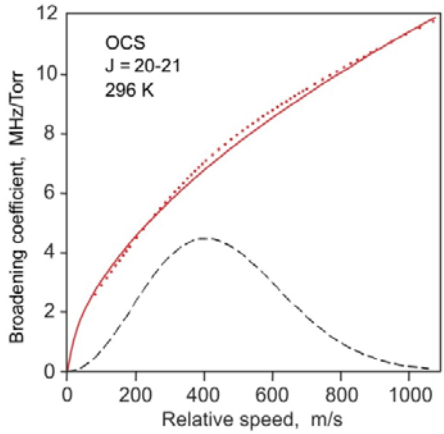

Fig. 1.12. The coefficient of collisional relaxation for J = 20—21 line of OCS molecule *versus* relative speed in the case of self-broadening. The solid line is the approximation of the theoretically calculated points by the function (1.88). The dashed curve is the Maxwell relative velocity distribution in arbitrary units. Adopted from Koshelev [2012].

It can be rigorously shown (Appendix A1) that averaging of the collisional relaxation rate over relative speeds gives exactly the same result as averaging the speeds of the molecules absorbing radiation (*'active molecules'*):

$$\langle \Gamma(\upsilon_r) \rangle = \langle \Gamma(\upsilon) \rangle. \tag{1.89}$$

This permits the use of (1.88) for the calculation of Γ_0 by means of (1.87). A simpler way to take into consideration the dependence of the relaxation rate of the molecules on their speed is to use the quadratic approximation of this dependence in the form [Rohart, 1994]:

$$\Gamma(\upsilon) = \Gamma_0 + \Gamma_2 \left[\left(\frac{\upsilon}{\upsilon_0} \right)^2 - \frac{3}{2} \right], \tag{1.90}$$

where υ_0 is the most probable speed of the active molecules and Γ_2 is the empirical parameter responsible for the speed dependence of the molecules' relaxation rate.

Note that line shifting should also be considered as the speed dependent effect making an impact on the molecular line shape because it originates from the same collisional interactions of molecules as the line broadening. The speed dependence of line shifting is modelled by equations similar to (1.88, 1.90).

A moving molecule absorbing radiation is in a flow of other molecules flying in the opposite direction. The speed of this flow and all the movement-related consequences, including the collisional relaxation, depend only on the intrinsic speed of the molecule in the space-fixed coordinate system. Therefore, this effect is sometimes referred to as '*the wind effect*' [Rautian, 2001].

Velocity-changing elastic collisions

The second effect influencing the molecular line shape is associated with the elastic collisions, during which, a molecule interacting with radiation does not change its internal state and oscillation phase (i.e., it persists to be coherent with the field). As was mentioned above, the fraction of such collisions in ordinary gases under normal conditions is small. Nevertheless, the collisions lead to changes in the velocity vector. As a result of these collisions, the molecule moves in a bounded spatial region, which according to the statistics always results in a decrease in the projection of its velocity onto the direction of radiation propagation. Ultimately, the speed of a molecule may decrease from a mean thermal

speed to a diffusion speed as a maximum. For the gas pressure at which the free path length of a molecule is shorter than half the radiation wavelength, the phase of the molecule's oscillations on collision is still in-phase with the field. Under these conditions elastic collisions do not result in the decay of coherence (molecules-oscillators synchronism); thus, the decrease in the speed leads to a reduced Doppler effect. This means that the spectral line corresponding to such molecules will be narrower than for the molecules experiencing inelastic collisions. The weaker the collisional relaxation, the stronger the narrowing effect. It is worth mentioning here the very illustrative analogy with an oscillator bouncing between the walls of a thin pillbox with a thickness less than a half wavelength of the oscillation. The analogy was put forward by Dicke [Dicke, 1953; Romer, 1955] who was the first to consider and study the effect, so it is often called the *Dicke narrowing effect*.

When modelling line shape with allowance for the Dicke effect, the strength of the collision, i.e., its efficiency with respect to the change of the velocity vector of the molecule interacting with the field, should be taken into account.

The model of strong (or hard) collisions implies that the molecule's speeds before and after collision do not correlate, they just follow the Maxwell distribution, i.e., the molecule completely forgets its initial velocity after each collision, while preserving coherence with the field. This approach was used in the works by Rautian and Sobelman [Rautian, 1966], and by Nelkin and Ghatak [Nelkin, 1964]. The hypothesis of weak (or soft) collisions implies that a molecule must experience multiple collisions before it completely loses the memory of its initial velocity. The corresponding line shape model was developed by Galatry [1961]. Although the considered models were derived from different assumptions on the character of collisions, they are equivalent in their application to experimental data and lead to similar results [Ngo, 2013]. Both models include, in addition to the ordinary parameter of collisional relaxation Γ_0, the narrowing parameter β_{opt} characterising the frequency of velocity-changing elastic collisions, which is often referred to as the *optical diffusion rate*. Let us recall again, that it is relevant exclusively to the molecules that experience changes in the velocity vector but preserve coherence to resonance radiation. Optical diffusion differs from gas-kinetic diffusion the rate of which is defined as

$$\beta_{kin} = \frac{kT}{MD} \tag{1.91}$$

where D is the *coefficient of mass diffusion* of absorbing molecules in ambient gas. The period of time corresponding to the gas-kinetic diffusion rate ($1/\beta_{kin}$) is the time over which the molecule completely forgets its initial velocity.

As $1/\Gamma_0$ is the average time over which the molecule loses its memory about the coherence with the field, it is apparent that Γ_0 cannot be much larger than β_{kin}, which is confirmed by numerous studies: Rohart [2007], D'Eu [2002], DeVizia [2011], Colmont [2001], Tran [2007], Hartmann [2008]. Since at each moment of time only part of the molecules experiences elastic collisions, β_{opt} shall always be smaller than β_{kin}, and the smaller the β_{opt}/β_{kin} ratio, the larger Γ_0/β_{kin}.

As the Dicke narrowing is caused exclusively by the narrowing of the shape of the Doppler broadened line, it is obvious that the effect manifests itself only at low enough pressures, when the collisional line width $\Delta\nu_c$ is smaller or around its Doppler width $\Delta\nu_D$. Under these conditions both narrowing mechanisms (the wind effect and the Dicke effect) act in gases simultaneously and manifest themselves in a similar way. Therefore, it is extremely difficult to determine their individual contribution to the experimental line shape, even if it is recorded with a high signal-to-noise ratio.

Note that there is no problem to create a model simultaneously taking into consideration both narrowing mechanisms in the approximation of their statistical independence (see, e.g., Ciurylo [1997] and Lance [1997]). The problem is that the velocity vector and the internal state of the molecules change as a result of the same collisions, so the correlation of both these mechanisms should be taken into consideration. Thus, in addition to the complicated expressions, one more variable parameter appears in line shape models (see, for example, Pine [1999, 2001]; Joubert [1999]; Ngo [2013]). The presence of several correlating variable parameters makes it possible to describe practically all experimentally observed lines within the noise level, but significantly complicates interpretation of the results. A more detailed overview of numerous models of the shape of resonant molecular lines, taking into account the Dicke and wind effects as well as the correlation between them, including the mathematical expressions needed for analysing the observed profiles, can be found in the monograph Hartmann [2008] and references therein.

Under the conditions of appreciable dominance of collisional broadening ($\Delta\nu_c >> \Delta\nu_D$), both the Dicke narrowing and the Doppler line broadening can be neglected. Therefore, the only known mechanism leading to the difference of the observable isolated resonant lines from the classical Lorentz profile is the wind effect. It influences the shape of all

collision-broadened lines of all gases; therefore, it should be taken into account at accurate modelling of absorption. The dominant contribution of the wind effect to line shape in a pure gas of polar molecules was demonstrated in the work Koshelev [2012] in an example analysing nearly all significant lines of the rotational spectrum of an OCS molecule, under conditions where the collisional broadening dominates and when it is comparable with the Doppler broadening.

The need to unify an exact line shape required for various spectroscopic applications stimulated the development of a universal model which is described in detail in Ngo [2013]. The model has a quite simple mathematical form with the use of standard functions, which ensures fast numerical computations comparable with calculating the Voigt profile. By zeroing the model parameters responsible for different narrowing mechanisms, it may be reduced to a still simpler form, neglecting the corresponding mechanisms in the analysis of observable lines. The model is called the Hartmann-Tran profile (HTP), after the names of its authors. In 2014, the International Union of the Theoretical and Applied Chemistry recommended the model for wide practical application [Tennyson, 2014]. This means that in the future the optical diffusion parameters, the parameters of the speed dependence of collisional relaxation, and the correlation parameters will be tabulated in the spectroscopic databases together with the other parameters of molecular lines of atmospheric gases.

Collisional coupling of molecular lines

All of the above regarding resonant molecular lines relates to *isolated lines.* This does not mean that a line contour does not overlap with other line contours and the contribution of the wings of neighbouring lines to the observed absorption is negligible. Moreover, the isolated lines may be quite close to each other and even merge into one line, but if the resulting absorption profile corresponds exactly to the sum of the contours of individual lines, then these lines are called isolated.

The difference between the isolated and non-isolated lines appears when a molecule interacting with the field makes a collisional transition to the states in which it will continue its resonant interaction (remain coherent) with the field.

Let us consider two pairs of energy levels between which radiative (with emission or absorption of a quantum) and non-radiative transitions allowed by the selection rules can take place, as shown in fig. 1.13.

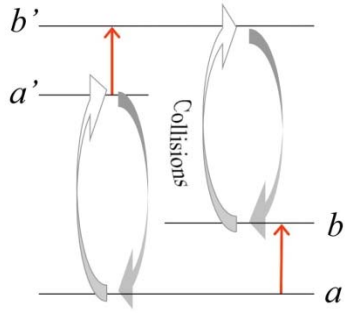

Fig. 1.13. An example of a pair of collisionally coupled molecular transitions. The allowed radiative and collisional transitions between the energy levels are shown by arrows.

The difference between the frequencies of the radiative transitions may be so large that at low pressures the contours of the corresponding lines do not overlap and, hence, the lines are isolated (fig. 1.14). We remind the readers that the energy level diagrams (fig. 1.13) change depending on the frequency of molecular collisions. The higher the collision frequency (the higher the pressure), the higher the energy uncertainty of each level, which means that the levels become thicker (1.57). With an increase in pressure, the levels eventually become so broad that the quanta with mean frequency of these two radiative transitions may be equiprobably absorbed by both transitions. In this case, the molecules may jump from level a to level b in two ways: 1) absorbing a quantum ν_{ab}, 2) making a collisional transition to level a', absorbing a quantum $\nu_{a'b'} = \nu_{ab}$ accompanied by the transition to level b' and making a subsequent collisional transition to level b. In other words, the molecules sitting at the level a can contribute to the radiation absorption with frequency $\nu_{a'b'}$ thanks to the collisional interaction with the neighbouring molecules. The situation is analogous for molecules sitting at the level a': they can affect quantum absorption ν_{ab} in a similar way. Under such conditions, the radiative transitions $a \rightarrow b$ and $a' \rightarrow b'$ cannot be regarded as isolated because of the population exchange between the transition levels which, as shown in section 1.2.1, are directly linked to the intensity of absorption lines. Such radiative transitions are collisionally coupled. Coupling of transitions entails the coupling of corresponding spectral lines.

Generally, the spectral intensity is borrowed from the periphery of a collisionally coupled spectral cluster (line doublet in the aforementioned model) to its centre. The effect comes into play when the lines overlap.

Even if the collisionally coupled lines are *resolved* (the number of lines is clear from the shape of the cluster), the absorption between them is higher than for the isolated lines and lower in the outer wings (the pair of the curves in the middle of fig. 1.14). This collisional effect has several names. It is called *collisional coupling*, line mixing, spectral exchange, or the line interference effect.

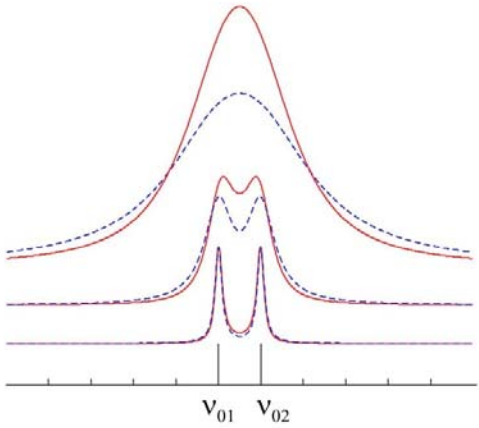

Fig. 1.14. The evolution of the absorption profile of collisionally coupled (solid curves) and isolated (dashed curves) lines at a successive 4-fold pressure increase.

A simple qualitative interpretation of the effect and the result of its manifestation in molecular spectra can be made using the example of a double-frequency oscillator in which the frequencies switch over from one to the other as a result of external action (collision), while the amplitude and phase of the oscillations remain unchanged (fig. 1.15). If the switching rate is low, i.e., the time between the 'collisions' is much longer than the period of oscillations, the spectrum corresponds to two overlapping lines at the frequencies consistent with the oscillator's frequencies. When the 'collision' rate becomes higher than the oscillation frequency, two sinusoids degenerate to a periodic function, the frequency of which is equal to the mean frequency of two initial oscillations. A further increase in the collision rate results in more harmonic oscillations at a mean frequency, that is, in spectrum narrowing. It should be emphasised that the oscillation phase is preserved. Without such phase continuity, the switching process is equivalent to the increase of collisional broadening of two isolated lines. This simple and meaningful model can be easily reproduced by the interested reader using a digital arbitrary wave function

generator (AWG). The result can be verified with a standard spectrum analyser.

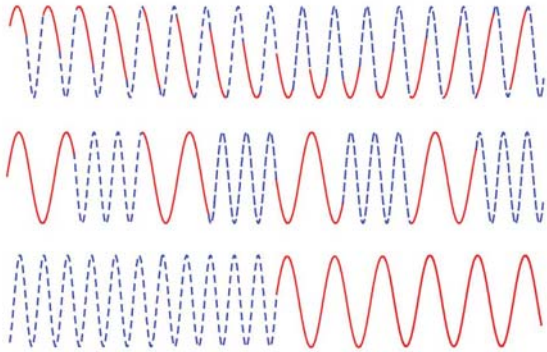

Fig. 1.15. Oscillations of a double-frequency oscillator without phase jumps during switching at a successive (upward) 4-fold increase of switching frequency (ν_{01} — solid curves, ν_{02} — dashed curves).

It is clear that the absorption lines of different molecules or isotopologues will not interfere. The principal condition for the effect to occur is allowed collisional transitions $a \rightarrow a'$ and $b \rightarrow b'$, i.e., the radiative transitions corresponding to them must be allowed by the selection rules.

Changes of the internal state of molecules on collisions were considered in detail in a series of works by Takeshi Oka [Oka, 1966, 1967, 1968; Lees, 1968; Daly, 1970], where it was demonstrated experimentally that the preferred collision-induced transitions predominantly follow the selection rule for the dipole radiative transitions. That is why the lines of *K*-multiplets of symmetric tops do not interfere with each other, even if the conditions of the experiment are such that all the lines of the multiplet merge into one [Tretyakov, 2008]. This occurs because of a small probability of collisional transitions between different *K*-sublevels of each *J*-state [Oka, 1968]. Under normal conditions, rotational lines with close frequencies belonging, for example, to different vibrational states will not interfere either. The energy level scheme in this case is exactly like in fig. 1.13, and all the transitions are allowed by selection rules. However, the probability of the collisional transition of a molecule to the excited vibrational state and back is negligibly small as the mean energy of thermal motion kT is usually much lower than the energy of vibrations.

A bright example of the interfering lines of atmospheric molecules in the millimetre and submillimetre wavelength ranges is the 60-GHz oxygen band formed by the lines of a ‘fine structure’ of rotational transitions of an

oxygen molecule [Van Vleck, 1947]. The fine structure appears because an oxygen molecule in ground electron state has a spin equal to 1. Therefore, according to the rule of summation of quantised angular momenta, the total momentum of a molecule at each fixed value of its orbital moment (characterising the molecule's rotation about the centre of mass) can have only three values corresponding to three possible orientations of the spin vector with respect to the orbital moment of the molecule. As a result, each rotational energy level of the molecule is split into three sublevels. At atmospheric pressure, the transitions between these sublevels form a broad band of merged lines with the centre near 60 GHz. As the transitions with the change of the molecule's orbital moment are also allowed, the coupling diagram looks similar to fig. 1.13, and all the lines of the fine structure are collisionally coupled and the observed profile of the absorption band differs strongly from the sum of the profiles of the lines belonging to it (fig. 1.16).

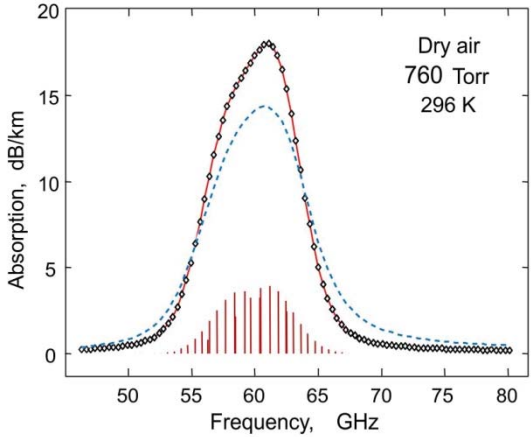

Fig. 1.16. The profile of a 60-GHz absorption band of oxygen in dry air. The circles correspond to the measurement data and the solid lines to the calculations taking into account the line interference effect. The dashed curve is the same spectrum calculated as a sum of lines neglecting interference. The vertical lines denote the positions and relative amplitudes of the lines forming the band. Adopted from Makarov [2013].

From the collisional nature of the effect, it follows that its manifestation is the more pronounced, the higher the gas pressure. In the paper by Rosenkranz [1975] it was shown that, for a relatively weak line coupling (this is fulfilled for the O_2 lines up to the atmospheric pressure), to the first approximation with respect to pressure, the influence of the

effect on the profile of a non-isolated collision-broadened spectral line may be taken into consideration by means of the parameter Y depending linearly on pressure:

$$I_c(\nu,\nu_0)=\frac{1}{\pi}\frac{\Delta\nu_c+Y\cdot(\nu-\nu_0)}{(\nu-\nu_0)^2+\Delta\nu_c^2},\quad Y=y\cdot p, \tag{1.92}$$

where y is the interference coefficient that is tabulated for each spectral line. In a somewhat more general form, this expression is used for taking into account collisional line coupling in all modern models of radiation propagation in the atmosphere.

An analogous, but a little more complex analytical expression for the line shape with allowance for the manifestations of the effect in the second order, with respect to pressure, was derived in the work of Smith [1981]. There are also more complex models that take into consideration line interference, which are based on a direct numerical solution of the basic equations describing the collisional interaction of molecules, rather than on a series expansion. The interested reader can find them in the monograph by Hartmann [2008] and the references therein.

The manifestation of the effect in the single line shape is equivalent to a linear antisymmetric distortion of the line shape relative to its centre. The distortion reaches its maximum at frequency detuning from the line centre approximately equal to the line collisional half width. That is at $(\nu-\nu_0)=\Delta\nu_c$. Under usual conditions the contribution of the line mixing effect to the line shape is significantly weaker than the contribution of coalitional line broadening. It follows from eq. (1.92) that in these conditions $Y\cdot(\nu-\nu_0)\ll\Delta\nu_c$, or $Y\ll 1$. Therefore, it may seem that the speed dependence of the line mixing effect can be thus neglected. However, the analysis of the magnitude of the latter effect in the 60-GHz oxygen band [Koshelev, 2021-1] shows its potential significance for strongly coupled lines such as the O_2 fine structure.

The manifestation of the effect of spectral exchange in the profile of the 60-GHz absorption band of oxygen will be addressed in more details in section 3.1.2.

1.2.3. Line shape parameters in gas mixtures

The shape of collision-broadened atmospheric lines should be analysed taking into account that the atmosphere is a mixture of a diverse range of gases. An average relative amount of its prevalent constituents is illustrated in fig. I.2 of the Introduction.

The radiation absorbing molecules that contribute to the spectral line intensity are called the *absorbers*. The molecules colliding with the absorbers that result in line broadening and shifting are called the *buffer molecules*. If the buffer and absorbing molecules are identical, the line is said to be studied under *self-broadening* conditions. Otherwise, we speak about broadening by buffer gases (sometimes referred to as the *foreign* gases).

If a molecule encounters only one partner at each collision (the *binary collision* approximation), then it can be considered that each gas constituent makes its own contribution to the collisional parameters of the studied line. So, for the width $\Delta\nu_c$ and central frequency shift $\nu_c - \nu_0$, the following relations hold true:

$$\begin{aligned} \Delta\nu_c &= \sum_i \gamma_i p_i, \\ \nu_c - \nu_0 &= \sum_i \delta_i p_i, \end{aligned} \tag{1.93}$$

where γ_i and δ_i are the coefficients of collisional broadening and shifting of the studied line of the i-th constituent of the gas mixture, and p_i is the partial pressure of this constituent in the mixture.

For the lines of water molecules that are the main absorbers of solar radiation and thermal radiation of the Earth, one can distinguish the contributions of self-broadening, self-shifting, dry air broadening, and shifting:

$$\begin{aligned} \Delta\nu_c &= \gamma_w p_w + \gamma_{air} p_{air}, \\ \nu_c - \nu_0 &= \delta_w p_w + \delta_{air} p_{air}, \end{aligned} \tag{1.94}$$

where γ_w, γ_{air}, and δ_w, δ_{air} are the coefficients of water line broadening and shifting under the conditions of self-pressure broadening and dry air pressure, respectively; p_w and p_{air} are the partial pressures of water vapour (absorbing gas) and dry air (buffer gas).

The coefficients of collisional broadening and shifting by air for atmospheric gases are tabulated in spectroscopic databases. As nitrogen and oxygen make the largest contribution to line broadening and shifting (all the other molecules of dry air constitute less than 1 % of its composition), γ_{air} and δ_{air} are often found from the relations

$$\begin{aligned} \gamma_{air} &= 0,79\gamma_{N_2} + 0,21\gamma_{O_2}, \\ \delta_{air} &= 0,79\delta_{N_2} + 0,21\delta_{O_2}, \end{aligned} \tag{1.95}$$

where γ_{O_2}, γ_{N_2} and δ_{O_2}, δ_{N_2} are the coefficients of water line broadening and shifting by nitrogen and oxygen pressure, respectively. A systematic error that may arise with the use of the expression (1.95) is different for different lines. Let us estimate this error for the 183-GHz diagnostic atmospheric line of water vapour using the experimental results obtained in Golybiatnikov [2005] and the known concentration of gas constituents of the Earth's atmosphere. Assuming the error of the parameter of line broadening by air calculated by the model (0.78084 N_2 + 0.209476 O_2 + 0.00934 Ar + 0.000314 CO_2 + 0.00003 Ne) to be zero, we find that a relative systematic error of broadening calculated by the simplified model (0.781 N_2 + 0.209 O_2 + 0.0096 Ar + 0.0004 CO_2) is +0.012 %. The use of the model (0.78 N_2 + 0.21 O_2 + 0.01 Ar) gives an error of –0.07 %, and the most commonly used model (0.79 N_2 + 0.21 O_2) corresponding to eq. (1.95) overestimates the broadening by 0.5 %.

1.2.4. Temperature dependence of line shape parameters

The qualitative manifestation of any collisional effect in line shape obviously depends on collision frequency. In an ideal gas at thermodynamic equilibrium at fixed pressure, the frequency of intermolecular collisions linearly depends on two factors: the molecular concentration and the speed of their translational motion. The concentration is inversely proportional to the gas temperature ($\sim T^{-1}$), and the speed is directly proportional to the square root of temperature ($\sim T^{0.5}$). Thus, the collision frequency is proportional to $T^{-0.5}$.

The collision of real molecules resembles a fast convergence of two quite dynamic nonrigid systems comprising a large number of oppositely charged particles. The result of their collision depends on the impact parameter, mutual orientation of these multiparticle molecules, as well as on their internal energy states that are most likely different, even for identical partners. Besides, the variety of populated energy states may change substantially depending on temperature. As a result, the cross section of the collisional interaction of molecules depends on the state and the speed of the absorber (section 1.2.2). That is, for the same collision frequency, the interaction cross section may be different for different temperatures. The exponent of the temperature dependence of collisional parameters in this case may differ significantly from the classical gas-kinetic value of –0.5. For example, for water molecule lines in ground vibrational state at frequencies up to 3 THz, the exponent of the broadening parameter temperature dependence by air pressure varies from –0.21 to –0.83, being –0.57 on average [Gordon, 2017].

For modelling absorption, the temperature dependence of collisional parameters is taken into consideration using the power functions. For broadening and shifting they have the following form

$$\gamma(T) = \gamma(T_0) \cdot \left(\frac{T_0}{T} \right)^{n_\gamma}, \qquad \delta(T) = \delta(T_0) \cdot \left(\frac{T_0}{T} \right)^{n_\delta}, \tag{1.96}$$

where $\gamma(T_0)$ and $\delta(T_0)$ are the values of the corresponding parameters at a given temperature T_0.

Such functions are the simplest approximations of real dependences in the vicinity of T_0. The exponents of temperature dependence are assumed to be positive in most cases, at least for pressure broadening. The largest amount of experimental data about line parameters was obtained in some interval around room temperature. That is why $T_0 = 300$ K in the majority of the propagation models. The theoretical analysis of the accuracy of such approximation at different deviations from T_0 was presented in work by Gamache [2009], where broadening of water vapour rotational lines by air was considered. It was shown that the expression (1.96) works rather well within the 30—50 K deviation from T_0, which is sufficient for atmospheric applications of spectroscopy in most cases. Note that a significant deviation of the behavior of the line shape parameters from eq. (1.96) can occur when considering temperature ranges of hundreds and thousands of Kelvins [Gamache, 2018].

It should be noted that the collisional line parameters and their temperature exponents are different for different buffer gases and vary from line to line, even if these lines correspond to the transitions of the same absorbing molecule.

Note that the information currently available on the temperature dependence of line frequency shifts by pressure is still very limited. For estimating the parameter n_δ one can use approximate theoretical considerations suggested in the work by Pickett [1980-1]. They are based on the fact that the speed dependence of the interaction cross section can be roughly approximated by a power function, and the temperature dependence of thermal speed is known. It should be kept in mind that only the relative speed of colliding molecules was taken into consideration, whereas the variation of their mutual orientation during the interaction (anisotropy of the interaction potential) was neglected. Under these approximations, the temperature dependence of the shifting parameter is related to the temperature dependence of broadening as $n_\delta \sim 1.5 n_\gamma + 0.25$,

i.e., shifting must have a stronger temperature dependence than broadening. For example, if n_γ is within the 0.6—0.8 interval, n_δ must be within the 1.15—1.45 interval. Taking into consideration the qualitative nature of this approach and absence of appropriate experimental data, the temperature dependence of the shifting parameter can be regarded to be not less than the temperature dependence of the broadening parameter, and unknown n_δ can be estimated using n_γ.

The approach using eq. (1.96) works if the line shift does not change its sign. The possibility of changing the sign of the pressure shift with the variation of temperature was predicted theoretically in Frost [1976] and observed in experiments in Baldacchini [1996] and Koshelev [2021]. In such cases, eq. (1.96) is not applicable, and more complex equations are proposed in Gamache [2018].

The temperature dependence of the line intensity of any molecule is determined primarily by populations of the upper and low transition levels (section 1.2.1). The dependence of the intensity on the energy of the low level and on the difference in the populations of the upper and low levels is generally applicable for all molecules and obeys the Boltzmann distribution. Note that the population difference factor is actually calculated through the energy of a quantum of resonance radiation. The temperature dependence of the partition function is another intensity influencing factor. It is slightly different for molecules of different types (see, for example, Townes [1955]). With this taken into account, neglecting low population of excited vibrational states, which is a rather good approximation for the majority of atmospheric molecules at normal temperatures, and making use of the fact that $h\nu << kT$ in the millimetre and submillimetre ranges, from (1.41) we obtain the following expression for line intensity:

$$S_{ab}(T) = S_{ab}(T_0)\left(\frac{T_0}{T}\right)^x \exp\left(\frac{E_a}{kT_0}\left(1-\frac{T_0}{T}\right)\right), \qquad (1.97)$$

where E_a is the energy of the low level, $x = 2$ for diatomic and linear molecules, and $x = 2.5$ for symmetric and asymmetric tops. This equation suits most of the spectroscopic applications based on the microwave technique. However, we should note that x includes the temperature dependence of the partition sum, which can vary within different temperature ranges. The corresponding corrections for most atmospheric molecules can be found using the partition sums theoretically calculated from 1 up to thousands of Kelvins [Gamache, 2017].

1.2.5. Some features of the shape of broad atmospheric lines

The shape of the collision-broadened line (1.79) was first suggested by Lorentz [1906], who believed that the state of molecules' distribution after collision is random. The Lorentz profile is derived under the impact approximation $\Delta\nu_c << \nu_0$.

A more accurate expression, which is more relevant for analysing broad atmospheric lines in the longwave part of the electromagnetic radiation spectrum, including the millimetre and submillimetre ranges, was derived by Van Vleck and Weisskopf [Van Vleck, 1945]. They noted that for the lines with $\Delta\nu_c \sim \nu_0$, the contribution of resonance at a negative frequency ($-\nu_0$) obtained from the solution of the equation of a damped harmonic oscillator is not negligibly small. So, the expression

$$I_c^{FL}(\nu,\nu_0)=\frac{1}{\pi}\left(\frac{\Delta\nu_c}{(\nu-\nu_0)^2+\Delta\nu_c^2}-\frac{\Delta\nu_c}{(\nu+\nu_0)^2+\Delta\nu_c^2}\right), \quad (1.98)$$

usually referred to as the *full Lorentz profile* is more correct for the collision-broadened line.

Besides, Van Vleck and Weisskopf took into account that, after each collision, the distribution of molecules corresponds to Boltzmann's distribution. The resulting line profile satisfying the normalisation condition (1.53) differs from the Lorentz profile mainly by the ν/ν_0 factor:

$$I_c^{VW}(\nu,\nu_0)=\frac{1}{\pi}\frac{\nu}{\nu_0}\left(\frac{\Delta\nu_c}{(\nu-\nu_0)^2+\Delta\nu_c^2}+\frac{\Delta\nu_c}{(\nu+\nu_0)^2+\Delta\nu_c^2}\right). \quad (1.99)$$

When modelling the profile of broad lines, it should be taken into consideration that the radiation quantum energy $h\nu_0$ that enters the tabulated integrated line intensity (1.41) cannot be regarded as constant, as the radiation frequency within the line contour changes markedly. Therefore, the multiplier ν/ν_0 also appears in the frequency dependence of the absorption coefficient (1.53):

$$\alpha_{line}(\nu)=\alpha_{ab}\frac{\nu}{\nu_0}I(\nu,\nu_0). \quad (1.100)$$

Let us also briefly mention the line profile obtained from the gas-kinetic equation:

$$I_c^G(\nu,\nu_0)=\frac{1}{\pi}\frac{4\nu^2\Delta\nu_c}{\left(\nu^2-\nu_0^2\right)^2+4\nu^2\Delta\nu_c^2}. \qquad (1.101)$$

This profile was derived by Gross [1955] under the impact approximation for lines of a purely rotational spectrum for which the energy of an absorbed quantum is small compared to the thermal energy, i.e., $h\nu << kT$. The profile proposed by Gross automatically took into account the additional frequency factor (1.100). This profile was frequently used for modelling atmospheric lines until the analysis of accurate experimental data demonstrated apparent advantages of the Van Vleck–Weisskopf profile [Hill, 1986] (see also section 3.1.2).

A more general case of line shape was proposed by Van Vleck and Huber [Van Vleck, 1977]. They showed that the Boltzmann distribution of molecules and balance between the absorbed and emitted radiation quanta per unit time should be taken into consideration. Additionally, there are other necessary conditions such as:

a) the ratio of the real and imaginary parts of the refractive index of gas (the Kramers–Krönig relation),

b) the *sum rule* according to which after collision the molecule can pass only to the existing energy levels,

c) under equilibrium conditions, a heated gas shall radiate according to the Planck formula for the *black body radiation*.

Equations for the absorption coefficient are derived using the autocorrelation function of the molecule's dipole moment (see section 1.2.2). The absorption coefficient normalised to the number of absorbing molecules is then written (omitting the minor constants depending on the system of units) in the form

$$\alpha(\omega) \propto \omega\left(1-e^{-\frac{\hbar\omega}{kT}}\right)F(\omega)\,,$$

where the first multiplier ω is related to the energy of radiation quantum, the second multiplier $\left(1-e^{-\frac{\hbar\omega}{kT}}\right)$ corresponds to the difference of populations of the upper and lower transition levels, and the third one $F(\omega)$ is the *spectral function* that is a Fourier image of the autocorrelation function of the dipole moment:

$$F(\omega)=\frac{1}{2\pi}\int_{-\infty}^{\infty}dt\,e^{-i\omega t}\langle\mu(0)\mu(t)\rangle\,,$$

where <…> denotes ensemble averaging.

The spectral function shall satisfy the relationship that is sometimes referred to as the principle of *detailed balance* between emitted and absorbed radiation:

$$F(-\omega) = F(\omega)e^{-\frac{\hbar\omega}{kT}},$$

which means that the probability of the stimulated transition from the lower to the upper level is $e^{\hbar\omega}$ times higher than the probability of the reverse transition. This can be taken into consideration by introducing the so-called *symmetrised spectral function*

$$F^s(\omega) = \frac{1}{2}\big(F(\omega) + F(-\omega)\big) = \frac{1}{2}\left(1 + e^{-\frac{\hbar\omega}{kT}}\right)F(\omega).$$

From this follows

$$F(\omega) = \frac{1}{\left(1+e^{-\frac{\hbar\omega}{kT}}\right)}\,F^s(\omega).$$

The substitution of this spectral function into the expression for the absorption coefficient yields

$$\alpha(\omega) \propto \omega\frac{\left(1-e^{-\frac{\hbar\omega}{kT}}\right)}{\left(1+e^{-\frac{\hbar\omega}{kT}}\right)}\big(F(\omega) + F(-\omega)\big) = \omega\ \mathrm{th}\left(\frac{\hbar\omega}{2kT}\right)\big(F(\omega) + F(-\omega)\big).$$

The autocorrelation function of the dipole moment of a molecule in simplest cases, such as a strongly rarefied gas or an ideal gas subject to Brownian motion, has analytical expressions that are clear from simple considerations (see, for example, Buldyreva [2011]). The corresponding spectral functions are the Doppler (1.71) and the Lorentz (1.79) profiles considered in section 1.2.2. This means, in particular, that a general expression for the shape of broad collision-broadened atmospheric lines is written as

$$\alpha_{line}(\nu) = \alpha_{ab}R(\nu)\frac{1}{\pi}\left(\frac{\Delta\nu_c}{(\nu-\nu_0)^2+\Delta\nu_c^2} + \frac{\Delta\nu_c}{(\nu+\nu_0)^2+\Delta\nu_c^2}\right), \qquad (1.102)$$

where

$$R(\nu) = \frac{\nu}{\nu_0}\frac{\tanh(h\nu/2kT)}{\tanh(h\nu_0/2kT)}. \qquad (1.103)$$

The expression (1.102) is universal for all wavelengths of electromagnetic radiation, it automatically transforms from the Van Vleck–Weisskopf form at $h\nu << kT$ to the Lorentz form at $h\nu >> kT$; and $R(\nu)$ is referred to as the *radiation term*.

1.2.6. Absorption modelling in a broad spectral range

The result of modelling an isolated resonant line using different profiles is presented in fig. 1.17. The parameters set in the model correspond approximately to the parameters of a hypothetic water vapour line at the frequency of 2000 GHz in the atmosphere under normal conditions. The following notion is taken for the profiles: the Van Vleck–Weisskopf profile (1.99) — VVW, solid curve; the truncated Van Vleck–Weisskopf profile (1.105) — VVW^{cut}, dotted curve; the Lorentz profile (1.79) — L, dashed curve; and the Gross profile (1.101) — GR, dash-dot curve (it coincides with the Lorentz profile in its full form (1.98). All the profiles take into account the relation (1.100). The dimensionless reduced frequency ν/ν_0 and the reduced absorption $\alpha(\nu)/\alpha(\nu_0)$ are used for the abscissa and the ordinate axes, respectively.

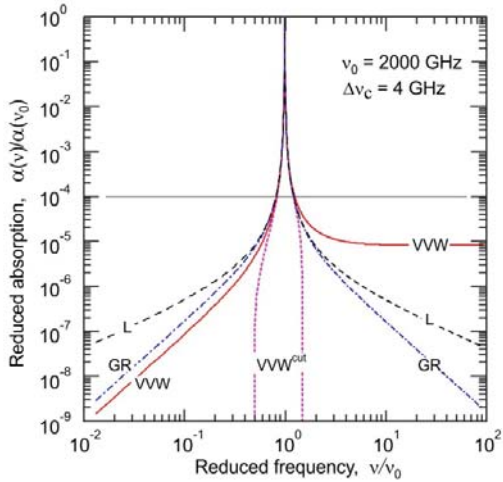

Fig. 1.17. Comparison of the collisional profiles of a resonant molecular absorption line in a broad frequency range.

All the profiles virtually coincide within approximately 20 % of the frequency detuning from the line centre ($0.8\nu_0 < \nu < 1.2\nu_0$), or until the absorption becomes less than 0.01 % of the maximum one. Significant

differences appear only in the far wings of the lines. For example, a slowly decaying high-frequency wing, that becomes constant at large detunings from the centre, and a low-frequency wing decaying faster than the other profiles, are typical for the Van Vleck–Weisskopf profile (1.99). At detuning from the line centre to the low-frequency region, the difference between the Lorentz and the Van Vleck–Weisskopf profiles grows rapidly and reaches an order of magnitude in the middle of the millimetre range (100 GHz, relative detuning ~70 %). This highlights the problem of broadband modelling of gas spectra. Questions arise about the adequacy of describing the resonant absorption of different models at different frequency detunings from the line centre, and the detuning at which the line wing should be considered as non-resonant absorption.

These issues are directly related to the validity range of the impact approximation used in the derivation of the resonant line shape by Lorentz, Van Vleck with Weisskopf and others, who theorised that the collision (breakdown of the oscillation train of a molecule-oscillator) occurs instantaneously. In fact, the collision may be considered as an impulse action of the field of one molecule on the other. The result of this action is a growing distortion of harmonic oscillations performed by the molecule before it 'feels' the approaching partner, which will finally restart the oscillator. It is hard to predict a spectral line shape of a molecule-oscillator with allowance for such action. It depends on many factors, including collisional parameters (relative speed, impact parameter), spatial configuration, and the internal energy of colliding partners. Nevertheless, it is clear that characteristic distinctions in line shape will appear in the far wings at a large frequency detuning from the centre determined by the duration of the action, which is approximately equal to the duration of the collision, τ_c. Thus, the profile obtained under the impact approximation is valid only near the line centre and for its near wings (within *line core*) in the frequency range meeting the condition

$$\left|\nu - \nu_0\right| << \frac{1}{2\pi\tau_c}. \qquad (1.104)$$

The fact that classical line shapes are inadequate and far wings need to be corrected was first revealed in the analysis of the experimentally observed absorption in the wings of carbon dioxide (see Winters [1964] and references therein). The development of relevant theoretical models can be traced, for instance, in work by Galtsev [1978] and in the references given there. It was shown, in particular, that the exponential decay of the line's far wing is connected with the duration of collision. Different aspects of modelling far wings of water vapour lines for

atmospheric applications were addressed in works by Clough [1980; 1989].

The qualitative behaviour of the far wings of a line can be demonstrated on a classical example of a molecule-oscillator interacting with external force (Appendix A2). If a collision is supposed to be non-instantaneous, the frequency dependence of a line wing will differ from $1/\nu^2$ typical for the Lorentz's wing. If the molecule-oscillator perturbation is increasing smoothly (i.e., the train of oscillations is decaying smoothly), the decay of the wing becomes exponential. If the perturbation has a non-monotonous behaviour, for example, the oscillations caused by molecular rotation with a period shorter or comparable with the duration of the collision, the far wing of the line will rise a little, relative to the Lorentz analogue at the detuning frequency equal to the frequency of these oscillations. The wing rise will inevitably be followed by an exponential decay at a larger detuning, as in the case of a smooth monotonous increase of the perturbation. From this it follows that, starting with a definite frequency detuning from the centre, the line wing calculated within the impact approximation should be corrected and will then break exponentially at detuning $\nu \sim (2\pi\tau_c)^{-1}$.

Despite the significant efforts made, the calculation of the far wing line shape is still one of the main problems to be solved in molecular spectroscopy. The known theoretical models, for example Tvorogov [1995] or Bogdanova [2010], are very sophisticated and too many empirical parameters are required for their application. *Ab initio* calculations are not available yet. For this reason, for the contribution of resonant lines to be taken into account, a simple 'truncated' line shape, in which the far wings of the line are cut at the frequency ν_{cut} (*cutoff frequency*), proposed in the work by Clough [1989], is often used in radiation propagation models. To avoid jumps of absorption in the modelled spectrum, the line is cut not only from the 'sides' but also from the 'bottom', so that at the detuning exceeding the cutoff frequency, the line absorption is considered to be zero. For example, a truncated Van Vleck–Weisskopf profile has the form

$$I_c^{VWcut}(\nu,\nu_0) = \frac{1}{\pi}\frac{\nu}{\nu_0}\left(I_c^{cut}(\nu,\nu_0) + I_c^{cut}(\nu,-\nu_0)\right),$$

$$I_c^{cut}(\nu,\nu_0) = \begin{cases} \dfrac{\Delta\nu_c}{(\nu-\nu_0)^2+\Delta\nu_c^2} - \dfrac{\Delta\nu_c}{\nu_{cut}^2+\Delta\nu_c^2}, & \text{for} \quad |\nu-\nu_0| \le \nu_{cut} \\ 0, & \text{for} \quad |\nu-\nu_0| > \nu_{cut} \end{cases} \tag{1.105}$$

For $\nu_{cut} \to \infty$, the truncated profile transforms to the initial one. The remaining part of the line profile after truncation ('pedestal' or 'plinth') is considered to be a non-resonant absorption that is modelled separately.

Note that, strictly speaking, the truncated line shapes do not satisfy the normalisation condition (1.53). The area under the truncated curve is always less than unity, i.e., this model of the spectrum will systematically underestimate resonant absorption. To minimise this error, the magnitude of the cutoff frequency is increased as much as possible. For example, $\nu_{cut} = 25$ cm^{-1} (or 750 GHz) is currently used for the water vapour lines in models of radiation propagation in the atmosphere [Clough, 1989; Rosenkranz, 1998]. The use of the truncated profile (1.105) with such a cutoff frequency for modelling, e.g., a water vapour line in the atmosphere leads to a loss of approximately 0.5 % of integrated intensity. It is of no practical significance for one line but may result in pronounced differences when modelling resonant absorption in a vibration-rotation spectral band. Recall that the cutoff frequency is directly related to the duration of collision and the aforementioned value of 25 cm^{-1} is equivalent to the case when H_2O molecule moving at an average thermal speed at room temperature propagates a distance of approximately ~1.8 Å. This is a little more than the characteristic geometric size of the (H_2O) molecule (~1.4 Å), but less than the radius of the excluded volume (~2.5 Å) and significantly less than the radius of the effective collisional cross section determined by the spectroscopic methods (~10 Å). This indicates that the used magnitude of the cutoff frequency may be somewhat overestimated.

1.3. Non-resonant absorption

Non-resonant absorption was first discovered in studies of infrared radiation absorption by water vapour. The studies were initiated in the 19-20th centuries and were aimed at exploring solar light transmission through the atmosphere [Tyndall, 1861]. Later it was found that, although water vapour constitutes only less than 0.5 % of the atmospheric mass, it is responsible for approximately 70 % of the radiation absorbed by the atmosphere and is the main constituent affecting the global energy budget (see, for example, Kiehl [1997]; Trenberth [2009]; L'Ecuyer [2015] and references therein). Moreover, water vapour is the principal atmospheric green-house gas with positive feedback that determines the weather and influences the climate of the Earth [Held, 2000].

The water molecules that make up atmospheric water vapour absorb radiation in all ranges from the microwave to the ultraviolet and beyond. This absorption occurs primarily due to the resonant spectral lines

corresponding to the molecular transitions to high rotational and vibrational energy levels. These lines are rather intense because a water molecule, despite its small mass, has a large permanent dipole moment. As this molecule is a light and highly nonrigid asymmetric top, its resonant lines are distributed quite uniformly throughout the range of electromagnetic waves. Nevertheless, the absorption spectrum of water features intense bands which, at low resolution, resemble a nearly periodic sequence of peaks diffusing with increasing frequency (fig. 1.18). These bands correspond to different vibrational modes of the molecule, i.e., to the nuclei movements resulting in stretch-shrink of the O—H bonds and change of the angles between them. The quasi-periodicity of the bands is explained by closeness of the frequencies of two of the three possible fundamental vibrations (symmetric $\nu_1 = 3657$ cm^{-1} and asymmetric $\nu_3 = 3756$ cm^{-1} stretching of O—H bonds) and approximately half the value of the frequency of the third deformation vibration corresponding to the change of the angle between the bonds $\nu_2 = 1595$ cm^{-1}. Each band consists of thousands of individual resonant vibration-rotation lines that are narrow (~ 0.1 cm^{-1}) under atmospheric conditions.

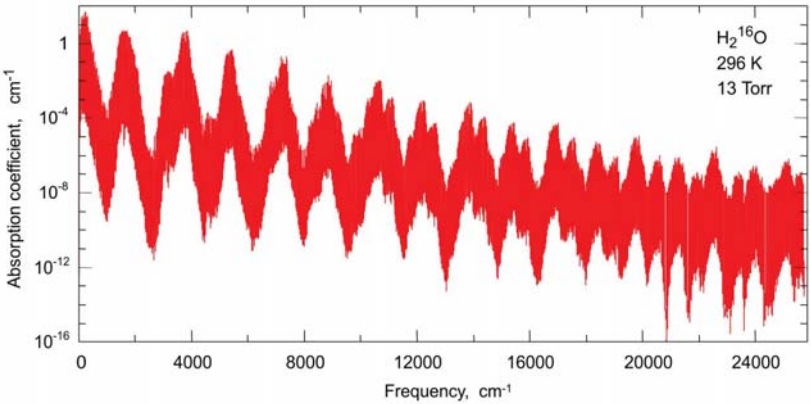

Fig. 1.18. The absorption spectrum of water vapour calculated using the HITRAN database [Gordon, 2017] for the main isotopologue.

These bands were observed at the end of the 19th century (see, for example, Rubens [1898]). In 1932, Brunt in his work [1932] noted that the spectrum looked as if the bands were arranged 'on a background of continuous absorption'. Such 'excess absorption' between the bands was mentioned approximately at the same time in the works by Elsasser [1938-1; -2], and a little later, in the middle of the 20th century it was revealed

that it is also present inside the bands appearing in the gaps between resonant lines [Van Vleck, 1947; Zhevakin, 1963]. Despite the development of increasingly more accurate resonant line shapes, this absorption did not find an explanation. In view of the smooth frequency dependence, it was called the *continuum absorption*, or just the continuum. In a broad spectral range, the water vapour continuum looks like a small base visible only on logarithmic scale, with a shape resembling the spectrum envelope on which resonant lines are arranged. Resonant absorption in the band centres can surpass the continuum by more than three orders of magnitude. In the gaps between the lines, however, this difference is much less. For example, in the *transparency microwindows* of the atmosphere in the millimetre wavelength range, the contribution of the continuum may even exceed the contribution of resonant lines by an order of magnitude.

The discrepancy between the data of observations and the models for the calculation of the energy balance of the Earth was the main headache of climatologists for several decades at the end of the 20th century (see, for example, Ramanathan [1997]). The 'anomalous' absorption of solar radiation by the atmosphere estimated at the end of the 1990s by data of numerous ground-based, airborne, and satellite stations amounted to 25—30 W/m^2, which greatly exceeded the needed accuracy of modelling [Ramanathan, 1997]. A major part of this value seemed to be due to a clear atmosphere [Arking, 1996].

The nature of the continuum has been actively discussed since its discovery, and the discussions are continued up to now (see, for example, the survey by Shine [2012], the work by Birk [2020] and references therein).

The explanation of the continuum by a large amount of unknown low-intensity resonant lines of a water molecule was debated by researchers in the 1940s [Strong, 1941; Cowling, 1942]. This explanation was fully rejected only recently, when modern methods of global computation of vibration-rotation spectra from first principles predicting all possible lines and bands, including those that have not been measured yet, almost reached experimental accuracy for the water molecule [Polyansky, 2012].

The hypothesis that the accumulated far wings of intense resonant lines are responsible for the continuum was first put forward by Elsasser [1938-1]. The hypothesis became popular because the traditional Lorentz and Van Vleck–Weisskopf line shapes were derived in the collision approximation, in which the duration of the collision τ_c is assumed to be negligibly small compared to the time between the collisions and, hence, these shapes are valid only at detuning from the central line frequency

much less than $(2\pi\tau_c)^{-1}$. So, the far line wings behaviour is uncertain. Some conclusions on the contribution of the far wings of resonant lines can be made on the basis of the calculations of absorption in the quasi-static approximation, assuming that during collision an absorbing molecule is in a permanent field of the other molecule. This approximation is valid only for a short instant of collision duration, so it allows for judgement on the absorption at the detuning from the central line frequency much larger than $(2\pi\tau_c)^{-1}$. Such calculations of water vapour were first performed by Rosenkranz [1985, 1987] and were further developed by Ma and Tipping in 1990-2008 ([Ma, 2008] and references therein). They are in satisfactory agreement with the observed continuum between the rotation-vibration bands but underestimate the absorption within the bands. A more accurate estimate of the wing contribution could be made on the basis of *ab initio* calculations of line shape. However, despite a substantial progress in this field, such calculations are currently possible only for small frequency detunings from the line centre (see, for instance, Hartmann [2013], Thibault [2020]).

1.3.1. Empirical description of the continuum

There is no reliable physical approach that would explain all known properties of the continuum. Therefore, for the continuum to be taken into consideration, all present-day models of radiation propagation in the atmosphere use empirical formulas, the parameters of which are determined experimentally. The problem is that the continuum cannot be measured directly. The currently accepted formal definition of the continuum absorption is written as

$$\alpha_{continuum} = \alpha_{total} - \sum \alpha_{lines}. \qquad (1.106)$$

The characteristic feature of this expression is that α_{total} is the measured quantity, whereas the continuum is all that remains after deduction from this quantity of the total calculated contribution of all resonant lines contributing to the measured absorption. The choice of the number of considered lines, their shape and parameters begin to play an important role as this directly influences the value of the obtained continuum. The uncertainty of the cutoff frequency of the resonant line wing considered in section 1.2.6 also affects the result. Thus, the obtained continuum is unambiguously related to the resonant absorption model used for its deduction from the total absorption.

Different empirical models are used for parametrisation of the continuum. Consider, as an example, the empirical model proposed by

Liebe [1984-1] for modelling the humidity-related continuum in the millimetre wavelength range. The model is constructed on the assumption that the continuum originates from the far wings of the water vapour resonant lines, located far beyond the range of consideration. In pure gas, the absorption coefficient in the far low-frequency wing of a collision-broadened line (eq. (1.102)) depends quadratically on frequency and is directly proportional to the Lorentz half-width $\Delta\nu_c$ that is directly proportional to pressure p (1.83) and to molecules' concentration n (1.41), that is also directly proportional to pressure. Therefore, the absorption can be represented as

$$\alpha_c(\nu, T) = C(T)p^2\nu^2, \tag{1.107}$$

where C is the temperature-dependent function found empirically. When modelling absorption in a mixture of two gases, one should take into account the relation (1.93):

$$\alpha_c(\nu, T) = \left(C_s(T)p_s + C_f(T)p_f\right)\cdot p_s\cdot\nu^2, \tag{1.108}$$

where C_s and C_f are the empirical functions corresponding to self-broadening and to broadening by foreign gas pressure, and p is the partial pressure. Taking into consideration the temperature dependence of broadening (1.96) and of line intensities (1.44), and keeping in mind that foreign gas can also possess resonant and continuum absorption we obtain

$$\alpha_c(\nu, T) = \left(C_{ss}p_{ss}^2\left(\frac{T_0}{T}\right)^{x_{SS}} + C_{fs}p_f p_s\left(\frac{T_0}{T}\right)^{x_{fs}} + C_{ff}p_f^2\left(\frac{T_0}{T}\right)^{x_{ff}}\right)\cdot\nu^2, \tag{1.109}$$

where C and x are the coefficients found empirically. The part of the temperature dependence of the absorption related to the line intensity $\alpha \sim T^{-3}$ ((1.44), with allowance for $n = p/kT$), is often written as a separate multiplier

$$\alpha_c(\nu, T) = \left(C_{ss}p_{ss}^2\left(\frac{T_0}{T}\right)^{x_{SS}} + C_{fs}p_f p_s\left(\frac{T_0}{T}\right)^{x_{fs}} + C_{ff}p_f^2\left(\frac{T_0}{T}\right)^{x_{ff}}\right)\cdot\left(\frac{T_0}{T}\right)^3\cdot\nu^2. \tag{1.110}$$

In compliance with this expression, in a particular case related to continuum parametrisation in the atmosphere, where the absorption in water vapour plays a dominant role ($s = H_2O$, $f = O_2 + N_2$), we speak about the component of the continuum with quadratic dependence on humidity,

with linear dependence on humidity, and the humidity-independent component, or the 'dry' continuum.

The second most known approach to the empirical description of the continuum is also based on the assumption that the continuum is a result of the unknown behaviour of the far wings of resonant lines. It is not limited to the millimetre and submillimetre waves and is used in the infrared region where far wings of the lines located higher or lower than the considered range can contribute to absorption. This approach is a logical continuation of the application of a truncated resonant line profile. The total absorption in the line is regarded to be a sum of the truncated profile (1.105) and the corrected pedestal remaining after cutting the Lorentz profile. An empirically determined χ-*function,* that is the function of frequency detuning from the line centre, is used for correction [Clough, 1989; Mlawer, 2012]. In fact, the function determines the shape of resonant line wings when the detuning from its centre is of the order of the cutoff frequency ν_{cut}. The function has variable parameters, which allow for the increasing or decreasing line wing decay as compared to the Lorentz wings of the pedestal (fig. 1.19). The parameters are regarded as the same for all lines. More details about the advantages and drawbacks of this method can be found in the monograph by Hartmann [2008]. Note that it is the only available approach that takes into account the contribution of line far wings to non-resonant absorption within the vibration-rotation bands in molecular spectra.

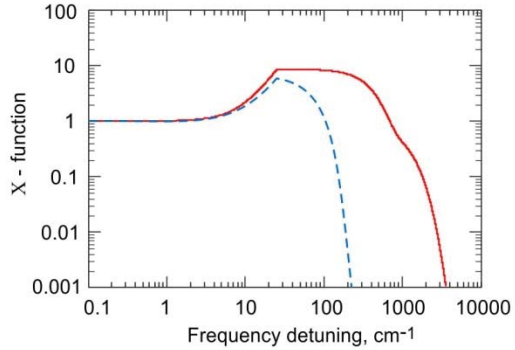

Fig. 1.19. The empirical functions of correcting far wings of water vapour resonant lines at self-broadening (solid curve) and at broadening by air (dashed curve) [Clough, 1989].

The drawback, common to all empirical models, is that they are reliable only in the region of parameters for which accurate experimental

data is available. Sufficiently good prediction accuracy may be expected in the case of interpolation of the results of measurement. The larger the interpolation range, the worse the prediction. It is not guaranteed that an empirical model will give correct results when the calculations are extrapolated to unexplored regions.

Besides, when an empirical model of the continuum is used, it is important to take into consideration the relationship between its coefficients and the model of resonant absorption. Otherwise, for example, valid correction of resonant line parameters in the used absorption model may worsen its agreement with the observed total absorption. Any change in the parameters responsible for resonant absorption should be accompanied by overdetermination of the coefficients of the empirical continuum.

It should be emphasised that all these problems arise because of the absence of adequate, physically justified, standard models of non-resonant absorption, including the models of resonant line far wings. Given such models, resonant and non-resonant absorption would be much more independent. For clarity, in this work the term *resonant absorption* is understood as the absorption in the vicinity of the central frequency of the spectral line. *Non-resonant absorption* is supplementary to resonant absorption, arising as a result of the interaction between molecules. *The continuum* is the empirically measured absorption (1.106), in which part of the resonant absorption, as well as the non-resonant absorption, may be present due to inaccurate determination of its components.

Since the interaction of two colliding molecules is the most likely cause of the problems in absorption modelling, the construction of a physically justified model of the continuum demands careful analysis of the processes occurring during collisions. In section 1.2.6 we have shown that the interaction of a molecule-absorber with a collision partner may be one of the mechanisms responsible for non-resonant absorption. In the next section, we will demonstrate that collisional interaction entails new phenomena causing non-resonant absorption and will consider the fundamentals of modelling the corresponding spectra.

1.3.2. Bimolecular absorption as the result of collisional interaction

Investigations into molecular interaction have a longstanding history (see, for example, Hirschfelder [1954] and Kaplan [2006]). Its ancient sources can be traced back to the philosophical epic ‘On the Nature of Things’ (‘De Rerum Natura’) written by Titus Lucretius Carus (99 BC– 55 BC). Isaac Newton (1643—1727) put forward the hypothesis on the

electromagnetic nature of the interaction of atoms. The Croatian scientist Rudjer Boskovic (1711—1787) developed the idea that all phenomena in gases arise from the spatial patterns of identical point particles (puncta) interacting in pairs according to an oscillatory law that determines their relative movement. The oscillating force increases up to infinity as particles approach each other and transforms into Newtonian attractive force at large distances. The forces acting between neutral atoms and molecules are called the Van der Waals forces. This is directly linked to Van der Waals' derivation in 1869 of the equation of state, taking into account the attraction between molecules as well as the finiteness of their volume, which according to today's level of knowledge, implies the appearance of significant intermolecular repulsive forces at a strong gas compression.

A self-consistent theory of intermolecular forces started to emerge after the creation of quantum mechanics. An approximate solution of the Schrödinger equation for the motion of an electron in the field of stationary nuclei makes it possible to find the dependence of the energy of the system on the distance between nuclei. In the simplest case of a diatomic molecule, this dependence is a characteristic curve (fig. 1.5) with a positive abscissa and ordinate semi-axes as asymptotes, and the minimum corresponding to the equilibrium internuclear distance, i.e., the balance of repulsion and attraction forces. This energy is potential energy for nuclei motion, or simply the *potential*. The interaction potential of two molecules is obtained analogously. A curve for the potential energy versus the distance between molecules' centres of mass should be determined for each fixed mutual orientation of the molecules. The intermolecular *interaction potential* is thus a multidimensional surface.

A simple approximate analytical expression for the intermolecular interaction potential explaining diversity of the experimental data on gas-kinetic properties of many gases was proposed by Lennard-Jones [Jones, 1924-1, -2], who is regarded to be the father of modern quantum chemistry. He conjectured that both the repulsive and the attractive parts of the interaction potential are the inverse power functions of intermolecular distance:

$$U(r) = 4D_e\left[\left(\frac{r_e}{r}\right)^{12} - \left(\frac{r_e}{r}\right)^{6}\right], \qquad (1.111)$$

where D_e is the depth of the potential well, r is the intermolecular distance, and r_e is the distance at which the interaction energy is equal to zero (equilibrium distance).

The Lennard–Jones potential is determined only by the distance between the interacting molecules and is independent of their mutual orientations, i.e., it is spherically symmetric (isotropic). Therefore, it is best suited for describing the interaction of symmetric nonpolar molecules, for example, inert gases. Nevertheless, this potential is frequently used for assessing the quantities related to the collisional interaction of molecules of all types.

For better understanding of the pair collisional interaction of molecules and its relation to nonideality of gases it is useful to get acquainted with the key work in this field, namely Storgyn [1959], where collisions of structureless monomers are analysed. The extension and subsequent generalisation of this work to the collisional interaction of nonpolar-polar and polar-polar molecules, as well as the interaction with ions using the Lennard–Jones potential, was attempted in work by Calo [1974]. Later, these ideas were more rigorously developed in the works by Vigasin and his colleagues (see Vigasin [2003] and references therein), who took interaction potential anisotropy into account and showed that the allowance for the rotational degrees of freedom of monomers significantly affects the results of collisions.

Below we will consider the basics of this approach.

What is going on during molecular collisions?

In air at atmospheric pressure and room temperature, an average intermolecular distance is about 30 Å, which is approximately ten times more than the gas-kinetic size of molecules. This means that the Earth's atmosphere is sufficiently rarefied to assume that only two molecules take part in most collisions, i.e., the collisional effects can be analysed using *pair interaction approximation*.

The result of the collision of two molecules in a gas is fully determined by their relative speed υ_r, impact parameter b_p, and interaction potential $U(r)$. Typical trajectories of motion corresponding to 'strong' (resembling the collision of billiard balls) and 'weak' (in the case of mutual attraction of the molecules only) collisions are presented in fig. 1.10. An intermediate case is also possible [Hirschfelder, 1948], when the molecules do not scatter at 'one touch collision', instead, there occurs *orbiting* (fig. 1.20).

It can be shown (see, e.g., Landau [1976]) that, if the distance between the colliding structureless molecules is considered as a function of time, then its kinematics is the same as that of the motion along one coordinate of a material point with reduced mass $\mu = m_1 m_2 / (m_1 + m_2)$ (where m_1 and m_2 are the masses of colliding molecules), and the kinetic energy

$K = \mu\upsilon_r^2/2$ in the field of the effective potential $U_{eff}(r, L_c) = U(r) + L_c/r^2$, where $L_c = Kb_p^2$. Assuming that the angular momentum of the colliding molecules is $M = \mu\upsilon b_p$ and the moment of inertia is $I = \mu r^2$, we obtain $L_c / r^2 = M^2/2I$, which corresponds to the energy of rotational motion of the interacting pair with respect to its centre of mass.

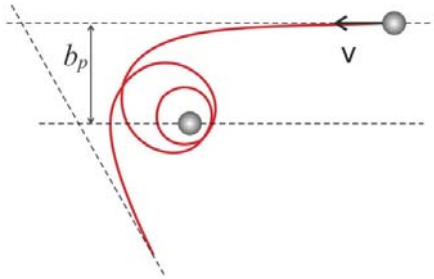

Fig. 1.20. An approximate trajectory of relative molecular motion on collisions corresponding to the case intermediate between the strong and weak collisions shown in fig. 1.10.

A typical family of the effective interaction potentials corresponding to the Lennard–Jones potential (6-12) and different values of L_c is presented in fig. 1.21.

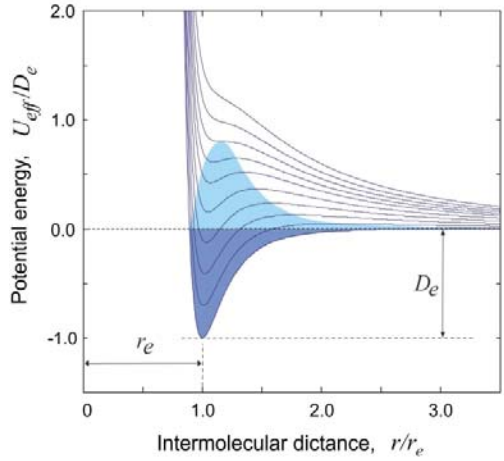

Fig. 1.21. The effective intermolecular interaction potentials for different values of angular momentum of the interacting pair. The energy of rotation about a common centre of mass $(L_c/r_e^2)/D_e$ changes from 0 (lowest curve) to 2.7 (uppermost curve). The shaded areas correspond to bound (dark grey) and quasi-bound (light grey) dimers and free pairs (unshaded area above the light grey).

The minimum and maximum of the potential curves at small values of L_c mean that the colliding molecular pair may be inside the potential well, forming a double molecule, i.e., a *dimer*. The kinetic energy of translational molecular motion in this case converts to the energy of molecular rotation about the common centre of mass. Such a dimer is unstable. Its total internal energy is higher than the dissociation energy, so by tunnelling through the potential barrier the dimer can spontaneously dissociate into two initial molecules. However, in the case of a lucky collision with a third molecule, the dimer can transfer the excess energy to it and will become stable. This means that molecular collisions in gases can lead to the merging of molecules into pairs, in other words to the formation of new molecules that will be new radiation absorbers with their own characteristic spectra.

Molecular pairs in gases may be classified by the value of total internal energy. If the total energy of a pair is lower than the energy of these molecules spaced apart by an infinite distance (‘zero’ energy), this pair forms a *bound* (sometimes referred to as truly bound), or a *stable* molecular complex that can dissociate only on collision with a third molecule. If the total energy of the pair is higher than the zero energy but lower than the energy of the effective potential maximum, then this pair is able to form a *quasi-bound*, or *metastable* molecular complex that can dissociate either on collision with a third molecule or spontaneously. The gas-kinetic and spectral properties of a metastable complex depend on the ratio of its lifetime and the average time between collisions. If the lifetime is longer than the time between collisions, the metastable complex behaves like bound complexes; otherwise, its properties are similar to those of two free molecules.

For large values of L_c, the effective potential has neither a minimum nor maximum. The molecular pair energy is too high for the formation of a complex, and the molecular collision looks like the collision of elastic spheres. Such a pair is called the *free molecular pair*.

The qualitative features of the collisional interaction of multiatomic molecules are approximately the same. With allowance for the anisotropy arising on collisions of multiatomic molecules, quasi-bound pair states may be formed not only as a result of molecular pair rotation, but also (even more readily) due to the internal degrees of freedom of monomers. In this case, the excess of the kinetic energy of the pair corresponding to the translational motion of monomers is converted to the internal rotation of the monomers in the dimer, relative to their common bond and/or to other degrees of freedom. As a result, the lifetime of a metastable dimer will increase significantly. Note that the collisions of multiatomic

molecules may give rise to absolutely new features that are not inherent in structureless monomers. For instance, the excess of the internal dimer energy, as compared to the dissociation energy concentrated in monomer rotation about the bond axis, can be arbitrary large up to infinity, but the dimer will not dissociate, which means that, in principle, the lifetime of a metastable dimer in such a state can be infinitely long. It should be noted, however, that for a metastable dimer to behave like a stable one, its lifetime should be longer than the average time between collisions.

In summary, we can classify all possible molecular pairs into three groups, taking into account their energy and angular momentum: (1) free molecular pairs; (2) metastable (quasi-bound) dimers; (3) stable (bound) dimers. The areas corresponding to these pair states for the simplest one-dimensional interaction potential (structureless monomers) are shown in fig. 1.21.

Generally, the interaction potential $U(r)$ depends on both the distance between the molecule's centre of mass and the number of internal angular coordinates t determining the orientation of the monomers relative to each other. For nonlinear molecules-monomers $t = 5$ (three coordinates for rotation of each monomer in space minus one because the rotation of one monomer can be taken from the position of the other), and for diatomic or linear molecules $t = 3$.

An approach to assessing the amount of different pair states was proposed in the work of Vigasin [1991]. According to this approach, the total energy of the interacting pair can be written as

$$H = U + E + L, \tag{1.112}$$

where E is the total kinetic energy of both monomers, including the energy of their rotation about the common intermolecular axis, and L is the energy of a two-dimensional rotation of a pair relative to the axis normal to the intermolecular axis. This rotation can be considered as the rotation of a slightly prolate asymmetric top. So, the state distribution of the pair approximately corresponds to the rotational distribution for diatomic molecules, which is Boltzmann's function

$$f(L) = \exp(-\frac{L}{kT}). \tag{1.113}$$

The internal energy E corresponds to a system with $t + 2$ degrees of freedom (two additional degrees of freedom correspond to the monomer motion along the intermolecular axis and to the pair rotation about this axis). Neglecting the interaction between the pair rotation as a whole and

the internal motion of monomers, the energy distribution function of states can be represented in the form [Landau, 1980]:

$$f(E) = E^{t/2} \exp(-\frac{E}{kT}). \quad (1.114)$$

Under the classical approximation, the total number of states (statistical weight) of the system can be found as

$$Z = \int \exp\left(-\frac{H}{kT}\right) dqdp, \quad (1.115)$$

where the integration is performed over all independent coordinates and impulses of the system. The total number of states can be represented as a sum of free, metastable, and bound states:

$$Z = Z_f + Z_m + Z_b. \quad (1.116)$$

If the form of the interaction potential $U(r)$ is known, the substitution of (1.112) into (1.115), allowance for (1.113) and (1.114), and the integration of (1.115) over the corresponding region of coordinates and impulses, allow statistical weights of all three types of pair states to be found in explicit form.

An exact form of an intermolecular interaction potential is currently one of the major problems of collision effects studies in modern spectroscopy. The *ab initio* methods of calculating the potential energy points for a multiplicity of mutual geometries of colliding molecules and further representation of the numerically obtained potential energy surface (PES) in functional form are known (see, e.g., Leforestier [2012]; Sumiyoshi [2015]). A fairly good surface can now be produced in reasonable time for relatively large molecular systems. However, each particular case is still considered as a distinguished result. Nevertheless, like in many other cases, reasonable simplification of a complex system allows one to draw qualitatively correct conclusions.

Relative fractions of pair states in different gases were calculated in the work of Vigasin [1991] in the approximation of a rigid rotor and a harmonic oscillator. The results of these calculations for water vapour are shown in fig. 1.22. They enable general conclusions about the temperature dependence of relative fractions of pair states. At extremely low gas temperatures, bound states dominate. With increasing temperature, their number decreases rather rapidly and becomes negligible at temperatures approximately corresponding to the doubled energy of dimer dissociation due to the breaking of the intermolecular bond ($kT \sim 2D_0$). As the temperature is increased, the metastable states first rapidly grow in number

due to the reducing fraction of bound states and dominate at temperatures approximately corresponding to the dissociation energy. Eventually, their amount slowly decreases as a result of the monotonic growth of the number of free pairs, whose contribution under ordinary atmospheric conditions is negligibly small and becomes significant only at very high temperatures. It is worth noting that all these features are more pronounced for nonlinear molecules that have more rotational degrees of freedom and, hence, form dimers more readily. Taking into account that monomer molecules can have vibrational degrees of freedom, as well as rotational ones, it may be expected that the shape of the curves will change at high temperatures: there will be still more dimers and fewer free pairs.

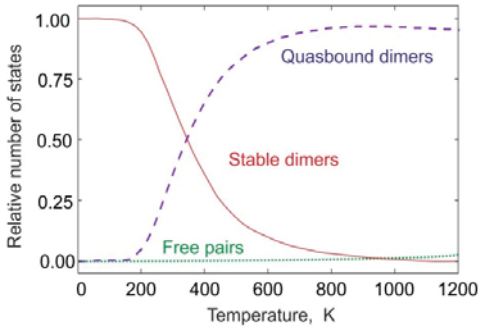

Fig. 1.22. Relative fractions of the pair states of H_2O molecules as a function of temperature [Vigasin, 1991]. The solid curve is for stable dimers, the dashed curve for quasi-bound dimers, and the dotted curve is for free pairs.

Note that the lifetime of metastable states is no less important for practical applications than the number of these states. The lifetime can be calculated from the probability of tunnelling through the potential barrier in each metastable state of the dimer, but this also requires an exact form of the interaction potential.

Virial equation of gas state and molecule dimerization

The thermodynamic equation of a gas state is directly related to collisional molecular interaction. It will be shown here that the amount of formed molecular complexes can be estimated on the basis of the empirical thermodynamic information on the properties of an imperfect gas.

Consider the equation of gas state written in virial form

$$\frac{pV_m}{RT} = 1 + \frac{B(T)}{V_m} + \frac{C(T)}{V_m^2} + \dots , \qquad (1.117)$$

where p, R, and V_m are, respectively, pressure, *gas constant* (sometimes referred to as a molar, universal, or ideal gas constant), and molar volume, and B and C are the second and third virial coefficients that are functions of temperature T. The term pV_m refers to the forces acting on the walls of a gas-containing vessel, RT refers to the kinetic energy of molecules, and all the other terms refer to the interaction of gas molecules with each other. In the case of an ideal gas, when molecules are considered as infinitely small material points and their interaction is instantaneous and elastic, only 1 remains in the right-hand side of the equation. As was shown above on an example of pair interactions, the collisional molecular interaction is neither instantaneous nor elastic. It is the mechanism that distinguishes real gases from ideal ones.

For estimating the number of dimers forming in gas under equilibrium thermodynamic conditions researchers use the concept *equilibrium constant,* which is introduced as follows. Consider the dimerization process as a reversible reaction of the joining together of two monomers:

$$\mathrm{M} + \mathrm{M} <=> \mathrm{D}\ ^{4}. \quad (1.118)$$

According to the Guldberg–Waage law of mass action, for this reaction the speed of dimer formation V_1 is equal to the product of the probability for each of the interacting molecules to get to the same point in space a_1, of the probability of formation of dimer a_2, and of the concentration of the interacting molecules $[\mathrm{M}] = n_m$:

$$V_1 = a_1 \cdot [\mathrm{M}] \cdot a_1 \cdot [\mathrm{M}] \cdot a_2 = a_1^2 a_2 \cdot n_m^2 \ . \qquad (1.119)$$

The speed of the dimer destruction reaction, V_2, is equal to the product of the probability of dissociation a_3 and of the dimer concentration $[\mathrm{D}] = n_d$:

$$V_2 = a_3 \cdot [\mathrm{D}] = a_3 \cdot n_d \ . \qquad (1.120)$$

These speeds are equal under the equilibrium conditions. The n_d / n_m ratio following from (1.119) and (1.120) at $V_1 = V_2$:

---

[4] Sometimes the left- and right-hand sides of the equation for this reaction are supplemented by the term '*TB*' corresponding to the so-called 'third body' needed for the formed molecule to get rid of the excess internal energy. Note that the properties of this third body are of no significance and do not affect the final result, as the reaction is reversible. The same collisional interaction can facilitate both creation of stable dimers and their destruction.

$$\frac{n_d}{n_m^2} = \frac{a_1^2 a_2}{a_3} = K_2^c \tag{1.121}$$

is a constant value at a given temperature. It is called the equilibrium constant of the reaction (1.118), or the *dimerization constant*. If the gas of the interacting molecules is considered a mixture of ideal monomers and dimers, then at a constant temperature their concentration is directly proportional to partial pressures. Therefore, the equilibrium constant can be defined by the partial pressures of the initial and final products of the reaction:

$$\frac{p_d}{p_m^2} = K_2^p = K_2 . \tag{1.122}$$

This definition of the equilibrium constant is more commonly accepted but less rigorous, as the reaction of joining together (1.118) is a result of molecular collisions, the number of which is proportional to the number density of molecules, rather than to the pressure that is less important in this case.

To elucidate the relationship between the dimer equilibrium constant and the second virial coefficient of the equation of state, let us look at Fowler's ideas [1939]. We assume, to begin with, that the difference of the gas from an ideal one is stipulated exclusively by the formation of dimers. In terms of intermolecular interactions this means that we ignore the intermolecular repulsive forces and assume that triple and higher order interactions may be neglected. Thus, the gas which consisted only of monomers under nonequilibrium initial conditions is considered a mixture of ideal monomers and dimers that readily transform one into another in the equilibrium state. Such a mixture meets the equation of state

$$pV = (\nu_m + \nu_d)RT , \tag{1.123}$$

where V is the volume of the mixture, and ν_m and ν_d correspond to the amount of monomer and dimer moles, respectively (hereinafter the subscripts m and d stand for monomers and dimers) formed under the equilibrium conditions from ν_0 moles of the initial gas. Using the definition of the amount of substance as a ratio of the substance mass m to the molar mass M and taking into account that $M = M_m$, we obtain for the mixture the following relationship

$$\nu_0 = \frac{m}{M} = \frac{m_m + m_d}{M} = \frac{\nu_m M_m + \nu_d M_d}{M} = \frac{\nu_m M_m + \nu_d 2M_m}{M_m} = \nu_m + 2\nu_d \,. \tag{1.124}$$

From the definition (1.122) with allowance for

$$\frac{p_m}{\nu_m} = \frac{p_d}{\nu_d} = \frac{RT}{V}\,, \tag{1.125}$$

we find

$$\nu_d = K_2 \cdot RT \frac{\nu_m^2}{V}\,. \tag{1.126}$$

For one mole of the initial gas, when $\nu_0 = 1$ and $V = V_m$, from the relations (1.124) and (1.126) we obtain a quadratic equation for ν_m:

$$2K_2 \frac{RT}{V_m}\nu_m^2 + \nu_m - 1 = 0\,, \tag{1.127}$$

that has only one positive root

$$\nu_m = \frac{V_m}{4K_2 \cdot RT}\left(\sqrt{1 + \frac{8K_2 \cdot RT}{V_m}} - 1\right). \tag{1.128}$$

Transforming the equation of state (1.123) to

$$\frac{pV_m}{RT} = \frac{\nu_m + 1}{2}\,, \tag{1.129}$$

substituting (1.124) into the obtained expression, and expanding its right-hand side in a power series of $1/V_m$ yields

$$\frac{pV_m}{RT} = 1 - K_2 \cdot RT \frac{1}{V_m} + 4\left(K_2 \cdot RT\right)^2 \frac{1}{V_m^2} + \ldots\,. \tag{1.130}$$

From the comparison of (1.130) and (1.117) follows

$$B(T) = -K_2 \cdot RT. \tag{1.131}$$

The allowance for repulsive forces at intermolecular interactions is directly related to the concept of the *excluded volume* b_0 introduced by Van der Waals, according to which the role of repulsion, i.e., the presence

of a repulsive part of the interaction potential, reduces to the fact that a molecule does not allow other molecules to penetrate into the volume occupied by it. The equation of the state of a hypothetic gas, with the repulsion following from (1.123) taken into account, will then transform to

$$p\left(V_m - b_0\right) = (\nu_m + \nu_d)RT\ , \tag{1.132}$$

which, like in the previous case, may be transformed to

$$\begin{aligned} \frac{pV_m}{\mathrm{RT}} &= \frac{\nu_m + 1}{2}\left(1 - \frac{b_0}{V_m}\right)^{-1} = \\ &= 1 + \left(b_0 - K_2 \cdot RT\right)\frac{1}{V_m} + \left(4K_2^2R^2T^2 - K_2 \cdot RTb_0 + {b_0}^2\right)\frac{1}{V_m^2} + \ldots\ . \end{aligned} \tag{1.133}$$

From this, follows

$$B(T) = b_0 - K_2 \cdot RT. \tag{1.134}$$

Using the methods of statistical mechanics (see, for example, Hill [1987]) it can be rigorously shown that the equilibrium constant K_2 may be represented as a sum of components of the corresponding metastable and bound dimers:

$$K_2 = K_m + K_b\ , \tag{1.135}$$

and that the second virial coefficient of equation (1.117) corresponds to all pair molecular interactions and, hence, by analogy with the total number of pair states (1.116), may be subdivided into three parts:

$$B(T) = B_f(T) + B_m(T) + B_b(T)\ , \tag{1.136}$$

where B_f is responsible for free pairs, i.e., for the collisions of free molecules, B_b takes into account the presence of bound molecular pairs (stable dimers) in the equilibrium state of the gas, and B_m allows for metastable dimers. The substitution of (1.135) into (1.134) and comparison of the obtained equality with (1.136) yields

$$B_b(T) = -K_b(T) \cdot RT\ ,\ B_m(T) = -K_m(T) \cdot RT\ ,\ B_f(T) = b_0\ . \tag{1.137}$$

From the expression (1.134), it follows that the total number of dimers formed in gas as a result of collisional interaction can be assessed by known values of excluded volume and of the second virial coefficient of the equation of state. Note that the expression (1.129) and, therefore

(1.134), was derived assuming that the amount of substance in the mixture of monomers and dimers is $\nu = \nu_m + \nu_d = \nu_0 = 1$. This is true only if the number of the forming dimers is so small that the change in the molar mass (or total number of particles) of the initial gas may be neglected.

A more detailed expression relating the dimer equilibrium constant, and the second virial coefficient was derived in the work of Leforestier [2014], in which the quantity

$$\alpha = \frac{2\nu_d}{\nu_0} \tag{1.138}$$

was used as the parameter characterising the number of dimers formed as a result of the reaction (1.118) in the initial nonequilibrium gas of monomers. The physical meaning of this parameter follows from the relation (1.124): α is the mass fraction of dimers (or equivalently, it is the relative fraction of monomers used for the formation of dimers). Then

$$\nu_m = \nu_0(1-\alpha),\ \nu_d = \nu_0\frac{\alpha}{2},\ \nu_m + \nu_d = \nu_0\left(1-\frac{\alpha}{2}\right). \tag{1.139}$$

Making use of the expressions (1.122), (1.123), (1.125), and (1.139) and taking into account

$$p = p_m + p_d, \tag{1.140}$$

we obtain

$$\nu_m + \nu_d = \nu_0\left(1 - pK_2\frac{(1-\alpha)^2}{1-\frac{\alpha}{2}}\right). \tag{1.141}$$

The virial equation of state (1.117) for the considered gas can be written in the form

$$pV = \nu\left[RT + B(T)p\right]. \tag{1.142}$$

The dimerization (merging) of molecules and their repulsion caused by the finiteness of their volume are the mechanisms responsible for the imperfect properties of a gas. If a small number of dimers are formed, the volume they occupy in space can be neglected in comparison to the volume occupied by monomers. Then, the virial equation of state of a weakly dimerising gas can be written as

$$pV = (\nu_m + \nu_d)RT + b_m\nu_m p_m, \tag{1.143}$$

where b_m is the second virial coefficient responsible for the monomer nonideality, provided it contains no dimers. It is actually the excluded monomer volume (cf. (1.132)).

The substitution of (1.141) into (1.143) and the allowance for

$$p_m \nu_m b_m = p\nu_0 b_m \frac{(1-\alpha)^2}{1-\frac{\alpha}{2}} \tag{1.144}$$

yield

$$pV = \nu_0 \left(RT + p\left(b_m - K_2 RT\right)\frac{(1-\alpha)^2}{1-\frac{\alpha}{2}} \right). \tag{1.145}$$

From the comparison of (1.145) and (1.142) follows

$$B(T) = \left(b_m - K_2 RT\right)\frac{(1-\alpha)^2}{1-\frac{\alpha}{2}}. \tag{1.146}$$

For $\alpha \to 0$, this expression transforms to the well-known relation (1.134) often used for estimates. It should be noted, however, that the relation (1.146) is derived under the same approximation $\nu = \nu_m + \nu_d \approx \nu_0$. This does not allow us to confidently assert that the relation (1.146) is more accurate than (1.134), as additional verification is needed to be sure.

The total amount of dimers in water vapour under given conditions (neglecting subdivision into bound and quasi-bound states) can be estimated by expressing the dimerization constant from (1.134) as

$$K_2(T) = \frac{b_0 - B(T)}{RT} \tag{1.147}$$

and using known data on the second virial coefficient (Appendix A4) and excluded volume (Appendix A5).

It is convenient to use for calculating the approximating function [Tretyakov, 2012]:

$$K_2(T) = \exp\left(\frac{\sum_{i=0}^{5} c_i T^i}{T} \right). \tag{1.148}$$

The numerical coefficients [5] $c_0 = 2183.3$, $c_1 = -12.66$, $c_2 = 0.012122$, $c_3 = -1.69 \cdot 10^{-5}$, $c_4 = 1.0485 \cdot 10^{-8}$, and $c_5 = -2.4717 \cdot 10^{-12}$ of the function are chosen so that its values correspond to the equilibrium constant in $(atm)^{-1}$ units. The deviation of the function (1.148) from the numerical data obtained from (1.147) does not exceed 0.8 % within the temperature range of 273—1275 K, and increases up to 10 % at extrapolation down to 200 K and up to 1500 K.

The found temperature dependence of K_2 is plotted in fig. 1.23 from which it follows, for example, that under normal room conditions at 21°C and a relative humidity of 50 %, when the partial pressure of water vapour is about 9 Torr, the partial pressure of dimers is approximately 5 mTorr. In section 3.2.2 it will be shown that such a small number of dimers permanently present in the equilibrium water vapour at typical atmospheric pressures is large enough for its contribution to be notable in the radiation absorption by the atmosphere observed in experiments.

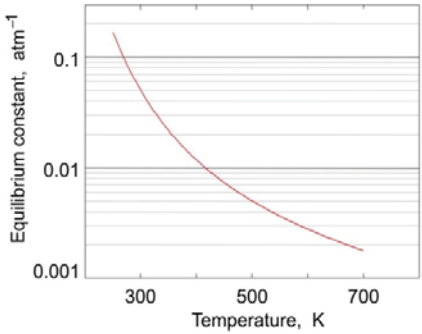

Fig. 1.23. Temperature dependence of the dimerization constant of water vapour determined by thermo-optical data on water vapour using the expression (1.147).

The expression (1.146) can be also used for estimating the equilibrium constant. It requires several successive iterations: first, the value of K_2 is found at $\alpha = 0$, then (1.146) is solved for α, and the result is substituted into (1.146) at the next iteration to determine the new value of K_2. The procedure is repeated until a steady-state value of K_2 is reached. The

[5] The values of the coefficients correspond to the fixed value $b_0 = 38.5$ cm^3/mol [Hirshfelder, 1942]. Allowance for the temperature dependence of excluded volume suggested in Leforestier [2014] almost does not affect the value of the equilibrium constant within the range of atmospheric pressures – the difference does not exceed 3 %.

obtained values of the dimerization constant are a little larger than the ones obtained from (1.147). The difference is approximately 17 % at 296 K and varies inversely to temperature variation.

Collisional molecular interaction in gas mixtures

The processes occurring during collisions of molecules of different kinds are, in principle, the same as for identical molecules. If the pair collision approximation is fulfilled, then in a gas mixture too, the equilibrium constants of stable and quasi-bound dimers consisting of two identical molecules are determined to the first approximation only by the squared value of the partial pressure of the respective monomer (expression (1.122)) and depend neither on gas-kinetic properties, nor on partial pressures of the other gases in this mixture. For quasi-bound dimers, this stability is explained by the pair nature of molecular interaction, according to which only two molecules take part in each collision. At least one more collision is needed for a stable dimer to be formed from a quasi-bound one. If the concentration of the considered molecules in gas is lower than the other ones, then the second collision of a quasi-bound dimer is likely to happen with a molecule of another kind. This means that the interaction potential and, hence the energy exchange, will differ from those in a pure gas. Nevertheless, reversibility of the reaction (1.118) should be taken into consideration. The same interaction potential will be responsible for the stable dimer destruction by molecules of this kind.

The only reason for the difference between the number of dimers forming in pure gas and in the presence of molecules of other gases is the appearance of the so-called *heterodimers*, i.e., double molecules formed by molecules of different gases. Heterodimers reduce the number of monomers available for the reaction of dimer formation (1.118). However, this decrease is insignificant in real weakly dimerising gases.

Shall triple molecules be taken into consideration?

If dimers are formed in an equilibrium gas, there always exists a probability of dimer collision with a monomer with the formation of a triple molecule (trimer) analogous to dimer formation. As a result of further collisions, the trimer may give birth to a tetramer, which gives birth to a pentamer, and so on. Despite the fact that molecular clusters are formed as a result of several collisions, their equilibrium constants may be

defined, by analogy with the dimerization constant (1.122), through the monomer and cluster partial pressures:

$$K_n^p = \frac{p_t}{p_m^n} = K_n, \qquad (1.149)$$

where n corresponds to the number of monomers in a cluster. As with dimers, these constants are functions of temperature.

It can be shown that the trimer equilibrium constant K_3 is related to the third virial coefficient of the equation of state (Appendix A3), the tetramer constant K_4 to the fourth virial coefficient, and so on.

To answer the question whether the clusters having higher order than dimers should be taken into consideration, let us analyse the contributions to the equation of state for water vapour of the second and third virial coefficients under atmospheric conditions. Water vapour is chosen for this analysis for several reasons: (a) its thermodynamic conditions are well studied; (b) water molecules more readily form clusters than molecules of other major atmospheric gases; (c) due to a larger dipole moment, water vapour complexes absorb significantly more radiation than complexes of other gases.

The majority of the moisture in the Earth's atmosphere is in the tropical region. Under these conditions (let us take a temperature of 37 °C and 100 % relative humidity for definiteness), the second term in the right-hand side of equation (1.117) is $-2.5 \cdot 10^{-3}$, and the third term is $-1.8 \cdot 10^{-5}$. This means that the triple interaction of water vapour molecules may be disregarded under all conditions typical for the atmosphere of the Earth. From this follows the conclusion that the non-resonant absorption in the clear Earth's atmosphere is caused predominantly by pairs of interacting molecules. That is why the term *bimolecular absorption* is frequently used in works devoted to the atmospheric continuum.

1.3.3. Principles of bimolecular absorption modelling

Following on from the previous section, for physically justified modelling of the spectrum of a bimolecular absorption, it is first necessary to construct an absorption model for each of the three possible pair states and then sum the results with the weights corresponding to the number of these states. Taking into consideration that the probability of a collision of molecules of two types in unit time per unit volume is directly proportional to the product of the concentrations (or partial pressures) of these molecules in a gas mixture, the spectrum of bimolecular absorption can be represented in the form

$$\alpha_{bimolecular} = \sum_{all\ pairs} \sum_{i=1}^{3} \left[C_i^{gas_1 - gas_2}(\nu, T) \cdot p_1 p_2 \right], \qquad (1.150)$$

where the first summation with respect to i gives the total spectrum of the three aforementioned pair states of the colliding molecules, that may be identical or may belong to different atmospheric gases (1 and 2), C_i are the spectra of the respective pair states allowing for the number of states, and p_1 and p_2 are the partial pressures of these gases; the second summation is done with respect to all possible pairs of atmospheric gases.

For the readers who want to learn more about the approaches to the rigorous theoretical calculation of bimolecular spectra we recommend the monograph by Frommhold [2006]. Below we give only an overview of what is known to date about the bimolecular absorption of the most abundant atmospheric molecules in the considered spectral range and how this absorption can be modelled.

Free molecular pair absorption

We remind the reader that here we speak only about additional absorption arising in a gas due to collisional molecular interaction. In the case of free molecular pairs, we deal with a single-approach collision with subsequent repulsion. As the molecules approach each other, additional short-term charge redistribution, i.e., additional polarisation, the magnitude of which is proportional to the interaction force, takes place in the molecule entering the field of the collision partner. As a result, the molecule more readily interacts with radiation, leading to an increase in absorption. The more collisions taking place per unit time, the more absorption occurs.

The appearance of a dipole moment is confirmed by the observation of the absorption bands in the spectra of these gases. The bands are exactly at the sites, where they would have been located if these molecules had dipole moments. The width and even the shape of the bands can be modelled approximately, using the known values of rotational constants of these molecules as a sum of the resonant lines corresponding to the transitions, allowed by the selection rules, uniformly broadened by the short lifetime of the collision-induced dipole moment (see, for example, Allin [1967]; Ho [1971]; Vigasin [1996]).

An example calculating the absorption spectrum caused by the dipole moment induced by intermolecular collisions in nitrogen, oxygen and in their mixture in the millimetre and submillimetre wavelength ranges can be found in the work of Boissoles [2003]. The result of this calculation for

the radiation absorption in a pure nitrogen is illustrated in fig. 1.24 for three temperatures. The calculations agree with the known experimental data [Buontempo, 1975; Stone, 1984] and with the recent results of numerical simulation of this absorption band using the full *ab initio* approach [Karman, 2015] and the method of classical scattering trajectories [Chistikov, 2019], on the basis of a full-dimensional anisotropic interaction potential.

Note that the absorption profile is in a good agreement with the shape of the spectrum envelope of a diatomic molecule. A stick diagram of the resonant rotational spectrum of N_2 molecule forbidden in the absence of collisions is also presented in fig. 1.24 for comparison (vertical bars on an arbitrary but corresponding scale along the ordinate in all the plots). The stick diagram was calculated using the relations (1.17), (1.21), and (1.24), the values of the rotational constants from Reuter [1986], and the selection rule $\Delta J = 2$ that must be fulfilled when the dipole moment of a nonpolar molecule is induced by the quadrupole moment of the collision partner (see, for example, Harries [1979]).

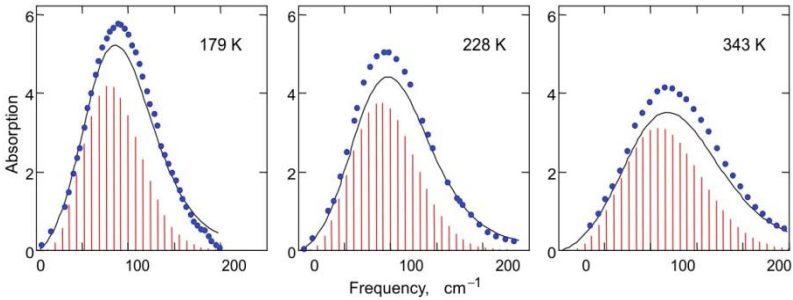

Fig. 1.24. The coefficient of collision-induced absorption of radiation by nitrogen normalised to density (in 10^{-6} cm^{-1}/Amagat^2 units) [6] at different temperatures. Solid curves — calculation from Boissoles [2003], dots — data from Borysow [1986].

A short-term increase of the dipole moment also occurs during collision of polar molecules. This additional, *induced dipole moment* causes additional absorption, which is expected to manifest itself as a weak 'base' in the region of resonant absorption bands coinciding with the

[6] An Amagat is a unit of gas number density measurement. 1 Amagat is numerically equal to the ideal gas density at a pressure of 1 atm and temperature 0 °C.

shape of the bands broadened by the short lifetime of the additional transient dipole moment.

For pure water vapour, the results of the computation of such absorption can be found in the work of Leforestier [2010]. They agree rather well with the simplest estimate of the collision-induced absorption spectrum calculated as the sum of pure rotational lines of a water molecule broadened by short collision time by Tretyakov [2015]. The estimate is based on the data of *ab initio* computations of Ikeda [2010], of the average dipole moment of water molecules at different densities and temperatures.

The results of calculations of the absorption caused by the induced dipole moment in nitrogen during the collision of nitrogen molecules with water molecules were reported in the work of Brown [2003].

In all cases, the results of computations and estimates indicate that, for the temperatures, pressures, and humidities typical for the Earth's atmosphere, absorption of this type has a much smaller magnitude than the observed continuum absorption.

Stable dimer absorption

Stable dimers are formed in an atmosphere as a result of intermolecular collisions. Their internal energy is lower than the dissociation energy and thus they are actually multiatomic molecules like many other molecules of atmospheric gases. The frequencies, intensities, and other parameters of resonant lines in their spectra may be calculated using the methods for ordinary molecules, this is confirmed by numerous studies of dimer spectra in cold molecular beams at a temperature of several Kelvins.

As was mentioned before, the continuum absorption of radiation by the atmosphere is determined primarily by its humidity. Therefore, the water dimers $H_2O—H_2O$ and heterodimers $H_2O—N_2$, $H_2O—O_2$, and others (that are sometimes called monohydrates of nitrogen, oxygen, and of other atmospheric molecules) are of major interest. Of them, water dimers are the best studied.

Water dimer and its spectrum

Investigations into the spectra of water dimers in cold molecular beams [Dyke, 1974; Fraser, 1989; Keutsch, 2003-1; Moudens, 2009], in matrices of noble gases [Bentwood, 1980; Bouteiller, 2011], and in helium nanodroplets [Kuyanov–Prozument, 2010] ascertained the nature of a water dimer as a physical entity, elucidated its equilibrium structure, gave

an insight into its complicated internal dynamics, and determined typical frequencies and intensities of the fundamental vibrations.

The dimer configuration was ascertained in the 1970s as a result of fitting the structural parameters satisfying the data of measurements of the frequencies of several groups of first rotational dimer lines observed in cold molecular beams [Dyke, 1974]. It was found that a dimer has an open structure (fig. 1.25), with the water monomers bound by a hydrogen bond so that one of them is a donor (giving a proton, the right molecule in fig. 1.25), and the other is an acceptor (receiving a proton, the left molecule in fig. 1.25). The benchmark parameters of the equilibrium dimer structure were found by high accuracy *ab initio* calculations in the work of Tschumper [2002]. A dimer molecule has a symmetry plane in which a donor and an oxygen atom of an acceptor are located. The acceptor symmetry axis is also located in this plane. The position of monomers in respect to each other is characterised by the distance between the oxygen atoms (2.9089 Å), by the angles between the monomer symmetry axis, and the axis passing through the centres of the oxygen atoms (the values of the angles are given in the figure). The positions of the atoms in the monomers are determined by the angle between the bonds (104.58° in the acceptor and 104.45° in the donor) and the lengths of the O—H bonds that are the same in the acceptor (0.9597 Å) and a little different in the donor (0.9581 Å for the bond of a 'free' proton and 0.9653 Å for the proton forming a hydrogen bond). For comparison, the most accurate calculations of the parameters of the equilibrium water molecule structure to date give the angle 104.50° and the bond length 0.95785 Å [Csaszar, 2005].

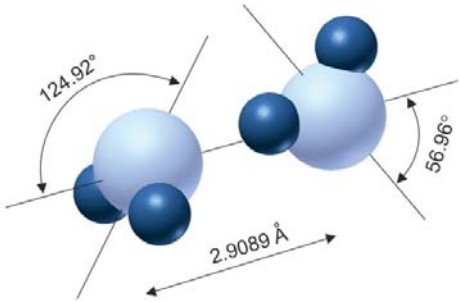

Fig. 1.25. The equilibrium structure of a water dimer from *ab initio* calculations [Tschumper, 2002].

The characteristic features of intramolecular dynamics of a water dimer were considered in detail in the works of Coudert [1990], Pugliano [1993],

Braly [2000-1, -2], Huang [2008-1], Kjaergaard [2008], Kelly [2010], and Leforestier [2012], and in the references therein.

The equilibrium structure of a dimer allows it to be classified as a slightly asymmetric prolate top with a permanent dipole moment directed almost along the top axis. As a dimer molecule has identical nuclei and a symmetry plane, it possesses eight energetically equivalent configurations. The transition from one configuration to another may occur as a result of tunnelling through three rather low potential barriers. Tunnelling through the lowest barrier (150—170 cm^{-1}) leads to proton exchange in the acceptor. The respective motion is called the *acceptor switching*. It splits each rotation-vibration dimer level into two. As a result of the second, most probable tunnel transition, the monomers exchange their roles — the acceptor becomes the donor, and vice versa. This motion is referred to as the *exchange*. It may proceed in two ways [Coudert, 1990], differing by the direction of monomers rotation about their symmetry axes. The barrier height is about 200 cm^{-1} and 400—500 cm^{-1}, respectively. This tunnelling leads to the further splitting of each of the two sublevels, arising from the acceptor switching into three 'sub-sublevels'.

An additional type of tunnelling in a dimer is the *bifurcation* motion, as a result of which, donor protons exchange places. According to various estimates, the height of the barrier ranges from 400 to 1000 cm^{-1}. This motion slightly shifts the sub-sublevels, but no further splitting occurs. A diagram of the splitting of a low rotational level in the ground vibrational state is presented in fig. 1.26. Symbols *A*, *B* and *E* designate the type of the level symmetry (corresponding to the symmetry of dimer wave functions in these states) according to the adopted classification [Fraser, 1991]; the statistical weights of the levels stipulated by the spins of the hydrogen atoms are given in parentheses. The approximate values of level splitting and shifts (in cm^{-1}) are shown on the right. For the levels with $|K| > 0$, the parity-related degeneracy is cancelled due to the asymmetry of the dimer, which leads to the additional splitting of sublevels with *A* and *B* symmetry into two and, as a result, each vibration-rotation level with $|K| > 0$ splits into 10, rather than 6 sublevels. The absolute value of all splittings varies strongly, depending on vibrational state.

The first analysis of all possible vibrations in the water dimer was undertaken in the work of Reimer [1984]. There exist 12 normal vibrational modes (fundamental oscillations). Six of them correspond to intramolecular vibrations of the O—H bonds of monomers, each of which can have symmetric, asymmetric, and bending vibrations. The frequencies of these modes are close to the fundamental vibration frequencies of the

monomer modes. The other six modes correspond to the low-frequency intermolecular oscillation of monomers in a dimer molecule (fig. 1.27).

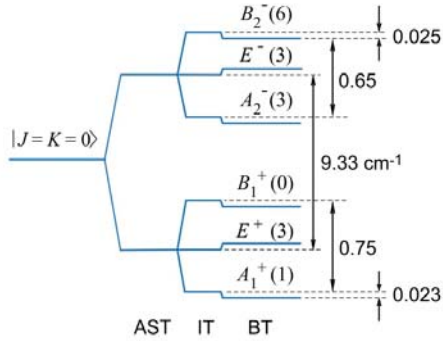

Fig. 1.26. Splitting of the low rotational level of the water dimer $J = 0$, $K = 0$ (J and K are the quantum numbers of the total angular momentum of the molecule and its projection onto the top axis as a result of tunnel motions designated as AST (acceptor switch tunnelling), IT (interchange tunnelling), and BT (bifurcation tunnelling).

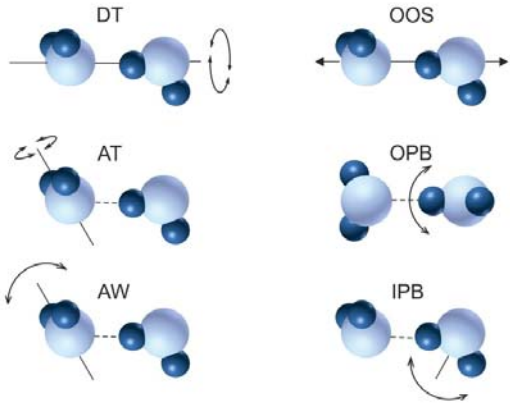

Fig. 1.27. Six normal vibrational intermolecular water dimer modes [Reimer, 1984]. The adopted notation: DT — donor torsion; OOS — O–O stretch; AW — acceptor wag; AT — acceptor torsion; IPB — in-plane bending; OPB — out-of-plane bending.

The calculated and measured normal-mode frequencies are listed in Table 1.1. The relative oscillator strength calculated in Kjaergaard [2008] is given in parentheses next to the calculated frequency. The most

accurate, for the time being, frequencies of the low-frequency fundamental intermolecular vibrations in a dimer can be found in work by Babin [2013].

Table 1.1. The frequencies (in cm^{-1}) and relative intensities of normal vibrational modes of water monomer and dimer

Monomer H_2O		Dimer $(H_2O)_2$			
mode[a]	experiment[b]	mode[c]	calculation[d]	experiment	
		ν_3 (ν_1, d)	3591 (28)	3601	[Buck, 2000]
		ν_1 (ν_3, d)	3711 (12)	3735	[Buck, 2000]
ν_1	3657.1 (0.4)	ν_2 (ν_1, a)	3634 (0.9)	3660	[Buck, 2000]
ν_3	3755.9 (9)	ν_9 (ν_3, a)	3725 (11)	3745	[Huang, 1989]
		ν_4 (ν_2, d)	1614 (7)	1616	[Bouteiller, 2004]
ν_2	1594.7 (13)	ν_5 (ν_2, a)	1603 (13)	1599	[Bouteiller, 2004]
		ν_{10} (OPB)	495 (14)	523	[Bouteiller, 2004]
		ν_6 (IPB)	304 (1.3)	311	[Bouteiller, 2004]
		ν_7 (OOS)	144 (12)	143	[Keutsch, 2003-2]
		ν_{11} (AT)	122 (21)	108	[Braly, 2000-2]
		ν_8 (AW)	121 (31)	103	[Braly, 2000-2]
		ν_{12} (DT)	85 (10)	88	[Braly, 2000-2]

[a] Designation of normal monomer modes: ν_1 — symmetric bond stretching, ν_3 — asymmetric stretching, ν_2 —bending;

[b] Data from the HITRAN database [Gordon, 2017];

[c] Designation of normal dimer modes and their description (in parentheses) indicating the respective normal modes of acceptor (a) and donor (e) molecules for intramolecular vibrations. The notation for the intermolecular vibrations is given in the caption to fig. 1.27.

[d] [Kjaergaard, 2008]

Note that, due to the strong anharmonism of intermolecular vibrations of a dimer, the combination modes of low-frequency oscillations can have a significant intensity comparable to the intensity of fundamental high-frequency oscillations. Therefore, the identification of higher-frequency modes, for example, the ones corresponding to in-plane and out-of-plane bendings cannot be considered final yet. The frequencies of these modes were measured only in cold neon and hydrogen matrices that may influence dimer vibrations; additionally, the identification of these modes has not been supported by rigorous *ab initio* calculations.

Four low-frequency modes are located within the 50—150 cm^{-1} range. These modes, their overtones, and combination vibrations form thousands of states, which at room temperature (thermal energy $kT \sim 200$ cm^{-1}) are sufficiently populated to make a notable contribution to the dimer

spectrum. In each of these states there is a full set of inversion-rotation levels the number of allowed transitions between which—and consequently, the number of resonant lines in the spectrum—exceeds the number of levels many times. Such a huge number of spectral lines under the conditions of inevitable collisional broadening results in a continuous resonance dimer spectrum uniformly spread over a wide spectral region, within the limits of its vibration-rotation bands. This allows us to consider the spectrum (at least in atmospheric applications) as one of the components of non-resonant absorption.

For a simple estimation of the dimer absorption coefficient in the region of its rotational spectrum, it is necessary to know the equilibrium structure and dipole moment of the dimer, including the dipole orientation with respect to the molecular axes. The structure of the dimer determines the general form of its rotational spectrum, and the dipole moment determines its integrated intensity. The structure of a water dimer is close to that of a strongly prolate symmetric top. The calculation of the energy levels and spectra for such a molecule in the rigid top approximation (see, for example, Townes [1955]) is not much more complicated than for a diatomic molecule (section 1.2.1). Values of rotational constants and dipole moment projections onto the principal axes of dimer rotation can be taken from the available measured and calculated data. The tunnelling effects, due to which the rotational levels of a dimer split into numerous sublevels, and a whole group of lines is observed in the spectrum instead of individual rotational lines, do not change the initial statistical weight of the levels. Therefore, the sum intensity of the group of lines is exactly equal to the intensity of the corresponding single rigid top line. Thus, as a first approximation, the allowance for the tunnelling effects is equivalent to uniform line broadening of the obtained rigid top spectrum up to total smearing of its rotational structure, where only its envelope remains but the integrated intensity of the spectrum is retained.

Such calculations for the water dimer can be found, for instance, in the works of Viktorova, [1970], Vigasin [1983], and Krupnov [2007]. An additional possibility of an internal hindered rotation, starting from torsional vibration of one monomer about the other, was taken into consideration in the work of Viktorova [1970].

The most complete and accurate, for the time being, *ab initio* calculations of a water dimer spectrum stick diagram for typical temperatures of the Earth's atmosphere based on the results of earlier theoretical and experimental studies are presented in work by Scribano [2007]. The prolate symmetric top approximation was also used in these calculations. All possible vibration-rotation-inversion dimer transitions up

to the frequency corresponding to the hydrogen bond dissociation energy (~1100 cm^{-1}) were explicitly taken into account in the calculations. The most accurate part of the calculations corresponds to the low-frequency part of the spectrum, i.e., to the millimetre and submillimetre regions, in which the impact of dimer nonrigidity on its spectrum is much weaker than in the infrared range.

For modelling the dimer spectrum, the parameter of collisional broadening of its resonant lines should be estimated. Following the work of Krupnov [2009], we use the well-known fact that the magnitude of the broadening parameter is approximately proportional to the dipole of the collision partners for the estimation. For example, the self-broadening of the line of an H_2O molecule (the dipole moment 1.87 D) is about 20 MHz/Torr [Gordon, 2017], and the line of a methylcyanide CH_3CN molecule (dipole moment 3.9 D) is approximately 50 MHz/Torr [Fabian, 1998]. Then, for a water dimer, the dipole moment of which was measured to be approximately 2.6 D [Odutola, 1980], the collisional line broadening parameter is expected to be about 30 MHz/Torr. (Note that this method gives an overestimated value of the parameter, as in the equilibrium water vapour dimers will most often collide with water monomers.)

The results of the calculations of water dimer spectra for the millimetre wavelength range with the use of the stick diagram from Scribano [2007], and the above line width estimates, are presented in fig. 1.28. They demonstrate the dependence of the dimer absorption spectrum on the pressure of the equilibrium water vapour. The quadratic dependence of the spectrum amplitude on pressure is quite expected (see the relation (1.122) determining the number of dimers). The dense and highly irregular, high-resolution spectrum (a small fragment at a pressure of 0.1 Torr is shown in the inset in fig. 1.28) is blurring with increasing pressure due to collisional broadening and fully transforms into a slowly varying non-resonant absorption already at the water vapour pressure of approximately 100 Torr. However, in the intermediate region of pressures, a sequence of characteristic equidistant peaks is observed in the dimer spectrum against the background of a non-resonant ‘base’.

The spectral analysis performed in the work of Krupnov [2009] demonstrates that each peak of this series is formed by a large number of the merged lines corresponding to the $J \to J+1$ transitions between the levels with E_1 symmetry (see fig. 1.26) and with different values of K in all possible vibrational states of the dimer. Fraser and co-authors [1989] showed that the frequencies of the lines of such transitions form quasi-equidistant sequences analogous to the spectra of polar diatomic molecules. The series with $K = 0$ in the ground vibrational state has the

highest intensity, which corresponds to the dimer molecule rotation about the axis with maximum moment of inertia. Consequently, the position of the spectral peaks is determined, to a great extent, by the frequencies of these transitions. With an increase of the molecule's rotation speed, the nonrigidity effects increase too, and the difference in the positions of molecular transitions of the same type in different vibrational states becomes increasingly more pronounced. This leads to gradual broadening of the rotational peaks in the dimer spectrum and their total blurring at frequencies higher than approximately 350 GHz (fig. 1.29).

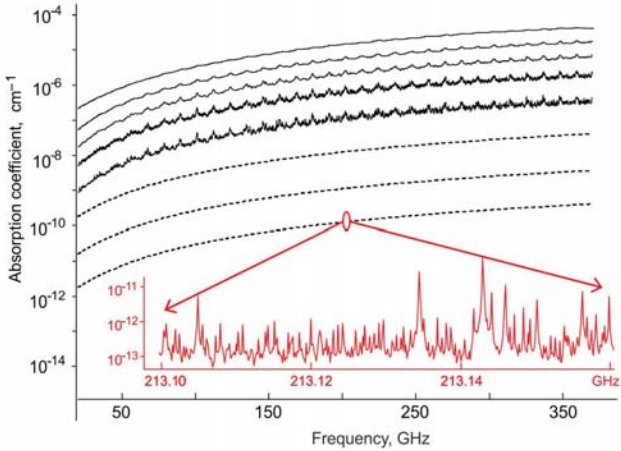

Fig. 1.28. The water dimer spectrum in equilibrium water vapour at pressures 0.1, 0.3, 1, 3, 7, 13, and 21 Torr (bottom-up) at room temperature calculated from first principles. For three lower spectra, only smoothed envelopes are plotted by the dashed curves. Inset: 60-MHz fragment of the spectrum at the pressure of 0.1 Torr. The upper spectrum corresponds to 80 Torr and 350 K.

Note that uncertainty of *ab initio* calculations and approximate estimates of collision broadening of dimer lines provide only a qualitative picture of the spectrum. Therefore, the authors of the calculations [Scribano, 2007] proposed, for the atmospheric applications using the wavelengths up to 1 mm, an empirical approximation of the expression in the form (1.109):

$$\alpha(\nu,T) = 7.27\cdot 10^{-8}\left(\frac{300}{T}\right)^{10.67} \nu^2 p_{H_2O}^2, \qquad (1.151)$$

which gives the value of the dimer absorption coefficient in water vapour (in dB/km) in the temperature range of 257—327 K, if the water vapour pressure p_{H_2O} is expressed in hectopascals (hPa) and frequency ν in GHz.

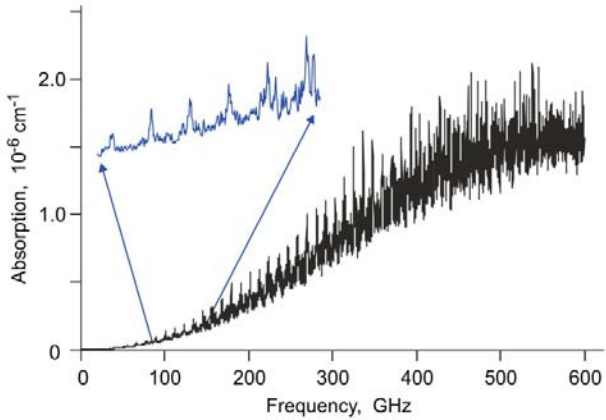

Fig. 1.29. The water dimer spectrum in equilibrium water vapour at T=270 K and pressure of 3 Torr calculated from first principles. Inset: a magnified fragment of the same spectrum. Adopted from Krupnov [2009].

A more detailed model of the spectrum, taking into account the presence of a sequence of peaks, was proposed in work by Odintsova [2014]. The model is based on the approximation of the rotational peaks in the spectrum of a stable dimer by a sum of Lorentz profiles, and of the remaining part of the spectrum by quadratic polynomial. In this model, the pressure dependence of the peak width and the temperature and pressure dependence of the spectrum intensity are taken into consideration empirically:

$$\alpha(\nu,T,p)=\left[4.29\cdot10^{-11}\nu^2\left(\frac{T_0}{T}\right)^{-3.8}+\sum_J\frac{I_J\gamma_J}{\left(\nu-\nu_J\right)^2+\gamma_J^2}\right]\cdot\left(\frac{T_0}{T}\right)^{13.5}\left(\frac{p}{p_0}\right)^2 . \quad (1.152)$$

Here, α is the absorption coefficient in cm^{-1}, ν is the frequency in GHz, p is the water vapour pressure in Torr, $T_0 = 296$ K, $p_0 = 13$ Torr, J is the number of the peak corresponding to the rotational quantum number of the transition $J \to J+1$,

$$\gamma_J=\left(0.108\cdot J-4.43\cdot10^{-5}\cdot J^3\right)+0.03\left(p-13\right) \quad (1.153)$$

is the effective peak width in GHz,

$$I_J = 6.3 \cdot 10^{-11} J^4 \exp\left(-0.0872 \cdot J\right) \tag{1.154}$$

is the peak intensity in cm^{-1}/GHz, and

$$\nu_J = 11.239 \cdot \left(J+1\right) + 8.68 \cdot 10^{-9} \cdot \left(J+1\right)^5 \tag{1.155}$$

is the central frequency of the peak in GHz.

The model agrees well with *ab initio* calculations of the spectra in the frequency range of 60-350 GHz for temperatures and pressures typical for the atmosphere of the Earth (fig. 1.30).

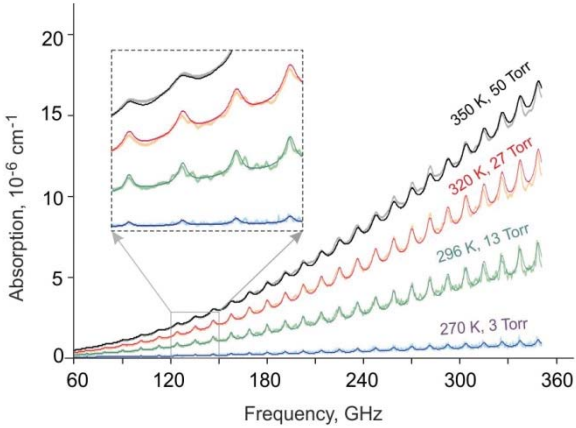

Fig. 1.30. The water dimer spectra calculated from first principles [Scribano, 2007] at different temperatures and pressures of water vapour (noisy lines) and the result of their approximation through the function (1.152) (smooth thin lines). Inset: the same spectrum on magnified scale. Adopted from [Odintsova, 2014].

The experimental observations of the water dimer spectrum in a warm water vapour (section 3.2.2) enabled the refinement of the coefficients of this model that can now be used for quantitative analysis of the continuum absorption in the pure water vapour and in the atmospheric air.

Heterodimers

The water heterodimers with molecules of atmospheric gases have been less investigated than water dimers $(H_2O)_2$. The analysis of the spectral lines recorded at a temperature of several kelvins in molecular beams using microwave spectrometers allowed for the determining of the rotational constants and the equilibrium structure (fig. 1.31) of H_2O—N_2

[Leung, 1989], $H_2O—O_2$ [Kasai, 2011], $H_2O—Ar$ [Fraser, 1990; Cohen, 1991; Cohen, 1993], $H_2O—CO_2$ [Peterson, 1984], and of many other heterodimers (see, for example, the surveys Potapov [2014; 2017] and references therein).

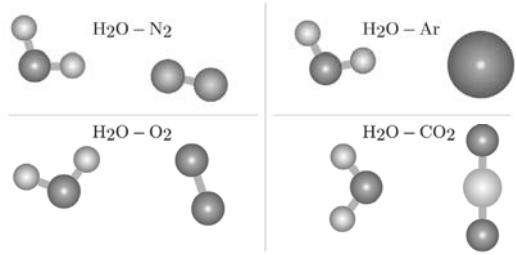

Fig. 1.31. The equilibrium structure of water heterodimers with molecules of major atmospheric gases according to the results of the work of Kjaergaard [2003]. The nuclei in all structures are in the plane of the picture.

The results of *ab initio* calculation of the structure, dipole moment, rotational constants, frequencies of fundamental vibrations, dissociation energy, and other parameters of water heterodimers with molecules of the major atmospheric gases can be found in the work of Kjaergaard [2003].

The heterodimer parameters obtained in this way, in combination with known data on air composition, allow us to estimate the abundance of these complexes in the atmosphere (fig. 1.32) through the methods of statistical thermodynamics (see, for example, Vaida [2000]; Klemperer [2006]).

Note that these calculations should be regarded as rough estimates for several reasons. The main reason is related to the stability of molecular complexes at relatively high (200–300 K) atmospheric temperatures. According to the available data [Kjaergaard, 2003], the binding energy of the complexes is 5.09 kcal/mol for $(H_2O)_2$, 0.72 for $H_2O—O_2$, 1.29 for $H_2O—N_2$, 0.32 for $H_2O—Ar$, and 2.73 for $H_2O—CO_2$, and the thermal energy kT at 250 K is 0.5 kcal/mol. It is clear that under these conditions a substantial part of the complexes is in short-lived metastable states. This raises the question as to whether the low-temperature structure of a weakly bound molecular complex can be used in these conditions for calculating its vibrational and rotational constants.

Moreover, the evaluation of the total number of states (mostly metastable) on the basis of methods of statistical physics, using a very approximate interaction potential and the rigid rotor and harmonic oscillator approximation is incorrect. Nevertheless, in view of the absence

of more accurate spectroscopic and thermodynamic data, statistical physics allows us to assess at least an order of magnitude of the studied phenomena.

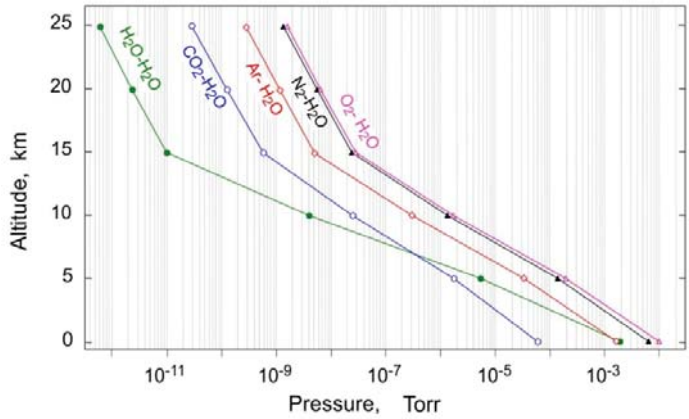

Fig. 1.32. The calculated partial pressures of heterodimers prevalent in the Earth's atmosphere at different heights [Kjaergaard, 2003].

According to estimates obtained in Svishchev [1998], Robinson [2003], Vaida [2000], and Sabu [2005] the concentration of the $H_2O—N_2$ and $H_2O—O_2$ heterodimers in air is much higher than the concentration of gases, such as methane (CH_4), nitrogen oxide (N_2O), carbon monoxide (CO), and various freons that are regarded to be of principal importance for the calculation of the greenhouse effect of the Earth's atmosphere.

The abundance of complexes and their structural parameters can be used to assess (also to an accuracy of the order of magnitude) their contribution to the total absorption of solar radiation by the atmosphere. Such estimates (see, for example, Kjaergaard [2003]) show that of all the heterodimers, the most absorbent are the $H_2O—N_2$ and $H_2O—O_2$ complexes. Their contribution to the atmospheric absorption is comparable to the contribution of a water dimer because of their significant abundance in the atmosphere. The contribution of the $H_2O—Ar$ complex is also noteworthy.

Metastable dimer related absorption

Recall that metastable (quasi-bound) molecules are double molecules. The total internal energy is higher than the dissociation energy of intermolecular bond. The internal energy includes the energy of pair

rotation as a whole and the energy distributed over internal degrees of freedom of the monomers forming such a molecular complex. The excess of this energy over the dissociation energy, for instance, when one monomer is rotating about the intermolecular axis, may be quite substantial as such a rotation does not break the bond. The lifetime of a metastable molecular complex strongly depends on the distribution of its internal energy. Obviously, the higher the energy of motion influencing the stretching of the intermolecular bond and the stronger this influence, the shorter the lifetime of the complex in this state. The average lifetime of metastable dimers is inversely proportional to the temperature of gas, as under the equilibrium thermodynamic conditions the internal energy is uniformly distributed over all degrees of freedom of the molecule.

The concept of the geometrical structure of complexes in metastable states is uncertain because of their anomalously high nonrigidity, even for weakly bound but stable dimers. Hence, standard spectroscopic methods of calculating the spectra based on the rigid top and harmonic oscillator approximation cannot be applied. *Ab initio* calculations using numerical methods of quantum chemistry traditional in molecular spectroscopy seem to be promising for metastable dimers. These methods have already enabled global calculation of vibration-rotation spectra of light molecules with a small number of atoms up to the dissociation energy. In this case the entire spectrum is computed at once. The accuracy of such calculations for a water molecule is close to the experimental one, as noted in Polyansky [2013]. It has been demonstrated that these methods can be extended to higher energies for any molecule, a water molecule is used as to demonstrate this in Zobov [2011]. Similar *ab initio*, although less accurate methods, were successfully used for calculating the absorption spectra of atmosphere-relevant pairs, such as N_2—N_2 [Karman, 2015] and O_2—O_2 [El-Kader, 2016], taking into account all possible bimolecular states.

Despite the enormous opportunities provided by modern computers, such calculations are still time and labour consuming. The more elementary particles are taken for calculations, the closer the energy of states under consideration is to the upper part of the potential and the higher the requirements for the calculation accuracy, the more resources are needed. Note that this dependence is significantly nonlinear. Therefore, even for a water dimer, such calculations can provide only a qualitative picture of the spectrum up to dissociation at best [Scribano, 2007], and only within the symmetric top approximation so far. The calculation of water dimer spectra in metastable states using this method is currently unfeasible.

An alternative method of theoretical characterisation of metastable dimers is based on molecular scattering calculations. Scattering is absolutely equivalent to the process of metastable molecule dissociation, if the time is reversed. Scattering calculations include detailed consideration of the inelastic molecular collision, taking into account the initial velocities of colliding partners, the impact parameter, and the binary interaction potential. Modern *ab initio* scattering calculation methods allow for comprehensive characterisation of quasi-bound states of a molecular complex which may be formed as a result of collision (see, e.g., Bergeat [2015], Ma [2015], Gao [2017]), including the lifetime and rotational states of both monomers in a broad range of colliding molecule energies. The method of classical trajectories calculation of molecular scattering using exact *ab initio* interaction potentials should be also mentioned (see Oparin [2017], Chistikov [2019], and references therein). It is currently used for calculating the bimolecular absorption spectra of the simplest nonpolar molecular systems, such as linear molecule–atom (CO_2—Ar [Oparin, 2017; Chistikov, 2020]) and diatom–diatom (N_2—N_2 [Chistikov, 2019]). This method requires significantly fewer resources than a full quantum mechanical approach and can be extended to all pair states of major atmospheric molecules. To the best of our knowledge, no theoretical calculations of any type are currently available for metastable dimers formed either by two H_2O molecules or by one H_2O molecule and one of any other molecule or atom (e.g., Ar).

For evaluation of absorption by metastable dimers in the case of the Earth's atmosphere or in similar cases when calculations are not available, the only option is to use qualitative 'finger' models which assume that a metastable state is intermediate between two free molecules and a stable dimer. In one extreme case, a dimer in such a state and an electromagnetic wave interacts like two unbound monomers. They can almost freely rotate in the close vicinity of each other. The average dipole moment of such a dimer is negligibly small, and its spectrum is quite close to the sum spectrum of both the monomers, with the spectral lines strongly broadened by the short lifetime of the metastable state [Ptashnik, 2011].

In the other extreme case, a metastable dimer differs from a stable one only by lifetime, i.e., it has the same structure, the same dipole moment and, hence, the same spectrum, but with additionally broadened lines [Vigasin, 1991]. The real spectrum must be intermediate between the spectra obtained from these two models.

Still another feature related to the radiation absorption by molecules in metastable states is worth noting. If the molecule's lifetime is shorter than one period of oscillations of electromagnetic radiation, the molecule will

perceive the field as a quasi-static one. The probability of absorption of a radiation quantum is very small in this case. This means that the number of metastable dimers per unit volume, which in these conditions may be detected spectroscopically, for example, by infrared radiation, will always be larger than by microwave radiation. The observed difference increases with increasing temperature as a result of the reduction of the average lifetime of metastable dimers.

CHAPTER 2

RESONATOR SPECTROMETER

2.1. Principle of operation

As the spectrum of a substance characterises its interaction with probing radiation, all available spectrometers can be divided into two main classes according to the principle of their operation. The first class includes instruments recording the spectrum by changes in the radiation properties. A typical example is a classical video spectrometer, in which a detector measures the power of the radiation transmitted through a gas. Spectrometers of the second-class trace changes in the macroscopic properties of the substance after its interaction with radiation. A typical example is a photoacoustic spectrometer, which measures the power of sound waves after absorption of light in a gas. However, there is a third way of spectrum recording by changes in the properties of the measuring element. Such instruments are called resonator spectrometers. As with the vibrations of a mechanical tuning fork, that sounds for a long time in air and rapidly damps when immersed in a viscous medium, the standing wave of electromagnetic radiation in the resonator decays faster when it is filled with absorbing gas. Interaction with matter leads to changes in the Q factor of the measuring resonant element. Therefore, this measurement method may be called the *resonance probe technique*[7].

The most intuitively clear definition of the Q factor or the quality of a resonant element is a dimensionless value corresponding to the duration of its 'sounding', which is characterised by a resonator time constant τ expressed through the number of oscillation periods T. The most commonly used definition of the resonator Q factor is the ratio of the resonance frequency f to its width Δf measured at half amplitude:

[7] Strictly speaking, resonant response is recorded through the power of the radiation transmitted through a resonator. The magnitude of this power changes when the resonator is filled with an absorbing substance. Therefore, one can formally assign resonator spectrometers to the first class.

$$Q = \frac{f}{\Delta f} = \frac{2\pi\tau}{T}. \qquad (2.1)$$

There are different ways of measuring a Q factor. One can find any Q-related parameter, for example, the damping ratio or time constant of eigenmodes [Meshkov, 2005], resonant response width [Mingelgrin, 1972; Read, 1988; Liebe, 1992; Bauer, 1993; Tretyakov, 2009] or the related resonance amplitude [Valkenburg, 1966; Bauer, 1986, 1991], but it is always necessary to register the resonator response to exciting radiation.

In the work of Dreizler [1986], it was shown that ultimate sensitivity of the spectroscopes is the same in temporal and frequency regimes of recording resonator response. So, the choice of the recording method depends mainly on how close to ultimate sensitivity a researcher can approach using available spectrometer components. Both methods will be considered below, with a little more attention given to measurements in the frequency domain as these are more common in resonator spectroscopy at millimetre and submillimetre wavelengths.

Let us show how the resonator Q factor and the parameters of resonator response are related to the absorption coefficient of the gas filling the resonator. This relationship can be readily found, as a high-Q resonator can be modelled to a high degree of accuracy as a classical damped oscillator excited by external harmonic driving force. For the field oscillation amplitude A, the expression

$$\frac{d^2}{dt^2}A + 2\gamma\frac{d}{dt}A + \omega_0^2 A = \frac{F}{m}\cdot\cos(\omega t) \qquad (2.2)$$

is valid in this case, where t is the time, ω and ω_0 are the angular frequencies of exciting radiation and of free oscillations of the field in the resonator, respectively, γ is the damping coefficient, m is regarded to be an oscillator mass characterising in our case the efficiency of coupling between external field and resonator, and F is the amplitude of external impact.

If the external exciting radiation is switched off after excitation of oscillations, the subsequent oscillations of the field amplitude will damp exponentially in conformity with the expression

$$A = A_0 \exp(-\gamma t)\cdot\cos(\Omega t + \varphi), \qquad (2.3)$$

where $\Omega = \sqrt{\omega_0^2 - \gamma^2}$.

Since the oscillation power W is proportional to the squared amplitude, the power will damp twice as fast:

$$W = W_0 \exp(-2\gamma t). \tag{2.4}$$

The time over which the radiation power in a resonator decreases e times is the resonator response time

$$\tau = 1/2\gamma, \tag{2.5}$$

and the distance passed during this time period by the radiation propagating at a speed c is its effective length

$$L_{\text{eff}} = c \cdot \tau. \tag{2.6}$$

One of the most important resonator characteristics is the relative radiation power loss during one full passage of the resonator by an electromagnetic wave ('single-pass' loss) defined as

$$P = \frac{1}{2}\frac{W_0 - W_1}{W_0}, \tag{2.7}$$

where W_0 is the radiation power at the initial moment of time, and W_1 is the radiation power after full passage of the resonator and returning to the same point in space with the same phase of oscillations. The factor 1/2 takes into account double radiation passage between the mirrors. The magnitude of this power can be found from (2.4), bearing in mind that the time spent on full passage is $T_1 = 2L/c$, where L is the distance between the mirrors or the resonator length. In high-Q resonators the radiation power decrease per one passage is very small: $2\gamma T_1 << 1$. Therefore, by expanding (2.4) in power series and neglecting minor terms we obtain $W_1 = W_0(1 - 4\gamma L/c)$. The substitution of this expression into (2.7) yields the relationship between loss and damping coefficient:

$$P = \frac{2\gamma L}{c}. \tag{2.8}$$

In the presence of external action, there appear, in addition to damped oscillations at resonator eigenfrequency, stimulated harmonic oscillations at the frequency of exciting radiation:

$$A = A_0 \exp(-\gamma t) \cdot \cos(\Omega t + \phi) + B \cdot \cos(\omega t + \varphi_1). \tag{2.9}$$

The stimulated oscillation amplitude is

$$B = \frac{F}{m\sqrt{\left(\omega^2 - \omega_0^2\right)^2 + \left(2\gamma\omega\right)^2}}. \tag{2.10}$$

It should be taken into consideration that in the vicinity of resonance $\omega \cong \omega_0$ and, hence, $\omega^2 - \omega_0^2 \approx 2\omega_0\left(\omega - \omega_0\right)$. Then, for the squared amplitude directly proportional to the energy of exciting radiation absorbed by the resonator per unit time we obtain

$$B^2 = \frac{F^2}{4m^2\omega_0^2} \cdot \frac{1}{\left(\omega - \omega_0\right)^2 + \gamma^2}. \tag{2.11}$$

The influence of the exponentially decaying term in eq. (2.9) can be eliminated, if step-by-step scanning of the exciting radiation frequency is so slow that at the end of each step the amplitude of natural oscillations can be neglected. In this case, in accordance with (2.11), the resonator response is a classical dispersion curve (Lorentz function) with half width at half amplitude γ. Note that the response amplitude at the resonance frequency is inversely proportional to the square of damping coefficient γ^2, and the resonance width is proportional only to the first power of γ, i.e., the resonance amplitude is more sensitive to the variation of γ. Passing from a circular to a linear frequency $\left(\omega = 2\pi f\right)$ and taking into consideration that for the resonance experimentally observed full width at half amplitude is $\Delta f = \gamma/\pi = (2\pi\tau)^{-1}$, from (2.8) we obtain a relationship between single-pass resonator loss and measured parameters:

$$P = \frac{2\pi L f_0}{cQ} = \frac{2\pi L}{c}\Delta f = \frac{L}{c\tau}. \tag{2.12}$$

It is interesting to note the relationship between the loss and the effective resonator length L_{eff}. The single-pass loss is actually part of the energy lost by radiation over distance L. The number of such parts that constitute total initial energy is $1/P$. From this, it follows that all the energy is lost when passing a path having length $L \times (1/P)$. Such an expression is obtained if (2.5) and (2.8) are substituted into the expression for the effective resonator length (2.6):

$$L_{\text{eff}} = \frac{L}{P}. \tag{2.13}$$

The radiation energy loss in a resonator comprises the inherent resonator loss and the radiation absorption loss in the gas filling the resonator:

$$P = P_{res} + P_{gas}. \tag{2.14}$$

The inherent resonator loss can be determined experimentally by pumping the resonator down to a deep vacuum or by filling it with a non-absorbing gas:

$$P_{res} = \frac{2\pi L f_0}{c Q_0} = \frac{2\pi L}{c}\Delta f_0 = \frac{L}{c\tau_0}. \tag{2.15}$$

The loss in gas, or the relative radiation power absorbed by gas in a single radiation passage through the resonator is found from (2.7) using the Bouguer—Lambert law (1.2):

$$P_{gas} = \frac{1}{2}(1 - e^{-2\alpha L}). \tag{2.16}$$

Under the conditions of small optical thickness ($2\alpha L << 1$), the expression (2.16) reduces to $P_{gas} = \alpha L$. Using this expression, and neglecting insignificant changes in the resonance frequency and in the radiation propagation speed, the absorption coefficient of a studied gas can be expressed through experimentally measured values of the resonator response parameters of a pumped-down resonator (marked by the subscript 0) and of a resonator filled with gas (marked by the subscript 1) in the form

$$\alpha = \frac{2\pi f_0}{c}\left(\frac{1}{Q_1} - \frac{1}{Q_0}\right) = \frac{2\pi}{c}\left(\Delta f_1 - \Delta f_0\right) = \frac{1}{c}\left(\frac{1}{\tau_1} - \frac{1}{\tau_0}\right). \tag{2.17}$$

Note that the resonator length does not enter the expression (2.17). This makes resonator spectrometers advantageous over all other spectrometer types for measuring the magnitude of absorption coefficient.

The small power loss approximation made in the derivation of the relations (2.12) and (2.17) is of no significant importance. It is used exclusively for obtaining simple and clear expressions relating the basic parameters of the resonator to each other and to the absorption coefficient of the gas filling the resonator. It can be shown (Appendix A6) that, if a high resonator *Q*-factor is maintained, the expression

$$\gamma = \gamma_{res} + \gamma_{gas} \tag{2.18}$$

is a more accurate analogue of (2.14), and there is no need to introduce in (2.17) the correction taking into account that the optical thickness of the gas may be not negligible.

An expression relating the absorption coefficient of gas and the amplitudes (Am) of resonant responses of a resonator with and without gas can be derived using the relation following from (2.1) and (2.11):

$$\frac{Q_0}{Q_1} = \sqrt{\frac{Am_0}{Am_1}}. \tag{2.19}$$

As the response amplitude is proportional to the amplitude of exciting force, only relative changes to the Q factor can be determined from the measurements. Hence, the amplitude should be calibrated to determine absorption in gas. This may be done, for instance, when measuring the Q factor of an empty resonator, for which resonance response width should be measured. Then an expression for the absorption coefficient analogous to (2.17) takes on the form

$$\alpha = \frac{2\pi f_0}{cQ_0}\left(\sqrt{\frac{Am_0}{Am_1}} - 1\right) = \frac{2\pi f_1}{cQ_1}\left(1 - \sqrt{\frac{Am_1}{Am_0}}\right). \tag{2.20}$$

The expressions in parentheses represent a relative change in the amplitude of the radiation that has passed through an absorbing medium. For a small absorption coefficient, this change corresponds to half of the relative change in the radiation power. If we compare (2.20) with the definition of the absorption coefficient (1.1), the multiplier before the parentheses can be considered as the reciprocal of a certain path length of this radiation, which is $(cQ)/(2\pi f)$. Exactly the same expression is obtained, if (2.15) is substituted into the formula for effective resonator length (2.13), and (2.1) is accounted for:

$$L_{eff} = \frac{cQ}{2\pi f}. \tag{2.21}$$

Then, the expression (2.20) transforms to

$$\alpha = \frac{1}{L_{eff}}\left(1 - \sqrt{\frac{Am_1}{Am_0}}\right) \tag{2.22}$$

from which it clearly follows that the higher the Q factor of the resonator or the greater the effective resonator length, the smaller the absorption coefficient can be measured.

Thus, we see an almost complete parallel with direct measurements of low absorption over long paths in the video-spectrometer regime: the longer the path length, the larger the optical thickness of the medium, and the lower the absorption can be recorded.

2.2. The main components of resonator spectrometer

2.2.1. Measuring cavity

Open quasi-optical Fabry–Perot resonators are most commonly used as sensitive components of resonator spectrometers in the millimetre and submillimetre wavelength ranges. Detailed theoretical analysis of such resonators can be found, for example, in the classical works of Kogelnik [1966] and Cullen [1979]. The most convenient for practical application are symmetric resonators having two identical spherically shaped concave mirrors. Sometimes it is no less convenient to use a combination of one spherical and one plane mirror. The structure of the field and the properties of such a resonator are analogous to the resonator of double length with two identical spherical mirrors. However, a resonator of smaller length has a rarer spectrum of eigenmodes and a smaller Q factor. The presence of a focusing mirror provides stable field oscillations in the resonator.

Stability of oscillations

When we speak about stability of oscillations, we mean that undamped field oscillations can exist in a resonator for unlimited time in the absence of inherent loss. The condition for stable oscillations in a resonator having length L with two identical spherical mirrors with curvature radius R_0 is

$$0 < \left(1 - \frac{L}{R_0}\right)^2 < 1, \tag{2.23}$$

from which, it follows that a resonator with mirrors of an arbitrary curvature is stable at any distance between them in the interval from 0 to $2R_0$. An exception is the point $L = R_0$ when the focal points of both mirrors coincide and are exactly in the cavity centre. Such resonators are referred to as *confocal*. Two borderline cases correspond to a) a resonator with plane mirrors ($R_0 = \infty$) that is unstable because of a possible field 'runaway' beyond the border of the mirror after a series of reflections; and b) a spherical or *concentric* resonator ($L = 2R_0$) in which a limiting mirror

diameter of $2R_0$ is attained at a given curvature, i.e., the mirrors are hemispheres.

Under paraxial approximation (weakly divergent beams) and conditions of negligibly small diffraction at the mirror edges (the diameter of the mirrors is made much larger than the characteristic size of field decay), the resonator eigenmodes are Gaussian beams [Kogelnik, 1966; Yu, 1982]. The *fundamental modes* are the solutions in which the dependence of the field intensity I on the distance from the resonator axis r is described by the Gaussian function:

$$\frac{I(r)}{I(0)} = \exp\left(-2\frac{r^2}{D_b^2}\right), \tag{2.24}$$

where D_b is the radius of a Gaussian beam (field '*spot size*'). It is determined by the distance from the beam axis at which the field amplitude decreases by e times. For the resonator with two identical spherical mirrors, the field spot size on the mirrors is related to the resonator parameters as

$$D_b = \sqrt{\frac{L\lambda}{\pi}}\sqrt{\frac{R_0^2}{L\left(2R_0 - L\right)}}, \tag{2.25}$$

where λ is the radiation wavelength. The minimal spot size (D_0) is in the middle of the cavity (*beam waist*):

$$D_0 = \sqrt{\frac{L\lambda}{2\pi}}\sqrt{\frac{2R_0 - L}{L}}. \tag{2.26}$$

Such fundamental modes are usually used for measuring absorption in resonator spectrometers. All the other modes that can be excited in a cavity are regarded as parasitic. Therefore, hereafter we will consider only such fundamental TEM_{00}-modes.

The size of the resonator mirrors determines the transverse size of the spectrometer gas cell. Therefore, for a given resonator length, mirrors with a curvature ensuring a minimal field spot size on the mirror are preferable. According to (2.25), this is attained at $R_0 = L$, which corresponds to the case of an unstable confocal cavity. The stability problem is solved by slight changes of the length. The resonator becomes stable, for example, at $R_0 = 0.8L$ or $R_0 = 1.2L$, while the size of the field spot on the mirror increases only by 1.6 %, compared to the minimal value. It should be taken into consideration that the closer the resonator to a confocal one, the

closer the frequencies of the fundamental and parasitic modes. This may result in a distorted resonator response (the stronger this is, the lower the Q-factor) and, hence, a systematic measurement error.

The Resonance frequencies of fundamental resonator modes f_q can be calculated assuming that, under resonance, an integer number q of radiation half-waves fit in between the resonator mirrors:

$$L = \frac{\lambda}{2} q \;\rightarrow\; f_q = \frac{c}{2L} q \,. \tag{2.27}$$

This general relation gives an accurate result only for resonators with parallel-plane mirrors of infinite aperture that are not used for high-Q resonators as a rule. For the calculation of resonance frequencies of a resonator with spherically curved mirrors, the expression (2.27) should be corrected [Cullen, 1979] with allowance for an increase in the resonator length. The resonator length increases as the spatial period of a standing wave in a Gaussian beam, especially in the *beam waist*, is larger than the wavelength in free space. For a resonator with two identical mirrors the resonance frequencies are

$$f_q = \frac{c}{2L}\left(q + \frac{1}{\pi} \arccos\left(1 - \frac{L}{R_0} \right) \right). \tag{2.28}$$

The relative accuracy of frequency calculations in this case is approximately $(\lambda/D_0)^5$. An expression from Yu [1982], taking into account wave front distortions at reflections, may be used if needed. This expression gives two orders of magnitude higher accuracy:

$$f_q = \frac{c}{2L}\left[q + \frac{1}{\pi} \arccos\left(1 - \frac{L}{R_0} \right) - \frac{\lambda}{4\pi^2 R_0} \right]. \tag{2.29}$$

The spectrum of resonator frequencies corresponding to its fundamental modes is equidistant, with the intermode distance $f_M = f_{q+1} - f_q = c/2L$.

In section 2.1 it was shown that for achieving maximal sensitivity of the resonator spectrometer and, hence, maximal measurement accuracy of the absorption coefficient, the maximal resonator Q factor is required. From the definition of the Q-factor (2.1) and the relations (2.27) and (2.15) we obtain

$$Q = \frac{\pi q}{P_{res}}. \tag{2.30}$$

From this, it follows that for achieving the maximal Q factor the resonator length should be increased to the furthest extent possible, and all its inherent losses should be minimised.

The resonator losses include: (1) reflection losses; (2) coupling losses; and (3) diffraction losses:

$$P_{res} = P_{reflection} + P_{coupling} + P_{difraction}. \quad (2.31)$$

Let us consider these three components in detail.

Reflection losses

Reflection losses are related to a finite ohmic conductance of mirror surfaces. Part of the power of the current induced on the mirror surface by incident radiation is lost on heating the mirror.

When a metal is interacting with an electromagnetic wave, *skin-effect* takes place (see, for example, Landau [1984]), i.e., the electromagnetic field penetrates the metal to a depth referred to as a skin-layer thickness. The skin-layer thickness for each metal is a function of electromagnetic radiation frequency and temperature of the metal. For far-IR radiation, including the millimetre and submillimetre wavelengths, at temperatures typical for the Earth's atmosphere, a normal skin-effect occurs when the free path of conduction electrons in the metal is much less than the thickness of the skin-layer. In this case, the reflection coefficient of coherent monochromatic radiation by the metal at normal radiation incidence on its surface can be assessed to a high degree of accuracy by the formula well known in the classical electrodynamics as the Hagen–Rubens formula (see Hagen [1903] and, e.g., Silveira [2010]):

$$R = 1 - 2\sqrt{\frac{f}{\sigma}}, \quad (2.32)$$

where f is the radiation frequency and σ is the metal conductivity in CGS units. Empirical values of conductivity (or resistivity inversely proportional to it) and its temperature dependence for most metals can be found in reference books. It is recommended to keep in mind that conductivity or reflection losses depend significantly on mirror technology and equation (2.32) is valid only for very pure metals.

Reflection losses relate to surface reflection coefficient R as

$$P_{refl} = 1 - R. \quad (2.33)$$

The choice of material for a mirror for a high-Q resonator of the millimetre or submillimetre range comes down to choosing a metal possessing the highest conductivity. The best materials for this purpose are (in descending order) silver, copper, gold, aluminium, and beryllium. Unfortunately, all of them except gold are gradually covered by an oxide layer. Nevertheless, mirrors of pure silver ensure the highest reflection coefficient. The use of a cheaper and easily processed brass with a further vacuum deposition of a rather thick (about 1 micron) layer of silver also gives satisfactory results. If the conditions of a particular experiment demand the Q-factor of the mirrors to be time invariable, to prevent oxidation the silver is coated by a thin (~10 nm) protective aluminium layer that is rapidly oxidised to aluminium oxide Al_2O_3. It is a dielectric too thin to make an impact on the reflection coefficient, but it safely protects the silver surface against further oxidation [Parshin, 2009].

The quality of a mirror surface affects not only the resonator Q-factor, but also the efficiency of excitation of its modes. Even small defects of surface shape (deviation from the plane or spherical shape) and its roughness (scratches) will lead to partial radiation scattering, thus inducing parasitic mode excitation. The best results are obtained from optical quality surfaces.

Coupling losses

These losses are the result of extraction from the resonator of part of the field oscillation energy through a coupling element. In some cases, it is convenient to use two coupling elements: one for exciting the resonator, the other for recording the resonator response. These elements may be either identical or have different properties and/or principle of operation. In either case, coupling losses of the resonator are a sum of losses in all coupling elements.

There are several variants of quasi-optical resonator coupling: through small holes in mirrors, through a partially transparent mirror, or by means of a thin dielectric plate or a film in a resonator.

The only advantage of coupling through a hole (*hole coupling*) is its simple implementation. The structures of the fields of exciting radiation and fundamental resonator modes are poorly matched in this case. Therefore, the efficiency of fundamental mode excitation is low. A significant proportion of the radiation power getting into the resonator is scattered over its volume, partially absorbed by the walls of the gas cell, and interferes with the resonator response. Many parasitic modes are excited in addition to the fundamental ones. Moreover, the hole coupling

poorly matches standard waveguides, which gives rise to standing waves in a waveguide tract and related variations of the value of coupling when the radiation frequency is changed. Nevertheless, hole coupling was used in the well-known worldwide resonator spectrometers, for instance, in the spectrometer designed by Hans Liebe (Institute for Communication Sciences, USA), who is one of the creators of the Millimeter-wave Propagation Model (MPM) of radiation propagation in the atmosphere [Liebe, 1975, 1984-1], in the spectrometer at the University of Lille, France [Bauer, 1986] which enabled the collection of a large amount of data on atmospheric continuum absorption, as well as in the spectrometers created in Cambridge, USA [Valkenburg, 1966], and at the University of Manchester, UK [Rezgui, 1995].

Partially transmitting plane mirrors are able, in principle, to better match the resonator field with input and output beams. Such mirrors are usually made in the form of a dense wire grid or mesh (see, for example, Braakman [2011]). A possible variant is photolithographic deposition onto a dielectric film of a thick (up to several microns) mesh or grid structure with a needed period. If the period of the structure is small, coupling will be broadband but the reflectivity of such a mirror will be too small for high-Q systems. The problem of back reflection of exciting radiation from the coupling element and the related formation of standing waves in the spectrometer waveguide tract remains unresolved. An example of using such a coupling is a resonator spectrometer created at the Jet Propulsion Laboratory in the USA [Read, 1988]. One of the mirrors of this resonator is made of a nickel mesh with a 27 μm step, 72 % transparency in the optical range and 2 and 0.6 % transparency at the frequencies of 120 and 60 GHz, respectively. A high resonator Q-factor (400000 at 120 GHz and 120000 at 60 GHz) at such large coupling losses is attained due to an increase of the resonator length up to approximately 3 m. A thin (less than a skin-layer thickness) metal wire deposited on a dielectric layer may also be used. Thin mirrors have large transmission losses and are very difficult to manufacture. It is next to impossible to produce two identical mirrors using the available technologies.

Film coupling is most acceptable for broadband high-frequency resonator spectroscopy. A thin dielectric film is stretched on a frame placed in the resonator at an angle such that exciting radiation reflected from the film should propagate along the resonator axis. The angle of 45° to the resonator axis is the simplest for alignment and the most optimal for matching [Schulten, 1966]. Matching of exciting radiation to the resonator field, i.e., agreement of the oscillation phase of the exciting beam with the resonator

field throughout the wave front is attained by superposing the size and position of the exciting beam with the resonator field spot on the film.

Film coupling has a number of advantages: minimum distortion of the structure of the resonator Gaussian beam; good matching between the resonator and the quasi-optical tract; a possibility of providing demanded coupling magnitude by choosing proper film material and its thickness; and absence of back reflection of exciting radiation to the waveguide tract of the spectrometer. Film coupling is used, for instance, in large-aperture resonator spectrometers created at the IAP RAS, Nizhny Novgorod [Dryagin, 1992; Krupnov, 2000; Tretyakov, 2009], and at the Ohio State University, USA [Meshkov, 2005].

When using a film as a coupling element it should be taken into consideration that the coupling coefficient (relative part of reflected power) is different for different polarisations of exciting radiation. Moreover, incursion of the phase of field oscillations during radiation propagation within the film is also different. As a result, changes in the polarisation of exciting radiation will lead to changes in the eigenmode frequencies and resonator Q-factor. To minimise systematic error associated with this effect when using a resonator spectrometer with film coupling for high-precision measurements, during frequency tuning it is necessary to control the consistency and invariance of the size and position of the exciting radiation beam spot on the coupling film as well as radiation polarisation.

Polytetrafluorethylene (Teflon), polyethylene terephthalate (lavsan, polyester) and polyimide are the most widely used materials for producing dielectric films for the millimetre and submillimetre wave technique. Dielectric parameters of thin films may vary significantly depending on thickness. Unfortunately, film parameters may vary in different batches and with different manufacturers.

The main downside of some dielectric films is the dependence of their parameters on environmental conditions. For example, lavsan and polyimide are hydrophilic materials, so their dielectric properties depend on humidity. Such dependence is less typical of Teflon films, which is why they are most often used as coupling films for studying absorbing properties of humid gases; to minimise possible systematic measurement error (see section 3.2.1). Besides, because of specific technology, most polymer films are roll materials and possess anisotropy [Vlasov, 2010]. This means that the spatial orientation of the film must coincide with or be orthogonal to the plane of polarisation of exciting radiation.

When a round hole in the centre of a mirror with a radius much smaller than beam radius is used as a coupling element, coupling loss can be

determined from the expression (2.24):

$$P_{coupling}^{hole} = 1 - exp\left(-2\frac{r_0^2}{D^2}\right) \approx 2\left(\frac{r_0}{D}\right)^2. \qquad (2.34)$$

In the case of partially transmitting mirrors, coupling loss is the transmission coefficient.

For calculating coupling losses using dielectric films we suppose that the resonator has a configuration depicted in fig. 2.1. Consider the case that is most important for practical application in a resonator spectrometer, when the polarisation of the electric field of exciting beam is parallel to the plane of the film (i.e., there is only *y*-component of polarisation). A dielectric film having thickness *d* is at an angle θ to the resonator axis, the *x* and *y* axes are in the plane of the mirror surface, x_1 and y_1 are in the plane of the film (the y_1 axis is parallel to the *y* axis), and the z_1 axis is normal to the plane of the film.

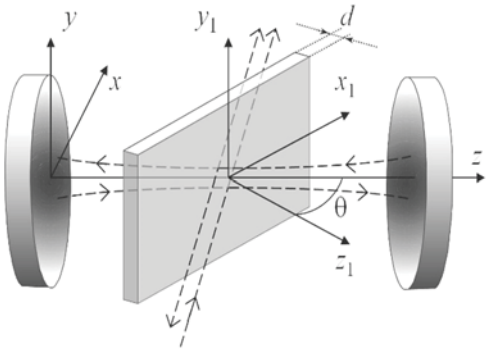

Fig. 2.1. Schematic of an open Fabry–Perot resonator with a thin dielectric coupling film. The dashed lines correspond to the beam path.

Assume that the dielectric permittivity tensor of the coupling film is diagonal in the $x_1y_1z_1$ reference frame, and its components are ε_{xx}, ε_{yy} and ε_{zz}. Then, making use of the Fresnel formulas (see, for example, Born [1959]) and neglecting the radiation absorption in the material of the film, we can obtain an expression for the coupling coefficient

$$R_c = \left(\left|r_{\|}\right|\right)^2 = \left(\left|\frac{R_{\|12} + R_{\|21}\exp(-2ikd\sqrt{\varepsilon_{yy} - \sin^2\theta})}{1 + R_{\|12}R_{\|21}\exp(-2ikd\sqrt{\varepsilon_{yy} - \sin^2\theta})}\right|\right)^2, \qquad (2.35)$$

where $k = \omega/c$ is the wave number, $r_{\|}$ is the ratio of the amplitudes of the electric field of reflected and incident plane waves reflected from a

dielectric layer, and $R_{\|}$ are the corresponding reflection coefficients at the gas-dielectric interface for considered waves:

$$R_{||12} = -R_{||21} = \frac{\varepsilon_{yy}\cos\theta - \sqrt{\varepsilon_{yy} - \sin^2\vartheta}}{\varepsilon_{yy}\cos\theta + \sqrt{\varepsilon_{yy} - \sin^2\vartheta}}. \qquad (2.36)$$

For small thicknesses ($kd << 1$), the coupling coefficient is proportional to the square of the film thickness.

For orthogonal polarisation (there is only x component of the electric field of exciting beam in the plane of the film), the expression for the coupling coefficient coincides with (2.35) to an accuracy of replacing ε_{yy} by ε_{xx}, and the expressions for the reflection coefficients $R_{\perp}$ at the gas-dielectric interface have the form

$$R_{\perp 12} = -R_{\perp 21} = \frac{\cos\theta - \sqrt{\varepsilon_{xx} - \sin^2\vartheta}}{\cos\theta + \sqrt{\varepsilon_{xx} - \sin^2\vartheta}}. \qquad (2.37)$$

The magnitude of coupling for this polarisation is much smaller than for the radiation polarised parallel to the plane of the film, as the angle of the radiation escape from the film is close to the angle of total internal reflection (Brewster angle).

In the case of negligibly small radiation absorption in a film, coupling losses P_c in the resonator are exactly equal to the coupling film reflection coefficient R_c.

Diffraction losses

Diffraction losses arise when part of the radiation power concentrated far from the centre of a Gaussian beam gets beyond the boundaries of resonator mirrors, given that the other resonator components are sufficiently far away from the beam field. Assuming that both resonator mirrors have equal radii r_m and the beam axis coincides with the axis passing through the centres of the mirrors, diffraction losses can be calculated as a volume integral of the Gaussian function (2.24) from the bounding radius r_c to the infinity:

$$P_{diffr} = exp\left(-\frac{2r_c^2}{\omega_g}\right), \quad \omega_g = \frac{\lambda r_m}{\pi}\sqrt{\frac{L}{2r_m - 1}}. \qquad (2.38)$$

Using this expression one can calculate the magnitude of diffraction losses and make them negligibly small by increasing the aperture of the resonator mirrors and coupling elements.

To illustrate relative contributions of different types of radiation losses, results of the computations of reflection, coupling, and diffraction losses in a resonator are presented in fig. 2.2. The results are given for a room-temperature, 40-cm-long vacuum resonator with two spherical mirrors 14 cm in diameter and a curvature radius of 24 cm made of pure silver, with a Teflon coupling film 6 μm thick at an angle of 45° to the resonator axis.

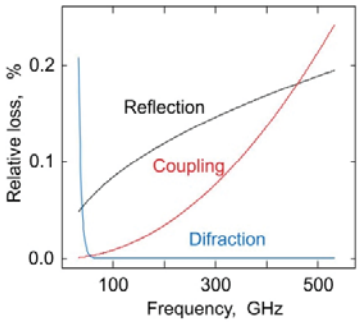

Fig. 2.2. Components of relative radiation power losses per one resonator passage.

An important resonator component providing high stability and accuracy of measurements is the *resonator frame*. It determines not only simplicity, operability, and reliable aligning of resonator mirrors and coupling elements, but also how temperature variations, external mechanical and acoustical noise jitter, and vibrations will affect the resonator response.

To minimise the impact of jitter and vibrations, the resonator mirrors are made non-adjustable. If spectrometer operation requires changing the resonator length, either both mirrors are rigidly fastened on massive metal bases or one of them is mounted on an element ensuring smooth movement of the mirror along the resonator axis. Absence of alignment imposes strict requirements to accuracy in manufacturing the components of the translation mechanism, bases, and mirrors, including those at the stage of mirror polishing and finishing. All mounting surfaces of the components must be strictly plane-parallel, and the mirror centres must coincide after superposition of the bases. Note that the use of spherical mirrors, which preserve stability of field oscillations at small adjustment errors, somewhat simplifies the task. However, maximum efficiency of operating mode excitation is achieved only in the case of ideal superposition of both mirror axes. The problems related to the requirement of plane-parallel and co-axial mirrors will be minimal and the best temperature stability of the resonator will be attained if the bases are interconnected by several rods of strictly equal lengths, and the end planes are strictly perpendicular to the axes [Schulten, 1965; Liebe, 1992; Tretyakov, 2009].

To minimise the influence of temperature drifts, the rods are made of invar (36/74 alloy of nickel and iron). In the –100 °C to +100 °C temperature interval, invar almost does not change its length (the thermal expansion coefficient is $1.2 \cdot 10^{-6}$ deg^{-1}). The direction of temperature drift

depends, among other factors, on which side of the bases the mirrors are fastened. Depending on the fastening point, relative changes in the base and mirror size may enter the resonator length as a sum or a difference, thereby making a cumulative or differential impact. This allows changes in the resonator length to be compensated for almost fully in the operating temperature range of the spectrometer.

If film coupling is used in the spectrometer, a special film fastening unit should be developed, which makes the frame design more complicated. In addition to film replacement and stretching, this unit is intended to adjust the coupling angle and to ensure that the axis of the film rotation is normal to the resonator axis; it must also be stable to mechanical vibrations and temperature variations. This also requires minimum alignment and maximum possible accuracy of manufacturing components. A film is usually clamped between two plane frames, stretched until an ideal smooth surface is attained, and fastened to the frame. The fastening when the axis of frame rotation intersects the resonator axis is the most convenient for alignment. The rotation of the frame with a film changes only the angles of exciting and output beams, it does not change the coupling spot position relative to the resonator.

2.2.2. Radiation source for cavity excitation

The radiation source for cavity excitation may be either continuous or pulsed. In either case, it must be a high-stability source. The pulse duration in spectrometers recording resonance in the time domain should be no less than the time of oscillation excitation in the resonator and the recording time of resonant response in the frequency domain. The recording time in the frequency domain depends on specific features of the radiation source and may be as short as measurements in the time domain.

The continuous wave (cw) source is more convenient in operation. The principal advantage of the cw source is the possibility to use the time of the experiment with maximum efficiency and, therefore, to attain ultimate parameters of the spectrometer determined only by basic principles of physics. For recording broadband spectra of a studied gas, radiation frequency tuning is highly important. Radiation power is determined primarily by the sensitivity of receiving circuits and must be sufficient to excite the resonator and register its response with a high signal-to-noise ratio (SNR). The resonator response shape observed at scanning radiation frequency (like in resonator spectrometers [Bauer, 1986; Read, 1988; Liebe, 1992; Alder, 1998; Nagarajan, 2017; Koshelev, 2018-1]) is a convolution of the true response shape and the shape of

radiation spectrum of the source. The closer the spectrum shape to the delta function, the more accurately the observed response corresponds to the true one. Therefore, radiation spectrum purity is a very important parameter. A narrow radiation spectrum is also of principal importance in spectrometers recording resonator response in the time domain (like in Meshkov [2005]), as it is closely connected with resonator excitation efficiency. That is why nearly all known resonator spectrometers use systems of source frequency stabilisation.

Frequency multipliers, Gann diodes, klystrons, backward-wave oscillators (BWO), and other devices are used as radiation sources. Despite the advance made in the development of semiconductor oscillators (see, for example, Samoska [2011] and references therein), BWOs are still the most suitable radiation sources for the wide-range millimetre and especially for the submillimetre wave spectroscopy thanks to their unique ability in electronic frequency tuning within a whole waveguide bandwidth [Krupnov, 2012]. Therefore, we will address BWO itself and its frequency stabilisation system in more detail.

Backward-wave oscillator

There are only two manufactures of BWOs in the world: Thomson-CSF in France and 'Istok' corporation in Russia (the town of Fryazino, Moscow region). A series of Fryazino BWOs (fig. 2.3) developed in the 1950-60s [Golant, 1965, 1969] spans the frequency range approximately from 40 GHz to over 1 THz at relative electronic frequency tuning of each tube up to 100 % (fig. 2.4) [Korolev, 2001].

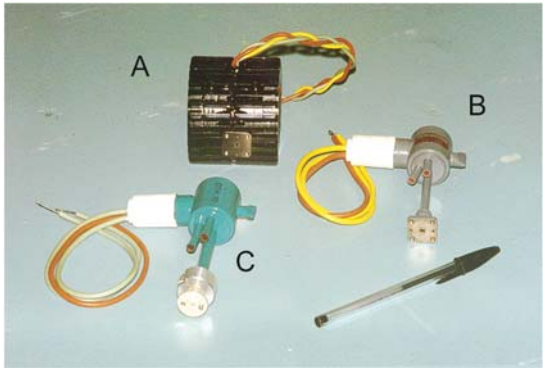

Fig. 2.3. Photographs of Fryazino BWO: *A* — 3 mm wavelength range BWO in a permanent magnet (packetized tube), *B* — 1 mm BWO, *C* — 0.3 mm BWO.

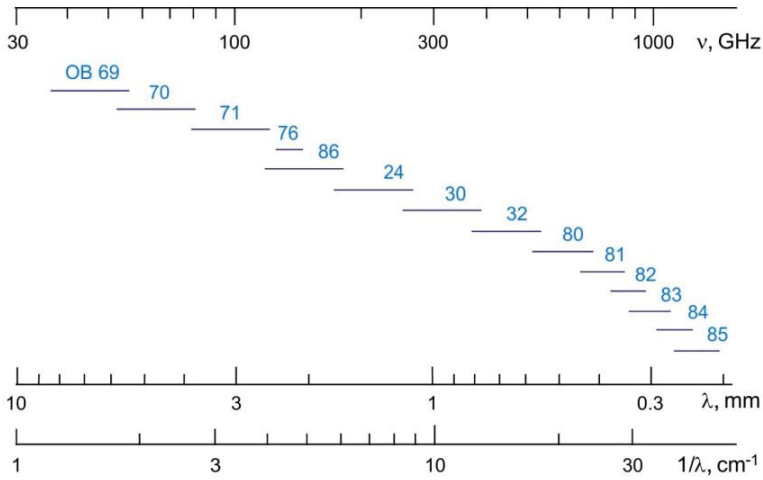

Fig. 2.4. Millimetre and submillimetre wave range spanned by a series of Fryazino BWOs.

In a BWO (fig. 2.5), radiation is generated as a result of long-term interaction of an electromagnetic wave with an electron beam whose electrons are gradually grouped into bunches. The phase velocity of the propagating waves is slowed down by a periodic waveguide structure to the speed of electron flight. Of all the waves with various frequencies generated by accelerated-decelerated electrons moving between the teeth of the slowing down structure (3D periodic waveguide), only the wave for which the phase velocity is equal to the velocity of electron bunches (*the condition of synchronism* between the wave and the electron bunches must be satisfied for wave amplification). The speed of the electrons is determined by the value of accelerating electric field that is specified by the voltage applied between the cathode and the anode. A change in the accelerating voltage leads to changes in the frequency of the generated radiation. The average slope of the frequency-voltage curve (fig. 2.6) is 50-100 MHz/V but may change tens of times within the operating range because of the individual features of the tube. Moreover, the slope may vary significantly at any frequency if part of the radiation is backreflected to the BWO.

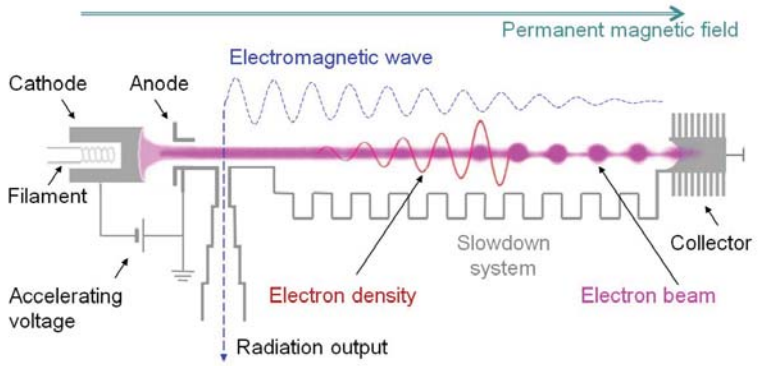

Fig. 2.5. BWO structure.

The power of the generated radiation is directly dependent on the current density of electron beams: the more electrons, the more energy they can transfer to the wave (fig. 2.7). The efficiency of electron-wave interaction, which also influences useful power, depends on many technological factors (quality of element manufacturing, accuracy of adjusting their relative position, etc.) and proper exploitation (strength and homogeneity of a magnetic field focusing the electron beam, accuracy of BWO alignment in the field, amongst other factors). Under optimal conditions, an average BWO power is from tens of milliwatts in the low-frequency part of the series to a few milliwatts for the highest-frequency tubes. Some samples are capable of generating several hundred milliwatts.

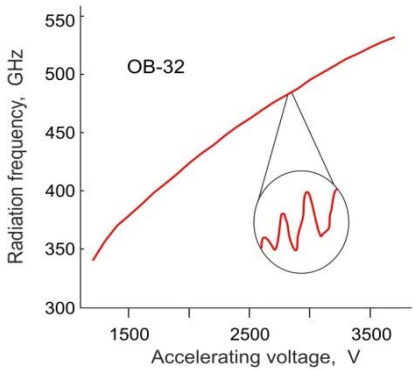

Fig. 2.6. Typical frequency-voltage characteristic of BWO.

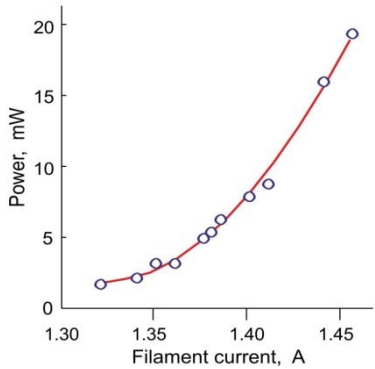

Fig. 2.7. Typical filament current dependence of submillimetre BWO radiation power.

Within the passport BWO range, its power can smoothly deviate from the average one by several decibels. These variations are not manifested in the records of narrow resonant lines.

For obtaining stable output power, a stabiliser of filament current heating a BWO cathode (electron gun) must be used. Still higher power stability can be additionally attained by means of thermal stabilisation of the BWO casing.

An electron beam is almost inertia-free. Therefore, any smallest and/or short-term voltage instability affects the radiation spectrum. Even the best conventional radio technical methods employed for manufacturing power supplies cannot ensure sufficiently high stability of accelerating voltage. The application of BWO for high-precision measurements requires the use of systems of fast automatic radiation frequency stabilisation and control. The best stabilisation and control characteristics are achieved using phase-locked loop (PLL) systems that will be considered below.

Phase-locked loop

It has already been mentioned that the characteristics of any resonant spectrometer depend to a great extent on the quality of the spectrum of radiation used for resonator excitation. There is a close relationship between the frequency and phase of harmonic signals. However, signal frequency can be estimated only after a full oscillation period, and accurate determination of frequency requires an average to be taken over many periods. But any change of frequency may be almost immediately revealed by changes in the oscillation phase in a small fraction of one period. Therefore, a system in which signal frequency stability is attained by active automatic control of its phase, ensures the best spectral characteristics. Such a system is called *the phase-locked loop* (PLL). Its design and operation principles deserve detailed consideration.

A PLL system was conceived by Henri de Bellescize in 1932 [Bellescize, 1932] as a method of receiving weak signals. Only later it was realised that the merits of the PLL system are paramount for stabilising reference oscillator frequency *without frequency error.*

This can be easily understood from the following considerations. Assume that a highly stable harmonic signal $S(t) = \mathrm{Sin}(\omega t + \varphi)$ is needed. The use of an automatic frequency stabilisation system (frequency locked loop, FLL) will introduce frequency uncertainty $\Delta\omega$, so the signal becomes $S(t) = \mathrm{Sin}[(\omega+\Delta\omega)t + \varphi]$. Similarly, the use of a PLL introduces phase uncertainty $\Delta\varphi$ leading to $S(t) = \mathrm{Sin}[\omega t + (\varphi+\Delta\varphi)]$. In both cases, the automatic system attempts to minimise either phase or frequency deviation

from the preset value. However, a mean value of the deviation never reaches zero because, according to the principle of operation of automatic control systems, it would require infinitely large signal amplification. The remaining deviation of $\Delta\omega$ is a systematic frequency error introduced by the FLL system, whereas $\Delta\varphi$ does not affect the signal frequency and can be neglected in most cases.

High stability of the frequency standard can be transferred practically to any point of the electromagnetic radiation range thanks to the PLL of the corresponding oscillators against the frequency standard harmonic. This advantage is used in all modern radiometers and is the basis of all high-precision microwave and optical frequency synthesisers. A frequency synthesiser is a tuneable, coherent radiation source with *quartz stability* (meaning that relative frequency uncertainty is on the order of 10^{-8}) that is the closest to an ideal source for radio engineering. Availability of frequency synthesisers is an important characteristic of mastering a frequency range.

Dozens, if not hundreds, of books are devoted to PLL systems. (see, e.g., Gardner [2005]). The mastering of the microwave range using PLL started in the 1950s, accompanying the expansion of radio methods to a higher frequency range [Peter, 1955]. Russia's first PLL of a microwave generator (10 GHz klystron) against the harmonic of a quartz oscillator (frequency ~75 MHz) was implemented by I.L. Bershtein and co-workers [Bershtein, 1958]. Their PLL had significant advantages over the earlier system developed by Peter and Strandberg [Peter, 1955], which in combination with a rational design and a simple adjustment technique made it suitable for commercial production. The development of this system can be traced by Krupnov [2001].

A PLL system is an automatic control system in which the phase of a controlled signal is continually electronically adjusted to the phase of a high-stability harmonic *reference signal*. The controlled signal frequency changes under the action *of control voltage*. Note that this is an important point: the signal source should be a *voltage controlled oscillator* (VCO). The automatic tuning is achieved by means of oscillations at a difference frequency between the controlled and reference signals referred to as the *beat-note voltage*. If the phases and, hence, frequencies of the signals coincide, there is no beat signal and the control voltage is equal to zero. The slightest offset of the frequency of the controlled signal from the frequency of the reference signal immediately gives rise to beat voltage that starts to build-up in direct proportion to the phase difference of the controlled and reference signals (the larger the initial offset, the higher the build-up rate). Until the signal phase difference reaches $\pi/2$, it is simply an

increase in the direct-current (DC) voltage. The sign of this voltage and the beat signal phase depend on the 'direction' of the initial offset, i.e., on whether the frequency of the controlled signal increases or decreases compared to the reference frequency. Control voltage is fed to the controlled signal oscillator. If the oscillator responds by a decrease of the initial frequency offset, then automatic tuning works. Otherwise, 'automatic detuning' takes place. However, a specific feature of PLL is that the system finds the 'operating point' itself. Automatic detuning persists only until the phase difference between the controlled and reference signals reaches $\pi/2$. After that the control voltage starts to decrease, automatic detuning slows down, and when the phase difference reaches π, automatic tuning sets in (fig. 2.8).

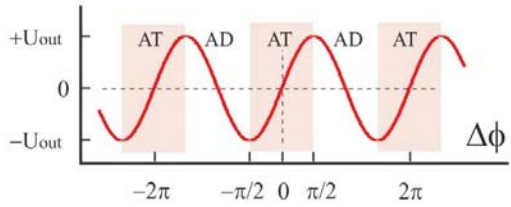

Fig. 2.8. Beat signal as a function of the phase difference between controlled and reference signals. The regions of automatic tuning (AT) and automatic detuning (AD) are shown by white and pink colours correspondingly.

If the system response to the frequency offset is insufficiently fast and the corresponding phase difference is more than $\pi/2$, automatic detuning occurs, which results in excitation of parasitic modulation of the frequency of the controlled oscillator. As the speed of response is finite even in the fastest of systems, there always exist noise components with characteristic frequencies, such that the system response will be too slow. This problem is solved by means of the frequency-dependent 'force' of the system reaction. Slow offsets are compensated with strong force, and fast ones with weak force; very fast offsets are ignored by the system. This is achieved through making the frequency dependence of the control signal gain decay by a definite law. Unity gain is attained exactly at the frequencies for which the system response delay corresponds to the phase shift by π. The required dependence is formed by a *proportionally integrating filter* (PIF), which allows for the correction of parameters of the control signal and, in particular, its bandwidth.

A block-diagram of the simplest PLL system is shown in fig. 2.9. A nonlinear element (for example, a diode in the simplest case), to which the controlled and reference signals are applied simultaneously, serves as a generator of a beat signal. The nonlinearity inherent in this element induces the appearance of current with difference frequency of these signals that is actually a beat-note signal.

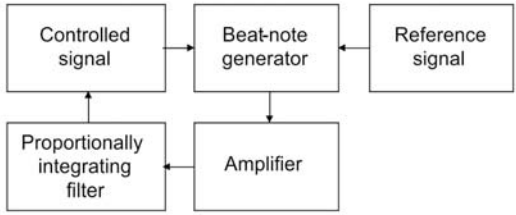

Fig. 2.9. Block-diagram of a PLL system.

The high slope of the voltage-frequency characteristic and the inertia-free electronic tuning inherent in BWO set rigorous requirements for the PLL system. The most essential of them is a high-speed response with characteristic times on the order of a microsecond and less. This means that the control bandwidth must exceed 1 MHz.

Superheterodyne beat-note detection

In PLL systems of high-frequency radiation sources, it is convenient to use, as a reference signal, the harmonic of a low-frequency synthesiser formed in the nonlinear element that receives the source radiation. A beat-note signal, whose frequency is the difference of the frequencies of reference signal harmonic and source radiation, is also formed in the same nonlinear element. The beat signal containing information about the phase difference of these signals is called in this case the *intermediate frequency* (IF) signal. A structure containing this nonlinear element with accessory terminals and joints is called a *multiplier-mixer* (see section 2.2.4 for detail). To increase a useful signal-to-noise ratio (SNR), the principle of superheterodyne detection of radiation at a high intermediate frequency is used. For this, the frequency of a difference signal is chosen in the interval from tenths to several gigahertz. The higher the frequency, the smaller magnitude of the current noise (inherent in all electronic systems) decaying in inverse proportion to frequency. This allows for the use of IF signal amplification present-day ultra-low noise amplifiers based on high electron mobility transistors (HEMT), whose intrinsic noise is comparable to the current noise of a conventional resistor cooled down to a

temperature of about 10 K, even at room temperature (see, e.g., the review of Shurakov [2016] and references therein). In PLL systems this amplifier is called the *intermediate frequency amplifier* (IFA). The amplified signal is compared with a high-stability reference signal, the frequency of which is exactly equal to the chosen frequency of the IF signal (f_{IF}) on a *phase detector*. A phase detector actually subtracts f_{IF} from the IF signal and forms a beat-note between the harmonic of the reference synthesiser and the source signal which, after amplification, is used for automatic correction of the source signal frequency.

In PLL systems of millimetre and submillimetre radiation sources, a microwave synthesiser (2-20 GHz) is usually used as a reference signal generator. Such a system of controlling radiation frequency (fig. 2.10) determines the following ratio of frequencies of the source radiation f_{source}, two reference signals (one of the microwave synthesiser f_{synth}, and one of the intermediate frequency f_{IF}):

$$f_{source} = n \cdot f_{synth} \pm f_{IF}, \quad (2.39)$$

where n is the integer corresponding to the number of the synthesiser harmonic. The sign is not critical for system operation, but important for the exact value of radiation frequency. The operator chooses the plus or minus sign. The corresponding frequency of the radiation source will always be either higher or lower than the frequency of the synthesiser harmonic. The beat-note signals will have the same frequency in either case. If the source frequency starts to increase, the frequency of the first beat-note signal increases too and the second one decreases, and vice versa. One of these two beat signals is chosen for operation and is sometimes called a *direct signal* or direct channel. The second beat signal is referred to as the *mirror signal.*

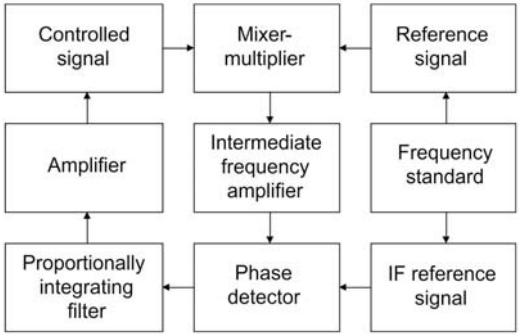

Fig. 2.10. Block-diagram of a PLL system with superheterodyne receiver.

In some cases, it is convenient to use stabilisation beat-notes between the harmonics of source radiation frequency and higher harmonics of a synthesiser signal which also arise in a multiplier-mixer. In this case, the relation (2.39) takes on the form

$$m \cdot f_{source} = n \cdot f_{synth} \pm f_{IF}, \qquad (2.40)$$

where m is the integer corresponding to the number of the harmonic of source radiation frequency.

Spectral characteristics

According to the principle of PLL system operation, all major spectral characteristics of the controlled source are determined by the corresponding characteristics of the reference signals. The PLL system tracks all slow drifts and short-term frequency offsets of reference signals and replicates them to the controlled source within the control bandwidth of the system. Therefore, when choosing reference signal sources, one should pay attention to their long-term stability and spectral purity. Instabilities of the principal reference signal (in our case it is a microwave synthesiser) are of still greater importance, as its frequency and all its instabilities are multiplied by the number of the harmonic. The contribution of PLL itself, in optimal operation mode, is negligible.

The accuracy with which the radiation frequency of the locked source follows the frequency of the reference synthesiser can be assessed by results of measurements of the IF signal spectrum in the PLL mode. In a properly working system, the spectrum width corresponds to the pulsations that cannot be compensated by the PLL system. For high-coherence sources such as klystrons or BWOs, this width is smaller than the minimal bandwidth of the best currently available, commercial spectrum analysers. An example can be found in the work of Lewen [1998], where the quality of BWO radiation frequency stabilisation was investigated. It was shown that the width of the IF spectrum at half maximum was 80 mHz after 30-min averaging. This means that the root mean square (rms) offset of the BWO radiation frequency from the frequency of the synthesiser harmonic was halved, i.e., 40 mHz only. The contribution of the PLL system at frequencies corresponding to the control bandwidth edge, where the reaction of the system is delayed by more than π, resulting in a small typical increase of noise that is easy to observe on a spectrum analyser, is more pronounced but less significant. The spectrum pattern (a typical example is given in fig. 2.11) strongly depends on the

resolution, analysed bandwidth, averaging time, and other characteristics of the analyser.

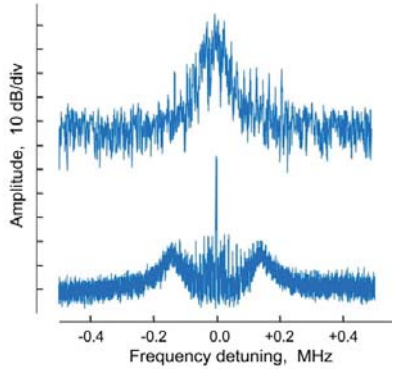

Fig. 2.11. Typical spectra of unstabilised (upper trace) and PLL-stabilised (bottom) radiation sources.

The phase noise N of a signal at frequency F_S is determined by the signal spectrum (fig. 2.12) as a ratio of the noise power density P_N in one side band at the frequency offset F_{off} from the signal frequency F_S within the 1-Hz bandwidth to the carrier signal power P_S expressed in decibels (dBc/Hz):

$$N = 10 \cdot \log_{10} \frac{P_N}{P_S}. \qquad (2.41)$$

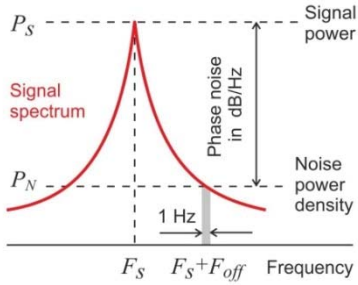

Fig. 2.12. Determining phase noise by signal spectrum.

Multiplication of signal frequency by n gives an n times increase in the amplitude of its instabilities and their power increases proportionally to squared amplitude, i.e., by n^2 times. From this and the definition (2.41) it follows that the phase noise of the multiplied signal increases by

20·log(n). Figure 2.13 shows by way of example an increase of the phase noise of the reference signal at frequency multiplication and the way a PLL system replicates it in the useful signal stabilised by the harmonic of the reference signal.

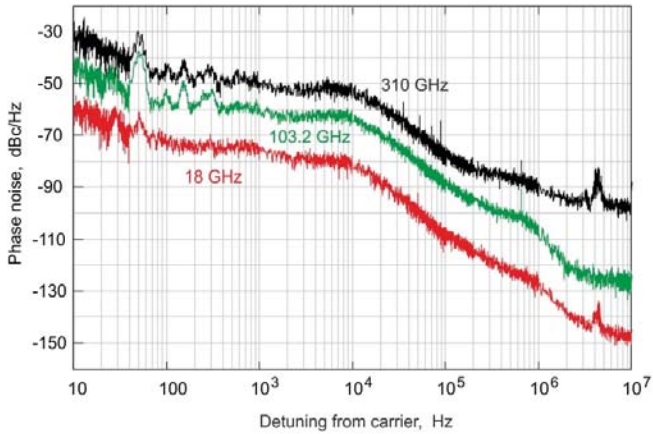

Fig. 2.13. Phase noise in spectra of beat-notes between the studied signals and the reference synthesiser (Wiltron 6769B) signal with negligible level of phase noise compared to the studied one.

One can see in fig. 2.13 the studied signals of the reference synthesiser (Agilent 8254A) operating at a frequency of 18 GHz; the third harmonic of the reference synthesiser operating at a frequency of 34.4 GHz obtained by passive multiplication in a nonlinear element (central trace); and the BWO at a frequency of 310 GHz PLL-stabilised against the ninth harmonic of the reference synthesiser operating at a frequency of 34.4 GHz (upper trace). The contribution of the PLL system manifests itself at detunings above 200 kHz as an increasing deviation of the upper trace from the one in the centre.

Frequency scanning

Following on from the expression (2.39), the frequency of a PLL-stabilised source can be changed in two ways. When the frequency of an IF reference signal is changed, the source frequency will change by exactly the same amount, and when the frequency of a microwave synthesiser is changed, the source frequency will change by n times more. Thus, a PLL system enables the scanning of the source frequency by rather

small steps in the vicinity of the resonator eigenmode, exactly like step recording of a narrow molecular line in microwave gas spectrometers. The principal difference between the resonator response and the rarefied gas response is that in the first case the frequency can vary for quite a number of reasons. For example, it may smoothly change due to the temperature drift that alters the resonator size, may fluctuate as a result of mechanical jitter and vibrations, or vary with a variation of the index of refraction of the gas filling the resonator. All this leads to distortion of the response shape and respective error in its parameter measurements. A natural solution to this problem is to record response over a time much shorter than the characteristic time of all instabilities. The experimental estimates showed that, under normal laboratory conditions, around a millisecond is a sufficiently small recording response time. It is shorter than typical periods of the mechanical vibrations of equipment components and electric pickup (the most bothersome is the pickup with mains frequency of 50 Hz and its harmonics).

Recall that the time period of frequency synthesis is one of the basic parameters of microwave synthesisers. On the set frequency command, the device starts to manipulate available reference signals synthesising a new frequency following a built-in algorithm. The signal frequency at the output of the device is indefinite over this period, it is slowly varying in an arbitrary way. In the best modern instruments, the time of synthesis is around several milliseconds. For reliable determination of resonator response parameters, recording should contain at least dozens, and better hundreds, of points. It should also be taken into account that in conventional microwave synthesisers the phase of the output signal after frequency switching does not correlate with the signal phase before switching. This means that, if such a signal is used for recording resonator response, then each change in frequency is followed by a pause, until the synthesis is completed and the resonator natural oscillations with the old phase are fully damped, and new oscillations are excited to a stationary level in a new phase.

Phase jumps free scanning

From the above, it follows that it is rather difficult to record undistorted resonator response using traditional PLL systems because conventional frequency synthesisers have a relatively long period of frequency switching. This stimulates the development of a system in which the transition from one frequency to another would take place in the PLL regime retaining the oscillation phase. This problem was effectively

solved using Direct Digital Synthesisers (DDS), made possible by the advance of high-speed microprocessor radio electronics.

The essence of DDS operation is the following. Using simple software, a digital processor coupled with a sufficiently accurate digital-analogue converter (DAC) calculates any preset time dependence of voltage and produces, at the output, a step signal synchronised with clock pulses. That is how present-day arbitrary waveform generators work. Limitations on step size and duration of nonperiodic signals are purely technical. If such a generator is commanded to draw a sinusoid with a preset period, its microprocessor with its own clock frequency will calculate the needed number of steps and their amplitudes. Further, the sine generation reduces to sending the corresponding commands to the DAC. To change the frequency at a given moment in time the processor changes the amplitudes of the subsequent steps, as is shown in fig. 2.14. The phase of the generated signal is retained automatically.

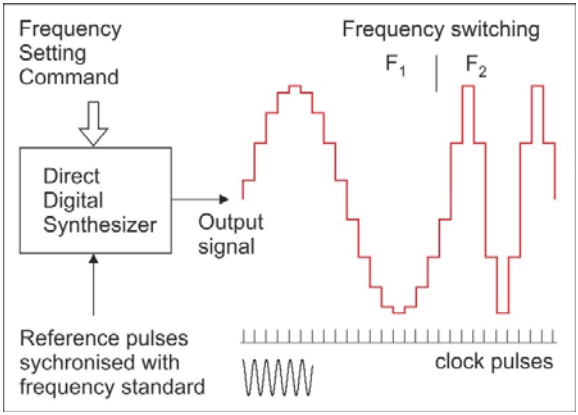

Fig. 2.14. The generation of harmonic signals by Direct Digital Synthesisers.

The signal frequency stability in this case corresponds to the stability of the clock frequency used by the processor, which may be locked, if needed, to the reference frequency standard. The switching speed, or more precisely the duration of the pause at the transition from one step sequence to another corresponding sinusoid with a different period, is limited only by the time of information rewriting to the DAC memory cells. Minimal time between the switchings depends on the speed with which the control processor calculates step parameters and transmits them to the DAC memory.

The use of a DDS as a reference IF signal oscillator in a PLL system enables fast *continuous-phase* scanning of source frequency without phase jumps. The frequency range of the present-day DDSs is determined by the speed of DAC operation and varies from tens to hundreds of megahertz. This imposes limitations on the bandwidth of continuous-phase scanning. The frequency scanning range may be expanded by dividing the frequency of the IF signal, using a digital divider before the signal is fed to the phase detector. Then the source frequency will be defined by

$$f_{source} = n \cdot f_{synth} \pm k \cdot f_{IF}, \qquad (2.42)$$

where k is the division ratio. The larger this coefficient, the broader the range of source frequency scanning by the same DDS. A block-diagram of a PLL system providing such a scanning mode is presented in fig. 2.15.

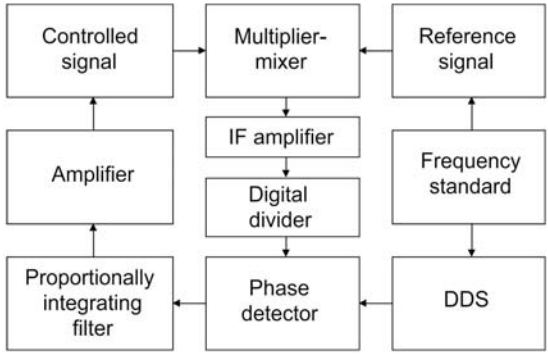

Fig. 2.15. PLL system for fast scanning of a controlled signal frequency without phase jumps at switchings within the IF amplifier transmission band.

Note that the scanning of exciting radiation frequency without phase jumps allows for the recording of resonant response over the time close to the physical limit corresponding to the time constant of the resonator, which is important for achieving ultimate sensitivity of the spectrometer.

Frequency manipulation

Frequency manipulation or stepwise back and forth periodic frequency switching is needed if the resonator response is registered in the time domain. In this regime one frequency coincides with the frequency of the resonator eigenmode, and the other is out of resonance. During the first half of the manipulation period, the radiation excites stimulated oscillations

of the field inside the resonator, which is followed by a decay of the field oscillations in the second half period. The field decay is registered by the detection system of the resonator spectrometer. In this mode, all the features of the PLL system operation enumerated above are exactly the same, as this regime is just a specific case of step scanning where the system makes one frequency step only. Note that the radiation phase conservation is not really important in this case because each excitation-decay cycle is independent.

2.2.3. Waveguide system

The waveguide line of a resonator spectrometer depends to a great extent on the choice of the type of coupling between resonator, exciting radiation, and detector. In the general case, its functions throughout the operating frequency range are the following: 1) the radiation transmission from a source to a resonator, where electromagnetic field oscillations at the fundamental mode will be excited; 2) the channelling of radiation carrying information about the resonator response to the exciting radiation and the delivery of the former radiation to a detector with minimum possible distortions.

Besides, in most of the known spectrometers used for investigating the atmosphere, the waveguide line has the third function, namely, splitting and delivery to the destination point of part of the radiation power sufficient for PLL operation or for any other control of the radiation frequency.

It should be taken into consideration that in real conditions some exciting radiation power may leak through the elements of the transmission line to the detector, bypassing the resonator and interfering with the useful signal. This leads to resonator response distortion, which is itself larger, the greater the leakage.

A decisive factor in the development of a waveguide line is the method of energy extraction from the radiation source (waveguide, antenna, beam). The majority of millimetre and submillimetre sources use waveguides for this purpose. They are convenient because a source readily joins the waveguides consisting of a set of standard elements. For example, rectangular waveguide outputs with standard cross sections are employed in the Fryazino BWOs (Table 2.1).

We remind the readers that the radiation with the wavelength λ cannot propagate in a rectangular waveguide with wall sizes a and b if $a < b < \lambda/2$ (waveguide-below-cutoff). An optimal cross section ($a \times b$) for a single-mode waveguide is $0.45\lambda \times 0.9\lambda$. With a decrease of λ, the number of modes that can propagate in the waveguide rapidly increases. The

following approximate relation can be used for estimations: $n_m \approx 2\pi(a \times b)/\lambda^2$.

Table 2.1. Frequency and wavelength ranges, output waveguide cross section, and approximate number of modes that can propagate in the waveguide for some Fryazino BWOs

f, GHz	λ, mm	*a*×*b*, mm	n_m
36—55	8.3—5.5	2.6×5.2	1—2
52—79	5.8—3.8	1.8×3.6	1—2
78—119	3.8—2.5	1.2×2.4	1—2
118—178	2.5—1.69	0.8×1.6	1—2
177—263	1.7—1.14	1.2×2.4	6—14
256—375	1.17—0.8	1.2×2.4	14—28
370—535	0.8—0.56	1.2×2.4	27—55
526—714	0.57—0.4	1.8×3.6	125—231

The analysis of Table 2.1 demonstrates that, even for millimetre wavelength BWOs with standard cross sections, the waveguides are oversized in the upper part of the operating range. Three BWO types operating in the range from 178 to 525 GHz have a waveguide with 1.2×2.4 mm section. As the frequency increases, the number of possible modes grows from 6 to 55. For all other higher-frequency tubes a 1.8×3.6 mm cross section is used, thus making the output still more oversized.

The manufacturer guarantees that, even in high-frequency BWOs, more than 90 % of output radiation power is in the fundamental TE_{01} mode. However, inevitable parasitic reflections at the elements of the transmission line induce excitation of numerous other modes in an oversized waveguide, disturbing the regular pattern of its field. The field distribution starts to change at frequency tuning, which results in an unstable radiation pattern of the beam formed by the transmission line and, hence, in a strong amplitude-frequency dependence of power and uncontrolled mismatch between exciting radiation and resonator field. The problems related to oversized output waveguides can be partially solved using smoothly tapering waveguide junctions to a single-mode cross section. However, in the submillimetre range, where there are no standard single-mode waveguide elements, quasi-optical elements are preferred.

As resonator response must be recorded with minimal distortions, it is important to minimise leakage of exciting radiation towards the receiver. Parasitic reflections in the waveguide line should be also minimised. This means that all the elements of the waveguide line should be carefully matched. Besides, Faraday isolators that transmit radiation in one direction

and block it in the opposite direction should be installed at the source output and in front of the receiver of the resonator output radiation. The requirement of minimal distortions also means that a waveguide line must be as short as possible, then the characteristic frequency period of standing waves in the waveguide arising due to uncontrolled parasitic re-reflections of radiation from its elements and their junctions will be the largest possible. The larger this period, the easier it will be to allow for or compensate the impact of the received radiation distortions.

It should be taken into consideration that all point-contact detectors used in the millimetre and submillimetre wave range have a current-voltage (C-V) characteristic close enough to a quadratic one (which ensures linear dependence of the output signal on the radiation power received by the detector) only at low (less than 1 mW) power levels. Consequently, a tuneable radiation power attenuator may be used in the waveguide line.

As was mentioned above, the configuration of the waveguide line depends on the choice of coupling with a resonator. The simplest solution is obtained in the case of hole coupling when one [Liebe, 1992] or two [Alder, 1998; Frenkel, 1966-1; Bauer, 1986] waveguides are placed in the central part of one of the resonator mirrors. The requirement of frequency scanning in a wide range implies the use of film coupling for exciting the resonator [Dryagin, 1992; Meshkov, 2005; Tretyakov, 2009; Nagarajan, 2017]. The size of the resonator field spot on the coupling film determines the size of the exciting beam. For efficient excitation, these sizes should be equal and the phase fronts of the exciting beam and of the resonator field should match each other. This is done by setting the corresponding output diameter and length of the horn-antennae to form the exciting beam from the fundamental mode of a rectangular waveguide. The horn is actually the converter of the fundamental waveguide mode to a beam that differs from an ideal (for resonator excitation) Gaussian beam by the phase front curvature. The curvature radius is approximately equal to the horn length. The longer the horn, the closer the beam is to a Gaussian one and the better the matching. Note that the increase of horn length contradicts the requirement for maximum short total length of the waveguide line. An optimal length is found as a result of a compromise, depending on the problem to be solved.

To achieve maximum spectrometer sensitivity, it is necessary to minimise inherent loss of the resonator. A possible way is to use one coupling element for both resonator excitation and registration of its response [Liebe, 1992; Tretyakov, 2009]. In the case of film coupling, this means that radiation from the resonator propagates simultaneously in two

directions: towards the exciting beam and in the opposite direction. The exciting and output beams have not only the same sizes but also the same axes. It is possible to record the response in a beam propagating in the same direction as the exciting beam [Nagarajan, 2017], but this will lead to its strong distortion due to the interference of two beams at the receiver point. The beams propagating towards each other can be separated, for example, using a wire grid polariser and a quasi-optical Faraday rotator of radiation polarisation [Hunter, 2007; Martin, 2009-2], as shown in fig. 2.16a. Vertically polarised radiation passes through the wire grid polariser and enters the quasi-optical rotator where the beam polarisation is rotated by +45°. This beam is directed to the Fabry–Perot resonator. The radiation returning back from the resonator and having the same polarisation passes back through the rotator, where it is rotated by another +45°. This beam is now horizontally polarised, so it is reflected by the grid polariser towards the detector.

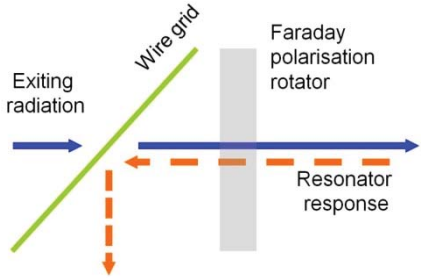

Fig. 2.16a. The separation of radiation beams by a wire grid polariser and a Faraday rotator of polarisation.

Another possible solution for separating these two beams is to use a quasi-optical 50 % beam splitter (or a four-way diplexer) as shown in fig. 2.16b.

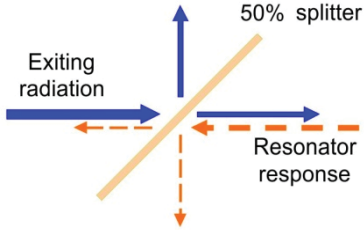

Fig. 2.16b. Beam path in a 50 % beam splitter.

The splitter is a flat plate transparent to radiation (e.g., mica, the thickness of which is chosen so that 50 % of the splitting occurs in the middle of the operating wavelength range) placed at an angle of 45° to the

beam axis. Half the power of the exciting beam is branched off by the plate and directed to the absorbing load. The best result is attained if the beam is directed to infinity by the mirror. One half of the output beam propagates towards the radiation source and is absorbed in the isolator, and the second half is directed towards the detector. This case has an advantage of a broader operation bandwidth and easier implementation, but a lower efficiency because only one quarter of the source power is used.

If the resonator response detector has an input waveguide with a single-mode cross section, then a horn like the one for exciting radiation should be used.

A PLL multiplier-mixer is formally a component that may belong either to the spectrometer waveguide line or to the radiation frequency control unit. The design of multiplier-mixers and ways of their connection will be considered in the next section.

2.2.4. Multiplier-mixer for PLL

A multiplier-mixer functionally belongs to a system of radiation frequency stabilisation and control. The properties of a multiplier-mixer are of key importance in providing stable operation of this system in a wide frequency range and ultimately determine radiation quality. Therefore, the principle of its operation, structure, and specific features of connection deserves special attention.

A mixer is actually the principal component of a *superheterodyne receiver* registering a controlled radiation signal. Historically, heterodyne and then superheterodyne receivers appeared with the advance of radio communication to replace much less sensitive conventional detector receivers.

In a detector receiver, a radio signal $V_s = A_s \cos(\omega_s t + \varphi_1)$ is applied to a nonlinear element. By virtue of its quadratic characteristic, the current flowing through the nonlinear element is proportional to the square of the applied voltage $I \sim (V_s)^2 \sim A_s^2$, i.e., the useful signal is directly proportional to the square of the radio signal amplitude.

An increase in sensitivity at heterodyning occurs due to the power of a stable signal from a local oscillator (heterodyne) connected to the receiver of radio signals. The heterodyne signal voltage $V_h = A_h \cos(\omega_h t + \varphi_2)$ is added to the voltage of the radio signal. The current flowing through the nonlinear element of the receiver, $I \sim (V_h + V_s)^2$, has a component directly

proportional to the product of voltages of the radio signal and the heterodyne: $I \sim 2V_h V_s$. By means of simple trigonometric relations we can show that this component contains a term with difference frequency $I \sim A_h A_s \cos\left[(\omega_h - \omega_s)t + \varphi\right]$. This current component resulting from the mixing of two signals is a useful signal of such a receiver. Its sensitivity may be increased by increasing the amplitude of a heterodyne signal. If the heterodyne frequency is exactly equal to the frequency of the radio signal carrying radiation, then such a receiver is referred to as a *heterodyne receiver*. The phase of a heterodyne signal may always be chosen so that cos φ = 1, hence, the gain of the useful signal in a heterodyne receiver as compared to a detector receiver will be $A_s A_h / A_s^2 = A_h / A_s$. In other words, the higher the heterodyne amplitude compared to the signal amplitude, the higher the gain.

If the heterodyne frequency slightly differs from the frequency of carrier radiation, the signal with difference frequency, called intermediate frequency signal, can be additionally amplified by means of a low-noise IFA and after that detected by a nonlinear element for extracting a useful radio signal. The amplitude of the useful signal in this case is proportional to the square of the product of amplitudes $I \sim \left(A_h A_s\right)^2$, and the gain of the useful signal compared to the detector receiver $\left(A_s A_h\right)^2 / A_s^2 = A_h^2$ is determined by the heterodyne power and does not depend on the magnitude of the radio signal.

Thus, the mixer serves to simultaneously receive a radio signal and a heterodyne signal and generate an IF signal. If a heterodyne signal is a harmonic of a low-frequency signal, an additional task of the mixer is the generation of harmonics, which is accomplished in the nonlinear element where the signals are mixed. The more the element characteristic differs from the linear one, the more effectively harmonics are formed and the larger their number. In this case, the mixer is called a *multiplier-mixer* or a harmonic mixer.

Let us formulate the requirements for a multiplier-mixer intended for operation with a PLL of the resonator spectrometer radiation source. They follow from the requirement of continuous, broadband, tuning-free operation.

1) The mixer shall operate throughout the frequency range of the radiation source without mechanical tuning. For example, for the Fryazino BWOs used as a radiation source, this means operation without adjustments within each waveguide sub-band of the spectrometer (Table 2.1).

2) The difference frequency, which is actually an intermediate frequency, must be sufficiently high to provide the required high-speed operation of the PLL. Let us assume, for example, that a 3 MHz control bandwidth is necessary for stable PLL operation. The system requires a high-frequency filter to exclude from the BWO radiation spectrum the frequency component of phase detector operation. Sufficient suppression of this component can be achieved if the operating frequency of the phase detector is 10 or more times higher than the highest frequency within the control bandwidth, i.e., beyond 3·10 = 30 MHz. If digital division of IF by k is used in the synchroniser for expanding the range of frequency scanning in the PLL mode, then the difference frequency generated by the multiplier-mixer should be higher than 30·k.

3) When scanning over the range, the heterodyne frequency (reference microwave synthesiser frequency) changes n times slower than the radiation frequency (equation (2.39)). Nevertheless, the range of tuning from the lowest f_{synth}^{min} to the highest f_{synth}^{max} synthesiser frequency is fairly large. A multiplier-mixer is supposed to perform efficient harmonic generation and signal mixing throughout the tuning range meeting the boundary conditions $(n+1)\cdot f_{synth}^{min} \le n\cdot f_{synth}^{max}$.

4) The radiation source power may vary significantly within the operating frequency range. The part of this power branched off in the waveguide line of the spectrometer for the PLL system should be sufficient for reliable operation of the multiplier-mixer throughout the frequency range without additional tuning.

It is worthy of note that millimetre wave multiplier-mixers are widely used for expanding the range of microwave measuring instruments, such as radiometers, spectrum analysers, frequency counters, power meters, and others. A large variety of multiplier-mixers in standard waveguide millimetre wave sub-bands, meeting the above-mentioned requirements to such instruments, has been developed and is commercially available (for example, produced by the leading manufacturers, including Quinstar, Millitech, Farran Technologies, and Vadiodes). The requirement of maximal efficiency of mixer operation in such instruments sets the condition according to which all the input radiation received by the mixer is converted to electric current flowing through its nonlinear element, and no back reflections are allowed. The mixer component acting as a receiving antenna is placed in the area of maximal electric field of the wave, thus making it maximum matched to the field of the input radiation propagating in the waveguide. A tapering waveguide, a ridged waveguide, or a smoothly narrowing microstrip line, located along the waveguide axis normally to its wide wall are used as field ‘concentrators’. Still another

element used for the back reflecting part of the power transmitted past the antenna is positioned so that the antinode of the formed standing wave should be in the antenna area. One or two planar diodes, the metallised beam leads of which play the role of a receiving antenna of input radiation, are used as a nonlinear element.

A heterodyne signal is a harmonic of a low-frequency synthesiser connected to the nonlinear element of the mixer by a coaxial connector positioned on the mixer casing. An IF signal is usually separated by a low pass filter placed inside the mixer and is extracted to another coaxial connector.

If the mixer is an inherent part of the system controlling or monitoring parameters of the radiation, only part (preferably a smaller part) of the radiation power should be forwarded to it. This necessitates the usage of a directional coupler in the spectrometer waveguide line (fig. 2.17). Despite the existence of standard directional couplers with different power dividing coefficients for all millimetre wave sub-bands, their application entails the additional elongation of the waveguide line, radiation power loss, and reflections from an additional flange to flange connection.

A multiplier-mixer in the form of a short waveguide section with minimal loss on radiation passage connected directly to the output source waveguide (fig. 2.17) is most suitable for systems controlling and monitoring radiation sources, including the system of spectrometer resonator frequency control.

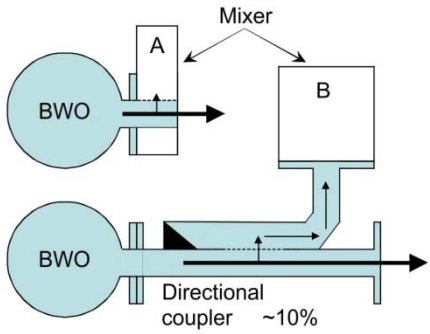

Fig. 2.17. Connecting a transmission-type (A) and a conventional (B) multiplier-mixer to a radiation source.

Such transmission-type multiplier-mixers were also developed for radiation frequencies up to ~180 GHz (see Tretyakov [2007-1]), but they have not been adopted by the industry yet.

Commercial multiplier-mixers with single-mode waveguides are available and may, in principle, be used for radiation frequencies significantly higher than 178 GHz. However, the design of most conventional wide-range mixers operating below 180 GHz allows them to be successfully used at frequencies up to 370 GHz as well, if a large part of the radiation power of a stabilised source directed to the mixer is at the fundamental waveguide mode. Thus, the problem of system operation within the 178– 370 GHz range comes down to the need to find a way for a wide-range separation of part of the radiation source without distorting its mode structure.

This scheme ceases to work beyond 370 GHz, primarily because of low efficiency of generating high harmonics of microwave synthesiser signal. Nevertheless, up to frequencies of approximately 500 GHz, conventional mixers of another type widely employed in microwave radiometers of the millimetre range (sometimes called *balanced mixers*) can also be used. Such a mixer is a key element of superheterodyne radiation receivers. It has two (often identical for better matching) waveguide inputs: one for a heterodyne signal, and the other for the radiation to be received. The frequency of the received radiation corresponds to the same waveguide range as the heterodyne frequency. A wire antenna (in other implementations it may be a microstrip line on a dielectric film in combination with a ridge or a smooth tapering of the waveguide short wall) is placed in the middle of the waveguide passing through the mixer normally to its wide wall. The received radiation and the heterodyne radiation are fed from two sides of the waveguide and directed towards each other. For the fundamental waveguide mode, the antenna is in the region of the maximal electric field propagating in the waveguide. The antenna is connected to a planar diode the second lead of which is connected to a strip line transmitting the difference signal formed in the diode to the output coaxial connector.

One can use as a heterodyne for such a mixer, for example, a signal of any synthesiser operating in the interval from 35 to 178 GHz on the basis of a primary radiation source and a PLL system (e.g., Krupnov [1994]). A good alternative to such synthesisers is a frequency multiplier. The development of high-frequency semiconductor electronics stimulated by the rapid advance of radio communication permits for the attainment of almost any desirable signal power in the frequency range up to 26 GHz. This allows for multiplying the frequency of a conventional microwave synthesiser effectively and obtaining at the multiplier output power sufficient for optimal operation of multiplier-mixers in the millimetre wave ranges up to 100– 200 GHz. Note that the spectral composition of

the multiplier output radiation is worse than in the primary radiation source because of the presence of harmonics of the initial signal.

2.2.5. Recording resonator response and determining its parameters

The requirements to this system and its specific implementation are almost independent of the domain (temporal or frequency) in which the resonant response is recorded. The description presented here corresponds to the detection of the response in the frequency domain but may be readily extended to the time domain.

The system has the following functions:

1) Undistorted detection of the resonator response at its excitation by continuous, coherent radiation frequency-scanned within the vicinity of one of the fundamental resonator modes. The resonator response should be detected without tuning throughout the operating frequency range of the exciting radiation. The scanning time and, hence, the time during which the resonant response should be recorded have upper and lower bounds. On the one hand, it must be much less than the period of characteristic mechanical and electric noise distorting the observed resonator response (section 2.2.2), that is around one millisecond. On the other hand, it cannot be less than the characteristic damping time of resonator self-oscillations that is about one microsecond.

2) The amplification of the resonator response signal to a needed level corresponding to the dynamic range of an ADC converter, digitising the resonator response signal synchronously with step scanning of the frequency of exciting radiation, and storing the signal in computer memory.

3) The determination of resonator response parameters. Of particular interest is resonance width, as it specifies the magnitude of radiation power loss measured by the spectrometer. The other parameters (centre frequency, amplitude, signal-to-noise ratio, and parameters of shape distortion) control operability of the system and are used to estimate measurement error.

4) The effective accumulation of a useful signal for reducing statistical measurement error and achieving maximal sensitivity of the spectrometer. This is attained by optimal noise filtration at all stages of signal recording and transformation, and by repetitive measurements of resonance parameters.

Detection system

The requirement for the resonator spectrometer to have a broad band impedes the usage of high-sensitivity heterodyne or superheterodyne receivers, as this entails the presence in the spectrometer of one more broadband frequency-tuned radiation source. Nevertheless, commercial vector network analysers receiving signals in this way have long been operating in part of the millimetre wavelength range (for example, Keysight Technologies Inc.) and are currently being developed for the submillimetre region. For example, such an analyser has been successfully employed in the Liebe resonator spectrometer [Liebe, 1992] for studying absorption in the atmospheric oxygen in the 54–66 GHz range. However, superheterodyne detection at harmonics can be implemented. In this case, a conventional multiplier-mixer (like for the PLL system) is used for detecting radiation coming out of the resonator. This detection method additionally requires a low-frequency synthesiser sweeping synchronously with the major radiation source.

In the first four standard waveguide sub-bands of the millimetre range from 36 to 178 GHz (Table 2.1), conventional commercial detectors based on point-contact or planar diodes of a single-mode waveguide for each sub-band can be used as receivers of the radiation after its passage through the resonator. The bandwidth (speed of operation) of such detectors can be limited by manufactures to decrease noise level. Bandwidths from 100 kHz to several megahertz are quite sufficient for undistorted resonance recording.

Commercial (much more costly) detectors can be used for operation in higher frequency subranges. However, in the 178–370 GHz subrange, if the source ensures sufficiently high power and its radiation has a good enough spatial mode structure, a standard 2-mm detector on a waveguide with 0.8×1.6 mm basic section may also be employed.

In the 350–500 GHz subrange, the power of wide-range tuneable radiation sources becomes, as a rule, much lower and does not exceed several milliwatts, even in BWOs, although an output BWO becomes still more oversized (Table 2.1). Commercial detectors on the basis of point contact or planar diodes operating at room temperature are currently too expensive. Alternative detection of radiation at frequencies beyond 370 GHz is to use a bolometer cooled by liquid helium. Germanium (Ge) or silicon (Si) bolometers have a higher sensitivity and a broader band (from 0.03 to 20 THz), but they are too slow. Bolometers based on indium antimonide (InSb) have a satisfactory response speed, sensitivity, and broad band. The best representatives, primarily thanks to the well-made

cryostat structure, are currently QMC Instruments bolometers. Their sensitivity is no less than 2000 V/W and equivalent noise power (radiation power equal to the power of intrinsic noise at the output of the system), is less than $1.2 \cdot 10^{-12}$ W·Hz$^{-1/2}$. The speed of response (the time during which a stationary response amplitude sets in when the power at the output is changed) is about 1 μs. The frequency characteristic of hot-electron InSb bolometers with non-resonant magnetic tuning allows for the detection of radiation within the 30–1500 GHz range without any tuning (fig. 2.18).

The application of such a bolometer in the 350–500 GHz subrange permits increasing the signal-to-noise ratio at recording resonant response by more than 2 orders of magnitude compared to the case of conventional room-temperature point-contact millimetre wave detectors. The radiation is fed to the bolometer quasi-optically through a circular window having a diameter of several centimetres, which enables simple alignment with the output resonator beam, for example, by means of a focusing mirror.

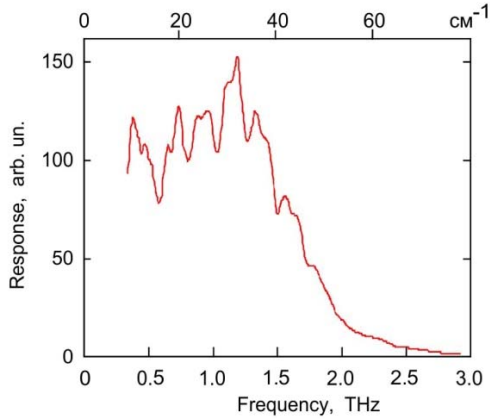

Fig. 2.18. A typical frequency characteristic of a QMC hot-electron InSb bolometer with non-resonant magnetic tuning, cooled by liquid helium.

For precision measurements it is important that the detector should not distort resonator response. Therefore, prior to using any detector, linearity of its characteristic must be carefully calibrated with respect to the dependence of the output signal on applied radiation power. A standard linear video amplifier of a detector signal, matching the detector at the input and ADC at the output and having a bandwidth corresponding to the detector speed completes the set of elements in the detection system.

Digitising resonance response and analysing its shape

The most accurate, commonly accepted way of analysing resonant response shape is to use the parameter variation method, i.e., optimisation or mathematical fitting of the parameters of a model function to experimental data. This method has, for a long time, been widely employed in molecular gas spectroscopy for determining parameters of observable lines and can be successfully used to analyse resonant response.

Experience shows that for analysing the shape of a resonant signal and determining its parameters with minimal systematic error, the signal recording should have at least several tens of points, the recording interval should be equal to about 10 resonance widths at half amplitude, and the signal-to-noise ratio must be at least a few dozen.

Digitising noise (the uncertainty of the signal amplitude corresponding to unity in the last digit) must be at least an order of magnitude less than the amplitude of the signal noise. All of the above means that signal response digitising demands an ADC having at least 1000 quantisation levels. A 12-bit ADC (4096 levels) is sufficient. Signal digitising should be performed synchronously with stepwise scanning of radiation frequency. Even if the radiation frequency is scanned without phase jumps, the time needed for the excitation of field oscillations in the resonator to a stationary level is of the order of the resonator time constant. Therefore, after each frequency step a pause should be made before starting to digitise the signal. The time of signal reading in present-day ADC is very short. It allows for making several consecutive readings of the signal amplitude at each step with subsequent averaging of the results. Several readings of the stationary signal amplitude at the same frequency allow, not only for the reduction of instrumental noise, but also for the evaluation of statistical uncertainty of the measurement.

To minimise systematic error when determining response parameters, the model function must exactly correspond to the shape of the observed signal. Consequently, its choice depends on both particular spectrometer configuration, including the features of radiation source and waveguide line, and the spectrometer operating mode. We will consider the Nizhny Novgorod spectrometer [Tretyakov, 2009] as an example demonstrating the way a model function is constructed and what should be taken into consideration.

As mentioned in section 2.2.4, for a low power (~1 mW) of detected radiation the current-voltage characteristic of all semiconductor diodes is close to a quadratic one. The voltage applied to a diode under the action of the field is directly proportional to the radiation amplitude, and the output signal proportional to the current is directly proportional to the squared

amplitude of the field or its power. According to the principle of operation (the change in the resistance of a semiconductor heated by radiation), the signal arising in the bolometer is also directly proportional to the power of incoming radiation. Therefore, the signal response shape of a high-Q resonator at sufficiently slow frequency scanning corresponds to the Lorentz function (2.11). It should be noted that the power of the radiation exciting the resonator is frequency dependent. This is inherent in any radiation source; in practice, however, this dependence is largely due to parasitic radiation reflections in the spectrometer waveguide line. It was verified experimentally that, if frequency scanning aimed at recording resonator response occurs in a relatively narrow frequency interval (1–10 MHz), then frequency dependence of radiation power may be represented to a high enough accuracy through a linear function. Consequently, in accordance with (2.11), the model function of the resonator response shall be multiplied by a linear function. It should also be taken into consideration that the resonator response signal at the ADC input may have a small invariable component. It can arise as a result of amplifier imperfections as well as due to electric pickups. That is why the model response function is supplemented with a constant additive term, which yields

$$M(f) = \frac{A_1 + A_2(f - f_0)}{(\Delta f/2)^2 + (f - f_0)^2} + A_3, \qquad (2.43)$$

where f is the radiation frequency; the centre frequency f_0, the total resonant response width Δf, and all A_i taking into account the frequency dependence of the radiation power and hardware effects are the variable parameters.

If exciting radiation gets into the detector as a result of insufficiently matched waveguide line in the spectrometer, the model function shall be supplemented with a linear, and possibly, even a quadratic frequency dependent term (see, for instance, Read [1988]).

To reduce statistical error in experiments, repeated measurements and averaging of the results are used as a rule. In the case of resonance width measurements, averaging can be done in two ways. The first way is to average the resonance width value obtained as a result of processing the recorded data at each single scanning of frequency. The second one is to superimpose the multiple recorded contours by their centres and then average them; the resonance width is found in the averaged recording. An example of such a recording through the Nizhny Novgorod spectrometer

[Krupnov, 2000] and the result of its processing by the function (2.43) are presented in fig. 2.19.

The analysis of fig. 2.19 allows for several conclusions:

1) The model function is in a good agreement with the data of the experiments.

2) The signal-to-noise ratio allows for the determination of a resonance width of around 100 kHz with a statistical uncertainty of 20 Hz.

3) The fitting residual[8] shows a symmetric increase of noise in the region of frequency detuning corresponding to the slopes of the resonant response. Such noise points to the appearance of the phase noise of the radiation source (see section 2.2.2) and indicates that accuracy of resonance width measurements can be increased by improving the quality of the radiation spectrum (see section 2.4.5).

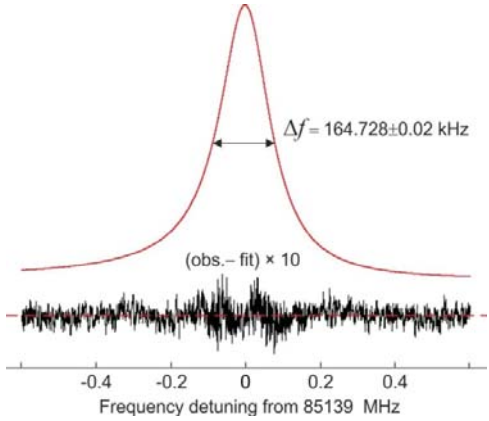

Fig. 2.19. The Fabry–Perot resonator response (500 averaged centred scans, each containing 512 points) (top) and the residual of fitting the shape to the model function (2.43) (bottom). Adopted from Krupnov [2000].

Note that the manifestation of phase noise, including any other frequency (parasitic radiation frequency modulation or PLL system excitation) or amplitude (fluctuations or regular power pulsations) noise can be seen directly on an oscilloscope screen. For this, only the alternating current (AC) component of the resonator response signal from the radiation detector should be observed in a stationary regime with the radiation frequency

[8] Hereafter, the fitting residual or the optimisation residual is understood as the difference between the experimentally obtained data and the theoretical calculations using the function optimised to these data.

scanning switched off. In this regime only a noise trace is visualised. If the trace width is monotonically increasing as the radiation frequency approaches resonance and reaches its peak at the resonance centre, this points to the presence of amplitude noise of the radiation exceeding the detector sensitivity. Amplitude pulsations induced by radiation power modulation manifest themselves analogously [Parshin, 2013]. If the trace width is increasing as the radiation frequency approaches resonance and reaches its maximum at a frequency detuning equal to its half width (where the resonance slope is at its maximum gradient), it is an indication of the radiation phase noise. The resonance slope here plays the role of a frequency discriminator transforming fluctuations of the signal phase (and/or frequency) to its amplitude.

Obviously, the resonance widths obtained by averaging multiple recordings and widths of multiply recorded shapes will coincide only in ideal, fully stationary conditions, where no systematic changes occur in the width of the resonance or in its centre frequency during measurement. Even when response recording takes minimal time, the systematic resonant frequency detuning caused, for example, by temperature drift, will result in a larger apparent resonant response width if the direction of frequency scanning coincides with the direction of resonant frequency detuning, and smaller if in opposing directions. So, it is reasonable to perform sequential scanning in both directions (with frequency increase and decrease) and to average the resulting resonance width values. To minimise measurement error caused by randomly varying walk-off speed, for example, due to mechanical jitter, such scanning (following a ‘saw-tooth’ law) and data acquisition should be repeated many times, averaging the measurement results. Values strongly differing from the average one resulting from strong distortion of resonance shape caused by rare irregular noise should be rejected.

The results of measuring the resonant response width of the Nizhny Novgorod spectrometer at ‘saw-tooth’ scanning of exciting radiation frequency and successive averaging of the measurement results depending on the number of averagings are presented in fig. 2.20. Different curves in the figure correspond to the treatment of the scans with increasing and decreasing frequency. One can see manifestations of relatively fast resonant frequency detuning. As a result of the frequency detuning, the difference between the resonance widths at back-and-forth frequency scans can amount to several hundred hertz. At the same time, the averaged dependence of the results of direct and back scans shows that after approximately 350 recordings the result ceases to depend on the direction of detuning and only

slowly varies within 10 Hz, which indicates that there was no pronounced systematic drift of the resonator length in the considered experiment.

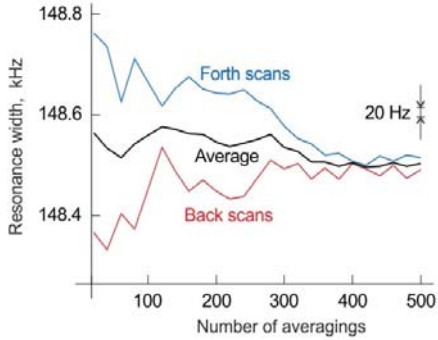

Fig. 2.20. An example of convergence of the results of measuring resonance width, corresponding to scanning with increasing (upper curve) and decreasing (lower curve) frequency in repeated data averaging. The line in the centre is the result of averaging. Adopted from Krupnov [2000].

2.3. Registering gas spectrum

In the previous sections of this chapter, we addressed measurements of the absorption coefficient of a gas filling a resonator at a definite spectral point corresponding to the frequency of the resonator eigenmode. It was assumed that the absorption coefficient does not depend on frequency within the range of recording resonant response. If it is necessary to determine gas spectrum, i.e., the frequency dependence of the absorption coefficient, the simplest way is to measure absorption by means of a resonator with a fixed length L at the frequencies of its successive longitudinal modes. This is equivalent to step-by-step recording of a gas spectrum in conventional spectrometers with a frequency synthesiser used as a radiation source. With such a spectrum measurement, the magnitude of the frequency step $c/2L$ in the resonator spectrometer corresponds to the difference in the frequencies of successive modes (equations (2.27)–(2.29)). This means, for example, that with the use of a 70 cm-long resonator, the magnitude of the frequency step in gas spectrum measurements will be ~200 MHz. Taking into consideration that under atmospheric pressure the width of spectral lines for most atmospheric molecules is about 3 GHz, such a frequency step provides the number of points in line shape recordings sufficient for reliable determination of its spectroscopic parameters. The easiest way to record a spectrum with a smaller frequency step is to increase the resonator length. For example, the resonator

assembled at the Ohio State University (USA) is 10 m long [Meshkov, 2005], and has the intermode distance of approximately 3 MHz, but there are natural limitations to this option.

Controlled tuning of resonator length seems to be more promising. Conventional precision mechanics ensures that the position of the resonator mirror is set to an accuracy of about 1 micron when the mirror is moved within 2 cm. When the length of a 70-cm resonator in the 2 mm wavelength range changes by 1 μm, the resonance frequency changes by ~0.2 MHz. As the coefficients of line broadening by pressure are on the order of 10 MHz/Torr for most atmospheric gases, a sufficient number of points in line profile recording may be obtained at a pressure of the studied gas mixture more than 1 Torr. A still higher frequency resolution can be attained if a mechanical tuner is supplemented by a piezoceramic movable element that can electronically, smoothly change its size typically within about 10 μm. This was done, for instance, in the resonator spectrometer at the University of Manchester (England) [Alder, 1998]. Such a combination allows the automatic adjustment of the resonator to the centre of the studied molecular line at radiation frequency scanning, which almost lifts the restriction on line width. Nevertheless, resonance frequency scanning is meaningless if the molecular line width is comparable to or less than the resonant response width. In this case, if the resonance and molecular line frequencies coincide, the absorption line is observed as a dip in the resonator response [Frenkel, 1966-1; Alder, 1998], and the parameters of its profile may be investigated by traditional molecular spectroscopy methods. A water vapour absorption line at a frequency of 183.31 GHz at room temperature on the background of resonator response is shown by way of example in fig. 2.21 for three different pressures [Dryagin, 1970]. The molecular line width at the lowest pressure is about 270 kHz; it is almost fully determined by the Doppler broadening (section 1.2.2). The resonance response width is approximately the same. It is worth noting that the nonlinear effect of saturated absorption in media (known as *Lamb dip* or *Doppler-free* spectroscopy) manifests itself in the centre of the line. Lamb dip arises as a result of the equalizing, under sufficiently intense radiation of the populations, of the transition levels of the molecules whose motion is perpendicular to the direction of radiation propagation; then a counter-propagating radiation beam passes the media without absorption.

Consider in more detail the simplest case when the spectrum is registered at the frequencies of the resonator eigenmodes with a fixed length, as the advantages of the resonator spectrometers over spectrometers

of other types are most apparent in this case, i.e., in the investigation of broad lines or non-resonant absorption smoothly varying with frequency.

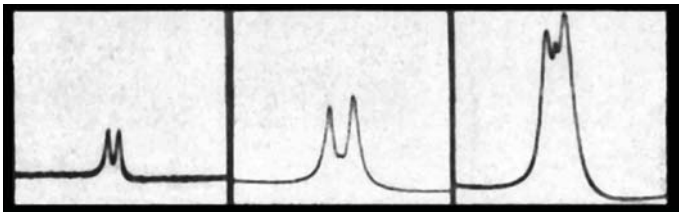

Fig. 2.21. The oscillograms of response of the resonator tuned to the frequency of the water vapour absorption line at 183.310 GHz at room temperature and three different pressures (from left to right: 0.1, 0.01, and 0.001 Torr) of water vapour filling the resonator [Dryagin, 1970].

If the studies are aimed at determining only the shape of gas spectrum rather than the absolute value of absorption coefficients, the resonator radiation loss can be calculated as shown in section 2.2.1. By transforming the expressions (2.14)-(2.16), we obtain that the response width Δf of the resonator filled with gas is related to the absorption coefficient α and to the resonator loss P_{res} by

$$\alpha = \Delta f \frac{c}{2\pi} - \frac{P_{\text{res}}}{L}. \qquad (2.44)$$

Thus, the process of determining the spectrum comes down to successive measurements of resonance widths at eigenmode frequencies and to simple calculations. The signal-to-noise ratio in the recorded spectrum of the studied gas is determined in this case, not only by the statistical error of resonance width measurements, but also by the small-scale amplitude-frequency dependence of the resonator loss caused by parasitic radiation reflections in the transmission line contributing to the resonator loss (section 2.2.3). These reflections in waveguides cannot be fully eliminated; therefore, the frequency dependence of resonator loss manifests itself in the gas spectrum as an additional instrumental noise. The influence of parasitic reflections can be reduced by decreasing (as far as it is allowed by the sensitivity of the resonator response detector) the magnitude of coupling, as well as by means of two Faraday isolators, one of which is placed at the detector input and the other at the output flange of the radiation source (fig. 2.28 in section 2.4.1).

Spectrum registering can take a rather long time. Small changes in the thermodynamic parameters of the studied gas (temperature, pressure, and humidity) that may occur over this period of time can lead to systematic

variation of the absorption and the related changes in the shape of the observed spectrum. Small changes can be taken into account and measurement results can be re-calculated to average conditions constant throughout the experiment through a model calculation of absorption. Atmospheric absorption and its constituents can be calculated, for example, via the MPM known worldwide [Liebe, 1989, 1992; Rosenkranz, 2017]. Possible inaccuracies of the used model introduce a negligibly small error in such a procedure.

An example of recording the spectrum of laboratory atmosphere at room temperature and atmospheric pressure in the 125–200 GHz range [Krupnov, 2000] is presented in fig. 2.22. In case of inaccurate calculation of resonator loss, the spectrum may be observed against the background of a function smoothly varying with frequency. This is taken into consideration in the analysis of the spectrum by means of a model function similarly to processing of the recordings of spectral lines in conventional microwave spectrometers, where they are observed against the background of parasitic signals. An analogous method is used for determining the parameters of resonator response (section 2.2.4).

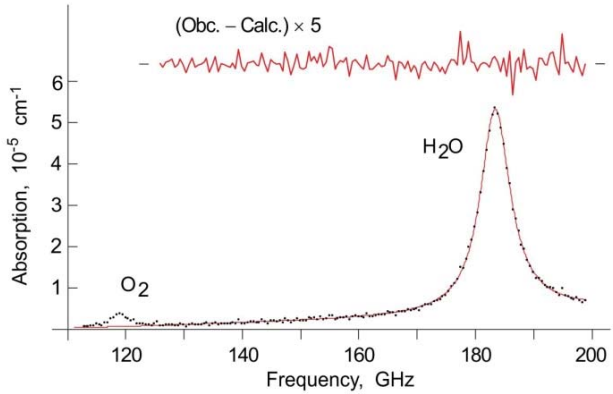

Fig. 2.22. The absorption spectrum of the atmosphere in the 125–200 GHz range (dots) obtained using the Fabry–Perot resonator by subtracting the calculated resonator loss. The solid curve corresponds to the model function optimised to the experimental points which is a sum of the Van Vleck–Weisskopf profile and the second-order polynomial with respect to frequency. The optimisation residual is shown at the top. Adopted from Krupnov [2000].

Gas spectrum can be determined more accurately if resonator loss is found experimentally. The technique of registering gas spectrum then follows directly from equation (2.17). First, the loss spectrum of the resonator (2.15) evacuated to a deep vacuum or filled with a non-absorbing gas (for example, argon) is measured by the resonant response widths. This spectrum is sometimes called the *baseline* of the spectrometer. After that, the resonator is filled with the studied gas and the spectrum of radiation loss in the resonator (2.14) is measured again. The difference between these two spectra gives the radiation loss spectrum in gas (2.16), which, given a small optical thickness, is linearly related to the absorption coefficient of the gas.

Note that the resonator eigenfrequencies during baseline registration slightly vary due to changes in the speed of light in the medium. This variation can be neglected as a rule as, for the index of refraction n of most gases, the condition $n - 1 << 1$ is fulfilled. Moreover, this variation can be eliminated by an appropriate choice of non-absorbing gas pressure during baseline registration.

To illustrate this measurement method, we present in fig. 2.23 an example of recording the spectrum of laboratory air at the atmospheric pressure in a frequency range of 110–200 GHz [Tretyakov, 2003]. In both recordings in the upper part of fig. 2.23 one can see the characteristic irregular amplitude-frequency dependence of the spectrum of resonator loss caused by parasitic radiation reflections in the waveguide. If the configuration of the resonator and of the entire quasi-optical transmission line whilst registering the baseline and the absorption spectrum of the studied gas do not vary (which is usually ensured by thermal stabilisation), then the parasitic reflections do not change either. They do not affect the final spectrum (in the lower part of fig. 2.23), as they are subtracted together with the baseline.

The standing waves influence can be eliminated better still by using their regular dependence on the distance between the radiation source and the resonator. If the source is moved along the axis of exciting radiation, there appears pure sinusoidal modulation of the resonator Q-factor. The regularity of this process allows for a substantial reduction in the related systematic measurement error by averaging the absorption coefficient determined by (2.17) for several predetermined values of the distance between the radiation source and the resonator within the full spatial period of the standing wave. The choice of distances should include an even number of points corresponding to opposite deviations of the Q-factor from its mean value, for example, to its minimum and maximum [Koshelev, 2018-1].

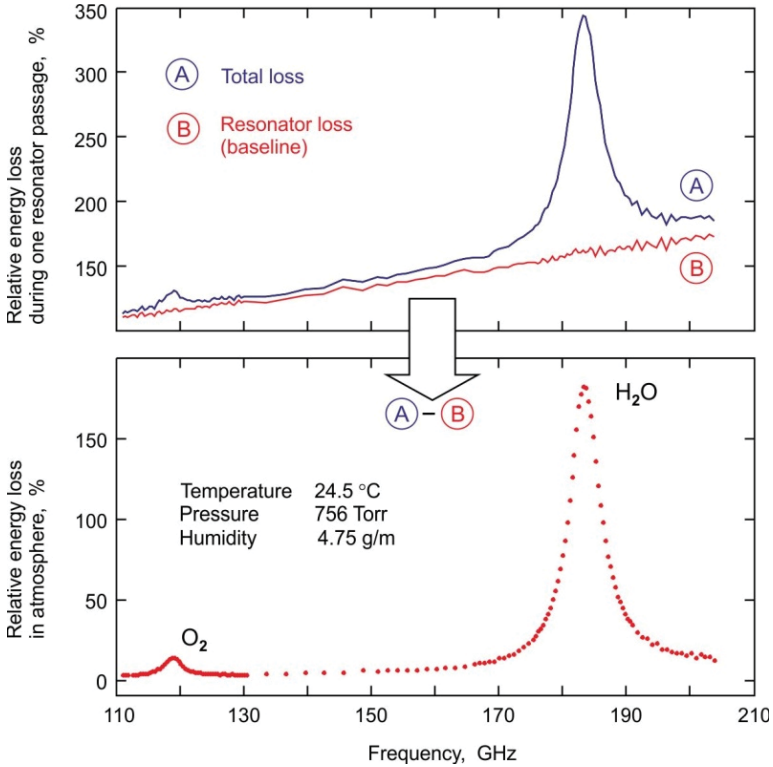

Fig. 2.23. An illustration of the principle of measuring gas absorption spectrum by a resonator spectrometer. Adopted from Tretyakov [2003].

This method of spectrum recording assumes that the studied gas does not significantly influence the resonator losses. However, there are exceptions. For example, if a resonator is filled with a gas mixture containing polar molecules (a water molecule is a prime example), they adhere to coupling elements and mirrors (surface adsorption), leading to changes in their properties and, hence, in the instrument baseline. The results of the measurements, in Tretyakov [2009], of the humidity dependence of an additional resonator loss arising when the resonator is filled with humid gas are shown in fig. 2.24 for several temperatures as a typical example of the problem. The comparison of fig. 2.24 and fig. 2.2, where the result of calculations of the loss of a resonator with close parameters is presented, demonstrates that the effect induced by water absorption may be significant.

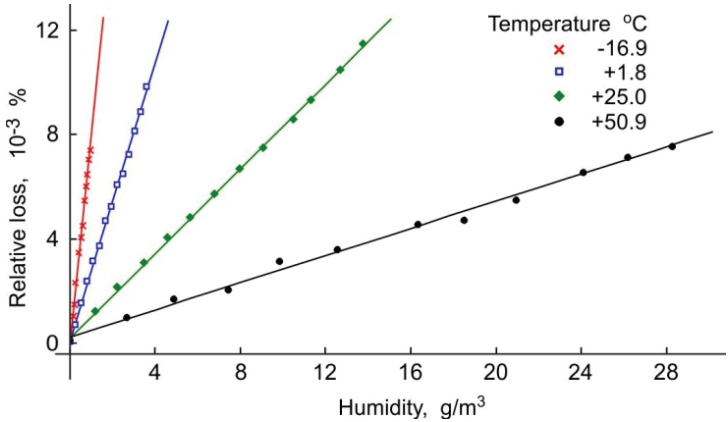

Fig. 2.24. Additional loss arising in the Fabry–Perot resonator filled with humid gas due to adsorption of water. Adopted from Tretyakov [2009].

This problem can be solved using a method of absorption measurements at different path lengths (the optical thickness variation method). The radiation loss during one passage of an empty resonator is determined only by the properties of its basic elements (section 2.2.1) and does not depend on the resonator length. The absorption loss in a gas filling the resonator is directly related to the optical thickness, i.e., to the resonator length.

We will show how the path variation method allows for the determination of the absorption coefficient of a gas at a small optical thickness, when all the expressions are quite clear. First, we will transform the expression (2.44) to the form

$$\Delta f = \frac{c}{2\pi}\left(\frac{P_{\text{res}}}{L} + \alpha\right). \qquad (2.45)$$

This indicates that, for the known length of the resonator, its loss and gas absorption coefficient can be regarded as two independent parameters. The values of these parameters can be unambiguously found in two ways: 1) the resonance width is measured for two values of length L_1 and L_2, and α and P_{res} are found from the solution of the system of two equations (2.45); 2) the resonance width is considered as a function of length. In this case, the values of the function are measured in a definite range of argument values, and α and P_{res} are found as the values of variable parameters giving the best fit of the model function (2.45) to the measured values.

The first method seems easier to use and more suitable for applications, as it can be implemented without mechanical changes of the resonator mirror position, which simplifies the spectrometer design and reduces measurement time. The second method ensures better control of measurements, which is advantageous for investigating the potential of the method. An example of its application is given in fig. 2.25, where the results of measuring response width of the resonator filled with laboratory air at atmospheric pressure and room temperature are plotted as a function of resonator length at the same fixed frequency of exciting radiation [Krupnov, 2000]. The resonator length in the figure is given in units of the number of radiation half-waves between the mirrors. One of the mirrors was sequentially moved along the resonator axis from one resonance to another. The value of the absorption coefficient determined in this experiment was $9.904(53)\cdot10^{-7}$ cm^{-1} (0.430(3) dB/km), which is in a good agreement with 0.443 dB/km calculated for the experimental conditions according to the MPM program [Liebe, 1989].

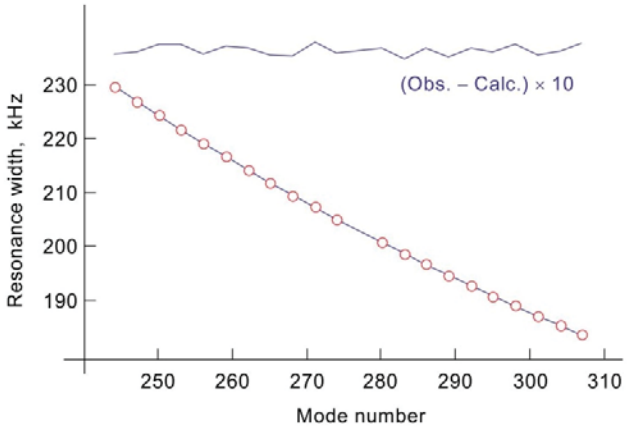

Fig. 2.25. The resonance width measured as a function of the number of radiation half-waves q between the resonator mirrors at a fixed frequency of 140.286 GHz (circles) and optimisation of the function (2.45) to the experimental points (line). The optimisation residue is shown at the bottom of the figure. Adopted from Krupnov [2000].

It should be taken into consideration that the movement of the mirror along the resonator axis does not change resonator loss only to the first approximation. The change in length leads to the change in the field spot size on the mirrors and on the resonator coupling elements, which in turn

changes diffraction loss. These changes, however, are regular and may be calculated to a high degree of accuracy (section 2.2.1). The resonator configuration can always be made so that the impact of the changes will be less than the statistical error of resonance width measurement.

The second method when solving the problem of resonator properties variation due to molecular adsorption was implemented in the work of Tretyakov [2009]. In this study the sensing element of the spectrometer is a module consisting of two resonators that are identical, except for the lengths which differ by exactly double (fig. 2.26). As well as the coupling elements and mirrors, the field distributions inside the resonators must be identical. This is attained by making the upper mirror of the short resonator flat. For a better match of the module to the waveguide system, a lens correcting the divergence of the exciting beam and providing identical conditions of coupling with both resonators can be placed at the module input. The measurements are performed at the frequencies of the short resonator eigenmodes which coincide with the frequencies corresponding to the modes of the long resonator. The parameters of the resonances of each resonator are measured sequentially, for which one of the resonators is damped (an absorber is inserted into the resonator) by a mechanical switch (fig. 2.26).

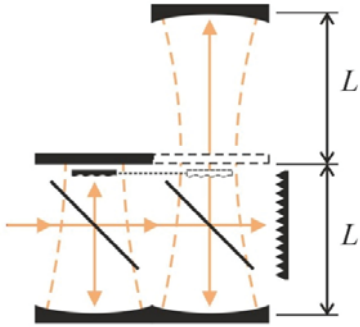

Fig. 2.26. A paired resonator module. The direction of Gaussian beam propagation is shown by arrows, and the distribution of the standing wave electric field by the long-dashed lines. The position of the resonator switch corresponds to the case when the short resonator is blocked and the long one is open. Adopted from Tretyakov [2009].

If we assume that the gas molecules are adsorbed by identical elements of the two resonators identically, then the additional loss P_{ads} caused by the adsorption will also be the same in both resonators. Then making use of the expressions (2.12), (2.14) and (2.15), for the losses of the empty and gas-filled resonators of the module we obtain the following relations

$$P_{\text{res1}} = \frac{2\pi L}{c}\Delta f_{01}; P_1 = P_{\text{res1}} + P_{\text{ads}} + P_{\text{gas1}} = \frac{2\pi L}{c}\Delta f_1$$

— for the resonator having length L and

$$P_{\text{res2}} = \frac{2\pi L}{c}\Delta f_{02}; P_2 = P_{\text{res2}} + P_{\text{ads}} + P_{\text{gas2}} = \frac{2\pi L}{c}\Delta f_2$$

— for the resonator having length 2*L*.

Using the above relations and the expression (2.16), in the approximation of a small optical thickness of the gas, we find the relation between the absorption coefficients of the gas and the measured resonator widths:

$$\alpha = \frac{2\pi}{c}\left[2(\Delta f_2 - \Delta f_{02}) - (\Delta f_1 - \Delta f_{01})\right]. \qquad (2.46)$$

The results of measurements of the absorption coefficient of the mixture of nitrogen and water vapour separately by means of (i) the resonators of the module and the relation (2.17), and (ii) using the method of length variation and the relation (2.46) are presented in fig. 2.27. One can see that a systematic error of absorption measurement caused by the adsorption of molecules of the studied gas can amount to hundreds of percent Tretyakov [2009].

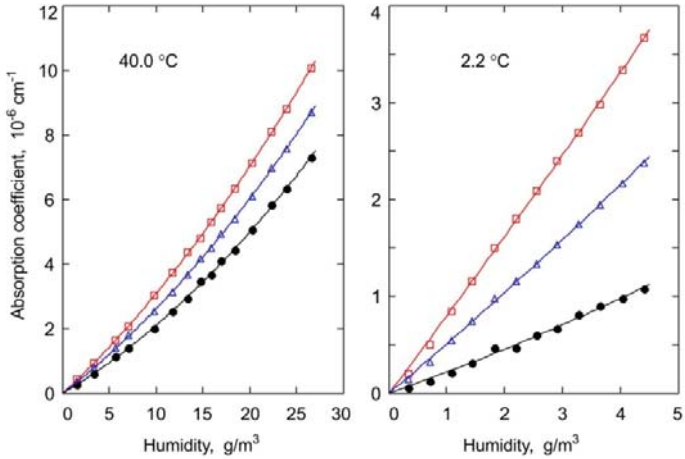

Fig. 2.27. The absorption coefficient of humid N_2 *versus* humidity at atmospheric pressure for 40 °C (*left*) and 2.2 °C (*right*). The measurements were made at a frequency of 130.38 GHz using three methods: by 0.35 m-long resonator (squares), 0.7 m-long resonator (triangles), and the method of length variations using both resonators (circles). Adopted from Tretyakov [2009].

2.4. Example of the resonator spectrometer

In the previous sections of this chapter, we considered the general principles of resonator spectrometer development and functioning, as well as possible options for the systems that may be included in its structure. Here we will describe an actual operating instrument — the spectrometer implemented at the IAP RAS in Nizhny Novgorod (Russia) that was conceived in 1999 for high-accuracy studies of the spectra of atmospheric gases and has been constantly developed and upgraded since [Krupnov, 1999, 2000; Shanin, 2003; Tretyakov, 2006, 2009; Parshin, 2009; Parshin, 2014; Koshelev, 2018-1]. Its characteristic features will be analysed in comparison with the best-known analogues, which will provide the opportunity for readers to get acquainted with several more resonator spectrometers. In conclusion we will discuss prospects for further development of the Nizhny Novgorod spectrometer.

2.4.1. Design principles

The spectrometer block-diagram is shown in fig. 2.28. The main spectrometer unit is a module consisting of two almost identical (including field structure) open Fabry–Perot resonators with film coupling, placed in a temperature-controlled vacuum chamber. Radiation losses in the resonator are reduced to minimum, so that up to frequencies of about 400 GHz they are almost fully determined by mirror reflection losses (see fig. 2.2) and are close to the smallest possible value for resonators with uncooled mirrors (fig. 2.29). The optical quality resonator mirrors were made using the same technology, from solid brass with a silver coating and a protective aluminium oxide coating. The mirror diameter is 140 mm, and the curvature radius is 490 mm.

The mirrors are rigidly fixed on three massive metal bases. The bases are connected by six invar rods, providing the requested rigidity of the resonator frame. The lengths of the resonators are 35 and 70 cm and may be changed, if needed, by moving the bases along the rods. The special fastening of the short resonator's flat mirror allows for the compensation of the different heat expansion of the rods and mirrors to ensure an invariable ratio of the resonator lengths when the temperature of the chamber is changed. The coupling element is a 5 μm thick Teflon film stretched over a frame and placed at an angle of 45° to the resonator axis. The field spot size on the coupling film for the specified mirror parameters and resonator size is several centimetres.

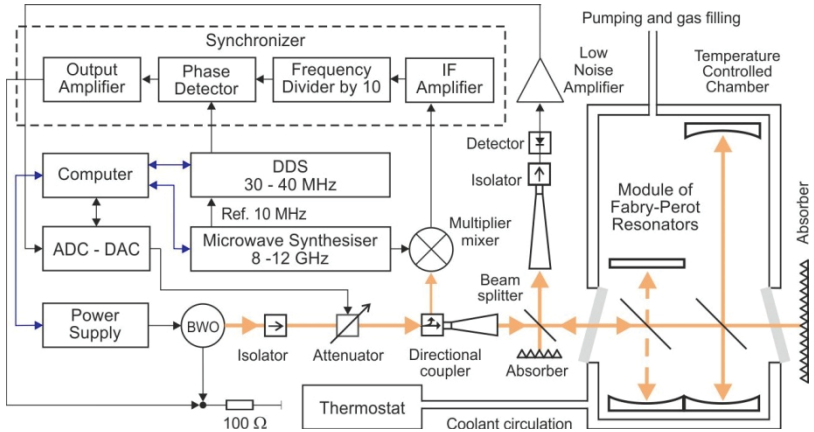

Fig. 2.28. The block-diagram of the Nizhny Novgorod resonator spectrometer.

The BWO-based frequency synthesiser is used as the radiation source. The BWO radiation frequency is stabilised by the PLL system against the harmonic of the microwave frequency synthesiser. Linear, step-by-step radiation frequency scanning in the PLL mode is performed by fast tuning without phase jumps of the frequency of the IF reference signal by means of a commercial direct digital synthesiser (DDS) PTS-10 (Programmed Test Sources Inc.), controlled via a fast synchronous parallel interface.

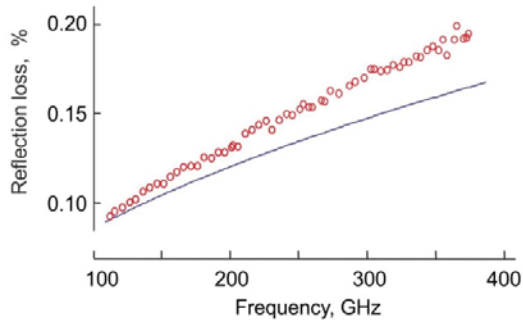

Fig. 2.29. The results of room temperature measurements [Parshin, 2014] of reflection losses for the mirrors of the Nizhny Novgorod spectrometer (circles) and the calculated dependence for ideal mirrors of pure silver (curve).

The absorption coefficient of the gas filling the resonator module is measured by the changes in the resonant response width. One or two resonators are used, depending on the tasks to be solved in experiment. The response is recorded at fast linear scanning of the exciting radiation frequency. The response width is found as a result of mathematical processing of its shape.

The minimum recording time of the resonator response (100–500 frequency steps) is determined by the time per step or the time between frequency switchings. The system allows, if necessary, for the reduction of this time down to 2–3 μs which is comparable to the resonator time constant. However, 45 μs per step were chosen in Koshelev [2018-1] as an optimal compromise in the current spectrometer configuration. This time is short enough to minimise the impact of the characteristic low-frequency mechanical and electrical noise distorting the resonator response. The influence of other factors leading to the resonance centre frequency drift during recording, such as, for example, thermal expansion, is eliminated by saw-tooth frequency scanning (with increasing and decreasing frequency) and subsequent averaging of the widths of the observed responses.

The spectrum of the studied gas is obtained as a set of points at the frequencies corresponding to the frequencies of the resonator eigenmodes with fixed length. The intermode distance corresponds to the resonator length and may vary from 200 to 400 MHz. The radiation frequency tuning from one resonator mode to another occurs automatically with the change of the frequency of the reference microwave synthesiser. This is accompanied by a short-term (~10 μs) break of the PLL, when the synthesiser power is corrected automatically using the result of pre-calibration to optimise the operation of the multiplier-mixer and to tune the power of the radiation exciting the resonator, as a result of which, the resonator response amplitude remains unchanged.

2.4.2. Backward-wave oscillator PLL

One of the fundamental elements of the PLL of the Nizhny Novgorod resonator spectrometer is its frequency synchroniser which combines an IF beat-signal amplifier (IFA), digital frequency divider, digital phase-frequency detector, proportional-integral filter, and output amplifier of the control signal, as well as a system indicating phase lock and normal operation of the entire PLL system. In addition, the synchroniser includes an automatic signal search and locking system which is activated, when the PLL mode fails, and periodically scans the synchroniser output voltage within the dynamic range of the output amplifier (about 10 V), thus

initiating the scanning of BWO radiation frequency (~500 MHz) and search for the IF signal. If a beat signal sufficient for normal operation appears at the synchroniser input, the PLL mode resets and the automatic searching system is switched off.

In the earlier stages of system development, an AD9850 microchip operating at a clock frequency up to 125 MHz seemed to have the most suitable parameters of all commercial DDSs as it permitted the synthesising of a signal with the option of fast frequency scanning without phase jumps in the 20–40 MHz range. The minimal frequency scanning step was merely 30 mHz, and the time between switchings was 58 μs. To expand the range of BWO radiation frequency scanning, the beat-signal between the harmonic of the microwave synthesiser and the BWO was digitally divided by 10. As a result, the expression (2.42) for the BWO radiation frequency in the PLL mode took the form

$$f_{\mathrm{BWO}} = n \cdot f_{\mathrm{syth}} \pm 10 \cdot f_{\mathrm{DDS}}\,. \qquad (2.47)$$

The application of a DDS as a source of the IF reference signal enabled fast frequency scanning without phase jumps of the millimetre and submillimetre source up to 200 MHz, around an arbitrary frequency point set by a microwave synthesiser within the BWO operating range.

BWO high-voltage power supplies have an insufficient voltage tuning speed to provide the required frequency control rate, therefore the PLL control signal is fed to an additional 100 Ohm resistor connected in-series with the BWO anode circuit; hence, it is algebraically subtracted from the high cathode voltage. As the BWO anode is connected to the BWO casing, it is under the control voltage. Consequently, a dielectric isolation is needed to separate the BWO and the waveguide line of the spectrometer. An alternative method of connecting PLL control voltage is to direct its low-frequency part to the analogue input of the high-voltage BWO power supply, and the high-frequency part to the BWO cathode. In this way, it is possible to use the high *voltage gain* of the power supply at low and medium frequencies. Then the amplifier of the high-frequency part of the control signal can be made less powerful, thus making the amplifier faster, which in turn will provide a broader control band and a higher quality of PLL operation. The downside of such a connection is the need to connect the amplifier output to the high-voltage conductor through an isolating capacitor. Careless switching of the high-voltage power supply, especially high-voltage breakdown that often occurs in BWOs, can damage the amplifier elements.

The general approach to stabilisation and control of the BWO radiation frequency in the spectrometer is the same for all frequency subranges.

However, the efficiency of generating the harmonics of the reference microwave synthesiser frequency decreases with an increase of the harmonic number. At frequencies beyond 400 GHz for the harmonic number 40 and higher, its power becomes insufficient for stable operation of the PLL system. This problem is solved by means of a commercial active frequency multiplier (‘Kvartz’, Nizhny Novgorod) of a microwave synthesiser signal with the output frequency in the 75–110 GHz range (fig. 2.30). This device consists of a cascade-connected passive frequency doubler of the 13.25–20 GHz range, a power amplifier for the 25–37 GHz range, and a passive frequency tripler. The input connector is coaxial, and the output one is a waveguide with a 1.25×2.5 mm section. The multiplier output power in the frequency range of 75–110 GHz smoothly varies between 2.2 and 4.5 mW at a constant power at the input of approximately 100 mW. Multipliers of this type are quite standard microwave components produced by many manufacturers (see, e.g., products from Radiometer Physics GmbH).

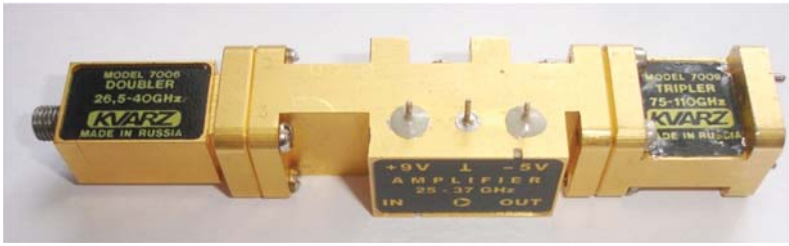

Fig. 2.30. The frequency multiplier of the microwave synthesiser used in the PLL system operating in the 350-520 GHz range. Adopted from Parshin [2013].

The frequency multiplier is connected to the multiplier-mixer based on a planar GaAs Schottky diode. The use of the frequency multiplier reduces the number of the operating harmonic in the multiplier-mixer down to 4-5 and provides stable functioning of the PLL system for many hours throughout the 350-520 GHz frequency range [Parshin, 2013].

2.4.3. Waveguide system

The use of a BWO as a radiation source and film coupling of the radiation and the resonator determines the configuration of the spectrometer waveguide system (section 2.2.3 and fig. 2.28). Each frequency subrange is determined by the waveguide section of the corresponding BWOs (Table 2.1). The waveguide system of each

subrange is assembled with the radiation source and receiver on a unified dielectric board, which allows for fast spectrometer retuning from one subrange to another.

A characteristic feature of the 36–178 GHz frequency range (four subranges) is that all the basic elements of the waveguide system — isolators, couplers, mixers, attenuators, and detectors — have standard single-mode waveguides like in the BWO. The only quasi-optical elements of the waveguide system are horns that match a Gaussian beam and waveguides, and a diplexer (50 % splitter) isolating the exciting radiation and the radiation that has passed through the resonator (fig. 2.16b). The multiplier-mixers of the PLL system are homemade transmission-type mixers also functioning as a directional coupler. Their design features and basic characteristics can be found in Tretyakov [2007-1].

The 177–263 GHz and 256–375 GHz subranges may be called transient. Starting from these frequencies, BWOs have oversized output waveguides with 1.2×2.4 mm section. However, the 'purity' of the mode composition of BWO radiation allows for the reduction of the waveguide size, without significant power loss, by installing a smooth tapering transition after the output flange of the BWO to a 0.55×1.1 mm cross section that is close to a single-mode waveguide for these frequencies, and then use available conventional waveguide elements, similar to those used in longer-wavelength subranges.

The attempt to replicate the transmission mixer design for the PLL system with a 0.55×1.1 mm cross section waveguide failed. The dimensions of standard planar diodes are too large for such a waveguide, which disturbs the optimal conditions for electrical current induction in the diodes at the radiation frequency. This problem is not a fundamental defect of the design as it may, in principle, be solved by developing a special pair of planar diodes. Attempts to use a transmission mixer with a 1.2×2.4 mm waveguide section connected to the BWO output in these subranges did not give a satisfactory result either. The power conversion in the mixer at these frequencies was extremely resonant, with deep dips caused by the mismatch between the mixer diodes and the BWO radiation due to the wavelength shortening that was much more than the one calculated. However, the test measurements demonstrated that the problem can be solved successfully by using a standard multiplier-mixer (see section 2.2.4) with a waveguide section of 1.2×2.4 mm. This means that a large portion of the BWO power within these ranges is really at the fundamental waveguide mode and the design of a standard mixer is insensitive enough to the radiation wavelength. Thus, the problem of system operation within the 178–260 and 260–370 GHz ranges comes

down to the need to find a possible way of broadband splitting-off of part of the radiation power without distorting its good mode structure. An acceptable solution was found by placing a conventional 20 % waveguide (0.55×1.1 mm) directional coupler after the tapering transition from the 1.2×2.4 mm to the 0.55×1.1 mm cross section at the BWO output. A reverse smooth transition from the 0.55×1.1 mm to the 1.2×2.4 mm cross section with the attached standard multiplier-mixer was connected to the side output of the coupler.

This scheme proved to be invalid in the 350–500 GHz range because of strongly irregular functioning of the directional coupler.

The range of frequencies beyond 370 GHz is characterised by a substantial decrease of the BWO output power (down to several milliwatts) and a pronounced reduction of the sensitivity of point-contact detectors caused by the rapidly growing parasitic capacitances in the diodes. As a result of the large size of the output waveguide, the BWO radiation is multimodal and has polarisation components along both waveguide walls, thus the actually used BWO output power is reduced further. Standard elements based on a single-mode waveguide are impracticable because of large losses. Therefore, a quasi-optical transmission line is used for operation in the 350–520 GHz frequency range (fig. 2.31). A gradually tapering waveguide junction *2* from the 1.2×24 mm to the 0.55×1.1 mm cross section is placed after the output flange of the BWO *1*. The junction acts as a mode filter reducing the number of possible waveguide modes by approximately five times. Further, the rectangular waveguide is transformed to a circular one by horn *3* shaping, at the output, a quasi-optical beam with a diameter of approximately 15 mm. About 50 % of the radiation is tapped by splitter *4* for the operation of the PLL system of the BWO. The other fraction of radiation passes through quasi-optical attenuator *5* followed by quasi-optical diplexer *6* separating the exciting and output beams, like in all the other frequency subranges. Idle outputs of the splitter and diplexer are blocked by matched loads (absorbers) *7*. The radiation from the resonator propagates to the receiver (InSb bolometer) through quasi-optical transmission line *8*. The radiation split-off for the PLL system passes through horn *9* and proceeds to the signal input of the 1.2×24 mm waveguide-based multiplier-mixer *10*, the heterodyne input of which is connected to the output of frequency multiplier *11* (fig. 2.30) whose input is connected to the microwave frequency synthesiser via isolator *12*. The signal output of the multiplier-mixer is connected to low-noise IFA *13*. The components of the submillimetre structure ‘OLIVE’ (IRE, Kharkov, Ukraine) have been used as elements of the quasi-optical line.

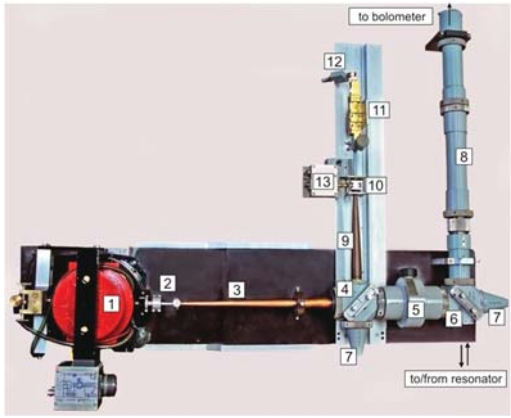

Fig. 2.31. The waveguide transmission line of the resonator spectrometer for the 350-500 GHz frequency range. Adopted from Parshin [2013].

For the operation of the PLL system in this frequency range, a multiplier-mixer developed for broadband, high resolution terahertz molecular gas spectrometry has been used. This multiplier-mixer has a waveguide input with a 1.2×2.4 mm cross section for a heterodyne signal and a quasi-optical input for submillimetre radiation [Krupnov, 2001]. Such mixers were successfully used in the well-known video spectrometers based on BWOs and a cooled bolometer in Cologne [Winnewisser, 1994], Kiel [Golubiatnikov, 2005-2] (Germany) and Lille [Bailleux, 1998] (France) Universities, and in other research centres.

2.4.4. Spectrometer capabilities as compared to the analogues

Here we will compare broadband spectrum recordings of atmospheric gases made by the Nizhny Novgorod spectrometer and by the three most well-known resonator spectrometers that have been successfully used for studying atmospheric absorption.

Technical and methodical features of spectrometers will be discussed, and a comparative analysis of their potential and basic parameters will be made.

The recording of the air absorption spectrum at atmospheric pressure and room temperature is presented in fig. 2.32. It is currently a unique recording for the width of the spectral range where the radiation wavelength varies by more than 10 times. This spectrum is a combination of recordings made in six spectral frequency subranges that can be regarded as a survey recording, demonstrating the spectrometer capabilities.

Well recognised in the spectrum are the characteristic lines corresponding to the radiation absorption by atmospheric gases. Detailed investigation of all these lines and of the observed non-resonant absorption will be considered in sections 3.1 and 3.2, respectively.

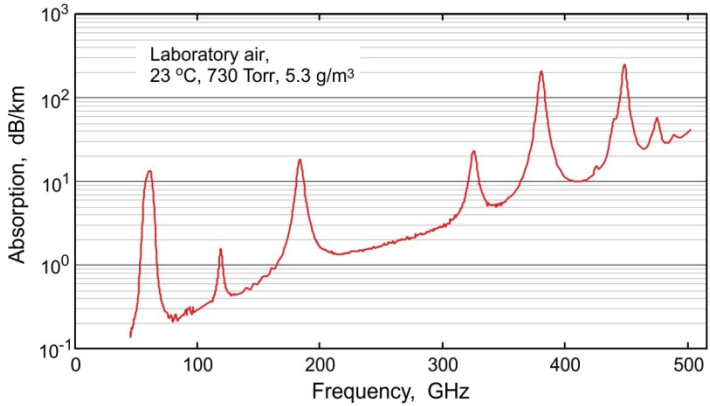

Fig. 2.32. Recording of the spectrum of atmospheric air with the Nizhny Novgorod resonator spectrometer.

The parameter most significant for the comparison of different spectrometers, besides their wavelength range, is the absorption coefficient sensitivity that is usually defined as a minimum detectable absorption corresponding to the absorption signal equal to the standard deviation of the hardware noise. However, it is important to distinguish between (a) the sensitivity routinely attained in spectrum studies called below 'real' sensitivity, (b) the record sensitivity demonstrated in targeted investigations, and (c) the ultimate sensitivity which can be attained for a specific spectrometer configuration under the condition of optimal operation of all its systems.

The real and record sensitivities differ mainly by the time spent on measurements. For increasing the sensitivity of any spectrometer, the method of useful signal accumulation is employed, i.e., averaging the results of measurements. If the experimental noise is *white*, i.e., its parameters are independent of time and its spectral components are distributed uniformly throughout the frequency range, its amplitude, according to the statistics, will decrease in direct proportion to the square root of the number of measurements if this number is sufficiently large. A natural limitation of this method of sensitivity increase is the duration of the period during which all the spectrometer components ensure its stable operation. Taking into consideration that direct comparison of the

sensitivity spectra of different spectrometers by their recordings is not quite legitimate, researchers sometimes indicate the time over which the declared sensitivity is achieved and for comparison they use the sensitivity normalised to the square root of the measurement time.

Ultimate sensitivity is characterised not only by the measurement time but also by the efficiency of using the time of the operating spectrometer for acquiring data about the absorption coefficient, i.e., the longer the technical pauses related to various switchings, adjustments, data transmission during spectrum recording, and other similar non-productive time losses, the farther the attained sensitivity from the ultimate one.

FASSST spectrometer

Two recordings of air absorption spectra with overlapping frequency ranges made with two resonator spectrometers are presented in fig. 2.33 on the same scale. Both the spectra were registered at atmospheric pressure, room temperature, and close humidity values. Spectrum *A* was obtained using the Nizhny Novgorod spectrometer [Tretyakov, 2003], and spectrum *B* the Ohio State University spectrometer [Meshkov, 2005] in which the resonator response was registered using the FAst Scan Submillimeter Spectroscopy Technique (FASSST) developed for high-resolution molecular gas spectroscopy [Albert, 1998].

Both recordings correspond to the 183–GHz diagnostic atmospheric water vapour line. At the bottom of the figure, one can see the spectrometer noises obtained as the difference between the observed spectrum and the model absorption.

A comparison of the recordings demonstrates that the real sensitivity of both spectrometers was approximately the same. This does not mean that the two spectrometers have the same record and ultimate sensitivities. Let us consider in more detail the principle of operation of the Ohio spectrometer and analyse how much time was spent on recording, what the non-productive time losses were, and what reserves can be used to increase the efficiency and sensitivity of each of the two spectrometers.

A simplified diagram of the Ohio spectrometer is shown in fig. 2.34. The resonator response in this spectrometer is recorded in the time domain. High sensitivity is attained by means of a 10-m symmetric Fabry–Perot resonator. The spherical resonator mirrors made of oxygen-free copper have a diameter of 30.5 cm and a curvature radius of 762 cm. The intermode distance is 15 MHz, which provides approximately 6000 fundamental longitudinal resonator modes within the 170–260 GHz interval corresponding to the frequency range of the BWO that serves as a

radiation source. The spectrometer has a quasi-optical waveguide line. Two thin-wire polarisers turned at an angle of 45° to each other together with the Faraday polarisation rotator act as an isolator, minimising radiation reflections in the excitation line. Film coupling (Mylar, 12 μm) of the resonator with the exciting radiation and hole coupling (3 mm in diameter) with the receiver of the resonator response are used. An InSb bolometer cooled by liquid helium serves as a receiver. The fractional radiation power loss per one pass through an empty resonator is less than 1 %, which ensures the Q factor over 5 mln. The contribution of diffraction losses starts to grow rapidly at frequencies below 190 GHz, thus impeding the use of the spectrometer with this resonator in lower-frequency subranges.

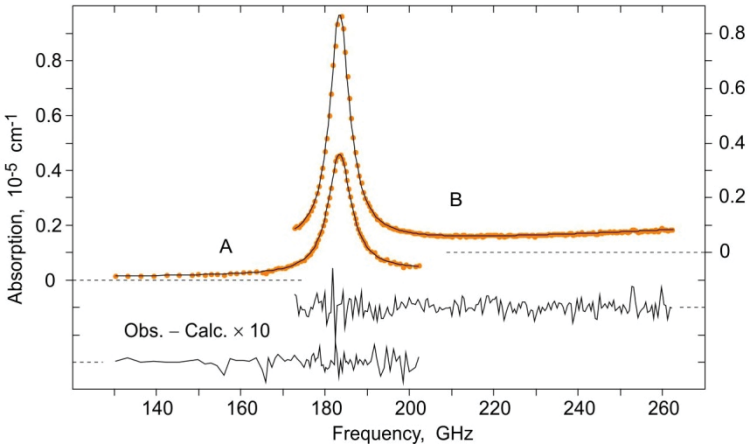

Fig. 2.33. Recordings of the atmospheric diagnostic line of water vapour made with the Nizhny Novgorod spectrometer (spectrum *A*, left) and with the Ohio spectrometer (spectrum *B*, right). The dots correspond to the experimentally measured absorption, and the curves to the calculated absorption optimised to the experimental data. The optimisation residue with a 10-fold magnification is shown at the bottom of the figure.

A resonator of such length is highly sensitive even to small fluctuations of ambient temperature. To minimise their influence, the vacuum chamber containing the resonator is placed in a thermostat with high-accuracy, active, processor-controlled temperature regulation which comprises electric heaters, fans, and heaters cooled by liquid nitrogen. As a result, a stable resonator temperature is maintained with ±0.5 °C error

and temperature gradients of no more than ±1 °C in the interval from –80 to +100 °C.

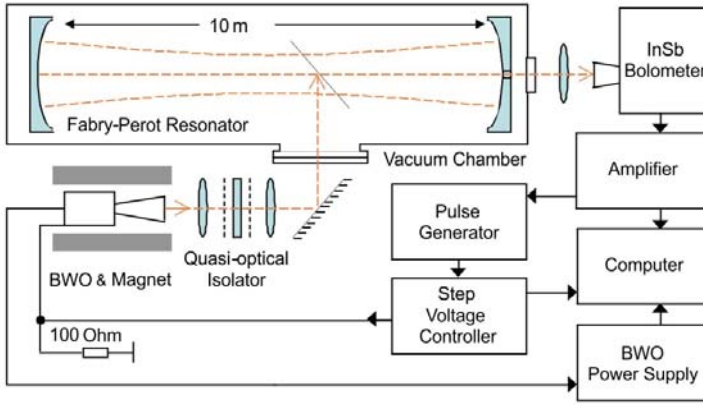

Fig. 2.34. Schematic diagram of the Ohio resonator spectrometer.

The principle of fast radiation frequency scanning (~30 GHz per second) allows for the employment of the fact that at small time intervals (smaller than the period of characteristic pulsations of power supply voltages) the radiation spectrum width of the BWO controlled only by a high-voltage source without automatic frequency control is much smaller that the intermode distance and the resonance width. The frequency-scanned radiation source passes through the resonances over a time comparable with the resonator time constant, which leads to successive excitation and 'ring-down' of field oscillations at the eigenmode frequencies, the decay time of which is measured in the spectrometer. Such an operation mode is attained in the spectrometer by means of a data acquisition system the trigger diagram of which is presented in fig. 2.35.

The cathode voltage controlling the BWO radiation frequency changes linearly with time. The signal appearing at the output of the detector registering the resonator response points to the excitation of field oscillations at one of the eigenmodes. As soon as this signal has reached a preset trigger level, a step voltage controller is activated and produces a voltage pulse applied to the BWO anode. As a result, the BWO radiation 'jumps away' from the resonance frequency. This changes the control voltage and results in a stepwise increase of the frequency of the BWO radiation. Such a frequency change corresponds to an instantaneous switching-off of the exciting resonator radiation. The leading edge of this

pulse triggers a device recording the time dependence of the detector signal amplitude, which corresponds to the decay of the power of free oscillations at the just-excited resonator mode and the trailing edge of the pulse stops recording. The process is repeated at the excitation of the next longitudinal resonator mode. Significant changes in the slope of the C-V characteristic (fig. 2.6), inherent in BWO, require the constant automatic tuning of the pulse duration so that, after a jump, the radiation frequency should always be within the intermode interval and should not coincide with the frequency of the succeeding mode. Fitting of the parameters of the exponential model function (2.4) to the registered responses allows for the determination of radiation losses in an empty resonator (or in a resonator filled with non-absorbing gas) and in a resonator filled with the studied gas and determining its absorption spectrum by their difference (2.17). The frequency is calibrated by the recording of a known gas spectrum at low pressure.

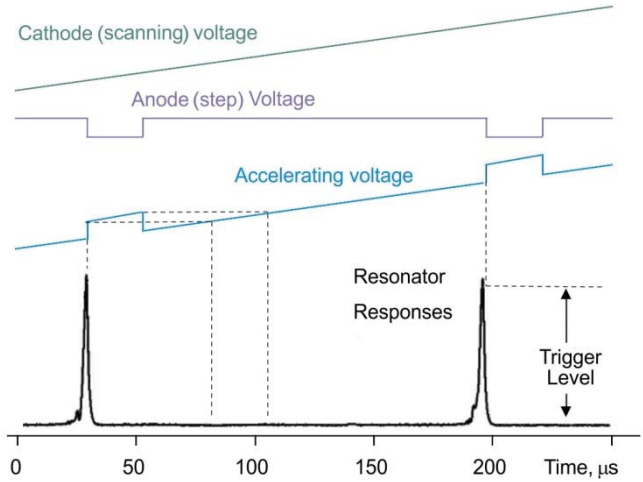

Fig. 2.35. The trigger diagram of the data acquisition system in the Ohio spectrometer [Meshkov, 2005].

The uncertainty of measuring the absorption coefficient at the frequency of each resonator mode, arising mainly due to the standing waves influencing the magnitude of coupling with the resonator, has been evaluated to be $2 \cdot 10^{-7}$ cm^{-1} [Meshkov, 2005]. It is the ultimate sensitivity specified by the principle of the spectrometer operation. Nevertheless, in the particular case of the Ohio spectrometer the real and record sensitivities characterised by the signal-to-noise ratio in the spectrum

recording can be more than the ultimate one. This has the following explanation. The standing radiation waves in the spectrometer waveguide line impede the attainment of a pronounced sensitivity gain by averaging the results of successive spectrum recordings, as the statistical noise associated with the signal-to-noise ratio when registering resonator response only slightly exceeds the systematic signal variations caused by the standing waves in the case of a single recording of the ring-down signal. Moreover, a complicated interference pattern of parasitic standing waves in a long spectrometer waveguide line and of regular fundamental resonator modes is very sensitive to mechanical jitter and to microscopic changes in any radiation-path-related size due to both residual temperature drifts and pressure variations in the course of filling the resonator with gas. Besides, the resonance frequencies change a little with a change in the index of refraction.

All this does not allow for the instrument baseline variations to be taken into account experimentally, as shown in fig. 2.23. Thus, it is a key limitation of spectrometer sensitivity. Nevertheless, the frequency period of the parasitic standing waves in a long spectrometer waveguide line is short, the component of the signal related to the standing waves has a quasi-periodic character, and the number of frequency points at which absorption is measured is very large. Therefore, in studies of the spectra with a typical scale of absorption variation much larger than the period of the standing waves, the magnitude of absorption can be averaged over groups of successive points. This increases the signal-to-noise ratio in the spectrum recording approximately in proportion to the square root of the number of averaged points. The spectrum *B* in fig. 2.33 was obtained at a single scanning of the entire considered frequency range. Approximately 6000 values of the obtained absorption were averaged over groups of 30 points. The instrument baseline deduced from the recording of the loss spectrum of the resonator with air was found analogously. The rms deviation of the as-obtained 187 experimental points in the 'noise path' of the spectrum (shown at the bottom of fig. 2.33) corresponds to the absorption of $2.9 \cdot 10^{-8}$ cm^{-1}. It is real spectrometer sensitivity for such spectra, which was also confirmed in the investigations of the oxygen spectrum at pressures above the atmospheric one [Meshkov, 2007]. The operating range of the spectrometer includes the line of molecular oxygen isotopologue $^{16}O^{18}O$ in a natural concentration that has absorption coefficient $2.3 \cdot 10^{-8}$ cm^{-1} in the centre. The spectrum of 6000 points is registered in a single scanning of the spectrometer range. As the oxygen line is very weak and broad and its shape need not be analysed, the recording can be averaged over groups of 100 points, which increases

sensitivity by about 10 times. Indeed, this line is observed in the experimental spectrum (fig. 12 from the work Meshkov [2007]) with the signal-to-noise ratio on the order of two, which corresponds to the sensitivity of approximately 10^{-8} cm^{-1}. This value is not a record one for the considered instrument either. For example, in the studies of absorption in dry nitrogen (section 3.2.1), the parameters of the continuum absorption, monotonically and weakly varying with frequency, were determined by averaging over numerous experiments performed at different pressures and temperatures. The total of about $6 \cdot 10^6$ point-measurements were taken throughout the spectra recordings within the operating frequency range of the spectrometer over the period of many days, which allowed for attaining the error of determining an absorption coefficient of $4.5 \cdot 10^{-9}$ cm^{-1} at a maximum experimental pressure of 3 atm and maximal experimental frequency of 260 GHz. This sensitivity follows from the continuum absorption uncertainty value of $0.013 \cdot 10^{-18}$ cm^{-1} $GHz^{-2}Torr^{-2}$ specified in Meshkov [2007].

Despite the fact that a single scanning of the studied frequency range takes only 3 s, the time needed for obtaining the spectrum of the studied gas is much longer. It includes the time needed for preparing and recording the spectrum of resonator loss (baseline) and the time for preparing and recording the spectrum used for frequency calibration of the resonator. In addition, long-lasting procedures of gas filling and pumping are also needed. Thus, the assertion made by the authors of the Ohio spectrometer (see, e.g., the abstract to Meshkov [2005]) that their instrument enables absorption measurements in the 170–260 GHz range over 3 s, is not quite correct.

The only possibility for enhancing the sensitivity of this spectrometer is the averaging of absorption values over groups of points within a single spectrum recording, which may be applied only in studies where absorption weakly varies with frequency.

One more basic feature of the Ohio spectrometer is worthy of note. During spectrum recording the radiation source scans the entire frequency range, including the sections between the fundamental modes of the resonator. The resonance response width can be assessed by its Q-factor of $5 \cdot 10^6$ and average operating frequency of 200 GHz using the expression (2.1). The obtained value of 40 kHz is almost 400 times less than the intermode interval. Obviously, in these conditions the useful time, i.e., the time needed for registering the resonator responses, is much shorter than the total scanning time. The limiting scanning speed is determined by the minimal time needed for the resonator excitation, which means that the time of resonance scanning (for certainty we take the frequency interval

equal to the resonant response width of 40 kHz) must be around the resonator time constant corresponding to $\tau \sim 4$ μs. The obtained estimate of a limiting scanning speed of 10 GHz/s agrees with the real speed used in the spectrometer. Assuming that the useful time includes the sum of the excitation time and the time of 'ring-down' (for estimates we can take the time of total oscillation damping to be 3τ), the useful-to-total time ratio or the spectrometer efficiency is approximately 1 %.

Let us now make an analogous analysis of recording *A* in fig. 2.33, obtained with the Nizhny Novgorod spectrometer [Tretyakov, 2003]. It contains 84 frequency points corresponding to the frequencies of the fundamental modes of a 40 cm long resonator in the 130–202 GHz range. The measurements were taken at all successive resonator modes near the water vapour line centre, whereas at the line wings, that are less informative for determining line parameters, part of the modes was omitted to shorten the recording time. The rms deviation of the points in the 'noise path' of this spectrum presented at the bottom of fig. 2.33 corresponds to the absorption of $2.6 \cdot 10^{-8}$ cm^{-1}. To obtain the spectrum at each of the 84 frequency points, 192 recordings of the resonator response in 512 frequency steps were made in each recording, with the frequency scanning speed of 60 μs per step. Thus, neglecting the time of radiation frequency switching from one resonator mode to another (which can be done in ~ 10 ms per one switching, hence, ~ 1 s for the entire range), a single scan of this frequency range takes about 500 s. Exactly the same time is needed to obtain the instrument baseline, and additional time for evacuating/filling the resonator with non-absorbing gas. It is difficult to assess the time needed for gas 're-filling'. It strongly depends on the used equipment and specific gas. However, other things being equal, the smaller the resonator size, the shorter this time. In practice, it takes a full working day, taking into account the time required to turn on the spectrometer and to prepare it for operation, to obtain spectra similar to those presented in the left and right parts of fig. 2.33.

Now consider potential reserves of the Nizhny Novgorod spectrometer for reduction of the time of spectrum recording. The great number of points for a single resonator response recording and multiple, repeated recordings were aimed at improving the statistical accuracy of determining the resonance width, which is determined primarily by the signal-to-noise ratio in the response recording. The experiments show that the use of a bolometer cooled by liquid helium instead of a commercial point-contact receiver in this frequency range increases the signal-to-noise ratio approximately by two orders of magnitude. An even better result can be obtained using a superheterodyne receiver (section 2.2.4). This provides

the basis for assessing the minimum time required to scan the entire specified spectral range, assuming that sufficient accuracy of determining the resonator parameters can be ensured by a single recording of the resonance with the increasing and decreasing frequency of 100 steps (number of points in the response recording) in each direction. This shortens the minimum time required for a single spectrum recording from 500 s to 1 s.

Further shortening of the spectrum recording time is also possible by increasing the speed of frequency scanning when recording the resonator response due to a decrease of the time interval between frequency switchings in DDS (section 2.4.5). The use of a commercial DDS PTS×10 (Programmed Test Sources, Inc.) computer, controlled via a high-speed interface in the modern version of the spectrometer instead of the former radio frequency DDS based on the AD9850 microchip, could reduce the time between frequency switchings to 3 μs [Koshelev, 2018-1]. Following this, one can expect at least a ten-fold (down to 0.1 s) reduction of the spectrum recording time. A still faster digital frequency scanning without phase jumps can be achieved by means of arbitrary function generators, in which the output signal is formed by a processor in an extensive memory of the device and then extracted by a high-speed DAC. The time between frequency switchings varies from tens to hundreds of nanoseconds and is restricted only by the speed of DAC response. Thus, the Nizhny Novgorod spectrometer operating in the PLL mode is also capable of ensuring radiation frequency scanning with limiting resonator speed determined by the resonator time constant. At such a fast scanning, the resonator response shape deviates from the Lorentz curve and may be taken into consideration in the numerical analysis of the response shape. It is worth mentioning that an increase in the spectrum recording speed is always accompanied by a decrease in the spectrometer sensitivity. Fast frequency scanning requires the fast registration of the response, i.e., a broadband receiver. The broader the band, the larger the receiver noise and the higher the uncertainty in determining the resonance parameters.

Recall that, in contrast to the Ohio spectrometer, the Nizhny Novgorod instrument scans the radiation frequency only in a minimum needed vicinity of the resonator mode, leaving aside the ‘void’ sections of the regular resonator eigenmode spectrum. The only non-productive time losses in this case are the intervals of frequency switchings from one resonator mode to another, but they can also be reduced to a minimum if the PLL is not lost (see section 2.2.2). The switching time is determined by the PLL speed and is approximately 1 μs, which means that these time losses may be made negligible compared to the useful time.

Note that the use of the PLL system for the radiation source is the key feature of the Nizhny Novgorod spectrometer that ensures its high sensitivity as it enables efficient accumulation of a useful signal and high-accuracy reproduction of the instrument baseline. This is possible because the repeated measurements are made strictly at the frequencies of the previous ones. The baseline in the Nizhny Novgorod spectrometer, like in the Ohio spectrometer, is specified by inevitable uncontrolled parasitic radiation reflections in the waveguide system. Nevertheless, the investigations have shown that with careful measurement of the baseline, the residual noise in the recorded spectrum is determined by the statistical uncertainty of resonant response width measurement. Consider as an example, the recording of the molecular oxygen line near 118 GHz [Koshelev, 2017] (fig. 2.36). The rms deviation of the experimental points in this recording from the model absorption corresponds to the absorption coefficient sensitivity of $4 \cdot 10^{-9}$ cm^{-1}, which coincides with the ultimate sensitivity of the Nizhny Novgorod spectrometer associated with the uncertainty of resonance width measurements (figs. 2.19 and 2.20).

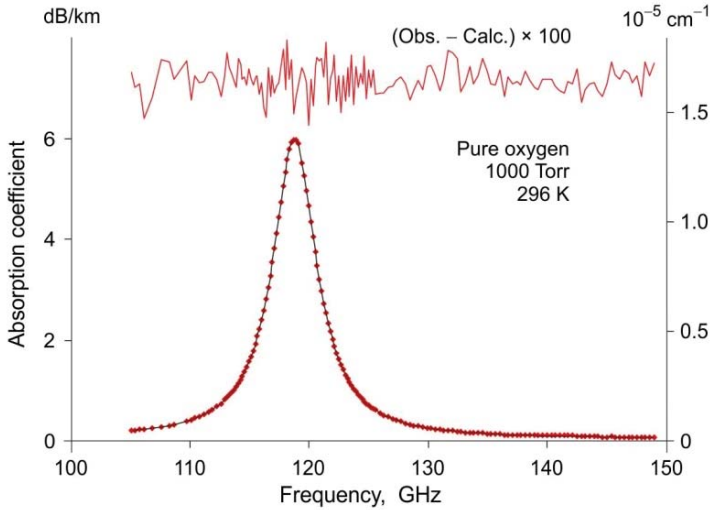

Fig. 2.36. Recording of the atmospheric oxygen line [Koshelev, 2017] with the Nizhny Novgorod spectrometer (dots) and the results of the line profile optimisation to the experimental data (solid curve). The upper trace is optimisation residue.

The above considerations lead to the conclusion that the spectrum *B* in fig. 2.33 is a recording with the sensitivity of the Ohio spectrometer that is

the maximum possible under these conditions, and the spectrum *A* is simply one of the routine recordings obtained with the Nizhny Novgorod spectrometer with a sensitivity lower than the ultimate one.

As a final note in the comparative analysis of the Nizhny Novgorod and Ohio spectrometers, we present estimates of the effective lengths of their resonators. The effective length of the Ohio spectrometer is readily determined by the formula (2.21) making use of its resonator *Q*-factor ($5 \cdot 10^6$) and taking, for definiteness, the resonance frequency of 180 GHz. This gives the effective length of 1326 m. The same value is obtained using the expression (2.12) and the mean value of empty resonator loss in the operating frequency range of the Ohio spectrometer of 0.0075 (this value is taken from fig. 2 of the paper [Meshkov, 2005]). The effective length of the Nizhny Novgorod spectrometer with the configuration used for recording the spectrum *A* in fig. 2.33 can be assessed analogously by losses of the empty resonator plotted in fig. 2.23, which gives the value of 260 m. So, its effective length is only 5 times shorter, whereas the real resonator length is 25 times shorter. Thus, the efficiency of the Ohio spectrometer is inferior to the Nizhny Novgorod spectrometer in the measurement time and in the resonator volume which demands huge efforts on its evacuation and maintenance of stable conditions.

Hans Liebe spectrometer

Let us now compare the Nizhny Novgorod spectrometer and the spectrometer developed by Hans Liebe at the Institute for Telecommunication Sciences (Boulder, USA) [Liebe, 1975, 1984-1, 1992]. It is one of the most thoroughly technically developed resonator spectrometers in the world. The results obtained using its most recent version formed the basis for the Millimeter-wave Propagation Model [Liebe, 1989, 1992] used worldwide. In his work [Liebe, 1984-1], Liebe stated that the spectrometer can operate in the 30–300 GHz range. However, from the publications, it appears Liebe performed his research using this spectrometer near 60 GHz and at the frequency of about 138 GHz. A simplified scheme of a Liebe spectrometer is shown in fig. 2.37.

A semiconfocal open Fabry–Perot resonator (fig. 2.38) is used as the measuring element of the Liebe spectrometer. Flat and spherical (curvature radius 40 cm) resonator mirrors, 10 cm in diameter, are made of brass polished to optical quality and are covered by silver. To reduce moisture adsorption, the mirrors can be heated independently of the chamber.

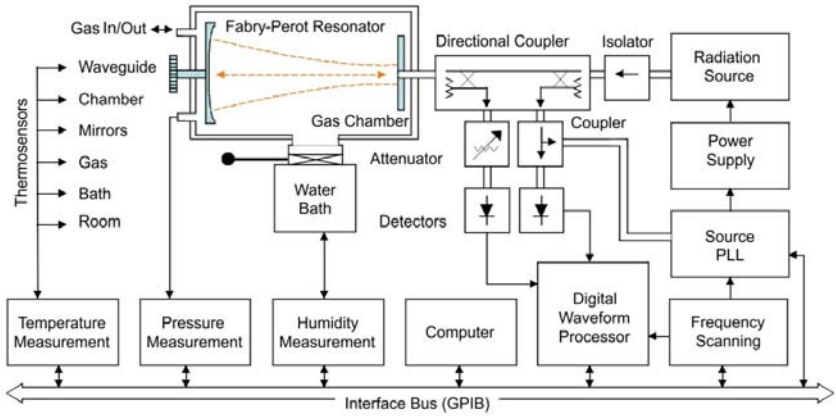

Fig. 2.37. Schematic of the Hans Liebe spectrometer [Liebe, 1987].

.

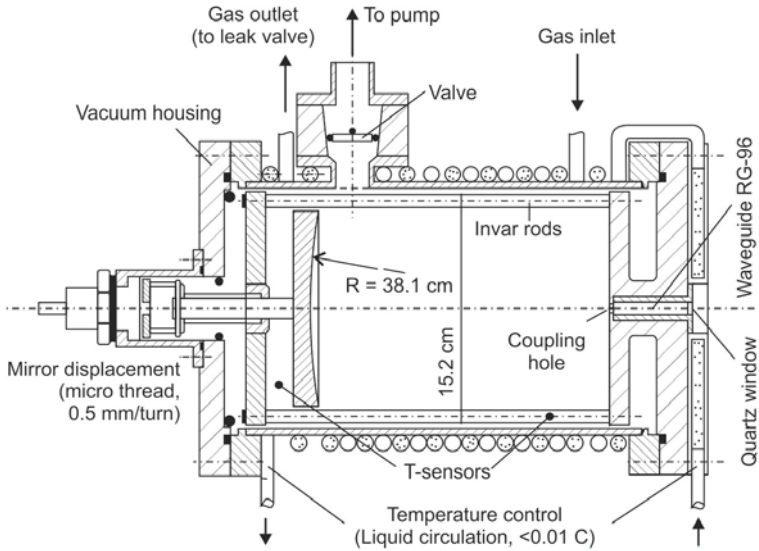

Fig. 2.38. The design of the Liebe spectrometer resonator module [Liebe, 1975].

The resonator frame is based on three invar rods. The distance between the mirrors is 20.5 cm and can be varied within ±1.2 cm by moving the spherical mirror using a micrometre screw, ensuring a setting

accuracy of approximately 1.3 μm. The resonator is placed in a vacuum chamber made of stainless steel and has a thermally conducting screen that may be thermally stabilised to an accuracy of 0.01 C, ensuring resonator length stability to an accuracy up to 0.7 nm during a 5-hour measurement cycle [Liebe, 1984-1]. The resonator is unresponsive to pressure drops from 0 to 2 atm.

The resonator is excited by hole coupling through an orifice with a diameter of 0.65 mm in the centre of the flat mirror. The resonator Q-factor is $\sim 3 \cdot 10^5$, time constant ~1 μs, and effective length ~240 m. The waveguide transmission line of the Liebe spectrometer is composed of standard waveguide single-mode sections. Standing waves in the waveguide system are minimised by an isolator placed after the radiation source. The exciting radiation and the resonator response are separated by a 4-pole directional coupler. A variable attenuator is installed before the receiver of the resonator response. A frequency multiplier connected to a microwave synthesiser of the 10—15 GHz range is used as a 60 GHz radiation source, and a klystron with centre frequency stabilised by a PLL system is used for studying absorption at a frequency of 138 GHz.

The spectrometer operates in the frequency domain: the resonator response is recorded at linear scanning of the frequency of exciting radiation. In an earlier spectrometer version, the resonator response at the frequency of 60 GHz was detected by a point-contact Schottky diode [Liebe, 1975], and at the frequency of 138 GHz by an InSb bolometer cooled by liquid helium [Liebe, 1984-1]. In the later version [Liebe, 1992], an automatic vector circuit analyser (allowing for simultaneous analysis of the amplitude and phase of the received signal) with a superheterodyne receiver at the input was used for detecting the resonator response and for analysing its shape. The resonator response was recorded in the course of stepwise (51 points with a step of 10 kHz) scanning of radiation frequency within ± 250 kHz relative to the response centre. 128 measurements were taken at each point with subsequent averaging of the results. To increase accuracy and evaluate statistical data uncertainty, the response was recorded 10 times. The response parameters were determined by optimising the parameters of the model function. According to Liebe's estimates, the spectrometer sensitivity in the studies of the 60 GHz frequency bands was better than $4.6 \cdot 10^{-8}$ cm^{-1} (0.02 dB/km) [Liebe, 1992], and $\sim 1.2 \cdot 10^{-7}$ cm^{-1} (0.05 dB/km) at 138 GHz [Liebe, 1984-1]. The sensitivity was estimated as the rms deviation of 10^7 results of measurements of the resonator response parameters made within one hour under the same thermodynamic conditions at the same frequency [Liebe, 1987]; hence, it corresponds to

the sensitivity to changes in the value of absorption (*variation sensitivity*) limited by the statistical accuracy of resonant response measurements.

To compare the capabilities of the latest version of the Liebe spectrometer and of the Nizhny Novgorod spectrometer, we will analyse the recordings of the spectrum of dry air in the vicinity of the absorption band of the atmospheric oxygen at about 60 GHz (fig. 2.39) obtained from these two spectrometers under identical conditions.

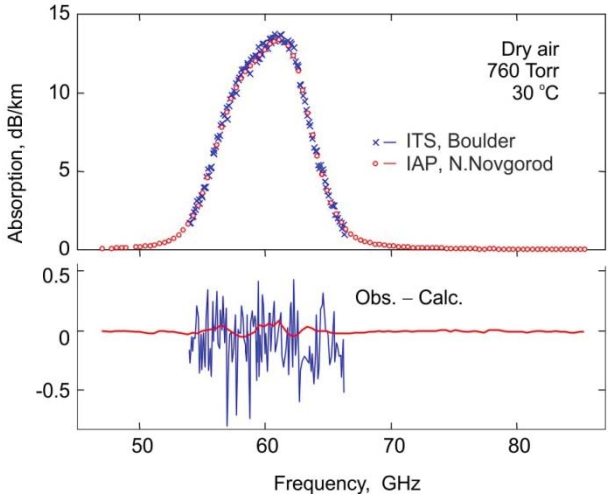

Fig. 2.39. Measurements of the air spectrum in the range of the 60-GHz absorption band of atmospheric oxygen made with the Nizhny Novgorod spectrometer (*dots*) [Makarov, 2011] and with the Liebe spectrometer (*crosses*) [Liebe, 1992] under the same conditions. The difference between the experimental and model spectra is shown at the bottom of the figure.

The recording made with the Liebe spectrometer contains 130 points within the 53.9–66.3 GHz range. The Nizhny Novgorod spectrum contains 98 points within the 46.5–85.3 GHz frequency range. The resonator in the Nizhny Novgorod spectrometer was 39.4 cm long and was placed in a thermally stabilised chamber providing temperature stability within 0.2 °C. The effective length of the empty resonator was about 320 m [Makarov, 2011]. Although the absolute magnitude of absorption is measured in both cases, the recordings coincide so that the difference between them is noticeable only after the subtraction of the calculated absorption (the lower part of fig. 2.39). Clearly, the difference manifest itself only in the statistical scatter of points, and the signal-to-noise ratio in

the recording of the Nizhny Novgorod spectrometer is about 10 times larger. The rms deviation of the points in the residue of the Liebe spectrum corresponds to the absorption of $5.4 \cdot 10^{-7}$ cm^{-1}, which is an order of magnitude larger than the estimated *variation sensitivity* of the spectrometer [Liebe, 1992]. An analogous value for the Nizhny Novgorod spectrometer is $4.7 \cdot 10^{-8}$ cm^{-1}. The systematic deviations of the residue of the Nizhny Novgorod spectrum from the zero-value noticeable near the band centre may be attributed either to inaccurate absorption modelling, or to unstable composition of the studied gas (see Makarov [2011] and section 3.1.2) and are not spectrometer noise. Therefore, in this case it is more precise to estimate the sensitivity of the Nizhny Novgorod spectrometer by the scatter of points in the 66– 85 GHz range, which gives the value of $1.7 \cdot 10^{-8}$ cm^{-1}, exceeding the variation sensitivity of this spectrometer by about 4 times.

Lille spectrometer

Still another instrument worthy of notice is the resonator spectrometer made at the Lille University, France [Bauer, 1986]. It was actively used for the investigation of the atmospheric absorption in the millimetre and submillimetre wavelength ranges. The schematic diagram of the Lille spectrometer is shown in fig. 2.40.

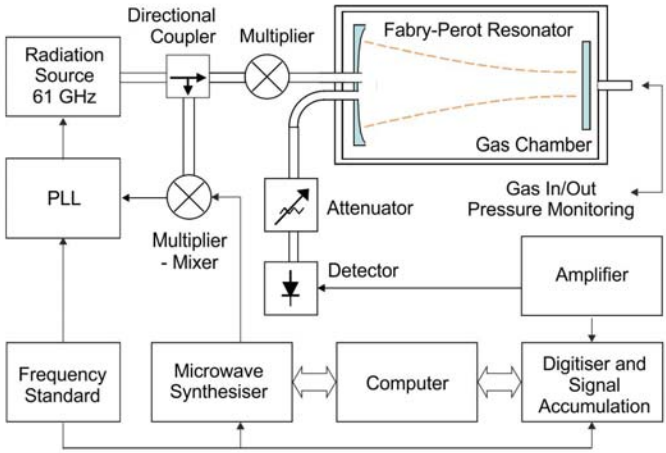

Fig. 2.40. Schematic diagram of the Lille spectrometer [Bauer, 1986].

A semiconfocal Fabry-Perot resonator is the measuring element of this spectrometer. Its optical-quality mirrors are covered with gold. The

diameters of the flat and spherical mirrors are 16 cm and 25 cm, respectively. The curvature radius of the spherical mirror is 160 cm. The distance between the mirrors is approximately 80 cm. The effective length of the resonator at the frequency of 180 GHz is about 200 m. The resonator is coupled to the exciting radiation source and the detector via two holes 1.4 mm in diameter located in the centre of the spherical mirror. Each hole is connected to the RG 99/U (3.099×1.549 mm) waveguide. The resonator is installed in a vacuum chamber made of stainless steel. The inner surface of the chamber and the resonator components are treated by a mixture reducing the adsorption of water molecules. The mirrors are heated for the same purpose. The temperature inside the chamber is maintained to an accuracy of ±0.05 °C to provide resonator stability during long-term measurements. A passive frequency doubler or tripler connected to a klystron is used as a radiation source in the 150–240 GHz range, and a BWO at a frequency near 350 GHz. The radiation frequency of the source is stabilised by a PLL system against a microwave synthesiser of the 4–18 GHz range. The waveguide system consists of standard single-mode sections. Schottky diodes serve as radiation detectors. The resonator response is recorded by linear step-by-step radiation frequency scanning and subsequent automatic digitising of the signal by a 256-channel system of data acquisition and accumulation. The response parameters are determined by analysing its shape.

This spectrometer can also be called a broadband spectrometer, but with a caveat. Despite the fact that the radiation sources used in the studies covered the 60–470 GHz frequency range with just small gaps, all the published measurements were made at only 9 frequency points in the 153–350 GHz interval. These points are marked by circles in fig. 2.41, demonstrating the results of measurements of the absorption coefficient of a mixture of nitrogen with water vapour at 5 % relative humidity, approximately room temperature, and atmospheric pressure [Bauer, 1986, 1991, 1993, 1995, 1996, 1998, 2001; Godon, 1992, 2000; Kuhn, 2002].

Estimates of the spectrometer sensitivity have not been reported in the literature but they can be made using the published measurement data. Each point in fig. 2.41 is the result of averaging of a series of measurements at 8-10 different temperatures (see the details in section 3.2.1). The rms deviation of the points of one series varies within broad limits from $2 \cdot 10^{-10}$ cm^{-1} to $1.1 \cdot 10^{-7}$ cm^{-1}. This points, on the one hand, to a very high statistical accuracy of measuring resonant response parameters (variation sensitivity) and, on the other hand, to uncontrolled systematic measurement error. This is also evidenced by the fact that the rms deviation of the difference between the experimental points and the model

absorption shown in fig. 2.41 is $2 \cdot 10^{-7}$ cm^{-1} (a special-purpose version of the Millimeter-wave Propagation Model that enables the calculation of absorption in humid nitrogen was used for the estimates). The authors believe that the main source of errors in their measurements was the uncontrolled variation of the value of coupling of the resonator with input and output radiation and changes in the composition of the mixture associated with water adsorption by the spectrometer components [Kuhn, 2002].

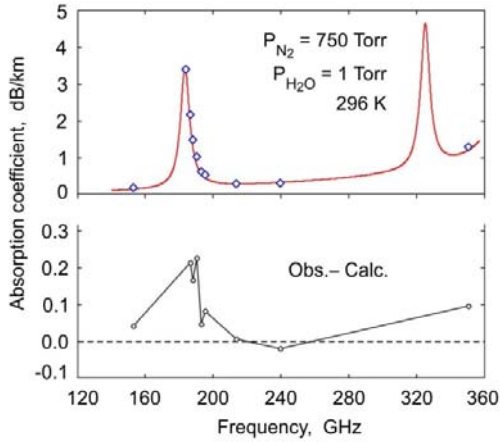

Fig. 2.41. The frequency range of the measurements made with the Lille spectrometer. The solid curve corresponds to the model absorption of the mixture of water vapour (1 Torr) with nitrogen (750 Torr) at 23 °C, and the measurement results are labelled by circles. The difference between the measured and calculated absorption is shown at the bottom.

Thus, comparison of each of the three instruments discussed above reveals the apparent advantages of the Nizhny Novgorod spectrometer, which are attributed to the following factors:

1) The decisive factor is the method of measuring the resonant response parameters, namely, fast precision saw-tooth scanning without phase jumps with increasing and decreasing frequency in the PLL mode and averaging of the width of the observed resonant responses. This key distinctive feature of the spectrometer allows for attaining the 20 Hz statistical accuracy of measuring resonant response width (figs. 2.19 and 2.20) corresponding to the spectrometer sensitivity to the change of the gas absorption coefficient of $4 \cdot 10^{-9}$ cm^{-1}.

2) The optimisation of the spectrometer waveguide system and the developed technique of taking its baseline into account minimised one of

the principal sources of systematic error associated with uncontrolled variation of the value of coupling between the resonator and the radiation source. This made it possible to achieve a statistical accuracy of 20 Hz when measuring the resonance width (fig. 2.36), in broadband spectra studies which is currently one of limitations of the spectrometer sensitivity.

3) The use of BWOs as radiation sources in combination with a waveguide line optimal for broadband studies provides unprecedented opportunities for continuous recording of spectra of studied gases throughout the operating frequency range (fig. 2.32).

2.4.5. Perspectives for further development

The main problem to be solved is a substantial non-productive loss of time at radiation frequency tuning at the transition from one resonator mode to another. Reducing the loss will help in attaining the ultimate speed of spectrum registering limited by the resonator quality. This will require increasing the frequency sweeping speed whilst recording the resonator response. Another direction is increasing the accuracy of determining resonant response parameters at a single recording, which is directly linked to an increase of the signal-to-noise ratio. One of the principal limiting factors in this case is the quality of the spectrum of the radiation exciting the resonator that may be increased by reducing phase noise in the reference signal of the PLL system (section 2.2.2). Here we will consider possible ways of improving the spectrometer characteristics in these three directions.

Reduction of time loss at frequency switching

Let us first consider time losses caused by the frequency switching corresponding to the transition from one resonator mode to another. They are accompanied by the break of the PLL not only related to the source of exciting radiation, but also to the loop of the reference signal generator in the microwave frequency synthesiser. Then the needed frequency is synthesised automatically with a new set of reference signals. The time of switching may vary from a few to tens of milliseconds, depending on the magnitude of reference frequency changes. For a more complete understanding of the capabilities of the resonator spectrometer, it is desirable to construct a radiation frequency control system that would allow fast switching without loss of the oscillation phase, if possible, over the entire operating frequency range of the BWO. The feasibility of

creating such a system by expanding the range of frequency scanning without phase jumps in a PLL system with DDS by digital division of the IF signal (see section 2.2.2 and fig. 2.15) was demonstrated in the works of Krupnov [2001] and Tretyakov [2006].

From the expressions (2.42) and (2.47) for the source radiation frequency in such a synthesiser it follows that the higher the DDS frequency (hence, the tuning range) and the larger the coefficient of the IF signal division, the larger the scanning bandwidth. Consequently, the operating frequency of the phase detector, the speed of the digital frequency divider, the central frequency, and the bandwidth of the IF beat signal amplifier must be increased. The parameters of basic microwave components are currently being rapidly improved, so the specific examples given below may be regarded as the lower bound of the available opportunities. Descriptions and characteristics of all the components needed for constructing such a high-speed synthesiser mentioned above can be found at the web sites of the major manufacturers (for example, Analog Devices or L3 Narda-MITEQ). The currently available DDS operating at a clock frequency of 3.5 GHz synthesise signals with a frequency up to 1750 MHz with $2 \cdot 10^{-10}$ Hz resolution and tuning time of several nanoseconds. There exists low-noise broadband IF amplifiers operating in the range up to 40 GHz, as well as digital dividers and phase detectors working with signals up to 70–80 GHz. Multiplier-mixers with an expanded range of the output IF signal can be chosen correspondingly. By modest estimates, these devices suggest the possibility of fast control of radiation frequency in the PLL mode with a switching time of less than a microsecond within 10–20 GHz.

In addition to the high-frequency elements, the PLL system capable of frequency tuning in such a wide range requires an additional component (terminal amplifier) capable of changing the voltage applied to the radiation source by a needed value during the switching time. For millimetre and submillimetre BWOs, frequency switching by 10 GHz means that the voltage should be changed by about 200 V. It is a rather complicated task to construct an amplifier that would combine such a dynamic range and required speed (the response time shall be less than 1 μs). Fortunately, such a regime of switching is not required for the resonator spectrometer.

Of practical interest is the regime in which the PLL system successively switches-over the radiation frequency from one resonator mode to another, followed by frequency scanning for recording the resonant response after each switching. The maximum change of the radiation frequency in this case corresponds to the intermode interval

which is about 300 MHz. This means that the fast change in voltage is approximately 6 V, i.e., it is within the width of the dynamic range of the conventional terminal amplifier of the PLL system. So, the switching can be made without breaking the loop, but an additional DC voltage component appears at the amplifier output. During frequency scanning within the vicinity of the resonance, the output signal of the high-voltage source has sufficient time to change, as a result of which the DC component at the amplifier output is eliminated, and the amplifier returns to the status ready for the next large switching. Thus, the entire BWO operation frequency range (~100 GHz) can be continuously swept with just a few slow (~10 ms) switchings, typical of conventional microwave synthesisers, with short-term PLL breaks every 10–20 GHz.

Scanning speed increase

Another option for reducing measurement time in the Nizhny Novgorod resonator spectrometer is to increase resonance recording speed. The DDS used in the spectrometer limits the frequency scanning speed because the minimum time between the switchings cannot be less than 2 μs, which is comparable to the resonator time constant. However, the rapid advance of the high-speed electronics suggests that still faster DDSs may emerge in the near future.

At a faster scanning, the field oscillations in the resonator do not have sufficient time to be excited up to a maximum level. The resonator response shape in this case will differ from the Lorentz one, which should be taken into consideration when determining the response parameters. The inertia of the devices (detector, video amplifier, ADC) recording the resonator response is another factor that should be taken into account as it is important for applications. Each of these devices will distort the resonator response if they have an insufficient reaction speed. Fortunately, in either case the response shape changes in a regular manner. Therefore, it can be calculated to a high enough accuracy by the preset resonator parameters, following the known law of frequency variation in the digital scanning of exciting radiation with a known step and retained oscillation phase. The inverse problem can also be solved, i.e., the resonator parameters can be found, by the shape of the observed signal. The derivation of the formulas needed for such calculations is given in Ovsyannikov [2005].

The degree of response distortion depends not only on the extent of frequency tuning per unit time and the reaction speed of the receiving circuit, but on the resonator response width too. Therefore, researchers

usually use a relative dimensionless speed V corresponding to the number of half widths of an undistorted resonant contour $\Delta f/2$ scanned over the time equal to a double resonator time constant 2τ. The results of calculations of the resonator response shape are shown in fig. 2.42 for three scanning speeds. The response shape for each speed is given for three different bandwidths of the recording device. The receiver bandwidth in kilohertz is specified near the peak of the corresponding response. The responses labelled by an asterisk were obtained neglecting the influence of the speed (bandwidth) of the receiving circuit. The responses presented in fig. 2.42 were calculated for the parameters close to the real ones for the Fabry–Perot resonator used in the Nizhny Novgorod spectrometer: resonance frequency 100 GHz, Q-factor 10^6, and time constant 0.8 μs; 200 frequency steps at 10 kHz each in all cases.

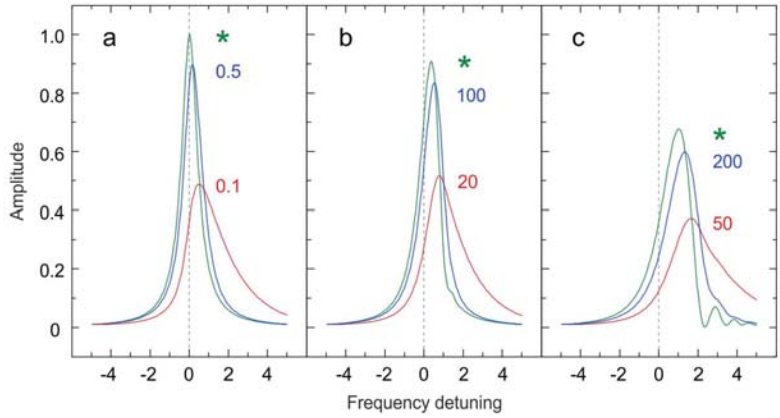

Fig. 2.42. The calculated resonant response shape for different scanning speeds (*a* – 0.027; *b* – 0.5, *c* – 2 relative units) of exciting radiation frequency and for different values of receiving circuits' bandwidth. The amplitude and detuning from the resonance frequency are normalised to the amplitude and half width of undistorted response, respectively. Adopted from Ovsyannikov [2005].

The response plotted in fig. 2.42, *a* corresponds to the time between the frequency switchings of 6 μs only. Nevertheless, under the given conditions, this may be regarded as slow scanning $V << 1$. The difference between the response labelled by the asterisk and the Lorentz function at the maximum point is 0.3 %, and the relative difference between the width of the observed response and the undistorted response is an order of magnitude less. With an increase of the speed up to $V \approx 1$, the amplitude of

the response starts to decrease, its width increases, and the peak shifts in the direction of the frequency scanning. For $V \approx 0.5$, oscillations with the amplitude and phase growing with increasing speed arise in the decaying wing of the response. The influence of the receiving bandwidth on the shape of the received signal (fig. 2.42) leads to response delay and spreading in the direction of frequency scanning. The receiver bandwidth needed for observing an undistorted response increases linearly with increasing V.

The optimal speed of scanning exciting radiation can be estimated in a numerical experiment. Assume that we are not restricted to narrow-band receiving circuits and have a high enough signal-to-noise ratio on a slowly recorded resonator response. Shortening the time of the experiment by increasing the speed of frequency scanning results in a decrease in the amplitude of resonator response and in an increase in its width due to the resonator inertia (fig. 2.42). The signal-to-noise ratio decreases in proportion to the amplitude and, hence, the accuracy of determining the attenuation parameter worsens. If loss in accuracy is undesirable, for maintaining the signal-to-noise ratio at the initial level (proportional to the square of relative amplitude changes), the number of averaged recordings should be increased, thus increasing the time of the experiment. If the response width is increased, the width of the scanning range should be increased too. To avoid the worsening of measurement accuracy, the number of frequency steps should be increased, which also results in an increase in the experiment time. The time of the experiment versus the relative frequency scanning speed V is plotted in fig. 2.43 on logarithmic scale. The time of the experiment T_{exp} in the figure is normalised to the duration of an analogous experiment at the frequency scanning speed corresponding to a switching time of 45 μs. The dependence is at its minimum at a scanning speed of about 2 relative units, which is optimal under the assumptions made above for the resonator parameters used in the described experiment.

One can see from the figure that the optimal speed increases the experiment time by more than two orders of magnitude, which may be used for shortening the experimental time and for observing the variation of absorption in real time.

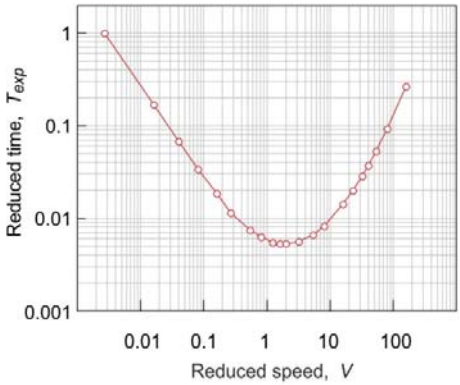

Fig. 2.43. Time of the experiment T_{exp} *versus* frequency scanning speed V, provided that the accuracy of determining the attenuation parameter is preserved. Adopted from Ovsyannikov [2005].

Increasing radiation purity

The appearance of exciting radiation phase noise on the slopes of the resonator response recording (fig. 2.19) indicates that the statistical uncertainty of determining the resonance parameters may be increased by using a radiation source with a purer spectrum. In section 2.2.2 it was shown that, with a correctly working PLL system, the radiation spectrum purity is almost fully determined by the quality of the spectrum of the reference signal.

Laser frequency combs generated by femtosecond (FS) lasers created new prospects for the accuracy and stability of frequency and time standards [Glauber, 2006]. In the works of Schibli [2008] and Martin [2009-2], it was shown that by using high speed PLL systems it is possible to obtain an intrinsic width of each component of the optical comb two orders of magnitude narrower than the maximum corresponding to the laser quantum noise. The absolute spectrum width of the comb component and the stability of its frequency are specified by the parameters of the reference radiation source to which the entire comb is phase-locked by the system. For example, the optical frequency standard [Young, 1999] with a radiation spectrum width of about 0.6 Hz at an average of over 32 s and with a frequency stability of about $3 \cdot 10^{-16}$ relative units per 1 s may be used as such a source.

Note that laser combs were used for precision measurements as well as for the generation of cw coherent radiation in the millimetre and submillimetre wavelength ranges (see, for example, Goyette [1995], Yasui

[2011], Song [2008], Mouret [2009], Makarov [2014], Füser [2014], Bartalini [2014] and references therein). Laser comb components can be used as reference signals for the frequency stabilisation of cw radiation sources. The high spectral purity and stability of the comb are transferred to the radiation of the cw source. For example, in the work of Millo [2009] it was shown that a 10 GHz signal source stabilised by a PLL system to one of the components of an FS laser frequency comb has a phase noise in the region of acoustic frequencies tens of decibels lower than in the best present-day microwave frequency synthesisers based on the traditional approach. Consequently, it seems promising to use the components of the frequency comb produced by the FS laser and transferred to the millimetre and submillimetre ranges as reference signals for the PLL of the radiation source used for exciting the resonator. Such an opportunity was for the first time demonstrated experimentally in the work by Tretyakov [2010] with the use of the setup shown schematically in fig. 2.44.

The BWO with a typical power of about 10 mW and 78–118 GHz radiation frequency is used as the source of radiation. A comb of optical frequencies is formed by the radiation of a Ti:Sapphire FS laser (pulse duration ~50 fs and average power ~100 mW). The pulse repetition rate (91577000.000 GHz) is stabilised by the PLL system against a signal of a microwave synthesiser synchronised with the rubidium atomic clock.

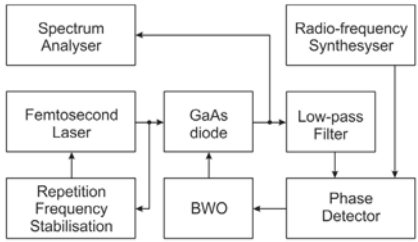

Fig. 2.44. Schematic of the PLL of BWO radiation against one component of a frequency comb produced by an FS laser. Adopted from Tretyakov [2010].

The laser comb is converted to the millimetre and submillimetre ranges (optical-terahertz conversion) in a commercial planar Schottky microwave diode, with a manufacturer-guaranteed cutoff frequency of 2-5 THz. Laser radiation is focused on a semiconductor (GaAs) in the contact area of the diode, giving rise to sub-picosecond pulses in the concentration of photoinduced carriers. The concentration and, hence, conductivity pulses form a comb of reference terahertz frequencies. The

stability of the terahertz comb is ensured by the stable intermode interval of the optical comb. The diode is located at the open edge of the waveguide of a broadband submillimetre multiplier-mixer. BWO radiation is transmitted through the waveguide to the back side of the diode, with the diode leads working as a receiving antenna. As the current in the diode is proportional to the product of the conductivity and voltage produced by the BWO radiation, there arise in the diode beats between the BWO signal and the corresponding component of the terahertz comb spectrum. In the experiment, the beat signal had the amplitude sufficient for phase locking the BWO radiation by a conventional synchroniser (section 2.4.2). The beat frequency (IF signal) was 30 MHz; the phase detector of the synchroniser worked at the same frequency. A low-pass filter with a cutoff frequency of 80 MHz at the synchroniser output blocked the ingress of the terahertz comb components to the phase detector. The bandwidth of the low-noise beat-note amplifier was about 10 MHz, providing sufficient isolation of the input signal from the mirror beats and from the beats between the BWO radiation and the other components of the terahertz comb. A radio-frequency synthesiser synchronised with the signal of the time and frequency standard was used as the source of the high-stability reference signal for the phase detector. The synthesiser provided a scan of the BWO radiation frequency within the 10–MHz bandwidth of the input signal amplifier.

CHAPTER 3

EXPERIMENTAL STUDIES OF ATMOSPHERIC ABSORPTION

A rigorous solution to the problem of radiation absorption by gas demands allowance for the motions of all molecules and their interaction with each other, which is currently unfeasible. A sufficiently good approximation for atmospheric applications is to divide the total absorption into two parts. The first part corresponds to the absorption that would be observed if the gas was almost perfect. Its molecules, though not material points, are very small spheres moving with mean thermal velocity. They do not interact with each other and absorb radiation over the time interval equal to the average time between collisions which occur instantaneously and do not result in molecule adhesion. In most cases, this part concerns the resonant interaction of molecules with radiation and resonant lines in their spectra. Minor collisional effects, such as line shifting, line mixing, the dependence of collisional cross section on molecular rotational state, etc., can be taken into account as corrections of the resonant line shape model through the corresponding parameters (see section 1.2).

The second part corresponds to the absorption arising when gas imperfection caused by pair interaction of molecules is taken into account (sections 1.2.6 and 1.3). The allowance for simultaneous interaction of three, four, and more molecules is meaningless for the Earth's atmosphere because of their negligibly small probability. In the majority of cases imperfect gas manifests itself as a small 'pedestal' under the resonance spectrum. This absorption varies smoothly with wavelength (or with frequency), from the visible to the microwave. That is why it is called *non-resonant absorption*, or *the continuum*.

According to this subdivision of the absorption, this chapter is also divided into two large parts.

Section 3.1 concerns the experimental study of resonant radiation absorption by molecules of atmospheric gases; we will speak about atmospheric lines. Although nearly all molecules are present in the Earth's atmosphere, only two gases are of major importance for the propagation of

millimetre and submillimetre radiation. These are water vapour (H_2O molecules) and oxygen (O_2). The spectra of these gases will be discussed in sections 3.1.1 and 3.1.2.

Particular attention will be paid to the results obtained by the resonator spectroscopy methods. Analogous data obtained using spectrometers of other types will be considered for comparison.

Nitrous oxide (N_2O) is another abundant atmospheric gas whose molecules have a dipole moment and, therefore, can resonantly interact with radiation and have a rotational spectrum. N_2O lines are visible in the upper rarefied layers of the atmosphere from satellites and contribute to the Earth's radiation balance. They should be taken into consideration in models of radiation propagation alongside the lines of other minor gas constituents of the atmosphere, such as ozone (O_3), sulphur dioxide (SO_2), ammonia (NH_3), carbon monoxide (CO), and others. However, a negligible volume content of nitrous oxide in the atmosphere (less than 10^{-5} %) excludes the possibility of observing resonant lines of N_2O in air under atmospheric pressure, even in the ultra-high-sensitivity resonator spectrometer considered in this book. Therefore, values of spectroscopic parameters of N_2O line as well as of other significant atmospheric molecules are determined at low pressures with spectrometers of other types and then extrapolated to the atmospheric conditions.

Section 3.2 is devoted to the experimental studies of the atmospheric continuum. Like in the case of resonant absorption, water vapour is the main contributor. Consequently, the atmospheric continuum can be divided into quadratic and linear parts with respect to humidity, corresponding to the so-called self- and foreign water vapour continua, respectively. The remaining humidity-independent part is called 'dry continuum'. The best-known studies aimed at determining quantitative characteristics of the continuum are reviewed. Particular attention is focused on the experiments which gave an insight into the physical origin of the continuum.

The results of most of the experimental studies considered in this chapter are compared with predictions from the radiation propagation models, which are developed on the basis of the Millimeter-wave Propagation Model most widely used, worldwide, for remote sensing of the atmosphere [Liebe, 1975, 1983, 1987, 1989, 1992, 1993; Rosenkranz, 1998; Tretyakov, 2005; Makarov, 2011; Rosenkranz, 2017]. The MPM was initially developed at the Institute for Telecommunication Sciences in Boulder (USA) by Hans Liebe, hence it is sometimes also called the Liebe model in his honour. Note that regarding the millimetre wave absorption by atmospheric oxygen, this model is unique. All the other propagation

models currently employed for atmospheric sounding use this part of the MPM. In most cases, the quality of the data obtained is assessed by comparing them with the MPM.

Another frequently mentioned source of data for comparison is HITRAN, a spectroscopic database for atmospheric applications [Gordon, 2017]. It is one of the most popular databases thanks to its accessibility and regular updates. It contains information on available experimental and theoretical data about molecular spectra. Each entry into the database is decided upon by an expert council, which critically assesses the quality of the new data and assigns an appropriate code of possible error. Historically such an assessment, as a rule, objectively reflects reality. However, in some cases, new high-accuracy experimental data fall outside the error interval given in the database.

3.1. Atmospheric lines

When speaking about the atmospheric lines of the millimetre and submillimetre wavelength ranges, researchers usually mean the most prominent spectral features, namely, the resonant lines of H_2O and O_2 molecules. The spectra of these molecules in atmospheric air under ordinary room conditions in a frequency range up to 1 THz are depicted in fig. 3.1.

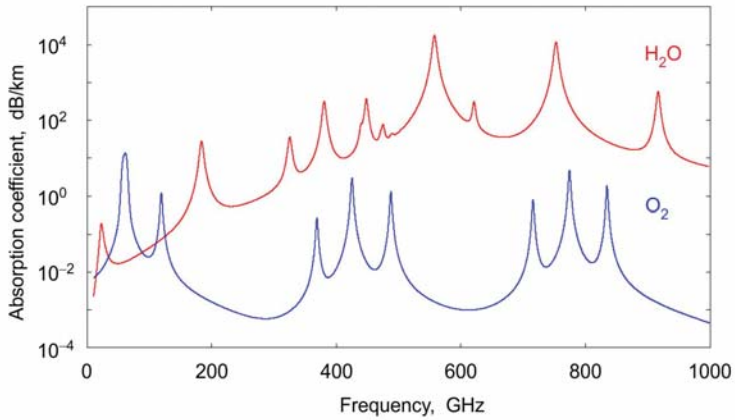

Fig. 3.1. Resonance spectra of oxygen and water vapour in the frequency range up to 1 THz in atmospheric air at a temperature of 27 ºC, pressure 750 mm Hg, and humidity 8 g/m^3 (calculated by MPM). Note the logarithmic vertical scale.

The spectra contain 11 strong lines of H_2O and 8 lines of O_2. Practically all of them are diagnostic lines that are used for remote sensing of the atmosphere for determining its humidity, temperature, and/or pressure profiles. Therefore, careful examination of each of them is an important scientific problem. Why do the spectra look like this, what kind of lines are they, why do they have such a shape, how does it change with temperature and pressure variation, how accurate are the parameters of these lines, how many significant spectral lines are actually contained in the spectra? Answers to these and many other questions will be given in sections 3.1.1 and 3.1.2.

The general approach to the experimental determination of the parameters of molecular spectral lines includes four principal stages: a) measuring the absorption coefficient of a studied gas under given thermodynamic conditions in a preset frequency range (section 2.3); b) creating a model function of the absorption coefficient (section 1.2), with the sought line parameters being the variables, corresponding most closely to the conditions of the experimental recording with allowance, if needed, for the specific features of the experiment; c) optimising (mathematical fitting) of the model function to the experimental data by minimising the rms deviation of the experimental points from the model function (this can be done using special-purpose software for spectral data processing, e.g., 'PeakFit' or 'TableCurve' developed at Systat Software Inc., or intrinsic data approximating functions from the general purpose mathematical software; and d) analysis of the optimisation results aimed at revealing the possible inadequacy of the model function or redundancy of the number of variable parameters, and assessment of statistical error in determining the parameters and the degree of their cross-correlation. After the final stage, the model function is corrected, if necessary, and the optimisation is repeated. The influence of cross-correlation may be reduced significantly, and more reliable values of sought line parameters may be obtained through the method of simultaneous optimisation of several spectra recorded in one experimental cycle that differ from each other, for example, by pressure, temperature, or even the composition of the studied gas [Benner, 1995; Plateaux, 2001; Jacquemart, 2001; Slocum, 2015]. Simultaneous processing allows for the use of *a priori* known dependences of the sought parameters on the varying conditions of spectrum recording.

3.1.1. Water vapour spectrum

The equilibrium structure of a water molecule (fig. 3.2) is specified by the hybridisation of electron orbitals of an oxygen atom when two atoms

of hydrogen are attached to it. Instead of the initial centrally symmetric structure of the O atom consisting of three *P* and one *S* orbitals resembling a cube, a new, also almost centrally symmetric structure comprising four hybrid *SP* orbitals is formed (*SP*3-hybridisation) which looks very much like a tetrahedron. Two vertexes of the tetrahedron correspond to the filled orbitals (each having two paired electrons) and the other two correspond to the initial *P* orbitals of two unpaired electrons of the O atom. H atoms with unpaired electrons are attached to these vertexes on the *S* orbitals forming covalent bonds between the atoms with common and paired electrons on the fully filled orbitals. In the equilibrium configuration of the water molecule, the angle between the bonds (104.53°) is a little smaller than it was in the tetrahedron (109.47°), and the distance between each H nucleus and O nucleus (bond length) is 0.95785 Å, which specifies the characteristic size of the H_2O molecule. The inner electron shell of the O atom with two paired electrons on the *S* orbital remains almost unperturbed. Oxygen pulls the electron density away from H atoms, as a result, the water molecule acquires a dipole moment directed along the symmetry axis of the molecule from oxygen to the hydrogens.

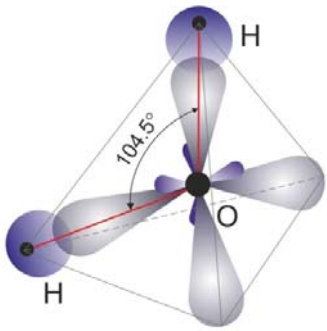

Fig. 3.2. Equilibrium structure of a water molecule. Schematic representation of *SP*-hybridised orbitals of the outer electron shell of O atom and *S* orbitals of H atoms. The inner electron shell of O atom is not shown.

From the spectroscopic point of view, a water vapour molecule belongs to the class of asymmetric tops as all its three principal moments of inertia are different. Since two light hydrogen atoms are present in the molecule, the rotational constants inversely proportional to the principal moments of inertia are fairly large. For the main isotopologue of the $H_2{}^{16}O$ molecule they are approximately 279.5, 437.2 and 823.0 GHz. The resulting rotational spectrum of the H_2O molecule is highly irregular, the lines are strongly spaced apart over the spectrum, and the effect of collisional coupling of the lines (section 1.2.2) in the water vapour spectrum is not observed in experiment. The theoretical calculations [Ma, 2014] also show that under the conditions of the Earth's atmosphere, this

effect can be disregarded, and the water vapour lines can be regarded as isolated.

The H_2O lines are quite intense, firstly, because of the large rotational constants resulting in a small partition sum (all gas molecules are distributed over a relatively small number of energy levels) and, secondly, because the molecule has a large dipole moment. The dipole moment magnitude of 1.8546(6) D, corresponding to the equilibrium molecule configuration, was measured using the Stark effect [Clough, 1973].

As is common for molecular spectroscopy, lines are identified using a combination of quantum numbers corresponding to the molecule transition from the lower to the upper rotational state. The rotational state of a classical asymmetric top is fully characterised by three projections of the total angular momentum onto the principal axes. The magnitude of the total angular momentum and its two projections can be used as an alternative. The quantum rotational state of an asymmetric top molecule is characterised analogously using the set of quantum numbers J, K_a, and K_c corresponding to the total angular momentum and its two projections onto the symmetry axis of the molecule in the approximation of a prolate and oblate symmetric top [Townes, 1955].

Three fundamental vibrational states of H_2O molecule (section 1.2.1) correspond to *symmetric stretch* (simultaneous periodic compression and stretching of both O—H- bonds), *asymmetric stretch* (compression of one O—H-bond accompanied by stretching of the other, and vice versa), and *bending* (harmonic changes of the angle between the O—H-bonds without changes in their length). The frequencies of these oscillations in $H_2{}^{16}O$ are approximately $\nu_1 = 109.6$, $\nu_3 = 112.6$, and $\nu_2 = 47.8$ THz, respectively. From this, it follows that all vibrational-rotational transitions of the molecule are far beyond the millimetre and submillimetre wavelength ranges, although due to intermolecular collisions part of the molecules are in excited vibrational states. The fraction of such molecules is small; for example, in an equilibrium water vapour at room temperature, the relative part of molecules in the lowest (fundamental bending) vibrational state is only about 0.03 %. The spectral lines corresponding to pure rotational transitions of such molecules can be observed in water vapour spectra (see, e.g., Serov [2014]) and, hence, should be taken into consideration in spectrum modelling. For identifying the corresponding lines, vibrational quantum numbers need to be specified. In the overwhelming majority of cases, when speaking about the spectrum of water vapour in the millimetre and submillimetre wavelength ranges, we mean rotational transitions in the fundamental vibrational state. A similar remark applies to the various isotopologues of the H_2O molecule. In the case of the natural abundance of

isotopes, the line of six ($H_2{}^{16}O$, $H_2{}^{18}O$, $H_2{}^{17}O$, $HD^{16}O$, $HD^{18}O$ and $HD^{17}O$, with a percentage of 99.73, 0.200, 0.03719, 0.03107, 0.0000623 and 0.00001159, respectively) out of nine stable isotopologues of H_2O can be observed in the spectra of water vapour, but the lines of the main isotopologue $H_2{}^{16}O$ are assumed by default. Thus, to identify, for example, the lowest frequency H_2O line in fig. 3.1, located near 22 GHz and belonging to the main isotopologue in the ground vibrational state, the notation corresponding to the change in the rotational state of the molecule $J'_{K'_a,K'_c} \leftarrow J_{K_a,K_c} = 6_{1,6} \leftarrow 5_{2,3}$ is used. In this transition, the total angular momentum increases, and values of its projections change.

Note yet another feature of the main isotopologue of a water molecule associated with the presence of a *spin* (an intrinsic form of angular momentum carried by particles) in the hydrogen nucleus. Each proton has a spin characterised by a quantum number 1/2 [9], due to which there are two spin isomers of the water molecule. Correspondingly, the nuclear spins of the protons in the molecule can be either parallel (the total nuclear spin is equal to unity) or antiparallel (the total spin is zero). The respective states are called *ortho-* and *para-states.* By virtue of the statistics related to permutations of identical nuclei, under ordinary conditions the ratio of the number of para- and ortho-states of molecules is 1/3. The transitions between these states are prohibited by the selection rules; therefore, water vapour can be considered as a mixture consisting of 25 % para-molecules and 75 % ortho-molecules of water (ortho-water and para-water).

The total angular momentum of the molecule, **F**, is a vector sum of the orbital moment **J** and the nuclear spin **I**. For the spin equal to unity, according to the general sum rule of moments, this means that only three values of the total angular momentum corresponding to three possible spin orientations with respect to the orbital moment are possible. Consequently, each rotational level in ortho-water splits into three sublevels (the quantum number F which in the considered case can take on three values $J-1$, J, and $J+1$ are used for their identification) between which regular transitions can occur. Such splitting is called the *hyperfine structure of rotational levels.* The corresponding hyperfine structure of spectral lines can be observed experimentally.

---

[9] We often say for simplicity that the proton spin is 1/2 or the molecular spin is 1, meaning the value of the quantum number, whereas the modulus of the angular momentum in these cases are equal to $\hbar\sqrt{\frac{1}{2}\left(\frac{1}{2}+1\right)}$ and $\hbar\sqrt{1(1+1)}$, respectively. Compare with eq. (1.15).

The allowed transitions are shown in the diagram in fig. 3.3 (bottom right). The arrows in the molecule diagram (top right) conventionally indicate that the proton spins are parallel. The most intense lines correspond to the $F' \leftarrow F$ transitions with the selection rule $\Delta F = 1$ (marked in the spectrum recording and shown by heavy black arrows in the level diagram).

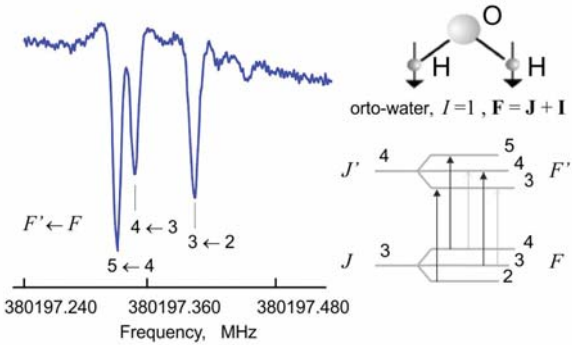

Fig. 3.3. Diagram of a hyperfine structure of ortho-water molecular levels on an example of the $4_{1,4} \leftarrow 3_{2,1}$ transition (*bottom right*) and the experimental spectrum [Golubiatnikov, 2006] of hyperfine components of the rotational line (*left)*.

The splitting is insignificant, so sub-Doppler spectroscopy methods ensuring a super high spectral resolution are used to study it (for example, Golubiatnikov [2006] and references therein), but its contribution may become noticeable at the accurate simulation of the shape of diagnostic atmospheric lines for interpreting the data of satellite observations. The levels of para-water do not split, and its lines do not have a fine structure.

The ortho- and para-water lines may be distinguished by the quantum numbers of the transitions. In the states with an even vibrational number V_3 (corresponding to the overtones of fundamental asymmetric stretch), K_a and K_c have different parity in ortho-molecules, and equal parity in para-molecules. In the states with odd V_3, contrariwise, different parity of K_a and K_c corresponds to para-molecules, and equal parity to ortho-molecules.

We believe that there is no reason to consider possible violation of the ortho-para ratio in atmospheric water vapour and, hence, changes in the intensity of diagnostic atmospheric lines. This follows from the fact that in liquid water the exchange of hydrogen atoms between the neighbouring molecules-monomers takes about 10 ps [Marx, 2006]. The exchange is fast in a solid phase as well, even if a water molecule contacts (is in the same matrix with) other molecules [Sliter, 2011]. If the para-ortho-balance

in the gas phase is disturbed for some reason, the proton exchange occurring on atmospheric dust, aerosols, in snowflakes, and in continuously forming and newly evaporating atmospheric micro-droplets will restore the 1/3 ratio following from the statistics.

By virtue of the abovementioned features of a water molecule, its lines can be found in all spectral ranges. For example, according to the HITRAN database, there are over 50 resonant lines of water vapour in the 20–300 GHz range traditional for microwave atmospheric radiometry, which can be investigated under usual conditions. However, only two of them are sufficiently intense for a radiometric analysis of atmospheric water. These are the $6_{1,6} \leftarrow 5_{2,3}$ line near the 22 GHz frequency and the $3_{1,3} \leftarrow 2_{2,0}$ line near 183 GHz (fig. 3.1). Both these lines are regarded to be the major diagnostic lines of atmospheric water vapour. The accuracy to which their parameters are known determines the accuracy of modelling atmospheric absorption and, hence, the accuracy of retrieving the profile of atmospheric humidity. Investigation of the parameters of these lines and comparative analysis of the results of these investigations deserve special attention.

The submillimetre wavelength range, which is currently also actively mastered by the radiometric methods and telecommunication, contains a tremendous amount of water vapour lines, including still more intense lines than in the millimetre domain, but they are less investigated as this range has always been less accessible using experimental techniques. Nevertheless, the general form of the atmospheric absorption spectrum at frequencies up to 1 THz is determined by 15 intense lines only. Almost all of them are clearly seen in fig. 3.1. These lines, which are of major interest for spectroscopic applications, will be considered in more detail in the next section. It contains a retrospective review of all known studies of atmospheric lines using resonator spectrometers, and the obtained line parameters are compared with data from other studies.

Experimental studies

22-GHz line

The spectral absorption line in water vapour near 0.78 cm^{-1} (23.3 GHz, ortho-water) was predicted theoretically in the first half of the 20th century on the basis of the measurements of the lines of rotational spectrum in the IR range (Dennison [1940] and references therein).

The first experimental study of this line was unexpectedly stimulated by the military for its needs associated with the development of powerful

1-cm range radiation sources for aircraft and marine radars. The tests showed that at some frequencies the radar sensitivity was strongly dependent on weather conditions, in particular, on air humidity. At that time the engineers developing radars knew nothing about atmospheric absorption lines, and it just so happened that the radar frequency coincided with the resonant line of water vapour. As chance would have it, scientists had the lucky opportunity to study and test the already developed radiation sources and all the related waveguide and other auxiliary equipment and techniques.

The radiation absorption by atmospheric air was measured in laboratory conditions at atmospheric pressure, a temperature of 45 ºC, and strongly varying (from 10 to 50 g/m^3) humidity in the 17–40 GHz frequency range [Becker, 1946]. The measurements were made using a non-tuneable volumetric resonator with a very high Q-factor ($Q \sim 600000$–800000) named 'echo-box', though it could as well be called a room as its walls, made of sheets of polished copper on a wooden frame, were about 2.5 m in size. The value of absorption was determined by the time of radiation power decay inside the resonator (section 2.1). For uniform energy distribution in the resonator, a 'mode mixer' was used, the parameters of which were very much like those of a powerful ceiling fan. The radiation power was measured with 360 thermocouples uniformly suspended all over the volume of the echo-box. A chromium-constantan thermocouple with flattened wires with a cross-section of 0.025×0.5 mm ensured the small-time constant needed for such measurements. The homogeneity of the studied gas mixture was maintained through a system of continuous circulation, which helped to moisten the air supplied to the echo-box. A significant radiation power reserve (up to 40 kW), as well as meticulous preparation and execution of the experiments ensured the very high, even by the most up-to-date criteria, quality of the obtained spectroscopic data.

In fig. 3.4 the data of measurements [Becker, 1946] are compared with the calculations of absorption by means of MPM.

The merit of the described study is the fact that the authors published not only the values of the determined spectral line parameters but also the results of absorption coefficient measurements. So, the data can be processed again and again to refine line and continuum parameters in this spectral range, with allowance for the regularly appearing new, more accurate data on the spectrum of the atmospheric air. For example, for determining the spectrometer baseline (see section 2.3) the absorbing chamber was filled with dry air. The recorded spectrum of the dry air (which contained, along with the contribution of resonator intrinsic loss,

absorption in the atmospheric oxygen) was subtracted from the recordings of the humid air spectra. The fact that the neighbouring 60 GHz absorption band of the atmospheric air was additionally broadened by the water vapour (Koshelev, [2015] and references therein) was not taken into consideration. This gave a small but systematic error in determining line parameters.

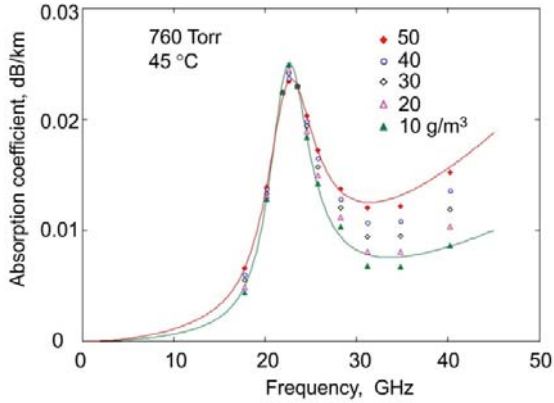

Fig. 3.4. The results of laboratory measurements [Becker, 1946] of radiation absorption in humid air in the vicinity of a 22 GHz line (symbols) and the calculated absorption using MPM for 50 (upper curve) and 10 (lower curve) g/m^3.

For retrieving the parameters of the observed line from the obtained data the following model function was used:

$$M(\nu) = C_1 \cdot \nu \cdot I_c^{VW}(\nu) + C_2 \cdot \nu^2 , \qquad (3.1)$$

where $I_c^{VW}(\nu)$ is the shape function of the Van Vleck–Weisskopf resonant line (1.99), and C_1 and C_2 are the coefficients, the values of which vary when the function is optimised to the experimental data together with central frequency ν_c and collisional halfwidth of the line $\Delta\nu_c$. The function (3.1) includes the expression (1.100) taking into account appreciable changes in the energy of the absorbed radiation quantum within the line contour. The second term simultaneously takes into consideration the contribution of the far wings of the other water vapour lines and continuum absorption (section 1.3.1). The results of the optimisation (3.1) to the experimental data shown in fig. 3.5 allow for the determination of all the principal line parameters at 45 ºC.

The integrated line intensity (fig. 3.5, *a*) normalised to air humidity is expected to be constant. The line intensity averaged over all experimental spectra is $4.41(10)\cdot10^{-25}$ cm/molec, which is only 3 % higher than the present-day value from the HITRAN database, recalculated to 45 ºC using eq. (1.97) and agrees with it within 3σ. Note that, according to the spectroscopists' estimates, the error of the calculated intensities given in HITRAN for diagnostic atmospheric water lines is approximately 1 %, although the expert council of the database suggested a more conservative estimate of 5–10 %.

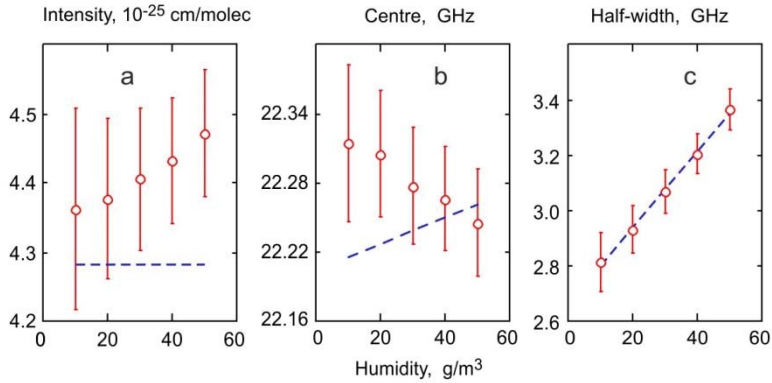

Fig. 3.5. Results of the optimisation of the parameters of the function (3.1) to the experimental data reported in the work of Becker [1946]. The vertical lines are the estimates of the statistical error of the parameter (rms deviation or 1σ). The dashed lines correspond to the present-day best expected values.

The frequency of the observed line centre and its width change with a humidity variation in accordance with (1.94). The frequency of the observed line centre (fig. 3.5, *b*) averaged over all experimental recordings is 0.743(2) cm^{-1} = 22.28(6) GHz, which is in agreement with the highly accurate value of the 'centre of mass' of the line 22235079.85(5) kHz, obtained from the results of the more recent measurements of the frequencies of hyperfine components of this line, using the method of Lamb dip [Kukolich, 1969], if they are averaged with the weights equal to their relative intensities. Note that Becker and Autler overestimated the error of frequency measurements at least two and a half times. The frequency of the observed centre can be considered the same in all the recordings, within the margins of statistical errors; nevertheless, it

systematically (almost linearly) decreased with increasing humidity, which corresponded to the self-shifting parameter $\delta_w = -1.61(14)$ MHz/Torr.

The line width (fig. 3.5, *c*) comprises of two parts responsible for self-broadening and broadening by air. The total gas pressure and its humidity were strictly controlled in the experiment, thus providing unambiguous finding of the parameters of collisional broadening by water vapour pressure $\gamma_w = 16.13(39)$ MHz/Torr and by air pressure $\gamma_a = 3.49(2)$ MHz/Torr.

The results of the study by Becker [1946] are also famous because, thanks to them, it became possible to confirm that the Van Vleck–Weisskopf line shape is better than the complete Lorentz [Van Vleck, 1945] or Gross [Gross, 1955] profiles for describing the shape of broad atmospheric lines of the millimetre and submillimetre wavelength ranges. This was done in the work of Hill [1986], where the parameter of asymmetry was used for comparing different line shapes. This parameter characterises linear distortion of the line at frequency detuning from its centre by the magnitude equal to the line half width:

$$R = \frac{I(\nu_0 + \Delta\nu) - I(\nu_0 - \Delta\nu)}{\big(I(\nu_0 + \Delta\nu) + I(\nu_0 - \Delta\nu)\big)/2}, \qquad (3.2)$$

where $I(\nu)$ is the function of line shape. The values of the parameter R for the Van Vleck–Weisskopf line shape agreed well with the data in the work of Becker [1946], whereas for the case of Lorentz or Gross shapes, the difference between the theoretical and measured R values was far beyond the maximum admissible experimental error.

The next comprehensive study of the parameters of this line was undertaken more than twenty years later [Liebe, 1969-1, 1969-2] using a dispersion spectrometer [Thompson, 1968] based on a high-Q resonator filled with the studied gas. The radiation source was a klystron with a frequency controlled either by a calibrated resonator (with a relative error of $\sim 5 \cdot 10^{-7}$) or by a wavemeter (with an error of $\sim 5 \cdot 10^{-6}$). The distinctive feature of this spectrometer, compared to those considered in Chapter 2, was that the directly measured value was a change in the frequency of the resonator eigenmode when it was filled with the studied gas (equations (2.27) – (2.29)). This change is caused by the variation of the refractive index n and, hence, of the speed of radiation propagation in the resonator $c = c_0/n$, where c_0 is the speed in vacuum. The absorption coefficient in the studied sample is determined unambiguously by the refractive index using the Kramers–Kronig relation for the complex dielectric permittivity of the medium (e.g., Landau [1984]). For increasing measurement accuracy, the principle of simultaneous excitation in the resonator of two modes at

multiple frequencies was used, so that the frequency of one mode was at the absorption line (at about 22 GHz), and the other outside it (near 11 GHz). This enabled the accurate measurement of the frequency shifting of the 22-GHz mode relative to the 11-GHz mode by the time between the pulses corresponding to the excitation of the high-frequency and low-frequency modes of the resonator. To calibrate the spectrometer, the resonator was filled with argon whose refractive index is frequency independent. The sensitivity of the spectrometer with respect to the absorption coefficient was estimated to be $5 \cdot 10^{-8}$ cm^{-1}.

The absorption was investigated at a temperature of 27 ºC in pure water vapour [Liebe, 1969-1] and in a mixture with all major atmospheric gases, including He and CO_2 [Liebe, 1969-2], which is important for the accurate calculation of the collisional line broadening by air. The measurements were made at relatively low pressures (about several Torr in gas mixtures and up to ~20 Torr in pure water vapour). The result of measuring the integrated line intensity — $4.226(85) \cdot 10^{-25}$ cm/molec — was 3.5 % lower than the present-day value from the HITRAN database.

The measured parameter of the line self-shifting $\delta_w = +1.38(15)$ MHz/Torr had a close absolute value, but the opposite sign compared to the result in the work mentioned above [Becker, 1946].

The parameters of collisional line broadening were $\gamma_w = 17.99(18)$ and $\gamma_a = 3.751(19)$ MHz/Torr. The value of γ_a was calculated from the parameters of line broadening by N_2, O_2, Ar, and CO_2 pressure measured in the work by Liebe [1969-2], taking into account their abundance in the atmosphere. Note that using calculations with the simplified expression (1.95) gives an error of about 0.5 %, which corresponds to the maximum statistical error of broadening parameter determined in the work by Liebe [1969-2].

The most recent study of this water vapour line, by Koshelev [2018-2], was made at pressures ranging from 1 mTorr up to 1 Torr using two apparatuses with complementary properties, namely, the video spectrometer and the spectrometer with radioacoustic detection of absorption (RAD spectrometer)[10]. A very good agreement of the air- and self-broadening parameters obtained in this study with the results of the pioneering work of Becker [1946] was demonstrated. The value and the sign of the self-shifting parameter were verified. The obtained value $\delta_w = +1.10(8)$ MHz/Torr is in a good agreement with the result in the work of Liebe [1969-1]. The speed dependence of broadening and shifting

[10] The principles of operation of these spectrometers are briefly described at the end of this section.

parameters for this line in pure water vapour and in air were determined for the first time.

183-GHz line

The presence of the water vapour absorption line near 6 cm^{-1} (para-water) also followed from the line measurements in the IR range [Dennison, 1940]. An approximate calculation of the line frequency (6.15 cm^{-1}) and line intensity[11] was performed in the work of King [1947]. This line was first observed in an experiment using a classical video spectrometer with harmonic generator [King, 1954] almost 10 years later than the line at 22 GHz. The approximate value of the absorption coefficient was confirmed, and the centre line frequency was found to be 183311.30(30) MHz. The frequency agrees rather well with the most accurate to date values of 183310.0906(15) MHz and 183310.087(1) MHz measured with the beam spectrometer [Huiszoon, 1971] and by the Lamb dip method [Golubiatnikov, 2006], respectively.

The parameters of the 183-GHz line at pressures up to the atmospheric one were investigated for the first time by Frenkel and Woods [Frenkel, 1966-1], who used a classical resonator spectrometer [Valkenburg, 1966]. The measurements were made at room temperature in pure water vapour and in its mixture with nitrogen, oxygen, and carbon dioxide. The absorption coefficient in the spectrometer was determined at the eigenmode frequencies of the open Fabry–Perot resonator through changes in the Q-factor of the resonator filled with absorbing gas. The available sources of coherent radiation allowed the absorption coefficient to be measured at points in the 100–300 GHz range. The Q-factor of the resonator consisting of one concave and one flat mirror about 23 cm in diameter, spaced apart by 60-75 cm was from 120000 to 330000 in the operating frequency range. The resonator was coupled to the radiation source and receiver through two open waveguides located in the middle of the flat mirror. The resonator length could be changed a little, so measurements could be made at both high and low pressures. The measured data are compared with the calculation by the MPM in fig. 3.6.

To measure the collisional broadening parameter, Frenkel and Woods took detailed measurements of absorption at small (from –200 to +300 MHz) detunings of the radiation frequency from the line centre. They used, for data analysis, the Van Vleck–Weisskopf model for the

[11] Recalculation of the found intensity taking into consideration the currently well-known centre frequency of the transition gives $7.894 \cdot 10^{-23}$ cm/molec, which is only about 1 % larger than the recent value from the HITRAN database.

shapes of the studied and the adjacent line at a frequency of 325 GHz (whose width was assumed to be like that of the 183 GHz line) and contained the additive term proportional to the squared frequency, which took into account the far wings of the other lines. The intensities of both lines were fixed at the calculated values obtained in the work by King [1947]. The following values of the broadening coefficients were obtained: $\gamma_w = 22(2)$, $\gamma_{N_2} = 4.4(2)$ and $\gamma_{O_2} = 2.7(2)$ MHz/Torr. According to these data, the line broadening by dry air pressure calculated using the approximate expression (1.95) was $\gamma_a = 4.04(20)$ MHz/Torr.

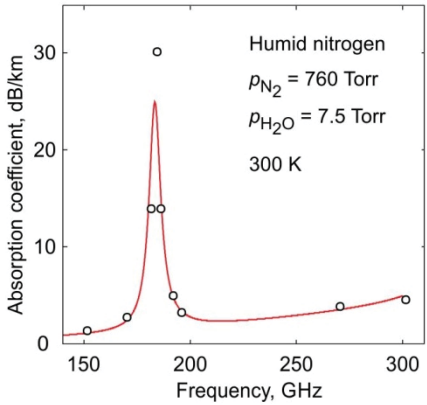

Fig. 3.6. The results of laboratory measurements of absorption [Frenkel, 1966-1] in humid nitrogen in the vicinity of the 183-GHz line (circles) and absorption calculated using MPM with allowance for changes in the model parameters when dry air was replaced by pure nitrogen (solid curve). Adopted from Tretyakov [2016].

The first continuous broadband (110–210 GHz) recordings of the 183 GHz line shapes at atmospheric pressure under relatively stable laboratory conditions became possible with the development of the Nizhny Novgorod resonator spectrometer (Chapter 2) [Krupnov, 2000; Tretyakov, 2003]. The measuring resonator in these experiments was isolated from the ambient air by a large plastic bag, through which the studied gas was continuously blown. About ten litres of gas per minute were consumed during spectrum recording and several times more when the sample was changed. It took several hours of continuous blowing to achieve stable thermodynamic conditions inside the bag. This method enabled the high-precision study of atmospheric lines with a desktop version of an open Fabry– Perot resonator long before the creation of an expensive

specialised gas pressure and temperature-controlled chamber. The constant refreshing of the sample under study, on the one hand, meant minimum problems associated with changes in the partial pressure of water vapour during the experiment due to adsorption and desorption by the spectrometer elements. On the other hand, it did not allow for avoiding small changes in the resonator loss when the dry non-absorbing gas used in recording the spectrometer baseline was replaced by the humid gas under study (see section 2.3). As the resonator losses are frequency dependent, it was necessary to supplement the model absorption function with the terms that would be constant and linear with respect to frequency. This could lead to systematic error in measuring the continuum but gave a negligible contribution when the parameters of the resonant lines were retrieved from the observed profile. The pressure of the studied gas corresponded exactly to the atmospheric pressure. It was measured by a carefully calibrated dial gauge to an accuracy of ± 0.5 Torr. The humidity of the gas was continuously monitored using a semiconductor sensor located near the central part of the resonator. The maximum error of relative humidity measurement, in accordance with the sensor manufacturer's warranty, was ± 1 % in the 10–90 % range and ± 2 % at a humidity of 0–10 %. Before entering the resonator, dry atmospheric gases were passed through a glass flask with double-distilled water. The change in the gas flow rate through the flask and the water temperature made it possible to vary the humidity of the studied gases over a wide range.

A specific feature of this method of research is that the complete draining of the resonator is impossible. Due to diffusion, molecules of atmospheric water vapour penetrate into a non-hermetic package. The spectrometer sensitivity to gas humidity is much higher than that of the sensor; therefore, water vapour lines are visible in the spectrum of the resonator loss, despite the fact that the indicator shows zero humidity. The lower the speed of the resonator blowing by dry gas, the higher the residual resonator humidity. The value of the residual moisture (which was 0.2–0.5 % of the saturating one, or 40–100 mg/m^3) was determined and taken into account by spectroscopic estimates of the signals from the observed lines and their known intensities, with an accuracy sufficient to make its impact on the results of processing of the studied spectra less than the statistical measurement error.

The broadband spectrum recording took several hours. The small absorption variations caused by temperature, humidity, and pressure drift were taken into consideration using the current MPM version in which the number of lines taken into account, and their parameters, were adjusted in accordance with the studied gas sample. Experimental or calculated data

on line shape parameters, for example, from HITRAN or Gamache [2003-1; 2003-2], were used if available. In their absence, empirical relations were used, taking into consideration that the efficiency of collisional broadening of water vapour lines in pure nitrogen is higher, and in oxygen is lower than in air.

To allow for the changes in the thermodynamic conditions of the studied gas during the experiment, the resulting absorption coefficient α was presented in the form

$$\alpha = \alpha_0 + \Delta\alpha \,, \tag{3.3}$$

where α_0 corresponds to the average set of thermodynamic parameters of gas for this experiment (temperature T_0, pressure P_0, humidity H_0), and $\Delta\alpha$ designates its variations corresponding to the deviation of the current parameters from the average ones calculated as

$$\Delta\alpha(T,P,H,\nu) = \mathrm{MPM}(T,P,H,\nu) - \mathrm{MPM}(T_0,P_0,H_0,\nu)\,. \tag{3.4}$$

Possible inaccuracies of model parameters (given that there is a small difference between the current and average parameters) make a negligible contribution to such a recalculation.

A large signal-to-noise ratio in the spectral recordings, achieved due to the high sensitivity of the spectrometer and the stability of the thermodynamic conditions of the gas under study, allowed for validating the shape functions of the resonant line used in propagation models by comparing them with the results of observations. The data were analysed using a model function which is the sum of the line profile (1.100) and the quadratic-frequency polynomial (including linear and constant terms) that takes into account the cumulative contribution to the observed absorption of the wings of other resonant atmospheric lines and of the continuum. An experimental recording of the line in laboratory atmospheric air and the results of its shape analysis using the full Lorentz (1.98), Van Vleck–Weisskopf (1.99), and Gross (1.101) profiles are shown in fig. 3.7.

The signal-to-noise ratio in the recording, defined as the ratio of the line amplitude at centre frequency to the rms deviation of the experimental points from the model function, is about 270. The results of the approximation of the observed absorption by different profiles coincide to an accuracy of the thickness of the smooth solid line in the lower part of fig. 3.7. The differences are visible in the fitting residues in the upper part of the figure. The model, using the Van Vleck–Weisskopf shape, fully agrees with the experimental data and gives an even noise residue in the frequency range of 18 lines' half widths from the centre downwards and 9

half widths upwards. The Lorentz and Gross shapes give indistinguishable residues with systematic deviations, especially noticeable in the near vicinity of the line centre and constituting approximately ± 0.3 % of the line amplitude.

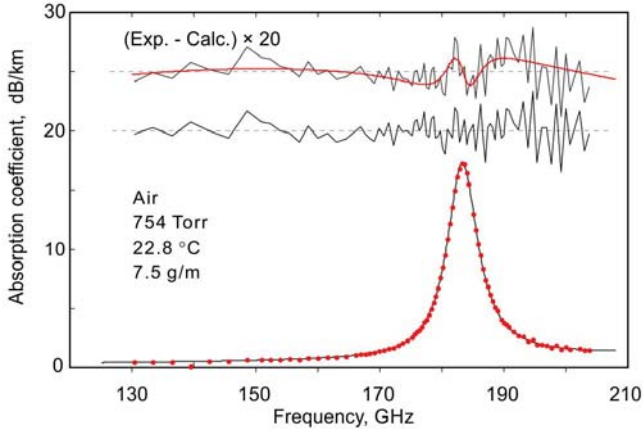

Fig. 3.7. Step-by-step recording (points) of the 183-GHz line of water vapour in atmospheric air and the result of its approximation by the model function (curve). The broken lines in the upper part of the figure show the magnified approximation residues with the use of the full Lorentz shape (upper) and the Van Vleck–Weisskopf (lower) shape; the smooth curve corresponds to the residue obtained if the absorption calculated using the Van Vleck–Weisskopf shape is approximated by the full Lorentz shape. Adopted from Tretyakov [2016].

Thus, the broadband recordings of the 183-GHz absorption line at atmospheric pressure obtained using a resonator spectrometer confirmed the conclusions of the work of Hill [1969], that the Van Vleck–Weisskopf model fits better the broad millimetre-wave atmospheric lines.

To measure line intensity, broadband recordings of its profile were made in a mixture of laboratory air with dry nitrogen at room temperature, atmospheric pressure, and various humidities ranging from 0.1 to 8.6 g/m^3 [Tretyakov, 2003]. The integrated intensity of the observed line was calculated from the amplitudes and widths found as a result of the optimisation of the model function using the relation (1.80). The values presented in fig. 3.8 demonstrate an almost perfect linear dependence on humidity, passing within the statistical error margin through the coordinate origin. The dots in the upper part of the figure show the measurement

results, and the straight line is their approximation by a linear function. The deviations of the experimental points from the line are shown on a magnified scale at the bottom of the figure. The vertical lines correspond to statistical measurement errors (3σ).

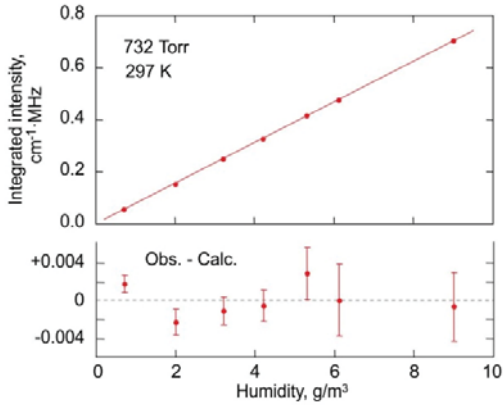

Fig. 3.8. The integrated intensity of the 183-GHz line *versus* humidity in a mixture of laboratory air with dry nitrogen. Adopted from Tretyakov [2003].

The line intensity normalised to the concentration of absorbing molecules, defined as the slope of the straight line that passes best through the experimental points with allowance for their errors, is $7.80(8)10^{-23}$ cm/molec, which is only 0.8 % higher than the present-day value from the HITRAN database. Such a good agreement between the result of direct experimental intensity measurement and the data from modern methods of calculation indicates the high quality of both. Such coincidences give the spectroscopists reason to believe that the real error with which the intensities of diagnostic atmospheric lines are known is about 1 %. Recall that the estimate of the possible intensity error for this line given in HITRAN is 5–10 %.

The centre frequency ν_c of the 183-GHz line observed in the experiments was consistently a little lower than the 'zero pressure' molecular transition frequency known from [Huiszoon, 1971]. In the first experiments [Krupnov, 2000], in which the spectrometer baseline was taken into account by calculating the intrinsic radiation losses in the resonator (section 2.3) and atmospheric air was the only analysed gas, this frequency shifting was attributed to unknown systematic errors of the

method. Further research [Tretyakov, 2003] was prepared and carried out more thoroughly. In addition to air, its principal components — nitrogen and oxygen — were used for analysing absorption. They were continuously blown through the spectrometer chamber to reduce the influence on the measurement result of the adsorption and desorption of the studied gases by the chamber walls and spectrometer elements. The spectrometer baseline was determined through experiments. The shifting of the line frequency centre observed in all the records was attributed to the collisional pressure shifting. The obtained values of the 183-GHz line shifting parameters by nitrogen, oxygen, and air pressure are listed in Table 3.1 together with the corresponding parameters of the collisional line broadening. These measurements can be considered to be the first laboratory measurements of the shifting parameter of one of the most important diagnostic atmospheric lines. Within the margin of statistical error, the obtained values of parameters are consistent with the results of later high-precision laboratory measurements [Golubiatnikov, 2005-1] at gas pressures up to several Torr using a spectrometer with radioacoustic detection of absorption (RAD spectrometer).

Table 3.1. Broadening and shifting of 183-GHz water vapour line by the pressure of atmospheric gases (data from the work of Tretyakov [2003])

Broadening gas	γ, MHz/Torr	δ, kHz/Torr	T, K
Nitrogen	4.24(4)	–91(24)	299.0
Oxygen	2.57(5)	–84(30)	298.6
Air	3.84(4)	–67(16)	298.0

It is interesting to note that the manifestation of the centre frequency shifting of the 183-GHz line was first reported [Pumphrey, 2000] at about the same time. Pumphrey and Bühler, who analysed the data of limb sounding of the atmosphere from satellites, found that the introduction of the shifting parameter in the absorption model improves its agreement with the experimental data. According to the records of the MLS radiometer aboard the UARS orbital satellite [Barath, 1993], $\delta_a =$ $= –0.19(4)$ MHz/Torr and analysis of the data of ATLAS/MAS radiometer [Croskey, 1992] aboard a space shuttle gave $\delta_a = – 0.27(5)$ MHz/Torr, which was consistent with the previous value within the error bars. Thus, both the sign and the order of magnitude of the effect were determined correctly. A characteristic feature of limb satellite measurements is a very large path length (up to hundreds of kilometres) on which the received signal is formed, ensuring high sensitivity to small absorptions using the method. Somewhat overestimating the capabilities of ‘space

spectrometers', Pumphrey and Bühler wrote: 'Certain parameters, including the pressure shifting, are hard to measure in the laboratory. Microwave limb-sounding instruments appear to be capable of providing a better measurement of the pressure shifting of the 183 GHz water vapour line than any laboratory technique of which we are aware' [Pumphrey, 2000].

325-GHz line

The position of the water line corresponding to the $5_{1,5}\leftarrow4_{2,2}$ rotational transition of a para-molecule was predicted, by the theoretical calculations based on IR-spectroscopic data, to be 325.5 GHz. It was first observed almost simultaneously in the mid-1960s by two different methods: using a BWO and an optoacoustic detector over an extended atmospheric path along the surface in field measurements [Ryadov, 1966] and a Stark video spectrometer with radiation at harmonic frequencies of a klystron in laboratory conditions under low-pressure water vapour [Lichtenstein, 1966]. The first method gave the estimate of the collisional broadening of the line by air pressure, and the second the estimate of the frequency of 325.1538(3) GHz, which was later determined more accurately to be 325152919(27) MHz in work by De Lucia [1972]. The most accurate value of the frequency of this transition of 325152.899(1) MHz to date was obtained using the Lamb dip method [Golubiatnikov, 2006]. The first laboratory measurement of the parameters of collisional line broadening by nitrogen and oxygen pressure and the assessment of their temperature dependence were also made at pressures lower than 1 Torr [Colmont, 1999].

The pioneer broadband (290–370 GHz) recordings of the absorption profile in the vicinity of this line, in mixtures of water vapour with nitrogen and oxygen at atmospheric pressure and different humidities, were made with the Nizhny Novgorod resonator spectrometer at room temperature [Koshelev, 2007]. The signal-to-noise ratio in the recordings was about 100. The procedure of working with the gases under investigation and obtaining the spectra was the same as in the study of the 183-GHz line. An example of spectrum recording is shown in fig. 3.9. One can see that under these conditions the shape of the 325-GHz line is under a strong influence of the low-frequency wing of the water vapour absorption line near 380 GHz corresponding to the $4_{1,4}\leftarrow3_{2,1}$ transition which is approximately an order of magnitude more intense. In addition, for accurate analysis of the shape of the observed 325-GHz line, it is important to take into account the absorption in the weak water vapour

line $10_{2,9} \leftarrow 9_{3,6}$ near 321 GHz (solid green curve in the lower part of the figure) which is practically invisible in the recording, as well as the wings of other resonant lines (dashed curve) and the continuum (dotted curve).

The line parameters were found using the following model function

$$M(\nu) = C_1 \cdot \nu \cdot I_c^{VW}(\nu) + I_{321}^{VW}(\nu) + I_{380}^{VW}(\nu) + C_2 \cdot \nu^2 + C_2 \cdot \nu + C_4 \,, \quad (3.5)$$

where the second and third terms are, respectively, the calculated absorption profiles of the 321-GHz and 380-GHz lines without variable parameters that were constructed on the basis of the Van Vleck–Weisskopf shape. The values of centre frequencies, the coefficients of collisional broadening and the shifting by nitrogen, oxygen, and water vapour pressure for these lines were taken from the results of their investigations performed in the same work at low pressures using the RAD spectrometer, and the intensity values were taken from the HITRAN database. The found collisional broadening and shifting coefficients of the 325-GHz line in nitrogen and oxygen coincided, within the experimental error, with the data measured with the RAD spectrometer (Table 3.2). The contribution of self-broadening and self-shifting was taken into account using the measurement data at low pressures. The found integrated intensity of the 325-GHz line was approximately 6 % less than the value from the HITRAN database.

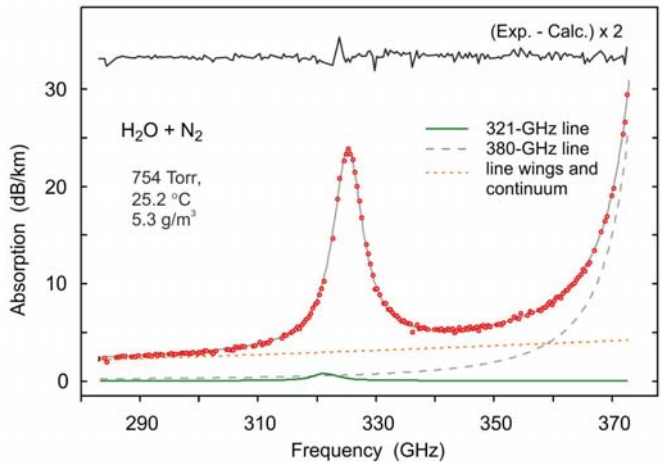

Fig. 3.9. Data of measurements (dots) of the spectra of the mixture of H_2O water vapour with N_2 in the vicinity of the 325-GHz line and their approximations by the model function (3.5). The broken line at the bottom of the figure is approximation residue. Adopted from Koshelev [2007].

Table 3.2. Collisional parameters of 325 GHz line (data from Koshelev, 2007)

Spectrometer	γ, MHz/Torr		δ, MHz/Torr		Intensity,
	H_2O-N_2	H_2O-O_2	H_2O-N_2	H_2O-O_2	cm/molec
Resonator	4.09(5)	2.29(4)	–0.037(11)	0.000(40)	$8.55(35)\cdot10^{-23}$
RAD	4.17(3)	2.33(2)	–0.020(7)	0.000(30)	—

380-GHz and 448-GHz lines

The lines corresponding to the rotational transitions of the water ortho-molecules $4_{1,4}\leftarrow3_{2,1}$ and $4_{2,3}\leftarrow3_{3,0}$ near 380 and 448 GHz (fig. 3.1) were predicted by the IR measurements, like in the previous cases. More accurately their position was determined by means of microwave video spectrometers operating at low pressures with the Doppler [Lichtenstein, 1966; De Lucia, 1972] and later with the sub-Doppler [Golubiatnikov, 2006] resolution. The obtained frequencies of 380197.356(5) and 448001.075 (5) MHz correspond to the 'centre of gravity' of the components of the hyperfine structure. The results of experimental studies of the collisional broadening of the 380-GHz line by the pressure of major atmospheric gases can be found in Ryadov [1968], Pearson [1969], Emery [1972], Bauer [1987].

The first high-sensitivity broadband (350–500 GHz) laboratory recordings of the spectra of air, humid nitrogen, and oxygen containing these lines at atmospheric pressure (fig. 3.10) were obtained using the Nizhny Novgorod resonator spectrometer at room temperature [Tretyakov, 2013-1]. The process was the same as with the two previous cases in broadband studies of 183-GHz and 325-GHz lines.

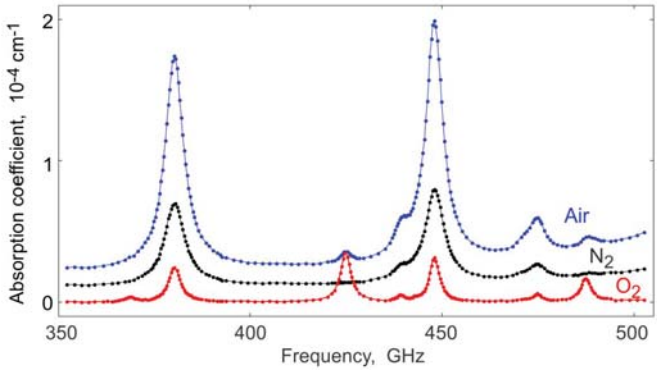

Fig. 3.10. The spectra of atmospheric air, nitrogen, and oxygen mixed with water vapour at atmospheric pressure, room temperature, and low humidity. The nitrogen and air spectra are elevated by 10^{-5} and $2\cdot10^{-5}$ cm^{-1}, respectively. Adopted from Tretyakov [2013-1].

With the advance into the short wavelength region, the spectrum analysis is becoming much more complicated, which is associated with the regular increase in line intensity (see section 1.2.1). Hence, there arises a need to allow for an increasingly larger number of lines in the considered spectral range. In this case, in addition to the two most intense water vapour lines at 380 GHz and 448 GHz, the spectrum recording features the lines of the $6_{4,3}\leftarrow5_{5,0}$ (439.2 GHz), $7_{5,2}\leftarrow6_{6,1}$ (443.0 GHz), $6_{4,2}\leftarrow5_{5,1}$ (470.9 GHz), $5_{3,3}\leftarrow4_{4,0}$ (474.7 GHz), and $6_{2,4}\leftarrow7_{1,7}$ (488.5 GHz) transitions. Six more lines become apparent in the optimisation residue, if they are not taken into account in the model. These are the lines of the $H_2{}^{16}O$ molecule: $7_{5,3}\leftarrow6_{6,0}$ (437.3 GHz), $8_{6,3}\leftarrow7_{7,0}$ (503.5 GHz) and $8_{6,2}\leftarrow7_{7,0}$ (504.5 GHz); of the $H_2{}^{18}O$ molecule: $4_{1,4}\leftarrow3_{2,3}$ (390.6 GHz) and $4_{2,3}\leftarrow3_{3,0}$ (489.0 GHz); and of the $HD^{16}O$ molecule: $2_{0,2}\leftarrow1_{1,1}$ (490.6 GHz) in the ground vibrational state which are present in water vapour, corresponding to the natural isotopic abundance. The lines of the first pure rotational triplet of the oxygen molecule near 368.5, 424.8 and 487.2 GHz located in this spectral range should also be taken into consideration. A detailed analysis of these lines, whose contribution to the observed absorption, especially in pure oxygen, is no longer small, will be made in section 3.1.3.

A number of the mentioned lines strongly overlap each other. The attempts to take into account all lines in the model function and simultaneous variation of their parameters cannot give reliable results because of cross-correlation. The multistep iterative approach, at which the observed spectra are ‘cleared’ to the maximum extent from weakly manifesting components using the MPM version adjusted to the gas under study and the values of the parameters of the intense lines remaining in the recording are determined and substituted into the MPM, proved to be more reliable. This allows the initial spectrum to be purified from the intense lines and the parameters of the weak lines to be determined more accurately. The procedure is repeated until the line parameters stop changing by significant values.

The parameters of the weak lines near 437.3, 503.5, 504.5, 390.6, 489.0, and 490.6 GHz could not be determined due to the insufficient signal-to-noise ratio. The absorption corresponding to these lines as well as to all the other intense lines of water vapour and oxygen beyond the considered range were calculated by the MPM and subtracted from all the observed spectra.

The 380-GHz and 448-GHz lines are very intense. Therefore, the absorption profile around these lines was recorded at low gas humidity so as not to go beyond the range of permissible changes in the magnitude of

the radiation power loss in the measuring resonator. The nitrogen humidity was about 0.69 g/m^3 (relative humidity being 3.4 %), air humidity was approximately 1.63 g/m^3 (relative humidity being 8.0 %), and, at oxygen spectrum recording, humidity changed from 0.13 to 0.22 g/m^3 (0.6—1.1 %). Under these conditions, the contribution of the continuum absorption (determined primarily by gas humidity) is also a minor constituent that can be calculated to a good enough accuracy by the MPM and subtracted from the observed spectra.

The model function used for the analysis of the obtained spectra was written in the form

$$M(\nu) = \sum_i C_i \frac{\nu}{\nu_{0i}} \left(I_c^{VW}(\nu) \right)_i + C_1 \cdot \nu + C_2 \qquad (3.6)$$

summing the Van Vleck–Weisshopf profiles of all the analysed lines. The additional terms with variable coefficients C_1 and C_2 allow for possible inaccuracy of calculating non-resonant absorption and unaccounted for changes in the spectrometer baseline during long-term spectrum recordings. The variable parameters for all the studied lines were the collisional line breadth $\Delta\nu_c$ and the position of the centre ν_c. The integrated intensities varied only for the 380-GHz and 448-GHz water lines and for the oxygen lines. For all the other water lines the fixed calculated values were used. The result of the analysis of the recorded spectrum of humid nitrogen is shown in fig. 3.11.

Broadband studies of the spectra at atmospheric pressure were carried out with a resonator spectrometer in the 350-510 GHz range along with measurements at low pressure (down to several Torr) with a RAD spectrometer. All water vapour lines within this spectral range that make a marked impact on the absorption profile under atmospheric pressure were investigated at low pressure. The values of the obtained parameters of collisional broadening and shifting of these water vapour lines were summarised by Tretyakov [2013-1].

The results of measurements with the two considered spectrometers agreed, within the measurement error margins, for all the parameters of the diagnostic atmospheric lines near 380 and 439 GHz, as well as for most other studied lines.

The values of the intensities of the 380-GHz and 439-GHz lines obtained in this research cannot be considered as the result of independent measurement, as the calculated values of line intensities were used for spectroscopic determination of gas mixture humidity and the respective correction of the indications of the humidity sensor.

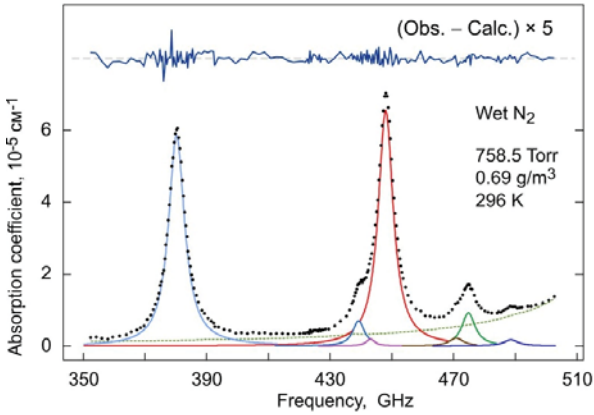

Fig. 3.11. The measured absorption in humid nitrogen at atmospheric pressure and room temperature (points) and seven constituents of its resonant spectral lines (solid curves), the parameters of which were determined by optimisation of the model (3.6) to the experimental points. The calculated contribution of the line wings outside the considered range and of the continuum is depicted by a smooth dotted curve. The optimisation residue is shown on a magnified scale at the upper part of the figure. Adopted from Tretyakov [2013-1].

Comparison with other experimental techniques

Let us now consider measurements of the principal molecular line parameters (intensity, collisional broadening, and shifting) using a broadband resonator spectrometer and compare it with the other techniques. The comparison will be made on an example of the most widely studied 183-GHz diagnostic atmospheric line using the results of all the works known to date.

There is a broad variety of spectrometers differing by one or another feature. However, besides the principle of 'probe resonance' underlying all resonator spectrometers (Chapter 2), only two approaches differing by the general physical principle of operation, which enable investigation of molecular spectral lines, can be distinguished.

The first approach is based on the analysis of the properties of the radiation that has passed through the substance. A typical example is a classical video spectrometer registering the power of coherent frequency-tuned radiation that has passed through a volume filled with absorbing gas. The spectrum of gas absorption coefficient can be found from the Bouguer–Lambert–Beer formula (1.2):

$$\alpha(\nu) = -\frac{1}{l}\ln\left(\frac{W(\nu)}{W_0(\nu)}\right), \tag{3.7}$$

where W and W_0 denote the radiation power measured as a function of frequency in two cases: when the volume is filled with studied gas and when it is empty. The merits of this method are its simplicity and a possibility of direct measurements of absorption coefficient.

The second approach is based on recording changes in the macroscopic properties of gas as a result of radiation absorption. An example of this is a RAD spectrometer (with radio acoustic detection of absorption) [Krupnov, 1979]. Radiation absorption leads to an increase in the internal molecular energy that is converted due to collisional relaxation to the translational energy of the molecules, i.e., the gas is heated. As a result, the pressure in a closed volume of the cell grows, which is registered by a high-sensitivity microphone. The output spectrometer signal S in this case is proportional to the power absorbed by the gas and can be presented, using the same relations, in the form

$$S \sim W_0 - W = W_0\left(1 - e^{-\alpha(\nu)l}\right). \tag{3.8}$$

Under the condition of a small optical depth ($\alpha l << 1$), the signal is directly proportional to the absorption coefficient:

$$S \sim W_0 \cdot \alpha(\nu) l. \tag{3.9}$$

The merit of this method is that the signal is directly proportional to the radiation power; hence, the spectrometer sensitivity can be increased by increasing the radiation power ([Golubiatnikov, 2020] and references therein). Note that, unlike the spectrometers of the first type, here the radiation power cannot be measured experimentally, as in this case there is no signal if there is no absorption. The frequency dependence of radiation power must be taken into account at the stage of spectrum processing by introducing into the model of the signal a multiplicative polynomial of the first or second order [Tretyakov, 2008]. This sets an upper limit on the width of the spectral line, i.e., on the pressure at which spectral line recording undistorted by hardware effects can be attained. Obviously, the higher the pressure of the gas under study, the stronger the collisional effects in the line shape and, consequently, the more accurately their parameters will be measured.

Uncontrolled and unavoidable reflections of radiation from spectrometer elements, leading to a complicated interference pattern of radiation in the spectrometer waveguide line, make the main contribution to the frequency

dependence of the radiation power. Note that the radiation interference is the main disturbing factor not only in spectrometers of the second type, but others as well. The possibility of measuring with spectrometers of the first type is rather limited, as the conditions of radiation propagation also change when the gas under investigation is pumped out. The refractive index of the medium varies as well. This alone is sufficient for the interference pattern in the waveguide line to change. In addition, small alterations in the geometric dimensions of the gas cell are possible due to a pressure drop or temperature drifts. The longer the cell, the stronger the impact of all these effects on the measurement result. This contradicts the sensitivity, which is directly proportional to the cell length in spectrometers of the first type and is necessary for obtaining line recordings with a signal-to-noise ratio sufficient for determining their parameters.

The results of studying the parameters of the 183-GHz line using video spectrometers at high pressures can be found in the work of Hemmi [1969] and Emery [1972]. In the first case, the cell length was 164 m and, in the second, 6 m. Typical data sets are given in fig. 3.12, where the results of calculating absorption following the MPM version adjusted for the same experimental conditions are shown for comparison. Similar recordings of the same lines using the Nizhny Novgorod resonator spectrometer can be seen in figs. 3.7 and 3.11.

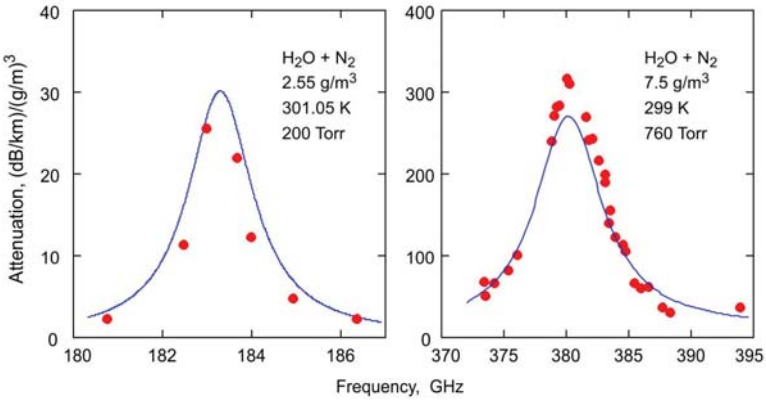

Fig. 3.12. Examples of absorption measurements (points) near diagnostic atmospheric lines at high pressures using video spectrometers ([Hemmi, 1969] *on the left* and [Emery, 1972] *on the right*) and the result of absorption calculation by the MPM version adjusted for the experimental conditions (curves).

These studies have convincingly demonstrated the futility of such attempts to obtain high-precision measurements of the parameters of spectral lines. A higher accuracy of determining line parameters using video spectrometers can be achieved, provided that the influence of the radiation interference on the observed line shape is insignificant, i.e., like in the case of the second type discussed above, at pressures such that the characteristic frequency scale of the power change is much larger than the range of the absorption line recording. The results of using video spectrometers for studying the parameters of the 183-GHz line under such conditions can be found in Rusk [1965], Bauer [1985; 1989], and Goyette [1990]. The cell length was 1 m or 2 m, 0.5 m and 0.6 m, respectively, and the gas pressure varied from tens to hundreds of millitorr. At such relatively low pressures, the Doppler broadening (section 1.2.2) has a noticeable influence on line shape, which has to be taken into account. A typical example of line recording is shown in fig. 3.13. The signal amplitude increasing abruptly with increasing frequency, many times higher than the amplitude of the line, has nothing to do with the absorption signal. It is a manifestation of radiation interference in the radiation transmission line of the spectrometer, unlike fig. 3.9 where a seemingly similar curve corresponds to the low-frequency wing of the intense 380-GHz line.

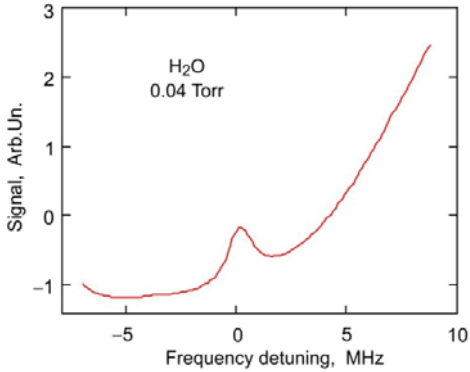

Fig. 3.13. An example of recording the 183-GHz line with a video spectrometer [Goyette, 1990]. Frequency detuning is from 183310 MHz.

Figure 3.13 shows how strong the influence of radiation interference may be in such experiments, even at very low pressures. It is clear that this influence can be a source of systematic error in measuring parameters. Nevertheless, allowance for the baseline using the expression (3.7), and

then taking into account possible ‘undercounting’ of the baseline by introducing an additional quadratic-frequency polynomial into the model function of the spectrum, enable the measuring of the collisional parameters of the line and their temperature dependence.

The intensity and collisional frequency shifting of the 183-GHz lines were not measured with video spectrometers in any of the known works because these parameters are hard to assess due to interference. The weak effect of the line frequency shifting is masked by the apparent displacement of the position of the line maximum due to the power ‘slope’. Measuring intensity with an uncertainty more than 10 % makes no sense, since the theory provides a higher accuracy. The accuracy of intensity measurement is limited by the accuracy with which the $W_0(\nu)$ function is known and its evaluation with an uncertainty of less than 10 % faces the difficulties listed above which are almost unresolvable. The only experimental measurements of the intensity of the 183 GHz lines were made with the Nizhny Novgorod resonator spectrometer [Tretyakov, 2003] with the uncertainty of approximately 1%, which corresponds to the inaccuracy of the best present day theoretical calculations [Lodi, 2011].

The RAD spectrometer is less susceptible to radiation interference. The fact is that in spectrometers of the first type, interference manifests itself at the location of the radiation receiver, specifically, at a certain point in space where the radiation detector is located. In the RAD spectrometer, the gas uniformly filling the entire cell is the radiation detector. The power of the radiation heating the gas may be different at different points of the cell due to interference, but only the average power over the entire volume, where the gas interacts with the radiation, affects the signal. Even the transverse size of the cell is much larger than the radiation wavelength; therefore, taking an average of the interference is very effective. The increase in the length of the radio acoustic cell aimed at increasing the sensitivity is limited by the fact that the elasticity of the microphone membrane at low pressures is always lower than the elasticity of the gas, and the microphone acts as a pressure receiver. The gain in pressure, which is a useful signal, does not increase with increasing cell length, since in most cases, with the exception of the most intense lines in the millimetre and submillimetre ranges ($\alpha \sim 1$ cm^{-1}), the gas absorbs radiation and is heated almost uniformly over the entire length of the cell. The increase in the total power absorbed by the gas with increasing cell length is compensated by the same increase in the volume of the heated gas. In the current spectrometer version, the cell length is 10 cm. For such a size, the characteristic period of standing waves is about 1.5 GHz. Considering that the characteristic value of the collisional broadening of the line is

10 MHz/Torr, assuming that the recording of the line shape within 10 of its widths is sufficient for reliable determination of its parameters, and that for minimal distortion of the line shape due to radiation interference this recording takes no more than 1/10 of the period of standing waves, we find that the gas pressure in the experiment should not exceed 1.5 Torr. It is several times higher than the maximum allowable pressure in video spectrometers and, together with a significantly weaker influence of radiation interference on the shape of the observed lines, ensures the RAD spectrometer superiority in determining collisional parameters of lines compared to video spectrometers. An example of recording the profile of the 183-GHz line with the RAD spectrometer is given in fig. 3.14. The results of using RAD for studying collisional parameters of the 183-GHz line can be found in the works of Krupnov [1992], Golubiatnikov [2005-1, and Koshelev [2021], where the parameters of broadening and shifting by pressure of the majority of atmospheric gases were measured and their speed and temperature dependence was investigated in the cases of self- and dry air pressure broadening.

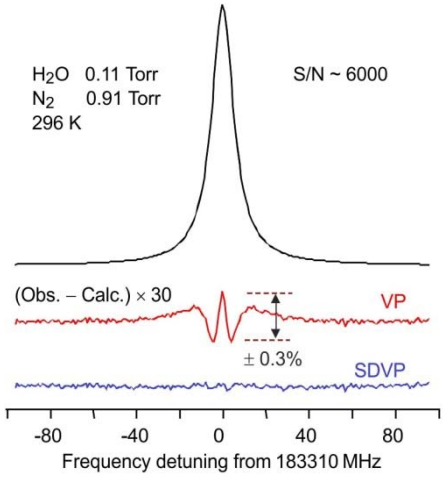

Fig. 3.14. 183-GHz line in humid nitrogen recorded with RAD spectrometer (upper curve) and optimisation residue for the Voigt profile (VP, central curve) and for the profile taking into account 'wind' effect (SDVP, section 1.2.2) (lower curve). The residues are presented with 30-fold magnification. Adopted from Tretyakov [2016].

The results of *field measurements* [Dryagin, 1966; Ryadov, 1975] carried out directly in the atmosphere following the video spectrometer scheme with a source and a radiation receiver spaced far apart along the Earth's surface can also be referred to the experimental determination of air pressure broadening of the considered line. The path length was 6 km and 1.6 km, respectively. A BWO was used as a radiation source, and a radiometer as a receiver. On the one hand, this measurement method partially eliminates the problem of radiation interference in the spectrometer waveguide line and has the advantage of the spectroscopy with a long radiation path length. On the other hand, in such measurements it is hard to maintain stable thermodynamic conditions for the studied gas and it is impossible to register their changes continuously throughout the radiation propagation path.

The results of measurements made in the work by Dryagin [1966] and the data from modelling with the updated MPM version under the same conditions are shown in fig. 3.15.

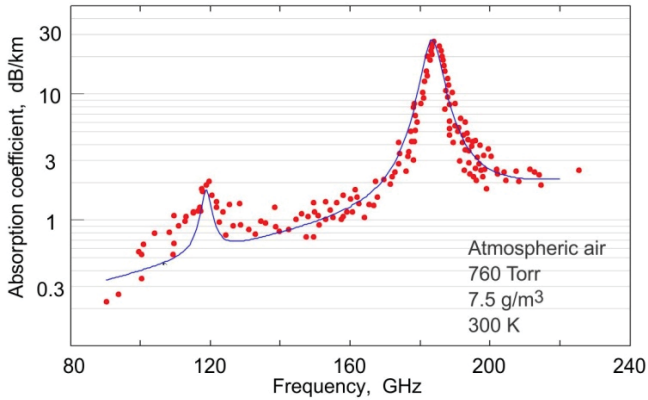

Fig. 3.15. The results of measurements (circles) of atmospheric absorption on the 6-km path along the surface (using data from figs. 1 and 2 from the work of Dryagin [1966]) and calculations (curve) for the same conditions with modern MPM.

It is even more difficult to analyse data of *radiometric measurements* of thermal radiation of air obtained using ground-based [Cruz-Pol, 1998; Payne, 2008] and satellite-borne [Pumphrey, 2000] instruments, as they depend dramatically on both, the model of atmospheric absorption and the model of the atmosphere itself. In such measurements, a calibrated highly sensitive and, as a rule, narrow-band radiation detector registers the

radiation of the molecules with rotational states being excited by collisions and relaxing at the spontaneous emission of a photon. At the same time, the observation paths are huge: they run vertically or at an angle through the entire thickness of the atmosphere. The complexity of the analysis and the uncertainty of gas parameters increase multiple times, compared to measurements on the paths along the surface, as all layers of the atmosphere with greatly differing thermodynamic conditions contribute to the received signal. Measurements of line parameters reduce in this case to the variation of the corresponding parameters of the model of atmospheric absorption. Note that incompleteness of the absorption model, uncertainty of its other parameters that are considered to be known and are fixed during such measurements, or inaccurate vertical distribution of absorbing molecules underlying the model can lead to significant systematic errors. However, despite all the difficulties, it was this method that made it possible to detect and measure the frequency shifting of the 183-GHz line by air pressure for the first time [Pumphrey, 2000].

Another source of experimental data for comparison may be spectral measurements of vibrational-rotational lines of water vapour in the IR range. The reason for this is the well-known fact that, when molecules collide, relaxation of their rotational state occurs much more easily than vibrational relaxation. A detailed analysis of this process in H_2O molecule was made in Gamache [2004-1, -2], where it was shown that, at least for lower vibrational states, the line broadening parameters differ notably from the parameters of the relevant lines of a pure rotational spectrum only for large values of the rotational quantum number J corresponding to the total angular momentum of the molecule. That is, the lines of all water molecule transitions between rotational levels with quantum numbers J, K_a, and K_c, same as of the 183-GHz line in the ground, and excited vibrational states, including fundamental oscillations and their first overtones, will have the collisional broadening parameters differing by no more than a few percent. Additionally, the spectral lines corresponding to similar transitions of different isotopologues of the molecule are almost equally broadened by pressure [Gamache, 2003-1, -2]. This means that the results of measurements of the collisional broadening of lines from Toth [1998, 2003, 2005, 2006] and Birk [2012], in which broadband vibrational-rotational spectra of water vapour in pure gas and in a mixture with major atmospheric gases were studied by means of Fourier-transform spectrometers, can be used for comparison. The line frequency shifting by gas pressure, on the contrary, strongly depends on the vibrational state of the molecule [Gamache, 2004-2], hence such a comparison is impossible.

For the comparison of collisional broadening parameters obtained by different researchers all data should to be brought to identical conditions. First of all, the value of the parameter obtained in experiment at a definite temperature should be recalculated, for example, to a temperature of 296 K adopted for most atmospheric databases using the relation (1.96). The values of the corresponding temperature exponents *n* from the works of Payne [2008], Goyette [1990] and Koshelev [2021] can be used for recalculation. Uncertainty of this data, as a rule, has a negligible effect on the result of the recalculation. To compare the parameters of line broadening and shifting by dry air pressure, it is also necessary to take into account the contributions from self-broadening and self-shifting which were not allowed for correctly or were neglected in some original works. In this case, the parameters from Golubiatnikov [2005-1] and Koshelev [2021] can be used to recalculate earlier data.

When the air broadening parameter is determined as a sum of the components corresponding only to a few major atmospheric gases, a correction related to insufficient adequacy of such a dry air model should be taken into consideration. The value of this correction for the 183-GHz line was estimated in section 1.2.3. The results of all known measurements of the collisional broadening parameters of the 183-GHz line by air and water vapour pressure recalculated in this way are shown in fig. 3.16. Data on the parameter of the line pressure shifting are much less known. All of them are listed in Table. 3.3.

Table 3.3. The coefficients of the frequency shifting of 183-GHz line by water vapour and air pressure at 296 K (in MHz/Torr).

Water vapour	Air	Reference
Less than +0.7		[Bauer, 1989]
	–0.19(4)	[Pumphrey, 2000], MAS
	–0.27(5)	[Pumphrey, 2000], MLS
	–0.069(16)	[Tretyakov, 2003]
+0.23(3)	–0.096(10)	[Golubiatnikov, 2005-1]
	–0.106	[Payne, 2008]
+0.145(7)	-0.0965(10)	[Koshelev, 2021]
	–0.106(390*)	HITRAN-2016

* Parameter uncertainty is assessed as the 0.039—0.39 MHz/Torr interval.

Figure 3.16 and Table 3.3 clearly demonstrate unknown systematic measurement errors actively discussed in the literature. The results even of the most meticulous measurements may differ from each other far beyond the stated error bars. The problem is that it is extremely difficult to assess systematic errors. Therefore, a statistical error corresponding to the scatter

of the obtained values relative to the used model is reported as a rule. The usual sources of systematic errors are the following:

a) uncontrolled variation of the spectrometer baseline caused by changes in the refractive index when the gas cell is filled with a studied sample, as well as by mechanical changes of the optical path length as a result of pressure drops or temperature drift;

b) inadequacy of the model used to describe the obtained data to the conditions of the experiment;

c) erroneous calibration of the measuring instruments;

d) the sources of systematic errors in the work with water vapour that are hardest to control are water molecule adsorption and desorption by the spectrometer elements, which may lead to changes in the water vapour partial pressure as well as to changes in the output signal of the spectrometer [Liebe, 1984-1, -2; Tretyakov, 2009].

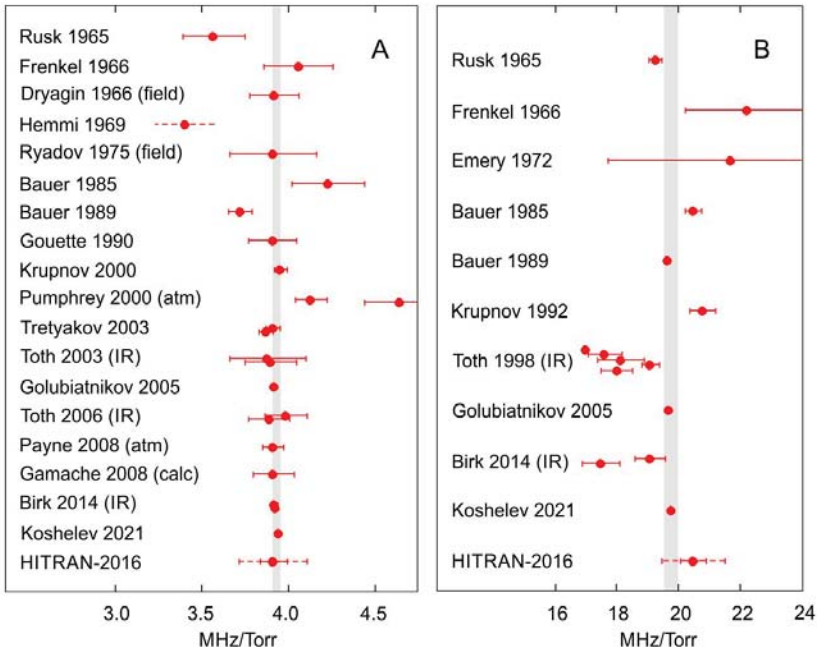

Fig. 3.16. The parameter of collisional broadening of 183-GHz line by dry air pressure (*a*) and water vapour pressure (*b*) at 296 K by results of different studies in chronological order. The shaded area corresponds to the most probable value of parameter and its error. Adopted from Tretyakov [2016].

That is why, for determining a reliable value of line parameters, multiple measurements should be performed under different experimental conditions using instruments based on different principles (see, for example, the review papers by Gamache [2004-1] and Payan [2005]).

The requirement of using different instruments shows the role of the broadband resonator spectrometers in the measurements of the parameters of isolated molecular lines. They are able to accurately determine line shape parameters at pressures much higher than typical operating pressures in other types of spectrometers. Of course, this does not exclude possible systematic errors. However, a combination of a resonator spectrometer with a spectrometer of another type ensures fast and efficient revealing and minimisation of possible sources of systematic errors.

The Nizhny Novgorod resonator spectrometer in combination with the RAD spectrometer make an *instrumental complex* [Parshin, 2009]. The results of using the complex to measure the parameters of pressure broadening and shifting of the 183-GHz line are shown in fig. 3.17, where the solid lines correspond to the approximation of the measurement results using the RAD spectrometer [Golubiatnikov, 2005-1] (empty symbols), which are extrapolated to the operating pressure range of the resonator spectrometer. The deviation of the results of measurements with the resonator spectrometer (filled symbols) [Tretyakov, 2003] from the extrapolation result is shown on magnified scale in the insets. The dashed lines in the insets correspond to the statistical uncertainty of the RAD spectrometer data. The vertical lines in the insets show the statistical uncertainty of the resonator data. At the bottom of the figure one can see the deviation of the experimental points from the lines.

The agreement, within statistical error, of the measurement results obtained with the spectrometers based on different physical principles and at pressures differing by more than 300 times means that systematic errors are minimal in both spectrometers. Such measurements significantly increase the reliability of determining line parameters. Confirmation of the high accuracy of measurements achieved with the use of the instrumental complex is demonstrated in fig. 3.16 *a*, from which it is clear that subsequent measurements did not refine the parameter value.

Careful analysis of fig. 3.16 also leads to definite conclusions about the possibilities of other methods of investigation. The most uncertain data were obtained with the use of video spectrometers, even when the statistical errors were small [Rusk, 1965; Hemmi, 1969; Bauer, 1985, 1989; Gouette, 1990]. Despite the seemingly high accuracy, the data could significantly (by more than 20 %) differ from each other. Measurements on extended paths along the surface [Dragin, 1966; Ryadov, 1975] give

unbiased parameter values, but cannot guarantee high accuracy. Judging by the parameter of air broadening (fig. 3.16 a), measurements of vibrational-rotational lines in the IR range [Toth, 1998, 2003, 2006; Birk, 2012] look promising. However, the self-broadening parameter (fig. 3.16 b), even with the most careful measurements [Birk, 2012], is different for the lines corresponding to the transitions with $\Delta J = -1$ and $\Delta J = +1$ and noticeably different from all the measurement results using other methods, which points to an imperfect adequacy of such a comparison. The values of the parameters obtained by limb satellite radiometric measurements [Pumphrey, 2000] are of the correct order of magnitude but may have a large systematic offset, which may be different for different data sets even with the same processing algorithm. Radiometric measurements at the zenith [Payne, 2008] are in a good agreement with high-precision laboratory measurements. However, this can only be a consequence of the fact that, when the model was optimised to the data of observations, the initial value of the parameter was taken from the calculations based on all laboratory measurements known at that time (in fig. 3.16, this value is designated as Gamache, 2008).

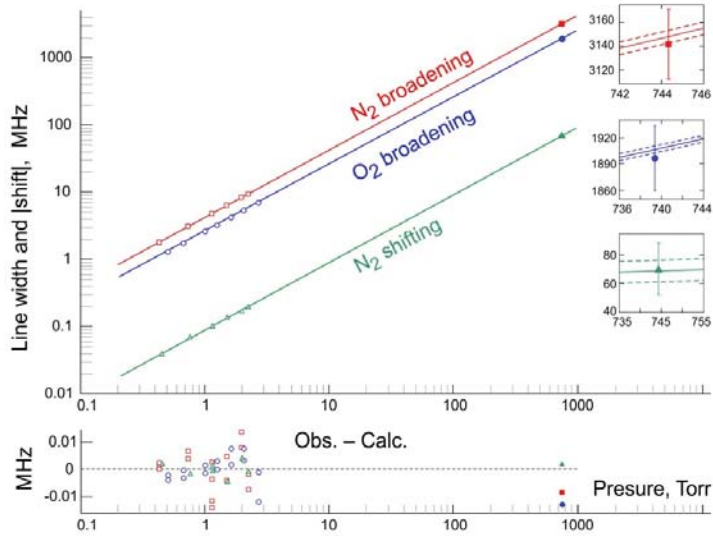

Fig. 3.17. Broadening and shifting modulus of 183-GHz line (line frequency shifting by nitrogen pressure is negative) by pressure of major atmospheric gases at room temperature by the results of measurements with the spectrometer complex. Adopted from Tretyakov [2016].

3.1.2. Oxygen spectrum

A molecule of oxygen (hereafter we speak about the main isotopologue of molecular oxygen $^{16}O_2$, the natural abundance of which is more than 99.5 %) is the second after water absorber of millimetre and submillimetre radiation in the Earth's atmosphere. Oxygen is a linear molecule composed of two identical atoms. By virtue of the symmetric structure, its electric dipole moment is equal to zero. The nuclear spin of each atom is also equal to zero. The outer electron shell of the oxygen atom is composed of six electrons, four of which are combined into two pairs (paired electrons), and the other two are free. Paired electrons differ from each other only by the spin direction. They form a stable system free of intrinsic magnetic moment and spin. There is a surprising and controversial fact that has not yet found a simple explanation (see the theory of molecular orbitals, for example, Barrett, 2002), when two oxygen atoms are combined into a molecule, on the one hand, a double covalent bond is formed with the energy approximately equal to the energy of pairing of two pairs of free electrons and, on the other hand, the oxygen molecule has magnetic moment and molecular spin as if it had two unpaired electrons. In molecules with an even total number of electrons, they are paired so that their total orbital moment and total spin are equal to zero,this is not the case with the oxygen molecule. Two electrons remain in a specific position. In the ground electron state of the molecule (usually designated as $^3\Sigma$), the total orbital moment of these electrons is zero, but their spins are parallel. The molecule has a total molecular spin S, characterised by quantum number equal to unity. As a result, the molecule has a magnetic dipole moment, which enables its interaction with electromagnetic radiation and ensures a rotational spectrum. Maxwell's equations are symmetric with respect to the electric and magnetic components of the field. However, the electric dipole unit (Debye) corresponds to approximately 100 units of magnetic dipole (*Bohr magneton*). Therefore, the efficiency of magnetic dipole interaction is small compared to that of the electric dipole. The magnetic dipole moment of oxygen is equal to two Bohr magnetons. Therefore, the intensity of oxygen lines is much less than the intensity of water vapour lines. By virtue of the fundamental principles of quantum mechanics associated with the identity of equivalent nuclei, there are no energy levels with an even quantum number characterising the rotational state of a molecule.

The vector of the total angular momentum of molecule **J** is composed of the orbital moment of molecule **N** characterising its rotation as a whole and spin **S**. As the value of the spin is equal to unity, according to the

angular momentum sum rule in quantum mechanics, only three combinations are possible: when the spin and the orbital moment are unidirectional (i), have opposite directions (ii), and are orthogonal (iii). The quantum number of the total angular momentum for each **N** can take on three values: $J = N + 1$, $J = N - 1$, and $J = N$. This means that each rotational state consists of three levels with different spin projections, i.e., the spin-rotational interaction in the O_2 molecule splits each rotational level of the molecule into three sublevels called *fine structure levels* (fig. 3.18).

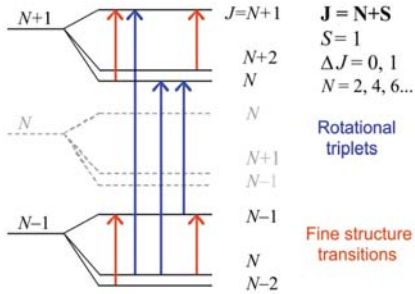

Fig. 3.18. A fragment of a diagram of rotational levels of an oxygen molecule. The symmetry-forbidden rotational level (even N) is shown by dashed lines. The arrows indicate the transitions allowed by the selection rule on absorption of a radiation quantum.

The selection rule for magnetic dipole transitions $\Delta J = 0, 1$ specifies two types of allowed transitions. These are transitions with a change in the rotational state (rotational transitions with a change in N) and transitions between the fine structure levels inside the rotational state (fine structure transitions without changes in N) corresponding to spin reorientation. The rotational transitions form characteristic triplets in the oxygen spectrum. The energies of purely rotational levels ($J = N$) and the corresponding transition frequencies can be calculated using the expressions (1.23) and (1.24). The distance between the lines in the triplets corresponds to the magnitude of fine splitting of the rotational levels, that is about 60 GHz. The first two triplets corresponding to the $N=3\leftarrow1$ and $N=5\leftarrow3$ transitions with centres near 420 and 780 GHz are seen in fig. 3.1. The magnitude of the fine level splitting weakly depends on the rotational state; therefore, all fine structure transitions have frequencies within the 5-mm wavelength range. The corresponding spectral lines at atmospheric pressure merge into a wide band centred near 60 GHz (fig. 3.1). The

exception is the line of the lowest transition $J=1\leftarrow 0$, $N=1$ whose frequency is approximately twice as large (118.75 GHz). A theoretical description of the magnitude of rotational levels splitting and expressions for calculating the frequencies of the fine structure lines in the oxygen spectrum can be found in Miller [1953]. The current, most accurate values of the rotational constants and the fine structure constants of the $^{16}O_2$ molecule are available from works by Drouin [2010], Miller [2012], and Yu [2014].

Among the fine structure transitions we can distinguish two series (sometimes called two *branches*) of transitions. Some of them are directed from the lower to the upper level of the fine structure, and the others from the middle to the upper level (fig. 3.18). Formally, they are distinguished by the sign of the change in the quantum number J: the transitions resulting in the total angular momentum decrease ($J\leftarrow J+1$, $\Delta N=0$ or $J'\leftarrow J=N\leftarrow N+1$) are designated as N^+, and the ones accompanied by an increase of the total angular momentum ($J\leftarrow J-1$, $\Delta N=0$ or $J'\leftarrow J=N\leftarrow N-1$) as N^-, respectively. The 60-GHz oxygen band in atmospheric air at several pressures, as well as the positions and relative intensities of the N^+- and N^--branches of the lines are depicted in fig. 3.19.

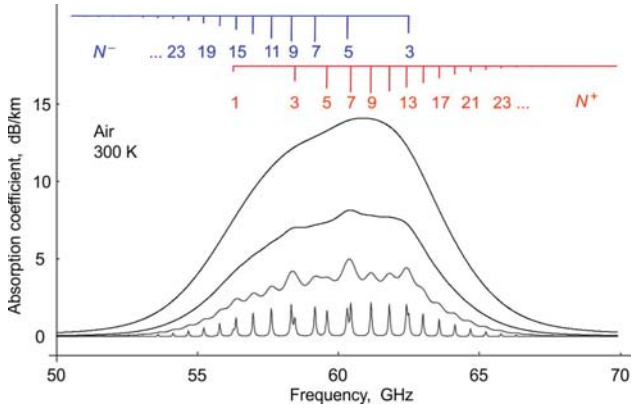

Fig. 3.19. 60-GHz oxygen band in atmospheric air at room temperature and pressures of 20, 200, 400 and 760 Torr (bottom-up) by MPM calculations. The vertical bars on top indicate the positions and relative intensities of the fine structure lines forming the band.

When discussing the oxygen spectrum, it should be taken into consideration that the matrix elements of the dipole moment (1.34) corresponding to the transition from the initial state to the same state

$\Delta N = 0$, $\Delta J = 0$ are nonzero for the magnetic dipole transitions. These are the so-called *non-resonant transitions*. As the molecule does not change its state, the centre frequency is strictly zero (that is why these transitions are sometimes called 'zero transitions')[12]. However, collisional interaction of molecules results in an uncertain energy of their states. Transitions with a nonzero change in energy meeting the selection rule $\Delta N = 0$, $\Delta J = 0$ are quite possible within this uncertainty. The non-resonant transition is absolutely similar to the resonant transition between two different energy levels, the energy uncertainty of which is due to collisions, and its profile is also described by the Van Vleck–Weisskopf profile. But in view of the zero-centre frequency of such a resonant line, its profile, even at small frequency detuning from 'resonance', degenerates into constant frequency-independent absorption. It has a monomolecular nature and should not be confused with the non-resonant absorption associated with nonideal gas (section 1.3). This absorption is called 'Debye' in honour of Peter Debye who, in fact, predicted this effect when analysing the dispersion properties of a polar liquid:

$$\alpha_D(\nu, p, T) = \frac{8\pi^2 n \mu^2}{3kTc} \frac{\gamma_D p}{\nu^2 + (\gamma_D p)^2}, \qquad (3.10)$$

where γ_D is actually the coefficient of collisional broadening of the absorption line at zero frequency (cf. (1.44) and (1.99)). The classical interpretation of the Debye absorption in oxygen was proposed by Van Vleck [1947]. The magnetic dipole moment caused by the motion of the electrons stipulating molecular spin is not so rigidly coupled with the molecule's frame as the electric dipole moment of polar molecules. Molecular collisions give rise to changes in the mutual orientation of the vectors of the orbital angular momentum **N** and spin vector **S**. The energy absorbed during non-resonant transitions is used to restore their original mutual orientation. In states with orthogonal arrangement of vectors **N** and **S** ($J = N$), the spin vector has more freedom due to the possibility of precession around **N**. Therefore, the transitions in the states with parallel **N** and **S** ($J = N \pm 1$), when more energy is needed to restore the collisional perturbation, make the greatest contribution to the non-resonant absorption. The intensities of non-resonant transitions are four to five orders of magnitude lower than the intensities of rotational transitions and

[12] The transition frequency enters line intensity as a multiplier. Therefore, the 'artificial frequencies' close to zero included in the spectroscopic databases for designation of the respective lines are used for calculating the intensities of non-resonant transitions.

of fine structure transitions; nevertheless, their contribution is noticeable in the experimentally observed oxygen absorption spectra.

There is still another feature in the spectrum of oxygen molecules that should be taken into account. All lines of the oxygen fine structure are not isolated, there is strong collisional coupling (interference, mixing or spectral exchange) between the lines (section 1.2.2). In the oxygen molecule, spin is weakly coupled with orbital moment. The spin vector precesses around the vector of angular momentum. The precession frequency corresponds to the magnitude of the fine level splitting. Collisions instantly (in a time much shorter than the precession period) change the orbital angular momentum of the molecule, whereas the spin cannot change just as quickly. A change in the rotational state of a molecule on collision leads only to an instantaneous change of the spin quantisation axis, which in this case coincides with the vector of the orbital moment, while the spin vector continues its motion with little or no change (cf. switching of a two-frequency oscillator in section 1.2.2 keeping in mind that the dipole monent interacting with radiation is caused by the molecular spin). The profiles of all the lines of oxygen fine structure overlap so that, at atmospheric pressure, they all merge into a wide structureless absorption band. The transitions between rotational levels, as well as the transitions between the levels of the fine structure, are collision-allowed. Thus, all the conditions for the collision coupling effect to occur are met.

A level diagram demonstrating collisional coupling of a series of N^+- and $(N+2)^-$-lines of fine structure is shown in fig. 3.20 (cf. fig. 1.13).

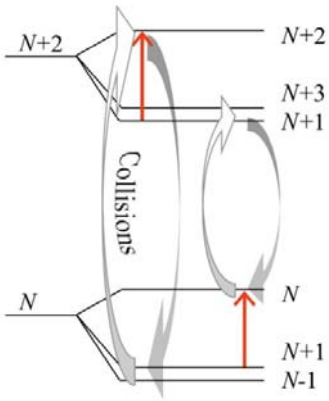

Fig. 3.20. Diagram of collisional coupling of a pair of transitions of the oxygen molecule fine structure. The allowed radiative and collisional transitions participating in spectral exchange are shown by arrows.

The diagram was constructed on the basis of the fact that the predominant transitions on collisions are the ones satisfying the selection

rules for radiative transitions, i.e., in most cases during collisions the molecule either passes to the neighbour rotational state or remains in the original state. It is known that even in polar molecules the collisional transitions with $\Delta J = 2, 3...$ are also allowed, although with a smaller probability. Due to the weak coupling of spin with orbital moment in the oxygen molecule, collisional transitions from any and to any sublevel of the fine structure within the nearest rotational states with $\Delta J = 2, 3, 4...$ are much more probable than similar collisional transitions of polar molecules. Based on this, one can easily draw a diagram similar to that in fig. 3.20 for the coupling of the three remaining pairs ($(N)^+$ and $(N+2)^+$; $(N)^-$ and $(N+2)^-$; $(N)^-$ and $(N+2)^+$) of fine-structure radiative transitions belonging to two neighbouring rotational states shown in fig. 3.18. The diagram of the collisional coupling between the N^+ and N^- transitions within the same rotational state is even simpler (fig. 3.21). Thus, all the lines of the oxygen fine structure, including a single line near 118.75 GHz are collisionally coupled. The higher the probability of the corresponding collisional transitions, the larger the relative number of gas molecules capable of making such transitions (that is, the larger the statistical weight of the corresponding levels), and the smaller the difference between the centre frequencies of the lines, the larger the coupling. Note that the collisional coupling affects the shape of the lines not only of ordinary resonant, but also of 'zero' transitions.

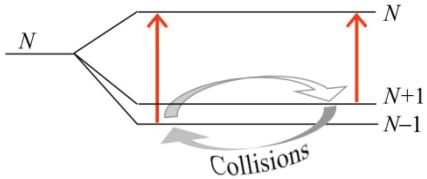

Fig. 3.21. Diagram of collisional coupling of the transitions of fine oxygen structure within one rotational state.

The result of the collisional coupling of a group of lines is generally described by the so-called *collisional relaxation matrix* (*collisional interaction matrix*). The size of the matrix is determined by the number of lines under consideration. Matrix rows and columns are numbered in accordance with the numbers of lines in the group. The elements of the matrix characterise coupling of the corresponding lines with each other. Their magnitude for each particular pair of lines is determined by the probability of the corresponding collisional transitions that provide line coupling (diagrams in figs. 3.20, 3.21, and their analogues). The diagonal

elements of the matrix, formally corresponding to the interaction of a line 'with itself', provide the collisional widths of the respective lines. The shape of the total absorption of the group of lines is numerically calculated through the elements of the relaxation matrix. If the lines of the group do not interact with each other, the matrix is diagonal, and the absorption profile is the sum of profiles of the individual lines. In the case of a weak interaction (only elements adjacent to the diagonal elements of the matrix are significant), one can obtain an analytical expression for the line profile and, as before, calculate the absorption band profile as the sum of the contributions of individual lines [Rosenkranz, 1975], taking into account only the main manifestation of the interference linear with respect to pressure (see (1.89), (1.92) and (1.100)):

$$\alpha^{band}(\nu)=\sum_i \frac{\alpha_{abi}}{\pi}\left(\frac{\nu}{\nu_{0i}}\right)^2\left(\frac{\Delta\nu_{ci}+Y_i\cdot(\nu-\nu_{0i})}{(\nu-\nu_{0i})^2+\Delta\nu_{ci}{}^2}+\frac{\Delta\nu_{ci}-Y_i\cdot(\nu+\nu_{0i})}{(\nu+\nu_{0i})^2+\Delta\nu_{ci}{}^2}\right). \quad (3.11)$$

Or, taking into consideration the second-order interference effects with respect to pressure [Smith, 1981]:

$$\alpha^{band}(\nu)=\sum_i \frac{\alpha_{abi}}{\pi}\left(\frac{\nu}{\nu_{0i}}\right)^2\left(\frac{\Delta\nu_{ci}\cdot(1+G_i)+Y_i\cdot(\nu-\nu_{0i}-D_i)}{(\nu-\nu_{0i}-D_i)^2+\Delta\nu_{ci}{}^2}+\frac{\Delta\nu_{ci}\cdot(1+G_i)-Y_i\cdot(\nu+\nu_{0i}-D_i)}{(\nu+\nu_{0i}+D_i)^2+\Delta\nu_{ci}{}^2}\right),$$

$$D=d\cdot p^2, \qquad G=g\cdot p^2, \quad (3.12)$$

where d and g are the second-order interference coefficients taking into account the centre frequency shift squared in pressure and line intensity variation.

If the interaction increases (for example, with an increase in gas pressure), the interaction matrix is filled up — all the elements distant from the diagonal become significant. Under these conditions, the resulting absorption profile can be calculated only numerically using the matrix elements.

The contributions of the line interference effect of the first- and second-order with respect to pressure to the profile of the 60-GHz band at atmospheric pressure and room temperature, corresponding to the expressions (3.11) and (3.12), are shown in fig. 3.22. The zero-order contribution corresponds to the sum of the line profiles neglecting the effect. The first-order correction corresponds to the difference between the absorption calculated by the formula (3.11) and the zero-order contribution. The second-order correction corresponds to the difference of the absorptions calculated by the formulas (3.11) and (3.12).

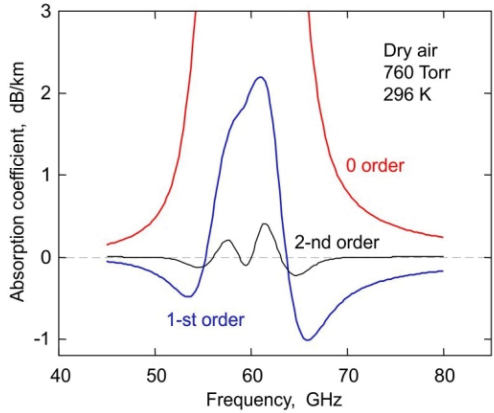

Fig. 3.22. The contributions of the collisional coupling of fine structure lines of oxygen of the first (long dashed curves) and second (solid curve) order in pressure to the absorption profile of 60-GHz band at atmospheric pressure and room temperature calculated using MPM. Adopted from Makarov [2020].

It was found experimentally that the temperature dependence of the parameters of line interference $Y(\mathrm{T})$ differs from the corresponding temperature dependence of the parameters of line broadening $\Delta\nu_c(T)$. This is indirect evidence of the fact that the line interference effect in the 60-GHz band is caused by collisional transitions of molecules not only to neighbouring, but also to other rotational levels. In either case, the temperature dependence of the collision frequency can be approximated by the simplest power law $(T_0/T)^{n_\gamma}$ (section 1.2.4). But the interference parameters may have an additional T-dependence as the probabilities of collisional transitions are related to the difference in the level populations, which is determined by the Boltzmann distribution $\sim \exp(\Delta E/kT)$. If the line interference is determined by the collisional transitions only to the neighbouring rotational levels, the contribution of the additional T-dependence is negligible, since $\Delta E << kT$. In other cases, it is necessary to take into account at least the next term of the power series expansion $(1 + \Delta E/kT)$. Therefore, for the T-dependence of the interference coefficients, the following expression is obtained

$$y(T) = \left(\frac{T_0}{T}\right)^{n_\gamma}\left(y_0 + y_1\frac{T_0}{T}\right) \qquad (3.13)$$

or more convenient for interpretation

$$y(T) = \left(\frac{T_0}{T}\right)^{n_\gamma} \left(y_0 + y_1\left(\frac{T_0}{T} - 1\right)\right), \tag{3.14}$$

where y_0 is the parameter of interference at temperature T_0, and y_1 is responsible for the additional T-dependence of the parameter. Analogous expressions for the T-dependence of the second-order interference parameters (d or g) differ from (3.13) and (3.14) only by $2n_\gamma$ instead of n_γ. This difference arises because the first-order coefficients are proportional to the sum of the terms which include individual elements of the collisional interaction matrix, each of which has T-dependence of collision frequency, and for the second-order coefficients the sum is comprised of the product of two elements. The expressions (3.13) and (3.14) are used for modelling absorption instead of their analogue (1.96), and the values of the coefficients y_0 and y_1 are found experimentally.

The stages of advancing the theoretical modelling of the 60-GHz absorption band can be traced through the works of Baranger [1958], Kolb [1958], Fano [1963], Ben-Reuven [1966], Gordon [1967], Rosenkranz [1975], [1988], Smith [1981], Makarov [2013], and Makarov [2020], and references therein.

The poorly studied effect of collisional coupling of lines, strongly manifested under ordinary atmospheric conditions, makes the 60-GHz band a unique spectroscopic object of study, as its manifestation in the spectra of other molecules can be observed mainly in the bands of vibrational-rotational spectra corresponding to the transitions with $\Delta J = 0$ (*Q-branches*) at ultrahigh (up to hundreds of atmospheres) pressures (see, for example, Buldyreva [2013]).

An important factor complicating experimental studies of the oxygen spectrum is that, due to the permanent magnetic dipole moment, an oxygen molecule is a *paramagnetic*, i.e., it is subject to the influence of magnetic field. This means that under normal conditions, as a result of the interaction with the Earth's permanent magnetic field, each J-level of the fine structure splits into $2J + 1$ sublevels (*the Zeeman effect*). The spectral lines will have the same splitting. Its magnitude for the lines corresponding to small N is of the order of several megahertz per Gauss [Hill, 1954]. Consequently, at pressures close to the atmospheric one, the homogeneous collisional broadening far exceeds the inhomogeneous broadening due to the Zeeman splitting, and the latter does not affect the shape of the observed spectrum.

In laboratory studies of collisional parameters of oxygen lines at low pressures, the Zeeman splitting can become a source of significant systematic errors if the gas cell of the spectrometer is not sufficiently well isolated from external magnetic fields (or they are not completely compensated by artificially created magnetic fields), and/or its elements retain residual magnetisation. For small magnetic fields, the splitting manifests itself and can be taken into account as an additional broadening of spectral lines (see, for example, Liebe [1993] and references therein).

When oxygen lines are observed in the atmosphere, the influence of the Earth's magnetic field will manifest itself at altitudes of about 40 km and higher (see, for example, Hartmann [1994]). Studies of the oxygen spectrum are also encouraged by the need for its accurate modelling for atmospheric spectroscopy applications, primarily for remote sensing. Oxygen spectral lines, like water vapour lines, are major diagnostic lines. Their main role in atmospheric sounding is to restore the vertical profile of temperature or pressure (depending on which of these parameters is considered to be known *a priori*). The potential of using oxygen lines in this way was noticed at the very beginning of the 'space age' in Meeks [1963].

At present, practically none of the atmospheric sounding satellites work without an 'oxygen thermometer' (radiometers on microwave oxygen lines) and many ground-based instruments use them as well (see, for example, Pardo [1998], Leslie [2004], Waters [2006], Cadeddu [2007], Shvetsov [2012], and Kulikov [2015]). One can get acquainted with modern remote 'oxygen gauges' of surface atmospheric pressure, for example, in Lawrence [2011] and references cited there.

Experimental studies

60-GHz band

Transition frequencies. Studies of the microwave spectrum of oxygen have a long history starting from the first half of the 20th century. The resonant absorption of radiation with a wavelength of about 0.5 cm, corresponding to the magnitude of fine splitting of the rotational levels of the oxygen molecule, was predicted theoretically [Van Vleck, 1934, 1947; Schlapp, 1937] on the basis of observations of the absorption bands formed as a result of the transitions between the lower electron states of atmospheric oxygen molecules in the sunlight [Dieke, 1927]. The first experimental confirmation of the fact that oxygen absorbs in the predicted range (48–72 GHz) and that the absorption coefficient (up to 76 dB/km at

the maximum in pure oxygen) approximately corresponds to the prediction and the average collisional line broadening is 0.8–2 MHz/Torr was obtained using a classical video spectrometer [Beringer, 1946]. These measurements were shortly confirmed by the field measurements of atmospheric absorption (measurement accuracy was 10–20 %) performed by the method of path length variation on the track along the surface 0.12–2.2 km long [Lamont, 1948]. The results of the first high-precision measurements of the frequencies of 25 lines (up to $N = 25$) from the fine structure spectrum at a low pressure with a Zeeman-modulated[13] video spectrometer can be found in Burkhalter [1950]. These data were consistently supplemented and refined by many researchers [Gokhale, 1951; Mizushima, 1954; Zimmerrer, 1961; West, 1966; Endo, 1982; Tretyakov, 2005]. The widest coverage of the rotational state of the molecule (up to N=39) was made in Endo [1982], where a Zeeman-modulated video spectrometer was also used. The smallest uncertainty in determining the frequencies (on the order of several kilohertz) of the most intense band lines with N values from 1 to 27 was achieved using the RAD spectrometer [Tretyakov, 2005]. The performed measurements showed no noticeable shifts in the line frequencies in the pressure of atmospheric gases. Through the obtained experimental data, a set of effective constants of fine splitting was determined, which can be used for calculating the positions of all significant lines of the fine structure of an oxygen molecule with an uncertainty of ~1 kHz, and for predicting the frequencies of lines that have not been measured to as high a degree of accuracy. The frequencies of the most significant lines found on the basis of these constants as well as the calculated values of the 60-GHz line intensities are presented in Appendix A7 (Table A7.1). The intensities are taken from the HITRAN database [Gordon, 2017]. Their uncertainty estimated by the spectroscopists is about 1 %.

Broadening coefficients. The history of measurements and consecutive refinements of the collisional broadening coefficients of individual 60-GHz band lines by the pressure of pure oxygen and other atmospheric gases can be traced through the works of Burkhalter [1950], Gokhale [1951], Anderson [1952], Hill [1954], Tinkham [1955], Zimmerrer [1961], Stafford [1963], Liebe [1977], Golubiatnikov [2003-1, -2], Tretyakov [2005], and Koshelev [2015, 2016, 2021-1]. The results of studying the

[13] The Zeeman modulation proved to be handy, not only because it enabled synchronous detection of a weak absorption signal at the modulation frequency, but also because the direct current component flowing through the modulator winding allowed, with a properly chosen spatial orientation of the gas cell, compensating the influence of the Earth's magnetic field.

temperature dependence of line broadening parameters can be found in Hill [1954], Tinkham [1955], Liebe [1975], and Koshelev [2016].

Line intensity gradually decreases with increasing rotational quantum number N (fig. 3.19), as a result of a decrease in the populations of the corresponding levels (section 1.2.1). The collisional broadening parameter also smoothly depends on the rotational state of the molecule. The most pronounced is the overall decrease of the parameter with increasing rotational excitation. This can be explained by a purely classical effect associated with the inertia of a top: the faster the rotation, the more stable its state, and the stronger the impact required to change the state of the top. The time of collisional relaxation of highly excited rotational states is longer and, hence, the broadening parameter is smaller.

Another well-known, more subtle inverse effect manifests itself against the background of a general decrease of line broadening with increasing rotational excitation. It is connected with the fact that the collisional interaction of the molecules rotating at the same speeds is closer to the static one and, therefore, is more efficient (*resonant rotational interaction*). The effect is most pronounced in pure gases at resonant interaction of molecules in the same states. By virtue of the uncertainty principle, a short collision time leads to uncertainty of the rotational state and, hence, resonant interaction can occur between the molecules that are not only in the same states, but also in states with similar rotational energy. The number of molecules with which the absorber molecules can interact resonantly depends on the rotational state of the absorber. The significant factors are the distance to the nearest levels and their populations. Since the energy difference between the neighbouring rotational states grows quadratically, it is obvious that the rotational resonance will be the strongest at small values of the rotational quantum number, when its increase is accompanied by an increase in the number of states resonant to it and in their population. Both these effects are common to most atmospheric molecules. The smoothness of the dependence of line broadening on rotational state allows for using empirical approximations of experimentally obtained data. This allows the experimental data on the broadening parameters to be extrapolated to the unexplored region of rotational quantum numbers. Generally, an expression of the form

$$\gamma(m) = \frac{\sum_{i=0}^{4} a_i m^i}{1 + \sum_{i=0}^{4} b_i m^i} \tag{3.15}$$

can be used as an approximating function. Here, m is the rotational quantum number, and a and b are variable parameters. For the broadening parameters of the 60-GHz oxygen band, lines one can also use a simpler version of (3.15):

$$\gamma(N) = a_1 + \frac{a_2}{1 + a_3 N + a_4 N^2 + a_5 N^4}. \qquad (3.16)$$

The coefficients of the function (3.16) used for the calculation of the parameters of fine structure line broadening by the pressure of the most common atmospheric gases and air were found in the works of Koshelev [2015, 2016, 2021-1] based on the analysis of the results of high-accuracy measurements (fig. 3.23). The values of the coefficients reproducing experimental data on line broadening from the works of Tretyakov [2005] and Koshelev [2015, 2016] (in MHz/Torr at 296 K) are listed in Table 3.4. The calculation error is ~ 1 % up to N = 19 and ~ 2 % up to N = 25. Calculations for $N > 25$ will actually be an extrapolation of experimental data, and their error will grow uncontrollably with increasing N. These studies have shown, in particular, that the line broadening coefficients of N^+- and N^- branches coincide within the measurement error (~ 1 %). This means that the cross section of the collisional interaction of O_2 molecules is determined mainly by their rotational state and does not depend on the orientation of the molecular spin. However, it was noted in Koshelev [2021-1] that N^- lines are systematically wider than N^+ lines, which should be taken into account in band-shape modelling for better accuracy.

Table 3.4. The coefficients of the empirical function (3.16) for the calculation of the parameters of collisional broadening of the fine structure lines of an oxygen molecule in different rotational states.

Coefficient	$\gamma_{O_2}(296)$	$\gamma_{N_2}(296)$	$\gamma_w(296)$	$\gamma_{air}(296)$*
a_1	1.263	0.960	1.140	1.132
a_2	1.129	1.471	1.528	1.348
a_3	0.186	0.141	0.101	0.188
a_4	$-7.1\cdot10^{-3}$	$-5.9\cdot10^{-3}$	$-4.78\cdot10^{-3}$	$-7.7\cdot10^{-3}$
a_5	$1.249\cdot10^{-5}$	$1.170\cdot10^{-5}$	$7.4\cdot10^{-5}$	$1.66\cdot10^{-5}$

* corresponds to the 79/21 mixture of N_2 and O_2.

It was revealed in the above experiments that the rotational state of molecules does not notably influence the temperature dependence of broadening, and the expression (1.96) with the same index of temperature dependence n_a = 0.754(12) can be used for modelling radiation absorption

in the atmosphere for all lines of the oxygen fine structure. In addition, the estimates of the shift of the line centre frequency confirmed that the magnitude of the linear in pressure shift did not exceed ±15 kHz/Torr for all lines.

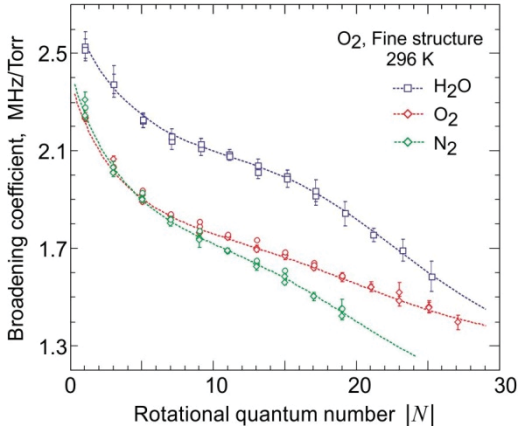

Fig. 3.23. The results of measuring collisional broadening of fine structure oxygen lines in pressure of the major atmospheric gases (circles – data from the work of Tretyakov [2005], rhombs – data from Koshelev [2015], squares – data from Koshelev [2016]) and their approximations by the function (3.16) with the coefficients from Table 3.4 (curves).

Parameters of collisional coupling. All the above-mentioned parameters of the O_2 fine structure lines were obtained at low (about several Torr) gas pressures when the collisional coupling did not manifest itself and the lines could be considered to be isolated.

The resonator spectroscopy for studying the 60-GHz band was first used at the Columbia University, USA with an 'echo box' [Artman, 1954] as a non-resonant resonator spectrometer similar to the one which allowed for obtaining the first high-precision data about the 22-GHz line of H_2O [Becker, 1946] (section 3.1.1). The feasibility of measuring the absorption in a wide range from several Torrs to the atmospheric pressure was demonstrated, which made it possible to record the absorption profile and determine the parameters of both individual lines and the entire band (fig. 3.24).

Comparison of the data obtained in [Artman, 1954] with recent data shows a good general agreement at high pressures but indicates possible systematic error in the investigation of individual lines. The authors

described, within the measurement error, the total absorption in the band as the sum of the Van Vleck–Weisskopf profiles for individual lines. They did not observe manifestations of the line interference effect, apparently due to the lack of accuracy in measuring the collisional broadening parameters.

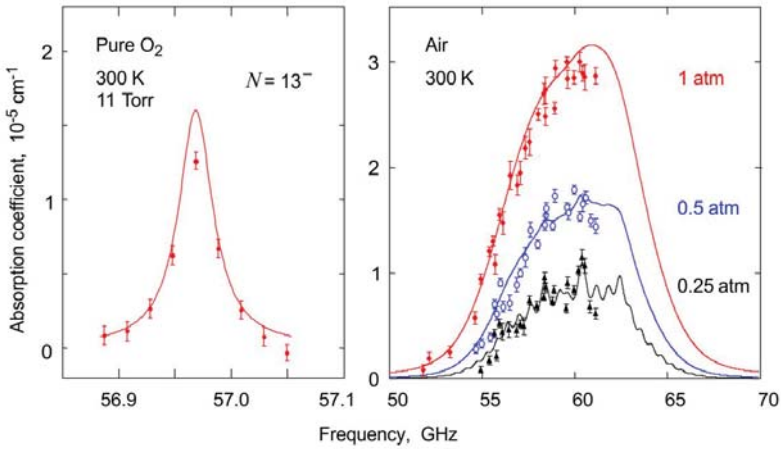

Fig. 3.24. The absorption measured with the 'echo-box' (symbols) [Artman, 1954] in pure oxygen near a single line (left) and in air within the 60-GHz band (right). Solid lines – the result of calculations using the present day MPM version.

The problem was revealed by radar operators in the 1960s (see Meeks [1963], Zhevakin [1966], Carter [1968], Reber [1972] and references therein) during the studies of atmospheric thermal emission and of the absorption by the atmosphere of 60-GHz components of the spectrum of solar radiation. Despite the instability and uncertainty of the thermodynamic conditions of the studied gas typical for field measurements, the possibility of analysing data obtained on very long paths ensured a high enough measurement accuracy. The difference of radiometric measurements from the model absorption calculated as a sum of profiles of individual band lines was systematically beyond the limits of measurement errors. The measured data indicated that the coefficient of collisional broadening of the O_2 fine structure lines (or the effective cross section of the collisional interaction of molecules) is pressure-dependent rather than a constant value which, in non-pressurised gases, is determined only by the properties of molecules (section 1.2.2). To achieve agreement with the model, the line broadening had to be reduced several times, starting from

the pressures at which the band lines begin to overlap (more than 10-20 Torr). This ‘phenomenon’ gave an impetus to theoretical studies. In 1967 Gordon [1967] proposed a theoretically substantiated explanation, which showed that it was not the strange behaviour of the collisional broadening but the previously unknown effect of collisional coupling of lines. The practical implementation of this theory to the spectrum of the fine structure of oxygen and the derivation of an analytical function convenient for modelling the shape of the resonant line (3.11), taking into account the effect of collisional coupling of the lines, were realised in 1975 [Rosenkranz, 1975].

Experimental confirmation of the developed theory of collisional coupling of oxygen fine structure lines was provided by the comprehensive study [Liebe, 1977] performed at the Institute of Telecommunications (USA) with a dispersive resonator spectrometer [Liebe, 1975]. The principal investigator of the research was Hans Liebe, an expert in practical modelling of the millimetre radiation propagation in the atmosphere and the creator of the MPM [Liebe, 1989] also responsible for its further development and refinement. The work of Liebe [1977] was actually the first systematic study of the parameters of individual band lines at pressures up to 20 Torr and of the absorption profile of the entire band at pressures up to the atmospheric one. The results clearly show that for quantitative measurements of the O_2 fine structure spectrum, the used resonator spectrometer had significant advantages over any other technique known by that time. It allowed, for the first time, the measuring of the refractive index for 11 major atmospheric gases and determining the dispersive characteristic of atmospheric air in the 40–140 GHz range. The high sensitivity of the spectrometer to absorption (the minimum detectable changes in the absorption coefficient was ±0.05 dB/km) made it possible to measure the broadening parameters and the intensities of the most intense lines of the 60-GHz band with a relative accuracy of 1–4 %. The measurements of line intensities confirmed the accuracy of the theoretical calculations [Van Vleck, 1947]. The centre frequencies of the lines measured with an uncertainty of 10 kHz confirmed and, for several lines, improved the results of the previous studies. A smooth dependence of the collisional self-broadening parameter of the oxygen fine structure lines on the rotational state of molecules was demonstrated for the first time, and the obtained values of the parameters are still in excellent agreement with present-day data. In accordance with the theoretical concepts of that time, the relative difference of the parameters of band line broadening by air pressure from self-broadening (the efficiency of broadening by air) was considered to be identical for all lines. The $\gamma_{air}/\gamma_{O2} = 0.96$ ratio,

experimentally determined in the work of Liebe [1975] for the line $N = 9^+$, is very close (according to modern data) to the value of this parameter for the most intense band lines (fig. 3.25).

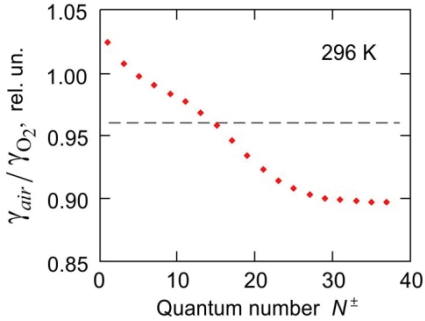

Fig. 3.25. The efficiency of air pressure broadening for the 60-GHz band lines. Points – current data (Table 3.4). Dashed line – experimentally determined value of 0.96 for $N = 9^+$ line [Liebe, 1975].

The temperature dependence of the air pressure broadening of all considered lines of the band was estimated by the results of studying the broadening of the $N = 9^+$ line in pure oxygen at four temperatures ranging from 252 K to 325 K. Fitting the expression (1.96) to these data with allowance for the measurement error gives n_γ = 0.84(4), which almost coincides within the uncertainty limits of the later measured value of 0.784(11) [Koshelev, 2016]. However, in the work of Liebe [1977], the value of n_γ was rounded up to 0.9, that was used in the early versions of MPM.

Analysis of the results of absorption measurements within the band profile in air at pressures of 100–800 Torr (the data in fig. 3.26 are given for 600 Torr) were used to determine, for the first time, values of the coefficients y_i (see (3.11), (1.92)) characterising the collisional coupling of oxygen lines to the first approximation (linear in pressure), which enabled adequate simulation of the atmospheric absorption in this spectral region.

The same experimental data were used in Rosenkranz [1988] for obtaining more accurate values of collisional coupling coefficients.

Is the first approximation of the shape of collisionally interacting lines (3.11) sufficient for simulating the profile of 60-GHz oxygen band in air, or are there conditions in the Earth's atmosphere for which a more accurate approximation (3.12), taking into account the second-order effects in pressure, is needed?

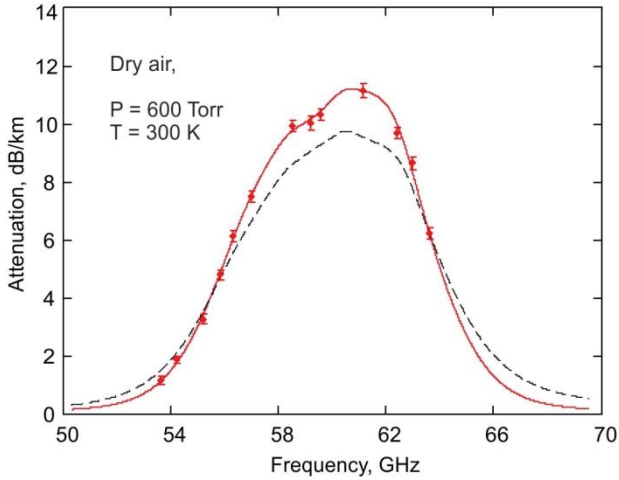

Fig. 3.26. The results of absorption measurements in atmospheric air in the 60-GHz range with a resonator spectrometer [Liebe, 1977] (points). Solid curve – calculation by the current MPM version; dashed curve – model absorption neglecting collisional coupling effect is given for comparison.

To answer this question a targeted study was undertaken at the Jet Propulsion Laboratory, Pasadena, California, USA [Read, 1988] using a specially developed resonator spectrometer. Its cavity length was 3 m, and one of the mirrors partially transmitted probe radiation (about 0.6 % at 60 GHz and 2 % at 120 GHz). The spectrometer sensitivity to changes in absorption was estimated to be ± 1 dB/km. Absorption measurements within the band were performed in pure oxygen at elevated pressures (about 2 atm.) and a low temperature (approximately –11 °C), when the collisional coupling effect was more pronounced than under normal conditions, and the coupling effect increased the absorption in the centre of the band by more than 30 % compared to the sum of profiles of the isolated lines.

The obtained data (fig. 3.27) confirmed that the first-order model [Rosenkranz, 1975] described the absorption observed in the oxygen band with a relative error of 10 % or less at a pressure of 2 atm. and even more precisely at lower pressures.

It is interesting to note that in the three above-mentioned studies of the 60-GHz band using resonator spectrometers (figs. 3.24, 3.26, and 3.27), the obtained experimental data were closer to the real values (i.e., agree

better with a more accurate present-day model) than to the absorption models obtained by the authors on the basis of these data or used for their interpretation.

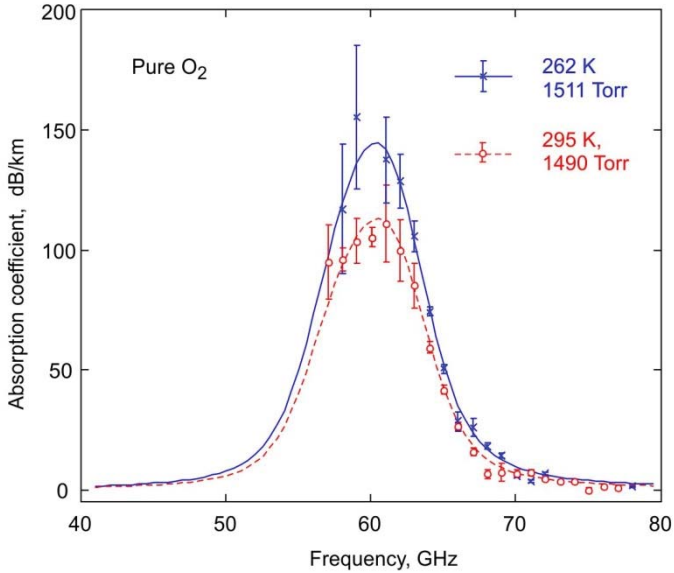

Fig. 3.27. Absorption in pure oxygen by data of the work of Read [1988] (points). The results of the calculations using a modern version of MPM are given for comparison.

The requirement for more accurate simulation of millimetre wave propagation in the atmosphere, raised by the rapidly developing methods of radiolocation and radiometry, led to the need to study the 60-GHz band at a qualitatively new level, including detailed spectral recordings of the absorption profile and their theoretical analysis in a wide range of temperatures and pressures. Such research was started at the Institute of Telecommunications Sciences under the leadership of Hans Liebe. A new resonator spectrometer (see section 2.4.3) having an absorption coefficient sensitivity of ± 0.02 dB/km at radiation power attenuations less than 3 dB/km or less than 2 % at greater attenuations was assembled. More than 5000 values of the radiation absorption coefficient in artificial air (a mixture of oxygen and nitrogen with the 20.45 to 79.55 ratio) were measured using the spectrometer in the 49–67 GHz frequency range with a step of 0.1 GHz. The measurements were carried out at eleven pressures

from 1.3kPa to 101 kPa (corresponding to the altitudes above the Earth's surface from 0 to 30 km with a step of 3 km) and at three temperatures of about 6, 30, and 54 ºC. The scientific report on this work and the experimental data obtained [Liebe, 1991] are available on the website of the Institute of Telecommunications Sciences.

The results corresponding to measurements at a temperature of 6.05 °C and an altitude above the Earth's surface from 0 (pressure of 760 Torr) to 15 km (pressure of 91 Torr) with a step of 3 km are shown by way of example in fig. 3.28, demonstrating an impressive amount and the high quality of the obtained data.

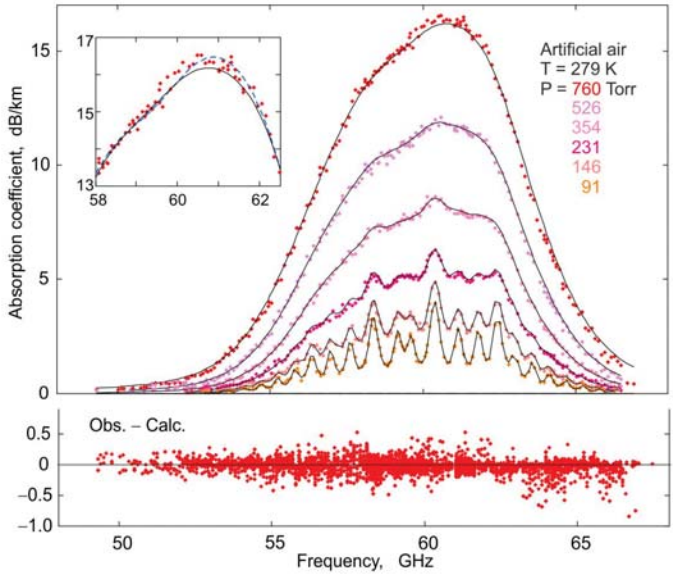

Fig. 3.28. Radiation power attenuation by atmospheric oxygen [Liebe, 1991]. Solid curves – calculation by MPM-92 [Liebe, 1992]. Inset – part of data for the pressure of 760 Torr. Dashed curve in the inset – calculations by the present day MPM version [Makarov, 2020] with allowance for the second-order in pressure interference of the lines. At the bottom – the deviation of the data [Liebe, 1991] from the calculation by MPM-92.

Based on these data, the coefficients of collisional coupling of lines were refined taking into consideration their temperature dependence, and a new version of the model of millimetre wave propagation in the atmosphere MPM-92 was created [Liebe, 1992]. The new model reduced

the standard deviation of experimental points from calculations (solid curves in fig. 3.28) by approximately a factor of two in comparison with the previous version of the MPM-89 model [Liebe, 1989]. Based on the good fit of the model to the obtained data, the authors of the MPM-92 noted that the approximation (3.11) was adequate under the conditions of the experiments. Nevertheless, the found values of the coefficients Y_i at atmospheric pressure were close to the upper limit, which restricted the region of applicability of the simplest (linear in pressure) approximation of the collisional coupling effect. A manifestation of the proximity to this limit is a small (0.2–0.3 dB/km) excess of the experimental points over the model calculations at the band maximum which was observed only at the lowest temperature and maximum pressure (the upper series in fig. 3.28), i.e., under the conditions of the strongest line interference.

The next cycle of experimental studies of the 60-GHz profile of absorption band was associated with the development of the Nizhny Novgorod resonator spectrometer [Krupnov, 1999, 2000] (section 2.4). The much higher sensitivity of the spectrometer as compared to all the earlier analogues promised new data that would contribute to quantitative and qualitative improvement of the description of radiation absorption by the atmosphere in this region of the spectrum.

The first trial experiments on *in situ* measurement of radiation absorption in the atmosphere using an uncovered Fabry-Perot resonator on a laboratory table [Krupnov, 1999, 2000] showed that there may appear to be systematic deviations of the experimental data from the results of the MPM-92 absorption calculations.

The first quantitative measurements of the band profile in pure oxygen and in atmospheric air performed using this spectrometer were presented in Tretyakov [2005]. The measuring resonator of the spectrometer was isolated from the ambient air by a polyethylene film. The spectrometer baseline (corresponding to the resonator losses) was determined experimentally when the resonator was filled with pure nitrogen. The gas sample with the temperature and pressure corresponding to the laboratory conditions was continuously blown through the cavity chamber. The relative humidity of the gas was continuously monitored by means of a high-precision semiconductor sensor (measurement error of 1–2 %). Technically pure oxygen and atmospheric air from a well-ventilated room were used in the study. The influence of small temperature, humidity, and pressure variations during the experiments on the measurement result was taken into account by calculating the corresponding absorption corrections by MPM (3.4).

The measured absorption profile of the band in atmospheric air was, on average, in good agreement with the previous measurements [Liebe, 1991] and with the calculations using the MPM-92 (fig. 3.29, curve *A*). However, the rms spread of the experimental points (~0.05 dB/km) was several times less than in the previous experiments. This revealed systematic deviations of the measurements from the model. The form of the deviations coincided to a great extent with the theoretically predicted [Smith, 1981] form of the correction to the absorption profile associated with the effect of collisional coupling of the band lines of the second-order in pressure (fig. 3.29, curve *C*). This coincidence allowed the researchers to claim the first experimental observation of the manifestation of this effect. However, with a shortfall of data needed for the development of an absorption model that would take into account the second-order effects, they restricted themselves to refining the first-order interference coefficients (fig. 3.29, curve *B*), which proved to be several percent larger for atmospheric air than the corresponding coefficients calculated by the MPM-92. For pure oxygen, the experimental values of *y* coefficients had never been reported before. The obtained values were approximately twice as large as their theoretical predictions made in the work of Smith [1991].

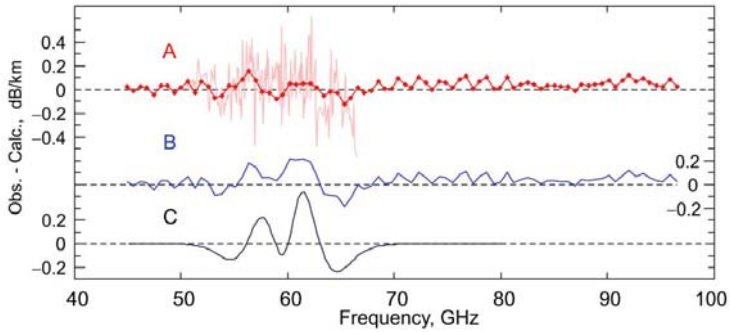

Fig. 3.29. The difference of the results of measuring the profile of 60-GHz band in atmospheric air at 755 Torr and 22 °C [Tretyakov, 2005] (points connected by a line) and the calculations by the MPM-92 and MPM-05 models (*A* and *B* respectively). An analogous difference for the data from Liebe [1991] at 760 Torr and 30 °C (light pink line) is shown in area *A*. The contribution of the second-order line interference effect [Makarov, 2011] to the band profile in the conditions of the experiment is shown by curve *C*.

It is interesting to note that the absorption model MPM-05, obtained in the work of Tretyakov [2005] at atmospheric pressure, gave more

pronounced systematic deviations from the experimental data (fig. 3.29, curve *B*) than its previous version (MPM-92 fig. 3.29, curve *A*). The reason was that the first- and second-order corrections were not completely orthogonal, and the second-order contribution could be partially taken into account by the first-order coefficients, as was the case in the development of the MPM-92.

Thus, it was shown that the second-order interference effect in the 60-GHz band of oxygen at atmospheric pressure cannot be considered negligible; it is a source of systematic errors in the available propagation models.

The experimental data needed for more accurate modelling of the collisional coupling of oxygen lines were obtained in the framework of the study by Makarov [2011]. In this work, the measuring resonator of the Nizhny Novgorod resonator spectrometer was placed in a temperature-controlled chamber, which provided more stable measurement conditions than in the previous experiments and allowed for studies of the spectra of atmospheric gases at atmospheric pressure in the temperature range from –30 to +60 °C. Fifteen recordings of the profile of the 60-GHz band in atmospheric air were obtained (fig. 3.30, *a*).

The outside air slowly blown through the chamber with the measuring resonator was used as the sample in the study. Its absorption coefficient was retrieved from the primary data by the same method as in Tretyakov [2005]. The basic feature directly related to measurements at low temperatures was air dehumidification. To do this, the air was passed through a copper tube cooled by liquid nitrogen. The atmospheric moisture froze in the tube, and the snowflakes flying out were trapped by a dense, dry, cold filter. Despite the careful selection of the degree of cooling and air flow rate, the data analysis showed that the oxygen concentration in the analysed gas varied from 20.5 to 21 % from day to day, which manifested itself in small (~ 0.3 dB/km) changes in the absorption in the centre of the band. This could be caused by the natural variations of the O_2 content in the urban air. However, the influence of the dehumidifier cannot be excluded. The temperature of liquid nitrogen (77.4 K) is slightly lower than the condensation temperature of oxygen (90.2 K), so it could freeze on the walls of the cold pipe. Therefore, the O_2 concentration was considered a variable parameter, the magnitude of which was retrieved spectroscopically on the basis of known band intensity. The best average incidence of the observed band profile with the calculation by the MPM-05 was used as a criterion. Hence, the integrated intensity of the band could not be verified in the experiment; the estimated error of its calculation is about one percent. The measurement error associated with

the uncertainty of O_2 concentration is expected to be about the same. Nevertheless, this circumstance could not influence the result of the study of the line interference effect, as such small changes markedly affect the amplitude of the band but change its shape negligibly.

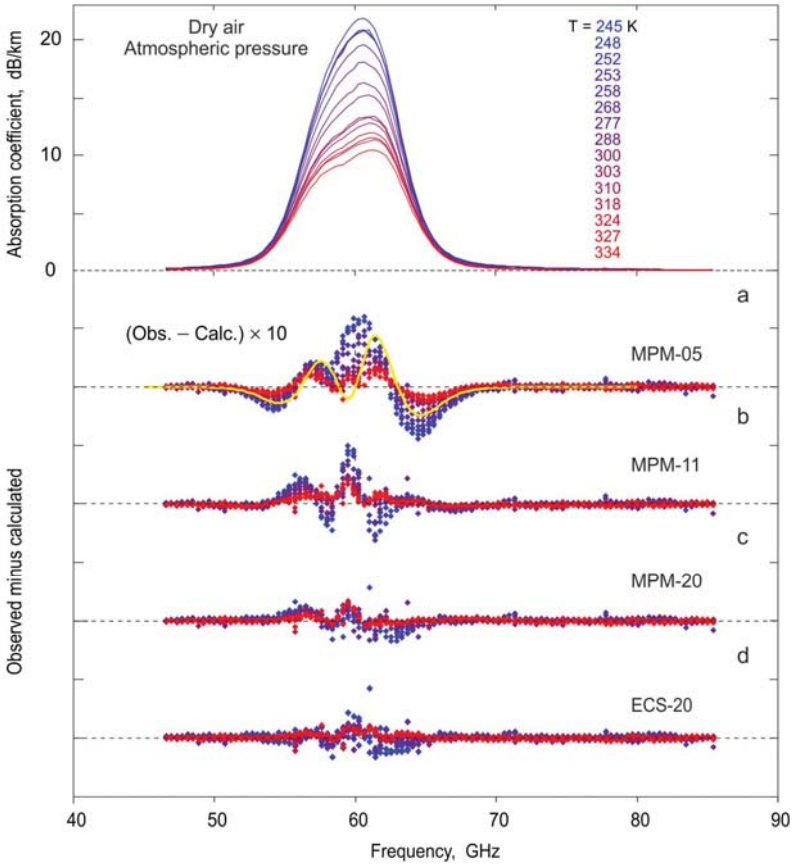

Fig. 3.30. Recordings [Makarov, 2011] of the 60-GHz band in dry air at atmospheric pressure and different temperatures (*a*) and the differences of the measured and calculated spectra using different absorption models (first-order Tretyakov [2005], second-order Makarov [2011], improved second-order and a generalised model Makarov [2020] — *b, c, d*, respectively). The solid curve in *b* is the contribution of the line interference effect of the second-order in pressure (fig. 3.22) calculated by MPM-11 for average experimental conditions.

Stable conditions provided a level of instrumental noise in spectrum recordings about five times lower than in earlier experiments. The absorption coefficient sensitivity was ~0.01 dB/km. So, the systematic differences of the first-order model (3.11) could be explicitly distinguished from the experimental data (fig. 3.30, *b*) and used for determining the coefficients of the second-order model (3.12).

Like in all previous studies, the collision coupling coefficients for each temperature simultaneously, for all band lines, were determined using a sequential iterative procedure of minimising the deviations of the experimental points from the corresponding calculated values (details can be found in Tretyakov [2005]; Makarov [2011]). The coefficients of the first (*y*) and second (*g* and *d)* order in pressure were determined simultaneously. The solution cannot be regarded as unique. Hence, it is important to distinguish between the error of the model coefficients and the error of calculating absorption using this model. Due to mutual correlation, underestimated values of some coefficients in absorption calculations may be compensated by overestimated values of the others. This means that the procedure determining interference parameters should be repeated, for example, in the case of refining line intensities or broadening coefficients. However, it can be considered that the obtained set of coefficients provides the best agreement of the model (3.12) with the available experimental data and corresponds to the theoretical principles used in the development of the model (3.12), in particular, to the smooth dependence of the coefficients on the quantum numbers of lines (fig. 3.31), which significantly reduces the number of degrees of freedom in search for a solution.

With the use of the found 15 sets of interference coefficients (*y, g*, and *d*) their temperature dependence was determined. The temperature dependence of the coefficients *y* normalised to $(300/T)^{0.8}$ for the lines $N = 1^+$, 17^+ and 17^- is plotted in fig. 3.32. The data were processed assuming that $n_\gamma = 0.8$ for all lines of the band.

There is almost no additional temperature dependence for the 1^+ line. This corresponds to the fact that the relation $\Delta E << kT$ is fulfilled for all collisional transitions ensuring the manifestation of the interference effect for this line. For lines with a larger orbital quantum number, the additional temperature dependence becomes significant. The values of the coefficients y_0, y_1, g_0, g_1, d_0, and d_1 corresponding to the expression (3.12) can be found in Makarov [2020].

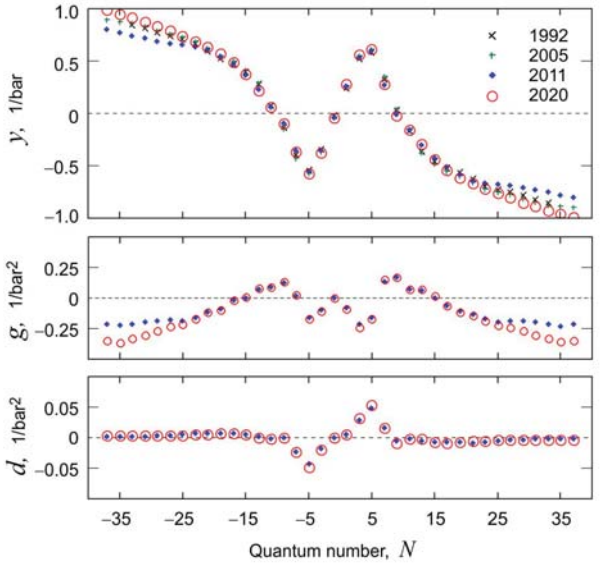

Fig. 3.31. The coefficients of collisional coupling of the first (*a*) and second (*b* and *c*) order for the oxygen fine structure lines at 300 K. The values of the quantum numbers N^+ and N^- are laid off on the x-axis on the right and left of zero, respectively. Open circles – values from Makarov [2020], crosses, pluses, and diamonds – values from Liebe [1992], Tretyakov [2005], and Makarov [2011].

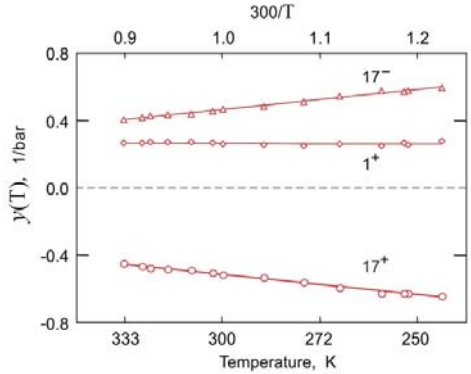

Fig. 3.32. Temperature dependence of the first-order interference coefficients y normalised to $(300/T)^{0.8}$ for the lines $N = 1^+$, 17^+ and 17^-. Symbols – values found from spectrum recordings (fig. 3.30, *a*), lines – the result of their linear approximation.

The as-obtained MPM model, allowing for the effect of interference of fine structure oxygen lines up to the second order in pressure, described experimental data much better than the previous model of the first-order MPM-05 (cf. fig. 3.31, *c* and *b*). The rms deviation of the entire array of experimental points was almost halved in the MPM-11 and reduced by about factor of 4 in the MPM-20. The greatest improvement of the description was achieved on the wings of the band, which is most valuable for the atmospheric remote sensing using radiometers of these ranges. Nevertheless, systematic discrepancies between the calculated and experimental profiles were observed near the band centre. The magnitude of the discrepancies increased with decreasing temperature. All this clearly indicated the inadequacy of the model and encouraged further development of the theoretical methods.

The next step in this direction was the development of an absorption model based on the energy correction sudden (ECS) formalism. The formalism rests upon the construction of a collisional interaction matrix of all significant lines and the calculation of absorption, including numerical inversion of the matrix (details can be found in Makarov [2013] and references therein). To simulate the 60-GHz band, lines of 7 branches were included in the interaction matrix, namely, N^+ and N^- branches, the corresponding branches with negative frequencies and three branches of non-resonant transitions ($J = N - 1$, $J = N$ and $J = N + 1$; $\Delta N = 0$; $\Delta J = 0$). The interaction with the rotational transition lines ($\Delta N = \pm 2$) was considered to be negligible. Forty-five lines up to $N = 90$ were taken into account in each branch. Thus, the interaction matrix contained $(7\times45)^2$ elements. Note that the atmospheric absorption should be calculated on the basis of at least two interaction matrices corresponding to the collisions of O_2 with O_2 and O_2 with N_2 molecules. However, in the absence of accurate experimental data on absorption in pure O_2, the only possible way is to build a matrix corresponding to collisions with a hypothetical 'air molecule', which, of course, is a significant approximation of the proposed model. It is justified by an insignificant difference in the collisional parameters of the corresponding lines (figs. 3.23 and 3.25). The diagonal elements of the interaction matrix corresponding to the collisional line broadening were regarded as known [Tretyakov, 2005] (the values for unmeasured lines were found by extrapolation) and were used to normalise the other elements. The semi-empirical design of matrix elements made use of three adjustable parameters. Their values were found from the experimental data obtained using the Nizhny Novgorod resonator spectrometer in Makarov [2011] by optimising the model for the experimental data at each temperature. The obtained sets of values for two

of the three sought parameters were temperature-independent within the statistical error of estimation, as was assumed in the construction of the model, and the third one showed a weak temperature dependence, which was fairly well approximated by a linear function. The algorithm for the numerical calculation of the profile of the 60-GHz band of atmospheric oxygen at an arbitrary given temperature and pressure based on the values of the found adjustable parameters is actually an absorption model. Its first version (ECS-13) was upgraded (ECS-20) on the basis of new experimental data. The model compliance with the experimental data is seen in fig. 3.30, *d*. The rms deviation of the experimental points from the calculation is notably smaller than in the MPM-20 and about half as small as in the MPM-11. The amplitude of systematic deviations does not exceed 0.2 dB/km, and their increase with decreasing temperature becomes much less pronounced.

Thus, the use of the ECS formalism has significantly improved the quality of modelling the absorption spectrum of the oxygen fine structure, with a significant decrease (about half compared to MPM-11 and MPM-20) in the number of empirically determined parameters. In fact, only four parameters are needed to describe the line interference effect. All the other parameters of the model (position, intensity, broadening coefficients, etc.) are similar to modelling a spectrum consisting of isolated lines. All this confirms that the ECS approach is more adequate than the previous models. The underside of this improvement is a noticeable increase in computation time. For example, the absorption corresponding to one of the experimental recordings shown in fig. 3.30 (about 100 frequency points) with an up-to-date personal computer by the MPM is calculated in a moment, whereas the use of ECS takes about a minute. It is highly likely that the computation time could be reduced in one way or another. For example, the same problem of reducing the time required to calculate the absorption using the Voigt profile (section 1.2.2) was successfully solved by analytical approximation [Humliček, 1982]. In any case, taking into account the rapid progress in computing technology, the duration of computation cannot be considered to be an essential drawback, provided it ensures the required accuracy.

118-GHz line

A single line of the oxygen fine structure ($N = 1^-$) near 118.75 GHz has been studied no less intensively than the 60-GHz band. It is a little more convenient for remote measurements of atmospheric temperature than the band for two reasons. Firstly, it is a single line, which greatly

simplifies the modelling of its profile. Secondly, its intensity is such that, even at the line centre frequency observed at the zenith, the Earth's atmosphere can still be considered transparent. For laboratory studies, a weak absorption coefficient in the centre of this line, which is merely about $1.4 \cdot 10^{-5}$ cm^{-1} even in pure O_2, on the contrary, creates additional difficulties.

The first observation of the 118-GHz line and the first estimates of the magnitude of its collisional broadening in pure O_2 [Anderson, 1951; Hill, 1954] were made using video spectrometers with Zeeman modulation. To increase the observed signal-to-noise ratio at least slightly, the oxygen was cooled down to –80 °C [Anderson, 1951], which gave a gain of about 60 % due to an increase in the relative population of the lower transition level.

The first comprehensive study which aimed, not only at refining the line parameters for remote sensing, but also at experimental verification of the existing theoretical models of its shape, was made at the University of Texas and presented in Schulze [1963]. The fact that the results were published in the journal 'Nature' indicates the high appreciation of the significance of the data. A classical video spectrometer with a harmonic generator and a superheterodyne receiver was used for the study. The specific feature of the work which provided high spectrometer sensitivity was a gas cell approximately 150 m long. The study was performed in pure dry oxygen at room temperature (300 K) in a very wide pressure range from 0.5 to 760 Torr. With the use of different methods of recording the absorption signal at low (0.5–6 Torr) and high (8–760 Torr) pressures, 1.90 and 2.08 MHz/Torr were obtained, respectively, for the collisional broadening coefficient, or 1.99 MHz/Torr using all the data. The data for measurements at pressures from 8 to 760 Torr presented in fig. 3.33 were recalculated to a pressure of 760 Torr, assuming that the line was pressure-broadened linearly and symmetrically relative to the centre (the maximum error of this recalculation was less than 0.07 dB/km, which is significantly less than the measurement error).

The optimisation of the Van Vleck–Weisskopf profile to the obtained data gave an appreciable systematic residue (the lower part of fig. 3.33), which allowed Schulze and co-author [Schulze, 1963] to speak about the insufficiently accurate correspondence of this theoretical line shape to the experiment, and to propose an empirically modified shape that improved the optimisation quality by approximately 20 %. Further studies using the Nizhny Novgorod resonator spectrometer showed the inconsistency of this modification.

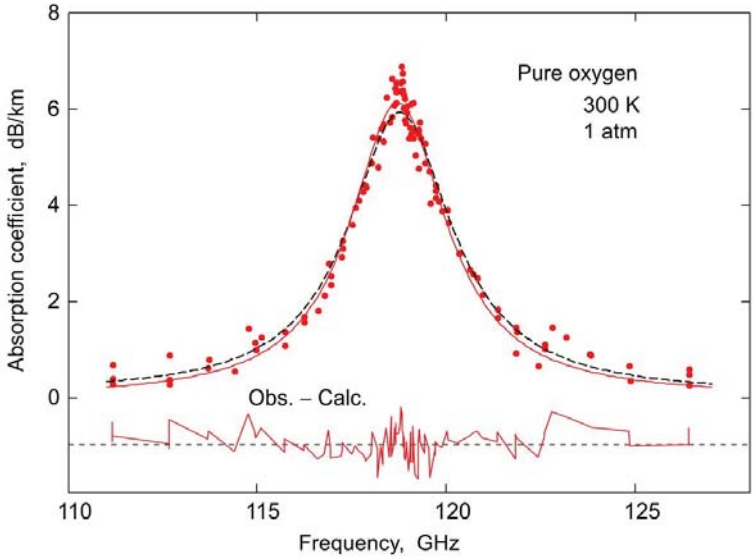

Fig. 3.33. Data of absorption measurements in pure O_2 [Schulze, 1963] recalculated to atmospheric pressure (points). Solid line – result of optimising the Van Vleck–Weisskopf profile to the measurement data; dashed curve – calculation by the MPM-05 model. The deviation of the data from the Van Vleck–Weisskopf profile is shown at the bottom of the figure.

The first application of resonator spectroscopy for the study of the 118-GHz line was also associated with an 'echo box' [Gimmestad, 1976]. Such a spectrometer was created at the Rutherford Appleton Laboratory (RAL), England. The effective path length was 100±1 m. The measurements were carried out in pure oxygen at 299±2 K and 50.1±0.1 Torr. The measurement results are presented in fig. 3.34 in comparison with the calculation by the MPM-05 model. The rms deviation of the experimental points from the calculation was 0.2 dB/km. However, when the broadening parameter was determined by varying the Lorentz profile parameters, the centre frequency and line intensity values known at that time were fixed and only the width was varied. This greatly reduced the error of determining the collision broadening parameter to 2.11 (5) MHz/Torr.

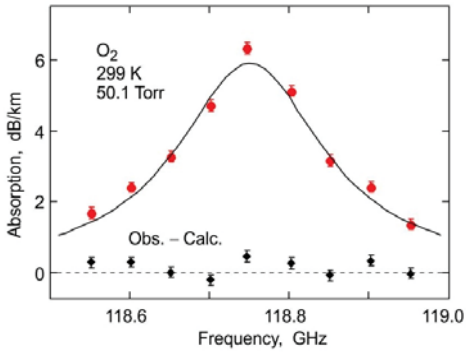

Fig. 3.34. Data of absorption measurements in pure O_2 [Gimmestad, 1976] (points) and calculation by MPM-05 (curve).

The first studies of collisional broadening of the 118-GHz line by the pressure of the major atmospheric gases (O_2, N_2, H_2O, Ar, and He) at room temperature (298±2 K) were made at the University of Texas with a compact resonator spectrometer (the distance between the mirrors was about 2 cm, this is approximately equal to their diameter) [Setzer, 1977]. The measurements were made at gas pressures (up to several Torr) such that the width of the observed line was less than the width of the resonance curve. So, the resonator served only as an increase in the interaction path length. The small resonator size allowed for the implementation of the method of Zeeman modulation and synchronous signal detection for line observation and, for the observed signal shape analysis, using an analytical expression typical of electron paramagnetic resonance spectrometers [Wahlquist, 1961], in which the collision width is a variable parameter. For the line broadening by O_2, N_2, and H_2O pressure, the obtained coefficients were 2.131 (37), 2.20 (10) and 2.30 (24) MHz/Torr, respectively.

The first experimental estimates of the temperature dependence of line broadening by O_2 and N_2 pressure were reported by Pickett [1981]. They were obtained using a conventional video spectrometer with a 50 cm-long cell at gas pressures within the 0.05–2 Torr range. The broadening parameter was determined by the *Pickett method* [Pickett, 1980-2]. The gist of this method is that the gas spectrum observed at a low pressure can be numerically recalculated to the spectrum observed at a high pressure by means of a convolution with the Lorentz profile, whose half width corresponds to the additional collisional broadening of the original spectrum. Theoretically, the application of the method solves the problems associated with the distortion of the observed line shape, for example, due to Zeeman splitting. However, at the same time, the convolution distorts

(smooths) the spectrometer baseline influenced by radiation interference which, practically, should not change with small changes in gas pressure. So, the measurement result can have related systematic errors. Pickett and co-authors presented the results of measurements from this method at three temperatures: 207, 281, and 295 K, which allowed them to determine the power exponents of the temperature dependence of broadening the 118-GHz line in O_2, N_2, and air. The resulting n_γ values were, respectively, 1.04(11), 0.61(9), and 0.70(9).

Another study of the 118-GHz line using the resonator spectroscopy was carried out at the Jet Propulsion Laboratory, USA [Read, 1988]. The absorption was determined by the change in the width of the resonant response when the resonator was filled with gas. The measurements were made in pure oxygen at pressures from 50 to 100 Torr, at room temperature (one measurement was made at 262 K), when the radiation frequency was shifted upwards and downwards from the line peak. The results recalculated to 300 K are presented in fig. 3.35, assuming that the line wings are symmetric with respect to its centre.

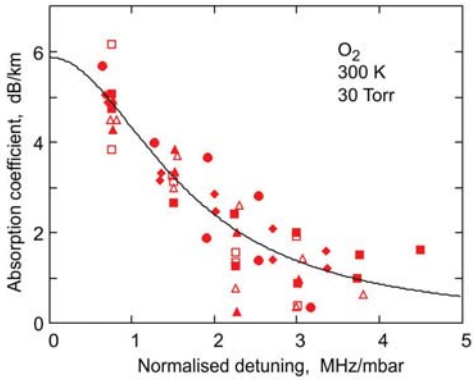

Fig. 3.35. Absorption in pure O_2 near the maximum of 118-GHz line (different symbols correspond to different measurement series [Read, 1988]). The curve is the result of calculations by the MPM.

With a rather large spread of experimental points ($\sigma \sim 1.5$ dB/km), the result of recalculating the data from [Read, 1988] to 296 K and averaging them with allowance for the reduced measurement error gives a broadening coefficient value of 2.25(20) MHz/Torr, in a good agreement with the present-day value of 2.22 MHz/Torr (formula (3.16) with the corresponding coefficients from Table 3.4), which indicates that there are no systematic measurement errors.

The next cycle of studying the parameters of the 118-GHz line is associated with the development of the Nizhny Novgorod resonator spectrometer (section 2.4). The first line recordings were made directly in the laboratory atmospheric air at room temperature and atmospheric pressure [Tretyakov, 2001]. The spectrometer baseline (corresponding to the inherent radiation loss in the cavity) was not measured in these experiments. The calculated frequency dependences of reflection coefficient, coupling and diffraction were used for its estimation. Inaccurate assessment of the baseline led to an uncertain absolute value of the measured absorption. Nevertheless, the wide frequency range of the recording allowed for the determination of the parameters of the oxygen line by its shape. The remaining systematic influence of the baseline was taken into account by introducing additional terms into the line shape model. The data obtained on different days under slightly different atmospheric conditions were recalculated using the MPM-92 to the same pressure and temperature (758 Torr, 21 ºC) average for this series of experiments and zero humidity. Then the Van Vleck–Weisskopf model with the addition of a function linear in frequency was optimised to them (all the parameters of the model were varied). The absorption irrelevant to the 118-GHz line was subtracted from the experimental data. The results of the most successful series of these experiments are presented in fig. 3.36. The signal-to-noise ratio was even slightly higher than in the Schulze–Tolbert experiments [Schulze, 1963]; but no systematic deviations from the classical theoretical Van Vleck–Weisskopf shape were observed (fig. 3.36). The coefficient of line broadening by air pressure was 2.14(7) MHz/Torr, which was in a good agreement with the results of the previous studies.

The line centre frequency was found to have shifted from the position of the line at low pressures. The value of the displacement was several times larger than the statistical measurement error and, in some experiments, reached 200 MHz. If the observed shift is interpreted as the result of collisional pressure shifting of line centre frequency, then it corresponds to the parameter –0.19(8) MHz/Torr.

A similar shift was observed in the Schultze–Tolbert experiments. For example, for the data shown in fig. 3.33 (partially recalculated from low pressures at which the shift should be smaller), it is 60 ± 20 MHz. It is interesting to note that the authors [Schulze, 1963] introduced significant corrections to the theoretical line shape but did not mention the experimentally observed displacement of its position, allowance for which improves the quality of the model optimisation approximately like the modification of the model suggested by them. A possible pressure shifting of the diagnostic atmospheric line frequency detected in this way, which is

fractions of megahertz per Torr, could make a noticeable impact on the atmospheric parameters retrieved from the remote sensing data [Krupnov, 2002-1]. In view of the importance of the issue and taking into account the possibility of direct measurement of such a significant shift at low pressures, the IAP RAS researchers performed a study using, in addition to the resonator spectrometer, the above-mentioned RAD spectrometer [Golubiatnikov, 2003-2; Tretyakov, 2004]. The measurements of the position of the line centre at pressures from 0.2 to 3.5 Torr with the RAD spectrometer showed that the magnitude of the shifting, linear with pressure, cannot exceed ±0.01 and ±0.015 MHz/Torr in pure oxygen and air, respectively. Consequently, the shifting of the line centre in the atmosphere cannot be more than 12 MHz.

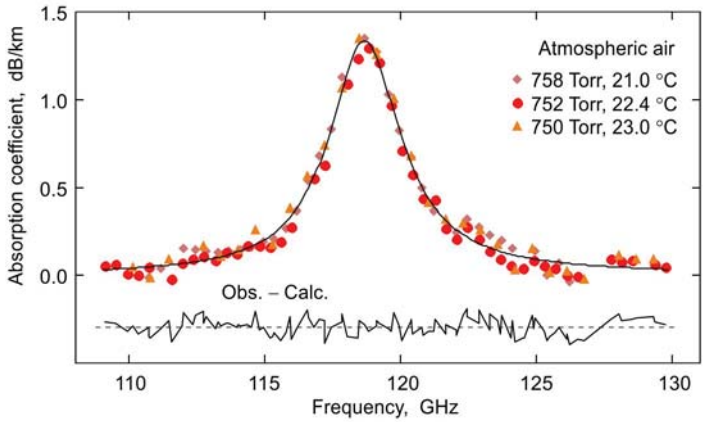

Fig. 3.36. Results of the first recordings of the 118-GHz line with the Nizhny Novgorod spectrometer [Tretyakov, 2001]. The data of three experiments (symbols) were recalculated to the absorption in a single isolated line in dry atmospheric air at 758 Torr, 21 °C. The difference between the data and the Van Vleck–Weisskopf contour fitted to them is shown at the bottom of the figure.

The key point which facilitated the resolution of this contradiction was analysis of the consequences of the impact of collisional coupling of oxygen fine structure lines on the shape of the 118-GHz line. Even at atmospheric pressure, the 1^- line looks like an isolated line, whose wings practically do not overlap with the 60-GHz band. At room temperature, the absorption in the wing of the band at a frequency of 118 GHz is less than 1 % of the line amplitude. Nevertheless, it was revealed that the coupling

effect is strong enough to manifest itself as the line peak shifts towards the band. Indeed, to the first approximation in pressure (see (3.11)), the manifestation of the effect of line coupling is similar to a linear distortion of the line shape relative to its centre. With an insufficient signal-to-noise ratio, the distortion of the line shape gets lost in noise and appears only as a shift in the position of its maximum. The magnitude of the displacement increases quadratically with increasing pressure (fig. 3.37).

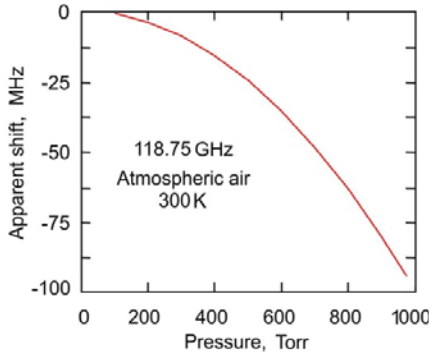

Fig. 3.37. Apparent shift of the 118-GHz line peak with increase in pressure due to the line coupling with the 60-GHz band.

The simulation of absorption using the MPM-92 predicted that, in air at room temperature and atmospheric pressure, the line maximum shifting should be about –50 MHz, and for detecting the difference of the line shape from the Van Vleck–Weisskopf profile under the same conditions, the signal-to-noise ratio (S/N) must be more than 100. The maximum expected shifting of the line centre in the studies using the RAD spectrometer is less than 1 kHz, and the difference of the line shape from the Lorentz profile could only appear for the S/N ratio as more than 20000. Thus, the performed analysis explained the observed facts, but required experimental verification. Line recording at atmospheric pressure using a resonator spectrometer with S/N > 100 seemed tangible, at least in pure O_2. In addition, the instrumental noise of the resonator spectrometer caused by an uncontrolled change in the coupling coefficient of the resonator and the exciting radiation as a function of frequency detected in the previous study (fig. 3.36) could be reduced by finding this dependence experimentally, by replacing the test gas in the resonator by a non-absorbing gas (section 2.3). This method was employed for the absorption measurements within the 20-GHz vicinity of the line in pure oxygen and in atmospheric air (nitrogen evaporating from liquid phase was used as a non-absorbing gas). The experiments were carried out at room temperature and atmospheric pressure. The examined gases were slowly blown through

a plastic bag covering the resonator. The recorded S/N ratio was about 500 for pure O_2 (fig. 3.38) and slightly less than 100 for air.

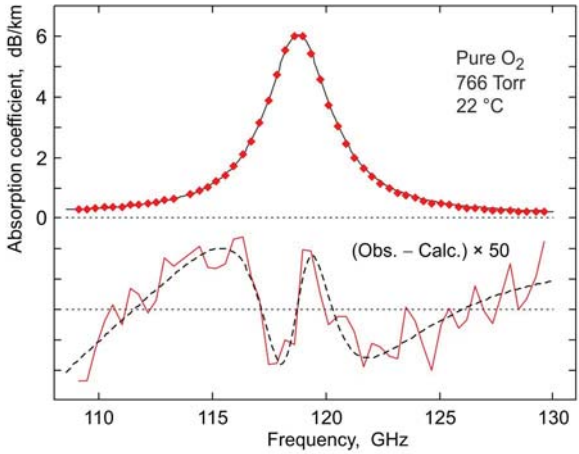

Fig. 3.38. Absorption in pure oxygen [Tretyakov, 2004] (points) and the corresponding calculation by MPM-05 (solid line). At the bottom – the difference between the observed line and the Van Vleck–Weisskopf profile fitted to the experimental points (broken line); the dashed line is the difference between the Van Vleck–Weisskopf profile and its analogue (3.11) taking into account the collisional coupling of the line.

The optimisation of the function (3.11) to the obtained data showed that it corresponds to the shape of the observed line to an accuracy of experimental noise, which was about 0.013 dB/km in the considered study. This enabled the first direct measurement of the theoretically predicted value of the interference parameter of the first-order and clearly demonstrated that the Van Vleck–Weisskopf profile was not suitable for modelling the 118-GHz line (fig. 3.38). The obtained values of the interference coefficients –4.6(4) and –5.9(29) 10^{-5} $Torr^{-1}$ for pure oxygen and air, respectively, were in a good agreement with the results of the earlier studies. Thus, in the MPM-92, the value $-3.1 \cdot 10^{-5}$ $Torr^{-1}$ was used for air. The theoretical value $-7.8 \cdot 10^{-6}$ $Torr^{-1}$ for oxygen was known from the work of Smith [1981]. The model function for processing the data of these experiments, in addition to the line shape function (3.11), included an additive second-order polynomial taking into account the influence of the wings of the neighbouring lines, as well as possible inaccurate allowance for the spectrometer baseline, and thus had 7 variable parameters. With the high S/N ratio in the obtained spectra the values of the collision

broadening parameters of the 118-GHz line were determined more accurately. The obtained values of 2.24(1) and 2.25(3) MHz/Torr were consistent, within statistical error margins, with the measurement data from the RAD spectrometer at low pressures, which increased reliability of the results significantly. The integrated line intensity at 24 ºC was found to be $0.997(20)\cdot10^{-26}$ cm/molec, which agrees well with the value of $0.9913\cdot10^{-26}$ cm/molec obtained by recalculating the HITRAN data for the temperature of the experiment. The line centre frequency within the measurement error coincided with its value known from the experiments at low pressures confirming that there was no shifting in the position of the line centre linear with pressure. Thus, the study resolved all the contradictions associated with the observation of this line and allowed its parameters to be refined significantly.

The next study of the 118-GHz line using the Nizhny Novgorod resonator spectrometer was concerned with measurements of the temperature dependence of the parameters of its shape in atmospheric air and pure oxygen. The results of this study were presented in two papers: Tretyakov, [2007-2] and Makarov [2008]. In both cases, the absorption measurements were made in the same frequency range and using the same method as in the previous work. At the beginning of this study, the measuring resonator was placed on the roof of a building where it was protected against wind and precipitations but was open to atmospheric air, which determined the thermodynamic parameters of the gas under study. The unpredictable weather conditions and natural temperature and pressure instability caused some difficulties which slowed down the work significantly and worsened the quality of the data. This encouraged the development of a simpler thermostat for the measuring resonator based on a domestic refrigerator which was used to continue the study. The refrigerator compressor was operating continuously, and the degree of chamber cooling was automatically regulated by periodic switching of the coolant. The flow was either passed by the chamber along the external ‘idle’ circuit, or along the working circuit through a large radiator installed in the chamber. A flexible heating element was attached to the radiator. The heating power was smoothly controlled by applied voltage. Stable temperature inside the chamber was maintained as a result of the balance between forced cooling and radiator heating, on the one hand, and the natural heat exchange between the chamber and the ambient laboratory air, on the other hand. Fans for mixing gas and reducing temperature gradients were installed in the chamber. Stable air temperature in the laboratory during the experiments was maintained by a domestic air conditioner. Such thermostabilisation in the semi-automatic mode maintained the

required temperature of the test gas in the chamber in the –30 to +60 °C range with an error of ~0.2°. As in all the previous experiments, gases were slowly blown through the chamber, thus providing the conditions for the measurements to be performed only at atmospheric pressure. The stable thermodynamic conditions of the gases being studied, as well as the stability of the waveguide path of the resonator excitation and the path of the response recording ensured the S/N ratios in the line recordings up to 800 in experiments with pure O_2 and, hence, a high statistical accuracy in determining line parameters. In all cases, the use of the line shape function (3.11) gave a noise-like optimisation residue, which confirmed the adequacy of this shape.

The results of measuring collisional line broadening coefficient in pure oxygen at atmospheric pressure as a function of temperature are presented in fig. 3.39 by squares and triangles [Tretyakov, 2007-2; Makarov, 2008]. The error bars for these points correspond to 1σ statistical measurement error. For comparison, the results of measurements in the ~ 0.2–2 Torr pressure range using the RAD spectrometer [Koshelev, 2015] are shown by diamonds; here, the error takes into account both statistical and possible systematic errors. The dashed line in the figure corresponds to the $2.244 \cdot (296/T)^{0.774}$ function.

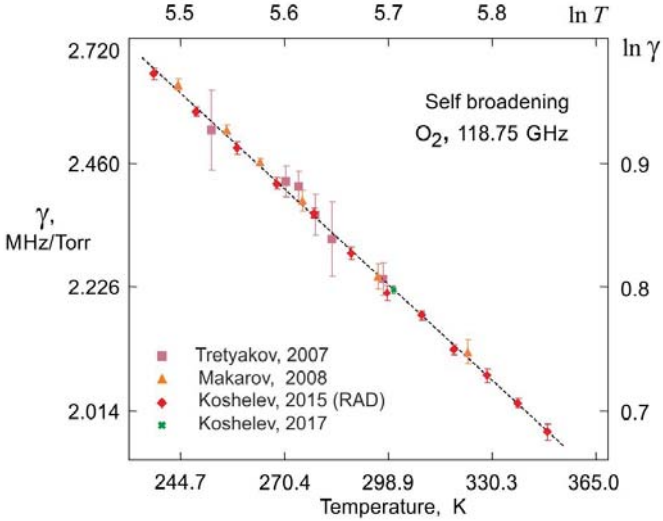

Fig. 3.39. The temperature dependence of the coefficient of collisional broadening of the 118-GHz line in pure O_2.

The optimisation of the coefficients of the power function (1.96) to all the data in fig. 3.39, with the weights inversely proportional to the squared uncertainty, gives $\gamma(296) = 2.244(2)$ MHz/Torr, $n_\gamma = 0.774(7)$ and shows that all the data are consistent with each other.

Due to the weak manifestation of the collisional coupling effect against the background of experimental noise shown at the bottom of fig. 3.38, the error of determining the value of the corresponding parameter is much larger than the line broadening parameter. The analysis of the results showed that for this line, like for $N = 1^+$ (fig. 3.32), with allowance for the expected temperature dependence $(T_0/T)^{n_\gamma}$ (3.13), the obtained line coupling parameter does not depend on temperature within the measurement error. The measurement data in pure oxygen recalculated to 300 K are presented in fig. 3.40, where the square, circles, and triangles are, respectively, the data of the works of Tretyakov [2004, 2007-2] and Makarov [2008]. The error bar corresponds to the 1σ statistical measurement error. The dashed line is the weighted average of $4.63(10)\cdot10^{-5}$ Torr^{-1} over all data.

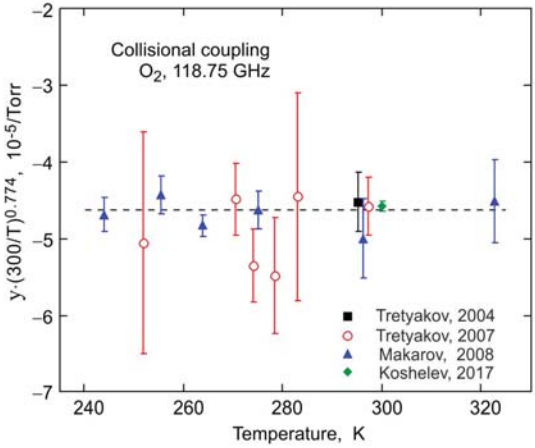

Fig. 3.40. The results of measurements of the collisional coupling coefficient of the 118-GHz line in pure O_2.

The line centre frequency at atmospheric pressure averaged over all experiments was 118.749(2) GHz, i.e., the line frequency shifting, linear with pressure, cannot exceed several kilohertz per Torr. The expression for the temperature dependence of the integrated intensity of the 118-GHz line is obtained from (1.41) taking into account the $Z(T)$ dependence and that $E_a = 0$ for this line:

$$S(T) = S(T_0)\frac{1}{T}\left(1-\exp\left(-\frac{h\nu_0}{kT}\right)\right). \qquad (3.17)$$

The integrated line intensity in these studies was determined assuming that the distortion in its shape due to collisional coupling is small and the simple relation (1.80) was used. The statistical measurement error in all the experiments in pure O_2 was less than 1 %. Moreover, in the second series of experiments carried out under stable laboratory conditions [Makarov, 2008], the rms deviation of the experimental points from the theoretical dependence (3.17) was less than 0.5 %, which is a sign of a high spectrometer potential. The results of measurements of the integral intensity of the 118-GHz line in pure O_2 using the Nizhny Novgorod resonator spectrometer [Makarov, 2008] are shown by circles in fig. 3.41. The dashed curve corresponds to the theoretical dependence of intensity on temperature (3.17) at $S(296) = 9.74\cdot10^{-26}$ cm/molec. The deviation of the experimental points from the theoretical curve is shown at the bottom of the figure. The error bars correspond to 3σ statistical measurement error.

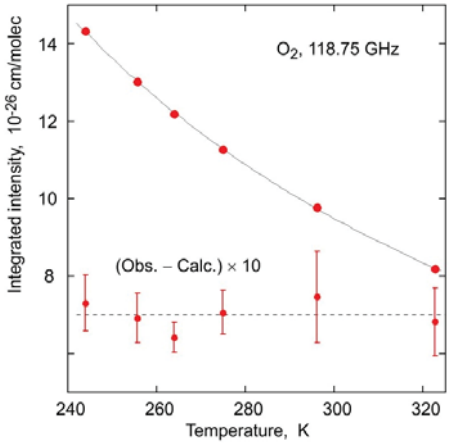

Fig. 3.41. The results of measurements of the integral intensity of the 118-GHz line with the Nizhny Novgorod spectrometer in pure O_2 at different temperatures [Makarov, 2008].

Given that the accuracy of the theoretical calculations of the intensity is approximately 1 %, the measurement results could refine the value of this line parameter. However, because of uncertain oxygen purity (a cheap, technically pure gas was used, in which the supplier-guaranteed concentration of O_2 was not less than 98 %), the error of the obtained values of intensity shall be estimated to be two to three percent due to possible systematic error. The agreement of the measurements and the calculations within such limits only confirms the accuracy of the latter.

The results of measurements of collisional parameters of the line in atmospheric air obtained by Makarov [2008] ($\gamma(300) = 2.25(1)$ MHz/Torr, $n_\gamma = 0.785(35)$, $y(300) = -5.5(3)\cdot10^{-5}$ Torr^{-1}) are less accurate than in pure oxygen owing to a lower concentration of O_2 and, hence, a lower S/N ratio in the line recording. Nevertheless, in this case too, a very good agreement of the line broadening parameters with the results of the later high-precision studies at low pressures by Koshelev [2016] can be noted.

It is interesting to note that almost simultaneously with this study, the temperature dependence of the 118-GHz line broadening by O_2 and N_2 pressure was carefully measured at the Jet Propulsion Laboratory with a classical Zeeman modulation video spectrometer [Drouin, 2007]. Hundreds of measurements were made in the temperature range of 200–300 K and pressures of 0.2–2.2 Torr. The broadening coefficient was determined by the above-mentioned method [Pickett, 1980-2, 1981], with the calculation of the convolution of the observed spectrum with the Lorentz profile. The obtained values of the broadening coefficients and the exponent of their temperature dependence ($\gamma_{O_2}(296) = 2.08(2)$ MHz/Torr, $n_{O_2} = 0.90(4)$ and $\gamma_{N_2}(296) = 2.06(2)$ MHz/Torr, $n_{O_2} = 1.00(5)$) differed significantly from the results in the work of Tretyakov [2004], known at that time and confirmed by later studies. As a possible source of systematic errors, Drouin and co-authors [Drouin, 2007] distinguish the distortions in the observed line shape induced by standing waves in the spectrometer transmission line. They estimated the maximum possible systematic measurement error of broadening coefficient to be 3 %. Comparison with the later data showed that the real error was several times more.

The next significant step towards refining knowledge on the 118-GHz line was made in the work of Koshelev [2017]. The line was studied in pure oxygen (higher than 99.995 %) at room temperature, when a new gas chamber with accurate pressure and temperature control was developed and implemented in the Nizhny Novgorod resonator spectrometer. Highly stable experimental conditions allowed for recording the line at atmospheric pressure with an unprecedented signal to noise ratio of about 2000. Analysis of the observed spectrum enabled further progress in the 118-GHz line shape description by revealing the manifestation of the ‘wind effect’ (the speed dependence of the collision cross section, Section 1.2.2), along with a considerable refinement of the other parameters, including pressure broadening, intensity, and line mixing. An example of line profile recording can be found in fig. 2.36. Neither the Van Vleck–Weisskopf profile (VVW) nor the Van Vleck–Weisskopf profile with allowance for the collisional coupling of the line (VVWLM) was able to

reproduce the observed line shape. A specially constructed Van Vleck–Weisskopf profile with allowance for the collisional coupling of the line and for the speed dependence of the collision cross section in quadratic approximation (qSDVVWLM) was used for analysing the spectra. The retrieved speed-dependent broadening parameters for this line (γ_0 = 2.271(7) and γ_2 = 0.172(2)) were found to be in a good agreement with the results of supplementary measurements at low pressures using a spectrometer with radio-acoustic detection of absorption. The line mixing coefficient y was assumed to be speed independent. It was found to be $4.71(3)\times10^{-5}$ 1/Torr, in agreement with the previous results (Fig. 3.40). The integrated line intensity was determined to be $0.9976(37)\cdot10^{-25}$ cm/molec in good agreement with the theoretical predictions, confirming the capability of the instrument to measure intensity at the sub-percent level.

A retrospective overview of all known results of measuring the collisional broadening of the 118 GHz line in pure oxygen and air is presented in fig. 3.42.

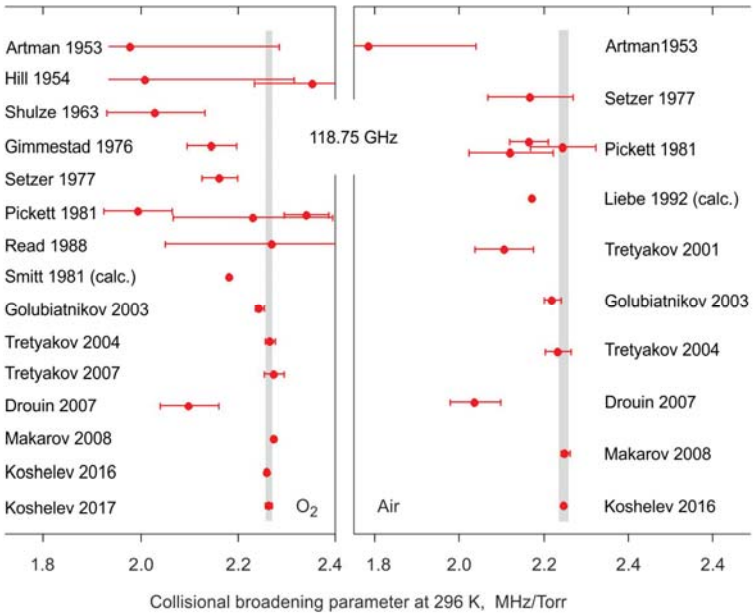

Fig. 3.42. The results of measurements of the coefficient of collisional broadening of the 118-GHz line by different researchers in chronological order recalculated to 296 K using $n_{O_2} = 0.765(7)$ and $n_{air} = 0.778(6)$ [Koshelev, 2016].

First rotational triplet

The position of the triplet lines was theoretically predicted to an accuracy of about 1 MHz in [Zimmerrer, 1961], where the value of the rotational constant B of the O_2 molecule was refined by means of accurate measurements of the frequencies of fine structure lines. The value of the centrifugal constant D was taken from [Babcock, 1948], where it was determined from the analysis of the UV range spectra containing lines corresponding to very high rotational states of the molecule.

The first experimental observations and measurements of the frequency of the centre, most intense line of the triplet were made several years after the prediction in McKnight [1968]. A video spectrometer with a 6-meter cell and Zeeman modulation was used for the observation. To increase line intensity, the cell was cooled to the liquid nitrogen temperature. Nevertheless, due to a very low S/N ratio, the systematic error in the frequency measurements was approximately 0.7 MHz, which was found in the subsequent study of the oxygen spectrum by the same group [Steinbach, 1973].

The results of the first measurement of the broadening coefficients of the most intense line of the triplet by the pressure of nitrogen and oxygen at 207 and 295 K were presented in the work [Pickett, 1981]. The measurement was made using a spectrometer with Zeeman modulation and the method of convolution of the observed spectrum with a Lorentz profile. The measurement error was about 10 %. Nevertheless, a large temperature range of the measurements allowed the authors to estimate the temperature dependence of the broadening.

In the next study of the collisional broadening of this line performed at room temperature and at low pressures, using the RAD spectrometer [Krupnov, 2002-2], the measurement accuracy was higher by about an order of magnitude. The values of the found broadening coefficients differed from the previous ones by about 25 %. The frequency of the transition was determined more accurately, and the magnitude of its linear pressure shifting was estimated to be -5 ± 40 kHz/Torr. These studies with the RAD spectrometer were continued in the frequency range up to 1.13 THz [Golubiatnikov, 2003-1], including measurements of the broadening parameters of the other two lines of the considered triplet and the positions of all rotational O_2 lines in the studied frequency range were updated. As a result, the rotational constants of the molecule were refined substantially.

The subsequent refinement of the rotational constants and, hence, of the position of the lines of the considered triplet, was associated with the

measurement of four more rotational O_2 lines, including a triplet near 1.8 THz [Drouin, 2010] made simultaneously in two laboratories with classical Zeeman modulation video spectrometers. The results of this study, together with frequencies of all other known oxygen transitions in the infrared, visible, and ultraviolet range, were used in a global model of the oxygen spectrum including data for its six most abundant isotopologues [Miller, 2012]. These two works confirmed the high accuracy of frequency measurements using the RAD spectrometer and showed that the 30-kHz estimate of the error in determining the triplet line positions may actually be several times less.

The temperature dependence of the broadening coefficients of the most intense line of the triplet was studied in Drouin's work [2007]. The measurements were made with a video spectrometer by the method used in Pickett [1991]. The obtained values of the exponents of temperature dependence 0.70(4), 0.76(4), and 0.72(4) for the line broadening coefficients in the pressure of nitrogen, oxygen, and air, respectively, are consistent within the statistical errors with the exponents (0.751(15), 0.765(11) and 0.754(11)) for similar fine structure lines [Koshelev, 2016], and the values of broadening coefficients allowing for possible 3 % systematic error, agree with the results of RAD spectrometer measurements [Krupnov, 2002-2; Golubiatnikov, 2003-1].

The first and, for the time being, the only study of the lines of the first rotational O_2 triplet by the resonator spectroscopy was performed using the Nizhny Novgorod spectrometer. The results of this study conducted at room temperature and atmospheric pressure in a continuously covered 350–500 GHz frequency range were presented by Tretyakov [2013-1]. The specific features of this work associated with the study of water vapour resonant lines at 380 and 448 GHz, located in this range, and a brief description of the method of determining line parameters can be found in section 3.1.1. The lines of the triplet were investigated in the winter atmospheric air and in pure oxygen. The air was sucked in from the street by a compressor. A cheap, technically pure gas was used to record the spectrum in oxygen (the O_2 content was more than 98 %). The investigated gases were slowly (15–20 l/min) blown through a plastic bag covering the measuring resonator. It was impossible to completely get rid of the water vapour in the gas, even when pure oxygen was studied. Water was present in the oxygen cylinder as well and diffused through the walls of the bag. This greatly complicated the analysis of the oxygen spectrum, since the water vapour lines, whose wings overlapped with O_2 lines in the spectrum recording, had comparable amplitudes with O_2 lines (fig. 3.10).

Nevertheless, with the use of the iterative procedure by means of the MPM (more details are available in section 3.1.1) the recorded spectra were 'cleaned' to the experimental noise level not only from H_2O lines but also from the continuum, including the far wings of the fine structure lines and other triplets (fig. 3.43).

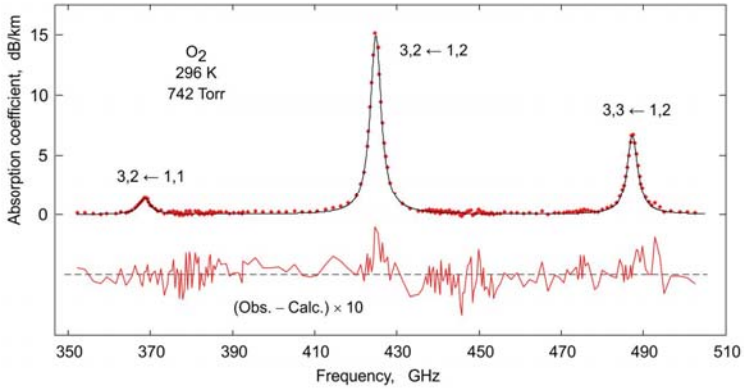

Fig. 3.43. The spectrum of the first rotational triplet of O_2 in a pure gas obtained with the resonator spectrometer. The quantum numbers of the corresponding *N', J'*← *N, J* transitions are indicated above the lines. The difference between the experimental spectrum and the calculation by MPM-05 with the parameters of the triplet lines from the works of Krupnov [2002-2] and Golubiatnokov [2003-1] is shown at the bottom of the figure. Adopted from Tretyakov [2013-1].

The line parameters were determined using the model function (3.6). The found coefficients of broadening by air and oxygen pressure coincided, within the 1σ statistical error margin, with the results of measurements of all lines using the RAD spectrometer [Krupnov, 2002-2; Golubiatnokov, 2003-1]. The shifts of the line centre frequencies linear in pressure did not exceed 50 kHz/Torr and were less than the statistical error of their determination for all the lines, which was also consistent with the RAD data. The line intensities measured at 296 K were in a good agreement with the calculated data from HITRAN (Table 3.5), which suggests that the accuracy of the calculations was much higher than the 10–20 % estimate of the uncertainty of intensities given for these lines in HITRAN. Note that the difference between the experimental and calculated (with the parameters from HITRAN) spectra (fig. 3.43) slightly decreased with an increase in the intensity of the lines by about 2 %.

In addition to the measured intensities and their statistical measurement errors (1σ), Table 3.5 contains the frequencies of the triplet lines corresponding to the calculation by the most accurate values of the rotational constants to date [Drouin, 2010].

Table 3.5. The frequencies and intensities of the lines of the first rotational triplet of O_2 in pure oxygen and air.

Frequency, MHz	$N', J' \leftarrow N, J,$	Oxygen	Air	HITRAN
		Intensity, 10^{-25} cm/molec		
368498.248(10)	3, 2 ← 1, 1	0.226(12)	–	0.2224
424763.022(10)	3, 2 ← 1, 2	2.500(11)	2.437(10)	2.425
487249.275(10)	3, 3 ← 1, 2	1.08(11)	1.00(10)	1.036

All the currently known results of measurements of the triplet line broadening coefficients can be compared using Table 3.6. The data listed in the table were recalculated to 296 K using the temperature dependence of the corresponding parameters of the fine structure lines from Koshelev [2016]. The discussion of the analogous results for the 183-GHz water vapour line (section 3.1.1) is also related to these data.

Table 3.6. The results of measurements of the coefficients of collisional line broadening of the first rotational oxygen triplet by oxygen, nitrogen, and air pressure.

Line	Gas	Source of information					
		[Pickett, 1981][a]	[Krupnov, 2002-2]	[Golubiatnikov, 2003-1]	[Drouin, 2007][b]	[Tretyakov, 2013-1]	HITRAN[c]
368 GHz	O_2			2.26(3)		2.25(16)	2.25
	N_2						
	Air						2.20
425 GHz	O_2	1.71(22)	2.19(1)		2.03(2+6)	2.18(14)	2.21
	N_2	2.58(28)	2.22(2)		2.18(2+6)		
	Air					2.14(7)	2.21
487 GHz	O_2			2.11(3)		2.14(3)	2.09
	N_2			2.18(10)			
	Air					1.93(30)	2.15

[a] Weighted mean values of measurements at 270 and 295 K.

[b] The first term in parentheses corresponds to the statistical, and the second term to the systematic measurement error.

[c] The uncertainty of the values is estimated to be 2-5 %.

3.2. The atmospheric continuum

For a deeper understanding of the material presented in this section, it is reasonable to briefly recall the meaning of the basic terms related to the atmospheric absorption to be considered.

The total absorption is an experimentally measured quantity for a given gas under given conditions. We will consider two classifications of the components of total radiation absorption by gas.

The first classification is based on the amount of gas monomer molecules involved in absorption of radiation quantum.

Monomolecular absorption is the absorption spectrum of monomer molecules. In the classical sense it is understood as the power spectrum of a train of oscillations of molecule-oscillator occurring from one collision to another and averaged over all kinds of oscillations breakdown scenarios. This time interval is called *mean free time*. Throughout this time, the dipole moment of the molecule interacts with the field. Uncertainty in the terminology and, as a result, of the interpretation of the absorption mechanism arises because collision does not occur instantaneously. Traditionally (see, for example, Vigasin [2003]), reference to the monomer resonance spectrum implies the presence in the gas of 'isolated monomers', i.e., molecules that do not perceive its neighbours. This means that only the unperturbed part is 'cut out' of the real train of oscillations of the molecule-oscillator. The train breaks down instantly (impact approximation). Such artificial distortion of the monomer oscillation train results in a significant distortion of the shape of the far wings of the line (Appendix A2). The respective absorption in the wings refers to another type, despite the fact that it is the result of the ongoing interaction of the field with a dipole of the same molecule. This molecule is now not isolated as it is in the field of the collision partner but it continues to interact with the field and related absorption has a monomolecular nature. The interaction with the collision partner changes the properties of molecule-oscillators. At the same time, in full conformity with the classical theory of oscillations, the trains of oscillations that smoothly occurred over the mean free path decay (neither instantly, nor monotonously) and there smoothly arise oscillations of a system of two molecules, which is the basis of the absorption corresponding to molecular pairs (cf. free and stimulated oscillations of classical oscillator). With this approach, the separation of the absorption into components seems feasible. It is natural to refer the power spectrum of complete trains of monomer oscillations to monomolecular absorption, which is done in this monograph. Like in the traditional approach, in the vicinity of the centre

of the resonant line, monomolecular absorption, to within small deviations at atmospheric pressures, corresponds to the spectrum of the idealised case of instantaneous collisions. For large detunings from the centre, in the region of the far wings, the monomolecular absorption may first slightly exceed the quadratically decaying absorption corresponding to the impact approximation, and then sharply, apparently exponentially, will tend to zero. Thus, the monomolecular absorption depends on the properties of the molecules surrounding the absorber molecule and will be different in different gas mixtures. Note that an analogous dependence on the composition of the mixture is also common for the case of instantaneous collisions of noninteracting monomers. It arises due to differences in the effective collision cross sections, which determines the broadening, shifting, and other collisional effects specifying the shape of the monomer lines within several full line widths at half maximum around its centre (this range is sometimes called the '*line core*').

Bimolecular absorption is the power spectrum of the train of oscillations produced simultaneously by two molecules. In this case, the interaction with the field is determined by the total dipole moment of the molecular pair. Note that stable dimers formed as a result of molecular collisions do not differ from ordinary molecules from the point of view of spectroscopy and the radiation absorption. They interact with the radiation from one collision to another, which corresponds to the absorption in the resonant lines of a double molecule. Nevertheless, with respect to atmospheric monomer molecules, this absorption is bimolecular and, therefore, supplementary to the monomolecular one. Due to high nonrigidity and a large number of internal degrees of freedom, double molecules have a huge number of lines that merge under atmospheric conditions into a smooth continuous spectrum weakly varying with frequency. Under these conditions, the dimer spectrum differs only slightly from the spectra of other components of bimolecular absorption, the smooth frequency dependence of which is explained by a very short time of the interaction of a pair of molecules with the field.

Multimolecular absorption is a more general case than bimolecular absorption. It arises when three or more molecules produce trains of oscillations simultaneously interacting with the radiation field. This classification is directly related to nonideal gas properties. The pressure of a real gas can be represented as a series expansion in powers of its concentration with the corresponding virial coefficients: $p = An + Bn^2 + Cn^3 + \ldots$ Analogously, the gas spectrum or the total absorption of radiation by gas can be expanded into the following components

$$\alpha_{total}(\nu) = \alpha_1(\nu)n + \alpha_2(\nu)n^2 + \alpha_3(\nu)n^3 + \ldots,$$

where $\alpha_1(\nu)$, $\alpha_2(\nu)$, and $\alpha_3(\nu)$ are the mono-, bi- and tri-molecular absorption spectra normalised to the number of particles, respectively. The virial coefficients enter the corresponding spectra as amplitude factors. Note that the spectra $\alpha_i(n)$ also include the dependence on concentration, for example, through the pressure dependence of collision-broadened resonant lines.

The second classification of total absorption relies on the pattern of the gas spectrum, which, as a rule, is represented by relatively narrow spectral lines against the background of absorption slowly varying with frequency.

Resonant absorption is the absorption in the vicinity of the centre frequency of the spectral lines of the molecules making up the gas mixture.

Non-resonant absorption is a combination of all other absorption mechanisms, except the resonant one, and can have components of both mono- and multimolecular absorption.

One more absorption type deserves separate consideration.

Debye absorption takes place in monomer molecules that can absorb radiation quanta within the limits of the uncertainty of molecular state energy level, which leads to the appearance of a 'resonant' collision-broadened line at zero frequency (in fact, this is a superposition of lines corresponding to all populated levels of a molecule), its wing rapidly degenerates into a frequency-independent absorption. The absorbed energy is expended on restoring the orientation of the molecule's axis of rotation which has deviated as a result of the collision. This absorption is monomolecular in nature, and non-resonant in appearance.

The continuum will traditionally be called the absorption which is empirically defined as the difference between the total absorption and the calculated sum of the lines of monomer molecules. All the above-mentioned components of the total absorption according to both classifications, as well as the Debye absorption, can be partially or fully present in the continuum due to the ambiguity of its definition.

3.2.1. Quantitative characteristics of the continuum

Taking into account the dominant role of water vapour molecules in the formation of the atmospheric continuum, the general expression commonly used for quantitative modelling of the atmospheric continuum can be obtained from the expression (1.150) which characterises bimolecular

absorption. It comprises three terms corresponding to the interactions of water molecules with each other (the term quadratic in humidity), water molecules with air molecules (the term linear in humidity), and dry air molecules between themselves (dry continuum term):

$$\alpha_{cont}(\nu,T) = C_w(\nu,T)\,p_w^2 + C_{air}(\nu,T)\,p_{air}p_w + C_{dry}(\nu,T)\,p_{air}^2, \quad (3.18)$$

where p_w and p_{air} are the partial pressures of water vapour and dry air, respectively.

It was established experimentally [Liebe, 1984-1; Rosenkranz, 1998; Kuhn, 2002; Koshelev, 2011] that in the millimetre wavelength range, the continuum absorption depends quadratically on frequency, and its temperature dependence within the range typical for the atmosphere can be modelled satisfactorily by the simplest power function, which allows the expression (3.18) to be represented in the form

$$\alpha_{cont}(\nu,T) = \left(C_w^0 \left(\frac{T_0}{T}\right)^{x_w} p_w^2 + C_{air}^0 \left(\frac{T_0}{T}\right)^{x_{air}} p_{air}p_w + C_{dry}^0 \left(\frac{T_0}{T}\right)^{x_{dry}} p_{air}^2 \right) \cdot \nu^2, \quad (3.19)$$

where C_w^0, C_{air}^0, C_{dry}^0, x_{air}, x_w, and x_{dry} are numerical coefficients. Note that in some works (for example, Rosenkranz [1998]), the $(T_0/T)^3$ factor corresponding to the temperature dependence of stimulated emission and absorption of radiation by molecules is given explicitly in the continuum parametrisation formulae, which leads to a decrease in the power exponents of the temperature dependence of all components of the continuum.

The expression (3.19) obtained from (1.150), assuming that the continuum is the result of bimolecular absorption, completely coincides with the expression (1.109), which is based on the hypothesis that the far wings of the resonant lines of atmospheric monomers (primarily H_2O molecules) provide the key mechanism responsible for the formation of the continuum. This lucky coincidence greatly simplifies the situation, as quantitative characteristics of the continuum can be determined in experiment without going deeply into its nature.

Humidity related continuum

The investigation of the continuum is a much more complicated and time-consuming task than the study of resonant lines. The problem is comprised of many factors which increase the complexity of the measurements as they all act simultaneously. The most significant of them

are: a) low magnitude of the absorption, b) weak frequency and strong temperature dependence, c) the need to accurately subtract the contribution of resonant absorption from the total observed absorption. When measurements are made in the open air, there also arises a most complicated problem of allowing for the attenuation of radiation associated with scattering and absorption by atmospheric aerosols[14]. Therefore, up to now, systematic laboratory studies of the humidity related atmospheric continuum in the millimetre and submillimetre wavelengths have been undertaken only by a few groups of researchers: at the Institute of Telecommunications, at the Universities of Lille, at the Ohio State University, at the Scientific Research Radiophysical Institute (NIRFI, Russia), and at the Institute of Applied Physics of the Russian Academy of Sciences in Nizhny Novgorod. In most cases, resonator spectrometers were used for measurements as they are most suitable for such work in the millimetre and long wavelength part of the submillimetre wavelength range. Only the NIRFI team, conducting the research in the most high-frequency part of this range, where continuum absorption quadratically increasing with frequency becomes quite intense, used multipass cells (such as the White gas cell [White, 1942]), the radiation path length in which was comparable to the effective path length of a high-Q resonator. A significant contribution to the refinement of the laboratory parameters of the continuum was made by field studies carried out over extended paths along the surface [Katkov, 1995; Manabe, 1989], as well as with ground-based radiometers [Westwater, 1990; Turner, 2009; Payne, 2011].

The first, and perhaps the most comprehensive study was the continuum research performed at the Institute of Telecommunications in 1970-1990 by Hans Liebe, whose main goal was to develop a model of millimetre wave propagation in the atmosphere for practical applications. The description of the resonator spectrometer used for measurements can be found in section 2.4.3. The measurements were made in the atmospheric transparency window near the frequency of 138 GHz. The preliminary results of measurements were reported in the work of Liebe [1984-1], and a few years later there appeared a detailed report on this study [Liebe,

[14] Under the conditions of a visually clear atmosphere, the influence of millimetre and submillimetre radiation scattering by small (the size up to 200 μm) particles may be neglected, as the wavelengths are much larger than the size of the scattering particles and they are not abundant. Therefore, aerosol absorption in these conditions is determined mainly by atmospheric humidity in liquid and solid phase. The methods with allowance for this part of the atmospheric absorption and the related issues were considered, for example, in the works of Liebe [1991-2] and Mätzler [2010].

1987]. The largest number of absorption measurements (about 2500) were made in pure water vapour and in a mixture with atmospheric air at six temperatures ranging from 282 K to 316 K, pressures up to 1.5 atm., and relative humidity of gases from 0 to 95 %. Besides, additional measurements of absorption in mixtures of water vapour with oxygen (at pressures up to 2.4 atm., which also allowed for the determination of values of the parameters of dry continuum), nitrogen, and argon were taken at 303 K. After subtracting the contribution of resonant lines, all numerical parameters of the expression (3.19) were found. The main results of these measurements are presented in fig. 3.44. Each point in the figures was obtained by averaging the data of numerous measurements. The solid lines were obtained by the approximation of the points by the corresponding components of the function (3.18). The dotted lines indicate the uncertainty interval.

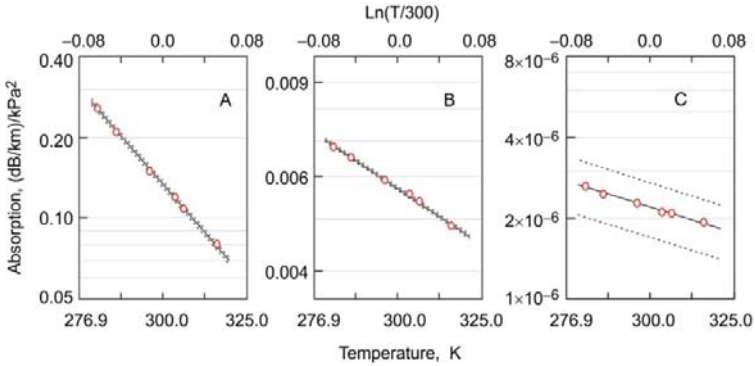

Fig. 3.44. The results of measuring the components of atmospheric continuum absorption at a frequency of 137.8 GHz [Liebe, 1987]: quadratic in humidity (*a*), linear in humidity (*b*) and humidity independent (*c)* components of absorption — summands of the function (3.18).

The next extensive cycle of studies of the continuum aimed at clarifying its physical nature was organised at the University of Lille in 1985-2002 [Bauer, 1986, 1991, 1993, 1995, 1996, 1998, 2001; Godon, 1992, 2000; Kuhn, 2002]. The used spectrometer is described in section 2.4.3. The measurements were carried out at atmospheric pressure at several frequency points in the 157–350 GHz range (fig. 2.41), at temperatures of 296–360 K. In most experiments, the absorption was measured in a mixture of water vapour and nitrogen at different humidities. Only at a frequency of 239 GHz were additional measurements made in mixtures of water vapour with carbon dioxide (CO_2) [Bauer, 1996], argon (Ar) [Bauer, 1998], methane (CH_4) [Godon, 2000], ethylene

(C_2H_4), and ethane (C_2H_6) [Bauer, 2001]. A summary of the work done and an attempt at a physical interpretation[15] of the observed continuum were given in [Bauer, 2001]. The results of absorption measurements in a mixture of water vapour and nitrogen related to the atmospheric continuum were summarised by Kuhn [2002]. Assuming that the quadratic dependence of the continuum absorption on frequency is preserved over the entire range of the measurements, the authors of that research cycle took into consideration the contribution of the resonant lines and found the continuum coefficients C_w, x_w, C_{N_2}, and x_{N_2}.

From the beginning of the 1970s to the end of the 1990s, a group of NIRFI scientists investigated the features of millimetre and submillimetre radiation absorption by air in windows of atmospheric transparency. The results of their laboratory studies [Furashov, 1985] are presented in fig. 3.45.

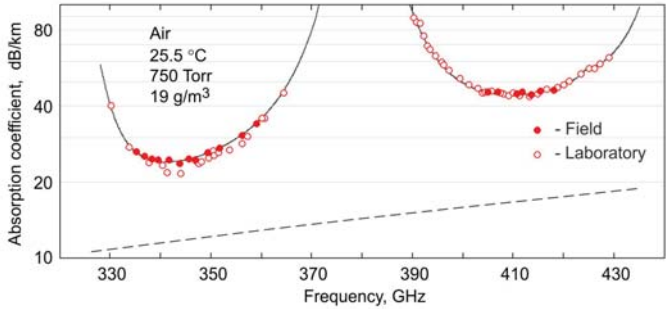

Fig. 3.45. Data of atmospheric absorption measurements [Furashov, 1984, 1985]. Field measurements — filled circles, laboratory measurements — empty circles. Calculations of the total absorption and the continuum using the present day MPM version — solid and dashed lines respectively.

The measurements were performed at room temperature, atmospheric pressure, and different air humidities under well controlled conditions using a multipass gas cell with the overall path length of approximately 140 m. The results of field measurements [Furashov, 1984] on a path along the surface of about 1 km are also given in fig. 3.45 for comparison. In all cases, the measurements were made through the scheme of the classical video spectrometer. A BWO was used as a radiation source, and an opto-acoustic detector as a receiver. Only the results of measurements of the total absorption and its subdivision into parts with linear and quadratic dependence on humidity were reported in these papers. The

[15] The authors erroneously interpreted the observed continuum as a collision-induced absorption, which was later criticised in the work [Vigasin, 2014].

contributions of the resonant lines and of the continuum were not separated. The data were recalculated for the same weather conditions using the MPM.

The results of the long-term field studies of the continuum quadratic in humidity performed by the NIRFI team can be found in the work of Katkov [1995], where data of absorption measurements in atmospheric transparency windows at 138, 247, 260, 340 and 410 GHz in the 270–310 K temperature range are presented. Based on the analysis of the obtained data (taking into account the calculated contribution of resonant lines and of the linear part of the continuum with respect to humidity[16]), the authors claim that under the conditions of the study, the power exponent of the temperature dependence of the quadratic part of the continuum with respect to humidity x_w does not go beyond the 10–15 interval. The authors note that x_w decreases with increasing frequency. However, the normalisation of the absorption obtained in their study to squared radiation frequency leads to the conclusion that all these data are in a good agreement, within the specified measurement errors (fig. 3.46).

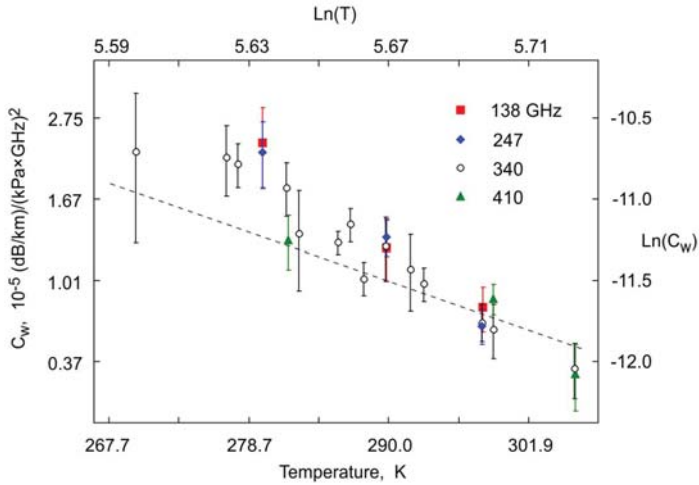

Fig. 3.46. The temperature dependence of the component of atmospheric continuum C_w quadratic with respect to the partial pressure of water vapour according to the data of figs. 1–3 from the work of Katkov [1995]. The solid line is the calculation from the present day MPM version.

[16] The difference between the calculated data presented in Table 2 from Katkov [1995] and the analogous data found using the updated MPM version does not exceed several percent, which indicates reliable results.

The results of the field study of atmospheric absorption, over a 21.4 km path along the surface in a mountainous part of Alaska in the temperature range of 4–32 °C and humidity of 3–21 g/m^3, were presented in the work of Manabe [1989]. The measurements were carried out at a frequency of 96.1 GHz using a classical video spectrometer scheme with a stabilised radiation source and a superheterodyne receiver. Periodic calibrations of the measuring equipment and active thermal stabilisation of the transmitting and receiving electronics ensured the baseline stability at a level less than 0.05 dB/km. The authors did not determine the continuum coefficients from their data but demonstrated a good agreement with the results of measurements and calculations from the MPM-87 [Liebe, 1987].

The studies of the atmospheric continuum with the use of ground-based radiometers directed vertically upwards (measurements at the zenith) and receiving the thermal radiation emitted by the atmosphere, while simultaneously measuring the atmospheric meteorological parameters using balloons with radiosondes, deserve separate consideration. A specific feature of these measurements is a much stronger dependence of the measurement result on the used absorption model than in radiometric measurements of the resonant line parameters. The results of the best-known measurements of the atmospheric brightness temperature obtained using ground-based stations at the end of the 20th century can be found in the work of Westwater [1990]. The measurements were carried out at frequencies of 20.6, 31.65, and 90.0 GHz in different climatic zones, which ensured a wide range of atmospheric temperatures and humidities. Data analysis allowed for the consideration of the advantages of one or another model used to simulate the thermal radiation of the atmosphere under the observation conditions. These data were used to refine the continuum coefficients in the MPM [Rosenkranz, 1998]. The obtained values of the coefficients are still used in this model. Examples of later, similar studies of the continuum can be found in work by Turner [2009], Payne [2011], and Wentz [2016] and references therein. The advanced capabilities of modern radiometric techniques allow for improving the agreement between the observation data and the model predictions by introducing additional multipliers to the continuum coefficients in the model. Note that the observed discrepancies may be caused not by an error in the coefficients, but by some factors and/or physical phenomena that affected the measurement results but were neglected in the model. Nevertheless, introduction of such multipliers for obtaining agreement between the experiment and the calculation in one transparency window

may also improve agreement in another, which is used as a justification for correcting the model.

The most recent laboratory study directly related to the parameters of the atmospheric continuum in the millimetre wavelength range is the cycle of measurements with the Nizhny Novgorod resonator spectrometer (section 2.4) in humid nitrogen. Only one measuring resonator with a fixed length was used in the first work of this cycle [Tretyakov, 2007]. This study showed that the results of measuring humid continuum, especially at low temperatures, may contain a significant systematic error associated with the adsorption of moisture by the resonator elements. This stimulated the development of a new differential measurement technique. Its main distinguishing feature is the simultaneous use in the spectrometer of two resonators that have the same field distribution but differ exactly twofold in length. Through the measurement principle, this method is equivalent to the path length variation method known in radiometry, which eliminates the effect of many systematic errors. The use of two resonators allowed eliminating the error (noted by the authors of all previous laboratory measurements of the continuum) associated with the adsorption of water molecules on mirrors and coupling elements of resonator spectrometers (section 2.3).

The results of long-term, regular studies of the continuum absorption of radiation in the 107–143 GHz range in humid nitrogen at atmospheric pressure and temperatures from 261 to 328 K (about a million single absorption measurements), performed using the two-resonator method, were presented in the work of Koshelev [2011]. The relative humidity of the studied mixture did not exceed 60 % to avoid the conversion of H_2O molecule adsorption by the surfaces of the resonator elements to moisture condensation. In the experimental data, this conversation manifests itself as a rapidly and nonlinearly increasing dependence of resonator loss on gas humidity. The spectrometer baseline was measured in pure nitrogen obtained by means of evaporation from liquid phase. This means that for finding total absorption, the contribution of dry continuum was subtracted simultaneously with the subtraction of the baseline, which simplified the interpretation of the data obtained.

For the convenience of comparing results, the list of the lines and the shape (1.105) were taken as the ones used for the calculation of resonant absorption in the work of Liebe [1987]. It was demonstrated that after subtracting the contribution of the H_2O resonant lines from the observed total absorption, the remaining continuum depended quadratically on frequency (fig. 3.47).

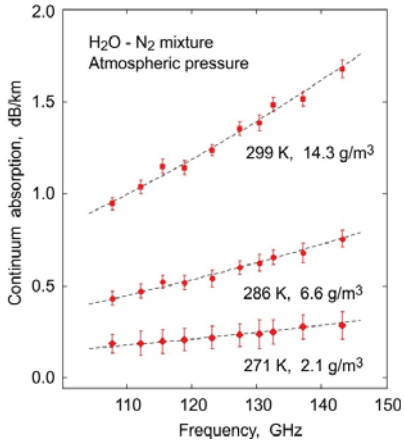

Fig. 3.47. Typical results of the continuum measurements in a mixture of water vapour and nitrogen for different combinations of temperature and humidity [Koshelev, 2011]. Dotted lines are the $y = ax^2$ function optimised to experimental data (points). Each point is the result of averaging of 256 individual measurements. The error corresponds to the rms deviation of individual measurements (1σ).

Each series of measurements analogous to that shown in fig. 3.47 allowed for obtaining coefficients characterising the continuum absorption in the studied frequency range at the corresponding temperature and humidity. Examples of the dependence of these coefficients on the partial pressure of water vapour at a constant temperature are shown in fig. 3.48.

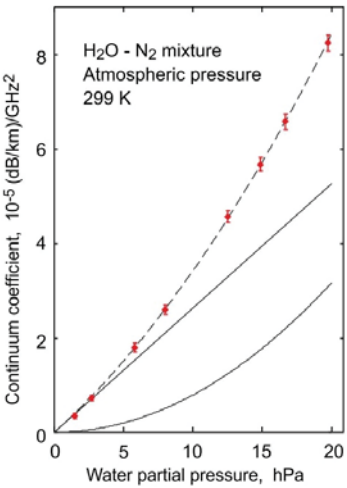

Fig. 3.48. Continuum coefficients in humid nitrogen *versus* partial pressure of water vapour [Koshelev, 2011] at three different temperatures. The error bars show rms deviation of the points from the $y = ax^2$ functions in the measurement series (fig. 3.47). Solid lines — subdivision of the 299-K dashed curve into linear and quadratic components.

According to the expression (3.19), these dependences had linear and quadratic components of humidity, which were found by the fitting

procedure and corresponded to the coefficients $C_w(T)$ and $C_{N_2}(T)$ (expression (3.18)) normalised to squared frequency at a given temperature. These coefficients, measured at different temperatures (fig. 3.49), were used to find the values of C_w, C_{N_2}, x_{N_2}, and x_w (expression (3.19)) needed for empirical modelling of the continuum. The results of the total absorption measurements were also presented in work by Koshelev [2011], enabling the refinement of the continuum coefficients when new data on resonant line parameters appear.

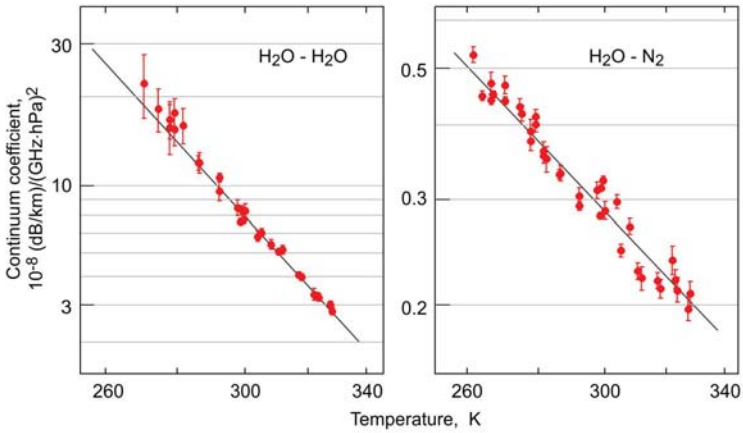

Fig. 3.49. The temperature dependence of the coefficients of continuum in humid nitrogen [Koshelev, 2011]. Each point is a coefficient for the term with quadratic (left graph) and linear (right graph) dependence on humidity of the function passing through the corresponding data series (fig. 3.48). Solid lines — the result of approximation of the points by the power function (3.19).

The result of the meticulous analysis of a series of laboratory data [Liebe, 1984-1, 1987; Bauer, 1993, 1995; Godon, 1992] on continuum absorption of centimetre and millimetre wave radiation by the atmosphere can be found in the work of Rosenkranz [1998, 1999]. The analysis was aimed at selecting the coefficients of the empirical model of the atmospheric continuum (3.19) which would be consistent with laboratory measurements and would provide the best fit of calculated absorption to results of radiometric measurements. The found coefficients are still used in the MPM.

A similar analysis of the same data, as well as results of more recent laboratory studies [Kuhn, 2003; Koshelev, 2011], with data of field

measurements on the path along the surface [Katkov, 1995] and with radiometric data [Turner, 2009; Payne, 2011; Wentz, 2016] are considered below. All the most known results of measurements of the continuum coefficients C_w and C_{air} at different temperatures, including the measurements mentioned in this section, are presented in fig. 3.50 which is analogous to figs. 2 and 5 from Rosenkranz [1998, 1999], respectively, with allowance for the $(T_0/T)^3$ factor common for all three components of the continuum mentioned above.

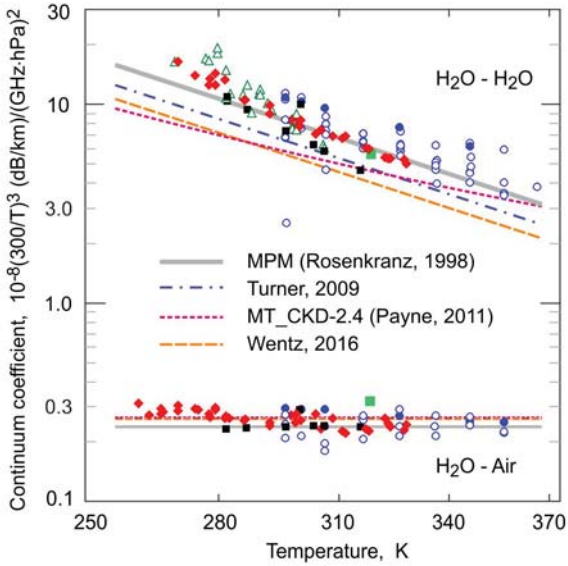

Fig. 3.50. The most known experimental data on the temperature dependence of the coefficients of the empirical model of atmospheric continuum (3.19): empty circles [Bauer, 1993, 1995; Godon, 1992]; small squares [Liebe, 1984-1, 1987]; large square [Becker, 1946]; filled circles [Kuhn, 2003]; triangles [Katkov, 1995]; rhombs [Koshelev, 2011]. Adopted from Tretyakov [2016].

The logarithmic scale used in fig. 3.50 allows for the consideration of the legitimacy of using the simplest power approximation $(T_0/T)^x$ for describing the temperature dependence of the continuum spectrum. For correct comparison of the results of continuum measurements in air and in humid nitrogen, data from Liebe [1987] were used, according to which, under identical conditions, the linear with the humidity component of the

continuum in nitrogen is 12 % larger than in air over a wide range of temperatures and humidities.

Despite the considerable scatter of experimental points from the mean magnitude of the absorption at a given temperature (30–50 % for the quadratic part (H_2O-H_2O) and 20–30 % for the linear part (H_2O-N_2)) it can be seen that, on average, different measurement series are in a good agreement. It is worthy of note that the most recent laboratory data on the quadratic part of the continuum [Koshelev, 2011] agree well with the data obtained in field conditions on an extended path along the surface [Katkov, 1995]. At room temperature, these two series of measurements gave almost the same value of the continuum absorption. The solid lines in the figure correspond to the modern version of the MPM. The MPM parameters were chosen on the basis of the above-mentioned analysis from Rosenkranz [1998]. The functions of the MPM look satisfactory in fig. 3.50, even taking into account the updated experimental data [Katkov, 1995; Kuhn, 2003; Koshelev, 2011]. Moreover, at temperatures above room temperature, the agreement can be considered good enough. At temperatures below room temperature, the results of all measurements are higher than predicted by the model. Furthermore, the most recent laboratory data from Koshelev [2011], supported by the field measurements from Katkov [1995] indicate that the part of the atmospheric continuum with quadratic humidity cannot be described by the power function $(T_0/T)^x$ which should look like a straight line on logarithmic scale. According to these data, the degree of the temperature dependence x_w in a temperature range of 300–330 K is 8.1(3), which is quite close to 7.5 from the MPM and in the 270–300 K range it is 10.6(6) which coincides, within uncertainty, with the value of 10.67 corresponding, according to the most accurate quantum-chemical calculations [Scribano, 2007], to the temperature dependence of millimetre wave absorption by stable dimers of water vapour.

Such a change in the power exponent of the temperature dependence of the continuum is due to the fact that the absorption by stable dimers dominates over other types of the bimolecular absorption at low temperatures but becomes small at high temperatures (fig. 1.22). The laboratory data from Kuhn [2003] and Koshelev [2011] also show that the growth of the linear part of the continuum with decreasing temperature is stronger than in the MPM.

For understanding whether the MPM's use of the continuum coefficients updated according to new laboratory and field experiments will lead to a better agreement with radiometric data let us address, for example, the work of Turner [2009]. Turner and co-authors showed that

the introduction of 0.79(18) and 1.11(10) multipliers into the quadratic and linear parts of the MPM continuum, respectively (dotted lines in fig. 3.50), significantly improves the agreement between the calculations of the brightness temperature of the atmosphere and the radiometry results at the zenith. Recall that the continuum coefficients are anti-correlated (expressions (1.108) and (3.18)). A decrease or an increase in the absorption model of one continuum component can be compensated by a corresponding increase or decrease of the other, so the total predicted atmospheric continuum remains approximately constant over a wide range of air humidities. A correction of the MPM based on measurements from Koshelev [2011] requires a simultaneous increase in both linear and quadratic humidity parts of the continuum, which will obviously lead to an increase in the total absorption and to a systematic discrepancy between the calculated and the measured brightness temperature. The converse statement is also true: the comparison of the result of the MPM correction based on radiometric data at the zenith with laboratory and field measurements reveals that the agreement with the model becomes worse, which is especially noticeable in the quadratic part (fig. 3.50), where the discrepancy goes beyond the permissible errors and becomes inadmissible. Similar results obtained in later and more accurate radiometric studies [Payne, 2011; Wentz, 2016] are shown in fig. 3.50 by dashed lines.

Radiometric measurements at the zenith made by different researchers in different places with different equipment under significantly differing atmospheric conditions, are consistent with each other. The general agreement of various laboratory and field measurements can be seen in fig. 3.50.

It is currently impossible to coordinate the results of these two different methods of studying atmospheric absorption with the use of a current absorption model. This issue was discussed in 2015 at the international conference dedicated to the problems of microwave radiometry of atmospheric humidity and was considered in the work of Brogniez [2016] and Tretyakov [2016]. The origin of the problem is, apparently, uncertainty of the model of atmospheric air, including insufficient accuracy of describing the distribution of thermodynamic parameters and the concentration of absorbing molecules with height rather than possible systematic errors of one or another experiment. Thus, the lack of an adequate model of the atmosphere is currently one of the factors constraining the process of improving accuracy of retrieving its parameters from radiometry data.

Summarising the analysis, we can say that within the framework of the available model of the atmosphere, the parameters of humidity related

continuum of the MPM suggested by Rosenkranz [1998] seem to be the most adequate compromise between the currently available laboratory, field, and radiometric data. We remind the readers that the values of the coefficients correspond to the calculation of the contribution of the resonant lines according to the MPM-98. Refinement of the parameters of the resonant lines requires adjustment of the continuum coefficients in accordance with the continuum definition (1.106). The accuracy limits of the modelling of radiometric data with such a set of parameters can be judged by fig. 6 from the work of Rosenkranz [1998], where the difference between the measured and calculated brightness temperature of the atmosphere observed at the zenith is shown in a wide range of humidities. The continuum parameters corresponding to the solid lines in fig. 3.50 were used for the calculations. The spread of the 'cloud' of experimental points throughout the considered range is about 6°. It can be seen against this background that at low and high humidity the calculation, on the average, is in a good agreement with the experiment. A systematic noticeable excess by approximately 2° of the experimental temperature over the calculated one is noticeable at intermediate humidities. This value corresponds to the uncertainty with which the radiation absorption by the atmosphere is currently modelled.

'Dry' continuum

Investigation of the 'dry' part of the atmospheric continuum is still more complicated and laborious because of its smallness, even compared with the 'moist' part. It is noteworthy that, despite the importance of the dry continuum for models of radiation propagation, its experimental studies in the millimetre wavelength range under conditions close to atmospheric ones were not performed until 2007 [Meshkov, 2007], and the meticulous work done at the Ohio State University with the use of a resonator spectrometer (section 2.4.3) is still the only study that provides comprehensive empirical information for dry continuum modelling.

In all previous studies that began with the works by Birnbaum (G. Birnbaum, National Bureau of Standards, USA), absorption was measured only in pure gases, in which nitrogen and oxygen are the main molecules responsible for the dry atmospheric continuum. For a very weak (but still growing as a function of squared pressure absorption) signal to become noticeable, measurements were made in pressurised gases. This demanded the development of special, small-size (a few centimetres) resonators allowing measurements to be carried out at pressures up to several hundreds of atmospheres (resonator designs for studying absorption in dry

atmospheric gases in the centimetre and millimetre wavelength ranges are described, for example, in [Bussey, 1959; Dagg, 1978]).

The first measurements of absorption in pure nitrogen were performed at a frequency of 24.35 GHz at room temperature and pressures up to 103 atm. [Birnbaum, 1962]. In a subsequent work [Ho, 1968] in measurements near 9.26 GHz at temperatures of 238–495 K and pressures up to 135 atm. the temperature dependence of nitrogen absorption was determined. A similar data set was obtained by Dagg [1975], where measurements were made near 70 GHz at temperatures of 208–333 K and pressures up to 300 atm. To verify the quadratic dependence of absorption on frequency, the same authors a little later carried out similar measurements at 140 GHz at room temperature [Dagg, 1978]. Measurements in a wider range at room temperature made by the video spectrometer scheme at a number of frequencies of within the 152–1200 GHz range using a 3-metre gas cell [Occelli, 1991] were less sensitive, but confirmed a quadratic increase of absorption with frequency.

The results of the first measurements in pure oxygen at 25 °C and pressures up to 8 atm. at a frequency of 2.3 GHz and up to 40 atm. at frequencies of 9.05 and 23.2 GHz can be found in the work of Maryott [1955]. A more thorough continuation of these studies also performed at room temperature, including measurements at frequencies near 2, 3, 9 and 23 GHz at pressures up to 70 atm., was reported in the work of Maryott [1960]. However, the physical interpretation of the obtained data is difficult even at present because of the significant contribution of resonant absorption in the 60 GHz wing of the oxygen band, which is strongly affected by collisional line coupling at such pressures (section 3.1.2).

The analysis of results of these measurements leads to the conclusion that they are in a good agreement with each other. The compliance is especially good for the data related to the millimetre and submillimetre ranges. However, the measurement error achieved in the study by Meshkov [2007] done with a resonator spectrometer is several times less, so the results of this study will be briefly discussed below.

The continuum coefficients in pure nitrogen (99.998 %), oxygen (99.993 %), and in their mixtures (79/21) were measured at frequencies within 170–240 GHz, temperatures 230–315 K and pressures up to 3 atm. In nitrogen at all pressures and temperatures, the measurement results confirmed the quadratic dependence of total absorption on frequency with a statistical error of less than 1 % and on pressure with an error less than 0.3 %. This allowed for the interpretation of the absorption as bimolecular, taking into account absence of resonant lines in nitrogen. It was assumed that the collision-induced component, that is a short-term polarisation of

molecules during collisions made the dominant contribution. The found temperature dependence of the absorption coefficient in nitrogen $C_{N_2-N_2}(T)$ is plotted in fig. 3.51 (upper solid curve). Using this dependence one can determine the coefficients of the expression (3.19) for the nitrogen continuum $C^0_{N_2} = 1.877(13)\cdot 10^{-18}$ cm^{-1}/(Torr$^2\cdot$GHz^2) at $T_0 = 300$ K and $x_{N_2} = 3.27(7)$.

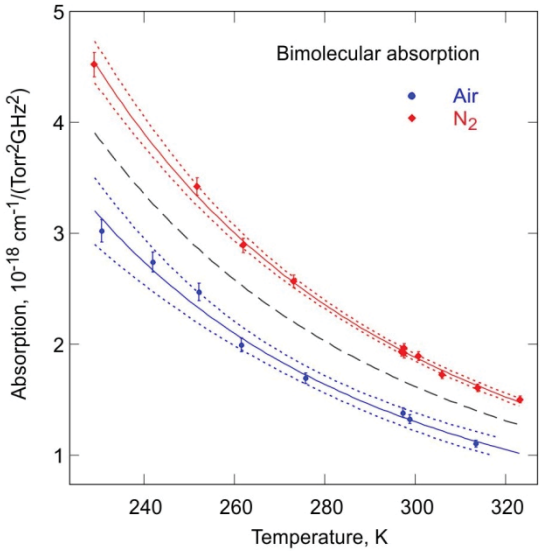

Fig. 3.51. Bimolecular absorption in pure nitrogen (upper solid curve) and in dry air (lower solid curve) normalised to squared frequency and pressure as a function of temperature [Meshkov, 2007]. Dotted lines are intervals of measurement uncertainty, the dashed line corresponds to the $0.84\cdot C_{N_2-N_2}$ dependence, which according to the calculations of collision-induced absorption [Boissoles, 2003] should correspond to 79/21 of N_2/O_2 mixture that is the equivalent of dry air.

The analysis of measurement results in pure oxygen is more complicated for several reasons: i) the collision-induced absorption in oxygen is much weaker than in nitrogen due to an almost 4 times smaller quadrupole moment of O_2 molecule than of N_2; ii) the contribution of the wings of the regular resonant lines of oxygen monomer is observable under experimental conditions; iii) a weak line around 233.95 GHz corresponding to the rotational transition of the $^{16}O^{18}O$ isotopologue in natural abundance falls into the frequency range of the study; and iv) the

Debye absorption inherent in oxygen, which, according to the preliminary estimates, was expected to dominate in experimental conditions. The parameters of the model function allowing for all these components of absorption with a minimum possible set of parameters were optimised to experimental data [Meshkov, 2007]. In this case, as in the previous studies, unambiguous interpretation of data encountered difficulties due to the strong mutual correlation of model coefficients arising mainly because it was impossible to accurately allow for the contribution of resonant absorption in O_2 lines. Hence, these measurements were called preliminary, and it was noted that the research should be continued in a wider range of frequencies and temperatures.

Absorption measurements in dry air are of greatest practical importance for atmospheric applications. These data were analysed in two stages. At the first stage, a frequency-independent component was retrieved from the total absorption, which, according to Meshkov [2007], should correspond to the Debye absorption by oxygen. The result is presented in fig. 3.52. It can be seen that, despite the considerable scatter of points associated with the correlation of the model parameters, the data obtained correspond well to the result of the calculation of the Debye absorption using the MPM. This component is calculated in the MPM by the expression corresponding to (3.10):

$$\alpha_D(\nu, p, T) = 2.552 \cdot 10^{-14} p^2 \left(\frac{300}{T}\right)^{2.8} \left(1 + \left(\frac{\gamma_D p}{\nu}\right)^2\right)^{-1}, \quad (3.20)$$

where ν is frequency in gigahertz, T is temperature in Kelvin, p is dry air pressure in Torr, γ_D = 7.47 MHz/Torr, and absorption is in reciprocal centimetres. At frequencies above 10 GHz, the last frequency-dependent factor can be neglected to an accuracy sufficient for present-day simulation of atmospheric absorption. Recall that, according to the adopted terminology, the Debye absorption is considered to be monomolecular as a result of the interaction of individual molecules with the field. Its square law variation with pressure is specified by the linear p-dependence of both intensity and collisional width of the line in the expression (3.10). At the next stage of data processing, based on the agreement of measurements and calculations (fig. 3.52), the Debye absorption calculated according to (3.20) was subtracted from the total absorption and the remaining part was interpreted as the bimolecular absorption depending quadratically on frequency and pressure [Meshkov, 2007]. Its temperature dependence is shown in fig. 3.51 (lower solid curve). The coefficients of the expression (3.19) derived from this

dependence for continuum radiation absorption in dry air are C^0_{dry} = = 1.30(4)·10^{-18} cm^{-1}/(Torr^2·GHz^2) for T_0=300 K and x_{dry}=3.35(11).

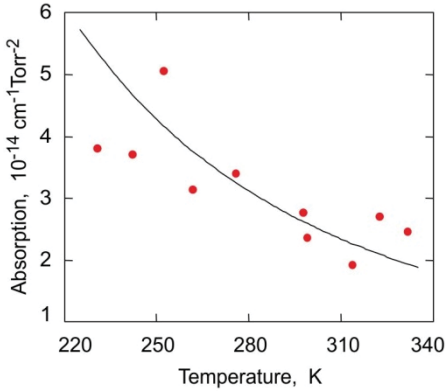

Fig. 3.52. The result of the retrieval of the frequency-independent part of absorption in the N_2/O_2 (79/21) mixture at 180–260 GHz [Meshkov, 2007] (circles) and the calculated temperature dependence of Debye absorption in dry atmosphere according to MPM (curve).

Reliability of the obtained values of continuum coefficients in dry air can be assessed in two ways. The first estimate is based on the assumption that the observed continuum is exclusively the result of collision-induced absorption. This allows for using the results of the work of Boissoles [2003], where such absorption was theoretically calculated for all possible collisional combinations: nitrogen with nitrogen, nitrogen with oxygen, and oxygen with oxygen. In dry air, which to a good accuracy can be considered to be a 79/21 percent mixture of nitrogen and oxygen, the bimolecular absorption can be represented as

$$\alpha_{air} = C_{N_2-N_2}p_{N_2}^2 + C_{N_2-O_2}p_{N_2}p_{O_2} + C_{O_2-N_2}p_{O_2}p_{N_2} + C_{O_2-O_2}p_{O_2}^2 = \\ = C_{N_2-N_2}0.79^2p^2\left(1 + \frac{C_{O_2-N_2}+C_{N_2-O_2}}{C_{N_2-N_2}}\frac{0.21}{0.79} + \frac{C_{O_2-O_2}}{C_{N_2-N_2}}\frac{0.21^2}{0.79^2}\right), \quad (3.21)$$

where all C are the spectra of the corresponding absorption components. The calculation shows that the ratio of these spectra up to frequencies of the order of several terahertz is almost independent of frequency, which means that all components have a nearly quadratic frequency dependence due to the radiation term. This ratio can be estimated as the ratio of the integrated intensities of the spectra, yielding

$$C_{O_2-N_2}/C_{N_2-N_2} = 0.106;$$
$$C_{O_2-O_2}/C_{N_2-N_2} = 0.129;$$
$$C_{N_2-O_2}/C_{N_2-N_2} = 1.143.$$

Substituting the found values into (3.21) and representing the collision-induced absorption in air in the millimetre and submillimetre ranges as a function growing quadratically with pressure $\alpha_{air} = C_{air}p^2$ give $C_{air} = 0.84C_{N_2-N_2}$. Then the spectrum of collision-induced absorption in air may be constructed from a spectrum in pure nitrogen $C_{N_2-N_2}$ which is known from the experiment. The spectrum C_{air} found in this way is shown in fig. 3.51 by a dashed line. It is a little outside of the experimental uncertainty range. Nevertheless, bearing in mind possible inaccuracy of calculations and the significant uncertainty of the contribution of monomolecular absorption in oxygen to the air continuum, the agreement can be regarded to be good.

Assessment of the magnitude of the monomolecular absorption uncertainty is the second possible estimate of reliability of the data obtained in Meshkov's work [2007]. This estimate can be made using the atmospheric absorption model MPM [Makarov, 2020], which enables separate calculation of all necessary absorption components (fig. 3.53). Obviously, the impact of the oxygen resonant line wings will be the strongest at maximal experimental pressure (3 atm.) and minimal temperature (230 K). Under these conditions, the contribution of the resonant monomolecular absorption is comparable to or even less than the Debye component. This is a manifestation of the collisional coupling effect which reduces absorption in the far wings of the interfering lines corresponding to ordinary resonant and 'zero' transitions. The influence of the latter is taken into account in the MPM through the coefficients of resonant line shape; therefore, only the total monomolecular absorption predicted by the model is physically meaningful. The integral contribution of monomolecular absorption is more than 30 % of bimolecular absorption. Hence, if it is taken into account incorrectly, the result of extracting the bimolecular absorption from the total absorption will be as incorrect. Uncertainty in the calculation of monomolecular absorption using the MPM becomes apparent when compared with similar calculations using a more accurate ECS model [Makarov, 2020] which predicts that the monomolecular absorption under these conditions should be less by about 60 %. This indicates that the frequency dependence of the monomolecular absorption was not taken into account when processing of

the obtained data in [Meshkov, 2007], which is clearly visible in fig. 3.53; moreover, its magnitude was overestimated by 60 % on average. The measurement results reported in the article referenced above allow for recalculating the obtained coefficients. This recalculation is reported by Tretyakov [2018]. It gives $C^0_{dry} = 1.63(4)\cdot 10^{-18}$ cm^{-1}/(Torr^{2}GHz^2) at $T_0 = 300$ K and $x_{dry} = 3.22(11)$, and the resulting recalculation of the temperature dependence of the continuum coefficient coincides within permissible errors with the theoretical prediction of $0.84\, C_{N_2\text{-}N_2}$, shown in fig. 3.51 by the dashed line. This agreement suggests that the dry air continuum coefficients obtained as a result of this recalculation are more accurate than the original ones. The given errors in the coefficients reflect only statistical uncertainty of the experimental data. The analysis shows that the real uncertainty of the C_{air} coefficient is hardly better than 10 %.

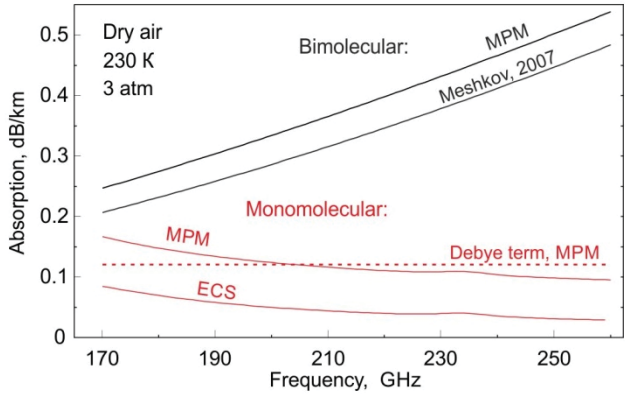

Fig. 3.53. The components of radiation absorption by dry air at 230 K and 3 atm. from [Meshkov, 2007] and by results of the calculations using the MPM and the ECS model [Makarov, 2020]. Adopted from Tretyakov [2018].

The next study of the millimetre-wave continuum absorption in dry nitrogen was undertaken with the Nizhny Novgorod resonator spectrometer [Serov, 2020]. It was performed in the 105-200 GHz frequency range, at temperatures varying within 265–310 K, and pressures from 500 Torr up to 1500 Torr. The results obtained were in a very good agreement with the absorption data from Meshkov [2007], complemented them in the frequency range and had a similar uncertainty. A unified data set from these two experimental studies was used for refining the dry air continuum

modelling. In particular, the empirical correction was introduced in the frequency dependence of the absorption, taking into account its increasing deviation from the quadratic function (eq. (3.19)) with the frequency increase in the submillimetre-wave range. The observed continuum absorption in pure N_2 was approximated by the following function

$$\alpha_{N_2-N_2}(\nu, p, T) = C_M \left(\frac{300}{T}\right)^n p^2 \frac{\nu^2}{2}\left(1 + \frac{1}{(1+\nu/450)^2}\right), \quad (3.22)$$

where frequency ν is in GHz, C_M =2.066×10^{-18} cm^{-1}/(Torr GHz)^2, and n = 3.27. The function can be used throughout the centimetre, millimetre and sub-millimetre ranges up to about 2 THz. For dry air continuum simulation, the aforementioned additional factor of 0.84 should be introduced into (3.22).

3.2.2. Physical origin of the continuum

The name of this section is historical rather than literal, as collisional (in particular, pair) interaction of molecules was mentioned at the earliest stages of research as a physical mechanism leading to the formation of continuum absorption. It proved to be the only possible mechanism after modern high-precision global calculations of vibrational-rotational spectra from first principles completely excluded the hypothesis of the origin of the continuum from a multitude of weak unknown resonant lines of a monomer. Therefore, when it comes to the nature of the continuum, it is usually understood as the distribution of the roles between various manifestations of the result of collisional interaction of molecules (sections 1.2.6 and 1.3.2). We remind the readers that these manifestations include undefined absorption in the far wings of the resonant lines of monomers, the absorption by double molecules (quasi-bound and stable dimers), and the absorption associated with an additional short-term collision-induced dipole moment in the monomers regarded to be free molecular pairs. Under ordinary conditions in water vapour, the last-named mechanism makes (according to estimates from Vigasin [1991], Leforestier [2010], and Tretyakov [2015]) a negligible contribution, so it cannot be retrieved from experimental spectra, at least at the current stage of research. In the two parts of this section, we will discuss observable manifestations in the continuum spectra of two other mechanisms related to dimers and far wings of monomers.

Spectral manifestations of stable water dimers

Many experimental studies of the atmospheric continuum have been undertaken, but only two works [Tretyakov, 2013-2; Serov, 2014] enabled unambiguous conclusions about its nature in the millimetre and submillimetre wavelength ranges. Both were carried out using the Nizhny Novgorod resonator spectrometer. The goal of the first work was the experimental verification of the presence in the spectrum of equilibrium water vapour of a periodic structure corresponding to a sequence of merged rotational lines of stable water dimers (section 1.3.3, figs. 1.28, 1.29).

The absorption periodicity followed from the results of quantum chemical calculations of the expected dimer spectrum [Scribano, 2007]. The possibility of preliminary spectrum simulation facilitated the solution of the problem [Krupnov, 2009]. In combination with known characteristics, this allowed for investigating into what frequency range and under what thermodynamic conditions it is most likely to detect a sequence of weak periodic peaks. The temperature and pressure were chosen for the following reasons. On the one hand, the lower the water vapour pressure, the narrower the characteristic peaks, which make it easier to detect them on a smoothly changing ‘pedestal’. However, collisional broadening of the peaks increases linearly and the amplitude quadratically with pressure. Therefore, it is obvious that if the peaks do not merge with each other, it is easier to detect them at highest possible humidity. On the other hand, the previous studies of humidity-related continuum showed that, when relative humidity exceeded 60 %, there appeared in the spectrum artefacts associated with moisture condensation on the elements of the measuring resonator. Vapour pressure can be increased by increasing its temperature, but this inevitably results in the significant complication of the set-up, as well as in an increase in the preparation and the duration of the experiment. These considerations determined the decision to start experiments at room temperature and 60 % humidity (pressure 12–13 Torr).

The choice of the frequency range for the first observation of the spectrum was a no less challenging problem. Recall that being a slightly asymmetric prolate top, a water dimer is very similar to a diatomic molecule. The studies of its rotational spectrum with molecular beam spectrometers at temperatures of several kelvins [Dyke, 1974; Fraser, 1989; Keutsch, 2003-1] revealed that the lines corresponding to numerous transitions with a successive increase in the total angular momentum are grouped around the lines of the transitions in which the dimer spins about

the axis with maximal moment of inertia, that is, it behaves like the simplest diatomic molecule. Note that such a pattern of rotational spectrum is typical not only for a water dimer, but also, for example, for its closest, most studied analogue – the H_2O—HF heterodimer (see papers by Belov [2007], Polyansky [2021], and references therein). Moreover, the spectra of ordinary molecules (weakly asymmetric tops) look similar, including the appearance at certain pressures of characteristic quasi-periodicity, which blurs with increasing frequency (interested readers may, for example, model the H_2CO spectrum using the HITRAN database). This means that the position of the maxima of the expected peaks in the dimer spectrum can be calculated quite well using the expression (1.22). The effective values of the rotational constants $B = 6160.6011(21)$ MHz and $D = 0.050079(91)$ MHz needed for this can be found by optimising (1.22) to the results of high-accuracy beam measurements [Dyke, 1974; Fraser, 1989; Keutsch, 2003-1] of the few first E^--type transitions ($J \to J+1$, $K = 0$). The results of this calculation are presented in Table 3.7.

Table 3.7. The measured and calculated values of the frequencies of rotational transitions of E^--type water dimers ($J \to J+1$, $K = 0$)

J	Measurement, MHz	Calculation, MHz
0	12321.00	12321
1	24640.81	24640.8
2	36958.13	36958.2
3	49271.94	49271.99
4	61580.86	61580.97
5	73884.03	73883.94
6	86179.95	86179.71
7	98467	98467.06
8	110745	110744.8
9	–	123011.7
10	–	135266.6
11	–	147508.3
12	–	159735.5
13	–	171947.2
14	–	184142.0
15	–	196318.7
16	–	208476.3
17	–	220613.4
18	–	232728.9
19	–	244821.5
20	–	256890.1

The observations at frequencies below 100 GHz did not seem promising in view of the low peak intensity, and above 400 GHz the spectrum lost its characteristic periodicity. Given possible calculation inaccuracy, the spectrum could become indistinguishable from experimental noise in these ranges. For reliable identification of the dimer spectrum, it was necessary to observe not just one, but a series of peaks. Thus, the choice of the frequency range was reduced to three intervals corresponding to the BWO bands used in the resonator spectrometer as radiation sources of 100–170, 170–260 and 260–380 GHz. The last one was excluded due to the presence of several intense lines of the H_2O monomer (fig. 3.1). The decisive factor in the choice between the two remaining ones was that the approximate frequency of the first rotational peak falling in the 100–170 GHz range was known from the low-temperature experiments [Keutsch, 2003-1].

Note that all the resonant lines of the monomer, including all its isotopologues and vibrational states, are well known in this frequency range. Only a few of them have an amplitude sufficient for them to be noticeable against the background of spectrometer noise. All of them belong either to an HDO molecule in the natural abundance of isotopes, or to the $H_2{}^{16}O$ molecule in the first excited bending vibrational state. The simulations showed that at the pressure chosen for the experiments, these lines can serve as useful markers on the spectrum recordings and do not interfere with the detection of dimeric peaks. For the calculation of the resonance spectrum of a monomer in this range, it is sufficient to take into account several dozen lines.

The very first experiment was a success. A sequence of four peaks clearly manifested itself in the recordings of the water vapour spectra in the 105–150 GHz frequency range after subtraction of the monomer contribution (fig. 3.54).

This sequence was simulated using a sum of Lorentz shapes at the frequencies of the expected dimeric peaks (Table 3.7, section 1.3.3). The positions of the peaks corresponded exactly to the frequencies of the dimer rotational lines known from low-temperature beam experiments (Table 3.7). The ‘contrast’ of the peaks was modest. They barely showed up with a signal-to-noise ratio of 2–3 (fig. 3.54). Numerous additional repeated experiments demonstrated that a series of characteristic peaks was observed in the water vapour spectrum after replacing essential spectrometer elements and after changes affecting the length of the spectrometer waveguide path. However, no characteristic peaks were observed under the same experimental conditions, if the spectrometer resonator was filled with nitrogen, which practically does not absorb radiation in this

wavelength range, or with argon instead of water. The intensity of the observed spectrum was consistent, within the measurement error, with the results of quantum chemical calculations of the dimer spectrum [Scribano, 2007], with the results of measurements of continuum absorption of radiation of this range in humid nitrogen [Koshelev, 2011], and multiply exceeded the absorption associated with the additional short-term collision-induced dipole moment in H_2O monomers [Leforestier, 2010; Tretyakov, 2015] (fig. 3.55).

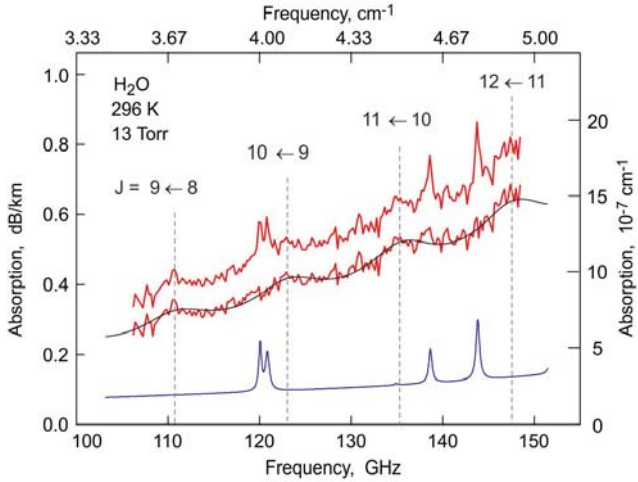

Fig. 3.54. Recording of water vapour spectrum (upper broken line) and the continuum spectrum (lower broken line) after subtraction of the calculated H_2O spectrum (lower solid line). The vertical lines correspond to the calculated frequencies of water dimer rotational transitions (Table 3.7). The smooth curve is a simplified model of dimer spectrum (section 1.3.3). Adopted from Tretyakov [2013-2].

This study provided the first undoubted confirmation that water dimers in the bound state are present in water vapour at room temperature in the amount consistent with the second virial coefficient of water vapour (equation (1.134)) [Tretyakov, 2012] and with quantum-chemical calculations [Scribano, 2006] and that, in line with the conclusions of the earlier theoretical studies [Viktorova, 1966; Vigasin, 1983; Scribano, 2007], the dimers determine the continuum absorption of millimetre waves by water vapour. Thus, as noted by Saykally [2013], it was a key step towards understanding their effect on solar absorption and chemistry in the atmosphere.

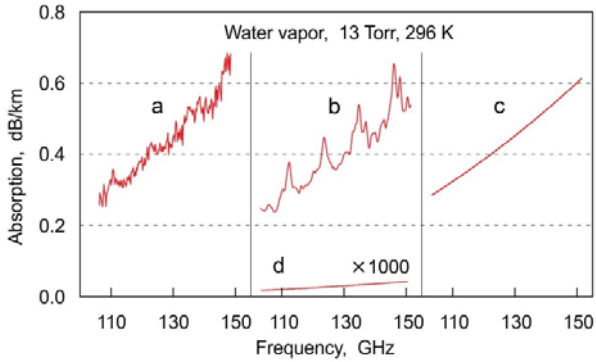

Fig. 3.55. Comparison of the observed spectrum of water vapour continuum (*a*) with the absorption found by the quantum-chemical methods [Scribano, 2007] (*b*, upper curve), with the part of the continuum with quadratic humidity in moist nitrogen [Koshelev, 2011] (*c*), and with collision-induced absorption increased by thousands of times [Leforestier, 2010] (*d*). Adopted from Tretyakov [2013-2].

The obvious difference between the experimental and the model spectra was that the width of the observed peaks was larger than of the calculated ones (fig. 3.55). The most likely reason is that the grouping of numerous lines of a very nonrigid $(H_2O)_2$ molecule into a quasi-periodic sequence of rotational peaks is less pronounced than predicted by the calculation. The narrower calculated peaks could be a result of using the symmetric top approximation. In addition, the anharmonicity of the little-studied low-frequency intermolecular vibrations and the related nonrigidity effects of the dimer structure could be underestimated.

On the one hand, the wider peaks made it difficult to observe and quantify the spectrum, but on the other hand, this indicated that higher-frequency recordings were preferable for analysis. The modelling showed that in this case, under the same conditions, the dimer lines should be more intense, and the broadening larger than the calculated ones suggested that the rotational peaks would not begin to split into components, as can be seen in the inset in fig. 1.29 but would still form a regular sequence.

A subsequent series of experiments on studying the water vapour spectrum conducted in the 190–260 GHz and 150–240 GHz frequency ranges [Serov, 2014; Koshelev, 2018] revealed nine more, as was expected, more intense rotational dimer peaks which are a continuation of the previously observed series (fig. 3.56).

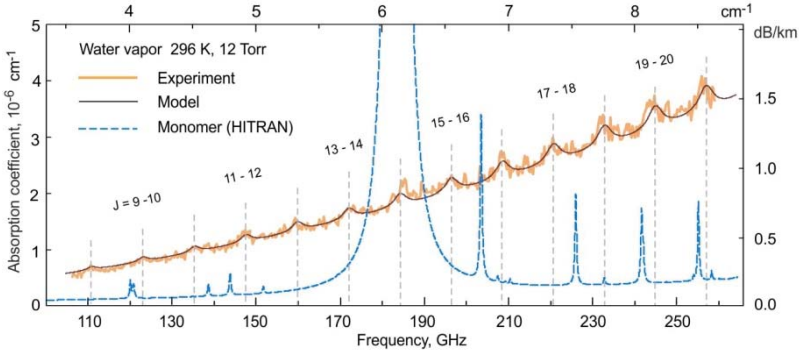

Fig. 3.56. Experimental dimer spectrum in water vapour (thick line). Thin line — approximation of the spectrum by (3.24). Dashed line — H_2O spectrum subtracted from the total absorption. Vertical dashed bars — position of E^--type rotational dimer transitions $J \rightarrow J+1$, $K=0$.

Most (about a dozen) spectra were recorded under the same conditions as in the previous work (at a temperature close to room temperature and a pressure of 12-13 Torr) using the same measuring resonator. The measurement technique conventional for resonator spectroscopy with a single resonator approximately 70 cm long was used in all these works. A single resonator was chosen to avoid increased duration of the experiment and deterioration of sensitivity of the instrument when radiation losses were measured simultaneously in two resonators (cf. section 3.2.1). There was no need for two resonators, as the absorption variations associated with dimeric peaks only slightly exceeded the maximum sensitivity of the spectrometer and refining the absolute value of non-resonant absorption by the method of variation of the resonator length was not the goal of the work. The goal of the study was to detect the sequence of peaks and analyse their position, shape, and amplitude, rather than measure absorption under the peaks. Nevertheless, the analysis of the obtained data showed that, even in this case, the measurement error of the absorption coefficient associated with possible adsorption of moisture on the resonator elements was small. This was confirmed by the fact that the absorption measured in these experiments in pure water vapour agreed well with the continuum component with quadratic humidity dependence (fig. 3.55, *a* and *b*) measured using the length variation method in humid nitrogen [Koshelev, 2011]. In addition, in Serov [2014] three recordings of the spectra were made at pressures of about 4, 27, and 34 Torr at temperatures approximately 7, 38, and 49 °C, respectively (fig. 3.57). The analysis of these data confirmed the main

conclusions of the previous work [Tretyakov, 2013-2] and enabled advancement in the quantitative analysis of the water dimer spectrum.

A simplified model of the dimer spectrum ((1.152)–(1.155)) [Odintsova, 2014] based on quantum-chemical calculations [Scribano, 2007] was used in the analysis. For adequate optimisation of this model to the experimental spectra of water vapour, the positions of the dimeric peaks should be refined.

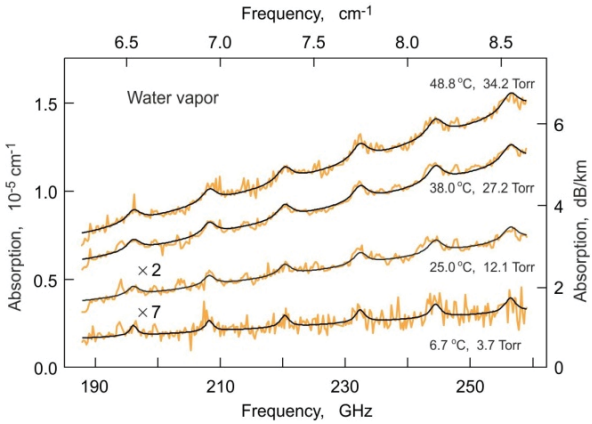

Fig. 3.57. The experimental recordings of water vapour spectrum [Serov, 2014] under different conditions (broken trace) after subtracting the monomer contribution and the result of their approximation by the model (smooth solid line). The spectra recorded at 6.7 and 25 °C are shown on 7- and 2-fold magnified amplitude scales, respectively.

With the use of the data from Table 3.7 and the results of experimental observations of the dimer spectrum at temperatures close to room temperature, it was found that the frequencies of the peaks in the observed sequence agree well with the expression

$$\nu_J = 12.326 \cdot (J+1) - 3 \cdot 10^{-4} \cdot (J+1)^3, \qquad (3.23)$$

equivalent to the expression (1.155). Besides, the model had to be supplemented with three more variable parameters taking into account:

1) the uncertainty of the value of the equilibrium constant of the dimers,
2) the uncertainty of the width of the rotational peaks of the dimer,
3) the uncertainty of the contribution to the observed absorption of the other components of the continuum, which, according to the previous studies, can be approximated by a function quadratic with respect to frequency. The resulting model of the water vapour spectrum after subtracting the monomer contribution had the following form

$$M(\nu) = A_1 \cdot \alpha(\nu, T, p, \nu_J, \gamma_J + A_2) + A_3 \cdot \nu^2 , \qquad (3.24)$$

where α is the function defined by the relations (1.152) – (1.154) and (3.23) and A_1—A_3 are the variable parameters of the model taking into account, respectively, the three factors listed above.

As already noted, the function α corresponding to the spectrum of a stable dimer also contains a smooth component, which grows quadratically with frequency and refers mainly to the *A*- and *B*-type rotational transitions (section 1.3.3). Note that one of the drawbacks of the Lorenz shape used to simulate rotational peaks in the dimer spectrum are long, slowly decaying wings, which (at large detunings from the centre) decrease quadratically with frequency. If such a model is optimised to experimental data, the variable parameters responsible for the intensity of a stable dimer spectrum (the first summand in (3.24)) and the rest of the non-resonant absorption (the second summand in (3.24)) are poorly determined due to cross-correlation. To avoid this drawback, Serov and co-authors [2014] developed an analogous model for the spectrum of bound dimers based on the sum of Gaussian functions (we will conventionally refer to the corresponding models as to Lorentzian and Gaussian). Both functions corresponded equally well to the *ab initio* spectrum of bound dimers [Scribano, 2007] in the considered range, and their use in the model (3.24) for processing experimental recordings yielded the same results within the margins of statistical error. This indicated that the correlation between the parameters of the dimeric and the remaining non-resonant absorption was insignificant, and the results obtained by the Lorentzian and Gaussian models of the dimer spectrum could be considered equivalent. An example of the result of optimisation of the Lorentzian model to the experimental records is shown in fig. 3.57.

The analysis of the variable parameters obtained by optimising the model (3.24) to the obtained experimental data provided several conclusions important for quantitative assessment of the water vapour continuum[17].

[17] Recall that the obtained results were based on quantum-chemical calculations [Scribano, 2007]. The error associated with the use of a simplified model of the interaction potential or with the method of calculating the dimer spectrum was automatically transferred to the model (3.23). The ratio of the intensities of the quasi-periodic component of the dimer absorption (*E*-type transitions) and of the smooth component (*A*- and *B*-type transitions) (section 1.3.3) makes the strongest impact on the result of the analysis.

The first of them concerns K_2^B, that is the equilibrium constant of stable dimers. The results of the *ab initio* calculation of K_2^B in a temperature range of 190–390 K were reported by Scribano [2006]. They were used in quantum-chemical calculations of the dimer spectrum [Scribano, 2007] and, hence, K_2^B (T) from later work by Scribano [2006] implicitly enters as a factor into the first term of the model (3.24). This means that the coefficients A_1 obtained by optimising the model to the observed spectra are, actually, the experimentally determined correction factors to the calculated values of K_2^B. The values of the constant found in this way are shown by diamonds in fig. 3.58. The average value over all experimental data and two models (Lorentzian and Gaussian) of the correction factor was 0.65(6). The dashed red line corresponds to the result of calculation from Scribano [2006] multiplied by 0.65. The other known data characterising the temperature dependence of the dimerization constant are also given in this figure for comparison. The thin solid blue curve and the circles were calculated according to (1.147) with *B(T)* from the empirical data from Tretyakov [2012] and from first principles from Leforestier [2014], respectively. These data are the upper limit for K_2^B as they characterise the total sum of dimers in stable and metastable states. The crosses show the values found by the measurements of the thermal conductivity [Curtiss, 1979] determined by all stable and partially by metastable dimers. The light blue dash-dotted and black dotted lines were obtained for stable dimers, respectively, from the association theory from Evans [2000] (corrected by accurate D_0 value determined later) and from classical calculations from Buryak [2015] using the interaction potential from the work by Góra [2014].

From fig. 3.58, it is clear that the experimental data on the temperature dependence of K_2^B in water vapour confirm the quantum-chemical calculations from Scribano [2006], taking into account the factor 0.65. Such a decrease was expected. The point is that the value $D_0 = 1234$ cm^{-1} was used for the dimer dissociation energy in the work [Scribano, 2006]. Later experimental studies, by Rocher-Casterline [2011] gave a value of 1105(10) cm^{-1}, which was confirmed by subsequent high-precision *ab initio* calculations by Leforestier [2012] that gave 1108 cm^{-1}.

The dimerization constant is related to the dissociation energy (see, for example, Scribano, 2006) as

$$K_2 \sim \exp\left(\frac{D_0}{kT}\right), \qquad (3.25)$$

from which, it follows that the correction factor for calculating the dimerization constant corresponding to the change in D_0 is exp((1108–1234)/kT)), which is from 0.52 to 0.59 in the temperature range of the experiment 280–322 K. This is consistent with the experimentally found value of 0.65(6) within the margin of statistical measurement error. Thus, the results of observations of the resolved rotational spectrum of dimers confirmed that the equilibrium constant of stable water vapour dimers can be calculated using the results of the work from Scribano [2006], which, taking into account the mentioned correction factor, are approximated by the expression

$$K_2^B(T) = 4.7856 \cdot 10^{-4} \cdot \exp\left(1669.8 / T - 5.10485 \cdot 10^{-3} T\right), \quad (3.26)$$

from which the value of the constant is obtained in units of atm^{-1}. The corresponding curve is shown in fig. 3.58 by a thick solid line.

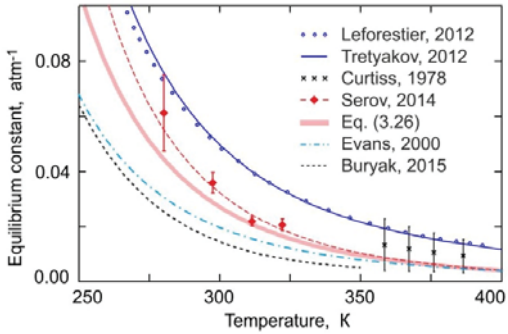

Fig. 3.58. Temperature dependence of the water vapour dimerization constant.

The second conclusion concerns the estimation of the mean collisional broadening of the dimer spectral lines in equilibrium water vapour. The estimate obtained from the pressure dependence of A_2 found using the Lorentzian and Gaussian models gave the values of 13(3) and 15(4) MHz/Torr, respectively. Note that this agrees remarkably well with the 14.3 MHz/Torr weighted mean self-broadening coefficient of the purely rotational spectrum of the H_2O molecule at 296 K. The population of the lower level of the corresponding rotational transition is taken as the weight, with allowance for the rotational degeneracy factor, so the weight is proportional to the probability of a collision with a molecule in this state. We remind the reader that under these conditions the dimer fraction in water vapour is less than 10^{-3} (section 1.3.2), and it is the H_2O molecules that are the major collisional partners of the dimer which determines broadening of the dimer spectrum. Such an estimate of the broadening parameter is valid, provided that the inhomogeneous broadening

of the rotational peak, determined by the frequency and intensity distribution of its constituent individual resonant lines, is much less than its homogeneous (collisional) broadening. Under the conditions of the considered experiments, the homogeneous-to-inhomogeneous broadening ratio is apparently small; moreover, it decreases with increasing frequency (peak number).

Another more rigorous method for estimating the mean coefficient of collisional line broadening of a dense dimer spectrum is the Pickett method [Pickett, 1980-2]. It is based on the possibility of calculating the homogeneous pressure broadening of any arbitrarily complex spectrum using a convolution of the original spectrum with a Lorentz shape having a half-width equal to the average broadening of individual lines of the spectrum. The spectrum recorded at a high pressure is compared with the convolution of the spectrum recorded at a low pressure. The width of the Lorentz function is the variable parameter. The ratio of the Lorentz function width to the difference of the pressures at which the spectra are recorded giving the best fitting result is the mean broadening parameter of the lines. The use of this method for the experimental spectra of a water dimer is illustrated in fig. 3.59. The parameter of broadening dimer lines by water vapour pressure found in this way and averaged over all pairs of available spectra was 13 MHz/Torr, which confirmed the validity of the estimate made using the above-mentioned method.

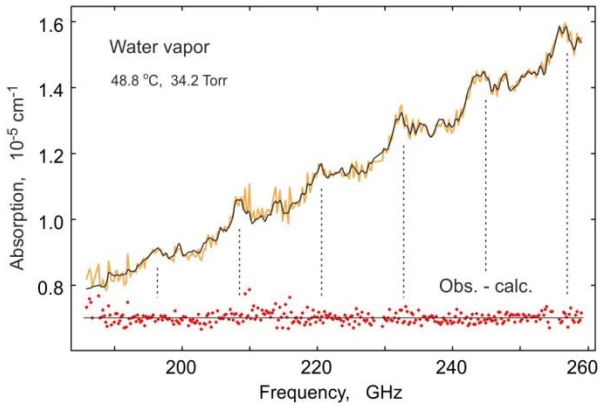

Fig. 3.59. The experimental recording of the spectrum of water vapour continuum [Serov, 2014] (broken line) and the result of optimisation of the model based on the convolution of the spectrum recorded at 298.3 K and 12.1 Torr (solid line). The difference between the observed and the calculated spectra is shown below by dots. The vertical lines are the positions of the E^--type water dimer lines $(J \rightarrow J+1, K=0)$.

It should be noted that the good agreement between the convolution models and the real spectra, as well as the agreement of the spectra recorded over a few years using significantly different equipment noted in [Koshelev, 2018], gives confidence that most large-scale inhomogeneities in the spectrum are typical spectral features or 'fingerprints' of dimers, rather than experimental noise.

The third conclusion is related to the resulting amplitude of the second term of the model (3.24). Approximately half of the observed continuum cannot be referred to stable dimers. From the previous assessments [Vigasin, 1991; Leforestier, 2010; Tretyakov, 2015], it follows that the contribution of 'free pairs', i.e., of the absorption caused by an additional transient dipole moment that appears in molecules during collisions, is negligible under the considered experimental conditions. Dimers in metastable states do contribute to the continuum. Their amount can be estimated through the equilibrium constant equal to the difference of the values between the blue and pink curves in fig. 3.58 and is comparable to the number of stable dimers. The simulation of the spectrum of metastable dimers using the simplest models discussed in section 1.3.3 (as a doubled monomer spectrum or as a bound dimer spectrum taking into account homogeneous broadening due to a short lifetime) showed that the 'metadimeric' mechanism alone is insufficient to explain the remaining part of the experimentally observed continuum. The emergence of an 'excess' continuum indicated for the first time that the total observed radiation absorption is not explained in the framework of the traditional concepts of monomolecular and bimolecular absorption in water vapour.

At the final stage of this experimental cycle, a series of measurements of the continuum in a mixture of water vapour with atmospheric air was carried out. The partial pressure of water vapour was approximately the same in all experiments (about 10 Torr), and the air pressure gradually increased almost to the atmospheric pressure. Quantitative analysis of these spectra is much more difficult than the analysis of the spectra of pure water vapour since the components corresponding to the collisional interaction of water molecules with nitrogen and oxygen molecules appear in the total absorption. These spectra, as well as the spectrum of water vapour, can have their characteristic features associated with collisional formation of poorly studied molecular complexes (heterodimers) $H_2O—N_2$ and $H_2O—O_2$. Only a mean non-resonant component increasing quadratically with frequency (the humidity-linear continuum) is known for these spectra (section 3.2.1). Its calculated value was subtracted from the experimental spectra along with resonant lines. Nevertheless, the quasi-

periodic spectrum typical of a water dimer was located, strictly speaking, on an unknown 'pedestal'. With a slight dilution of water vapour with air (approximately up to 80 Torr), the impact of this pedestal was small, and the obtained spectra were analysed using the convolution model. This allowed for the determination of an approximate value of the mean collisional broadening coefficient of water dimer lines by air pressure. It was approximately half as large as for broadening by water vapour pressure. This value was used to analyse spectra at higher air pressures. For this, it was necessary to determine the 'shape' of the pedestal, which was done empirically, considering that the characteristic frequency scale of pedestal changes is much larger than the scale of the changes corresponding to the rotational peaks in the dimer spectrum. The dimer spectrum calculated by the convolution model for the experimental conditions was subtracted from the observed spectrum, and the rest was approximated by a sextic polynomial. The obtained function described 'slow' absorption variations with frequency, without affecting its small-scale changes associated with possible inaccuracy of the dimeric spectrum subtraction. After subtracting this function from the original spectra, they were analysed using the Lorentz model of the dimer spectrum and the convolution model. The result is presented in fig. 3.60.

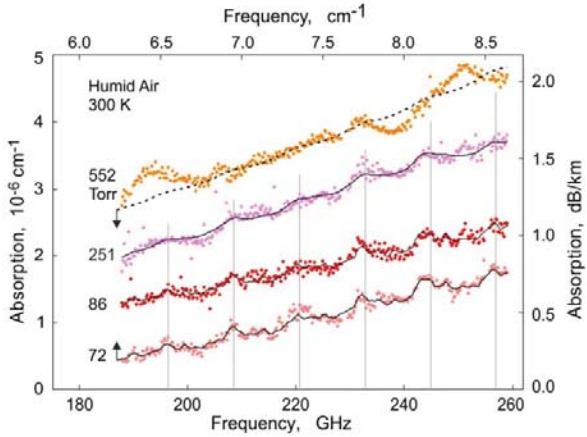

Fig. 3.60. The recordings of humid air spectra at room temperature (dots) and optimised model functions obtained by the convolution with the result of averaging the spectra recorded in pure water vapour (solid lines) at a pressure of about 10 Torr. The lower and upper spectra are shifted down by 10^{-6} and up by $5 \cdot 10^{-7}$ cm^{-1}, respectively. Adopted from Serov [2014].

No trace of the dimer spectrum was detected in the spectrum recording at 552 Torr. This is due to the fact that, at this pressure, the estimated width of the dimeric peak exceeds the distance between the peaks and the dimer spectrum is almost completely blurred by collisional broadening (the modelled dimer spectrum under these conditions is shown by a dotted line). The analysis of the remaining three recordings somewhat clarified the mean coefficient of dimer spectrum broadening by air pressure, which was found to be 6.3(21) MHz/Torr, and the dimerization constant of water vapour in air was verified. The uncertainty was about 20 %, but the average value of the constant exactly coincided with the value obtained from the analysis of the pure water vapour spectra. This confirmed that the 'third body' in the formation of a dimer (the most likely collision partner of the water dimer in air is a nitrogen or oxygen molecule) only takes excess energy but does not affect the equilibrium constant value.

Thus, resonator spectroscopy enabled the obtainment of unique experimental data describing the spectral properties of a water dimer under conditions close to atmospheric ones. A regular continuous sequence consisting of 13 peaks predicted by modern quantum-chemical calculations as a superposition of resonant rotational lines of a stable dimer was experimentally recorded in the spectra of water vapour in the 110–260 GHz range. The shape of the spectrum of a 'warm' water dimer in the specified frequency range was determined thanks to the sufficient signal-to-noise ratio in the recorded spectra and their reproducibility over a wide range of temperatures (288–322 K) and pressures (3.7–34.2 Torr). This can be used in the future as a reliable support for improving accuracy of the calculations from first principles. Analysis of the spectra allowed for the determination of, for the first-time, average values for the parameters of the collisional broadening of dimer lines by water vapour and air pressure.

The experimental confirmation that the dilution of water vapour with air does not alter the total intensity of the dimer spectrum and only leads to homogeneous broadening and the related 'smoothing' of the spectrum is of great importance for practical applications. The coefficients of the simplified model of a dimer spectrum [Odintsova, 2014], needed for its use in modelling the propagation of radiation in the atmosphere, were refined.

The most important result of this work in the field of fundamental spectroscopy was the discovery of 'excess' continuum in water vapour, which indicated that, in the framework of the established concepts, it is impossible to give a consistent description of the observed absorption. This allowed for the formulation of the problem and stimulated the study,

the results of which are summarised in the next section. It is not related to resonator spectroscopy but is directly relevant to the issues addressed here.

The contribution of resonant line far wings

To find a way for solution of the problem of the water vapour 'excess continuum' detected in the millimetre wavelength range, it is necessary to analyse the continuum spectrum over the entire range of the H_2O molecule rotational spectrum. This should be done analogously to the analysis of the continuum in the millimetre range, taking the results of this analysis into account. The main indications that such an analysis could provide an answer to the question on the nature of the excess continuum are the following two facts: 1) the monomer spectrum in this area is well studied; 2) the spectrum of a stable dimer in this region is known from quantum-chemical calculations [Scribano, 2007], and the information about it is supported by direct measurements in the millimetre-wave range. To eliminate the fundamental uncertainties associated with the use of approximate models for interpreting absorption at the edge of the band, the study should be performed in a wide spectral range. For example, any bell-shaped function can be used for the crude qualitative description of the profile of the envelope of an individual band of a vibrational-rotational spectrum (e.g., the simulation of vibrational-rotational bands of a dimer spectrum by the Lorentz function in [Ptashnik, 2011; Odintsova, 2013]). Satisfactory agreement can be obtained for the band as a whole, but significant divergences may be observed in its wings.

The rotational spectrum of the H_2O molecule extends from the radio band up to frequencies of 20–30 THz. Continuum absorption in its low-frequency part (approximately up to 0.4–0.5 THz) can be considered to be quite well studied (section 3.2.1). The results of several single (poorly consistent either with each other or with measurement data in the millimetre range) measurements of absorption in water vapour in transparency microwindows are known in the 0.4–1.5 THz range (see Burch, 1981; Slocum, 2015 and references therein) and in the 0.6–2.6 THz range [Podobedov, 2008]. There was no experimental information about the continuum in the region of the maximum of the rotational H_2O spectrum (3–6 THz) corresponding to the region of the 'spectroscopic gap' (in related areas of physics it is often called the 'terahertz gap'), which is called so because of the lack of suitable radiation sources. The results of the continuum study in the range of the high-frequency wing of the band (10–40 THz) were reported by Burch [1981]. So, the results of

the previous studies did not provide the information needed for the analysis.

The Fourier spectrometers using a synchrotron as a broad-band bright radiation source seemed to be the only possible way to obtain new experimental data in a required range, with a sensitivity that would allow the continuum spectrum to be quantitatively analysed after subtracting the monomer resonant absorption. The proposal for performing such a study at the SOLEIL synchrotron was supported. The details of this work and the results obtained during three measurement companies can be found in papers by Odintsova [2017, 2019, 2020]. A conventional water sample and ^{18}O enriched water sample (97 % enrichment) were used for cross-checking the obtained data. The spectra of $H_2{}^{16}O$ and $H_2{}^{18}O$ molecules are different but the interaction potential is practically the same, so the bimolecular spectra of these water isotopologues are expected to be very close.

With the use of the synchrotron, it became possible to register the absorption spectra of water vapour and to retrieve from them the continuum in a uniquely wide frequency range of 0.4–17 THz (or 14–500 cm^{-1} that are frequency units traditional for IR spectroscopy, corresponding to the reciprocal of the radiation wavelength in centimetres). The study was performed at room temperature using a Bruker IFS-125 HR spectrometer equipped with a multipass gas cell with an effective interaction path length of 151.8(15) m. Given hard constraint on the dedicated synchrotron time, the selection of optimal experimental conditions was a critical task complicated by the specific features of water vapour continuum studies. To ensure high sensitivity, the spectrum, on the one hand, had to be recorded at maximum possible path length and maximum possible water vapour pressure, as the magnitude of the continuum increases in proportion to squared pressure. On the other hand, the recording should remain spectroscopically informative, that is, for controlling reliability of the obtained data, the shape of at least part of the observed resonant lines must be analysed. For this, the optical thickness of the gas must be less than 10. The spectrum should not exhibit the adsorption-related effects, especially water vapour condensation, i.e., the maximum humidity should be no more than 60–65 % of the saturating one. At least two spectrum recordings at different pressures are required to verify that the observed continuum depends quadratically on pressure, which means that it is specified by bimolecular absorption rather than by experimental artefacts. Using the results of extensive modelling of expected spectra, three recordings were made in the 14–35 cm^{-1} range (in the coherent radiation mode of synchrotron electron bunches) at pressures

of about 8, 10 and 12 Torr, and three in the 40–650 cm^{-1} range (in the standard synchrotron mode) at pressures of 2, 4 and 6 Torr. The value of pressure less than in the low-frequency experiment follows from the condition of maintaining spectroscopic informativity in the range of higher-intensity resonant lines. Additionally, a series of short-term recordings in the 40–650 cm^{-1} range at gradually increasing pressure was made for verification of the continuum pressure dependence.

The continuum was determined as the difference between the total observed and calculated resonant absorption in monomer lines. The monomer spectrum was calculated using the HITRAN data (all significant lines of the five most abundant isotopologues of H_2O) and the 'truncated' Van Vleck–Weisskopf profile (1.105). In the range of 14–35 cm^{-1}, the continuum was determined in all parts of the spectrum where the optical depth was less than unity (fig. 3.61). In the 40–500 cm^{-1} range, the continuum was retrieved, as is usually done in the IR range [Burch, 1981; Podobedov, 2008; Ptashnik, 2011, Baranov, 2008], as the difference between the observed and calculated absorption only in the spectrum minima corresponding to the transparency microwindows between the resonant lines (it is believed that this minimises the impact of the uncertainty of resonant line parameters). A very good quadratic pressure dependence of the resulting absorption continuum, as well as close similarity of the two isotopologue continua were demonstrated.

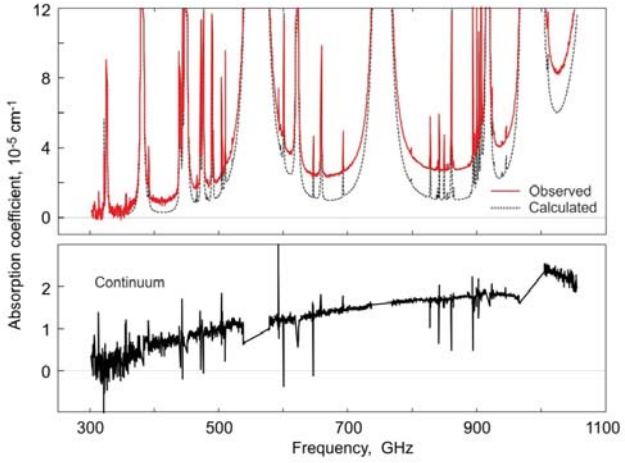

Fig. 3.61. Top – water vapour spectrum at 296 K and 11.3 Torr according to Odintsova [2019] (solid line – experimental recording, dotted line – resonant absorption calculation. Bottom – continuum absorption determined as the difference between the two upper spectra (bold noise line).

The continuum found in this way is compared with all the best-known data from the previous experimental studies in fig. 3.62. The results of the calculations by the MT-CKD model of the continuum used worldwide for atmospheric applications (see, for example, Mlawer, 2012 and references therein) are also shown by the solid line for comparison with the experimental data. The other method of resonant absorption calculation in MT-CKD is taken into account.

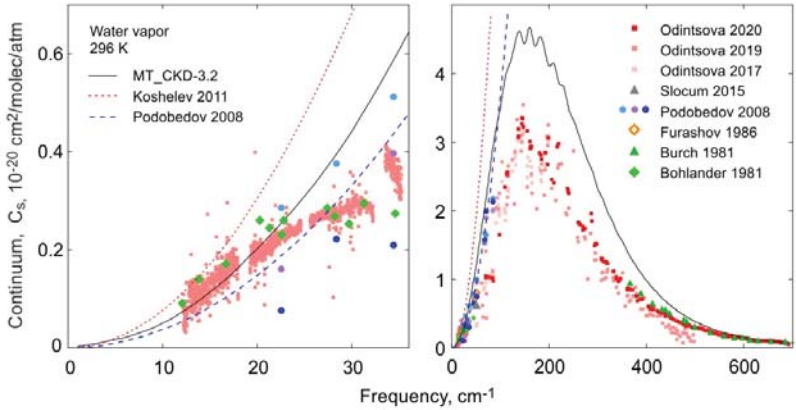

Fig. 3.62. Water vapour continuum in the region of rotational spectrum of H_2O molecule according to all best-known studies. The left panel is a zoomed-in part of the right panel.

Despite the considerable scatter of points, it can be seen that, on the whole, all the experimental data agree well with each other and provide an insight into the water vapour continuum in this part of the spectrum. Systematic measurement error can be traced, for example, in the 40–80 cm^{-1} range, where the data obtained by Podobedov [2008] are higher than the measurement results from Slocum [2015]. The data reported by Slocum [2015] were obtained in a relatively narrow (about 3 cm^{-1}) frequency range, but the results of the simultaneous processing of 145 spectra recorded with a good signal-to-noise ratio in the pressure range of 2–15 Torr and with the path length varying from 2 to 8 m demonstrate that they are quite reliable and in a good agreement with the new data. It is also shown that the MT-CKD semiempirical model overestimates the continuum absorption significantly, by 30 % to 100 %. The new measurements fill the 90–350 cm^{-1} gap where the water vapour continuum was not measured before.

It is worth noting that the value of these measurements with a synchrotron is not limited to the complementary and correcting function. The results of measurements in the 14–35 cm^{-1} range (fig. 3.62, left panel) resolved one of the long-standing contradictions of the continuum of the millimetre and submillimetre wavelengths. Namely, the theoretical assumptions and measurements in the millimetre range indicated that the continuum should grow quadratically with increasing frequency. However, the early measurements performed at several points in the submillimetre range [Llewellyn-Jones, 1978; Burch, 1981; Furashov, 1966] pointed to some 'slowing down' of the growth. Moreover, a systematic study of the continuum performed at 22–86 cm^{-1} [Podobedov, 2008] confirmed the absorption growth quadratic with frequency but the found continuum coefficient C_w^0 proved to be approximately twice less than from measurements in the millimetre-wave range. The impossibility of resolving this problem without additional experimental data is, in particular, confirmed by the fact that the semiempirical MT-CKD model predicted a quadratic growth of the continuum for the millimetre and submillimetre wavelengths, but with an average value of the coefficient, as seen in fig. 3.62, left panel.

The fact that the 'slowing down' of the continuum growth was not accepted by the community is due in part to all sorts of artefacts and systematic errors in the studies of the water vapour spectrum, especially in the submillimetre range that is hard-to-reach even today. One example (see the review by Tretyakov [2014]) is the erroneous detection of dimeric bands in the absorption spectrum of water vapour published in 'Nature' [Gebbie, 1969]. Apparently for the same reason, data from the series of measurements by R.A. Bohlander [Burch, 1981] (shown by green rhombs in fig. 3.62) demonstrating a smooth transition in the 20 cm^{-1} region from the rapidly growing quadratic dependence in the millimetre range to a slow growth at shorter wavelengths were not published and unfairly forgotten. New data from Odintsova [2017; 2019] confirmed the reality of this transition, thus reconciling the results of the earlier studies.

To get an insight into the nature of this specific feature of the continuum spectrum, let us again refer to the work of Scribano [2007], devoted to quantum-chemical calculations of the spectrum of stable dimers. In the previous section, it was noted that this spectrum has much in common with the spectra of weakly asymmetric prolate tops, including their characteristic quasi-periodicity corresponding to the rotation about the axis with maximal moment of inertia. Based on this similarity, it can be argued that the envelope of the water dimer rotational spectrum will also have a characteristic bell-shaped appearance (fig. 1.4), reaching its

maximum near 16 cm^{-1} at room temperature. In this region of the calculated dimer spectrum (fig. 13 from Scribano [2007]), a wide 'hill'[18] is observed against the background of a general increase in intensity due to the overlapping of the lines of *A*- and *B*-type transitions of bound water dimer (fig. 1 from Odintsova [2014]). Obviously, the calculated dimer spectrum can be compared with the spectrum of the observed continuum only, like in the analysis of quasi-periodicity of the water vapour continuum in the millimetre range, i.e., taking into account details of the calculation and additional absorption mechanisms that become apparent during the experiment (section 3.2.1). In particular, the observed hill must be slightly higher in frequency (the rotational constant *B* of the dimer spectrum is about 9 % larger than that obtained in the calculations), wider (for the same reason why the rotational peaks turned out to be wider) and must be located on top of the 'pedestal' of the absorption with comparable magnitude and growing with frequency (corresponding to the absorption by quasi-bound dimers and, possibly, by the far wings of monomer lines). With all this taken into consideration, we can say that the shape, size, and position of the specific feature observed in the spectrum of water vapour continuum in the 14–35 cm^{-1} range agree with the results of *ab initio* calculations. The agreement is even more pronounced if the observed and calculated spectra are compared after removal of their frequency dependence inherent in the radiation term, which is universal for all molecular absorbers and thus can hide individual spectral features [Frommhold, 2006]. In the millimetre-submillimetre-wave range this universal dependence is very close to the frequency-squared one. The spectra normalised by squared frequency are compared in fig. 3.63, where a very good agreement of the observed continuum with the results of *ab initio* calculations of water dimer spectrum is an independent experimental confirmation of the manifestation of dimeric absorption in the equilibrium water vapour and dominating contribution of dimers to the observed continuum in this domain. In addition, this agreement adds confidence that the result of dimer spectrum calculations [Scribano, 2007] can be used for interpreting the continuum in a higher frequency region as well.

[18] This feature of the dimer spectrum was also predicted in the earlier calculations [Viktorova, 1970; Vigasin, 1983], in which a simplified dimer model was used.

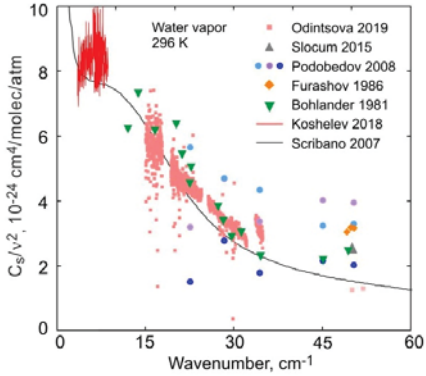

Fig. 3.63. Water vapour continuum normalised by squared frequency.

Considering that the magnitude of the water vapour continuum in the region of the monomer rotational spectrum is established, we can turn to analysis of its components presented in fig. 3.64. The shape of all components is similar to that of the continuum; therefore, for approximate estimates of the contributions of the components, we will use their relative amplitude in the region of the peak. According to the results of the calculations from Leforestier [2010], the absorption related to the collision-induced dipole moment (the interaction of the molecules forming free pairs) is about 0.1 % (dotted curve in fig. 3.64 with 100-fold magnification). Note that this is an upper estimate, since the calculation does not take into account the collisional formation of dimers, which reduces significantly the manifestation of the effect [Tretyakov, 2015]. For the calculation of the total dimeric absorption (including bound and quasi-bound states) we use known data on the second virial coefficient [Tretyakov, 2012], equilibrium constant [Serov, 2014], the spectrum of stable dimers [Scribano, 2007] (the solid curve at the bottom of fig. 3.64), as well as the two simplest models of metastable dimers (section 1.3.3) in which the spectrum of metastable dimers is calculated like that of stable ones (long-dashed curve) or like a double monomer spectrum (dash-dotted curve). This allows for attributing to dimeric absorption 30 to 55 % of the observed continuum. According to modern concepts, the wings of the monomer resonant lines correspond quite well to the Lorentz or Van Vleck–Weisskopf model up to detuning of 25 cm^{-1} from the centre — this is the value used for the cutoff frequency in the calculations of the monomer spectrum for retrieving the continuum. Uncertainty starts with detunings exceeding 25 cm^{-1}; however, it was found [Winters, 1964] that the rate of absorption decay in the wings of real lines increases up to an

exponential value. So, real absorption is smaller than predicted by the Lorentz function. Such behaviour is called ‘sub-Lorentzian’. This means that the upper estimate of the contribution of the resonant lines to the continuum is attained if their wings are approximated by the Lorentz function up to infinite detunings. The calculation shows that increasing the cutoff frequency up to more than 100 cm^{-1} almost ceases to influence the result, i.e., the maximal uncertainty of the far wings contribution can be roughly assessed as the difference of two monomer spectra calculated with a wing cutoff frequency of 100 and 25 cm^{-1}. The resulting maximal estimate of the impact of the far wings is approximately 10 % of the continuum.

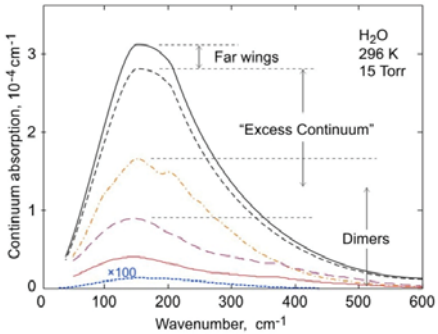

Fig. 3.64. Water vapour continuum in the region of rotational spectrum of H_2O molecule and its components. The upper solid and dashed lines are the result of approximation of measurements [Odintsova, 2017; Odintsova, 2019] with a wing cutoff frequency of 25 and 100 cm^{-1}. The lower lines denote model bimolecular absorption spectra (see the body of the text).

In summary, we find that about half of the continuum observed in experiment has no explanation in the framework of the modern concepts.

Note that the above estimates are basically qualitative in nature, as they imply the validity of spectrum calculations [Scribano, 2007] and the accuracy of the equilibrium constant correction [Serov, 2014] of stable dimers discussed in the previous section. Nevertheless, the magnitude of the found ‘excess continuum’ is too large to be explained by inaccuracies of the assumptions and data used for the evaluation. This suggests that the excess continuum is quite possible.

Since there was no reason for a significant (several-fold) increase of the estimate of dimeric absorption, the most likely explanation of the excess continuum was an underestimation of the contribution of the resonant line far wings due to uncertainty of their assessment in the

framework of the established concepts (section 1.2.6). This hypothesis could be verified by an analogous qualitative analysis of the total continuum absorption in two bands of fundamental vibrations of H_2O corresponding to bending (~1595 cm^{-1}) and stretching of bonds (antisymmetric ~3756 cm^{-1} and almost 20 times less intense symmetric ~3651 cm^{-1}), since the features of the shape of the far wing lines are expected to manifest themselves in all these spectral ranges in the same or very similar way. The continuum spectrum in these areas was relatively well studied (see, for example, the review from Shine [2012] and references therein). A complicating circumstance was that the amount of information about the dimer spectrum was significantly less than in the region of the rotational H_2O band. Nevertheless, the calculated data [Kjaergaard, 2008] on the position and integral intensity of the main dimer bands, partially confirmed experimentally, enabled such an analysis [Ptashnik, 2011]. With the restriction on the total amount of dimers determined by the value of the second virial coefficient (section 1.3.2) taken into consideration, a later works from Shine [2016], Ptashnik [2019], and Simonova [2022] showed that the excess continuum also occurs in these and other H_2O bands.

Evidence in favour of the hypothesis about the role of monomer far wings in the formation of excess continuum could be a model of far wings shape universal for all three (rotational and two fundamental vibrational) spectral bands of the H_2O molecule, which would give a quantitative explanation of the magnitude of the continuum within the most significant part of the band. Such a model was proposed in the work of Serov [2017].

The simulation was based on the ideology of the continuum description using an empirically fitted χ function [Clough, 1989] by which the remainder of the truncation of the line shape function in the impact approximation is multiplied. That is, the resonant absorption in the region of detunings $|\nu - \nu_0| \le \nu_{cut}$ is modelled using the line lists from the HITRAN database as the profile (1.103) with truncation (1.105). To obtain monomolecular absorption, the result of the modelling should be complemented with the modified wings:

$$\alpha_{wing}(\nu,\nu_0) = a_{ab} R(\nu,\nu_0)\cdot\left(I_c(\nu,\nu_0)\chi(\nu,\nu_0) + I_c(\nu,-\nu_0)\chi(\nu,-\nu_0)\right),$$

$$\chi(\nu,\nu_0) = \left(1 + A\cdot\frac{|\nu-\nu_0|}{\Delta\nu_{wing}}\right)\cdot\exp\left(-\frac{(\nu-\nu_0)^2}{\Delta\nu_{wing}^2}\right), \qquad (3.27)$$

where I_c is the Lorentz function (1.79) for $|\nu - \nu_0| > \nu_{cut}$ and the $I_c(\nu_{cut}, \nu_0)$ constant for $|\nu - \nu_0| \le \nu_{cut}$; the parameters A and $\Delta\nu_{wing}$ are responsible for the amplitude (in arbitrary units) and the width of the region of the wing

where real absorption is larger than predicted by the Lorentz function (the super-Lorentzian wing). For convenience of comparison with the previous works, the cutoff frequency ν_{cut} of the resonant line wing was considered to be 25 cm^{-1}.

The form of the χ function in the expression (3.27) was chosen such that the resulting line shape should have the simplest expression for simulation and should not contradict the currently known information about possible behaviour of the far wings (section 1.2.6). With the use of the function (3.27), the spectra of the water vapour continuum in the rotational band at room temperature [Odintsova, 2019] and in fundamental vibrational bands of H_2O molecule (the room temperature data from Ptashnik [2011]) were analysed. The absorption by bound dimers in the rotational band was simulated based on quantum-chemical calculations from Scribano [2007], and in the vibrational bands a simplified model from Ptashnik [2011] was used according to which the dimer spectrum was represented by a sum of Lorentz profiles with known integrated intensities at frequencies of vibrational dimer modes (data of calculations from Kjaergaard [2008], and experiments from Bouteiller [2011] and Kuyanov–Prozument [2010] were used). The width of the profiles of all dimeric bands of 54 cm^{-1} was the best fit to the experimental data. To estimate the contribution of metastable dimers in all bands, the model of a doubled monomer spectrum uniformly broadened by the characteristic lifetime of the metastable state was employed (the width of all lines was assumed to be 10 cm^{-1}). The concentration of metastable dimers was determined by the data on the second virial coefficient of water vapour from Tretyakov [2012], the dimerization constant of bound dimers (3.26), and the excluded volume from Leforestier [2014]. The constants A and $\Delta\nu_{wing}$ of the function of excess continuum (3.27) were found iteratively from the condition of the best fit to the experimental data. The magnitude of $\Delta\nu_{wing}$ was determined 'manually' to be 11 cm^{-1} and fixed for all three bands, and the parameter A was determined by optimising the model to the experimental data. The obtained values of A were 13 for the rotational band, and 32 and 18.5 for the bands 1600 and 3600 cm^{-1}, respectively.

The proposed empirical model of the resonant line wings is, upon the whole, well suited for describing the continuum absorption in the vicinity of the water monomer band centres. Depending on the band, the excess continuum ranges from 20 to 50 % of the total observed continuum. The amplitude coefficient A does not change within its 50 % uncertainty. All the found values of A correspond to 22(10). A large, at first sight, uncertainty magnitude is readily justified by the use of approximate purely empirical models.

The correspondence of the proposed model with $\Delta\nu_{wing} = 14$ cm^{-1} and $A = 19$ to the continuum in these three bands is shown in fig. 3.65.

All this suggests that the nature of the observed excess continuum is monomolecular absorption that can be explained assuming a slight modification of the shape of the resonant line wing. This change is many orders of magnitude less than the amplitude of the line itself, and its relative contribution to the integrated intensity of the line is of the order of 0.001, which is much less than the uncertainty with which the intensities of the resonant lines are known. An indirect confirmation of the monomolecular nature of the excess continuum is also the fact that the model spectrum (fig. 3.65, left panel) better fits the experimentally found continuum points than the smooth curve, which is expected for traditionally considered bimolecular absorption components.

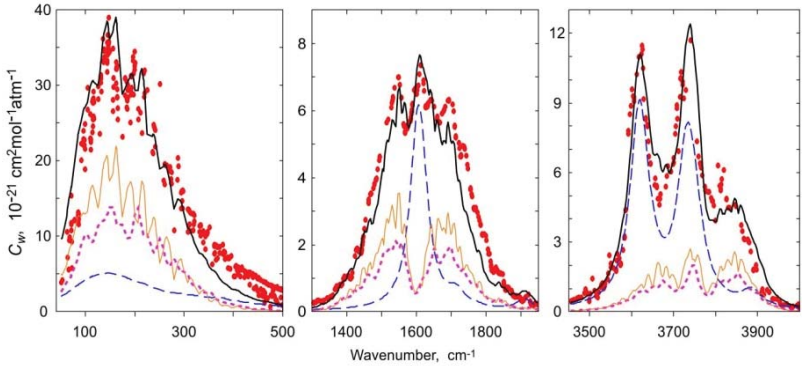

Fig. 3.65. Water vapour continuum spectra at room temperature (points are experimental data from Odintsova [2017; 2019] and Ptashnik [2011]) and their approximation by a model (bold solid curve), including the contributions of stable (dashed curve) and metastable (dotted curve) dimers and far wings of monomer lines (thin solid curve) calculated by model (3.27).

It should be emphasised that the model (3.27) does not pretend to rigorously describe all available experimental data in all frequency ranges. Moreover, we remind the reader that the most probable (although still unconfirmed by rigorous theoretical calculations) mechanism of the super-Lorentzian behaviour of the line wing is the influence of molecular rotation during collision (section 1.2.6). From this it follows, in particular, that the wing shape should depend on the rotational state of the absorbing molecule and, therefore, will be different for different lines, changing within the spectral band. Nevertheless, the simplest empirical model (3.27)

enables a qualitative demonstration that the excess continuum absorption observed in the region of water vapour rotational spectrum and in the region of the fundamental vibrational-rotational bands can be explained within the framework of a unified approach as the contribution of the undefined far wings of monomer resonant lines which were not taken into account. Note that similar ideas were used in the later work by Tran [2017] for analysis of the HCl rotational band broadened by Ar and similar conclusions were made.

Summing up the above, the following conclusions can be made:

1. The main result is the hypothesis according to which two mechanisms — dimeric absorption and uncertain absorption in the far wings of intense monomer lines — are equally responsible for the formation of the water vapour continuum that determines to a great extent the properties of the atmospheric continuum. Both mechanisms were actively discussed by the scientific community for many decades, but were considered opposing (see, for example, the reviews from Shine [2012], Tretyakov [2014] and references therein). However, the neglection of either of them makes an adequate description of available experimental data impossible. The 'fingerprints' of dimers (confirmed by *ab initio* calculations) are the characteristic spectral features that manifest themselves in the continuum spectra both, in the region of a purely rotational band [Serov, 2014; Odintsova, 2019] and within the fundamental vibration bands of H_2O molecules [Ptashnik, 2011]. These features cannot be explained by absorption in monomers. The description of the continuum only with the help of the dimeric model also fails [Shine, 2016; Ptashnik, 2019; Simonova, 2022]. The number of dimers required to explain the magnitude of the observed absorption greatly exceeds the maximum determined by the value of the second virial coefficient of the equation of state of water vapour, which is well known from experiments and is confirmed by *ab initio* calculations. Thus, both these mutually complementary mechanisms should be fully taken into account in models of radiation propagation in the atmosphere.

2. The simplest semi-empirical models of the continuum components and the methods of calculation discussed in this section are very useful tools for qualitative analysis (at the level of the physical description of the main manifestation of the effect) of the experimentally observed absorption and for setting a correspondence between its resonant and non-resonant components and the respective physical mechanisms. However, these models are too primitive and cannot be used to accurately describe absorption in the entire spectral range of electromagnetic radiation and in the entire range of atmospheric conditions.

3. At present, the primary step towards constructing a long awaited physically based radiation propagation model with high accuracy and predictive power for modern atmospheric applications is to carry out meticulous *ab initio* calculations of the shape of a monomolecular absorption line taking into consideration the behaviour of far wings and with subsequent generalised parametrisation of the results of calculations. Semi-classical trajectory calculations using the real potential of intermolecular interaction [Ivanov, 2016; Oparin, 2017; Chistikov, 2019, 2020] seem to be most promising for this purpose.

4. To verify the calculations, as well as to clarify the contributions of the other components of the continuum, high-sensitivity, wide-range studies of the continuum spectrum are required. Examples of such studies in the infrared range clearly demonstrating advantages of resonator spectroscopy can be found in the review by Shine [2016] and references cited there. A key factor is to conduct experiments in a wide temperature range, as different components of the continuum must have different temperature dependence.

CONCLUSION

In conclusion, we highlight the most significant contributions of resonator spectroscopy to the study of spectral features of atmospheric absorption in the millimetre and submillimetre wavelength ranges.

From the point of view of the fundamental spectroscopy, the most important result of the resonant line studies is the experimental confirmation of the validity of theoretical calculations of the shape of broad atmospheric lines. The resonator spectroscopy data provided proof that the Van Vleck–Weisskopf shape is more adequate for describing an isolated line profile than the Lorenz or Gross shape, and that the Rosenkranz line shape (3.11) can be used for the description of the profile of collisionally coupled lines. These two-line shapes are used in all present-day models of atmospheric absorption.

The second most important but, apparently, the first in demand, is a high-precision study of the collisional coupling of fine structure lines of atmospheric oxygen. It allowed for finding quantitative parameters that are currently used in all models of millimetre and submillimetre radiation propagation.

The third significant contribution is the validation of the parameters of collisional line broadening and shift measured at low pressures. The analysis of the data presented, for example, in Tables 3.2 and 3.6, demonstrates that in many cases the accuracy of measurements with the RAD spectrometer is even higher than with the resonator spectrometer. However, the credibility of these data (especially in the case of frequency shifts linear in pressure that are very small for atmospheric lines) is much higher if they coincide within the statistical error with the data of resonator spectroscopy. That is why the frequency shift of diagnostic lines by pressure, that was earlier considered to be negligible, is now taken into account in the propagation models.

Finally, the line intensities have been verified in experiment. No other method can compete with the resonator spectrometer in the measurement accuracy of this line parameter, as the measured absorption coefficient is independent of resonator length. According to the HITRAN spectroscopic database, indefiniteness of the intensities of millimetre and submillimetre lines of H_2O molecule is at the present 5-10 %, and of oxygen 10-20 %. Indirect estimates based on the analysis of broadband vibrational-rotational spectra and high-precision measurements of individual lines in

the IR region (see, e.g., Polyansky [2015]), give reason to believe that, actually, the accuracy of present-day calculations is approximately an order of magnitude higher. Nevertheless, only the results of intensity computations with data of direct measurements by the resonator method can give confidence that the error of diagnostic line modelling associated with the use of calculated line intensities will not exceed 1 %.

A deeper insight into the physical nature of the humidity-related continuum is one of the major long-standing problems in molecular spectroscopy. In the field of continuum studies in the millimetre and submillimetre wavelength ranges, resonator spectroscopy is almost beyond competition. The application of other methods only confirmed and/or supplemented the information obtained. The frequency, pressure, and temperature dependence of the continuum investigated with the resonator spectrometer enabled the finding of values of all empirical coefficients of the continuum for radiation propagation models.

With the use of the resonator spectroscopy, it became possible to confirm the hypothesis regarding the essential role of water vapour dimers in the formation of the atmospheric continuum that has been actively debated for more than half a century and to come close not only to a complete understanding of its nature, but also to a quantitative assessment of its main components.

APPENDICES

The materials presented in Appendices may be useful for the readers interested in practical details and for those who want to get a deeper insight into the processes and ideas considered in the book. The Appendices can help answer questions such as: What were the conclusions made in the main sections of the monograph based on? Where did the formulas come from? How were the estimates made and what approximations were used for this? The last Appendix provides information about line parameters that may be useful for solution of the tasks related to atmospheric absorption modelling.

A1. Collisional relaxation rate averaging over relative and absolute speeds of molecules-absorbers

The lifetime of a molecule in a given state (the more so when it is coherent with the field), in most cases, almost coincides with the time between collisions and depends on molecular speed. On collision, the state relaxes. The mean relaxation rate in an ensemble of molecules is found by its averaging over all possible speeds of molecules with the corresponding weight determined by the velocity distribution function.

We will show that the relaxation rate averaging over absolute values of absorbing molecules speed υ gives the result identical to the averaging over their relative speeds υ_r, i.e., $\langle \Gamma(\upsilon) \rangle_{\upsilon} = \langle \Gamma(\upsilon_r) \rangle_{\upsilon_r}$.

By definition

$$\left\langle \Gamma(\upsilon) \right\rangle_{\upsilon} = \int f\left(\upsilon\right)\ \Gamma\left(\upsilon\right) d\upsilon\,, \tag{A1.1}$$

$$\left\langle \Gamma(\upsilon_r) \right\rangle_{\upsilon_r} = \int f\left(\upsilon_r\right)\ \Gamma\left(\upsilon_r\right) d\upsilon_r\,, \tag{A1.2}$$

where the functions $f\left(\upsilon\right)$ and $f\left(\upsilon_r\right)$ are, respectively, probability distributions of absolute and relative speeds of absorbing molecules.

Let us make use of the conditional probability distributions $f(\upsilon_r \left| \upsilon \right.)$ and $f(\upsilon \left| \upsilon_r \right.)$, which mean the probability that a molecule has the relative speed υ_r, given that its absolute speed is υ and vice versa.

Apparently

$$\int f(\upsilon)\ d\upsilon = \int f(\upsilon_r)\ d\upsilon_r = \int f(\upsilon_r|\upsilon)\ d\upsilon_r = \int f(\upsilon|\upsilon_r)\ d\upsilon = 1\,. \quad \text{(A1.3)}$$

From the properties of conditional probability follows

$$d\upsilon \cdot f(\upsilon)\ d\upsilon_r f(\upsilon_r|\upsilon) = d\upsilon_r f(\upsilon_r)\ d\upsilon \cdot f(\upsilon|\upsilon_r). \quad \text{(A1.4)}$$

As

$$\Gamma(\upsilon) = \int f(\upsilon_r|\upsilon)\cdot\Gamma(\upsilon_r)d\upsilon_r\ ,$$

from (A1.1) follows

$$\langle\Gamma(\upsilon)\rangle_\upsilon = \int\int f(\upsilon) f(\upsilon_r|\upsilon)\cdot\Gamma(\upsilon_r)d\upsilon_r d\upsilon\ .$$

Making use of the relation (A1.4) we obtain

$$\langle\Gamma(\upsilon)\rangle_\upsilon = \int\int f(\upsilon_r) f(\upsilon|\upsilon_r)\cdot\Gamma(\upsilon_r)d\upsilon_r d\upsilon\ . \quad \text{(A1.5)}$$

Taking into account (A1.3), the expression (A1.5) reduces to

$$\langle\Gamma(\upsilon)\rangle_\upsilon = \int f(\upsilon_r)\cdot\Gamma(\upsilon_r)\ d\upsilon_r\ , \quad \text{(A1.6)}$$

which, according to the definition (A1.2), is $\langle\Gamma(\upsilon_r)\rangle_{\upsilon_r}$.

A2. How the far wings of resonant lines can behave

The far wings, i.e., the power spectrum of a periodic process (rotation, vibration, and so on) occurring during the molecule–field interaction at large frequency detunings from the centre of a resonant line, correspond to the fast components of this process at collision. We will consider how the finiteness of the collision time affects line shape on an example of the simplest qualitative model of a molecule-oscillator interacting with external harmonic force (electromagnetic wave) for a rather long period of time τ (the time between collisions):

$$\ddot{x} + \omega_0^2 x = \frac{1}{m} F(t)\cdot\cos\ \omega t, \quad \text{(A2.1)}$$

where ω_0 is the angular frequency of the oscillator; ω is the angular frequency of the external force; and m is the oscillator effective mass representing the efficiency of the molecular interaction with the field. This

inessential constant factor will be further omitted, as here we are interested in line shape only.

The energy acquired by the oscillator from the external force can be calculated using the following formula (e.g., Landau, 1976):

$$\Delta W(\omega) = \frac{1}{2}\left| \int_{-\tau/2}^{\tau/2} F(t)\cos\omega t \cdot \mathrm{e}^{-i\omega_0 t} dt \right|^2 . \qquad \text{(A2.2)}$$

For finding the energy acquired from the field by an ensemble of such molecules-oscillators subject to random perturbations (analogue of equilibrium gas), the obtained expression is, as a rule, averaged using the Poisson distribution for the number of molecules-oscillators that can interact with the field over the time between the collisions, τ, under the conditions of random, kind of Brownian motion (it is assumed that after the collision the oscillator 'gets out of the game'):

$$R(\tau) = \frac{1}{\tau_0}\exp\left(-\frac{\tau}{\tau_0}\right), \qquad \text{(A2.3)}$$

where τ_0 is the average time between molecular collisions (cf. (1.62)). For the average energy acquired by gas as a function of frequency (corresponding to line shape in gas) we have

$$\Delta\overline{W}(\omega) = \int_0^\infty \Delta W(\omega)\cdot R(\tau) d\tau . \qquad \text{(A2.4)}$$

Consider first the simplest case corresponding to the impact approximation:

$$\begin{aligned} F_0(t) &= 1, \text{ for } -\tau/2 \le t \le \tau/2 \\ &= 0 \quad \text{for other values of } t, \end{aligned} \qquad \text{(A2.5)}$$

which means that a molecule-oscillator interacts with the field only during the time τ between two instantaneous collisions (fig. A2.1, upper plot).

The integrals in (A2.2) and (A2.4) for the function F_0 are taken analytically. For the energy of a single oscillator, we obtain

$$\Delta W = \frac{1}{2}\left|\frac{1}{2}\int_{-\tau/2}^{\tau/2}\left(\exp[i(\omega-\omega_0 t)] + \exp[-i(\omega+\omega_0)t]\right)dt\right|^2 =$$

$$= \frac{1}{2}\left(\frac{\sin^2\frac{(\omega-\omega_0)\tau}{2}}{(\omega-\omega_0)^2} + \frac{\sin^2\frac{(\omega+\omega_0)\tau}{2}}{(\omega+\omega_0)^2} + \frac{\cos\omega_0\tau - \cos\omega\tau}{\omega^2-\omega_0^2}\right). \qquad \text{(A2.6)}$$

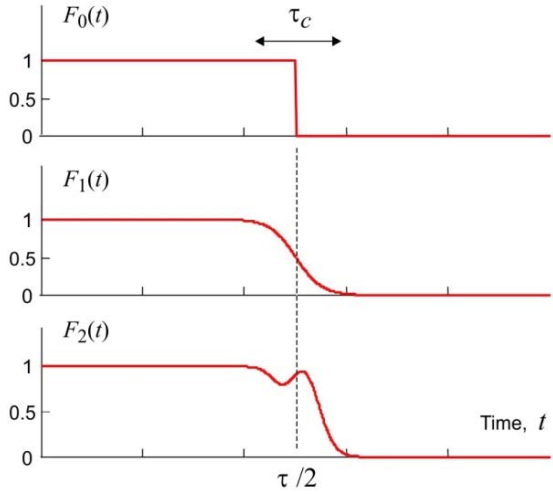

Fig. A2.1. The function of 'switching' the molecule-oscillator state for different collision scenarios (instantaneous, smooth monotonic, nonmonotonic). Only the part corresponding to 'switching off' is demonstrated. At 'switching on', the function is exactly the same but inverted in time.

Substituting (A2.6) into (A2.4) and using the relation $1/\tau_0 << \omega_0$, which means that the resonant line width is much less than its centre frequency (that is always met under the conditions typical for molecular gas spectroscopy), yields

$$\Delta\bar{W} = \frac{1}{\tau_0}\int_0^\infty \Delta W \exp\left(-\frac{\tau}{\tau_0}\right)d\tau$$
$$\approx \frac{1}{4}\cdot\left(\frac{1}{(\omega-\omega_0)^2+1/\tau_0^2}+\frac{1}{(\omega+\omega_0)^2+1/\tau_0^2}\right) \qquad \text{(A2.7)}$$

This confirms that, under the impact approximation implying that the gas molecules collide instantaneously, the line shape corresponds to the classical Lorentz profile.

Let us now assume that the oscillator transition from the state when it interacts with external force to the state of rest occurs smoothly over a period of time (fig. A2.1, middle plot). For this, the external force function will be written, for example, by means of hyperbolic tangents in the form

$$F_1(t) = \frac{1}{2}\left(\tanh\left(\frac{4t + 2\tau}{\tau_c} \right) - \tanh\left(\frac{4t - 2\tau}{\tau_c} \right) \right), \qquad \text{(A2.8)}$$

where τ_c is the typical transition time corresponding to the duration of the collision.

Modern computational means readily provide numerical solutions to (A2.2) and (A2.4) without long analytical calculations. The result will be demonstrated for the following parameters: $\tau_0 = 2\pi \cdot 3 \cdot 10^{12}$ rad/s, $\tau_0 = = 10^{-9}$ s, and $\tau_c = 1.5 \cdot 10^{-12}$ s, which correspond approximately to the resonant line of H_2O in pure water vapour at room temperature and pressure of about 10 Torr in the region of maximum intensity of rotational spectrum with central frequency $\nu_0 = 100$ cm^{-1} and collisional halfwidth 160 MHz. The line shape (A1.10) for these parameters for the function F_1 is shown in fig. A2.2.

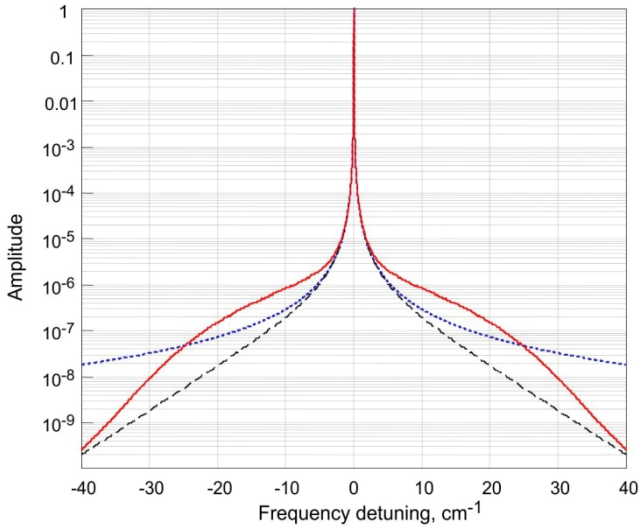

Fig. A2.2. The shape of a molecule-oscillator resonant line at different scenarios of switching of the exciting external force presented in fig. A2.1. Solid, dashed, and dotted lines correspond to nonmonotonic (F_2), smooth monotonic (F_1), and instantaneous (F_0) scenarios.

One can see that at detunings larger than $1/(2\pi\tau_c) \sim 4$ cm^{-1} the line wing is lower than the Lorentz function. Such behaviour is called *sub-Lorentzian*. Linearity of the wing decay on the logarithmic scale of the

graph points to the exponential decrease of the corresponding absorption. This indicates that the resonant absorption is fairly well localised in the spectral region. Formally, the exponentially decaying wing, similarly to the Lorentz one, is infinite, but its contribution to absorption at large detunings from the centre is negligible.

Note that the sub-Lorentzian behaviour of the far wing occurs for any monotonic transition function. For example, if the function is linear in time t, then the wing decays proportionally to the 4-th power of frequency detuning.

Let us further assume that the molecule-oscillator will not only feel the smoothly increasing influence of the approaching collision partner that will help the molecule to get out of the interaction with the field but will also feel the partner's rotation. In other words, suppose that the external force switches on and off with oscillations, rather than monotonically (see fig. A2.1, lower plot). For this, we will supplement the function F_1 switching the molecule-oscillator state with the component providing periodical oscillations during switching:

$$F_2(t) = F_1(t) + \frac{A_0}{2}\left[\exp\left(-\frac{16\left(t-\frac{\tau}{2}\right)^2}{\tau_c^2}\right)\cdot\sin^2\left(\frac{2\pi t}{T_0}-\varphi\right)+\right.$$

$$\left.+\exp\left(-\frac{16\left(t+\frac{\tau}{2}\right)^2}{\tau_c^2}\right)\cdot\sin^2\left(\frac{2\pi t}{T_0}+\varphi\right)\right], \qquad \text{(A2.9)}$$

where A_0, T_0, and φ are the parameters responsible for the amplitude, period, and initial phase of the oscillations. Numerical values of these parameters for modelling line shape were chosen to provide the best fit to the observed absorption in rotational and fundamental vibrational bands of water vapour (section 3.2.2).

Despite the seemingly small change in the form of the switching function (fig. A2.1), its result is quite significant (fig. A2.2). A gently sloping hump with a characteristic width depending on collision time is formed in the line wing at the detuning frequency equal to the oscillation frequency of the second term of the function F_2. In this detuning region, the line wing is higher than the Lorentz function (*super-Lorentzian*

behaviour). The deviation of the obtained wing from the Lorentz one in relative units is shown in fig. A2.3. Such line wing behaviour points to a qualitative similarity of the obtained result with the empirical description of the water vapour continuum using the χ-functions (section 1.3.1). Quantitative comparison is illegitimate as dimer absorption was not taken into account when choosing parameters of the χ-functions.

Note that only the smoothness of the switching process and the presence of oscillations are of principal importance in both cases. Although the specific form of the function $F(t)$ affects the result, it is chosen merely for simplicity and convenience of mathematical representation.

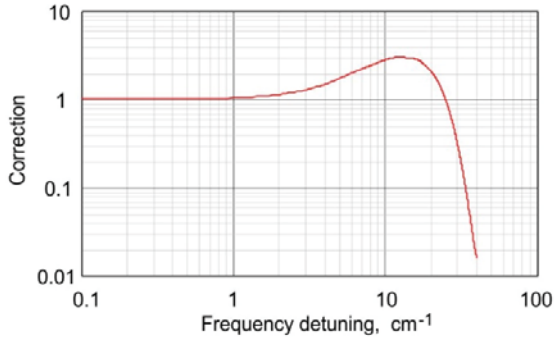

Fig. A2.3. The line wing shape ratio at nonmonotonic (F_2) and instantaneous (F_0) switching-off of external force, which is actually a correcting factor of the far wings of the Lorentz shape (analogue of the χ-function, cf. fig. 1.19)

Despite the plausibility of the resulting picture, one should not forget that this is just a model. The sub-Lorentzian behaviour of the far wings (exponential decay at large detunings) is confirmed by analysis of the experimental data on absorption in the far wings of rotational-vibrational bands (e.g., of CO_2, H_2O molecules) and can be regarded as proven. The super-Lorentzian behaviour is needed for the explanation of the experimentally observed continuum within the H_2O spectral bands (section 3.2.2). Obviously, oscillations of the interaction force are possible. Examples of harmonic perturbations of resonance frequency during molecular collisions can be found in the results of classical trajectory calculations [Ivanov, 2016]; the nonmonotonic behaviour of the switching function, very similar to the one presented in the lower graph in fig. A2.1, calculated for a real molecular line was considered in the monograph by Hartmann [2008] (see p. 51). However, it is not yet clear how these

perturbations affect the shape of the far wing, so this mechanism of the appearance of a super-Lorentzian wing is regarded to be a hypothesis.

A3. The relationship between the coefficients of virial equation of gas state and the equilibrium constants K_2, K_3, and b_0

Suppose that gas in the equilibrium state is a mixture of ideal monomers, dimers, and trimers. The interaction of free molecules can be taken into account as an effective excluded volume b_0. The equation of state for such gas can be written in the form

$$p\left(V - b_0\right) = \left(\nu_1 + \nu_2 + \nu_3\right) RT \,,$$

where (as well as in all the following equations of this section) the monomer, dimer, and trimer are designated by the indices 1, 2, and 3, respectively.

The amount of matter in moles is

$$\nu = \frac{m}{M} = \frac{m_1 + m_2 + m_3}{M} =$$

$$= \frac{\nu_1 M_1 + \nu_2 M_2 + \nu_3 M_3}{M} \approx \frac{\nu_1 M_1 + \nu_2 2M_1 + \nu_3 3M_1}{M_1} = \nu_1 + 2\nu_2 + 3\nu_3 \,.$$

In molar concentrations $n_{1,2,3} = \dfrac{\nu_{1,2,3}}{V}$ we obtain

$$n = n_1 + 2n_2 + 3n_3 \,, \qquad \text{(A3.1)}$$

$$p\left(1 - \frac{b_0}{V}\right) = \left(n_1 + n_2 + n_3\right) RT \,. \qquad \text{(A3.2)}$$

The equilibrium constants are defined as

$$K_2 = K_2^c = \frac{n_2}{n_1^2} \,, \quad K_3 = K_3^c = \frac{n_3}{n_1^3} \,.$$

Note that the designation of the equilibrium constants adopted here for simplification of subsequent expressions differs from that used in section 1.3.2, where they were defined through partial pressures. In the used approximation, when gas is considered as a mixture of ideal monomers, dimers and trimers, the constants defined through concentrations and pressures are uniquely related as

$$pV = \nu RT \to n = \frac{p}{RT}, \quad K_2^c = K_2^p RT, \quad K_3^c = K_3^p \left(RT\right)^2.$$

From (A3.1) we obtain

$$n = n_1 + 2K_2 n_1^2 + 3K_3 n_1^3 = n(n_1), \tag{A3.3}$$

and from (A3.2)

$$\frac{p}{RT} = \frac{n_1 + K_2 n_1^2 + K_3 n_1^3}{\left(1 - \frac{b_0}{V}\right)}. \tag{A3.4}$$

For one mole of the initial monomer gas ($V = V_m$) $n = \frac{1}{V_m}$, from (A3.4) and (A3.3) we find

$$\frac{pV_m}{RT} = \frac{p}{RT} \cdot \frac{1}{n} = \frac{n_1 + K_2 n_1^2 + K_3 n_1^3}{\left(1 - \frac{b_0}{V_m}\right) \cdot \left(n_1 + 2K_2 n_1^2 + 3K_3 n_1^3\right)} = \frac{n_1 + K_2 n_1^2 + K_3 n_1^3}{\left(1 - b_0 n\right) \cdot \left(n_1 + 2K_2 n_1^2 + 3K_3 n_1^3\right)} =$$

$$= \frac{n_1 + K_2 n_1^2 + K_3 n_1^3}{\left(1 - b_0 \cdot \left(n_1 + 2K_2 n_1^2 + 3K_3 n_1^3\right)\right) \cdot \left(n_1 + 2K_2 n_1^2 + 3K_3 n_1^3\right)} = F(n_1). \tag{A3.5}$$

We can express n_1 through n from the cubic equation (A3.3), substitute it into (A3.5), and expand the result in power series of n. As an alternative we can use an inverse function

$$n = f(n_1), \quad n_1 = f^{-1}(n).$$

By definition, the expansion in power series is

$$F\left(n_1(n)\right) = F\left(n_1(n)\right)\Big|_{n=0} + \left.\frac{dF}{dn}\right|_{n=0} \cdot n + \frac{1}{2} \cdot \left.\frac{d^2F}{dn^2}\right|_{n=0} \cdot n^2 + \ldots.$$

According to the rules of taking derivatives of a complex function we have

$$\frac{dF\left(n_1(n)\right)}{dn} = \frac{dF(n_1)}{dn_1} \cdot \frac{dn_1}{dn} = \frac{dF}{dn_1} \cdot \left(\frac{dn}{dn_1}\right)^{-1}; \tag{A3.6}$$

$$\frac{d^2F(n_1(n))}{dn^2}=\frac{d}{dn}\left(\frac{dF}{dn_1}\cdot\left(\frac{dn}{dn_1}\right)^{-1}\right)=\frac{d^2F}{dn_1^{\,2}}\cdot\frac{dn_1}{dn}\cdot\left(\frac{dn}{dn_1}\right)^{-1}+\frac{dF}{dn_1}\cdot\frac{d}{dn}\left(\left(\frac{dn}{dn_1}\right)^{-1}\right)=$$

$$=\frac{d^2F}{dn_1^{\,2}}\cdot\left(\frac{dn}{dn_1}\right)^{-2}+\frac{dF}{dn_1}\cdot\frac{d}{dn_1}\left(\left(\frac{dn}{dn_1}\right)^{-1}\right)\cdot\frac{dn_1}{dn}=\frac{d^2F}{dn_1^{\,2}}\cdot\left(\frac{dn}{dn_1}\right)^{-2}+\frac{dF}{dn_1}\cdot\frac{d}{dn_1}\left(\left(\frac{dn}{dn_1}\right)^{-1}\right)\cdot\left(\frac{dn}{dn_1}\right)^{-1}. \tag{A3.7}$$

Thus, finding the expansion coefficients of the function F in power series of n comes down to taking partial derivatives of $F(n_1)$ and $n(n_1)$ with respect to n_1, which is an easy task:

$$\frac{dn}{dn_1}=1+4K_2n_1+9K_3n_1^2\,. \tag{A3.8}$$

$$\frac{dF}{dn_1}=\left[\begin{array}{c}\dfrac{\dfrac{d}{dn_1}\left(n_1+K_2n_1^2+K_3n_1^3\right)}{\left(n_1+2K_2n_1^2+3K_3n_1^3\right)-b_0\cdot\left(n_1+2K_2n_1^2+3K_3n_1^3\right)^2}-\\ -\left(\dfrac{d}{dn_1}\left(\left(1-b_0\cdot\left(n_1+2K_2n_1^2+3K_3n_1^3\right)\right)\cdot\left(n_1+2K_2n_1^2+3K_3n_1^3\right)\right)\right)\cdot=\\ \cdot\dfrac{n_1+K_2n_1^2+K_3n_1^3}{\left(\left(n_1+2K_2n_1^2+3K_3n_1^3\right)-b_0\cdot\left(n_1+2K_2n_1^2+3K_3n_1^3\right)^2\right)^2}\end{array}\right]=$$

$$=\left[\begin{array}{c}\dfrac{1+2K_2n_1+3K_3n_1^2}{\left(n_1+2K_2n_1^2+3K_3n_1^3\right)-b_0\cdot\left(n_1+2K_2n_1^2+3K_3n_1^3\right)^2}-\\ -\left(1+4K_2n_1+9K_3n_1^2-2b\left(1+4K_2n_1+9K_3n_1^2\right)\left(n_1+2K_2n_1^2+3K_3n_1^3\right)\right)\cdot\\ \cdot\dfrac{n_1+K_2n_1^2+K_3n_1^3}{\left(\left(n_1+2K_2n_1^2+3K_3n_1^3\right)-b_0\cdot\left(n_1+2K_2n_1^2+3K_3n_1^3\right)^2\right)^2}\end{array}\right] \tag{A3.9}$$

The expression for the second virial coefficient $B=\left.\dfrac{dF}{dn}\right|_{n=0}$ is found by substituting (A3.9) and (A3.8) into (A3.6) and letting n_1 go to zero (at $n\to0$ $n_1\cong n$):

$$B=b_0-K_2\,.$$

Analogously, we calculate $\frac{d^2F}{dn_1^2}$, use the result with (A3.8) and (A3.9) in (A3.7) and for n_1 tending to zero, obtain the sought expression for the third virial coefficient

$$C = \frac{1}{2} \cdot \frac{d^2F}{dn^2}\bigg|_{n=0} = b_0{}^2 + 4K_2^2 - b_0K_2 - 2K_3 .$$

A4. Empirical parametrisation of the second and third virial coefficients of the water vapour equation of state on the basis of known thermodynamical data

Taking into consideration the relationship between molar density (ρ_m) and molar volume ($V_m = 1/\rho_m$), equation (1.117) can be written in the form

$$\frac{p}{\rho_m RT} = 1 + B(T)\rho_m + C(T)\rho_m^2 + ... \qquad \text{(A4.1)}$$

From this follows that $B(T)$ and $C(T)$ can be found through the first and second partial derivatives of the left-hand side of equation (A4.1) with respect to molar density:

$$B(T) = \lim_{\rho_m \to 0}\left[\frac{d}{d\rho_m}\left(\frac{p}{\rho_m RT}\right)\right], \quad C(T) = \frac{1}{2}\lim_{\rho_m \to 0}\left[\frac{d^2}{d\rho_m^2}\left(\frac{p}{\rho_m RT}\right)\right]. \quad \text{(A4.2)}$$

The most complete compilation of known thermodynamic data on water vapour was done in the work of Wagner [2002]. The data obtained in this work are regarded as reference ones. They can be extracted numerically from the public database NIST Chemistry Webbook in the interval of temperatures 273—1275 K and pressures 0—1000 MPa (~10^4 atm.). According to the description, the relative data uncertainty is less than 0.1 %. The database software for each given temperature allows for calculating up to two hundred (p, ρ_m) points with the number of significant digits up to 12. This is sufficient for approximating the points by the polynomial of degree 6-8 and uniquely calculating the values of B and C by formula (A4.2) using standard software.

For convenience of computations the obtained values of $B(T)$ can be approximated by an analytical function, for example, of the form [Tretyakov, 2012]:

$$F_1(T) = \left(\frac{100}{T}\right)^s \cdot \sum_{i=0}^{9} a_i T^i \,, \qquad \text{(A4.3)}$$

where a_i are adjustable coefficients (Table A4.1), $s = 6$ for $B(T)$, and $s = 9$ for $C(T)$. The polynomial degree and the number of significant digits in the coefficients are chosen so that the relative deviation of the function from the found values of B and C does not exceed the relative accuracy of the initial thermodynamic data (0.1 %) throughout the temperature and pressure interval. Such parametrisation more accurately corresponds to the initial thermodynamic data than the previous analogues (see, for example, Harvey, 2004).

Table A4.1. Coefficients of the approximating function (A4.3) for $B(T)$ and $C(T)$ for the temperature interval 273 — 1275 K

	$B(T)$, $cm^3 \cdot mole^{-1}$	$C(T)$, $cm^6 \cdot mole^{-2}$
s	6	9
a_0	$-7.04242 \cdot 10^6$	$-5.2331832 \cdot 10^{11}$
a_1	$8.345651 \cdot 10^4$	$4.079161 \cdot 10^9$
a_2	$-4.212794 \cdot 10^2$	$-1.7322727 \cdot 10^7$
a_3	$1.242946 \cdot 10^0$	$4.6636033 \cdot 10^4$
a_4	$-2.409822 \cdot 10^{-3}$	$-8.3911426 \cdot 10^1$
a_5	$3.017768 \cdot 10^{-6}$	$1.0171702 \cdot 10^{-1}$
a_6	$-2.518957 \cdot 10^{-9}$	$-8.0946594 \cdot 10^{-5}$
a_7	$1.350628 \cdot 10^{-12}$	$4.1124096 \cdot 10^{-8}$
a_8	$-4.134191 \cdot 10^{-16}$	$-1.2609901 \cdot 10^{-11}$
a_9	$5.530774 \cdot 10^{-20}$	$1.9229771 \cdot 10^{-15}$

The curves for the second and third virial coefficients *versus* temperature and the deviation of the numerical values, obtained by empirical data from the approximating function (A4.3), are plotted in fig. A4.1. Note that the approximation function (A4.3) gives qualitatively correct dependences at extrapolation to higher temperatures (up to ~1800 K for $B(T)$ and to ~1400 K for $C(T)$), as well as to much lower temperatures.

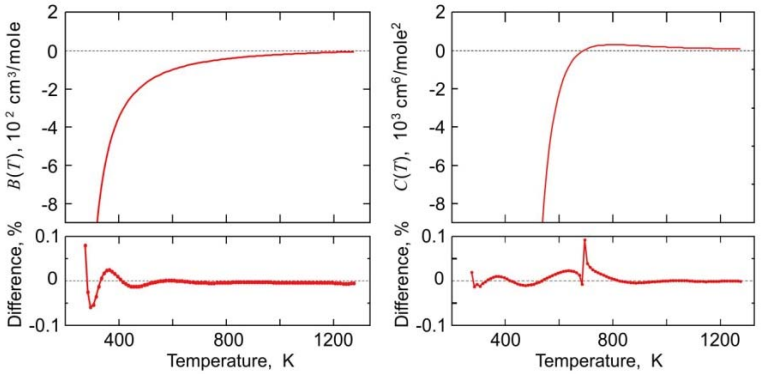

Fig. A4.1. The second (*a*) and third (*b*) virial coefficients of the equation of state for water vapour (upper curves) and percentage deviation of the numerical values obtained by empirical data [Wagner, 2002] using expression (A4.1) from the approximating function (A4.3) with the coefficients from Table A4.1 (lower curves). Adopted from Tretyakov [2012].

A5. Assessment of excluded water vapour volume

The simplest assessment of the magnitude of excluded volume for water vapour follows from the analytical solution of the Van der Waals equation of state for the conditions of coexistence of liquid, solid and gas phases of the matter (critical or triple point), i.e., temperature and pressure take on critical values:

$$b_0 = \frac{RT_c}{8p_c}. \qquad \text{(A5.1)}$$

The values of critical parameters for water vapour are well known [Wagner, 2002]: $T_c = 647.096$ K, $p_c = 22.0640$ MPa. Their substitution into (A5.1) yields $b_0 = 30.481$ cm^3/mole constant for all temperatures. Under the assumptions made for the derivation of the Van der Waals equation, this value can be treated as the physical volume occupied by a molecule into which other molecules cannot penetrate.

A more accurate interpretation of the excluded volume as an effective volume determined by the range of attraction forces, or in other words, of the volume of molecular interaction b_a which depends, in particular, on the dipole moment of molecules was proposed by Hirschfelder [1942]. Using the experimental data on the water vapour state, Hirschfelder and co-authors found the interaction volume to be 38.5 cm^3/mole. Being the most

plausible one, this value was used for the calculation of water vapour parameters in many works up to the beginning of the 21st century [Scribano, 2006; Harvey, 2004].

The analogy between the terms *interaction volume,* introduced by Hirschfelder and co-authors [Hirschfelder, 1942], and *interaction cross-section* (see section 1.2.2), as well as the relationship of this volume with the dipole moment of the molecule and the interaction forces, may cause misunderstanding. For example, if the volume of collisional interaction is calculated as a volume of a sphere having radius equal to the mean radius of the collisional cross section of water vapour molecules in different rotational states at room temperature, then it will be 120 times larger than the effective excluded volume specifying the gas-kinetic properties of vapour. The point is that the interaction cross section of polar molecules is determined by the dipole field, which is slowly decaying with distance, even taking into account molecular rotation. Even at long distances this field is sufficient for changing the rotational state of colliding molecules. Therefore, in discussions concerning the excluded volume, which determines the kinetic properties of gas, it is more appropriate to speak about the range of repulsive forces. These forces associated with the overlapping of electronic orbitals in the interacting molecules are very short-term ones (for example, for the Lennard–Jones potential (1.111) the repulsive force decreases as $1/r^{12}$), but they determine the distance of minimal approach of molecules on collisions and, hence, the magnitude of the effective excluded volume [Tretyakov, 2012].

Consequently, the radius of the effective excluded volume can be estimated from the equilibrium distance between the monomers in the dimer, which corresponds to the balance of the forces of attraction and repulsion at zero temperature. This distance is known with good accuracy for many molecules from spectroscopic experiments with low-temperature molecular beams. For example, for a water dimer this distance is 2.978 Å [Keutsch, 2003-1]. Obviously, this value is the upper limit for the radius of the sphere of effective gas–kinetic interaction. The distance of the minimal approach of monomers is a little less than the equilibrium value. In a dimer, this distance depends on its internal energy, and when free molecules collide, it is determined by their total kinetic energy. For example, for the Lennard–Jones potential (6-12), the distance of the minimal approach for the achievable energies is 80–85 % of the equilibrium value (fig. 1.21). Correspondingly, the radius of the sphere of effective gas–kinetic interaction of water molecules at high temperatures can be estimated to be 2.38–2.53 Å, and the volume of the sphere will be 34–41 cm^3/mol, which perfectly coincides with the values of 30.5 and

38.5 cm^3/mol mentioned above that were obtained, respectively, from the solution of the Van der Waals equation and on the basis of empirical thermodynamic data. At low temperatures, the distance of the closest approach of water molecules during collisions almost does not differ from the equilibrium internuclear distance of the dimer, and the corresponding excluded volume is approximately 67 cm^3/mol. At high temperatures, the distance of closest approach is almost constant, which is due to a very rapid increase in the repulsive forces when molecules approach each other. Thus, with an increase in temperature, the excluded volume will first sharply (probably exponentially) change from ~67 to ~37 cm^3/mol, and then it will decrease slowly, remaining almost unchanged [Tretyakov, 2012].

These considerations were used in the work of Leforestier [2014] for the calculation of the excluded volume in the classical sense, defined as half the volume of a sphere of radius equal to the distance of the closest approach of rigid spherical molecules. The distance of the closest approach of gas molecules in a 'head-on' collision was calculated from the condition that the total average kinetic energy of the relative translational motion of the molecule $3kT/2$ converts into the potential interaction energy. To understand where this energy value comes from, recall that the average kinetic energy of the translational motion of ideal gas molecules in 3D space, in accordance with the law of equidistribution of energy over degrees of freedom, is known to be $3kT/2$. The average energy of relative motion of the interacting molecules is characterised, on the one hand, by the reduced mass (1.12), which is twice less than the mass of one molecule and, on the other hand, by the fact that the relative velocity of molecules is the root of 2 larger than the absolute speed. The value of $mV^2/2$ turns out to be the same for both average and relative average energy. The interaction potential obtained on the basis of *ab initio* calculations was used for the calculations by Leforestier [2012]. The result is shown in fig. A5.1.

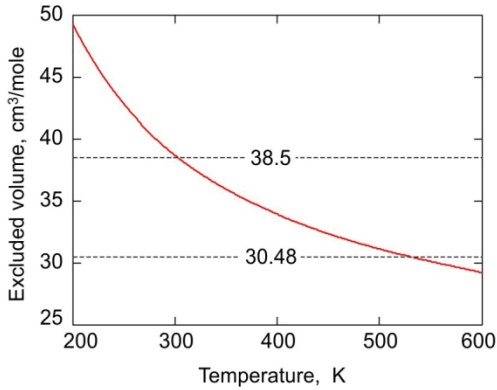

Fig. A5.1 Temperature dependence of the classical excluded volume of equilibrium water vapour as a function of temperature according to the results of calculations by Leforestier [2014] using the most accurate intermolecular interaction potential to date. Horizontal lines — estimates obtained on the basis of the analyses of empirical data from Hirschfelder [1942] (upper line) and from the solution of the van der Waals equation (A5.1) for known critical parameters of water vapour (lower line).

For practical application of the results of numerical calculations it is handy to use the approximating empirical function

$$b_0(T) = \exp\left(\frac{135 + 3.26T - 1.84\cdot 10^{-4}T^2}{T}\right) \text{ [cm}^3\text{/mol]}, \qquad \text{(A5.2)}$$

which deviates from the numerical data from Leforestier [2014] by fractions of a percent.

This estimate confirms the values of the excluded volume obtained from the previous considerations.

Note that all the estimates given here are rather approximate. Their use for calculating the values of the dimerization constant based on the expression (1.147) is justified only by the fact, that under ordinary atmospheric conditions, $b_0 << B$. The calculation of the excluded volume, i.e., of the number of free pair states of molecules at each given temperature, is approximately as complex as direct calculation of the dimerization constant. Such calculations require knowledge of the full-size interaction potential and adequate consideration of bound and metastable pair states [Vigasin, 2012]. Despite the importance of this issue for fundamental and applied spectroscopy, and the fact that the calculation

procedure is transparent, it demands substantial computing resources and time costs, and has not been implemented until now.

A6. Field damping in a resonator with continuous and discrete losses

Consider a symmetric Fabry-Perot resonator having length L, with identical mirrors and hole coupling on each mirror to simplify the consideration and formulas. Suppose that the steady-state oscillations of the field in the resonator at the frequency of one of its eigenmodes are excited by coherent monochromatic radiation. We will consider the propagation of the wave inside the resonator, starting from the surface of one of the mirrors after the radiation has been turned off. If the resonator is empty, the wave passes from one mirror to the other without attenuation. When the wave is reflected from the mirror, there occurs an amplitude jump, as part of the wave energy has been spent on electron current induction in the mirror (reflection losses), another part on extracting the radiation from the resonator through the coupling hole (coupling losses), and the third part has been lost because the mirror has a finite size, and the part of the radiation outside its boundary escaped from the resonator (diffraction losses). All losses inherent in such a resonator can be characterised by one loss factor r corresponding to the change of the initial field amplitude A_0 at a single reflection

$$A = rA_0. \tag{A6.1}$$

After reflection, the wave propagates back to the first mirror without a decrease in the amplitude. On reflection, the amplitude again decreases by r times. In this way the wave amplitude changes discretely on each passage through the resonator (fig. A6.1, upper step line).

The values of the wave amplitudes after successive reflections are described by

$$A_n = A_0 \mathrm{e}^{-\gamma_0 T n}, \tag{A6.2}$$

where n = 0, 1, 2… is the integer corresponding to the number of reflections, T is the time of radiation propagation from one mirror to the other, and

$$\gamma_0 = -\frac{1}{T} ln\left(\frac{1}{r}\right) \tag{A6.3}$$

is the damping constant of field oscillations in an empty resonator (cf. (2.3)). The function continuous in time corresponding to such discrete changes is shown by the upper solid curve in fig. A6.1.

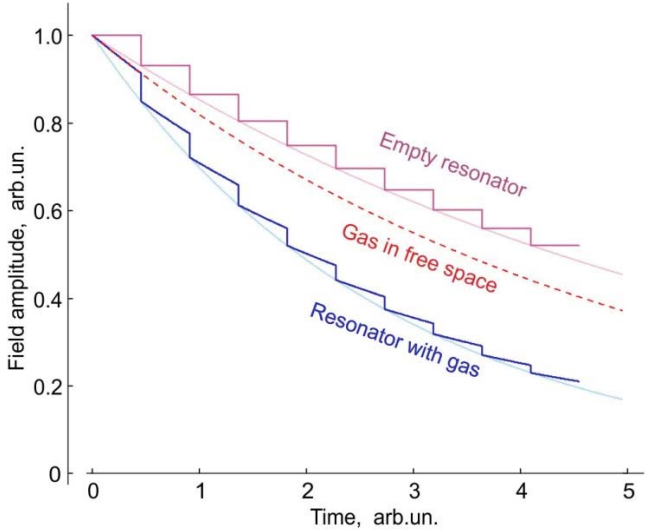

Fig. A6.1. The evolution of the field standing wave amplitude in a resonator with and without gas after the exciting radiation has been switched off. The steps correspond to the wave reflection at the mirror.

If the radiation at the resonance frequency is propagating in free space through a gas with absorption coefficient α, then the field amplitude decreases continuously in time in accordance with the Bouguer-Lambert law (eq. (1.2)):

$$A = A_0 \mathrm{e}^{-\frac{\alpha}{2}ct}, \qquad \text{(A6.4)}$$

where the multiplier 1/2 takes into consideration that the amplitude of the absorbed field decreases twice slower than its power proportional to the squared amplitude. This dependence is shown by the dash-dot curve in fig. A6.1. If this gas fills the resonator under consideration, then the field amplitude will change continuously while the radiation is propagating between the mirrors and in jumps during reflections, as shown by the lower step curve in fig. A6.1.

The change in the field amplitude over the time $T_1=2T=2L/c$ (corresponding to one full bypass of the resonator by the field and return

to the same point in space with the same phase, as defined in section 2.1) is

$$\frac{A}{A_0} = r^2\, \mathrm{e}^{-\frac{\alpha}{2}cT_1} = \mathrm{e}^{-(\gamma_0 T_1 + \alpha L)}, \qquad \text{(A6.5)}$$

where two reflections (eqs. (A6.1) - (A6.2)) and the path $2L$ passed by the radiation through the absorbing gas (eq. (A6.4)) are taken into account.

On the other hand, according to (2.3), the change of the field amplitude is

$$\frac{A}{A_0} = \mathrm{e}^{-\gamma T_1}, \qquad \text{(A6.6)}$$

where γ is the damping constant of the resonator filled with gas. From (A6.5) and (A6.6) it follows

$$\alpha L = (\gamma - \gamma_0)T_1 \text{ or } \alpha = \frac{2}{c}(\gamma - \gamma_0). \qquad \text{(A6.7)}$$

The expression (2.17) derived in section 2.1 in the small resonator losses approximation can be obtained directly, without approximations from (A6.7), with allowance for the relationship of the field damping constant with the resonator Q factor, resonant response width Δf, and resonator time constant τ:

$$\gamma = \pi f_0 Q^{-1} = \pi \Delta f = (2\tau)^{-1}.$$

Assuming that $\alpha c/2$ is the damping constant of the radiation amplitude in gas, we can transform the expressions (A6.7) into (2.18).

One should not forget about the approximation of a single-frequency oscillator (equation (2.2)), on the basis of which all these relations, including (2.18) and (2.14), were derived. In practical terms, this means that the contribution of the adjacent modes of the resonator must be negligible.

A7. Spectroscopic parameters of H_2O and O_2 lines in the millimetre – submillimetre wave range for atmospheric absorption modelling

Table A7.1. Frequencies of the most significant lines of the fine structure of $^{16}O_2$ molecule and their intensities at 296 K weighted according to the natural terrestrial isotopic abundances

N^-	Frequency MHz	Intensity, 10^{-27} cm/molec	N^+	Frequency MHz	Intensity 10^{-27} cm/molec
1^-	118750.335(3)	100.0	1^+	56264.774(2)	27.39
3^-	62486.254(2)	84.04	3^+	58446.589(2)	75.43
5^-	60306.057(2)	113.3	5^+	59590.983(2)	111.3
7^-	59164.205(2)	125.5	7^+	60434.778(2)	131.3
9^-	58323.877(2)	122.4	9^+	61150.562(2)	134.8
11^-	57612.487(2)	108.1	11^+	61800.158(2)	124.5
13^-	56968.212(2)	87.64	13^+	62411.221(2)	105.3
15^-	56363.399(2)	65.77	15^+	62997.984(2)	82.23
17^-	55783.815(2)	45.93	17^+	63568.526(2)	59.69
19^-	55221.384(3)	29.95	19^+	64127.775(2)	40.61
21^-	54671.180(3)	18.28	21^+	64678.910(2)	25.61
23^-	54130.024(4)	10.47	23^+	65224.078(3)	15.21
25^-	53595.775(4)	5.631	25^+	65764.779(3)	8.487
27^-	53066.933(4)	2.849	27^+	66302.096(4)	4.452
29^-	52542.418(5)	1.357	29^+	66836.834(4)	2.198
31^-	52021.429(6)	0.6086	31^+	67369.601(5)	1.022
33^-	51503.360(7)	0.2574	33^+	67900.868(5)	0.4481
35^-	50987.745(10)	0.1027	35^+	68431.006(6)	0.1853
37^-	50474.215(14)	0.0387	37^+	68960.312(7)	0.0723
39^-	49962.477(21)	0.0138	39^+	69489.029(10)	0.0267
41^-	49452.294(29)	0.0046	41^+	70017.354(15)	0.0093

Table A7.2. Line shape parameters for three rotational triplets of $^{16}O_2$ at 296 K

ν_0, MHz	Intensity*, 10^{-25} cm/molec	E_{low}*, cm^{-1}	γ_{air}, MHz/Torr	n_{γ}^{air}*, unitless	γ_{self}, MHz/Torr	$N',J' \leftarrow N,J$
368498.245(20)	0.2223	3.9611	2.21(2)	0.72	2.25(3)	3,2 – 1,1
424763.023(20)	2.425	2.0843	2.21(2)	0.72	2.19(1)	3,2 – 1,2
487249.270(30)	1.036	2.0843	2.16(10)	0.72	2.11(3)	3,3 – 1,2
715392.980(70)	0.6275	18.3372	2.08*	0.72	2.10(10)	5,4 – 3,3
773839.510(60)	3.961	16.3876	2.18(10)	0.72	2.03(6)	5,4 – 3,4
834145.560(50)	1.365	16.3876	1.98(10)	0.72	1.96(10)	5,5 – 3,4
1061123.830(50)	0.9096	44.2117	1.97*	0.72	1.97(10)	7,6 – 5,5
1120714.836(40)	4.91	42.2240	2.00(10)	0.72	1.96(6)	7,6 – 5,6
1179879.019(50)	1.543	42.2240	1.96*	0.72	1.93*	7,7 – 5,6

* Data from HITRAN-2016.

Table A7.3. The set of self-consistent parameters of the O_2 fine structure lines for modelling the 60-GHz band shape in the atmosphere by eq. (3.12). Adopted from Makarov [2020]

N	Intensity, 10^6 kHz/kPa	γ_{air}, GHz·bar^{-1}	y_0, bar^{-1}	y_1, bar^{-1}	g_0, bar^{-2}	g_1, bar^{-2}	d_0, GHz· bar^{-2}	d_1, GHz· bar^{-2}
1^-	940.3	1.685	-0.041	0	-0.0007	0	-0.00028	-0.00039
1^+	543.4	1.703	0.277	0.124	-0.0901	-0.045	0.00597	0.009
3^-	1503.0	1.513	-0.372	-0.00202	-0.103	0.007	-0.0195	-0.012
3^+	1442.1	1.495	0.559	-0.00812	-0.239	0.033	0.0318	0.016
5^-	2103.4	1.433	-0.573	0.0447	-0.172	0.081	-0.0475	-0.027
5^+	2090.7	1.408	0.618	-0.0927	-0.172	0.162	0.0541	0.029
7^-	2379.9	1.353	-0.366	0.264	0.0279	0.179	-0.0232	0.006
7^+	2438.0	1.353	0.278	-0.351	0.15	0.225	0.0154	-0.015
9^-	2363.7	1.303	-0.0895	0.359	0.132	0.054	0.0007	0.010
9^+	2479.5	1.319	-0.0209	-0.416	0.17	0.003	-0.00842	-0.014
11^-	2120.1	1.262	0.0601	0.326	0.0871	0.0004	-0.0025	-0.013
11^+	2275.9	1.265	-0.152	-0.353	0.0686	-0.047	-0.0014	0.013
13^-	1746.6	1.238	0.216	0.484	0.0827	-0.034	-0.0004	0.004
13^+	1915.4	1.217	-0.293	-0.503	0.0674	-0.071	-0.002	-0.005
15^-	1331.8	1.207	0.373	0.579	0.00685	-0.18	0.005	0.010
15^+	1490.2	1.207	-0.436	-0.59	0.016	-0.21	-0.0066	-0.010
17^-	945.3	1.137	0.491	0.616	-0.0211	-0.285	0.0072	0.010
17^+	1078.0	1.137	-0.542	-0.619	-0.0663	-0.323	-0.008	-0.011
19^-	627.1	1.101	0.571	0.611	-0.0953	-0.363	0.0064	0.008
19^+	728.7	1.101	-0.613	-0.609	-0.115	-0.38	-0.007	-0.009
21^-	389.7	1.037	0.636	0.574	-0.118	-0.378	0.0056	0.003
21^+	461.3	1.038	-0.67	-0.568	-0.14	-0.387	-0.0060	-0.003
23^-	227.3	0.996	0.69	0.574	-0.173	-0.392	0.0047	0.0009
23^+	274.0	0.996	-0.718	-0.566	-0.186	-0.394	-0.0049	-0.0009
25^-	124.6	0.955	0.74	0.601	-0.217	-0.424	0.0040	0.0017

Continued on the next page

Table A7.3. (Continued)

N	Intensity, 10^6 kHz/kPa	γ_{air}, GHz·bar^{-1}	y_0, bar^{-1}	y_1, bar^{-1}	g_0, bar^{-2}	g_1, bar^{-2}	d_0, GHz· bar^{-2}	d_1, GHz· bar^{-2}
25^+	153.0	0.955	-0.763	-0.591	-0.227	-0.422	-0.0041	-0.0016
27^-	64.29	0.906	0.788	0.627	-0.234	-0.465	0.0036	0.0024
27^+	80.40	0.906	-0.807	-0.615	-0.242	-0.46	-0.0037	-0.0023
29^-	31.24	0.858	0.834	0.643	-0.266	-0.51	0.0033	0.0024
29^+	39.80	0.858	-0.849	-0.629	-0.272	-0.50	-0.0034	-0.0024
31^-	14.32	0.811	0.876	0.65	-0.301	-0.55	0.0032	0.0021
31^+	18.56	0.811	-0.887	-0.635	-0.304	-0.54	-0.0032	-0.0020
33^-	6.193	0.764	0.915	0.653	-0.334	-0.58	0.0030	0.0017
33^+	8.172	0.764	-0.922	-0.636	-0.333	-0.56	-0.0030	-0.0016
35^-	2.529	0.717	0.95	0.654	-0.361	-0.62	0.0028	0.0013
35^+	3.397	0.717	-0.955	-0.635	-0.358	-0.59	-0.0029	-0.0012
37^-	0.975	0.669	0.987	0.643	-0.348	-0.69	0.0029	0.0005
37^+	1.334	0.669	-0.988	-0.623	-0.344	-0.65	-0.0029	-0.0004

Table A4. Line shape parameters of the most significant $H_2{}^{16}O$ lines in the subTHz range at 296 K

ν_0, MHz $J'_{K'_aK'_c} \leftarrow J_{K_aK_c}$	Intensity, 10^{-23} cm/molec	E_{low}, cm^{-1}	γ_{air}, MHz/Torr	n_γ^{air}, unitless	γ_{self}, MHz/Torr	n_γ^{self}, unitless	δ_{air}, MHz/Torr	δ_{self}, MHz/Torr
22235.07985* 6_{16}–5_{23}	0.04454	446.5107	3.584(52)	0.70(5)	17.71(5)	1.2(5)	–0.03(4)	+1.10(8)
183310.087(1) 3_{13}–2_{20}	7.736	136.1639	3.945(6)	0.71(7)	19.75(2)	0.83(1)	–0.097(1)	+0.145(7)
321225.676(6)* 10_{29}–9_{36}	0.2554	1282.9188	3.22(7)	0.73	14.15(3)	-	–0.19(3)	+0.37(10)
325152.899(1) 5_{15}–4_{22}	9.077	315.7795	3.76(2)	0.74	18.51(3)	-	–0.017(7)	+1.76(10)
380197.356(5)* 4_{14}–3_{21}	82.62	212.1564	3.834(12)	0.54	18.59(9)	-	–0.094(2)	+0.31(5)
439150.795(5)* 6_{43}–5_{50}	7.128	742.0762	2.74(3)	0.69	12.08(5)	-	+0.07(2)	+0.22(5)
443018.355(5)* 7_{52}–6_{61}	1.481	1045.0578	2.43(2)	0.70	10.61(2)	-	+0.19(2)	–0.31(5)
448001.075(5)* 4_{23}–3_{30}	86.33	285.4186	3.48(1)	0.57	17.34(3)	-	–0.13(2)	–0.82(4)
470888.903(2) 6_{42}–5_{51}	2.734	742.073	2.89(3)	0.73	12.93(4)	-	+0.08(2)	–0.62(8)

Continued on the next page

* Centre of gravity of hyperfine components

Table A4. (Continued)

ν_0, MHz $J'_{K'_aK'_c} \leftarrow J_{K_aK_c}$	Intensity, 10^{-23} cm/molec	E_{low}, cm^{-1}	γ_{air}, MHz/Torr	n_γ^{air}, unitless	γ_{self}, MHz/Torr	n_γ^{self}, unitless	δ_{air}, MHz/Torr	δ_{self}, MHz/Torr
474689.108(1) 5_{33}–4_{40}	10.90	488.1342	3.16(2)	0.71	14.98(6)	-	–0.04(2)	–0.96(10)
488491.128(3) 6_{24}–7_{17}	2.211	586.4792	4.49(5)	0.75	18.1(2)	-	–0.09(5)	–0.48(10)
556935.995(15) 1_{10}–1_{01}	5238	23.7944	4.17(2)	0.75	18.4(2)	-	+0.25(2)	–2.26(4)
620700.807(150) 5_{32}–4_{41}	56.72	488.1077	3.29	0.79	15.9(2)	-	-	+1.85(10)
752033.113(14) 2_{11}–2_{02}	3454	70.0908	4.152(46)	0.77	18.11(15)	-	+0.22(3)	1.17(3)
916171.582 4_{22}–3_{31}	142.6	285.2193	3.59	0.79	18.5	-	-	-

* Centre of gravity of hyperfine components

REFERENCES

[Albert, 1998] Albert S., Petkie D. T., Bettens R. P. A., Belov S. P., De Lucia F. C. FASSST: A new gas-phase analytical tool. *Analytical Chemistry*. 1998. Vol. 70, No. 21. P. 719A—727A.

[Alder, 1998] Alder J. F., Baker J. G. Quantitative millimetre wavelength spectrometry. Part IV. Response curves for oxygen in carbon dioxide and nitrogen at 60 GHz. *Analytica Chimica Acta.* 1998. Vol. 367. P. 245—253.

[Allin, 1967] Allin E. J., May A. D., Stoichef B. P., Stryl J. C., Welsh H. L. Spectroscopy research at the McLennan physical laboratories of the University of Toronto. *Applied Optics*. 1967. Vol. 6, iss. 10. P. 1597—1608.

[Anderson, 1951] Anderson R. S., Johnson C. M., Gordy W. Resonant absorption of oxygen at 2.5-millimeter wavelength. *Phys. Rev*. 1951. Vol. 83. P. 1061—1062.

[Anderson, 1952] Anderson R. S., Smith W. V., Gordy W. Line-breadths of the microwave spectrum of oxygen. *Phys. Rev*. 1952. Vol. 87, No. 4. P. 561—658.

[Arking, 1996] Arking A. Absorption of solar energy in the atmosphere: Discrepancy between model and observations *Science*. 1996. Vol. 273. P. 779—782.

[Artman, 1954] Artman J. O., Gordon G. P. Absorption of microwaves by oxygen in the millimeter wavelength region. *Phys. Rev*. 1954. Vol. 96, No. 5. P. 1237—1245.

[Babcock, 1948] Babcock H. D., Herzberg L. Fine structure of the red system of atmospheric oxygen bands. *Astrophysical J*. 1948. Vol. 108. P. 167—190.

[Babin, 2013] Babin V., Leforestier C., Paesani F. Development of a “first principles” water potential with flexible monomers: Dimer potential energy surface, VRT spectrum, and second virial coefficient. *J. Chem. Theory Comput*. 2013. Vol. 9. P. 5395—5403.

[Bailleux, 1998] Bailleux S., Bogey M., Bolvin H., Civis S., Cordonnier M., Krupnov A. F., Tretyakov M. Yu., Walters A., Coudert L. H. Sub-millimeter wave spectroscopy of the Ar...H_3^+ and Ar...D_3^+ ionic complexes. *J. Mol. Spectrosc*. 1998. Vol. 190. P. 130—139.

[Baldacchini, 1996] Baldacchini G., Buffa G., D'Amato F., Pelagalli F., Tarrini O. Variations in the sign of the pressure-induced lineshifts in the ν_2 band of ammonia with temperature. *J Quant Spectrosc Radiat Transfer*. 1996 V.556 P. 741-743.

[Baranger, 1958] Baranger M. Problem of overlapping lines in the theory of pressure broadening. *Phys. Rev*. 1958. Vol. 111, No. 2. P. 494—504.

[Baranov, 2008] Baranov Yu. I., Lafferty W. J., Ma Q., Tipping R. H. Water-vapor continuum absorption in the 800–1250 cm^{-1} spectral region at temperatures from 311 to 363 K. *J. Quant. Spectrosc. Radiat. Transfer*. 2008. Vol. 109. P. 2291—2302.

[Barath, 1993] Barath F. T., Chavez M. C., Cofield R. E., Flower D. A., et al. The upper atmosphere research satellite microwave limb sounder instrument *J. Geophys. Res*. 1993. Vol. 98(D6). P. 10751—10762.

[Barrett, 2002] Barrett J. Atomic structure and periodicity. Cambridge: Royal Society of Chemistry, 2002. P. 153. (Basic concepts in chemistry. Vol. 9 of Tutorial chemistry texts).

[Bartalini, 2014] Bartalini S., Consolino L., Cancio P., De Natale P., et al. Frequency-comb-assisted terahertz quantum cascade laser spectroscopy. *Phys. Rev.* X. 2014. Vol. 4. Art. 021006.

[Bauer, 1985] Bauer A., Godon M., Duterage B. Self- and air-broadened linewidth of the 183 GHz absorption in water vapor. *J. Quant. Spectrosc. Radiat. Transfer*. 1985. Vol. 33, No. 2. P. 167—175.

[Bauer, 1986] Bauer A., Duterage B., Godon M. Temperature dependence of water-vapor absorption in the wing of the 183 GHz line. *J. Quant. Spectrosc. Radiat. Transfer*. 1986. Vol. 36, No. 4. P. 307—318.

[Bauer, 1987] Bauer A., Godon M., Kheddar M. Temperature and perturber dependences of water-vapor 380 GHz-line broadening. *J. Quant. Spectrosc. Radial. Transfer*. 1987. Vol. 37, No. 6. P. 531—539.

[Bauer, 1989] Bauer A., Godon M., Kheddar M., Hartmann J.-M. Temperature and perturber dependences of water vapor line-broadening. Experiments at 183 GHz; calculations below 1000 GHz. *J. Quant. Spectrosc. Radiat. Transf*. 1989. Vol. 41, No. 1. P. 49—54.

[Bauer, 1991] Bauer A., Godon M. Temperature dependence of water-vapor absorption in linewings at 190 GHz. *J. Quant. Spectrosc. Radiat. Transfer*. 1991. Vol. 46, No. 3. P. 211—220.

[Bauer, 1993] Bauer A., Godon M., Carlier J., Ma Q., Tipping R. H. Absorption by H_2O and H_2O—N_2 mixtures at 153 GHz. *J. Quant. Spectrosc. Radiat. Transfer*. 1993. Vol. 50. P. 463—475.

[Bauer, 1995] Bauer A., Godon M., Carlier J., Ma Q. Water vapor absorption in the atmospheric window at 239 GHz. *J. Quant. Spectrosc. Radiat. Transfer*. 1995. Vol. 53. P. 411—423.

[Bauer, 1996] Bauer A., Godon M., Carlier J., Gamache R. R. Absorption of a H_2O—CO_2 mixture in the atmospheric window at 239 GHz; H_2O–CO_2 linewidths and continuum. *J. Mol. Spectrosc.* 1996. Vol. 176. P. 45—57.

[Bauer, 1998]. Bauer A., Godon M., Carlier J., Gamache R. R. Continuum in the windows of the water vapor spectrum. Absorption of H_2O–Ar at 239 GHz and linewidth calculations. *J. Quant. Spectrosc. Radiat. Transfer*. 1998. Vol. 59, No. 3—5. P. 273—285.

[Bauer, 2001] Bauer A., Godon M. Continuum for H_2O–X mixtures in the H_2O spectral window at 239 GHz; X = C_2H_4, C_2H_6. Are collision-induced absorption processes involved? *J. Quant. Spectrosc. Radiat. Transfer.* 2001. Vol. 69. P. 277—290.

[Becker, 1946] Becker G. E., Autler S. H. Water vapor absorption of electromagnetic radiation in the centimeter wave-length range. *Phys. Rev*. 1946. Vol. 70, No. 5—6. P. 300—307.

[Beers, 1959] Beers Y. Theory of the cavity microwave spectrometer and molecular frequency standard *Rev. Sci. Instrum*. 1959. Vol. 30. P. 9—16.

[Bellescize, 1932] de Bellescize H. La réception synchrone *L'Onde Électrique*. 1932. Vol. 11. P. 230—240.

[Belov, 2007] Belov S. P., Demkin V. M., Zobov N. F., Karyakin E. N., et al. Microwave study of the submillimeter spectrum of the H_2O—HF dimer. *J. Mol. Spectrosc*. 2007. Vol. 241. P. 124—135.

[Benedict, 1970] Benedict W. S., Clough S. A., Frenkel L., Sullivan T. E. Microwave spectrum and rotational constants for theground state of D_2O. *J. Chem. Phys*. 1970. Vol. 53. P. 2565.

[Benner, 1995] Benner D. C., Rinsland C. P., Devij V. M., Smith M. A. H., Atkins D. A multispectrum nonlinear least squares fitting technique. *J. Quant. Spectrosc. Radiat. Transfer.* 1995. Vol. 53, No. 6. P. 705—721.

[Ben-Reuven, 1966] Ben-Reuven A. Impact broadening of microwave spectra. *Phys. Rev.* 1966. Vol. 145, No. 1. P. 7—22

[Bentwood, 1980] Bentwood R. M., Barnes A. J., Orville-Thomas W. J. Studies of intermolecular interactions by matrix isolation vibrational spectroscopy. *J. Mol. Spectrosc*. 1980. Vol. 84. P. 391—404.

[Berestetskii, 1982] Berestetskii V. B., Lifshitz E. M., Pitaevskii L. P. *Quantum Electrodynamics*. Vol. 4 (2nd ed.), Butterworth-Heinemann, 1982. ISBN 978-0-7506-3371-0.

[Bergeat, 2015] Bergeat A., Onvlee J., Naulin C., van der Avoird A., Costes M. Quantum dynamical resonances in low-energy CO(j = 0) + He inelastic collisions. *Nature Chemistry*. 2015 V. 7. No. 4. P. 349—353. DOI: 10.1038NCHEM.2204.

[Beringer, 1946] *Beringer R.* The absorption of one-half centimeter electromagnetic waves in oxygens. *Phys. Rev*. 1946. Vol. 70, No. 12. P. 53—57.

[Berman,1972] *Berman P. R.* Speed-dependent collisional width and shift parameters in spectral profiles *J. Quant. Spectrosc. Radiat. Transfer*. 1972. Vol. 12. P. 1331.

[Bershtein, 1958] Bershtein I.L., Sibiryakov V. L., *Radiotekh. Elektron*., 3, 290 (1958) (In Russian).

[Birk, 2012] Birk M., Wagner G. Temperature-dependent air broadening of water in the 1250—1750 cm^{-1} range. *J. Quant. Spectrosc. Radiat. Transfer*. 2012. Vol. 113. P. 889—928.

[Birk, 2020] Birk M., Wagner G., Loos J., Shine K. P. 3 μm water vapor self- and foreign-continuum: New method for determination and new insights into the self-continuum. *J. Quant. Spectrosc. Radiat. Transfer*. 2020. Vol. 253. Art. 107134.

[Birnbaum, 1962] Birnbaum G., Maryott A. A. Collision-induced microwave absorption in compressed gases. II. Molecular electric quadrupole moments. *J. Chem. Phys*. 1962. Vol. 36. P. 2032—2036.

[Bogdanova, 2010] Bogdanova Ju. V., Rodimova O. B. Line shape in far wings and water vapor absorption in a broad temperature interval. *J. Quant. Spectrosc. Radiat. Transfer*. 2010. Vol. 11. P. 2298—2307.

[Boissoles, 2003] Boissoles J., Boulet C., Tipping R. H., Brown A., Ma Q. Theoretical calculation of the translation-rotation collision-induced absorption in N_2–N_2, O_2–O_2, and N_2–O_2 pairs. *J. Quant. Spectrosc. Radiat. Transfer*. 2003. Vol. 82. P. 505—516.

[Bonch-Bruevich, 1965] Bonch-Bruevich A.M., Khodovoi V.A. Multiphoton processes. *Soviet Physics. Uspekhi.* 1965. V.85. No.1 P. 3-64.

[Born, 1959] Born M., Wolf E. 1959. *Principles of Optics*. Pergamon Press.

[Borysow, 1986] Borysow A., Frommhold L. Collision-induced rototranslational absorption spectra of N_2–N_2 pairs for temperatures from 50 to 300 K. *Astroph. J*. 1986. Vol. 311. P. 1043—1057.

[Bouguér, 1729] Bouguer P. *Essai d'Optique, sur la gradation de la lumiere*. Paris, France: Claude Jombert, 1729. P. 16—22.

[Bouteiller, 2004] Bouteiller Y., Perchard J. P. The vibrational spectrum of $(H_2O)_2$: Comparison between anharmonic *ab initio* calculations and

neon matrix infrared data between 9000 and 90 cm^{-1}. *Chem. Phys*. 2004. Vol. 305. P. 1—12.

[Bouteiller, 2011] Bouteiller Y., Tremblay B., Perchard J. P. The vibrational spectrum of the water dimer: Comparison between anharmonic ab initio calculations and neon matrix infrared data between 14000 and 90 cm^{-1}. *Chem. Phys*. 2011. Vol. 386. P. 29.

[Braakman, 2011] Braakman R., Blake G. A. Principles and promise of Fabry–Perot resonators at terahertz frequencies. *J. Appl. Phys*. 2011. Vol. 109. Art. 063102.

[Braly, 2000-1] Braly L. B., Cruzan J. D., Liu K., Fellers R. S., Saykally R. J. Terahertz laser spectroscopy of the water dimer intermolecular vibrations. I: $(D_2O)_2$. *J. Chem. Phys*. 2000. Vol. 112. No. 23. P. 10293—10313.

[Braly, 2000-2] Braly L. B., Liu K., Brown M. G., Keutsch F. N., Fellers R. S., Saykally R. J. Terahertz laser spectroscopy of the water dimer intermolecular vibrations. II: $(H_2O)_2$. *J. Chem. Phys*. 2000. Vol. 112. No. 23. P. 10314—10326.

[Brogniez, 2016]. Brogniez H., English S., Mahfouf J.-F., Behrendt A., et al. A review of sources of systematic errors and uncertainties in observations and simulations at 183 GHz. *Atmospheric Measurement Techniques* (EGU). 2016. Vol. 9. P. 2207—2221.

[Brown, 2003] Brown A., Tipping R. H. "Collision-induced absorption in dipolar molecule–homonuclear diatomic pairs". In *Weakly interacting pairs: unconventional absorbers of radiation in the atmosphere* edited by C. Camy-Peyret and A. A. Vigasin. P. 93—99. Dordrecht: Kluwer Academic, 2003.

[Brunt, 1932] Brunt D. Notes on radiation in the atmosphere *Q. J. R. Meteorol. Soc*. 1932. Vol. 58. P. 389—420.

[Buck, 2000] Buck U., Huisken F. Infrared spectroscopy of size-selected water and methanol Clusters. *Chem. Rev*. 2000. Vol. 100. P. 3863—3890.

[Buldyreva, 2011] Buldyreva J., Lavrentieva N., Starikov V. *Collisional line broadening and shifting of atmospheric gases. A practical guide for line shape modelling by current semi-classical approaches*. Imperial College Press: World Scientific, 2011.

[Buldyreva, 2013] Buldyreva J. V., Gennadiev N. A., Filippov N. N. Line-mixing in absorption bands of linear molecules diluted in high-density rare gases: Measurements and modeling for OCS–He. *J. Chem. Phys*. 2013. Vol. 138. Art. 164117.

[Bunker, 2004] Bunker F. Jensen. P. *Molecular Symmetry and Spectroscopy*. 2-nd ed. Ottawa: NRC Reseach Press, 1988.

[Buontempo, 1975] Buontempo U., Cunsolo S., Jacucci G., Weis J. J. The far infrared absorption spectrum of N_2 in the gas and liquid phases. *J. Chem. Phys*. 1975. Vol. 63. P. 2570.

[Burenin, 1981-1] Burenin A.V., Karyakin E.N., Krupnov A.F., Shapin S.M., Valdov A.N. Submillimeter microwave spectrum and spectroscopic constants of the OCS molecule. Less abundant isotopic species of the molecule. *J. Mol. Spectrosc*. 1981. Vol. 85. P. 1–7.

[Burenin, 1981-2] Burenin A.V., Valdov A.N., Karyakin E.N., Krupnov A.F., Shapin S.M. Submillimeter microwave spectrum and spectroscopic constants of the OCS Molecule. Isotopic species $^{16}O^{12}C^{33}S$ and $^{18}O^{12}C^{32}S$. *J. Mol. Spectrosc*. 1981. Vol. 87. P. 312–315.

[Burkart, 2014] Burkart J., Romanini D., Kassi S. Optical feedback frequency stabilized cavity ringdown spectroscopy. *Opt. Lett*. 2014. Vol. 39. No. 16. P. 4695–4698.

[Burkhalter, 1950] Burkhalter J. H., Anderson R. S., Smith W. V., Gordy W. The fine structure of the microwave absorption spectrum of oxygen. *Phys. Rev*. 1950. Vol. 79, No. 4. P. 651—655.

[Burch, 1981] Burch D. E. Continuum absorption by atmospheric H_2O. *Proceedings SPIE*. 1981. Vol. 277: Atmospheric Transmission. P. 28—39.

[Buryak, 2015] Buryak I., Vigasin A. A. Classical calculation of the equilibrium constants for true bound dimers using complete potential energy surface. *J. Chem. Phys*. 2015. Vol. 143. Art. 234304.

[Bussey, 1959] Bussey H. E., Birnbaum G. Cavity resonators for dielectric spectroscopy of compressed gases. *Review of Scientific Instruments*. 1959. Vol. 30. P. 800—804.

[Cadeddu, 2007] Cadeddu M. P., Payne V. H., Clough S. A., Cady-Pereira K., Liljegren J. C. Effect of the oxygen line-parameter modeling on temperature and humidity retrievals from ground-based microwave radiometers. *IEEE Transactions on Geoscience and Remote Sensing*. 2007. Vol. 45, No. 7. P. 2216—2223.

[Calo, 1974] Calo J. M., Brown J. H. The calculation of equilibrium mole fractions of polar-polar, nonpolar-polar, and ion dimers. *J. Chem. Phys*. 1974. Vol. 61. P. 3931—3941.

[Camy-Peyret, 2003] Camy-Peyret C. and Vigasin A. A. *Weakly Interacting Molecular Pairs: Unconventional Absorbers of Radiation in the Atmosphere.* Dordrecht: Kluwer Academic, 2003. (NATO ARW Proceedings Series).

[Carter, 1968] Carter C. J., Mitchell R. L., Reber E. E. Oxygen absorption measurements in the lower atmosphere. *Journal of Geophysical Research*. 1968. Vol. 73, No. 10. P. 3113—3120.

[Chistikov, 2019] Chistikov D. N., Finenko A. A., Lokshtanov S. E., Petrov S.V., Vigasin A.A. Simulation of collisioninduced absorption spectra based on classical trajectories and ab initio potential and induced dipole surfaces. I. Case study of N_2–N_2 rototranslational band. *J. Chem. Phys.* 151 2019 194106

[Chistikov, 2020] Chistikov D. N., Finenko A. A., Kalugina Y. N., Lokshtanov S. E., Petrov S. V., Vigasin A. A. Simulation of collision-induced absorption spectra based on classical trajectories and ab initio potential and induced dipole surfaces II. Case study of CO_2–Ar rototranslational band. *J. Chem. Phys.* 2020; Submitted.

[Ciurylo, 1997]. Ciurylo R., Szudy J. Speed-dependent pressure broadening and shift in the soft collision approximation. *J. Quant. Spectrosc. Radiat. Transfer*. 1997. Vol. 57. P. 411—423.

[Clough, 1973] Clough S. A., Beers Y., Klein G. P., Rothman L. S. Dipole moment of water from Stark measurements of H_2O, HDO, and D_2O. *J. Chem. Phys.* 1973. Vol. 59. P. 2254—2259.

[Clough, 1980] Clough S. A., Kneizys F. X., Davies R., Gamache R., Tipping R. "Theoretical line shape for H_2O vapor: Application to the continuum". In *Atmospheric Water Vapor* ed. by A. Deepak, T. D. Wilkerson, and L. H. Ruhnke. P. 25—46. N. Y.: Academic Press, 1980. (Proceedings of the International Workshop on Atmospheric Water Vapor, Vail, Colorado, September 11–13, 1979).

[Clough, 1989] Clough S. A., Kneizys F. X., Davies R. W. Line shape and the water vapor continuum. *Atmos. Res.* 1989. Vol. 23. P. 229—241.

[Cohen, 1991] Cohen R. C., Saykally R. J. Multidimensional intermolecular dynamics from tunable far–infrared laser spectroscopy: Angular-radial coupling in the intermolecular potential of argon–H_2O. *J. Chem. Phys*. 1991. Vol. 95. P. 7891—7906.

[Cohen, 1993] Cohen R. C., Saykally R. J. Determination of an improved intermolecular global potential energy surface for Ar–H_2O from vibration–rotation–tunneling spectroscopy. *J. Chem. Phys.* 1993. Vol. 98. P. 6007—6030.

[Colmont, 1999] Colmont J.-M., Priem D., Wlodarczak G., Gamache R. R. Measurements and calculations of the halfwidth of two rotational transitions of water vapor perturbed by N_2, O_2, and air. *J. Mol. Spectrosc*. 1999. Vol. 193. P. 233—243.

[Colmont, 2001] Colmont J. M., D'Eu J.-F., Rohart F., Wlodarczak G., Buldyreva J. N_2- and O_2-broadenings and lineshapes of the 551.53-GHz line of ^{14}NO. *J. Mol. Spectrosc*. 2001. Vol. 208. P. 197—208.

[Góra, 2014] Góra U., Cencek W., Podeszwa R., van der Avoird A., Szalewicz K. Predictions for water clusters from a first-principles two-

and three-body force field. *J. Chem. Phys*. 2014. Vol. 140. Art. 194101.

[Coudert, 1990] Coudert L. H., Hougen J. T. Analysis of the microwave and far infrared spectrum of the water dimer. *J. Mol. Spectrosc*. 1990. Vol. 139. P. 259—277.

[Coudert, 2009] Coudert L. H., Belov S. P., Willaert F., McElmurry B. A., Bevan J. W., Hougen J. T. Submillimeter spectrum and analysis of vibrational and hyperfine coupling effects in $(HI)_2$ *J. Chem. Phys. Lett*. 2009. Vol. 482. P. 180—188.

[Cowling, 1942] Cowling T. G. The absorption of water vapour in the far infra-red. *Reports on Progress in Physics*. 1942. Vol. 9. P. 29—41.

[Croskey, 1992] Croskey C. L., Kampfer N., Belivacqua R. M., Hartmann G. K., et al. The Millimeter wave Atmospheric Sounder (MAS): a shuttle-based remote sensing experiment. *IEEE Trans. Microwave Theory Techn.* 1992. Vol. 40, No. 6. P. 1090—1100.

[Cruz-Pol, 1998] Cruz-Pol S. L., Ruf C. S., Keihm S. J. Improved 22–32 GHz atmospheric absorption model. *Radio Sci.* 1998. Vol. 33, No. 5. P. 1319—1333.

[Csaszar, 2005] Csaszar A. G., Czako G., Furtenbacher T., Tennyson J., et al. On equilibrium structures of the water molecule. *J. Chem. Phys*. 2005. Vol. 122. Art. 214305.

[Cullen, 1979] Cullen A. L., Yu P. K. Complex source-point theory of the electromagnetic open resonator. *Proc. R. Soc. Lond. A*. 1979. Vol. 366. P. 155—171.

[Curtiss, 1979] Curtiss L. A., Frurip D. J., Blander M. Studies of molecular association in H_2O and D_2O vapors by measurements of thermal conductivity. *J. Chem. Phys*. 1979. Vol. 71. P. 2703—2711.

[Dagg, 1975] Dagg I. R., Reesor G. E., Urbaniak J. L. Collision induced absorption in N_2, CO_2, and H_2 at 2.3 cm^{-1}. *Can. J. Phys*. 1975. Vol. 53. P. 1764—1776.

[Dagg, 1978] Dagg I. R., Reesor G. E., Wong M. A microwave cavity measurement of collision-induced absorption in N_2 and CO, at 4.6 cm^{-1}. *Can. J. Phys*. 1978. Vol. 56. P. 1037—1045.

[Daly, 1970] Daly P. W., Oka T. Microwave studies of collision-induced transitions between rotational lewels. VII. Collisions between NH_3 and nonpolar molecules. *J. Chem. Phys*. 1970. Vol. 53, No. 8. P. 3272—3278.

[D'Eu, 2002] D'Eu J.-F., Lemoine B., Rohart F. Infrared HCN lineshapes as a test of Galatry and speed-dependent Voigt profiles. *J. Mol. Spectrosc*. 2002. Vol. 212. P. 96—110.

[De Lucia, 1972] De Lucia F. C., Helminger P., Cook R., Gordy W. Submillimeter microwave spectrum of $H_2{}^{16}O$. *Phys. Rev. A*. 1972. Vol. 5, No. 2. P. 487—490.

[Dennison, 1940] Dennison D. M. The infra-red spectra of polyatomic molecules. Part II. *Rev. Mod. Phys*. 1940. Vol. 12, No. 3. P. 175—214.

[De Vizia, 2011] De Vizia M. D., Rohart F., Castrillo A., Fasci E., Moretti L., Gianfrani L. Speed-dependent effects in the near-infrared spectrum of self-colliding $H_2{}^{18}O$ molecules. *Phys. Rev. A*. 2011. Vol. 83. Art. 052506.

[Dicke, 1953] Dicke R. H. The effect of collisions upon the Doppler width of spectral line. *Phys. Rev.* 1953. Vol. 89. P. 472—473.

[Dieke, 1927] Dieke G. H., Babcock H. D. The structure of the atmospheric absorption bands of oxygen. *Proc. Nat. Acad. Sci*. 1927. Vol. 13. P. 670—678.

[Dreizler, 1986] Dreizler H. Experiences with microwave Fourier transform spectroscopy of molecular gases. *Mol. Phys*. 1986. Vol. 59. P. 1—28.

[Drouin, 2007] Drouin B. J. Temperature dependent pressure induced linewidths of $^{16}O_2$ and $^{18}O^{16}O$ transitions in nitrogen, oxygen and air. *J. Quant. Spectrosc. Radiat. Transfer*. 2007. Vol. 105. P. 450—458.

[Drouin, 2010] Drouin B. J., Yu S., Miller C. E., Müller H. S. P., Lewen F., Brünken S., Habara H. Terahertz spectroscopy of oxygen, O_2, in its $^3\Sigma_g^-$ and $^1\Delta$ electronic states. *J. Quant. Spectrosc. Radiat. Transfer*. 2010. Vol. 111. P. 1167—1173.

[Dryagin, 1966] Dryagin Yu. A., Kislyakov A. G. Kukin L. M., Naumov A. I., Fedoseev L. I. Measurements of the atmospheric absorption in the range 1.36-3.0 mm. *Soviet Radiophysics.* 1966. V.9. No. 6. P. 624–627.

[Dryagin, 1970] Dryagin Yu. A. Frequency measurement with a high-quality Fabry-Perot resonator. *Radiophysics and Quantum Electronics*. 1970. V. 13, No. 1. P. 107—110.

[Dryagin, 1992] Dryagin Yu. A., Parshin V. V. A method to measure dielectric parameters in 5–0.5 mm wavelength band. *International Journal of Infrared and Millimeter Waves*. 1992. Vol. 13, No. 7. P. 1023—1032.

[Dyke, 1974] Dyke T. R., Muenter J. S. Microwave spectrum and structure of hydrogen bonded water dimer. *J. Chem. Phys*. 1974. Vol. 60. P. 2929—2930.

[El-Kader, 2016] El-Kader M.S.A. Theoretical calculation of the rototranslational collision-induced absorption (CIA) spectra in O_2–O_2

pairs. *Z. Phys. Chem*. 2016; 230(8): 1099–1109. DOI 10.1515zpch-2015-0674

[Elsasser, 1938-1] Elsasser W. M. Far infrared absorption of atmospheric water vapor. *Astrophys. J*. 1938. Vol. 87. P. 497—507.

[Elsasser, 1938-2] Elsasser W. M. Note on atmospheric absorption caused by the rotational water band. *Phys. Rev*. 1938. Vol. 53. — P. 768.

[Emery, 1972] Emery R. Atmospheric absorption in the region of 1 mm measurements wavelength. *Infrared Physics*. 1972. Vol. 12. P. 65—79.

[Endo, 1982] Endo Y., Mizushima M. Microwave resonance lines of $^{16}O_2$ in its electronic groung state ($X^3\Sigma_g^-$). *Japanese Journal of Applied Physics*. 1982. Vol. 21, No. 6. P. L379—L380.

[Evans, 2000] Evans J. T., Vaida V. Aggregation of water molecules: Atmospheric implications. *J. Chem. Phys*. 2000. Vol. 113, No. 16. P. 6652—6659.

[Fabian, 1998] Fabian M., Morino I., Yamada K. M. T. Analysis of the line profiles of CH_3CN for the J = 5–4 and J = 6–5 rotational transitions. *J. Mol. Spectrosc*. 1998. Vol. 190. P. 232—239.

[Fano, 1963] Fano U. Pressure broadening as a prototype of relaxation. *Phys. Rev*. 1963. Vol. 131, No. 1. P. 259—268.

[Fowler, 1939] Fowler R. H., Guggenheim E. A. *Statistical thermodynamics*. 1939. N. Y.: Macmillan Co: Cambridge University Press, 693 p.

[Fraser, 1989] Fraser G. T., Suenram R. D., Coudert L. H. Microwave electric-resonance optothermal spectroscopy of $(H_2O)_2$. *J. Chem. Phys*. 1989. Vol. 90. P. 6077—6085.

[Fraser, 1990] Fraser G. T., Lovas F. J., Suenram R. D., Matsumura K. Microwave spectrum of Ar–H_2O: Dipole moment, isotopic studies, ^{I7}O quadrupole coupling constants. *J. Mol. Spectrosc*. 1990. Vol. 144. P. 97—112.

[Fraser, 1991] Fraser G. T. $(H_2O)_2$: spectroscopy, structure and dynamics. *Int. Rev. Phys. Chem*. 1991. Vol. 10. P. 189—206.

[Frenkel, 1966-1] Frenkel L., Woods D. Microwave absorption by H_2O vapor and its mixtures with other gases between 100 and 300 Gcs. *Proc. IEEE*. 1966. Vol. 54, No. 4. P. 498—505.

[Frenkel, 1966-2] Frenkel L., Woods D. Microwave absorption in compressed CO_2. *J. Chem. Phys*. 1966. Vol. 44. P. 2219.

[Frommhold, 2006] Frommhold L. *Collision-induced absorption in gases*. 2006. N.Y.: Cambridge University Press.

[Frost, 1976] Frost B. S. A theory of microwave lineshifts. *J. Phys. B: Atom. Mol. Phys.* 1976.V. 96. P. 1001—1020.

[Füser, 2014] Füser H., Bieler M. Terahertz frequency combs theoretical aspects and applications. *J. Infrared Millim. Terahz. Waves*. 2014. Vol. 35. P. 585—609.

[Furashov, 1966] Furashov N. I., Sverdlov B. A., Chernyaev S. N.. Absorption of electromagnetic radiation by pure water vapor at frequencies near 1.5 THz. *Radiophysics and Quantum Electronics*. 1996. Vol. 39. P. 754—759.

[Furashov, 1984] Furashov N. I., Katkov V. Y., Ryadov V. Ya. On the anomalies in submillimeter absorption spectrum of atmospheric water vapor. *Int. J. Infrared Millim. Waves*. 1984. Vol. 5, No. 7. P. 971—984.

[Furashov, 1985] Furashov N. I., Katkov V. Yu. Humidity dependence of the atmospheric absorption coefficient in the transparency windows centered at 0.88 and 0.73 mm. *Int. J. Infrared Millim. Waves*. 1985. Vol. 6, No. 8. P. 751—764.

[Galatry, 1961] Galatry L. Simultaneous effect of Doppler and foreign gas broadening on spectral lines. *Phys. Rev*. 1961. Vol. 122. Art. 1218.

[Galtsev, 1978] Galtsev A. P. Tsukanov V. V. Calculation of shape of IR gas absorption bands by method of statisticall molelling. *Optics and Spectroscopy.* 1978. Vol. 45, No. 1. P. 75—80 (In Russian).

[Gamache, 2000] Gamache R. R., Kennedy S., Hawkins R., Rothman L. S. Total internal partition sums for molecules in the terrestrial atmosphere. *Journal of Molecular Structure*. 2000. Vol. 517518. P. 407—425.

[Gamache, 2003-1] Gamache R. R., Fischer J. Half-widths of $H_2{}^{16}O$, $H_2{}^{18}O$, $H_2{}^{17}O$, $HD^{16}O$, and $D_2{}^{16}O$. I. Comparison between isotopomers. *J. Quant. Spectrosc. Radiat. Transfer*. 2003. Vol. 78. P. 289—304.

[Gamache, 2003-2] Gamache R. R., Fischer J. Half-widths of $H_2{}^{16}O$, $H_2{}^{18}O$, $H_2{}^{17}O$, $HD^{16}O$, and $D_2{}^{16}O$. II. Comparison with measurement. *J. Quant. Spectrosc. Radiat. Transfer*. 2003. Vol. 78. P. 305—318.

[Gamache, 2004-1] Gamache R. R., Hartmann J.-M. An intercomparison of measured pressure-broadening and pressure-shifting parameters of water vapor. *Can. J. Chem*. 2004. Vol. 82. P. 1013—1027.

[Gamache, 2004-2] Gamache R. R., Hartmann J.-M. Collisional parameters of H_2O lines: effects of vibration. *J. Quant. Spectrosc. Radiat. Transfer*. 2004. Vol. 83. P. 119—147.

[Gamache, 2017] Gamache R. R., Roller C., Lopes E., Gordon I. E., et al. Total internal partition sums for 166 isotopologues of 51 molecules important in planetary atmospheres: Application to HITRAN2016 and beyond. *J. Quant. Spectrosc. Radiat. Transfer.* 2017. Vol. 203. P. 70—87.

[Gamache, 2018] Gamache R. R., Vispoel B. On the temperature dependence of half-widths and line shifts for molecular transitions in the microwave and infrared regions. *J. Quant. Spectrosc. Radiat. Transfer*. 2018. Vol. 217. P. 440—452.

[Gao, 2017] Gao Z., Loreau J., van der Avoird A., van de Meerakker S.Y.T. Direct observation of product-pair correlations in rotationally inelastic collisions of ND_3 with D_2. *Phys Chem Chem Phys*. 2019. Vol. 21. Art. 14033. DOI: 10.1039c8cp07109h.

[Gardner, 2005] Gardner F. M. *Phaselock Techniques* (Third Edition). 2005. John Wiley & Sons. Print ISBN:9780471430636

[Gamache, 2009] Gamache R. R., Laraia A. L. N_2-, O_2-, and air-broadened half-widths, their temperature dependence, and line shifts for the rotation band of $H_2{}^{16}O$. *J. Molec. Spectrosc*. 2009. Vol. 257. P. 116—127.

[Gebbie, 1969] Gebbie H. A., Burroughs W. J., Chamberlain J., Harris J. E., Jones R. G. Dimers of the water molecule in the Earth's atmosphere. *Nature*. 1969. Vol. 221. P. 143—145.

[Gilbert, 1970] Gilbert J. A microwave saturation spectrometer for the measurement of linewidth and absolute intensity. *Rev. Sci. Instr*. 1970. Vol. 41, No. 7. P. 1050—1065.

[Gimmestad, 1976] Gimmestad G. G., Llewellyn-Jones D. T., Gebbie H. A. Millimetre wave oxygen attenuation measurements. *J. Quant. Spectrosc. Radiat. Transfer*. 1976. Vol. 16. P. 899—900.

[Glauber, 2006] Glauber R. J. One hundred years of light quanta. *Rev. Mod. Phys*. 2006. Vol. 78. P. 1267—1278.

[Godon, 1992] Godon M., Carlier J., Bauer A. Laboratory studies of water vapor absorption in the atmospheric window at 213 GHz. *J. Quant. Spectrosc. Radiat. Transfer*. 1992. Vol. 47. P. 275—285.

[Godon, 2000] Godon M., Bauer A., Gamache R. R. The continuum of water vapor mixed with methane: absolute absorption at 239 GHz and linewidth calculations. *J. Molec. Spectrosc*. 2000. Vol. 202. P. 293—302.

[Gokhale, 1951] Gokhale B. V., Strandberg M. W. P. Line breadths in the 5-mm microwave absorption of oxygen. *Phys. Rev*. 1951. Vol. 84. P. 844.

[Golant, 1965] Golant M. B., Vilenskaya P. L., Zyulina E. A., Kaplun Z. F., *et al*. *Prib. Tekh. Eksp*. 1965. Vol. 4. P. 136—139; (In Russian. English translation - "*Sovjet Physics—Pribory*")

[Golant, 1969] Golant M. B., Alekseenko Z. T., Korotkova Z. S., Lunkina L. A., *et al. Prib. Tekh. Eksp*. 1969. Vol. 3. P. 231—232. (In Russian. English translation - "*Sovjet Physics—Pribory*")

[Golubiatnikov, 2003-1] Golubiatnikov G. Yu., Krupnov A. F. Microwave study of the rotational spectrum of oxygen molecule in the range up to 1.12 THz. *J. Mol. Spectrosc*. 2003. Vol. 217. P. 282—287.

[Golubiatnikov, 2003-2] Golubiatnikov G. Yu., Koshelev M. A., Krupnov A. F. Reinvestigation of pressure broadening parameters at 60-GHz band and single 118.75 GHz oxygen lines at room temperature. *J. Mol. Spectrosc*. 2003. Vol. 222. P. 191—197.

[Golubiatnikov, 2005-1] Golubiatnikov G. Yu. Shifting and broadening parameters of the water vapor 183-GHz line ($3_{13} - 2_{20}$) by H_2O, O_2, N_2, CO_2, H_2, He, Ne, Ar, and Kr at room temperature. *J. Mol. Spectrosc*. 2005. Vol. 230, No. 2. P. 196—198.

[Golubiatnikov, 2005-2] Golubiatnikov G. Yu., Lapinov A. V., Guarnieri A., Knochel R. Precise Lamb-dip measurements of millimeter and submillimeter wave rotational transitions of $^{16}O^{12}C^{32}S$. *J. Mol. Spectrosc*. 2005. Vol. 234. P. 190—194.

[Golubiatnikov, 2006] Golubiatnikov G. Yu., Markov V. N., Guarnieri A., Knoechel R. Hyperfine structure of $H_2{}^{16}O$ and $H_2{}^{18}O$ measured by Lamb-dip technique in the 180–560 GHz frequency range. *J. Mol. Spectrosc*. 2006. Vol. 240. P. 251—254.

[Golubiatnikov, 2020] Golubiatnikov G.Yu., Koshelev M.A., Tsvetkov A.I., Fokin A.P., Glyavin M.Yu., Tretyakov M.Yu. Sub-Terahertz high-sensitivity high-resolution molecular spectroscopy with a gyrotron. *IEEE Trans. THz Sci. Technol*. 2020. Vol. 10, No. 5. P. 773-783. DOI: 10.1109TTHZ.2020.2984459.

[Gordon, 1967] Gordon R. G. On the pressure broadening of molecular multiplet spectra. *J. Chem. Phys*. 1967. Vol. 46. P. 448—455.

[Gordon, 1968] Gordon R.G. "Correlation functions for molecular motion" in *Advances in magnetic resonance*. 1968. Ed. J.S. Waugh. V. 3. Elsevier. P. 1-42. DOI: 10.1016B978-1-4832-3116-7.50008-4.

[Gordon, 2017] Gordon I. E., Rothman L. S., Hill C., Kochanov R. V., *et al*. The HITRAN2016 Molecular Spectroscopic Database. *J. Quant. Spectrosc. Rad. Transfer*. 2017. Vol. 203. P. 3—69.

[Gordon, 2021] Gordon I. E., Rothman L. S., Hargreaves R.J., Hashemi R., *et al*. The HITRAN2020 Molecular Spectroscopic Database. *J. Quant. Spectrosc. Rad. Transfer*. 2021. DOI: 10.1016/j.jqsrt.2021.107949

[Gordy, 1984] Gordy W., Cook R. L. *Microwave molecular spectra*. 1984. N.Y.: J. Wiley and Sons Inc.

[Goyette, 1990] Goyette T. M., De Lucia F. C. The pressure broadening of the $3_{13} - 2_{20}$ transition of water between 80 and 600 K. *J. Mol. Spectrosc*. 1990. Vol. 143, No. 2. P. 346—358.

[Goyette, 1995] Goyette T. M., Guo W., De Lucia F. C., Swartz J. C., *et al.* Femtosecond demodulation source for high resolution submillimeter spectroscopy. *Appl. Phys. Lett*. 1995. Vol. 67. P. 3810—3812.

[Gross, 1955] Gross E. P. Shape of collision-broadened spectral lines. *Phys. Rev*. 1955. Vol. 97, No. 2. P. 395—403.

[Hagen, 1903] Hagen E., Rubens H. Über Beziehungen des Reflexions- und Emissionsvermögens der Metalle zu ihrem elektrischen Leitvermögen. *Annalen der Physik*. 1903. Vol. 316, No. 8. S. 873—901.

[Harries, 1979] Harries J. E. The temperature dependence of collision-induced absorption in gaseous N_2. *J. Opt. Soc. Am*. 1979. Vol. 69, No. 3. P. 386—393.

[Hartmann, 1994] Hartmann G. K., Degenhardt W., Zwick R., Liebe H. J., Hufford G. A., Cotton M. G. Zeeman splitting of the 61 GHz (9+) O_2 line in the upper atmosphere measured by MAS. *IGARSS '94. Surface and Atmospheric Remote Sensing: Technologies, Data Analysis and Interpretation*. 1994. Vol. 3. P. 1338—1340. (IEEE Conference Publications: Geoscience and Remote Sensing Symposium, 1994).

[Hartmann, 2008] Hartmann J.-M., Boulet C., Robert D. *Collisional effects on molecular spectra: Laboratory experiments and models, consequences for applications*. 2008. Amsterdam: Elsevier.

[Hartmann, 2013] Hartmann J.-M., Tran H., Ngo N. H., Landsheere X., *et al. Ab initio* calculations of the spectral shapes of CO_2 isolated lines including non-Voigt effects and comparisons with experiments. *Physical Review A*. 2013. Vol. 87. Art. 013403.

[Harvey, 2004] Harvey A. H., Lemmon E. W. Correlation for the second virial coefficient of water. *J. Phys. Chem. Ref. Data*. 2004. Vol. 33. P. 369—376.

[Held, 2000] Held I. M., Soden B. J. Water vapor feedback and global warming. *Annu. Rev. Energy Environ*. 2000. Vol. 25. P. 441—475.

[Hemmi, 1969] Hemmi C. O., Straiton A. W. Pressure broadening of 1.63-mm water vapor absorption line. *Radio Sci*. 1969. Vol. 4. P. 9—15.

[Herzberg, 1949-1] Herzberg G. *Molecular spectra and Molecular Structure: Spectra of Diatomic Molecules*. 1979. Boston, MA: Springer.

[Herzberg, 1949-2] Herzberg G. *Infrared and Raman Spectra of polyatomic molecules.* 1945. NY: D. Van Nostrand Company.

[Hill, 1954] Hill R., Gordy W. Zeeman effect and line breadth studies of the microwave lines of oxygen. *Phys. Rev*. 1954. Vol. 93, No. 5. P. 1019—1022.

[Hill, 1986] Hill R. J. Water vapor-absorption line shape comparison using the 22-GHz line: The Van Vleck–Weisskopf shape affirmed. *Radio Science*. 1986. Vol. 21, No. 3. P. 447—451.

[Hill, 1987] Hill T. L. *Statistical Mechanics: Principles and Selected Applications* (Dover Books on Physics) 1987. NY: Dover Inc. ISBN-13: 978-0486653907

[Hirschfelder, 1942] Hirschfelder J. O., McClure F. T., Weeks I. F. Second virial coefficients and the forces between complex molecules. *J. Chem. Phys*. 1942. Vol. 10. P. 201—211.

[Hirschfelder, 1948] Hirschfelder J. O., Bird R. B., Spotz E. L. The transport properties for non-polar gases. *J. Chem. Phys*. 1948. Vol. 16. P. 968—981.

[Hirschfelder, 1954] Hirschfelder J. O., Curtiss C. H., Bird R. B. *Molecular theory of gases and liquids*. 1954. NY: Jon Wiley & Sons, Inc.

[Ho, 1968] Ho W., Kaufman I. A., Thaddeus P. Pressure induced microwave absorption in N_2. *J. Chem. Phys*. 1968. Vol. 49. P. 3627—3631.

[Ho, 1971] Ho W., Birnbaum G., Rosenberg A. Far-infrared collision-induced absorption in CO_2. I. Temperature dependence. *J. Chem. Phys*. 1971. Vol. 55. P. 1028—1038.

[Huang, 1989] Huang Z. S., Miller R. E. High resolution near-infrared spectroscopy of water dimer. *J. Chem. Phys.* 1989. Vol. 91. P. 6613—6631.

[Huang, 2008-1] Huang X., Braams B. J., Bowman J. M., Emerson C. L., *et al.* New *ab initio* potential energy surface and the vibration-rotation-tunneling levels of $(H_2O)_2$ and $(D_2O)_2$. *J. Chem. Phys*. 2008. Vol. 128. Art. 034312.

[Huang, 2008-2] Huang X., Schwenke D. W., Lee T. J. An accurate global potential energy surface, dipole moment surface, and rovibrational frequencies for NH_3. *J. Chem. Phys*. 2008. Vol. 129. Art. 214304.

[Huiszoon, 1971] *Huiszoon C.* A high resolution spectrometer for the shorter millimeter wavelength region Rev. Sci. Instrum. 1971. Vol. 42, iss. 4. P. 477—481.

[Humliček, 1982] Humliček J. Optimized computation of the Voigt and complex probability functions. *J. Quant. Spectrosc. Radiat. Transfer*. 1982. Vol. 27, No. 4. P. 437—444.

[Hunter, 2007] Hunter R. I., Robertson D. A., Goy P., Smith G. M. Design of high-performance millimeter wave and sub-millimeter wave quasi-optical isolators and circulators. *IEEE Microwave Theory and Techniques*. 2007. Vol. 55, No. 5. P. 890—898.

[Ikeda, 2010] Ikeda T., Katayama Y., Saitoh H., Aoki K. High-temperature water under pressure. *J. Chem. Phys.* 2010. Vol. 132. Art. 121102.

[Ivanov, 2016] Ivanov S. V. Quasi-bound complexes in collisions of different linear molecules: Classical trajectory study of their manifestations in rotational relaxation and spectral line broadening. *J. Quant. Spectrosc. Radiat. Transfer*. 2016. Vol. 177. P. 269—282.

[Jacquemart, 2001] Jacquemart D., Mandin J.-Y., Dana V., Picqué N., Guelachvili G. A multispectrum fitting procedure to deduce molecular line parameters: Application to the 3-0 band of $^{12}C^{16}O$. *Eur. Phys. J. D*. 2001. Vol. 14. P. 55—69.

[Jacquinet-Husson, 2011] Jacquinet-Husson N., Crepeau L., Armante R., Boutammine C., *et al*. The 2009 edition of the GEISA spectroscopic database. J. Quant. Spectrosc. Radiat. Transfer. 2011. Vol. 112. P. 2395—2445.

[Jacquinet–Husson, 2016] Jacquinet-Husson N., Armante R., Scott N. A, Chedin A, *et al.* The 2015 edition of the GEISA spectroscopic database. *Journal of Molecular. Spectroscopy*. 2016. Vol. 327. P. 31—72.

[Jensen, 2000] Jensen P., Bunker P. *Computational Molecular spectroscopy*. 2000. Ed. by. Chichester. UK: Wiley and Sons Ltd.

[Jones, 1924-1] Jones J. E. On the determination of molecular fields. I. From the variation of the viscosity of a gas with temperature. *Proceedings of the Royal Society of London. Series A*. 1924. Vol. 106. P. 441—462.

[Jones, 1924-2] Jones J. E. On the determination of molecular fields. II. From the equation of state of a gas. *Proceedings of the Royal Society of London. Series A*. 1924. Vol. 106, No. 738. P. 463—477.

[Joubert, 1999] Joubert P., Bonamy J., Robert D., Domenech J. L., Bermejo D. A partially correlated strong collision model for velocity- and state-changing collisions application to Ar-broadened HF rovibrational line shape. *J. Quant. Spectrosc. Radiat. Transfer*. 1999. Vol. 61. P. 519—531.

[Kaplan, 2006]. Kaplan I. G. *Intermolecular Interactions: Physical Picture, Computational Methods and Model Potentials.* 2006. NY: John Wiley & Sons, Ltd

[Karman, 2015] Karman T., Miliordos E., Hunt K. L. C., Groenenboom G. C., van der Avoird A. Quantum mechanical calculation of the collision-induced absorption spectra of N_2–N_2 with anisotropic interactions. *J. Chem. Phys.* 2015. Vol. 142. Art. 084306.

[Kasai, 2011] Kasai Y., Dupuy E., Saito R., Hashimoto K., *et al.* The H_2O–O_2 water vapour complex in the Earth's atmosphere. *Atmos. Chem. Phys*. 2011. Vol. 11. P. 8607—8612.

[Kassi, 2012] Kassi S., Campargue A. Cavity ring down spectroscopy with $5 \cdot 10^{-13}$ cm^{-1} sensitivity *J. Chem. Phys*. 2012. Vol. 137. Art. 234201.

[Katkov, 1995] Katkov V. Yu., Sverdlov B. A., Furashov N. I. Experimental estimates of the value and temperature dependence of the air-humidity quadratic component of the atmospheric water-vapor absorption coefficient in the frequency band of 140–410 GHz. *Radiophysics and Quantum Electronics*. 1995. Vol. 38. P. 835—844.

[Kelly, 2010] Kelly R. E. A., Tennyson J., Groenenboom G. C., van der Avoird A. Water dimer vibration–rotation tunnelling levels from vibrationally averaged monomer wavefunctions. *J. Quant. Spectrosc. Radiat. Transfer*. 2010. Vol. 111. P. 1262—1276.

[Keutsch, 2003-1] Keutsch F. N., Goldman N., Harker H. A., Leforestier C., Saykally R. J. Complete characterization of the water dimer vibrational ground state and testing the VRT(ASP-W)III, SAPT-5st, and VRT(MCY-5f) surfaces. *Mol. Phys*. 2003. Vol. 101. P. 3477—3492.

[Keutsch, 2003-2] Keutsch F. N., Braly L. B., Brown M. G., Harker H. A., *et al.* Water dimer hydrogen bond stretch, donor torsion overtone, and "in-plane bend" vibrations. *J. Chem. Phys*. 2003. Vol. 119. P. 8927—8937.

[Khintchine, 1934] Khintchine A. Korrelationstheorie der stationären stochastischen prozesse. *Mathematische Annalen*. 1934. Vol. 109. P. 604—615.

[Kiehl, 1997] Kiehl J. T., Trenberth K. E. Earth's annual global mean energy budget. *Bull. Am. Meteorol. Soc.* 1997. Vol. 78. P. 197—208.

[King, 1947] King G. W., Hainer R. M. Expected microwave absorption coefficients of water and related molecules. *Phys. Rev*. 1947. Vol. 71, No. 7. P. 433—443.

[King, 1954] King W. C., Gordy W. One-to-two millimeter wave spectroscopy. IV. Experimental methods and results for OCS, CH_3F and H_2O. *Phys. Rev*. 1954. Vol. 93, No. 3. P. 407—412.

[Kjaergaard, 2003] Kjaergaard H. G., Robinson T. W., Howard D. L., Daniel J. S., Headrick J. E., Vaida V. Complexes of importance to the absorption of solar radiation. *J. Phys. Chem. A*. 2003. Vol. 107. P. 10680—10686.

[Kjaergaard, 2008] Kjaergaard H. G., Garden A. L., Chaban G. M., Gerber R. B., *et al.* Calculation of vibrational transition frequencies and

intensities in water dimer: Comparison of different vibrational approaches. *J. Phys. Chem*. A. 2008. Vol. 112. P. 4324—4335.

[Klemperer, 2006] Klemperer W., Vaida V. Molecular complexes in close and far away. *P. Natl. Acad. Sci. USA* (PNAS). 2006. Vol. 10328. P. 10584—10588. DOI: 10.1073pnas.0508231103.

[Kogelnik, 1966] Kogelnik H., Li T. Laser beams and resonators. *Proceedings of the IEEE*. 1966. Vol. 54, No. 10. P. 1312—1329.

[Kolb, 1958] Kolb A. C., Griem H. Theory of line broadening in multiplet spectra. *Phys. Rev*. 1958. Vol. 111. P. 514—521.

[Korolev, 2001] Korolev A. N., Zaitsev S. A., Golenitskij I. I., Zhary Y. V., *et al*. Traditional and novel vacuum electron devices. *IEEE Transactions on Electron Devices*. 2001. Vol. 48, No. 12. P. 2929—2937.

[Koshelev, 2007] Koshelev M. A., Tretyakov M. Yu., Golubiatnikov G. Yu., Parshin V. V., Markov V. N., Koval I. A. Broadening and shifting of the 321-, 325- and 380-GHz lines of water vapor by the pressure of atmospheric gases. *J. Mol. Spectrosc*. 2007. Vol. 241. P. 101—108.

[Koshelev, 2011] Koshelev M. A., Serov E. A., Parshin V. V., Tretyakov M. Yu. Millimeter wave continuum absorption in moist nitrogen at temperatures 261–328 K. *J. Quant. Spectrosc. Radiat. Transfer*. 2011. Vol. 112. P. 2704—2712.

[Koshelev, 2012]. Koshelev M. A., Tretyakov M. Yu., Rohart F., Bouanich J.-P. Speed dependence of collisional relaxation in ground vibrational state of OCS: Rotational behavior. *J. Chem. Phys*. 2012. Vol. 136. Art. 124316.

[Koshelev, 2015] Koshelev M. A., Vilkov I. N., Tretyakov M. Yu. Pressure broadening of oxygen fine structure lines by water. J. *Quant. Spectrosc. Radiat. Transfer*. 2015. Vol. 154. P. 24—27.

[Koshelev, 2016] Koshelev M. A., Vilkov I. N., Tretyakov M. Yu. Collisional broadening of oxygen fine structure lines: The impact of temperature. *J. Quant. Spectrosc. Radiat. Transfer.* 2016. Vol. 169. P. 91—95.

[Koshelev, 2017] Koshelev M. A., Delahaye T., Serov E. A., Vilkov I. N., Boulet C., Tretyakov M. Yu. Accurate modelling of the diagnostic 118-GHz oxygen line for remote sensing of the atmosphere. *J. Quant. Spectrosc. Radiat. Transfer*. 2017. Vol. 196. P. 78–86.

[Koshelev, 2018-1] Koshelev M. A., Leonov I. I., Serov E. A., Chernova A. I., *et al*. New frontiers of modern resonator spectroscopy. *IEEE Trans. on Terahertz Sci. Technol*. 2018. Vol. 8, No. 6. P. 773—783.

[Koshelev, 2018-2] Koshelev M. A., Golubyatnikov G. Yu., Vilkov I. N., Tretyakov M. Yu. Line shape parameters of the 22-GHz water line for

accurate modeling in atmospheric applications. *J. Quant. Spectrosc. Rad. Transfer*. 2018. Vol. 205. P. 51–58.

[Koshelev, 2021] Koshelev M. A., Vilkov I. N., Makarov D. S., Tretyakov M. Yu., *et al.* Water vapor line profile at 183-GHz: temperature dependence of broadening, shifting, and speed-dependent shape parameters. *J. Quant. Spectrosc. Rad. Transfer*. 2021. Vol. 260. Art. 107472.

[Koshelev, 2021-1] Koshelev M. A., Vilkov I. N., Makarov D. S., Tretyakov M.Yu., P.W. Rosenkranz. Speed-dependent broadening of the O_2 fine-structure lines. *J. Quant. Spectrosc. Rad. Transfer*. 2021. Vol. 264. Art. 107546.

[Krupnov, 1979] Krupnov A. F. "Modern submillimeter microwave scanning spectroscopy". In *Modern aspects of microwave spectroscopy,* ed. by G. W. Chantry. P. 217—256. L.: Acdemic Press, 1979.

[Krupnov, 1992] Krupnov A. F., Markov V. N. Temperature behavior of the 3_{13}-2_{20} water vapor spectral line self-broadening. *Atmospheric and oceanic optics*. 1992. Vol. 5, No. 2. P. 140.

[Krupnov, 1994] Krupnov A. F., Pavlovsky O. P. Commercial frequency synthesizer of the 118–178 GHz range. *Int. J. Infrared Millim. Waves*. 1994. Vol. 15, No. 10. P. 1611—1624.

[Krupnov, 1999] Krupnov A. F., Tretyakov M. Yu., Parshin V. V., Shanin V. N., Kirillov M. I. Precision resonator microwave spectroscopy in millimeter and submillimeter range. *Int. J. Infrared Millim. Waves*. 1999. Vol. 20, No. 10. P. 1731—1737.

[Krupnov, 2000] Krupnov A. F., Tretyakov M. Yu., Parshin V. V., Shanin V. N., Myasnikova S. E. Modern millimeterwave resonator spectroscopy of broad lines. *J. Mol. Spectrosc*. 2000. Vol. 202. P. 107—115.

[Krupnov, 2001] Krupnov A. F. Phase lock-in of mmsubmm backward wave oscillators: development, evolution and applications. *Int. J. Infrared Millim. Waves*. 2001. Vol. 22, No. 1. P. 1—18.

[Krupnov, 2002-1] Krupnov A. F., Shvetsov A. A. Asymmetry of 118 GHz line in the earth atmosphere: pressure shift as a new element in atmospheric lines. *Radio Science*. 2002. Vol. 37, No. 4. Art. 1056.

[Krupnov, 2002-2] Krupnov A. F., Golubiatnikov G. Yu., Markov V. N., Sergeev D. A. Pressure Broadening of the Rotational Line of Oxygen at 425 GHz. *J. Mol. Spectrosc*. 2002. Vol. 215. P. 1—3.

[Krupnov, 2007]. Krupnov A. F., Zobov N. F. On a possibility of experimental observation of individual rotational lines of water dimer in the equilibrium gas phase. *Atmospheric and oceanic optics*. 2007. Vol. 20, No. 9. P. 703—706.

[Krupnov, 2009] Krupnov A. F., Tretyakov M. Yu., Leforestier C. Possibilities of observation of discrete spectrum of water dimer at equilibrium in millimeter-wave band. *J. Quant. Spectrosc. Radiat. Transfer*. 2009. Vol. 110. P. 427—434.

[Krupnov, 2012] Krupnov A. F., Tretyakov M. Yu., Belov S. P., Golubiatnikov G. Yu., *et al.* Accurate broadband rotational BWO-based spectroscopy. *J. Mol. Spectrosc*. 2012. Vol. 280. P. 110—118.

[Kuhn, 2002] Kuhn T., Bauer A., Godon M., Buehler S., Kunzi K. Water vapor continuum: absorption measurements at 350 GHz and model calculations. *J. Quant. Spectrosc. Radiat. Transfer*. 2002. Vol. 74. P. 545—562.

[Kukolich, 1969] Kukolich S. G. Measurement of the molecular *g* values in H_2O and D_2O and hyperfine structure in H_2O. *J. Chem. Phys*. 1969. Vol. 50. P. 3751—3755.

[Kulikov, 2015] Kulikov M. Yu., Krasil'nikov A. A., Shvetsov A. A., Fedoseev L. I., *et al*. Simultaneous ground-based microwave measurements of the middle-atmosphere ozone and temperature. *Radiophysics and Quantum Electronics*. 2015. Vol. 58, No. 6. P. 409—417.

[Kuyanov-Prozument, 2010] Kuyanov-Prozument K., Choi M. Y., Vilesov A. F. Spectrum and infrared intensities of OH-stretching bands of water dimers. *J. Chem. Phys*. 2010. Vol. 132. Art. 014304.

[Lamont, 1948] Lamont H. R. L. Atmospheric absorption of microwaves. *Phys. Rev*. 1948. Vol. 74. P. 353.

[Lance, 1997] *Lance B.* On the Speed-Dependent Hard Collision Lineshape Models: Application to C_2H perturbed by Xe B. Lance, G. Blanquet, J. Walrand, J. Bouanich J. Mol. Spectrosc. 1997. Vol. 185. P. 262—271.

[Landau, 1976] Landau L. D., Lifshitz E. M. *Mechanics.* (3rd ed.). (1976). Amsterdam: Elsevier (Butterworth-Heinemann) ISBN 978-0-7506-2896-9.

[Landau, 1977] Landau L. D., Lifshitz E. M. *Quantum Mechanics: Non-Relativistic Theory.* (3rd ed.). (1977). Pergamon Press. ISBN 978-0-08-020940-1.

[Landau, 1980] Landau L. D., Lifshitz E. M. *Statistical Physics.* (3rd ed.). (1980). Amsterdam: Elsevier (Butterworth-Heinemann). ISBN 978-0-7506-3372-7.

[Landau, 1984] Landau L. D., Lifshitz E. M., Pitaevskii L.P. *Electrodynamics of Continuous Media*. (2nd ed.). (1984). Elsevier (Butterworth-Heinemann). ISBN 978-0-7506-2634-7.

[Lawrence, 2011] Lawrence R., Lin B., Harrah S., Hu Y., Hunt P., Lipp C. Initial flight test results of differential absorption barometric radar for remote sensing of sea surface air pressure. J. Quant. Spectrosc. Radiat. Transfer. 2011. Vol. 112. P. 247—253.

[L'ecuyer, 2015] L'ecuyer T.S., Beaudoing H.K., Rodell M., Olson W., et al. The observed state of the energy budget in the early twenty-first century. *Journal of Climate*. 2015. Vol. 28. P. 8319—8346

[Lees, 1968] Lees R. M., Oka T. Microwave triple resonance: Direct observation of $\Delta J = 2$ collision-induced transitions. *J. Chem. Phys*. 1968. Vol. 49. P. 4234—4235.

[Leforestier, 2010] Leforestier C., Tipping R. H., Ma Q. Temperature dependences of mechanisms responsible for the water-vapor continuum absorption. II. Dimers and collision-induced absorption. *J. Chem. Phys*. 2010. Vol. 132. Art. 164302.

[Leforestier, 2012] Leforestier C., Szalewicz K., van der Avoird A. Spectra of water dimer from a new *ab initio* potential with flexible monomers. *J. Chem. Phys*. 2012. Vol. 137. Art. 014305.

[Leforestier, 2014] Leforestier C. Water dimer equilibrium constant calculation: a quantum formulation including metastable states. *J. Chem. Phys*. 2014. Vol. 140. Art. 074106.

[Leslie, 2004] Leslie R. V. NPOESS aircraft sounder testbed-microwave: observations of clouds and precipitation at 54, 118, 183, and 425 GHz. *IEEE Trans. Geosci. Rem. Sens*. 2004. Vol. 42, No. 10. P. 2240—2247.

[Leung, 1989] Leung H. O., Marshall M. D., Suenram R. D., Lovas F. J. Microwave spectrum and molecular structure of the N_2–H_2O complex. J. Chem. Phys. 1989. Vol. 90. P. 700—712.

[Lewen, 1998] Lewen F., Gendriesch R., Pak I., Paveliev D. G., Hepp M., Schieder R., Winnewisser G. Phase locked backward wave oscillator pulsed beam spectrometer in the submillimeter wave range. *Rev. Sci. Instrum*. 1998. Vol. 69, No. 1. P. 32—39.

[Liebe, 1969-1] Liebe H. J., Thompson M. C., Dillon T. A. Dispersion studies of the 22 GHz water vapor line shape: I. The Lorentzian behavior. *J. Quant. Spectrosc. Radiat. Transfer*. 1969. Vol. 9. P. 31—47.

[Liebe, 1969-2] Liebe H. J., Dillon T. A. Accurate foreign-gas broadening parameters of the 22-GHz H_2O line from refraction spectroscopy. *J. Chem. Phys*. 1969. Vol. 50. P. 727—732.

[Liebe, 1975] Liebe H. J. Pressure-scanning mm-wave dispersion spectrometer. *Rev. Sci. Instrum*. 1975. Vol. 46, No. 7. P. 817—825.

[Liebe, 1977] Liebe H. J., Gimmestad G. G., Hopponen J. D. Atmospheric oxygen microwave spectrum – experiment versus theory. *IEEE Trans. Antennas and Propagation*. 1977. Vol. 25, No. 3. P. 327—335.

[Liebe, 1983] Liebe H. J. Atmospheric EHF window transparencies near 35, 90, 140, and 220 GHz. *IEEE Trans. Antennas and Propagation*. 1983. Vol. 31, No. 1. P. 127—135.

[Liebe, 1984-1] Liebe H. J. The atmospheric water vapor continuum below 300 GHz. *Int. J. Infrared. Millim. Waves.* 1984. Vol. 5, No. 2. P. 207—227.

[Liebe, 1984-2] Liebe H. J., Wolfe V. L., Howe D. A. Test of wall coatings for controlled moist air experiments. *Rev. Sci. Instrum*. 1984. Vol. 55, No. 10. P. 1702—1705.

[Liebe, 1987] Liebe H. J., Layton D. H. Millimeter-wave properties of the atmosphere: Laboratory studies and propagation modeling. Institute for Telecommunication Sciences. Boulder, 1987. NTIA Report 87-224.

[Liebe, 1989] Liebe H. J. MPM – an atmospheric millimeter-wave propagation model. *Int. J. Infrared Millim. Waves.* 1989. Vol. 10, No. 6. P. 631—650.

[Liebe, 1991-1] Liebe H. J., Hufford G. A., De Bolt R. O. The atmospheric 60-GHz oxygen spectrum: modeling and laboratory measurements. Institute for Telecommunication Sciences. Boulder, 1991. NITA Report 91-272.

[Liebe, 1991-2] Liebe H. J., Hufford G. A., Manabe T. A model for the complex permittivity of water at frequencies below 1 THz. *Int. J. Infrared Millim. Waves*. 1991. Vol. 12, No. 7. P. 659—675.

[Liebe, 1992] Liebe H. J., Rosenkranz P. W., Hufford G. A. Atmospheric 60 GHz oxygen spectrum: new laboratory measurement and line parameters. *J. Quant. Spectrosc. Radiat. Transfer.* 1992. Vol. 48, No. 56. P. 629—643.

[Liebe, 1993] Liebe H. J., Hufford G. A., Cotton M. G. Propagation modeling of moist air and suspended waterice particles at frequencies below 1000 GHz. *AGARD Conf. Proc*. 1993. Vol. 542. P. 3.1—3.10.

[Lichtenstein, 1966] Lichtenstein M., Derk V. E., Gallagher J. J. Millimeter wave rotational transitions and the Stark effect of the water molecule. *J. Mol. Spectrosc*. 1966. Vol. 20. P. 391—401.

[Llewellyn-Jones, 1978] Llewellyn-Jones D. T., Knight R. J., Gebbie H. A. Absorption by water vapour at 7.1 cm^{-1} and its temperature dependence. *Nature.* 1978. Vol. 274, No. 5674. P. 876—878.

[Lodi, 2011] Lodi L., Tennyson J., Polyansky O. L. A global, high accuracy *ab initio* dipole moment surface for the electronic ground

state of the water molecule. *J. Chem. Phys*. 2011. Vol. 135, No. 3. Art. 034113.

[Lorentz, 1906] Lorentz H. A. Absorption and emission lines of gases. *Proc. Amst. Acad. Sci*. 1906. Vol. 8. P. 591—611.

[Ma, 2008] Ma Q., Tipping R. H., Leforestier C. Temperature dependences of mechanisms responsible for the water-vapor continuum absorption. I. Far wings of allowed lines. *J. Chem. Phys*. 2008. Vol. 128. Art. 124313.

[Ma, 2014] Ma Q., Boulet C., Tipping R. H. Effects on calculated half-widths and shifts from the line coupling for asymmetric-top molecules. *J. Chem. Phys*. 2014. Vol. 140. Art. 244301.

[Ma, 2015] Ma Q., van der Avoird A., Loreau J., Alexander M.H., van de Meerakker S., Dagdigian P.J. Resonances in rotationally inelastic scattering of NH_3 and ND_3 with H_2. *J. Chem. Phys*. 2015. Vol. 143. Art. 044312. doi: 10.10631.4927074

[Makarov, 2008] Makarov D. S., Koval I. A., Koshelev M. A., Parshin V. V., Tretyakov M. Yu. Collisional parameters of the 118 GHz oxygen line: temperature dependence. *J. Mol. Spectrosc*. 2008. Vol. 252. P. 242—243.

[Makarov, 2011] Makarov D. S., Tretyakov M. Yu., Rosenkranz P. W. 60-GHz oxygen band: precise experimental profiles and extended absorption modeling in a wide temperature range. *J. Quant. Spectrosc. Radiat. Transfer*. 2011. Vol. 112. P. 1420—1428.

[Makarov, 2013] Makarov D. S., Tretyakov M. Yu., Boulet C. Line mixing in the 60-GHz atmospheric oxygen band: Comparison of the MPM and ECS model. *J. Quant. Spectrosc. Radiat. Transfer*. 2013. Vol. 124. P. 1—10.

[Makarov, 2014] Makarov D. S., Tretyakov M. Yu., Shkaev A. P., Kiselev A. M., Stepanov A. N., Parshin V. V. Femtosecond laser comb based subterahertz synthesizer. *Appl. Phys. Lett*. 2014. Vol. 105. Art. 063502.

[Makarov, 2020] Makarov D. S., Tretyakov M. Yu., Rosenkranz P. W. Revision of the 60-GHz atmospheric oxygen absorption band models for practical use. *J. Quant. Spectrosc. Rad. Transfer.* 2020. Vol. 243. Art. 106798.

[Manabe, 1989] Manabe T., Debolt R. O., Liebe H. J. Moist-air attenuation at 96 GHz over a 21-km line-of-sight path. *IEEE Trans. Anten. Propag*. 1989. Vol. 37, No. 2. P. 262—266.

[Margenau, 1969] Margenau, H. Kestner, N. *Theory of inter-molecular forces* (2nd ed.) 1969. Pergamon Press. ISBN: 9781483151700

[Martin, 2009-1] Martin M. J., Foreman S. M., Schibli T. R., Ye J. Testing ultrafast mode-locking at microhertz relative optical linewidth. *Opt. Express*. 2009. Vol. 17. P. 558—561.

[Martin, 2009-2] Martin D.H., Wylde R.J. Wideband circulators for use at frequencies above 100 GHz to beyond 350 GHz. *IEEE Transactions on Microwave Theory and Techniques.* 2009. Vol. 57, No. 1. P. 99—108.

[Maryott, 1955] Maryott A. A., Birnbaum G. B. Microwave absorption in compressed oxygen. *Phys. Rev*. 1955. Vol. 99, No. 6. P. 1886.

[Maryott, 1960] Maryott A. A., Birnbaum G. B. Microwave absorption in compressed oxygen. *J. Chem. Phys*. 1960. Vol. 32. P. 686—691.

[Marx, 2006] Marx D. Proton transfer 200 years after von Grotthuss: insights from *ab initio* simulations. *Chem. Phys. Chem*. 2006. Vol. 7. P. 1848—1870.

[Mätzler, 2010] Mätzler C., Rosenkranz P. W., Cermak J. Microwave absorption of supercooled clouds and implications for the dielectric properties of water. *J. Geophys. Res*. 2010. Vol. 115. Art. D23208.

[May, 2013] May A. D., Liu W.-K., McCourt F. R. W., Ciuryło R., Sanchez-Fortún Stoker J., Shapiro D., Wehr R. The impact theory of spectral line shapes: a paradigm shift. *Can. J. Phys*. 2013. Vol. 91. P. 879—895.

[McKnight, 1968] McKnight J. S., Gordy W. Measurement of the submillimeter-wave rotational transition of oxygen at 242 kMcsec. *Phys. Rev. Lett*. 1968. Vol. 21, No. 27. P. 1787—1789.

[Meeks, 1963] Meeks M. L., Lilley A. E. The microwave spectrum of oxygen in the Earth's atmosphere. *J. Geophys. Res*. 1963. Vol. 68, No. 6. P. 1683—1703.

[Meshkov, 2005] *Meshkov A. I.* Broadband absolute absorption measurements of atmospheric continua with millimeter wave cavity ringdown spectroscopy A. I. Meshkov, F. C. De Lucia Rev. Sci. Instrum. 2005. Vol. 76. Art. 083103.

[Meshkov, 2007] Meshkov A. I., De Lucia F. C. Laboratory measurements of dry air atmospheric absorption with a millimeter wave cavity ringdown spectrometer. *J. Quant. Spectrosc. Radiat. Transfer*. 2007. Vol. 108. P. 256—276.

[Miller, 1953] Miller S. L., Townes C. H. The microwave absorption spectum of $(O^{16})_2$ and $O^{16}O^{17}$. *Phys. Rev*. 1953. Vol. 90, No. 4. P. 537—541.

[Miller, 2012] Yu S., Miller C. E., Drouin B. J., Müller H. S. P. High resolution spectral analysis of oxygen. I. Isotopically invariant

Dunham fit for the $X^3\Sigma^-_g$, $a^1\Delta_g$, $b^1\Sigma^+_g$ states. *J. Chem. Phys*. 2012. Vol. 137. Art. 024304. doi: 10.10631.4719170.

[Millo, 2009] Millo J., Boudot R., Lours M., Bourgeois P. Y., Luiten A. N., Le Coq Y., Kersalé Y., Santarelli G. Ultra-low-noise microwave extraction from fiber-based optical frequency comb. *Optics Lett.* 2009. Vol. 34. P. 3707—3709.

[Mingelgrin, 1972] Mingelgrin U., Gordon R. G., Frenkel L., Sullivan T. E. Microwave spectrum of compressed O_2-foreign gas mixtures in the 48–81 GHz region. *J. Chem. Phys*. 1972. Vol. 57, No. 7. P. 2923—2931.

[Mizushima, 1954] Mizushima M., Hill R. M. Microwave Syectrum of O_2. *Phys. Rev*. 1954. Vol. 93, No. 4. P. 745—748.

[Mlawer, 2012] Mlawer E. J., Payne V. H., Moncet J.-L., Delamere J. S., Alvarado M. J., Tobin D. C. Development and recent evaluation of the MT–CKD model of continuum absorption. *Philos. Trans. R. Soc. A*. 2012. Vol. 370. P. 2520—2556.

[Moudens, 2009] Moudens A., Georges R., Goubet M., Makarewicz J., Lokshtanov S. E., Vigasin A. A. Direct absorption spectroscopy of water clusters formed in a continuous slit nozzle expansion. *J. Chem. Phys*. 2009. Vol. 131. Art. 204312.

[Mouret, 2009] Mouret G., Hindle F., Cuisset A., Yang C., Bocquet R., Lours M., Rovera D. THz photomixing synthesizer based on a fiber frequency comb. *Opt. Express*. 2009. Vol. 17. Art. 22031.

[Nagarajan, 2017] Nagarajan S., Neese C. F., De Lucia F. C. Cavity-Based Medium Resolution Spectroscopy (CBMRS) in the THz: A bridge between high- and low-resolution techniques for sensor and spectroscopy applications. *IEEE Transactions on Terahertz Science and Technology.* Vol. 7, No. 3, P. 233—243. doi: 10.1109TTHZ.2017.2680841.

[Ngo, 2013] Ngo N. H., Lisak D., Tran H., Hartmann J.-M. An isolated line-shape model to go beyond the Voigt profile in spectroscopic databases and radiative transfer codes. *J. Quant. Spectrosc. Radiat. Transfer*. 2013. Vol. 129. P. 89—100.

[Nelkin, 1964] Nelkin M., Ghatak A. Simple binary collision model for Van Hove's $Gs(r, t)$. *Phys. Rev. A*. 1964. Vol. 135. P. 4—9.

[Occelli, 1991] Occelli R., Chaaban H., Moynault J. M., Coulon R., Balsamo A. Submillimetric and millimetric collision-induced absorption spectra in compressed gaseous nitrogen using very low-frequency optical source. *Can. J. Phys*. 1991. Vol. 69. P. 1264—1272.

[Odintsova, 2013] Odintsova T. A., Tretyakov M. Yu. Evidence of true bound and metastable dimers and trimers presence in high temperature

water vapor spectra. *J. Quant. Spectrosc. Radiat. Transfer*. 2013. Vol. 20. P. 134—137.

[Odintsova, 2014] Odintsova T. A., Tretyakov M. Yu., Krupnov A. F., Leforestier C. The water dimer millimeter-wave spectrum at ambient conditions: A simple model for practical purposes. *J. Quant. Spectrosc. Radiat. Transfer*. 2014. Vol. 140. P. 75—80.

[Odintsova, 2017] Odintsova T. A., Tretyakov M. Yu., Pirali O., Roy P. Water vapor continuum in the range of rotational spectrum of H_2O molecule: new experimental data and their comparative analysis. *J. Quant. Spectrosc. Radiat. Transfer*. 2017. Vol. 187. P. 116—123.

[Odintsova, 2019] Odintsova T. A., Tretyakov M. Yu., Zibarova A. O., Pirali O., Roy P., Campargue A. Far-infrared self-continuum absorption of $H_2{}^{16}O$ and $H_2{}^{18}O$ (15–500 cm^{-1}). *J. Quant. Spectrosc. Rad. Transfer*. 2019. Vol. 227. P. 190—200.

[Odintsova, 2020] Odintsova T. A., Tretyakov M. Yu., Simonova A. A., Ptashnik I. V., Pirali O., Campargue A. Measurement and temperature dependence of the water vapor self-continuum between 70 and 700 cm^{-1}. *J. Mol. Struct*. 2020. Vol. 1210. Art. 128046.

[Odutola, 1980] Odutola J. A., Dyke T. R. Partially deuterated water dimers: microwave spectra and structure. *J. Chem. Phys*. 1980. Vol. 72, No. 9. P. 5062—5070.

[Oka, 1966] Oka T. Observation of preferred collisional transitions in ethylene oxide by the use of microwave double resonance. *J. Chem. Phys*. 1966. Vol. 45. P. 754—755.

[Oka, 1967] Oka T. Microwave studies of collision-induced transitions between rotational levels. II. Observations in H_2CO, HCN, and H_2CCO. *J. Chem. Phys*. 1967. Vol. 47, No. 1. P. 13—26.

[Oka, 1968] Oka T. Microwave studies of collision-induced transitions between rotational levels. IV. Steady-state measurements in NH_3. *J. Chem. Phys*. 1968. Vol. 48, No. 11. P. 4919—4928.

[Oparin, 2017] Oparin D. V., Filippov N. N., Grigoriev I. M., Kouzov A. P. Effect of stable and metastable dimers on collision-induced rototranslational spectra: carbon dioxide-rare gas mixtures. *J. Quant. Spectrosc. Radiat. Transfer*. 2017. Vol. 196. P. 87—93.

[Ovsyannikov, 2005] Ovsyannikov R. I., Tretyakov M. Yu. Determination of loss in a Fabry-Perot resonator from its response to exciting radiation with a fast-scanned frequency. *Journal of Communications Technology and Electronics*. 2005. Vol. 50, No. 12. P. 1400—1408.

[Pumphrey, 2000] Pumphrey H. C., Bühler S. Instrumental and spectral parameters: their effect on and measurement by microwave limb

sounding of the atmosphere. *J. Quant. Spectrosc. Radiat. Transfer*. 2000. Vol. 64. P. 421—437.

[Papoušek, 1982] Papoušek D., Aliev M. R. *Molecular vibrational-rotational spectra.* 1982. Prague: Vydala Academia.

[Pardo, 1998] Pardo J. R., Gérin M., Prigent C., Cernicharo J., Rochard G., Brunel P. Remote sensing of the mesospheric temperature profile from close-to-nadir observations: Discussion about the capabilities of the 57.5–62.5 GHz frequency band and the 118.75 GHz single O_2 line. *J. Quant. Spectrosc. Radiat. Transfer*. 1998. Vol. 60, No. 4. P. 559—571.

[Parshin, 2009] Parshin V. V., Tretyakov M. Yu., Koshelev M. A., Serov E. A. Instrumental complex and the results of precise measurements of millimeter- and submillimeter-wave propagation in condensed media and the atmosphere. *Radiophysics and Quantum Electronics*, 2009. Vol. 52, No. 8. P. 525–535.

[Parshin, 2013] Parshin V. V., Tretyakov M. Yu., Koshelev M. A., Serov E. A. Modern resonator spectroscopy at submillimeter wavelengths. *IEEE Sensors Journal*. 2013. Vol. 13, No. 1. P. 18—23.

[Parshin, 2014] Parshin V. V., Serov E. A., Bubnov G. M., Vdovin V. F., Koshelev M. A., Tretyakov M. Yu. Cryogenic resonator complex. *Radiophysics and Quantum Electronics*. 2014. Vol. 56, No. 8–9. P. 554—560.

[Payan, 2005] Payan S., De La Noe J., Hauchecorne A., Camy-Peyret C. A review of remote sensing techniques and related spectroscopy problems. *CR Physique*. 2005. Vol. 6. P. 825—835.

[Payne, 2008] Payne V. H., Delamere J. S., Cady-Pereira K. E., Gamache, *et al*. Air-broadened half-widths of the 22- and 183-GHz water-vapor lines. *IEEE Transactions on Geoscience and Remote Sensing*. 2008. Vol. 46, No. 11. P. 3601—3617.

[Payne, 2011] Payne V. H., Mlawer E. J., Cady-Pereira K. E., Moncet J.-L. Water vapor continuum absorption in the microwave. *IEEE Transactions on Geoscience and Remote Sensing*. 2011. Vol. 49, No. 6. P. 2194—2208.

[Pearson, 1969] Pearson J. E., Llewellyn-Jones D. T., Knight R. J. Water vapour absorption near a wavelength of 0.79 mm. *Infrared Physics*. 1969. Vol. 9. P. 53—58.

[Pearson, 1970] Pearson R., Sullivan T., Frenkel L. Microwave spectrum and molecular parameters for $^{14}N_2{}^{16}O$. *J. Mol. Spectrosc*. 1970. Vol. 34. P. 440—449.

[Peixoto, 1992] Peixoto J. P., Oort A. H. *Physics of Climate*. 1992. N.Y.: American Institute of Physics.

[Perin, 2001] Perin A. “Review on the Existing Spectroscopic Databases for Atmospheric Applications” in *Spectroscopy from Space* ed. by J. Demaison, et al. 2001. Dordrecht: Kluwer Academic Publishers, Vol. II, No. 20. P. 235—258. (NATO Science Series).

[Peter, 1955] Peter M., Strandberg M. W. P. Phase stabilization of microwave oscillators. *Proc. IRE.* 1955. Vol. 43, No. 7. P. 869—873.

[Peterson, 1984] Peterson K. I., Klemperer W. Structure and internal rotation of H_2O–CO_2, HDO–CO_2, and D_2O–CO_2 van der Waals complexes. *J. Chem. Phys*. 1984. Vol. 80. P. 2439—2445.

[Pickett, 1980-1] Pickett H. M. Effects of velocity averaging on the shapes of absorption lines. *J. Chem. Phys*. 1980. Vol. 73. Art. 6090.

[Pickett, 1980-2] Pickett H. M. Determination of collisional linewidths and shifts by a convolution method. *Applied Optics*. 1980. Vol. 19, No. 16. P. 2745—2749.

[Pickett, 1981] Pickett H. M., Cohen E. A., Brinza D. E. Pressure broadening and its implications for cosmic background measurements. *The Astrophysical Journal*. 1981. Vol. 248. P. L49—L51.

[Pine, 1999] Pine A. S. Asymmetries and correlations in speed-dependent Dicke-narrowed line shapes of argon-broadened HF. *J. Quant. Spectrosc. Radiat. Transfer*. 1999. Vol. 62. P. 397—423.

[Pine, 2001] Pine A., Ciurylo R. Multispectrum fits of Ar-broadened HF with a generalized asymmetric lineshape: Effects of correlation, hardness, speed dependence, and collision duration *J. Mol. Spectrosc*. 2001. Vol. 208. P. 180—187.

[Plateaux, 2001] Plateaux J.-J., Regalia L., Boussin C., Barbe A. Multispectrum fitting technique for data recorded by Fourier transform spectrometer: application to N_2O and CH_3D. *J. Quant. Spectrosc. Radiat. Transfer*. 2001. Vol. 68. P. 507—520.

[Podobedov, 2008] Podobedov V. B., Plusquellic D. F., Siegrist K. E., Fraser G. T., Ma Q., Tipping R. H. New measurements of the water vapor continuum in the region from 0.3 to 2.7 THz. *J. Quant. Spectrosc. Radiat. Transfer.* 2008. Vol. 109. P. 458—467.

[Polyansky, 2012] Polyansky O. L., Zobov N. F., Mizus I. I., Lodi L., *et al.* Global spectroscopy of the water monomer. *Philos. Trans. R. Soc. Lond., A*. 2012. Vol. 370. P. 2728—2748.

[Polyansky, 2013] Polyansky O. L., Ovsyannikov R. I., Kyuberis A. A., Lodi L., Tennyson J., Zobov N. F. Calculation of rotation-vibration energy levels of the water molecule with near-experimental accuracy based on an *ab initio* potential energy surface. *J. Chem. Phys. A*. 2013. Vol. 117, No. 39. P. 9633—9643.

[Polyansky, 2015] Polyansky O. L., Bielska K., Ghysels M., Lodi L., *et al.* High-accuracy CO_2 line intensities determined from theory and experiment. *Phys. Rev. Lett*. 2015. Vol. 114. Art. 243001.

[Polyansky, 2021] O. L., Ovsyannikov R. I., Tennyson J., Belov S. P., Tretyakov, M.Yu. Makhnev V. Yu., Zobov N. F. Variational analysis of HF dimer tunneling rotational spectra using an *ab initio* potential energy surface. *J. Molec. Spectrosc.* 2021. Vol. 379. Art. 111481.

[Potapov, 2014] Potapov A., Asselin P. High-resolution jet spectroscopy of weakly bound binary complexes involving water. *International Reviews in Physical Chemistry*. 2014. Vol. 33, No. 2. P. 275—300.

[Potapov, 2017] *Potapov A.* Weakly bound molecular complexes in the laboratory and in the interstellar medium: A lost interest? *Molecular Astrophysics*. 2017. Vol. 6. P. 16—21.

[Ptashnik, 2011] Ptashnik I. V., Shine K. P., Vigasin A. A. Water vapour self-continuum and water dimers: 1. Analysis of recent work. *J. Quant. Spectrosc. Radiat. Transfer*. 2011. Vol. 112. P. 1286—1303.

[Ptashnik, 2019] Ptashnik I. V., Klimeshina T. E., Solodov A. A., Vigasin A. A. Spectral composition of the water vapour self-continuum absorption within 2.7 and 6.25 μm bands. *J. Quant. Spectrosc. Radiat. Transfer*. 2019. Vol. 228. P. 97—105.

[Pugliano, 1993] Pugliano N., Cruzan J. D., Loeser J. G., Saykally R. A. Vibrational and K_a' dependencies of the multidimensional tunneling dynamics in the 82.6 cm^{-1} intermolecular vibration of the water dimer-d_4. *J. Chem. Phys.* 1993. Vol. 98. P. 6600—6617.

[Ramanathan, 1997] Ramanathan V., Vogelmann A. M. Greenhouse effect, atmospheric solar absorption and the Earth's radiation budget: From the Arrhenius–Langley era to the 1990s. *Ambio*. 1997. Vol. 26, No. 1. P. 38—46.

[Rautian, 1966] Rautian S.G., Sobel'man I.I. The effect of collisions on the Doppler broadening of spectral lines. *Sov. Phys. Usp*. 1967. V. 9. P. 701–716.

[Rautian, 2001] Rautian S. G. Universal asymptotic profile of a spectral line under a small Doppler broadening. *Optics and Spectroscopy* 2001. V. 90. No. 1. P. 30—40.

[Razavy, 2003] Razavy, M. 2003. *Quantum theory of tunneling*. World Scientific. ISBN 978-981-238-019-7.

[Read, 1988] Read W. G., Hillig K. W., Cohen E. A., Pickett H. M. The measurement of absolute absorption of millimeter radiation in gases: The absorption of CO and O_2. *IEEE Trans. Anten. Propagat*. 1988. Vol. 36, No. 8. P. 1136—1143.

[Reber, 1972] Reber E. E. Absorption of the 4- to 6-millimeter wavelength band in the atmosphere *Journal of Geophysical Research*. 1972. Vol. 77, No. 21. P. 3831—3845.

[Reimer, 1984] Reimer J. R., Watts R. O. The structure and vibrational spectra of small clusters of water molecules. *Chem. Phys*. 1984. Vol. 85. P. 83—112.

[Reuter, 1986] Reuter D., Jennings D. E., Brault J. W. The $v = 1 \leftarrow 0$ quadrupole spectrum of N_2. *J. Mol. Spectrosc.* 1986. Vol. 115. P. 294—304.

[Rezgui, 1995] Rezgui N. D., Allen J., Baker J. G., Alder J. F. Quantitative millimetre wave spectrometry. Part I: Design and implementation of a tracked millimetre wave confocal Fabry–Perot cavity spectrometer for gas analysis. *Analytica Chimica Acta*. 1995. Vol. 311. P. 99—108.

[Robinson, 2003] Robinson T. W., Kjaergaard H. G. High level *ab initio* studies of the low-lying excited states in the H_2O–O_2 complex. *J. Chem. Phys*. 2003. Vol. 119. P. 3717—3720.

[Rocher-Casterline, 2011] Rocher-Casterline B. E., Ch'ng L. C., Mollner A. K., Reisler H. Determination of the bond dissociation energy (D_0) of the water dimer, $(H_2O)_2$, by velocity map imaging. *J. Chem. Phys*. 2011. Vol. 134. Art. 211101.

[Rohart, 1994] Rohart F., Mäder H., Nicolaisen H.-W. Speed dependence of rotational relaxation induced by foreign gas collisions: Studies on CH_3F by millimeter wave coherent transients. *J. Chem. Phys*. 1994. Vol. 101, No. 8. P. 6475—6486.

[Rohart, 2007] Rohart F., Nguyen L., Buldyreva J., Colmont J.-M., Wlodarczak G. Lineshapes of the 172 and 602 GHz rotational transitions of $HC^{15}N$. *J. Mol. Spectrosc*. 2007. Vol. 246. P. 213—227.

[Romer, 1955] Romer R. H., Dicke R. H. New technique for high-resolution microwave spectroscopy. *Phys. Rev.* 1955. V. 99, No. 2. P. 532—536.

[Rose, 1955] Rose, M. E. 1955. *Multipole Fields*. NY: John Wiley & Sons.

[Rosenkranz, 1975] Rosenkranz P. W. Shape of the 5 mm oxygen band in the atmosphere. *IEEE Trans. Anten. Propagat*. 1975. Vol. 23, No. 4. P. 498—506.

[Rosenkranz, 1985] Rosenkranz P. W. Pressure broadening of rotational bands. I. A statistical theory. *J. Chem. Phys*. 1985. Vol. 83. P 6139—6144.

[Rosenkranz, 1987] Rosenkranz P. W. Pressure broadening of rotational bands. II. Water vapor from 300 to 1100 cm^{-1}. *J. Chem. Phys*. 1987. Vol. 87. P. 163—170.

[Rosenkranz, 1988] Rosenkranz P. W. Interference coefficients for overlapping oxygen lines in air. *J. Quant. Spectrosc. Radiat. Transfer*. 1988. Vol. 39, No. 4. P. 287—297.

[Rosenkranz, 1998] Rosenkranz P. W. Water vapor microwave continuum absorption: A comparison of measurements and models. *Radio Science*. 1998. Vol. 33, No. 4. P. 919—928.

[Rosenkranz, 1999] Rosenkranz P. W. Correction to "Water vapor microwave continuum absorption: A comparison of measurements and models". *Radio Science*. 1999. Vol. 34, No. 4. P. 1025.

[Rosenkranz, 2017] Rosenkranz P.W. Line-by-line microwave radiative transfer (nonscattering). Remote sensing code library. doi:10.21982m81013. 2017.

[Rothman, 2009] Rothman L. S., Gordon I. E., Barbe A., Benner D. C., Bernath P. F., Birk M. et al. The HITRAN 2008 molecular spectroscopic database. *J. Quant. Spectrosc. Radiat. Transfer*. 2009. Vol. 110. P. 533—572.

[Rothman, 2013] Rothman L. S., Gordon I. E., Babikov Y., Barbe A., Benner D. C., Bernath P. F., Birk M., et al. The HITRAN 2012 molecular spectroscopic database. *J. Quant. Spectrosc. Radiat. Transfer*. 2013. Vol. 130. P. 4—50.

[Rubens, 1898] Rubens H., Aschkinass E. Beobachtungen uber Absorption und Emission von Wasserdampf und Kohlensaure im ultrarothen Spectrum. *Ann. Phys*. 1898. Vol. 300, No. 3. S. 584—601.

[Rusk, 1965] Rusk J. R. Temperature and Zeeman measurements on the 1.64-mm H_2O absorption line. *J. Chem. Phys*. 1965. Vol. 43, No. 8. P. 2919—2920.

[Ryadov, 1966] Ryadov. V. Ya., Furashov N. I. The width of the water vapour line $\lambda = 0.92$ mm. *Soviet Radiophysics*. 1966. V. 9, No. 6. P. 621—623.

[Ryadov, 1968] Ryadov. V. Ya., Furashov N. I. Investigation of the width and intensity of the atmospheric water vapor spectral line $\lambda = 12.67$ cm^{-1}. *Optics and Spectroscopy*. 1968. V. 24, No. 2. P. 186—194. (In Russian)

[Ryadov, 1975] Ryadov V.Ya. Furashov. N. I. About widths and intensities of submillimeter-wave absorption lines of rotational spectrum of water vapour. *Izv. Vuz. Radiofiz*. 1975. V. 18. No. 3. P. 358—370.

[Sabu, 2005] Sabu A., Kondo S., Saito R., Kasai Y., Hashimoto K. Theoretical study of O_2–H_2O: Potential energy surface, molecular vibrations, and equilibrium constant at atmospheric temperatures. *J. Phys. Chem. A.* 2005. Vol. 109. P. 1836—1842.

[Samoska, 2011] Samoska L. A. An overview of solid-state integrated circuit amplifiers in the submillimeter-wave and THz regime. *IEEE Trans. Terahertz Sci. Technol*. 2011. Vol. 1, No. 1. P. 9—24.

[Saykally, 2013] Saykally R. J. Viewpoint: Simplest water cluster leaves behind its spectral fingerprint. *Physics.* 2013. Vol. 6. Art. 22.

[Serov, 2014] Serov E. A., Koshelev M. A., Odintsova T. A., Parshin V. V., Tretyakov M. Yu. Rotationally resolved water dimer spectra in atmospheric air and pure water vapour in the 188–258 GHz range. *Phys. Chem. Chem. Phys*. 2014. Vol. 16. P. 26221—26233.

[Serov, 2017] Serov E. A., Odintsova T. A., Tretyakov M. Yu., Semenov. V.E. On the origin of the water vapor continuum absorption within rotational and fundamental vibrational bands. *J. Quant. Spectrosc. Rad. Transfer*. 2017. V. 193. P. 1—12.

[Schibli, 2008] Schibli T. R., Hartl I., Yost D. C., et al. Optical frequency comb with submillihertz linewidth and more than 10 W average power. *Nature Photonics*. 2008. Vol. 2. Art. 355.

[Schlapp, 1937] Schlapp R. Fine structure in the $^3\Sigma$ ground state of the oxygen molecule, and the rotational intensity distribution in the atmospheric oxygen band. *Phys. Rev*. 1937. Vol. 51, No. 3. P. 342—345.

[Schulten, 1965] Schulten G. II. Anwendungen der dielektrischen Leitung. *Philips' Technische Rundschau*. 1965. V. 26, No. 12. S. 33—40.

[Schulten, 1966] Schulten G. Resonators for mm waves and their use for the observation of gas resonances. *Frequenz.* 1966. Vol. 20. P. 10—22.

[Schulze, 1963] Schulze A. E., Tolbert C. W. Shape, intensity and pressure broadening of the 2.53-millimetre wave-length oxygen absorption line. *Nature*. 1963. Vol. 200, No. 4908. P. 747—750.

[Scribano, 2006] Scribano Y., Goldman N., Saykally R. J., Leforestier C. Water dimers in the atmosphere. III. Equilibrium constant from a flexible potential. *J. Phys. Chem*. A. 2006. Vol. 110. P. 5411—5419.

[Scribano, 2007] Scribano Y., Leforestier C. Contribution of water dimer absorption to the millimeter and far infrared atmospheric water continuum. *J. Chem. Phys*. 2007. Vol. 126. Art. 234301.

[Serov, 2020] Serov E. A., Balashov A. A., Tretyakov M. Yu., Odintsova T. A., Koshelev M. A., Chistikov D. N., Finenko A. A., Lokshtanov S. E., Petrov S. V., Vigasin A. A. Continuum absorption of millimeter

waves in nitrogen. *J. Quant. Spectrosc. Radiat. Transfer*. 2020. V. 242. Art. 106774.

[Setzer, 1977] Setzer B. J., Pickett H. M. Pressure broadening measurements of the 118.750 GHz oxygen transition. *J. Chem. Phys*. 1977. Vol. 67. P. 340—343.

[Shanin, 2003] Shanin V. N., Dorovskikh V. V., Tretyakov M. Yu., Parshin V. V., Shkaev A. P. An automated millimeter-wave resonator spectrometer for investigating the small absorption in gases. *Instruments and Experimental Techniques*. 2003. V. 46, No. 6. P. 798—803.

[Shine, 2012] Shine K. P., Ptashnik I. V., Rädel G. The water vapour continuum: brief history and recent developments. *Surveys in Geophysics*. 2012. Vol. 33, No. 34. P. 535—555.

[Shine, 2016] Shine K. P., Campargue A., Mondelain D., McPheat R. A., Ptashnik I. V., Weidmann D. The water vapour continuum in near-infrared windows. Current understanding and prospects for its inclusion in spectroscopic databases. *J. Mol. Spectrosc*. 2016. Vol. 327. P. 193—208.

[Shurakov, 2016] Shurakov A., Lobanov Y., Goltsman G. Superconducting hot-electron bolometer: from the discovery of hot-electron phenomena to practical applications. *Superconductor Science and Technology*. 2016. Vol. 29, No. 2. Art. 194303.

[Shvetsov, 2012] Shvetsov A. A., Karashtin D. A., Fedoseev L.I., Mukhin D.N., Skalyga N.K., Bolhsakov O.S., Feygin A. M. Ground-based sounding of the middle-atmosphere thermal structure in the frequency range 50–60 GHz. *Radiophysics and Quantum Electronics*. 2012. Vol. 54, No. 89. P. 569—576.

[Silveira, 2010] Silveira F. E. M., Kurcbart S. M. Hagen–Rubens relation beyond far-infrared region. *Europhysics Letters*. 2010. Vol. 90. Art. 44004.

[Simonova, 2022] Simonova A. A., Ptashnik I. V., Elsey J., McPheat R. A., Shine K. P., Smith K. M. Water vapour self-continuum in near-visible IR absorption bands: Measurements and semiempirical model of water dimer absorption. *J. Quant. Spectrosc. Radiat. Transfer*. 2022. Vol. 277. Art. 107957.

[Sliter, 2011] Sliter R., Gish M., Vilesov A. F. Fast nuclear spin conversion in water clusters and ices: a matrix isolation study. *J. Phys. Chem*. A. 2011. Vol. 115. P. 9682—9688.

[Slocum, 2015] Slocum D. M., Giles R. H., Goyette T. M. High-resolution water vapor spectrum and line shape analysis in the Terahertz region. *J. Quant. Spectrosc. Radiat. Transfer*. 2015. Vol. 159. P. 69—79.

[Smith, 1981] Smith E. W. Absorption and dispersion in the O_2 microwave spectrum at atmospheric pressures. *J. Chem. Phys*. 1981. Vol. 74, No. 12. P. 6658—6673.

[Song, 2008] Song H.-J., Shimizu N., Furuta T., Suizu K., Ito H. Broadband-frequency-tunable sub-Terahertz wave generation using an optical comb, AWGs, optical switches, and a uni-traveling carrier photodiode for spectroscopic applications. J. *Lightwave Technol*. 2008. Vol. 26. P. 2521—2530.

[Stafford, 1963] Stafford L. F., Tolbert C. W. Shapes of oxygen absorption lines in the microwave frequency region. *J. Geophys. Res*. 1963. Vol. 68, No. 11. P. 3431—3435.

[Steinbach, 1973] Steinbach W., Gordy W. Millimeter and submilimeter-wave spectrum of $^{18}O_2$. *Phys. Rev. A*. 1973. Vol. 8, No. 4. P. 1753—1758.

[Stone, 1984] Stone N. W. B., Read L. A. A., Anderson A., Dagg I. R., Smith W. Temperature dependent collision-induced absorption in nitrogen. *Can. J. Phys*. 1984. Vol. 62. P. 338—347.

[Storgyn, 1959] Storgyn D. E., Hirschfelder J. O. Contribution of bound, metastable, and free molecules to the second virial coefficient and some properties of double molecules. *J. Chem. Phys*. 1959. Vol. 31. P. 1531—1545.

[Strong, 1941] Strong J. Study of atmospheric absorption and emission in the infrared spectrum. *J. Franklin. Inst.* 1941. V. 232. P. 1—22.

[Sumiyoshi, 2015] Sumiyoshi Y., Endo Y. Three-dimensional potential energy surface of Ar–CO. *J. Chem. Phys*. 2015. Vol. 142. Art. 024314.

[Svishchev, 1998] Svishchev I. M., Boyd R. J. Van der Waals complexes of water with oxygen and nitrogen: Infrared spectra and atmospheric implications. *J. Phys. Chem. A*. 1998. Vol. 102. P. 7294—7296.

[Tennyson, 2014] Tennyson J., Bernath P. F., Campargue A., Császár A. G., et al. Recommended isolated-line profile for representing high-resolution spectroscopic transitions. *Pure Appl. Chem.* 2014. Vol. 86, No. 12. P. 1931—1943.

[Tennyson, 2016] Tennyson, J., Yurchenko, S. N., Al-Refaie, A. F., Barton, E. J., et al. The ExoMol database: Molecular line lists for exoplanet and other hot atmospheres. *Journal of Molecular Spectroscopy*. 2016. V. 327. P. 73—94.

[Thibault, 2020] Thibault F., Martínez R.Z., Bermejo D., Wcisło P. Line-shape parameters for the first rotational lines of HD in He. *Molecular Astrophysics.* 2020. Vol. 19. Art. 100063.

[Thompson, 1968] Thompson M. C., Vetter M. J. Dual mode microwave cavities for dispersion measurement. *Rev. Sci. Instr*. 1968. Vol. 39. P. 1333—1335.

[Tinkham, 1955] Tinkham M., Strandberg M. P. Line breadths in the microwave magnetic resonance spectrum of oxygen. *Phys. Rev*. 1955. Vol. 99, No. 2. P. 537—539.

[Toth, 1998] Toth R. A., Brown L. R., Plymate C. Self-broadened widths and frequency shifts of water vapor lines between 590 and 2400 cm^{-1}. *J. Quant. Spectrosc. Radiat. Transfer*. 1998. Vol. 59, No. 6. P. 529—562.

[Toth, 2003] Toth R. A., Brown L. R. Oxygen broadening parameters of water vapor: 1212–2136 cm^{-1}. J. Mol. Spectrosc. 2003. Vol. 218. P. 135—150.

[Toth, 2005] Toth R. A. Measurements and analysis (using empirical functions for widths) of air- and self-broadening parameters of H_2O. *J. Quant. Spectrosc. Radiat. Transfer*. 2005. Vol. 94. P. 1—50.

[Toth, 2006] Toth R. A., Brown L. R., Smith M. A. H., Devic V. M., Benner D. C., Dulick M. Air-broadening of H_2O as a function of temperature: 696–2163 cm^{-1}. *J. Quant. Spectrosc. Radiat. Transfer*. 2006. Vol. 101. P. 339—366.

[Townes, 1955] Townes C. H., Schawlow A. 1955. *Microwave spectroscopy*. N. Y.: McGrow-Hill.

[Tschumper, 2002] Tschumper G. S., Leininger M. L., Hoffman B. C., Valeev E. F., Schaefer H. F., Quack M. Anchoring the water dimer potential energy surface with explicitly correlated computations and focal point analyses. *J. Chem. Phys*. 2002. Vol. 116. P. 690—701.

[Tran, 2007] Tran H., Bermejo D., Domenech J.-L., Joubert P., Gamache R. R., Hartmann J.-M. Collisional parameters of H_2O lines: Velocity effects on the line-shape. *J. Quant. Spectrosc. Radiat. Transfer*. 2007. Vol. 108. P. 126—145.

[Tran, 2017] Tran H, Li G, Ebert V, Hartmann J-M. Super- and sub-Lorentzian effects in the Ar-broadened line wings of HCl gas. *J. Chem. Phys.* 2017. Vol. 146. Art. 194305.

[Trenberth, 2009] Trenberth K. E., Fasullo J. T., Kiehl J. Earth's global energy budget. *Bulletin of the American Meteorological Society*. 2009. Vol. 90, No. 3. P. 311—324.

[Tretyakov, 2001] Tretyakov M. Yu., Parshin V. V., Shanin V. N., Myasnikova S. E., Koshelev M. A., Krupnov A. F. Real atmosphere laboratory measurement of the 118-GHz oxygen line: shape, shift, and broadening of the line. *J. Mol. Spectrosc*. 2001. Vol. 208, No. 1. P. 110—112.

[Tretyakov, 2003] Tretyakov M. Yu., Parshin V. V., Koshelev M. A., Shanin V. N., Myasnikova S. E., Krupnov A. F. Studies of 183 GHz water line: broadening and shifting by air, N_2 and O_2 and integral intensity measurements. *J. Mol. Spectrosc*. 2003. Vol. 218. P. 239—245.

[Tretyakov, 2004] Tretyakov M. Yu., Golubiatnikov G. Yu., Parshin V. V., Koshelev M. A., Myasnikova S. E., Krupnov A. F., Rosenkranz P. W. Experimental study of line mixing coefficient for 118.75 oxygen line. *J. Mol. Spectrosc*. 2004. Vol. 223. P. 31—38.

[Tretyakov, 2005] Tretyakov M. Yu., Koshelev M. A., Dorovskikh V. V., Makarov D. S., Rosenkranz P. W. 60-GHz oxygen band: precise broadening and central frequencies of fine structure lines, absolute absorption profile at atmospheric pressure, revision of mixing coefficients. *J. Mol. Spectrosc*. 2005. Vol. 231. P. 1—14.

[Tretyakov, 2006] Tretyakov M. Yu., Parshin V. V., Koshelev M. A., Shkaev A. P., Krupnov A. F. Extension of the range of resonator scanning spectrometer into submillimeter band and some perspectives of its further developments. *J. Mol. Spectrosc*. 2006. Vol. 238. P. 91—97.

[Tretyakov, 2007]. Tretyakov M. Yu., Koshelev M. A., Koval I. A., Parshin V. V., Dryagin Yu. A., Kukin L. M., Fedoseev L. I. Continuum absorption in a mixture of nitrogen and water vapor in the range from 100 to 210 GHz. *Atmospheric and oceanic optics*. 2007. Vol. 20, No. 2. P. 89—93.

[Tretyakov, 2007-1] Tretyakov M. Yu., Tretyakova S. E., Fedorenko E. F. Transmission-type harmonic mixers of mm-wave range. *Int. J. Infrared Millim. Waves*. 2007. Vol. 28. P. 839—847.

[Tretyakov, 2007-2] Tretyakov M. Yu., Koshelev M. A., Koval I. A., Parshin V. V., Kukin L. M., Fedoseev L. I., Dryagin Yu. A., Andriyanov A. F. Temperature dependence of pressure broadening of 1^- oxygen line at 118.75 GHz. *J. Mol. Spectrosc*. 2007. Vol. 241. P. 109—111.

[Tretyakov, 2008] Tretyakov M. Yu., Koshelev M. A., Makarov D. S., Tonkov M. V. Precise measurements of collision parameters of spectral lines with a spectrometer with radioacoustic detection of absorption in the millimeter and submillimeter ranges. *Instruments and Experimental Techniques*. 2008. Vol. 51, No. 1/ P. 78—88.

[Tretyakov, 2009] Tretyakov M. Yu., Krupnov A. F., Koshelev M. A., Makarov D. S., Serov E. A., Parshin V. V. Resonator spectrometer for precise broadband investigations of atmospheric absorption in discrete

lines and water vapor related continuum in millimeter wave range. *Rev. Sci. Instrum*. 2009. Vol. 80, No. 9. Art. 093106.

[Tretyakov, 2010] Tretyakov M. Yu., Shkaev A. P., Kiselev A. M., Bodrov S. B., Andrianov A. V., Makarov D. S. Frequency stabilization of a primary subterahertz oscillator by a frequency comb of a femtosecond laser. *JETP Letters*. 2010. Vol. 91, No. 5. P. 222—225.

[Tretyakov, 2012] Tretyakov M. Yu., Serov E. A., Odintsova T. A. Equilibrium thermodynamic state of water vapor and the collisional interaction of molecules. *Radiophysics and Quantum Electronics*. 2012. Vol. 54. No. 10. P. 700—716.

[Tretyakov, 2013-1] Tretyakov M. Yu., Koshelev M. A., Vilkov I. N., Parshin V. V., Serov E. A. Resonator spectroscopy of the atmosphere in the 350–500 GHz range. *J. Quant. Spectrosc. Radiat. Transfer*. 2013. Vol. 114. P. 109—121.

[Tretyakov, 2013-2] Tretyakov M. Yu., Serov E. A., Koshelev M. A., Parshin V. V., Krupnov A. F. Observation of the rotationally resolved spectrum of the water dimer at room temperature. *Phys. Rev. Letters*. 2013. Vol. 110. Art. 093001.

[Tretyakov, 2014] Tretyakov M. Yu., Koshelev M. A., Serov E. A., Parshin V. V., Odintsova T. A., Bubnov G. M. Water dimer and the atmospheric continuum. *Physics – Uspekhi.* 2014 Vol. 57, No. 11. P. 1083—1098.

[Tretyakov, 2015] Tretyakov M. Yu., Sysoev A. A., Odintsova T. A., Kyuberis A. A. Collision-Induced dipole moment and millimeter and submillimeter continuum absorption in water vapor. *Radiophysics and Quantum Electronics.* 2015. Vol. 58, No. 4. P. 262—276.

[Tretyakov, 2016] *Tretyakov M. Y.* Spectroscopy underlying microwave remote sensing of atmospheric water vapor J. Mol. Spectrosc. 2016. Vol. 328. P. 7—26.

[Tretyakov, 2018] Tretyakov M. Yu., Zibarova A. O. On the problem of high-accuracy modeling of the dry air absorption spectrum in the millimeter wavelength range. *J Quant Spectrosc Radiat Transf.* 2018. Vol. 216. P. 70—75.

[Turner, 2009] Turner D. D., Cadeddu M. P., Löhnert U., Crewell S., Vogelmann A. M. Modifications to the water vapor continuum in the microwave suggested by ground-based 150-GHz observations. *IEEE Transactions on Geoscience and Remote Sensing*. 2009. Vol. 47, No. 10. P. 3326—3337.

[Tvorogov, 1995] Tvorogov S. D., Rodimova O. B. Spectral line shape. I. Kinetic equation for arbitrary frequency detunings. *J. Chem. Phys*. 1995. Vol. 102, No. 22. P. 8736—8745.

[Tyndall, 1861] Tyndall J. On the absorption and radiation of heat by gases and vapours and on the physical connexion of radiation, absorption and conduction. *Phil. Trans. R. Soc. Lond.* 1861. Vol. 151. P. 1–136.

[Vaida, 2000] Vaida V., Headrick J. E. Physicochemical properties of hydrated complexes in the Earth's atmosphere. *J. Phys. Chem. A*. 2000. Vol. 104, No. 23. P. 5401—5412.

[Valkenburg, 1966] Valkenburg E. P., Derr V. E. A high-Q Fabry–Perot interferometer for water vapor absorption measurements in the 100 Gcs to 300 Gcs frequency range. *Proc. IEEE*. 1966. Vol. 54, No. 4. P. 493—498.

[Van Vleck, 1934] Van Vleck J. H. Magnetic dipole radiation and the atmospheric absorption bands of oxygen. *The Astrophysical Journal*. 1934. Vol. 80, No. 5. P. 161—170.

[Van Vleck, 1945] Van Vleck J. H., Weisskopf V. F. On the shape of collision-broadened lines. *Revs. Modern Phys*. 1945. Vol. 17. P. 227—236.

[Van Vleck, 1947] Van Vleck J. H. The absorption of microwaves by oxygen. *Phys. Rev*. 1947. Vol. 71, No. 7. P. 413—424.

[Van Vleck, 1977] Van Wleck J. H., Huber D. L. Absorption, emission, and linebreadths: A semihistorical perspective. *Rev. Mod. Phys*. 1977. Vol. 49, No. 4. P. 939—959.

[Viktorova, 1966] Viktorova A. A., Zhevakon S. A. Absorption of microradiowaves in air by water dimers. *Proc. USSR Acad. Sci.* 1966. V. 171, No 5. P. 1061—1064. *(in Russian)*

[Viktorova, 1970] Viktorova A. A. Ratational spectrum of water dimer. *Proc. USSR Acad. Sci.*. 1970. V. 194, No 3. P. 540—543. *(in Russian)*

[Vigasin, 1983] Vigasin A. A., Chlenova G. V. Rotational spectrum of $(H_2O)_2$ at atmospheric conditions. *Izv. AN USSR. Physicsc of the atmosphere and ocean*. 1983. Vol. 19, No. 7. P 703—708. (*in Russian*).

[Vigasin, 1991] Vigasin A. A. Bound, metastable and free states of bimolecular complexes. *Infrared Phys.* 1991. Vol. 32. P. 461—470.

[Vigasin, 1996] Vigasin A. A. On the nature of collision-induced absorption in gaseous homonuclear diatomics. *J. Quant. Spectrosc. Radiat. Transfer*. 1996. Vol. 56. P. 409—422.

[Vigasin, 2003] Vigasin A. A. "Bimolecular absorption in atmospheric gases" in Weakly interacting molecular pairs: unconventional absorbers of radiation in the atmosphere. eds. Camy-Peyret C., Vigasin A. A.. 2003. Dordrecht: Kluwer Academic, P. 23—47.

[Vigasin, 2012] Vigasin A. A. On the concept of excluded volume for weakly associating gas. *Molecular Physics.* 2012. Vol. 110, No. 23. P. 2957—2961.

[Vigasin, 2014] Vigasin A. A. Water vapor continuum: Whether collision-induced absorption is involved? *J. Quant. Spectrosc. Radiat. Transfer*. 2014. Vol. 148. P. 58—64.

[Vlasov, 2010] Vlasov S. N., Parshin V. V., Serov E. A. Methods for investigating thin dielectric films in the millimeter range. *Technical Physics.* 2010, Vol. 55, No. 12. P. 1781—1787.

[Wagner, 2002] Wagner W., Pruss A. The IAPWS formulation 1995 for the thermodynamic properties of ordinary water substance for general and scientific use. *J. Phys. Chem. Ref. Data*. 2002. Vol. 31. P. 387—535.

[Wahlquist, 1961] Wahlquist H. Modulation broadening of unsaturated lorentzian lines. *J. Chem. Phys.* 1961. Vol. 35. Art. 1708.

[Waters, 2006] Waters J. W., Froidevaux L., Harwood R. S., Jarnot R. F., Pickett H. M., et al. The Earth observing system microwave limb sounder (EOS MLS) on the Aura satellite. *IEEE Transactions on Geoscience and Remote Sensing*. 2006. Vol. 44, No. 5. P. 1075—1092.

[Wentz, 2016] Wentz, F. J., Meissner T. Atmospheric absorption model for dry air and water vapor at microwave frequencies below 100 GHz derived from spaceborne radiometer observations. *Radio Sci*., 2016. Vol. 51. P. 381—391.

[West, 1966] West B. G., Mizushima M. Absorption spectrum of the oxygen molecule in the 55–65-Gcsec region. *Phys. Rev*. 1966. Vol. 143. P. 31.

[Westwater, 1990] Westwater E. R., Snider J. B., Falls M. J. Ground-based radiometric observations of atmospheric emission and attenuation at 20.6, 31.65, and 90.0 GHz: A comparison of measurements and theory. *IEEE Trans. Anten. Propag*. 1990. Vol. 38, No. 10. P. 1569—1580.

[White, 1942] White J. Long optical paths of large aperture. *J. Opt. Soc. Am*. 1942. Vol. 32, No. 5. P. 285—288.

[Wiener, 1930] Wiener N. Generalized harmonic analysis. *Acta Mathematica*. 1930. Vol. 55. P. 117—258.

[Winnewisser, 1997] Winnewisser G., Belov S. P., Klaus Th., Schieder R. Sub-Doppler measurements on the rotational transitions of carbon monoxide. *J. Mol. Spectrosc*. 1997. Vol. 184. P. 468—472.

[Winters, 1964] Winters B. H., Silvermans S., Benedicts W. S. Line shape in the wing beyond the band head of the 4.3 mkm band of CO_2. *J. Quant. Spectrosc. Radiat. Transfer*. 1964. Vol. 4. P. 527—537.

[Yasui, 2011] Yasui T., Takahashi H., Kawamoto K., Iwamoto Y., Arai K., Araki T., Inaba H., Minoshima K. Widely and continuously tunable terahertz synthesizer traceable to a microwave frequency standard. *Opt. Express*. 2011. Vol. 19, No. 5. P. 4428—4437.

[Young, 1999] Young B. C., Cruz F. C., Itano W. M., Bergquist J. C. Visible lasers with subhertz linewidths. *Phys. Rev. Lett*. 1999. Vol. 82. Art. 3799.

[Yu, 1982] Yu K., Cullen A. L. Measurement of permittivity by means of an open resonator. I. Theoretical. *Proc. R. Soc. London, Ser. A.* 1982. Vol. 380. P. 49—71.

[Yu, 2014] Yu S., Drouin B.J., Miller C.E. High resolution spectral analysis of oxygen. IV. Energy levels, partition sums, band constants, RKR potentials, Franck–Condon factors involving the $X^3\Sigma^-_g$, $a^1\Delta_g$ and $b^1\Sigma+_g$ states. *J. Chem. Phys.* 2014. Vol. 141. Art. 174302.

[Zhevakin, 1963] Zhevalin C. A., Naumov A. P. About absorption coefficient of electromagnetic waves by water vapour in the range 10 mkm – 2 cm. *Izv. VUZov. Radiofizika*. 1963. Vol. 6, No. 4. P. 674—694 (*in Russian*).

[Zhevakin, 1966] Zhevakin S. A., Naumov A. P. Absorption of 3 mm – 7.5 mm waves in the Earth's atmosphere. *Soviet Radiophysics*. 1966. Vol. 9. P. 271—281.

[Zimmerrer, 1961] Zimmerrer R. W., Mizushima M. Precise measurement of the microwave absorption frequencies of the oxygen molecule and the velocity of light. *Phys. Rev*. 1961. Vol. 121, No. 1. P. 152—155.

[Zobov, 2011] Zobov N. F., Shirin S. V., Lodi L., Silva B. C., Tennyson J., Csaszar A. G., Polyansky O. L. First-principles vibration-rotation spectrum of water above dissociation. *Chem. Phys. Lett*. 2011. Vol. 507. P. 48—51.